NUCLEAR REACTIONS OF ASTROPHYSICAL INTEREST

EDITED BY: Scilla Degl'Innocenti, Livio Lamia and Rosario Gianluca Pizzone
PUBLISHED IN: Frontiers in Astronomy and Space Sciences and Frontiers in Physics

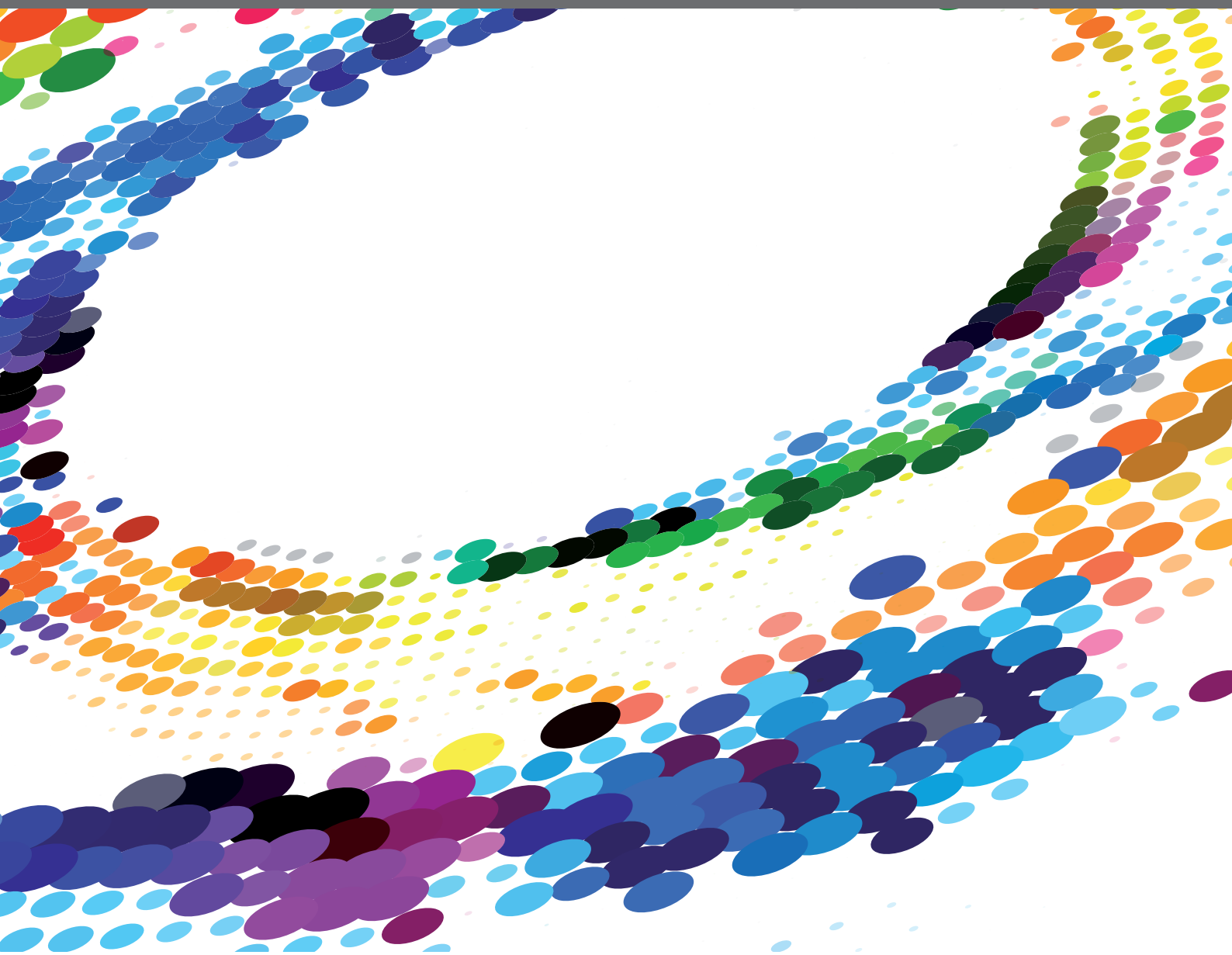

frontiers Research Topics

frontiers

ISSN 1664-8714
ISBN 978-2-88971-119-2
DOI 10.3389/978-2-88971-119-2

About Frontiers

Frontiers is more than just an open-access publisher of scholarly articles: it is a pioneering approach to the world of academia, radically improving the way scholarly research is managed. The grand vision of Frontiers is a world where all people have an equal opportunity to seek, share and generate knowledge. Frontiers provides immediate and permanent online open access to all its publications, but this alone is not enough to realize our grand goals.

Frontiers Journal Series

The Frontiers Journal Series is a multi-tier and interdisciplinary set of open-access, online journals, promising a paradigm shift from the current review, selection and dissemination processes in academic publishing. All Frontiers journals are driven by researchers for researchers; therefore, they constitute a service to the scholarly community. At the same time, the Frontiers Journal Series operates on a revolutionary invention, the tiered publishing system, initially addressing specific communities of scholars, and gradually climbing up to broader public understanding, thus serving the interests of the lay society, too.

Dedication to Quality

Each Frontiers article is a landmark of the highest quality, thanks to genuinely collaborative interactions between authors and review editors, who include some of the world's best academicians. Research must be certified by peers before entering a stream of knowledge that may eventually reach the public - and shape society; therefore, Frontiers only applies the most rigorous and unbiased reviews.
Frontiers revolutionizes research publishing by freely delivering the most outstanding research, evaluated with no bias from both the academic and social point of view. By applying the most advanced information technologies, Frontiers is catapulting scholarly publishing into a new generation.

What are Frontiers Research Topics?

Frontiers Research Topics are very popular trademarks of the Frontiers Journals Series: they are collections of at least ten articles, all centered on a particular subject. With their unique mix of varied contributions from Original Research to Review Articles, Frontiers Research Topics unify the most influential researchers, the latest key findings and historical advances in a hot research area! Find out more on how to host your own Frontiers Research Topic or contribute to one as an author by contacting the Frontiers Editorial Office: frontiersin.org/about/contact

NUCLEAR REACTIONS OF ASTROPHYSICAL INTEREST

Topic Editors:
Scilla Degl'Innocenti, University of Pisa, Italy
Livio Lamia, University of Catania, Italy
Rosario Gianluca Pizzone, Laboratori Nazionali del Sud (INFN), Italy

Citation: Degl'Innocenti, S., Lamia, L., Pizzone, R. G., eds. (2021). Nuclear Reactions of Astrophysical Interest. Lausanne: Frontiers Media SA.
doi: 10.3389/978-2-88971-119-2

Table of Contents

frontiers in Astronomy and Space Sciences

EDITORIAL
published: 10 June 2021
doi: 10.3389/fspas.2021.691596

Editorial: Nuclear Reactions of Astrophysical Interest

Scilla Degl'Innocenti[1]*, *Livio Lamia*[2,3,4] *and Rosario Gianluca Pizzone*[3]

[1]*Dipartimento di Fisica, Universitá di Pisa, Pisa, Italy,* [2]*Dipartimento Fisica e Astronomia "Ettore Majorana", Universitá degli Studi di Catania, Catania, Italy,* [3]*Laboratori Nazionali del Sud, INFN, Catania, Italy,* [4]*Centro Siciliano di Fisica Nucleare e Struttura della Materia-CSFNSM, Catania, Italy*

Keywords: reaction rates, stellar models, stellar nucleosynthesis, primordial nucleosynthesis, nuclear astrophysics

Editorial on the Research Topic

Nuclear Reactions of Astrophysical Interest

Several astrophysics theoretical predictions are strictly dependent on the availability of theoretical/experimental information about fusion cross sections at the energies of astrophysical interest; suffice to say that the development of stellar astrophysics during the first decades of the 20th century is mainly due to the insight that stars are powered by thermonuclear reactions.

The most of the elements present in the Universe are formed through nuclear fusions among charged nuclei and nuclear/neutron captures on nuclides in stellar cores; the fusion energies are well below the Coulomb barrier for reactions among charged particles. Moreover some reactions involve weak interactions with a consequent strong reduction of the reaction rate. Thus the measurement of cross sections at astrophysical interest is a challenge which requires the installation of the detectors underground to reduce the background due to cosmic rays and the development of "ad hoc" detection methods. Moreover suitable formalism for nuclear astrophysics calculations must be developed.

Thus nuclear astrophysics is an inter-disciplinary field which connects astrophysics (mainly stellar physics and cosmological nucleosynthesis) to experimental techniques of low energy cross section measurements and nuclear physics theory. In the last 2 decades the measurements/calculations of many cross sections of astrophysical interest have been greatly improved, however in several cases the still present uncertainties affect in a not negligible (or in some cases in a severe) way, the predictions for stellar characteristics and element nucleosynthesis.

This Research Topic summarizes the present situation for research fields in which the sinergy between nuclear physics and astrophysics is especially evident. In details it will cover the fundamental topics listed below:

- primordial nucleosynthesis: the formation of elements in the early Universe is explored in terms of its dependence on nuclear inputs. In particular the primordial lithium problem is addressed in terms of recent observations as well as an up-to-date compilation of nuclear reaction rates of interest arising from direct and indirect measurements;
- solar and stellar models: stellar models are investigated with a balanced focus on both massive and smaller mass stars. Their importance for nucleosynthesis is examined in details with big attention paid to the role of nuclear inputs in different phases of stellar evolution. Other important current issues are also addressed such as transport mechanisms, opacities, surface abundance patterns and measurements, etc. The role of stars in advanced evolutionary phases (Asymptotic Giant Branch) as source of presolar oxyde grains is discussed also in dependence

Edited by:
Michele Viviani, National Institute of Nuclear Physics of Pisa, Italy

Reviewed by:
Pierre Descouvemont, Université libre de Bruxelles, Belgium

***Correspondence:**
Scilla Degl'Innocenti
scilla.deglinnocenti@unipi.it

Specialty section:
This article was submitted to Nuclear Physics, a section of the journal Frontiers in Astronomy and Space Sciences

Received: *06 April 2021*
Accepted: *31 May 2021*
Published: *10 June 2021*

Citation:
Degl'Innocenti S, Lamia L and Pizzone RG (2021) Editorial: Nuclear Reactions of Astrophysical Interest. Front. Astron. Space Sci. 8:691596. doi: 10.3389/fspas.2021.691596

of relevant nuclear reaction rates. Solar models and solar neutrino production are also reviewed with special attention to recent developments.;

- the importance of light elements in nuclear astrophysics: light elements (Li, Be and B) play an important role in various stellar physics and cosmological problems. In this research topic the different aspects of the issue will be addressed from their cosmological importance to the role of Li, Be and B surface abundances in stars as possible trackers of internal mixings and other stellar processes. Particular attention will be devoted to the dependence of light element abundances on nuclear reaction rate measurements. The observational techniques and the results for surface light elements abundances in stars of different types and belonging to different Galactic populations will be also described.
- neutron mergers in binary systems emerged recently as a fundamental mechanism for nucleosynthesis of heavy elements in the Universe; in 2017 one of such systems was discovered for the first time by the LIGO-Virgo collaboration as souce of gravitational waves as well as the production place for r-process nucleosynthesis;
- direct and indirect measurements of nuclear cross sections at astrophysical energies are fundamental to model stellar structure and evolution since nuclear reaction rates determine the nucleosynthesis processes as well as the energy production in stars. Moreover also cosmological nucleosynthesis is affected by nuclear cross section values. The measurement of neutron or charged particle induced reactions at astrophysical energies is a very challenging task. To this purpose direct measurements must be performed underground (e.g., the LUNA facilities) and powerful indirect methods (e.g., Trojan Horse Method (THM), Asymptotic normalization Coefficient (ANC), Transfer reactions) are used as complementary tools to determine the reaction rates at energies far below the Coulomb barrier (in the case of charged particles interactions);
- theoretical methods for nuclear astrophysics provide the framework that allowed indirect methods to be developed and applied in experimental nuclear astrophysics. They are also a precious tool in the cases in which extrapolations are mandatory. A dedicated review will offer a bird-eye view of their achievements and applications in nuclear astrophysics.

The aim of the Research Topic is many-fold: 1) to made available to people who adopt theoretical stellar and/or nucleosynthesis models an evaluations of the still present theoretical uncertainties due to errors in nuclear cross sections. These uncertainties will be also compared to the ones due to the indetermination on other input quantities for models. 2) To summarize the "status of art" of the experimental measurements for nuclear cross sections relevant for stellar physics and primordial nucleosynthesis. 3) to focus on the synergic efforts driven by direct and indirect methods in nuclear astrophysics in order to measure cross sections of astrophysical interest at the Gamow energies. This is of great importance for reaction induced on stable nuclei (like the ones which are dealt with in this work) and is the only way for understanding explosive nucleosynthesis (mainly driven by reactions on unstable nuclei interacting with charged particles or neutrons). 4) To offer to astrophysicists a comprehensive view of experimental results and a description of recent outcomes for nuclear astrophysics open problems and vice-versa to offer to nuclear physicists a clear view of the demands of nuclear inputs for our understanding of the Universe.

We believe that the synergic efforts of the two communities as well as the building up of a *common foundation* for new generations of investigators will lead to a stronger nuclear astrophysical community which may be one of the keys to a better understanding of the physical processes taking place in the Universe.

AUTHOR CONTRIBUTIONS

SDI, LL and RP conceived the research topic together and wrote the present editorial synergically.

FUNDING

This work has been partially supported by INFN (Iniziativa specifica TAsP) and the Pisa University project PRA 2018/2019 "Le stelle come laboratori cosmici di fisica fondamentale".

ACKNOWLEDGMENTS

LL acknowledges the program "Starting Grant 2020" by University of Catania.

Conflict of Interest: The authors declare that the research was conducted in the absence of any commercial or financial relationships that could be construed as a potential conflict of interest.

frontiers in Astronomy and Space Sciences

REVIEW
published: 24 April 2020
doi: 10.3389/fspas.2020.00009

Nuclear Reactions of Astrophysical Interest

*Pierre Descouvemont**

Physique Nucléaire Théorique et Physique Mathématique, Université Libre de Bruxelles, Brussels, Belgium

We present different reaction models commonly used in nuclear astrophysics, in particular for the nucleosynthesis of the light elements. Nuclear reactions involved in stellar evolution generally occur at energies much lower than the Coulomb barrier. This property makes the cross sections extremely small, and virtually impossible to be measured in the laboratory. We start with a general discussion of low-energy scattering, and define the various cross sections required for reaction networks (essentially radiative capture and transfer reactions). Then we present specific models. Microscopic theories are based on fundamental principles, such as a nucleon-nucleon interaction, and an exact account of the antisymmetrization between all nucleons. In this context, most calculations performed so far have been done in the cluster approximation, but recent works, referred to as "*ab initio*" models, go beyond this approximation. Microscopic models can be simplified by neglecting the internal structure of the colliding nuclei, which leads to the potential model, also named the optical model. An alternative approach for the theoretical analysis of the experimental data is based on the phenomenological R-matrix theory, where parameters are fitted to the existing data, and then used to extrapolate the cross sections down to stellar energies. Indirect approaches, such as the Trojan Horse method, are briefly outlined. Finally, we present some typical applications of the different models.

Keywords: nuclear reactions, nuclear astrophysics, scattering models, capture reactions, transfer reactions, indirect methods

OPEN ACCESS

Edited by:
Rosario Gianluca Pizzone, Laboratori Nazionali del Sud (INFN), Italy

Reviewed by:
Stefan Typel, Technische Universität Darmstadt, Germany
Marco La Cognata, Laboratori Nazionali del Sud (INFN), Italy

***Correspondence:**
Pierre Descouvemont
pdesc@ulb.ac.be

Specialty section:
This article was submitted to Nuclear Physics, a section of the journal Frontiers in Astronomy and Space Sciences

Received: *16 January 2020*
Accepted: *10 March 2020*
Published: *24 April 2020*

Citation:
Descouvemont P (2020) Nuclear Reactions of Astrophysical Interest. Front. Astron. Space Sci. 7:9. doi: 10.3389/fspas.2020.00009

1. INTRODUCTION

Nuclear reactions are responsible for the nucleosynthesis, i.e., for the formation of the elements in the Universe (Bethe, 1939; Burbidge et al., 1957). Big-Bang nucleosynthesis mainly produces ^{2}H, ^{3}He, and α particles. This primordial nucleosynthesis is followed by the formation of early stars where elements up to Fe are produced. Heavier elements are then synthesized by various processes, such as neutron capture (Reifarth et al., 2018), neutrino-induced reactions (Alvarez-Ruso et al., 2018), explosive events in supernovae (Wiescher et al., 2012), and the rapid-neutron process in neutron-star mergers (Thielemann et al., 2017). Astrophysical scenarios and stellar models are discussed in many textbooks (see e.g., Clayton, 1983; Rolfs and Rodney, 1988; Iliadis, 2007; Thompson and Nunes, 2009) and review articles (see e.g., Aprahamian et al., 2005; José and Iliadis, 2011; Wiescher et al., 2012).

The role of nuclear physics in astrophysics is fundamental, and this discipline is referred to as nuclear astrophysics. It essentially started with the pioneering work of Bethe (1939). Later, the various cycles of stellar evolution were described in the seminal review by Burbidge et al., known as B^{2}FH (Burbidge et al., 1957). Many observational properties find their origin in nuclear physics. (i) A typical example is the 0_2^+ level of ^{12}C, known as the Hoyle state (Hoyle, 1954), which was predicted from the observed ^{12}C abundance in the Universe, and found

experimentally later. The formation of ^{12}C is currently well-understood from the triple α process. (ii) From the observed abundances of the elements, a gap between masses 5 and 8 is explained by the particle instability of ^{5}He and ^{5}Li. (iii) In the high-mass region of the abundance distribution, peaks are clearly observed, and are explained by the existence of magic numbers in nuclear physics. Magic nuclei are strongly bound, and therefore difficult to destroy by photodissociation. (iv) The abundance distribution also presents an "even-odd" effect, even nuclei being more abundant; again the origin of this effect stems from nuclear binding energies since odd-mass nuclei are less bound and therefore more fragile than even-mass nuclei. Recent reviews on nuclear astrophysics can be found in Bertulani and Kajino (2016) and Liccardo et al. (2018).

Stellar models require many nuclear inputs. A huge number (up to several thousands) of reaction rates, involving charged particles (protons and alphas) and neutrons, are needed in nucleosynthesis networks (Wiescher et al., 2012). Reactions involving charged particles are transfer and capture processes. The former stem from the nuclear force, and the latter from the electromagnetic interaction. When both channels are open, the transfer cross section is always much larger than the capture cross section. A challenge for nuclear physicists is to determine the cross sections at stellar energies, which are in general much lower than the Coulomb barrier. Except in a few cases, direct measurements in this low-energy range (referred to as the "Gamow peak") are not possible, since the cross sections are too low to be measured in the laboratory. Although experimental techniques have been strongly developed over the last decades (Broggini et al., 2010), a theoretical support is often necessary to complement the data, and in particular to extrapolate them down to stellar energies.

Owing to the experimental difficulties associated with direct measurements, several indirect techniques have been developed: the Trojan Horse method (Baur, 1986; Tumino et al., 2013; Spitaleri et al., 2019), the Coulomb breakup method (Baur et al., 1986), or the Asymptotic Normalization Coefficient method (ANC, see Mukhamedzhanov et al., 2001). The main advantage of these indirect approaches is to circumvent the smallness of the cross sections. However, they require a precise theoretical modeling to determine the relevant cross sections from the data.

The calculation of the cross sections is of course based on the scattering theory. Various models are being used in the literature. Owing to the low energies relevant in nuclear astrophysics, and to the low level densities, the optical model (also referred to as "potential model") can be used for capture reactions (Tombrello and Parker, 1963; Bertulani, 2003). Heavy-ion fusion reactions are also described by this model, even if different variants exist (Canto et al., 2006). Impressive developments have been performed in the framework of microscopic models, which present an important predictive power since they rely on a nucleon-nucleon interaction only. Solving a many-body Schrödinger equation for scattering states is however a difficult task, and the cluster approximation (Horiuchi et al., 2012) is used in most calculations. However, recent works succeeded to address, in a microscopic theory, the ^{2}H(d,γ)^{4}He (Arai et al., 2011), ^{3}He(d,p)^{4}He (Navrátil and Quaglioni, 2012), and ^{3}He(α,γ)^{7}Be (Neff, 2011; Dohet-Eraly et al., 2016) reactions without the cluster approximation. Recent progress has been made in Effective Field Theories (Zhang et al., 2018). These calculations are highly computer demanding, and are currently limited to low-mass systems.

The models discussed above are, in principle, independent of experimental data. In practice, however, available data are used to assess their reliability, and/or to tune some important parameter(s). In contrast, the phenomenological R-matrix theory (see for example Barker and Kajino, 1991; Descouvemont and Baye, 2010) explicitly relies on the existence of data, but is an efficient tool to analyse reactions of astrophysical interest. The cross sections can be parameterized by a small number of real, energy-independent, parameters. This fitting procedure requires the availability of experimental data, but in general allows a reliable extrapolation down to stellar energies. The R-matrix theory deals with capture, transfer and elastic scattering on an equal footing. In practice, however, the R-matrix theory is limited to reactions where the level density is limited (typically up to a few levels per MeV).

When the mass increases, the level density is in general too large for cluster models or for an R-matrix approach. In that situation, the cross section essentially depends on properties of the compound nucleus. Here the shell model (Richter et al., 2011) provides information on resonance properties, such as energies, spins, widths, etc. An extension to the continuum has been developed (Chatterjee et al., 2006). The Hauser-Feshbach formalism (Rauscher et al., 1997) is also widely used in high-mass systems, with a high level density.

A specificity of nuclear astrophysics is to require a large number of reaction rates. These reaction rates are obtained from various sources, experimental as well as theoretical. A link between nuclear physics and astrophysics can be established by compilations, where the authors provide an evaluation of the available data, and recommend reaction rates. The first compilations were performed by the Caltech group (Caughlan and Fowler, 1988), and then improved in various ways: evaluation of uncertainties, improved numerical treatment, update of experimental data, etc. Some compilations address specific reactions, such as Big-Bang nucleosynthesis (Descouvemont et al., 2004; Coc et al., 2012) or solar fusion reactions (Adelberger et al., 2011), but other works cover a wider range (Angulo et al., 1999; Longland et al., 2010).

In this review, we discuss the current status of reaction models in nuclear astrophysics. We focus on charged-particle induced reactions, which represent one of the main inputs in stellar evolution. In section 2, we present an overview of the different cross sections involved in the nucleosynthesis. In section 3 we briefly describe some theoretical models used for nuclear reactions. Applications are presented in section 4. The conclusion and outlook are presented in section 5.

2. CROSS SECTIONS FOR NUCLEAR ASTROPHYSICS

2.1. Scattering Wave Functions

In this section, we present an outline of the reaction theory needed for nuclear astrophysics. In particular, we are dealing

with low energies, around and below the Coulomb barrier. The goal is to model different processes, such as transfer or capture reactions. We start from a general formalism of scattering theory, and then apply it to different models. This outline is of course very brief, and we refer to textbooks (e.g., Satchler, 1983; Canto and Hussein, 2013) for a more detailed presentation.

The main goal of scattering models is to solve the Schrödinger equation

$$H\Psi = E\Psi \tag{1}$$

for positive energies E (this energy is defined from the reaction threshold). In this equation, H is the Hamiltonian, and Ψ is the nucleus-nucleus wave function. For the sake of simplicity we assume here that the internal structure of the colliding nuclei is neglected and that the spin of the target is zero. Consequently, the Hamiltonian only depends on the relative coordinate $\boldsymbol{r}$. For a system with charges (Z_1e, Z_2e) and nucleon numbers (A_1, A_2), it is written as

$$H = -\frac{\hbar^2}{2\mu m_N}\Delta_r + V_N(r) + V_C(r), \tag{2}$$

where, m_N is the nucleon mass and $\mu = A_1A_2/(A_1 + A_2)$ is the dimensionless reduced mass of the system. In Equation (2), $V_N(r)$ and $V_C(r)$ are the nuclear and Coulomb potentials, respectively. In general $V_N(r)$ depends on the angular momentum and on the spin. A partial wave with total spin J and angular momentum L is given by

$$\Psi_L^{JM}(\boldsymbol{r}) = \frac{1}{r}g_L^J(r)\big[Y_L(\Omega_r) \otimes \chi_s\big]^{JM}, \tag{3}$$

where the spinor χ_s is associated with the spin. In most cases, $s = 0$ or $s = 1/2$ (the latter case covers the frequent situation of nucleon scattering). The relative function $g_L^J(r)$ is given by the one-dimension Schrödinger equation

$$-\frac{\hbar^2}{2\mu m_N}\left(\frac{d^2}{dr^2} - \frac{L(L+1)}{r^2} + V_N(r) + V_C(r)\right)g_L^J(r) = Eg_L^J(r), \tag{4}$$

and must be solved for scattering states ($E > 0$) or for bound states ($E < 0$) with the corresponding boundary conditions. Efficient techniques are based on the Numerov algorithm (Raynal, 1972) or on the R-matrix method (Descouvemont and Baye, 2010).

At large distances, the nuclear potential V_N in (2) is negligible. For a scattering state, the radial wave function tends to

$$g_L^J(r) \xrightarrow[r\to\infty]{} I_L(kr) - U_L^J O_L(kr), \tag{5}$$

where $I_L(x)$ and $O_L(x)$ are the incoming and outgoing Coulomb functions (see section 2.2), and U_L^J is the scattering matrix (in single-channel calculations, it is a 1×1 matrix). The scattering matrix depends on the nuclear potential, and provides the elastic cross sections. For real potentials, usually used in astrophysics, we have the property

$$|U_L^J| = 1. \tag{6}$$

The phase shift δ_L^J is defined from

$$U_L^J = \exp(2i\delta_L^J), \tag{7}$$

and is real. At energies above the Coulomb barrier, complex potentials are often used. The imaginary part simulates absorption, and the model is referred to as the "optical model" (Satchler, 1983). In that case, we have

$$|U_L^J| \leq 1, \tag{8}$$

and the phase shift contains an imaginary part.

Generalizations can be performed in various directions. A first possibility is to extend the wave function (3) to multichannel calculations as

$$\Psi_L^{JM}(\boldsymbol{r}) = \frac{1}{r}\sum_{cLI} g_{cLI}^J(r)\left[Y_L(\Omega_r) \otimes \left[\phi_c^{I_1} \otimes \phi_c^{I_2}\right]^I\right]^{JM}, \tag{9}$$

where $\phi_c^{I_1}$ and $\phi_c^{I_2}$ are the internal wave functions with spins I_1 and I_2, and where I is the channel spin. Equation (4) is replaced by a system of coupled equations.

In Equations (3) and (9), antisymmetrization effects between the target and the projectile are neglected. However, they can be partly simulated by an appropriate choice of the nucleus-nucleus potential (Friedrich, 1981; Baye, 1987). A second generalization aims to explicitly include antisymmetrization effects. In microscopic cluster models (Descouvemont and Dufour, 2012), the wave function is defined as

$$\Psi_L^{JM} = \mathcal{A}\frac{1}{r}\sum_{cLI} g_{cLI}^J(r)\left[Y_L(\Omega_r) \otimes \left[\phi_c^{I_1}(\boldsymbol{\xi_1}) \otimes \phi_c^{I_2}(\boldsymbol{\xi_2})\right]^I\right]^{JM}, \tag{10}$$

where $\mathcal{A}$ is the A-nucleon antisymmetrization operator. The internal wave functions are defined in the shell model and depend on a set of internal coordinates ($\boldsymbol{\xi_i}$). We will briefly describe microscopic models in section 3.

2.2. General Properties of Low-Energy Reactions

Before discussing applications specific to nuclear astrophysics, we address here some general properties of the cross sections at low energies, typical of stellar conditions. In this energy regime, the scattering between charged particles is essentially governed by the Coulomb interaction. In other words, we can neglect the structure of the nuclei, and reduce the Schrödinger equation to a two-body problem. For a given angular momentum L, the wave function depends on the relative coordinate $\boldsymbol{r}$. The radial Schrödinger equation only involves the Coulomb potential and reads, at c.m. energy E,

$$-\frac{\hbar^2}{2\mu m_N}\left(\frac{d^2}{dr^2} - \frac{L(L+1)}{r^2}\right)g_L(r) + \frac{Z_1Z_2e^2}{r}g_L(r) = Eg_L(r), \tag{11}$$

where we have dropped index J. The solutions of Equation (11) are the regular and irregular Coulomb functions $F_L(\eta, kr)$ and

$G_L(\eta, kr)$ (Thompson, 2010). They depend on the wave number k, and on the Sommerfeld parameter η

$$k = \sqrt{\frac{2\mu m_N E}{\hbar^2}},$$
$$\eta = \frac{Z_1 Z_2 e^2}{\hbar v} \approx 0.158\, Z_1 Z_2 \sqrt{\frac{\mu}{E}}\ (E \text{ in MeV}), \qquad (12)$$

where $v = \hbar k/\mu m_N$ is the relative velocity.

From the Coulomb functions, one defines the incoming and outgoing functions as

$$I_L(\eta, x) = G_L(\eta, x) - iF_L(\eta, x),$$
$$O_L(\eta, x) = G_L(\eta, x) + iF_L(\eta, x). \qquad (13)$$

The penetration factor P_L and the shift factor S_L are obtained, at a radius a, from

$$P_L(E, a) = ka/[F_L^2(\eta, ka) + G_L^2(\eta, ka)]$$
$$S_L(E, a) = [F_L(\eta, ka)F'_L(\eta, ka) + G_L(\eta, ka)G'_L(\eta, ka)]\, P_L(E, a), \qquad (14)$$

where the prime denotes the derivative with respect to ka. The penetration factor can be approximately interpreted as the probability to cross the Coulomb barrier, and therefore strongly depends on energy (strictly speaking, however, P_L is not a probability since it may be larger than unity). Below the Coulomb barrier, it essentially depends on energy as

$$P_L(E, a) \sim \exp(-2\pi\eta). \qquad (15)$$

This term represents the main contribution to the energy dependence for $L = 0$. Higher-order corrections can be found in Clayton (1983) and Afanasjev et al. (2012). The penetration factor is illustrated in **Figure 1** for a light system p+^{12}C, and for an heavier system α+^{12}C. The Coulomb barriers are around 1.6 and 3.2 MeV, respectively. As expected, the centrifugal barrier reduces the penetration factor. This effect is stronger for light systems, where the reduced mass is small. Some dependence upon the radius a shows up, but is weak at very low energies.

The fast energy dependence (15) is common to all low-energy cross sections. For this reason, nuclear astrophysicists use the S factor

$$S(E) = \sigma(E)E\exp(2\pi\eta), \qquad (16)$$

which presents a smooth energy dependence for non-resonant reactions. It contains the nuclear information on the reaction.

Resonances play an important role in many reactions. Near a resonance energy E_R in a partial wave J_R, a cross section $\sigma(E)$ can be written at the Breit-Wigner approximation as

$$\sigma(E) \approx \frac{\pi}{k^2}\frac{2J_R+1}{(2I_1+1)(2I_2+1)}\frac{\Gamma_i(E)\Gamma_f(E)}{(E-E_R)^2+\Gamma(E)^2/4}, \qquad (17)$$

where Γ_i and Γ_f are the partial widths in the initial and final channels, Γ is the total width, and (I_1, I_2) are the spins of the colliding nuclei. This definition is valid for transfer as well as for capture reactions. In both cases, the entrance width $\Gamma_i(E)$ is a particle width, often a proton or an alpha width. Its energy dependence is given by

$$\Gamma_i(E) = \Gamma_i\frac{P_L(E, a)}{P_L(E_R, a)} = 2\gamma_i^2 P_L(E, a), \qquad (18)$$

where Γ_i is the width at energy E_R, and γ_i^2 is called the reduced width (Descouvemont and Baye, 2010). Notice that the energy variation slightly depends on the radius a. The Breit-Wigner approximation is a particular case of the more general R-matrix theory (Lane and Thomas, 1958; Descouvemont and Baye, 2010), where several resonances may overlap.

According to Equation (15), the width of a resonance gets very narrow when the energy decreases. The reduced width γ_i^2 reflects the cluster structure of the resonance (Descouvemont and Baye, 2010) and is defined even for bound states (in that case the total width is $\Gamma_i = 0$ since the penetration factor vanishes). It does not depend on energy. Consequently, even a state presenting a strong cluster structure may be characterized by a small total width

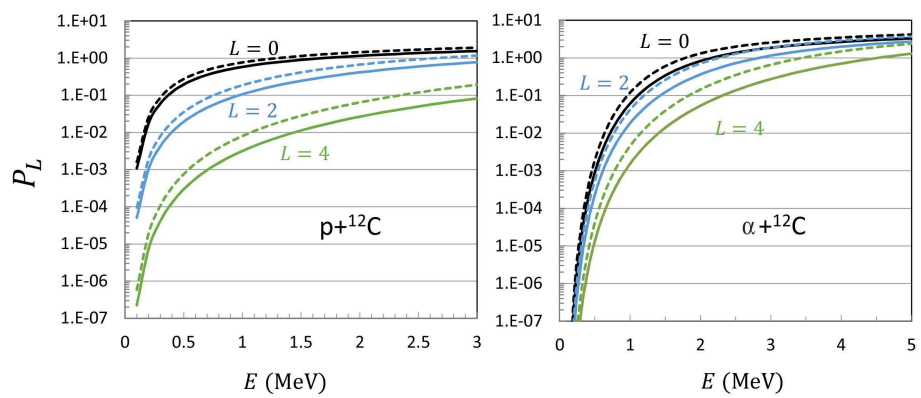

FIGURE 1 | Penetration factor (14) for the p+^{12}C **(left)** and α+^{12}C **(right)** systems. Solid and dashed lines correspond to $a = 5$ fm and $a = 6$ fm, respectively.

if it is located at low energies. As the entrance width depends on the penetration factor, the fast Coulomb dependence is also removed in the resonant S factor [Equation (16) with the cross section (17)].

In transfer reactions, $\Gamma_f(E)$ is also a particle width, and the previous discussion is still valid. Notice that, in general, the L values are different (see a discussion and examples in Descouvemont, 2003). However, the Q value must be taken into account as

$$\Gamma_f(E) = 2\gamma_f^2 P_L(E+Q,a) \tag{19}$$

where γ_f^2 is the reduced width of the resonance in the exit channel. If the threshold energy Q is large (typically a few MeV), the corresponding penetration factor presents a slow energy dependence, and the final width is approximated by a constant. This is not true in a few specific reactions, where the Q value is small (or even negative), and where the energy dependence of (19) is not negligible (an example is ^{17}O(α,n)^{20}Ne where Q = 0.586 MeV).

In capture reactions, the width of the exit channel Γ_f is the γ width. The energy dependence is given by the theory of electromagnetic transitions and reads

$$\Gamma_\gamma(E) = \Gamma_\gamma \left(\frac{E-E_f}{E_R-E_f} \right)^{2\lambda+1}, \tag{20}$$

where Γ_γ is the γ width at the resonance energy, λ is the order of the electromagnetic transition, and E_f the energy of the final nuclear state ($E_f < 0$). In general this energy dependence is rather weak, and can be neglected. Owing to the lower amplitude of the electromagnetic interaction compared to the nuclear force, γ widths are in general much lower than particle widths (in light nuclei $\Gamma_\gamma \lesssim 1$ eV).

The total width $\Gamma(E)$ in (17) is in general defined as the sum of the partial widths,

$$\Gamma(E) = \Gamma_i(E) + \Gamma_f(E). \tag{21}$$

If more than two channels are open, the total width should include all partial widths of the resonance.

2.3. Radiative-Capture Reactions

Radiative-capture reactions play an important role in the nucleosynthesis (Iliadis, 2007). They can be seen as a transition from an initial scattering state to a final bound state of the system. This process arises from the electromagnetic interaction, and can therefore be treated in the perturbation theory (Rose and Brink, 1967). If H_e is the photon-emission Hamiltonian for the nuclear system, the capture cross section to a final state with spin J_f and parity π_f is given by

$$\frac{d\sigma_c}{d\Omega_\gamma}(E,J_f\pi_f) = \frac{k_\gamma}{2\pi\hbar}\frac{1}{(2I_1+1)(2I_2+1)} \times \sum_{q\nu_1\nu_2 M_f} |\langle \Psi^{J_f M_f \pi_f} | H_e(q,\Omega_\gamma) | \Psi^{\nu_1\nu_2}\rangle|^2, \tag{22}$$

where Ω_γ is the photon angle, $q = \pm 1$ is the photon polarization, and $\Psi^{J_f M_f \pi_f}$ the final-state wave function. Here ν_1 and ν_2 are the spin projections of the colliding nuclei.

To compute the cross section, the initial wave function $\Psi^{\nu_1\nu_2}$ is expanded in partial waves, and the electromagnetic operator is expanded in multipoles $\mathcal{M}^\sigma_{\lambda\mu}$ (Rose and Brink, 1967). At the long wavelength approximation, the electric ($\sigma = E$) and magnetic ($\sigma = M$) multipole operators are given by

$$\mathcal{M}^E_{\lambda\mu} = e\sum_i^A g_\ell(i)\, r_i^\lambda Y^\mu_\lambda(\Omega_{r_i}),$$
$$\mathcal{M}^M_{\lambda\mu} = \mu_N \sum_i^A \left[\frac{2}{\lambda+1} g_\ell(i) \boldsymbol{\ell}_i + g_s(i)\boldsymbol{s}_i \right] \cdot \boldsymbol{\nabla} r_i^\lambda Y^\mu_\lambda(\Omega_{r_i}), \tag{23}$$

with

$$g_\ell(i) = 1/2 - t_{iz},$$
$$g_s(i) = g_p(1/2 - t_{iz}) + g_n(1/2 + t_{iz}), \tag{24}$$

where t_{iz} is the isospin projection of nucleon i, and g_p, g_n are the gyromagnetic factors of the proton ($g_p = 5.586$) and of the neutron ($g_n = -3.826$) ($\mu_N = e\hbar/m_N c$ is the nuclear magneton). Equations (23) are written in the framework of a microscopic approach. Simplified expressions, valid for two-particle systems can be found (e.g., in Bertulani, 2003; Descouvemont, 2003). After integration over the photon angle Ω_γ, the total cross section is given by

$$\sigma_c(E,J_f\pi_f) = \frac{2J_f+1}{(2I_1+1)(2I_2+1)}\frac{8\pi}{\hbar} \times \sum_{\sigma\lambda J_i L_\omega L_\omega} \frac{k_\gamma^{2\lambda+1}}{2L_\omega+1}\frac{(\lambda+1)}{\lambda(2\lambda+1)!!^2} |\langle \Psi^{J_f\pi_f} || \mathcal{M}^\sigma_\lambda || \Psi^{J_i\pi_i}_{L_\omega I_\omega}(E)\rangle|^2, \tag{25}$$

where J_i and π_i are the spin and parity in the entrance channel, and where L_ω and I_ω are the channel spin and the orbital momentum. The summations in (25) are limited by the usual selection rules

$$|J_i - J_f| \le \lambda \le J_i + J_f,$$
$$\pi_i\pi_f = (-)^\lambda \text{ (for } \sigma = E),$$
$$\pi_i\pi_f = (-)^{\lambda+1} \text{ (for } \sigma = M). \tag{26}$$

In addition, the long-wavelength approximation ($k_\gamma R \ll 1$, where R is a typical dimension of the system) strongly reduces the summation over λ. In many cases, a single multipole is important.

As in the previous subsection we only give the integrated cross section, where no interference between multipoles and partial waves shows up. In contrast, the differential cross section (22) involves interference terms (see more detail in Descouvemont, 2003).

2.4. Transfer Reactions

In a transfer reaction (also denoted as "rearrangement reaction"), some nucleons are exchanged between the target and the projectile. A typical example in astrophysics is the ^{13}C(α,n)^{16}O reaction, where two protons and one neutron are stripped from the α particle to ^{13}C, to produce ^{16}O. Transfer processes arise from the nuclear interaction and the corresponding cross sections are usually much larger than the capture cross sections, arising from the electromagnetic interaction. For example, the ^{13}C(α,n)^{16}O cross section is larger by several order of magnitude than the ^{13}C(α,γ)^{17}O cross section.

If $\Omega = (\theta,\phi)$ is the relative direction of the nuclei in the final channel, the transfer cross section (Descouvemont and Baye, 2010) is given by

$$\frac{d\sigma_t}{d\Omega}(E,i\to f) = \frac{\pi}{k^2}\frac{1}{(2I_1+1)(2I_2+1)}\sum_j A_j(E)\,P_j(\cos\theta), \quad (27)$$

where the anisotropy coefficients $A_j(E)$ are defined as

$$A_j(E) = \frac{1}{4\pi}\sum_{J\pi\ell LI}\sum_{J'\pi'\ell'L'I'}(-)^{I-I'}Z(j,J,J',\ell,L,I)\,Z(j,J,J',\ell',L',I') \\ U^{J\pi}_{i\ell I,f\ell' I'}(E)\,U^{J'\pi'*}_{iLI,fL'I'}(E). \quad (28)$$

and $\boldsymbol{U}^{J\pi}$ represents the collision matrix generalized to multichannel systems. Coefficients Z are defined as

$$Z(j,J,J',\ell,L,I) = [(2J+1)(2J'+1)(2\ell+1)(2L+1)]^{1/2} \\ <\ell\,0\,L\,0|j\,0>\begin{Bmatrix}\ell & L & j\\ J' & J & I\end{Bmatrix}. \quad (29)$$

Again, definition (27) is model independent. The choice of the model only affects the collision matrix. As for radiative capture, the important quantity in astrophysics is the integrated cross section

$$\sigma_t(E,i\to f) = \frac{\pi}{k^2}\sum_{J\pi}\frac{2J+1}{(2I_1+1)(2I_2+1)}\sum_{LL'II'}|U^{J\pi}_{iLI,fL'I'}(E)|^2. \quad (30)$$

The discussion of subsection 2.3 remains valid: in general a few terms are important in (30), since only low L values contribute at energies below the Coulomb barrier.

2.5. Fusion Reactions

A number of nuclear reactions that occur in stars are fusion reactions, involving light to medium-mass nuclei. Important examples are the carbon and oxygen burning processes in massive stars. The angular momentum and energy-dependent transmission coefficient $T_f(L,E)$ is then used in the cross section formula to obtain the fusion cross section σ_f

$$\sigma_f(E) = \frac{\pi}{k^2}(1+\delta_{12})\sum_L(2L+1)T_f(L,E), \quad (31)$$

where $\delta_{12} = 1$ for symmetric systems and 0 otherwise. For symmetric systems the sum runs over even L values only.

Within an optical model approach to fusion (in that case, $|U^J_L| < 1$), the transmission coefficient is given by

$$T_f(L,E) = 1 - |U^J_L|^2. \quad (32)$$

However, at very low energies, $U^J_L \approx 1$, and this technique is not accurate. From the continuity equation, the transmission coefficient (32) is strictly equivalent to

$$T_f(L,E) = -\frac{2}{\hbar v}\int |g_L(r)|^2 W(r)dr, \quad (33)$$

where $W(r)$ is the imaginary part of the optical potential that represents absorption due to fusion, and $g_L(r)$ is the exact (single-channel) wave function (Hussein, 1984; Canto et al., 2006).

2.6. Weak-Capture Cross Sections

For low-mass stars, the nucleosynthesis is initiated by the p(p,$e^+\nu$)d reaction, which occurs through the weak interaction. Since the corresponding Hamiltonian is much smaller than the nuclear and electromagnetic Hamiltonians, the cross section is very small. Estimates in optimal experimental conditions (Rolfs and Rodney, 1988) predict one event per 10^6 years! Fortunately, theoretical models are quite accurate (Kamionkowski and Bahcall, 1994; Marcucci et al., 2013). The cross section is shown to be proportional to

$$\sigma_{pp}(E) \sim |<\Psi^{1^+}_d||\mathcal{M}_F + \lambda^2\mathcal{M}_{GT}||\Psi_{pp}(E)>|^2, \quad (34)$$

where $\Psi^{1^+}_d$ is the deuteron wave function, $\Psi_{pp}(E)$ is the $p-p$ scattering wave function and $\mathcal{M}_F$ and $\mathcal{M}_{GT}$ are the Fermi and Gamow-Teller operators, respectively. In (34), λ^2 is the ratio of axial-vector to vector coupling constants. A recent calculation (Gaspard et al., 2019) provides $S(0) \approx 3.95\times10^{-25}$ MeV-b, which is considerably lower than values obtained for capture or transfer reactions.

3. REACTION MODELS IN NUCLEAR ASTROPHYSICS

3.1. Microscopic Models

Microscopic models are based on fundamental principles of quantum mechanics, such as the treatment of all nucleons, with exact antisymmetrization of the wave functions. Neglecting three-body forces, the Hamiltonian of a A-nucleon system is written as

$$H = \sum_{i=1}^{A} T_i + \sum_{i<j=1}^{A} V_{ij}, \quad (35)$$

where T_i is the kinetic energy and V_{ij} a nucleon-nucleon interaction (Wildermuth and Tang, 1977).

The Schrödinger equation associated with this Hamiltonian cannot be solved exactly when $A > 3$. For very light systems ($A \sim 4-5$) efficient methods (Kievsky et al., 2008) exist, even for continuum states (Navrátil et al., 2010). However, most

reactions relevant in nuclear astrophysics involve heavier nuclei, essentially with nucleon or α projectiles. Recent developments of *ab initio* models (see e.g., Caurier and Navrátil, 2006; Navrátil and Quaglioni, 2011) are quite successful for spectroscopic properties of low-lying states. These models make use of realistic interactions, including three-body forces, and fitted on many properties of the nucleon-nucleon system. Recent works succeeded in applying *ab initio* calculations to nuclear astrophysics (see e.g., Arai et al., 2011; Neff, 2011; Dohet-Eraly et al., 2016; Marcucci, 2018). However, a consistent description of bound and scattering states of an A-body problem remains a challenging task (Navrátil et al., 2010), in particular for transfer reactions.

In the cluster approximation, it is assumed that the nucleons are grouped in clusters (Wildermuth and Tang, 1977; Descouvemont and Dufour, 2012). The internal wave functions of the clusters are denoted as $\phi_i^{I_i\pi_i\nu_i}(\boldsymbol{\xi_i})$, where I_i and π_i are the spin and parity of cluster i, and $\boldsymbol{\xi_i}$ represents a set of their internal coordinates. In a two-cluster system, a channel function is defined as

$$\varphi_{LI}^{JM\pi}(\Omega_r,\boldsymbol{\xi_1},\boldsymbol{\xi_2}) = \left[Y_L(\Omega_r)\otimes[\phi_1^{I_1\pi_1}(\boldsymbol{\xi_1})\otimes\phi_2^{I_2\pi_2}(\boldsymbol{\xi_2})]^I\right]^{JM}, \quad (36)$$

where different quantum numbers show up: the channel spin I, the relative angular momentum L, the total spin J and the total parity $\pi = \pi_1\pi_2(-)^L$.

As discussed in section 2.1, the total wave function of the A-nucleon system is written, in a microscopic cluster model, as

$$\Psi^{JM\pi} = \sum_{cLI}\Psi_{cLI}^{JM\pi} = \sum_{cLI}\mathcal{A}\,g_{cLI}^{J\pi}(r)\,\varphi_{cLI}^{JM\pi}(\Omega_r,\boldsymbol{\xi_1},\boldsymbol{\xi_2}), \quad (37)$$

which corresponds to the Resonating Group (RGM) definition (Horiuchi, 1977; Descouvemont and Dufour, 2012). Index c refers to different two-cluster arrangements, and $\mathcal{A}$ is the antisymmetrization operator. In most applications, the internal cluster wave functions $\phi_i^{I_i\pi_i\nu_i}$ are defined in the shell model. Accordingly, the nucleon-nucleon interaction must be adapted to this choice, which leads to effective forces, such as the Volkov (Volkov, 1965) or the Minnesota (Thompson et al., 1977) interactions. The relative wave functions $g_{cLI}^{J\pi}(r)$ are to be determined from the Schrödinger equation, which is transformed into a integro-differential equation involving a non-local potential (Horiuchi, 1977). In practice, this relative function is expanded over Gaussian functions (Wildermuth and Tang, 1977; Dufour and Descouvemont, 2011), which corresponds to the Generator Coordinate Method (GCM). The numerical calculations can be made systematic with the GCM, which is not the case for the RGM.

The main advantage of cluster models with respect to other microscopic theories is their ability to deal with reactions, as well as with nuclear spectroscopy. The first applications were done for reactions involving light nuclei, such as d, ^{3}He or α particles (Liu et al., 1981; Hofmann and Hale, 1997). More recently, much work has been devoted to the improvement of the internal wave functions: multicluster descriptions (Descouvemont and Baye, 1994), large-basis shell model extensions (Descouvemont, 1996), or monopolar distortion (Baye and Kruglanski, 1992).

3.2. The Potential Model

Solving the Schrödinger equation associated with a many-body system is a difficult problem, which does not have an exact solution when the nucleon number is larger than three. The potential model is fairly simple to use, and has been applied to several reactions in low-energy nuclear physics (Tombrello, 1965; Bertulani, 2003). The basic assumptions of the potential model are: (i) the nucleon-nucleon interaction is replaced by a nucleus-nucleus force $V(r)$, which depends on the relative coordinate r only; (ii) the wave functions of the unified nucleus can be described by a cluster structure with $A_1 + A_2$ nucleons; (iii) the internal structure of the nuclei does not play any role. Since we are dealing with low energies, the potential is in general real. The extension to higher energies, which requires complex potentials to simulate absorption channels, is known as the optical model. A generalization to coupled-channel problems is also possible, but seldom used in nuclear astrophysics.

The radial function $g_L^{J\pi}(r)$ for bound and scattering states is deduced from Equation (4). According to the application, the choice of the nuclear contribution is guided by experimental constraints. In radiative-capture calculations it is crucial to reproduce the final-state energy. If phase shifts are available, they can be used to determine the initial potential.

Besides experimental constraints, the nucleus-nucleus potential must follow requirements arising from microscopic arguments (Kukulin et al., 1983; Baye and Descouvemont, 1985). In the microscopic wave function (37), it can be shown that, under some assumptions, there are non-vanishing radial functions $g_{cLI}^{J\pi}(r)$ which yield $\Psi_{cLI}^{JM\pi} = 0$ after application of the antisymmetrization operator $\mathcal{A}$. These radial functions are called "forbidden states," and their number depends on the system and on the angular momentum. To illustrate the problem, let us consider the α+p system where the α particle is described in the shell model. Since the s-shell is filled by the α orbitals, the external proton cannot occupy this s-shell state, which corresponds to a forbidden state. We refer the reader to Buck et al. (1977), Kukulin et al. (1983), and Baye and Descouvemont (1985) for more information. The occurrence of forbidden states can be simulated by an adequate choice of the potential. According to Buck et al. (1977), the potential must contain a number of bound states n_r, equal to the number of forbidden states. This prescription leads to deep potentials, since they involve additional (unphysical) bound states. The calculation of n_r is in general not obvious, except for nucleus-nucleon systems.

In this simple model, the capture cross sections are deduced from integrals involving scattering functions $g_{L_iI}^{J_i\pi_i}(r)$ at energy E, and bound-state wave functions $g_{L_fI}^{J_f\pi_f}(r)$

$$I_{if}^{\lambda}(E) = \int g_{L_i}^{J_i\pi_i}(E,r)r^{\lambda}g_{L_f}^{J_f\pi_f}(r)dr. \quad (38)$$

We refer to Bertulani (2003) for more detail.

The main advantage of the potential model is its simplicity. However, it assumes from the very beginning that the final bound state presents the two-body structure of the entrance channel. This is also true for resonances, which must be described by

the adopted nucleus-nucleus structure. This hypothesis is not always valid. In the $^{16}O(\alpha,\gamma)^{20}Ne$ reaction for example, the 0_1^+ ground state and the 0_4^+ broad resonance are well described by an $\alpha+^{16}O$ structure, but the 0_2^+ and 0_3^+ resonances would require other configurations, such as $\alpha+^{16}O^*$ or $p+^{19}F$. This problem is more and more frequent as the level density increases. Another well-known example is the $^{15}O(\alpha,\gamma)^{19}Ne$ reaction where most of the ^{19}Ne low-lying states can be accurately reproduced by an $\alpha+^{15}O$ structure, but where the resonance important for astrophysics ($3/2^+$ at $E_{c.m.} = 0.50$ MeV) most likely presents another structure (Dufour and Descouvemont, 2000).

3.3. The Phenomenological *R*-Matrix Method

The *R*-matrix method is well-known in atomic and nuclear physics (Descouvemont and Baye, 2010). The basic idea is to divide the space in two regions: the internal region (with radius a), where the nuclear force is important, and the external region, where the interaction between the nuclei is governed by the Coulomb force only. Although the *R*-matrix parameters do depend on the channel radius a, the sensitivity of the cross section with respect to its choice is quite weak. In the *R*-matrix method, the energy dependence of the cross sections is obtained from Coulomb functions, as expected from the Schrödinger equation.

In the phenomenological variant of the *R*-matrix method, the physics of the internal region is determined by a number N of poles, which are characterized by their energies E_λ and reduced widths $\gamma_{\lambda i}$. In a multichannel problem, the *R*-matrix at energy E is defined as

$$R_{ij}(E) = \sum_{\lambda=1}^{N} \frac{\gamma_{\lambda i}\gamma_{\lambda f}}{E_\lambda - E}, \tag{39}$$

which must be determined for each partial wave $J\pi$ (not written for the sake of clarity). Indices i and f refer to the initial and final channels. The pole properties are associated with the physical energy and width of resonances, but not strictly equal. This is known as the difference between "formal" and "observed" parameters, deduced from experiment.

The scattering matrices, and therefore the cross sections, are directly determined from the R matrices in the different partial waves (see Lane and Thomas, 1958; Descouvemont and Baye, 2010 for detail). When a single-channel is involved ($i = f = 1$), the scattering matrix is written as

$$U = \frac{I(ka)}{O(ka)} \frac{1-(S-iP)R}{1-(S+iP)R}, \tag{40}$$

where $P(E)$ and $S(E)$ are the penetration and shift factors, respectively. In that case, the *R*-matrix has a dimension 1×1. This definition can be easily extended to multichannel calculations (Descouvemont and Baye, 2010). The phase shift is defined by

$$U = \exp(2i\delta) = \exp(2i(\delta_{\rm HS} + \delta_{\rm R})), \tag{41}$$

where δ_{HS} is the hard-sphere phase shift which is obtained with $R = 0$, and therefore with $\gamma_{\lambda i} = 0$. The hard-sphere and *R*-matrix phase shifts are obtained from

$$\delta_{\rm HS} = -\arctan\frac{F(ka)}{G(ka)},$$
$$\delta_{\rm R} = \arctan\frac{PR}{1-SR}. \tag{42}$$

Let us discuss the calculation of resonance properties. The pole energies E_λ and reduced widths γ_λ (see Equation 39) are associated with the poles of the *R*-matrix, and therefore depend on the conditions of the calculation, such as the radius a. In a single-channel problem, the resonance energies E_i^r, also referred to as the "observed" energies, are defined as the energies where the *R*-matrix phase shift is $\delta_R = \pi/2$. According to (42), $E_i^{\rm r}$ are therefore solutions of the equation

$$S(E_i^{\rm r})R(E_i^{\rm r}) = 1. \tag{43}$$

On the other hand, the "observed" width enters the Breit-Wigner parameterization near the resonance energy

$$\delta_{\rm R}(E) \approx \arctan\frac{\Gamma_i(E)}{2(E_i^{\rm r}-E)}, \tag{44}$$

which gives, by using (42)

$$\Gamma_i(E) = 2P(E)\frac{R(E_i^{\rm r})}{\left[S(E)R(E)\right]'_{E=E_i^{\rm r}}} = 2P(E)\,\tilde{\gamma}_i^2, \tag{45}$$

and defines $\tilde{\gamma}_i^2$ as the "*observed*" reduced width of the resonance. We also have

$$\Gamma_i(E) = \Gamma_i\frac{P(E)}{P(E_i^{\rm r})}, \tag{46}$$

where Γ_i is the width calculated at the resonance energy.

If the pole number N is larger than unity, or in multichannel calculations, the definition of $E_i^{\rm r}$ and of $\tilde{\gamma}_i^2$ is not analytical and requires numerical calculations (Angulo and Descouvemont, 2000; Brune, 2002). We illustrate here a simple but frequent situation of a single-channel calculation with $N = 1$. The phase shift (42) is

$$\delta_{\rm R}(E) = \arctan\frac{\Gamma_1(E)}{2(E_1 - E - \gamma_1^2 S(E))}, \tag{47}$$

which is equivalent to (44) if we set

$$E_1^{\rm r} = E_1 - \tilde{\gamma}_1^2 S(E_1^{\rm r})$$
$$\tilde{\gamma}_1^2 = \gamma_1^2/\left(1+\gamma_1^2\,S'(E_1^{\rm r})\right), \tag{48}$$

where $S'(E) = dS/dE$. These formulas provide a simple link between calculated and observed values. To derive (48) we have used the Thomas approximation where the shift factor is linearized near $E_1^{\rm r}$ as

$$S(E) \approx S(E_1^{\rm r}) + (E - E_1^{\rm r})S'(E_1^{\rm r}). \tag{49}$$

This approximation is in general quite accurate. The term $\tilde{\gamma}_1^2 S'(E_1^{\rm r})$ is called the shift factor; it is proportional to the reduced width and is therefore large for strongly deformed states. With Equation (48), the fitting procedure can be used from the observed parameters. It presents important simplifications when some of the parameters (such as bound-state or resonance energies) are known from experiment, and therefore should be constant during the fit.

The phenomenological R-matrix method can be applied to transfer as well as to capture reactions. It is usually used to investigate resonant reactions but is also suited to describe non-resonant processes. In the latter case, the non-resonant behavior is simulated by a high-energy pole, referred to as the background contribution, which makes the R-matrix nearly energy independent. In nuclear astrophysics, a famous application is the $^{12}C(\alpha,\gamma)^{16}O$ reaction. Experimental cross sections are available down to $E \approx 1$ MeV, whereas the relevant stellar energy is close to 0.3 MeV. The R-matrix parameters are fitted to the available data, and then used to extrapolate the cross section to stellar energies (see a review in deBoer et al., 2017).

3.4. Indirect Methods

The main problem of nuclear astrophysics is the smallness of the cross sections at stellar energies. Further, in some reactions the availability of the required beam at the right energy may be difficult to obtain. These issues spurred interest in devising indirect methods (Tribble et al., 2014; Mukhamedzhanov and Rogachev, 2017), whereby the induced desired reaction is extracted from another reaction. We give below a brief overview of some indirect methods.

3.4.1. The Trojan Horse Method

The basic idea behind the Trojan Horse Method (Baur, 1986; Typel and Baur, 2003; Tumino et al., 2013; Spitaleri et al., 2019) is to use the three-body reaction,

$$a + A \rightarrow b + (x + A) \rightarrow b + (c + C), \tag{50}$$

to extract the cross section of the desired $x+A \rightarrow c+C$ two-body reaction. In the entrance channel, nucleus a presents a cluster structure $a = b + x$, and cluster x is transferred to the target A. In this process, cluster b acts as a spectator.

Using the Plane Wave Impulse Approximation and the spectator model (Typel and Baur, 2003), the cross section of process (50) is factorized as

$$\frac{d^3\sigma}{dE_c d\Omega_c d\Omega_C} = K \left(\frac{d\sigma}{d\Omega}\right)_{\rm off} |\Phi(\boldsymbol{k}_{xb})|^2, \tag{51}$$

where K is a kinematic factor. In this equation, $\left(\frac{d\sigma}{d\Omega}\right)_{\rm off}$ is the half-off-energy-shell differential cross section for the two-body reaction, $x + A \rightarrow c + C$, and $\Phi(\boldsymbol{k}_{xb})$ is the Fourier transform of the ground state wave function of nucleus $a(= b + x)$.

The main advantage of the Trojan Horse Method is that the cross section (51) is not affected by Coulomb effects, and is therefore more accessible than cross sections of astrophysical interest. Dividing it by a calculated $K|\Phi(\boldsymbol{k}_{xb})|^2$ provides the desired cross section $\left(\frac{d\sigma}{d\Omega}\right)_{\rm off}$. We refer the reader to Tribble et al. (2014) and Spitaleri et al. (2019) for recent reviews. The Trojan Horse Method has been applied to many reactions (see a review in Tumino et al., 2013). A recent example is the measurement of the ^{2}H(d,p)^{3}H and ^{2}H(d,n)^{3}He cross sections from 2 keV to 1.5 MeV (Tumino et al., 2011). An ^{3}He beam was used to measure the three-body ^{2}H(^{3}He,p^{3}H)^{1}H and ^{2}H(^{3}He,n^{3}He)^{1}H cross sections. Here nucleus a is ^{3}He=d+p, and the deuteron cluster (x in our notations) is transferred to the target. This approach provides ^{2}H(d,p)^{3}H and ^{2}H(d,n)^{3}He cross sections free of electron screening effects.

3.4.2. Coulomb Dissociation

The Coulomb breakup method (Baur et al., 1986, 2001) has been suggested in experiments using radioactive beams to address the problem of small cross sections. The photodissociation reaction

$$c + \gamma \rightarrow a + b \tag{52}$$

represents the reverse process of the capture reaction

$$a + b \rightarrow c + \gamma, \tag{53}$$

and their cross sections σ_d and σ_c are related by the balance theorem

$$\sigma_d(E) = \frac{(2I_a+1)(2I_b+1)}{2(2I_c+1)} \frac{k^2}{k_\gamma^2} \sigma_c(E), \tag{54}$$

where I_i represents the spin of nucleus i In most applications, the photon wavelength k_γ is much larger than the particle wavelength k, which means that

$$\frac{k^2}{k_\gamma^2} \gg 1, \tag{55}$$

and σ_d is significantly larger than σ_c. This method is therefore a good way to compensate the smallness of capture cross sections at low energies. It is, however, limited to capture reactions toward the ground state of nucleus c.

The ^{6}Li$\rightarrow\alpha$+d breakup reaction was used to assess the method (Kiener et al., 1991), and reinvestigated recently (Hammache et al., 2010). Coulomb breakup has also been used with radioactive beams, to investigate reactions, such as ^{14}O$\rightarrow^{13}$N+p (Motobayashi et al., 1991; Kiener et al., 1993) or ^{8}B$\rightarrow^7$Be+p (Motobayashi et al., 1994; Kikuchi et al., 1998; Schümann et al., 2006). The importance of the nuclear interaction on the Coulomb dissociation has been discussed, for example, in Kumar and Bonaccorso (2012).

3.4.3. The Asymptotic Normalization Coefficient (ANC) Method

At large distances, the radial wave function for bound states tends to a Whittaker function (Abramowitz and Stegun, 1972); we have

$$g_L^{J\pi}(r) \xrightarrow[r\rightarrow\infty]{} C_L^{J\pi} W_{-\eta,L+1/2}(2k_B r), \tag{56}$$

where $C_L^{J\pi}$ is the so-called "asymptotic normalization coefficient" (ANC). For weakly bound states, the exponential decrease is slow, and the main contribution to the electromagnetic matrix elements arises from large distances. The capture cross section is then essentially determined by the ANC. A typical example is the ^{7}Be(p,γ)^{8}B reaction, where the ^{8}B ground state is bound by 137 keV only. Of course, this is true at very low energies only (typically $\leq$ 100 keV); for higher energies, the inner part of the wave function and, consequently, the nuclear interaction play a role.

When the external-capture approximation is valid, the capture cross section to a final state f can be written as

$$\sigma_c(E, J_f\pi_f) \approx |C_{L_f}^{J_f\pi_f}|^2 \tilde{\sigma}_c(E, J_f\pi_f), \quad (57)$$

where $\tilde{\sigma}_f(E, J_f\pi_f)$ is independent of the model; its energy dependence is given by the properties of the Coulomb functions (Baye and Brainis, 2000). The measurement of the ANC is based on transfer reactions where a nucleon of the projectile is transferred to the target. Energies must be large enough to ensure a peripheral process which is sensitive to the external part of the wave functions only. An example is the ^{7}Be(^{3}He,d)^{8}B reaction which has been used to determine the ANC of ^{8}B (Mukhamedzhanov et al., 1995).

4. APPLICATIONS

4.1. Applications of Microscopic Models

The knowledge of the ^{2}H(d,γ)^{4}He, ^{2}H(d,p)^{3}H, and ^{2}H(d,n)^{3}He cross sections at astrophysical energies is of great interest. Aside from the astrophysical interest, the ^{2}H(d,γ)^{4}He capture reaction is extremely important from the nuclear physics viewpoint because its cross section at low energies (below 0.3 MeV) is expected to be dominated by D-wave components in the α particle. Hence it should be very sensitive to the tensor force in the NN interaction (Sabourov et al., 2004).

An ab initio model has been used to study the phase shifts of the p+^{3}He (Arai et al., 2010) and d+d, p+^{3}H, n+^{3}He (Arai et al., 2011) systems. For the two-body NN interaction V_{ij}, two different realistic potentials are used: AV8′ (Pudliner et al., 1997) and G3RS (Tamagaki, 1968), that consist of central, tensor, and spin-orbit components. Because the main aim is to clarify the role of the tensor force, it is useful to compare results obtained with the realistic interactions with that of an effective NN interaction that contains no tensor force. The MN central potential (Thompson et al., 1977) is adopted with the standard value for the admixture parameter $u = 1$.

The ^{2}H(d,p)^{3}H and ^{2}H(d,n)^{3}He reactions play an important role in Big-Bang nucleosynthesis. As the observed D/H ratio is currently known with 1.5% accuracy, a high precision is required for the reaction rates. The cross sections have been measured by several groups (Leonard et al., 2006; Tumino et al., 2014), but the extrapolations down to low energies are still uncertain. A compilation of the latest data has been undertaken to reduce the extrapolation uncertainties (Coc et al., 2015). The ^{2}H(d,p)^{3}H and ^{2}H(d,n)^{3}He S factors are presented in **Figure 2**. They mainly occur from the transitions of the $d + d$ $^5S_2$ channel to the D-wave continuum of p+^{3}H or n+^{3}He, which is due to the tensor force. Without the tensor force, these cross sections cannot be reproduced.

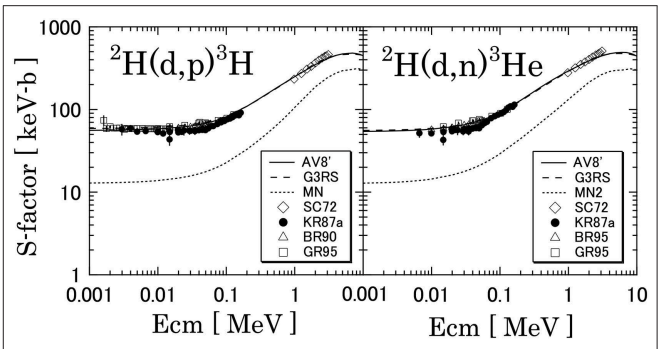

FIGURE 2 | ^{2}H(d,p)^{3}H and ^{2}H(d,n)^{3}He astrophysical S-factors calculated with the realistic AV8′+ G3RS potential (solid lines) and with the effective MN potential (dotted lines). See Angulo et al. (1999) for the experimental data. Reprinted figure with permission from Arai et al. (2011). Copyright (2011) by the American Physical Society.

More recently, the ^{3}He(α,γ)^{7}Be and ^{3}H(α,γ)^{7}Li cross sections were computed in the no-core shell model (NCSM) (Dohet-Eraly et al., 2016). The authors used a renormalized chiral nucleon-nucleon interaction. In addition to NCSM states, which are optimized for bound states of the seven-nucleon systems, a specific treatment of the α+^{3}He and α+^{3}H configuration is introduced, yielding the NCSM with continuum. With this correction, bound-state properties and elastic phase shifts are well-reproduced. **Figure 3** shows the corresponding S-factors, which are compared with previous *ab initio* models (Nollett, 2001; Neff, 2011). Significant differences exist, due to convergence problems and to the use of different nucleon-nucleon interactions.

4.2. Applications of the Potential Model

The first applications of the potential model were devoted to the ^{3}He(α,γ)^{7}Be (Tombrello and Parker, 1963; Buck et al., 1985) and the ^{7}Be(p,γ)^{8}B (Robertson, 1973; Typel et al., 1997) reactions. Both reactions are essentially non-resonant at low energies, and the final bound states can be fairly well-described by a two-cluster structure. Most applications in the literature are performed with local potentials. More recently, the influence of the non-locality was investigated by Tian et al. (2018). Applications to fusion reactions can be found, for example, in Chien et al. (2018) (single-channel model) and Assunção and Descouvemont (2013) (multichannel model).

We present in **Figure 4** the ^{3}He(α,γ)^{7}Be S-factor computed with the potential of Buck et al. (1985), and compare with some experimental data sets. The goal is not to provide a fit of the data, but rather to illustrate the use of the potential model in a simple example. The α+^{3}He potential contains a spin-orbit term; it reproduces several spectroscopic properties of ^{7}Be and of ^{7}Li. We show separately the contributions of the s wave ($L_i = 0, J_i = 1/2^+$) and of the d wave ($L_i = 2, J_i = 3/2^+, 5/2^+$). Around $E = 0$ the main contribution comes from

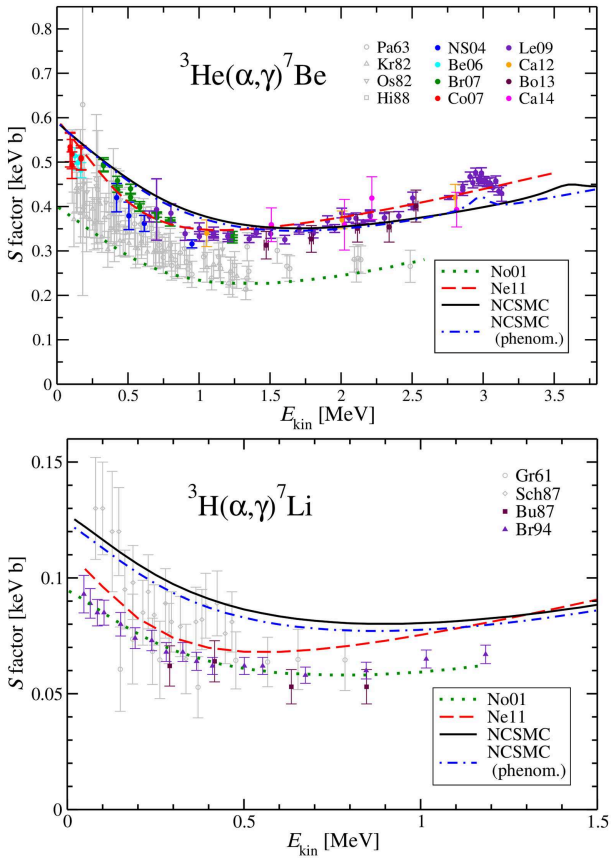

FIGURE 3 | ^{3}He(α,γ)^{7}Be and ^{3}H(α,γ)^{7}Li *S*-factors computed with the No Core Shell model (solid lines). The other lines represent alternative calculations (see Dohet-Eraly et al., 2016 for details and for the references to the data). Reprinted from Dohet-Eraly et al. (2016) with permission from Elsevier.

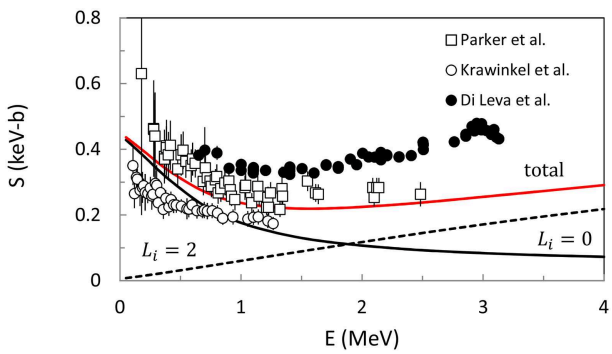

FIGURE 4 | ^{3}He(α,γ)^{7}Be *S*-factor computed in the potential model. The $L_i = 0$ and $L_i = 2$ components are shown separately. The data are taken from Parker and Kavanagh (1963), Kräwinkel et al. (1982), and Di Leva et al. (2009).

$L_i = 0$, but $L_i = 2$ cannot be neglected at energies where data are available.

As discussed in section 3, the capture cross sections are determined from integrals involving the initial and final wave functions. Let us define

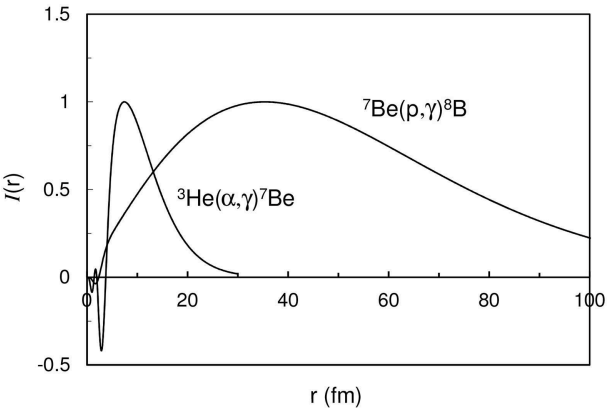

FIGURE 5 | Integrand (58) at 0.02 MeV for ^{7}Be(p,γ)^{8}B, and at 0.1 MeV for ^{3}He(α,γ)^{7}Be ($\lambda = 1$). The normalization is arbitrary.

$$I(r) = g^{J_f}(r) r^{\lambda} g^{J_i}(r), \tag{58}$$

whose integral provides the electric component of the cross section. In **Figure 5**, we present this integrand for typical energies. For the ^{3}He(α,γ)^{7}Be reaction, the maximum of $I(r)$ is located near $r_{max} = 10$ fm. At low energy the initial function $g^{J_i}(r)$ decreases rapidly in the nuclear region; conversely, the final function $g^{J_f}(r)$ is maximal in this region, and exponentially decreases as

$$g^{J_f}(r) = C_f \, W_{-\eta,\ell_f+1/2}(2k_B r) \sim C_f \, \exp(-k_B r)/\rho^{\eta}, \tag{59}$$

where k_B is the wave number of the bound state. The decrease is therefore faster for large k_B values, and hence for large binding energies. For very low binding energies, such as in ^{8}B (−137 keV), we have $r_{max} \approx 40$ fm and integrand (58) is non-negligible up to 150 fm. Accordingly, integrals (38) must be performed up to large r values to ensure the convergence.

4.3. Applications of the *R*-Matrix Method

Besides the typical application of the *R*-matrix to the ^{12}C(α,γ)^{16}O reaction (deBoer et al., 2017), various reactions have been analyzed recently in the *R*-matrix approach. Some examples are ^{14}N(p,γ)^{15}O (Li et al., 2016) or ^{13}C(p,γ)^{14}N (Chakraborty et al., 2015). Here we discuss in more detail a recent *R*-matrix analysis of the ^{18}O(p,α)^{15}N cross section which has been measured in the underground laboratory of the Gran Sasso (LUNA) (Bruno et al., 2019). This reaction influences the abundances of ^{15}N, ^{18}O and ^{19}F isotopes, critical to constrain a wide variety of stellar models.

At stellar temperatures, the rate is mainly determined by the properties of three $1/2^+$ ($\ell = 0$) resonances at center of mass energies 0.143, 0.610, and 0.800 MeV. For the latter two resonances, results on their energy and partial widths are inconsistent (La Cognata et al., 2008), and important differences have also been reported between the cross sections of different

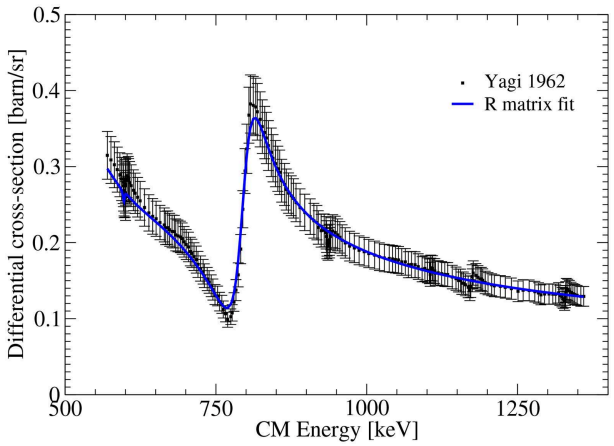

FIGURE 6 | ^{18}O(p,p)^{18}O differential cross section at $\theta = 140°$ with the *R*-matrix fit. The data are taken from Yagi (1962). Reprinted from Bruno et al. (2019) with permission from Elsevier.

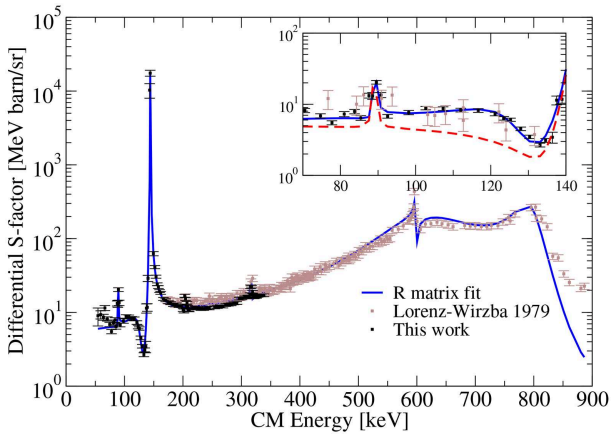

FIGURE 7 | ^{18}O(p,α)^{15}N differential *S*-factor at $\theta = 135°$ with the *R*-matrix fit. The red dashed lined in the inset shows the effect of removing the new state at $E = 106$ keV. Reprinted from Bruno et al. (2019) with permission from Elsevier.

datasets at low energies. The main goal of Bruno et al. (2019) was to measure the non-resonant component of the cross section of the ^{18}O(p,α)^{15}N reaction at proton beam energies from $E_p = 360$ to 60 keV, extending the range of direct measurements to stellar energies. From the cross section measurements, the strength of resonances of astrophysical interest could be determined.

An important advantage of the *R*-matrix theory is that some parameters are common to different reactions. In the present case, resonance energies, and proton widths are common to the ^{18}O(p,p)^{18}O and ^{18}O(p,α)^{15}N cross sections. Only the α widths are specific to ^{18}O(p,α)^{15}N. This property therefore provides several constraints on the parameter sets. Ideally, the cross sections should be measured at several angles, which permits to add further constraints.

The LUNA data and the fits of the ^{18}O(p,p)^{18}O and ^{18}O(p,α)^{15}N cross sections are shown in **Figures 6**, **7**, respectively. Several resonances are included in the fit (see Bruno et al., 2019 for detail). Both fits are excellent, with common parameters (energies and proton widths of resonances). The new data set (Bruno et al., 2019) suggest a new resonance at $E_{cm} = 110$ keV.

5. CONCLUSION

Nuclear astrophysics is a broad field, where many nuclear inputs are necessary. In particular, charged-particle cross sections are quite important, and difficult to measure, owing to the low energies and cross sections. Another characteristic of nuclear astrophysics is that there is almost no systematics. In the low-mass region, each reaction presents its own peculiarities and difficulties, in the theoretical as well as in the experimental viewpoints. Nevertheless some hierarchy can be established among reactions of astrophysical interest. Transfer reactions, arising from the nuclear interaction, present cross sections larger than capture cross sections which have an electromagnetic origin. In addition, the resonant or non-resonant nature of a reaction also affects the amplitude of the cross section.

We have discussed different theoretical models often used in nuclear astrophysics. The potential model and the *R*-matrix method are widely applied in this field; they are fairly simple and well-adapted to low-energy reactions. On the other hand, microscopic cluster models have a stronger predictive power, since they only rely on a nucleon-nucleon interaction, and on the assumption of a cluster structure for the nucleus. Finally, indirect methods are more and more developed since they overcome the major difficulty of nuclear astrophysics, i.e., the smallness of the cross sections.

A very impressive amount of work has been devoted to nuclear astrophysics in the last decades. Although most reactions involving light nuclei are sufficiently known, some reactions, such as ^{12}C(α,γ)^{16}O or ^{12}C+^{12}C, still require much effort to reach the accuracy needed for stellar models. In the nucleosynthesis of heavy elements (*s* process, *p* process), further problems arise from the level densities and the cross sections should be determined from statistical models. A better knowledge of these cross sections represents a challenge for the future.

AUTHOR CONTRIBUTIONS

The author confirms being the sole contributor of this work and has approved it for publication.

FUNDING

This work was supported by the Fonds de la Recherche Scientifique-FNRS under Grant Numbers 4.45.10.08 and J.0049.19. Computational resources have been provided by the Consortium des Équipements de Calcul Intensif (CÉCI), funded by the Fonds de la Recherche Scientifique de Belgique (F.R.S.-FNRS) under Grant No. 2.5020.11 and by the Walloon Region. PD was Directeur de Recherches of F.R.S.-FNRS, Belgium.

REFERENCES

Abramowitz, M., and Stegun, I. A. (1972). *Handbook of Mathematical Functions*. London: Dover.

Adelberger, E. G., Balantekin, A. B., Bemmerer, D., Bertulani, C. A., Chen, J. W., Costantini, H., et al. (2011). Solar fusion cross sections II: the pp chain and CNO cycles. *Rev. Mod. Phys*. 83:195. doi: 10.1103/RevModPhys.83.195

Afanasjev, A. V., Beard, M., Chugunov, A. I., Wiescher, M., and Yakovlev, D. G. (2012). Large collection of astrophysical *S* factors and their compact representation. *Phys. Rev. C* 85:054615. doi: 10.1103/PhysRevC.85.054615

Alvarez-Ruso, L., Sajjad Athar, M., Barbaro, M. B., Cherdack, D., Christy, M. E., Coloma, P., et al. (2018). NuSTEC[1] White Paper: Status and challenges of neutrino–nucleus scattering *Prog. Part. Nucl. Phys*. 100, 1–68. doi: 10.1016/j.ppnp.2018.01.006

Angulo, C., Arnould, M., Rayet, M., Descouvemont, P., Baye, D., Leclercq-Willain, C., et al. (1999). A compilation of charged-particle induced thermonuclear reaction rates. *Nucl. Phys. A* 656, 3–183. doi: 10.1016/S0375-9474(99)00030-5

Angulo, C., and Descouvemont, P. (2000). *R*-matrix analysis of interference effects in ^{12}c(α,α)^{12}c and ^{12}c(α,γ)^{16}o. *Phys. Rev. C* 61:064611. doi: 10.1103/PhysRevC.61.064611

Aprahamian, A., Langanke, K., and Wiescher, M. (2005). Nuclear structure aspects in nuclear astrophysics. *Prog. Part. Nucl. Phys*. 54, 535–613. doi: 10.1016/j.ppnp.2004.09.002

Arai, K., Aoyama, S., and Suzuki, Y. (2010). Microscopic cluster model study of ^{3}He + *p* scattering. *Phys. Rev. C* 81:037301. doi: 10.1103/PhysRevC.81.037301

Arai, K., Aoyama, S., Suzuki, Y., Descouvemont, P., and Baye, D. (2011). Tensor force manifestations in *Ab Initio* study of the ^{2}H(*d*,γ)^{4}He, ^{2}H(*d*,*p*)^{3}H, and ^{2}H(*d*,*n*)^{3}He reactions. *Phys. Rev. Lett*. 107:132502. doi: 10.1103/PhysRevLett.107.132502

Assunção, M., and Descouvemont, P. (2013). Role of the hoyle state in ^{12}C + ^{12}C fusion. *Phys. Lett. B* 723, 355–359. doi: 10.1016/j.physletb.2013.05.030

Barker, F. C., and Kajino, T. (1991). The 12C(α,γ)16o cross section at low energies. *Aust. J. Phys*. 44, 369–396. doi: 10.1071/PH910369

Baur, G. (1986). Breakup reactions as an indirect method to investigate low-energy charged-particle reactions relevant for nuclear astrophysics. *Phys. Lett. B* 178, 135–138. doi: 10.1016/0370-2693(86)91483-8

Baur, G., Bertulani, C. A., and Rebel, H. (1986). Coulomb dissociation as a source of information on radiative capture processes of astrophysical interest. *Nucl. Phys. A* 458, 188–204. doi: 10.1016/0375-9474(86)90290-3

Baur, G., Hencken, K., Trautmann, D., Typel, S., and Wolter, H. H. (2001). Electromagnetic dissociation as a tool for nuclear structure and astrophysics. *Prog. Part. Nucl. Phys*. 46, 99–108. doi: 10.1016/S0146-6410(01)00113-2

Baye, D. (1987). Supersymmetry between deep and shallow nucleus-nucleus potentials. *Phys. Rev. Lett*. 58, 2738–2741. doi: 10.1103/PhysRevLett.58.2738

Baye, D., and Brainis, E. (2000). Zero-energy determination of the astrophysical s factor and effective-range expansions. *Phys. Rev. C* 61:025801. doi: 10.1103/PhysRevC.61.025801

Baye, D., and Descouvemont, P. (1985). Antisymmetrization effects in radiative capture reactions. *Ann. Phys*. 165, 115–147. doi: 10.1016/S0003-4916(85)80007-5

Baye, D., and Kruglanski, M. (1992). α + α scattering in a microscopic model with monopolar distortion. *Phys. Rev. C* 45, 1321–1332. doi: 10.1103/PhysRevC.45.1321

Bertulani, C. A. (2003). RADCAP: A potential model tool for direct capture reactions. *Comput. Phys. Commun*. 156, 123–141. doi: 10.1016/S0010-4655(03)00441-7

Bertulani, C. A., and Kajino, T. (2016). Frontiers in nuclear astrophysics. *Prog. Part. Nucl. Phys*. 89, 56–100. doi: 10.1016/j.ppnp.2016.04.001

Bethe, H. A. (1939). Energy production in stars. *Phys. Rev*. 55, 103. doi: 10.1007/BF01325636

Broggini, C., Bemmerer, D., Guglielmetti, A., and Menegazzo, R. (2010). LUNA: Nuclear astrophysics deep underground. *Ann. Rev. Nucl. Part. Sci*. 60, 53–73. doi: 10.1146/annurev.nucl.012809.104526

Brune, C. R. (2002). Alternative parametrization of *R*-matrix theory. *Phys. Rev. C* 66:044611. doi: 10.1103/PhysRevC.66.044611

Bruno, C. G., Aliotta, M., Descouvemont, P., Best, A., Davinson, T., Bemmerer, D., et al. (2019). Improved astrophysical rate for the ^{18}O(*p*,α)^{15}N reaction by underground measurements. *Phys. Lett. B* 790, 237–242. doi: 10.1016/j.physletb.2019.01.017

Buck, B., Baldock, R. A., and Rubio, J. A. (1985). Cluster model of A = 7 nuclei and the astrophysical s factor for ^{3}He(α,γ)^{7}Be at zero energy. *J. Phys. G* 11, L11–L16. doi: 10.1088/0305-4616/11/1/003

Buck, B., Friedrich, H., and Wheatley, C. (1977). Local potential models for the scattering of complex nuclei. *Nucl. Phys. A* 275, 246–268. doi: 10.1109/TNS.1977.4329048

Burbidge, E. M., Burbidge, G. R., Fowler, W. A., and Hoyle, F. (1957). Synthesis of the elements in stars. *Rev. Mod. Phys*. 29, 547–650. doi: 10.1103/RevModPhys.29.547

Canto, L. F., Gomes, P. R. S., Donangelo, R., and Hussein, M. S. (2006). Fusion and breakup of weakly bound nuclei. *Phys. Rep*. 424, 1–111. doi: 10.1016/j.physrep.2005.10.006

Canto, L. F., and Hussein, M. S. (2013). *Scattering Theory of Molecules, Atoms and Nuclei*. Singapore: World Scientific Publishing.

Caughlan, G. R., and Fowler, W. A. (1988). Thermonuclear reaction rates v. *At. Data. Nucl. Data Tables* 40, 283–334. doi: 10.1016/0092-640X(88)90009-5

Caurier, E., and Navrátil, P. (2006). Proton radii of ^{4,6,8}He isotopes from high-precision nucleon-nucleon interactions. *Phys. Rev. C* 73:021302. doi: 10.1103/PhysRevC.73.021302

Chakraborty, S., deBoer, R., Mukherjee, A., and Roy, S. (2015). Systematic *R*-matrix analysis of the ^{13}C(p,γ)^{14}N capture reaction. *Phys. Rev. C* 91:045801. doi: 10.1103/PhysRevC.91.049905

Chatterjee, R., Okolowicz, J., and Ploszajczak, M. (2006). Description of the ^{17}F(p,γ)^{18}Ne radiative capture reaction in the continuum shell model. *Nucl. Phys. A* 764, 528–550. doi: 10.1016/j.nuclphysa.2005.10.002

Chien, L. H., Khoa, D. T., Cuong, D. C., and Phuc, N. H. (2018). Consistent mean-field description of the ^{12}C +^{12} C optical potential at low energies and the astrophysical *s* factor. *Phys. Rev. C* 98:064604. doi: 10.3952/physics.v57i4.3597

Clayton, D. D. (1983). *Principles of Stellar Evolution and Nucleosynthesis*. Chicago, IL: The University of Chicago Press.

Coc, A., Goriely, S., Xu, Y., Saimpert, M., and Vangioni, E. (2012). Standard big bang nucleosynthesis up to cno with an improved extended nuclear network. *Astrophys. J*. 744:158. doi: 10.1088/0004-637X/744/2/158

Coc, A., Petitjean, P., Uzan, J. P., Vangioni, E., Descouvemont, P., Iliadis, C., et al. (2015). New reaction rates for improved primordial D/H calculation and the cosmic evolution of deuterium. *Phys. Rev. D* 92:123526. doi: 10.1103/PhysRevD.92.123526

deBoer, R. J., Görres, J., Wiescher, M., Azuma, R. E., Best, A., Brune, C. R., et al. (2017). The ^{12}C(α,γ)^{16}O reaction and its implications for stellar helium burning. *Rev. Mod. Phys*. 89:035007. doi: 10.1103/RevModPhys.89.035007

Descouvemont, P. (1996). Application of an extended cluster model to the ^{8}Li(α,n)^{11}B reaction. *Nucl. Phys. A* 596, 285–298. doi: 10.1016/0375-9474(95)00409-2

Descouvemont, P. (2003). *Theoretical Models for Nuclear Astrophysics*. New York, NY: Nova Science.

Descouvemont, P., Adahchour, A., Angulo, C., Coc, A., and Vangioni-Flam, E. (2004). Compilation and *R*-matrix analysis of big bang nuclear reaction rates. *At. Data Nucl. Data Tables* 88, 203–236. doi: 10.1016/j.adt.2004.08.001

Descouvemont, P., and Baye, D. (1994). ^{7}Li+ p and ^{7}Be+ n reactions in a microscopic three-cluster model. *Nucl. Phys. A* 573, 28–46. doi: 10.1016/0375-9474(94)90013-2

Descouvemont, P., and Baye, D. (2010). The *R*-matrix theory. *Rep. Prog. Phys*. 73:036301. doi: 10.1088/0034-4885/73/3/036301

Descouvemont, P., and Dufour, M. (2012). *Clusters in Nuclei, Vol. 2, Lecture Notes in Physics, Vol. 848*. Berlin; Heidelberg: Springer.

Di Leva, A., Gialanella, L., Kunz, R., Rogalla, D., Schürmann, D., Strieder, F., et al. (2009). Stellar and primordial nucleosynthesis of ^{7}*be*: Measurement of ^{3}*he*(α,γ)^7*be*. *Phys. Rev. Lett*. 102:232502. doi: 10.1103/PhysRevLett.102.232502

Dohet-Eraly, J., Navrátil, P., Quaglioni, S., Horiuchi, W., Hupin, G., and Raimondi, F. (2016). ^{3}He(α,γ)^{7}Be and ^{3}H(α,γ)^{7}Li astrophysical *S* factors from the no-core shell model with continuum. *Phys. Lett. B* 757, 430–436. doi: 10.1016/j.physletb.2016.04.021

Dufour, M., and Descouvemont, P. (2000). The ^{15}N(α,γ)^{19}F and ^{15}O(α,γ)^{19}Ne reactions in a microscopic multicluster model. *Nucl. Phys. A* 672, 153–164. doi: 10.1016/S0375-9474(00)00054-3

Dufour, M., and Descouvemont, P. (2011). Low-lying resonances in the 16b nucleus. *Phys. Lett. B* 696, 237–240. doi: 10.1016/j.physletb.2010.12.032

Friedrich, H. (1981). Microscopic nucleus-nucleus potentials. *Phys. Rep*. 74C, 209–275. doi: 10.1016/0370-1573(81)90131-9

Gaspard, D., Sparenberg, J. M., Wenda, Q., and Baye, D. (2019). Complex-energy analysis of proton-proton fusion. *Phys. Rev. C* 100:035805. doi: 10.1103/PhysRevC.100.035805

Hammache, F., Heil, M., Typel, S., Galaviz, D., Sümmerer, K., Coc, A., et al. (2010). High-energy breakup of ^{6}Li as a tool to study the big bang nucleosynthesis reaction ^{2}H(α,γ)^{6}Li. *Phys. Rev. C* 82:065803. doi: 10.1103/PhysRevC.82.065803

Hofmann, H. M., and Hale, G. M. (1997). Microscopic calculation of the 4he system. *Nucl. Phys. A* 613, 69–106. doi: 10.1016/S0375-9474(96)00418-6

Horiuchi, H. (1977). Kernels of gcm, rgm and ocm and their calculation methods. *Prog. Theor. Phys. Suppl*. 62, 90–190. doi: 10.1143/PTPS.62.90

Horiuchi, H., Ikeda, K., and Katō, K. (2012). Recent developments in nuclear cluster physics. *Prog. Theor. Phys. Suppl*. 192:1. doi: 10.1143/PTPS.192.1

Hoyle, F. (1954). On nuclear reactions occuring in very hot stars.i. the synthesis of elements from carbon to nickel. *Astrophys. J. Suppl*. 1:121. doi: 10.1086/190005

Hussein, M. S. (1984). Theory of the heavy-ion fusion cross section. *Phys. Rev. C* 30:1962. doi: 10.1103/PhysRevC.30.1962

Iliadis, C. (2007). *Nuclear Physics of Stars*. Weinheim: Wiley-VCH Verlag GmbH.

José, J., and Iliadis, C. (2011). Nuclear astrophysics: the unfinished quest for the origin of the elements. *Rep. Prog. Phys*. 74:096901. doi: 10.1088/0034-4885/74/9/096901

Kamionkowski, M., and Bahcall, J. N. (1994). The rate of the proton-proton reaction. *Astrophys. J*. 420:884. doi: 10.1086/173612

Kiener, J., Gils, H. J., Rebel, H., Zagromski, S., Gsottschneider, G., Heide, N., et al. (1991). Measurements of the coulomb dissociation cross section of 156 mev ^{6}Li projectiles at extremely low relative fragment energies of astrophysical interest. *Phys. Rev. C* 44, 2195–2208. doi: 10.1103/PhysRevC.44.2195

Kiener, J., Lefebvre, A., Aguer, P., Bacri, C. O., Bimbot, R. B., Borderie, G. B., et al. (1993). Determination of the ^{13}N(p, γ)^{14}O reaction rate through the coulomb break-up of a ^{14}O radioactive beam. *Nucl. Phys. A* 552, 66–81. doi: 10.1016/0375-9474(93)90331-Q

Kievsky, A., Rosati, S., Viviani, M., Marcucci, L. E., and Girlanda, L. (2008). A high-precision variational approach to three- and four-nucleon bound and zero-energy scattering states. *J. Phys. G* 35:063101. doi: 10.1088/0954-3899/35/6/063101

Kikuchi, T., Motobayashi, T., Iwasa, N., Ando, Y., Kurokawa, M., Moriya, S., et al. (1998). Further measurement of the ^{7}Be(p,γ)^{8}B cross section at low energies with the coulomb dissociation of ^{8}B. *Eur. Phys. J. A* 3, 213–215.

Kräwinkel, H., Becker, H. W., Buchmann, L., Görres, J., Kettner, K. U., Kieser, W. E., et al. (1982). The ^{3}He(α,γ)^{7}Be reaction and the solar neutrino problem. *Zeit. Phys. A* 304, 307–332. doi: 10.1007/BF01421513

Kukulin, V. I., Neudatchin, V. G., Obukhovski, I. T., and Smirnov, Y. F. (1983). *Clusters as Subsystems in Light Nuclei*. Braunschweig: Vieweg.

Kumar, R., and Bonaccorso, A. (2012). Interplay of nuclear and coulomb effects in proton breakup from exotic nuclei. *Phys. Rev. C* 86:061601. doi: 10.1103/PhysRevC.86.061601

La Cognata, M., Spitaleri, C., Mukhamedzhanov, A. M., Irgaziev, B., Tribble, R. E., Banu, A., et al. (2008). Measurement of the 20 and 90 kev resonances in the ^{18}O(p,α)^{15}N reaction via the trojan horse method. *Phys. Rev. Lett*. 101:152501. doi: 10.1103/PhysRevLett.101.152501

Lane, A. M., and Thomas, R. G. (1958). R-matrix theory of nuclear reactions. *Rev. Mod. Phys*. 30, 257–353. doi: 10.1103/RevModPhys.30.257

Leonard, D. S., Karwowski, H. J., Brune, C. R., Fisher, B. M., and Ludwig, E. J. (2006). Precision measurements of ^{2}H(d,p)^{3}H and ^{2}H(d,n)^{3}He total cross sections at big bang nucleosynthesis energies. *Phys. Rev. C* 73:045801. doi: 10.1103/PhysRevC.73.045801

Li, Q., Görres, J., deBoer, R. J., Imbriani, G., Best, A., Kontos, A., et al. (2016). Cross section measurement of ^{14}N(p,γ)^{15}O in the cno cycle. *Phys. Rev. C* 93:055806. doi: 10.1103/PhysRevC.93.055806

Liccardo, V., Malheiro, M., Hussein, M., Carlson, B., and Frederico, T. (2018). Nuclear processes in astrophysics: Recent progress. *Eur. Phys. J. A* 54:221. doi: 10.1140/epja/i2018-12648-5

Liu, Q. K. K., Kanada, H., and Tang, Y. C. (1981). Microscopic study of ^{3}He(α,γ)^{7}Be electric-dipole capture reaction. *Phys. Rev. C* 23, 645–656. doi: 10.1103/PhysRevC.23.645

Longland, R., Iliadis, C., Champagne, A., Newton, J., Ugalde, C., Coc, A., et al. (2010). Charged-particle thermonuclear reaction rates: I. monte carlo method and statistical distributions. *Nucl. Phys. A* 841, 1–30. doi: 10.1016/j.nuclphysa.2010.04.008

Marcucci, L. E. (2018). Recent progress in ab-initio studies of nuclear reactions of astrophysical interest with a $\leq$ 3. *J. Phys. Conf. Series* 981:012019. doi: 10.1088/1742-6596/981/1/012019

Marcucci, L. E., Schiavilla, R., and Viviani, M. (2013). Proton-proton weak capture in chiral effective field theory. *Phys. Rev. Lett*. 110:192503. doi: 10.1103/PhysRevLett.110.192503

Motobayashi, T., Iwasa, N., Ando, Y., Kurokawa, M., Murakami, H., Gen, J. R., et al. (1994). Coulomb dissociation of ^{8}B and the ^{7}Be(p,γ)^{8}B reaction at low energies. *Phys. Rev. Lett*. 73, 2680–2683. doi: 10.1103/PhysRevLett.73.2680

Motobayashi, T., Takei, T., Kox, S., Perrin, C., Merchez, F. K., Ieki, D. R., et al. (1991). Determination of the astrophysical ^{13}N(p,γ)^{14}O cross section through the coulomb dissociation method. *Phys. Lett. B* 264, 259–263. doi: 10.1016/0370-2693(91)90345-Q

Mukhamedzhanov, A. M., Gagliardi, C. A., and Tribble, R. E. (2001). Asymptotic normalization coefficients, spectroscopic factors, and direct radiative capture rates. *Phys. Rev. C* 63:024612. doi: 10.1103/PhysRevC.63.024612

Mukhamedzhanov, A. M., and Rogachev, G. V. (2017). Radiative capture reactions via indirect methods. *Phys. Rev. C* 96:045811. doi: 10.1103/PhysRevC.96.045811

Mukhamedzhanov, A. M., Tribble, R. E., and Timofeyuk, N. K. (1995). Possibility to determine the astrophysical s factor for the ^{7}Be(p,γ)^{8}B radiative capture from analysis of the ^{7}Be(^{3}He,d)^{8}B reaction. *Phys. Rev. C* 51, 3472–3478. doi: 10.1103/PhysRevC.51.3472

Navrátil, P., and Quaglioni, S. (2011). Ab initio many-body calculations of deuteron-^{4}He scattering and ^{6}Li states. *Phys. Rev. C* 83:044609. doi: 10.1103/PhysRevC.83.044609

Navrátil, P., and Quaglioni, S. (2012). *Ab Initio* many-body calculations of the ^{3}H(d,n)^{4}He and ^{3}He(d,p)^{4}He fusion reactions. *Phys. Rev. Lett*. 108:042503. doi: 10.1103/PhysRevLett.108.042503

Navrátil, P., Roth, R., and Quaglioni, S. (2010). Ab initio many-body calculations of nucleon scattering on ^{4}He, ^{7}Li, ^{7}Be, ^{12}C, and ^{16}O. *Phys. Rev. C* 82:034609. doi: 10.1103/PhysRevC.82.034609

Neff, T. (2011). Microscopic calculation of the ^{3}He(α,γ)^{7}Be and ^{3}H(α,γ)^{7}Li capture cross sections using realistic interactions. *Phys. Rev. Lett*. 106:042502. doi: 10.1103/PhysRevLett.106.042502

Nollett, K. M. (2001). Radiative α-capture cross sections from realistic nucleon-nucleon interactions and variational monte carlo wave functions. *Phys. Rev. C* 63:054002. doi: 10.1103/PhysRevC.63.054002

Parker, P. D., and Kavanagh, R. W. (1963). He^3(α,γ)Be^7 reaction. *Phys. Rev*. 131, 2578–2582. doi: 10.1103/PhysRev.131.2578

Pudliner, B. S., Pandharipande, V. R., Carlson, J., Pieper, S. C., and Wiringa, R. B. (1997). Quantum monte carlo calculations of nuclei with $a < 7$. *Phys. Rev. C* 56:1720. doi: 10.1103/PhysRevC.56.1720

Rauscher, T., Thielemann, F. K., and Kratz, K. L. (1997). Nuclear level density and the determination of thermonuclear rates for astrophysics. *Phys. Rev. C* 56, 1613–1625. doi: 10.1103/PhysRevC.56.1613

Raynal, J. (1972). *Computing as a Language of Physics, Trieste 1971*. Vienna: IAEA. 281.

Reifarth, R., Erbacher, P., Fiebiger, S., Göbel, K., Heftrich, T., Heil, M., et al. (2018). Neutron-induced cross sections. *Eur. Phys. J. Plus* 133:424. doi: 10.1140/epjp/i2018-12295-3

Richter, W., Brown, B. A., Signoracci, A., and Wiescher, M. (2011). Shell-model studies of the rp reaction ^{25}Al(p,γ)^{26}Si. *Prog. Part. Nucl. Phys*. 66, 283–286. doi: 10.1016/j.ppnp.2011.01.021

Robertson, R. G. H. (1973). Proton capture by ^{7}Be and the solar neutrino problem. *Phys. Rev. C* 7, 543–547. doi: 10.1103/PhysRevC.7.543

Rolfs, C., and Rodney, W. S. (1988). *Cauldrons in the Cosmos*. Chicago, IL: The University of Chicago Press.

Rose, H. J., and Brink, D. M. (1967). Angular distributions of gamma rays in terms of phase-defined reduced matrix elements. *Rev. Mod. Phys*. 39, 306–347. doi: 10.1103/RevModPhys.39.306

Sabourov, K., Ahmed, M. W., Canon, S. R., Crowley, B., Joshi, K., Kelley, J. H., et al. (2004). Experimental and theoretical study of the ^{2}H($\vec{d},\gamma$)^{4}He reaction below $E_{\text{c.m.}} = 60$ keV. *Phys. Rev. C* 70:064601. doi: 10.1103/PhysRevC.70.064601

Satchler, G. R. (1983). *Direct Nuclear Reactions*. Oxford: Oxford University Press.

Schümann, F., Typel, S., Hammache, F., Sümmerer, K., Uhlig, F., Böttcher, I., et al. (2006). Low-energy cross section of the ^{7}Be(p,γ)^{8}B solar fusion reaction from the coulomb dissociation of ^{8}B. *Phys. Rev. C* 73:015806. doi: 10.1103/PhysRevLett.73.015806

Spitaleri, C., La Cognata, M., Lamia, L., Pizzone, R. G., and Tumino, A. (2019). Astrophysics studies with the trojan horse method. *Eur. Phys. J. A* 55:161. doi: 10.1140/epja/i2019-12833-0

Tamagaki, R. (1968). Repulsive core of effective alpha-alpha potential and the pauli principle. *Suppl. Prog. Theor. Phys*. E68, 242–258. doi: 10.1143/PTPS.E68.242

Thielemann, F., Eichler, M., Panov, I., and Wehmeyer, B. (2017). Neutron star mergers and nucleosynthesis of heavy elements. *Ann. Rev. Nucl. Part. Sci*. 67, 253–274. doi: 10.1146/annurev-nucl-101916-123246

Thompson, D. R., LeMere, M., and Tang, Y. C. (1977). Systematic investigation of scattering problems with the resonating-group method. *Nucl. Phys. A* 286, 53–66. doi: 10.1016/0375-9474(77)90007-0

Thompson, I., and Nunes, F. (2009). *Nuclear Reactions for Astrophysics: Principles, Calculation and Applications of Low-Energy Reactions*. Cambridge: Cambridge University Press.

Thompson, I. J. (2010). *NIST Handbook of Mathematical Functions*. Cambridge: Cambridge University Press.

Tian, Y., Pang, D. Y., and Ma, Z. Y. (2018). Effects of nonlocality of nuclear potentials on direct capture reactions. *Phys. Rev. C* 97:064615. doi: 10.1103/PhysRevC.97.064615

Tombrello, T. A. (1965). The capture of protons by 7Be. *Nucl. Phys*. 71, 459–464. doi: 10.1016/0029-5582(65)90733-9

Tombrello, T. A., and Parker, P. D. (1963). Direct-capture model for the $He^{3}(\alpha,\gamma)Be^{7}$ and $T(\alpha,\gamma)Li^{7}$ reactions. *Phys. Rev*. 131, 2582–2589. doi: 10.1103/PhysRev.131.2582

Tribble, R. E., Bertulani, C. A., Cognata, M. L., Mukhamedzhanov, A. M., and Spitaleri, C. (2014). Indirect techniques in nuclear astrophysics: a review. *Rep. Prog. Phys*. 77:106901. doi: 10.1088/0034-4885/77/10/106901

Tumino, A., Spartá, R., Spitaleri, C., Mukhamedzhanov, A. M., Typel, S., Pizzone, R. G., et al. (2014). New determination of the ^{2}H(d,p)^{3}H and ^{2}H(d,n)^{3}He reaction rates at astrophysical energies. *Astrophys. J*. 785:96. doi: 10.1088/0004-637X/785/2/96

Tumino, A., Spitaleri, C., Cherubini, S., Gulino, M., La Cognata, M., Lamia, L., et al. (2013). New advances in the trojan horse method as an indirect approach to nuclear astrophysics. *Few Body Syst*. 54, 745–753. doi: 10.1007/s00601-013-0690-5

Tumino, A., Spitaleri, C., Mukhamedzhanov, A. M., Typel, S., Aliotta, M., Burjan, V., et al. (2011). Low-energy fusion reactions via the trojan horse method. *Phys. Lett. B* 700, 111–115. doi: 10.1016/j.physletb.2011.05.001

Typel, S., and Baur, G. (2003). Theory of the trojan-horse method. *Ann. Phys*. 305, 228–265. doi: 10.1016/S0003-4916(03)00060-5

Typel, S., Wolter, H. H., and Baur, G. (1997). Higher-order effects in the coulomb dissociation of 8b into ^{7}Be+P. *Nucl. Phys. A* 613, 147–164. doi: 10.1016/S0375-9474(96)00415-0

Volkov, A. B. (1965). Equilibrium deformation calculations of the ground state energies of 1p shell nuclei. *Nucl. Phys*. 74, 33–58. doi: 10.1016/0029-5582(65)90244-0

Wiescher, M., Käppeler, F., and Langanke, K. (2012). Critical reactions in contemporary nuclear astrophysics. *Ann. Rev. Astron. Astrophys*. 50, 165–210. doi: 10.1146/annurev-astro-081811-125543

Wildermuth, K., and Tang, Y. C. (1977). *A Unified Theory of the Nucleus*. Braunschweig: Vieweg.

Yagi, K. (1962). Analysis of elastic scattering of protons by o18 and the energy levels of f19. *J. Phys. Soc. Japan* 17:604. doi: 10.1143/JPSJ.17.604

Zhang, X., Nollett, K. M., and Phillips, D. R. (2018). Models, measurements, and effective field theory: Proton capture on ^{7}Be at next-to-leading order. *Phys. Rev. C* 98:034616. doi: 10.3952/physics.v58i1.3647

Conflict of Interest: The author declares that the research was conducted in the absence of any commercial or financial relationships that could be construed as a potential conflict of interest.

frontiers in Astronomy and Space Sciences

REVIEW
published: 29 October 2020
doi: 10.3389/fspas.2020.560149

Direct and Indirect Measurements for a Better Understanding of the Primordial Nucleosynthesis

Roberta Spartá[1,2], Rosario Gianluca Pizzone[1], Carlos A. Bertulani[3], Suqing Hou[4], Livio Lamia[1,2,5] and Aurora Tumino[1,6]*

[1] Laboratori Nazionali del Sud, Istituto Nazionale Fisica Nucleare, Catania, Italy, [2] Dipartimento Fisica e Astronomia "Ettore Majorana", Universitá degli Studi di Catania, Catania, Italy, [3] Department of Physics and Astronomy, Texas A&M University, Commerce, TX, United States, [4] Key Laboratory of High Precision Nuclear Spectroscopy, Institute of Modern Physics, Chinese Academy of Sciences, Lanzhou, China, [5] Centro Siciliano di Fisica Nucleare e Struttura della Materia, Catania, Italy, [6] Facoltá di Ingegneria e Architettura, Universitá degli Studi di Enna "Kore", Enna, Italy

The Big Bang Nucleosynthesis (BBN) model is a great success of nuclear astrophysics due to the outstanding agreement between observational and predicted light elements abundances. One exception, however, is the so-called "lithium problem." In this context, experimental efforts to measure the relevant reactions have been brought to an increased level of accuracy in measuring primordial abundances, and the introduction of indirect methods has allowed researchers to overcome the natural limitations of direct measurements in the energy range of interest for BBN. Here we review the results obtained from the application of the Trojan Horse Method to some of the most influential reactions of the standard network, such as ^{2}H(d,p)^{3}H, ^{2}H(d,n)^{3}He, ^{3}He(d,p)^{4}He, ^{7}Li(p,α)^{4}He, and ^{7}Be(n,α)^{4}He. The relevant cross sections have been then used as new inputs to a classical BBN code, resulting in important constraints that make suggestions for a possible solution for the lithium problem outside of nuclear physics.

Keywords: primordial nucleosynthesis, reaction rates, primordial abundances, lithium problem, R-matrix

OPEN ACCESS

Edited by:
Francesca Sammarruca, University of Idaho, United States

Reviewed by:
Roelof Bijker, National Autonomous University of Mexico, Mexico
Grant James Mathews, University of Notre Dame, United States

***Correspondence:**
Rosario Gianluca Pizzone
rgpizzone@lns.infn.it

Specialty section:
This article was submitted to Nuclear Physics, a section of the journal Frontiers in Astronomy and Space Sciences

Received: *08 May 2020*
Accepted: *17 August 2020*
Published: *29 October 2020*

Citation:
Spartá R, Pizzone RG, Bertulani CA, Hou S, Lamia L and Tumino A (2020) Direct and Indirect Measurements for a Better Understanding of the Primordial Nucleosynthesis. Front. Astron. Space Sci. 7:560149. doi: 10.3389/fspas.2020.560149

1. INTRODUCTION

Big Bang Nucleosynthesis (BBN) occurred when our universe was able to produce nuclei that happened just after the baryogenesis, most probably from the second to the 20th minute after the *Bang*, while temperature fell from more than 10^9–10^8 K. BBN has been widely studied for decades due to its importance for the understanding of the whole Big Bang Model, being one of its three mainstay pieces of evidence, together with the galactic recession and the Cosmic Microwave Background (CMB). As it is the oldest, it is a valuable tool with which to constrain the physical evolution of the *Big Bang*.

The model actually describing BBN is one of the major successes of nuclear astrophysics as a discipline, especially considering its Standard version (SBBN), which is the most accepted by the community. For this model to be *Standard*, it is necessary that the baryon-to-photon number densities ratio $\eta = \frac{n_B}{n_\gamma}$ is uniform in space and time during BBN; the neutrinos families N_ν are three (this is known from the measurement of the Z_0 width at CERN Tanabashi et al., 2018), as predicted by the Standard Model for Particle Physics, and no other particle is present in remarkable abundance except of neutrinos ν; And the neutron half-life τ_n has a value of 879.4 $\pm$ 0.6 s (Particle Data Group mean average from 2018 and 2019 updates), which significantly influences the weak

interaction rate and the reaction rates of light elements synthesis and destruction. Moreover, SBBN is based on General Relativity and ΛCDM cosmology. Recent and complete reviews for SBBN are given in Cyburt et al. (2016) and Pitrou et al. (2018). This success relies on the outstanding agreement between what is predicted as the output, namely, the primordial abundances of the elements produced during BBN, and the same abundances resulting from the current observations (and brought back with other models to the primordial values). This is true not only for the compliance of nuclear physics and astronomy results but also for the model parameters obtained with methods completely outside of nuclear astrophysics, such as the CMB evaluation from the Planck satellite of $\eta \cdot 10^{-10} = 6.12 \pm 0.06$ (Planck Collaboration et al., 2018), impressively concordant with the BBN model result of $5.8 \leq \eta \cdot 10^{-10} \leq 6.5$, which was given in Cooke et al. (2018) and obtained by taking advantage of the most recent and precise measurements of the deuterium primordial abundance. With this recent and precise evaluation of η from the Planck mission, it is now possible to consider SBBN as a parameter-free model, described with computer programs where outputs are the desired primordial abundances and inputs are the cosmological parameters and the rates of the reactions through which light elements are produced.

The only thorn in our side is the Cosmological Lithium Problem, namely the discrepancy of a factor three between what is observed (as an example see Sbordone et al., 2010) and what is predicted by SBBN. Since the early 1980s the Spite plateau, i.e., the nearly constant lithium abundance with decreasing metallicity in halo stars, was assumed as a signature of primordial lithium. Since then, observational developments have confirmed its existence and its predicted cosmologic role. Nevertheless, what is calculated in BBN models is systematically higher than what is observed in halo stars and is assumed to be primordial. In recent times, much effort has been put to shore up the model, and, from an observational point of view, it is now claimed to have reached a precision of a few percent for some elements (Aver et al., 2015; Cooke et al., 2018). Currently, the nuclear measurements part appears to be one of the main sources of uncertainty, as it is difficult to obtain all the involved cross sections with the same degree of precision. Together with nuclear cross sections measurements (some involving the radioactive isotope ^{7}Be interaction with neutron), relevant uncertainties in the prediction of primordial ^{7}Li also arise from stellar physics (e.g., observations, stellar rotation, and transport mechanisms) that are far from being understood.

In fact, to study the origin and evolution of the light element abundances in the galaxy, one should take into account several competing processes besides the Big Bang cosmic-ray production, stellar depletion, and nucleosynthesis all of which are linked to the cosmic and chemical evolution (see e.g., Boesgaard et al., 2004 for a review).

In general, theoretical analyses of light element abundances in stars are still limited by the lack of precise information on the efficiency of envelope convection, microscopic diffusion, and radiative acceleration and on the possible presence of additional mixing mechanisms (e.g., induced by the stellar rotation, see Cayrel et al., 1999). Moreover, the predicted light element depletion strongly depends on the adopted physical input (besides nuclear reaction rates), such as the equation of state and the opacity of the stellar matter, which is still affected by relevant uncertainties (see e.g., Pinsonneault, 1997 for some results of evolutionary models). It is therefore not surprising that discrepancies persist between the predicted and observed light element abundances even for the determination of solar ^{7}Li abundance or in the case of open clusters and halo or disk stars. It is also important to stress that for all the other primordial isotopes, predicted values of abundances and observed ones (in the appropriate astrophysical site) do match.

Despite all the efforts devoted to reduce the uncertainties, in most of the cases, directly measured cross sections are inadequate in the energy range of interest for BBN due to natural limitations, such as the Coulomb barrier presence for charged particle induced reactions, which reduces the cross sections to values so small that they are almost impossible to measure. However, direct measurement data sets have been selected here for all the reactions analyzed with the aim of discerning which set is still valid or not.

Recently, indirect measurements have been performed to overcome these difficulties, particularly using the Trojan Horse Method (THM). This has been applied to some of the most influential reactions of the SBBN network, such as ^{2}H(d,p)^{3}H, ^{2}H(d,n)^{3}He, ^{3}He(d,p)^{4}He, ^{7}Li(p,α)^{4}He as first (Pizzone et al., 2014), and then extended to ^{7}Be(n,α)^{4}He and ^{3}He(n,p)^{3}H. This extension takes advantage of the new applications of the THM to neutron-induced and radioactive-beam-induced reactions, which substantially widens the THM scope to almost all the interesting reactions for astrophysical scenarios. Cross sections thus obtained have been compared with direct measurements and used as new inputs for a classical BBN code. Here we review the main results of the measurements above together with the conclusions that can be drawn from the calculation outcome. In particular, we discuss the resulting constraints that suggest a possible solution for the lithium problem outside of nuclear physics.

2. NUCLEAR MEASUREMENT PROBLEMS

Particle interaction in the BBN environment took place with thermal energy $E \sim k_B T$ as kinetic energy, meaning that $10^{0 \div 2}$ keV is the range of astrophysical interest (BBN universe had temperatures $T \sim 10^{8 \div 9}$ K), which is what laboratory experiments should concentrate on to better understand this first nuclear astrophysics scenario.

Unfortunately, it is very difficult, when not impossible, to have accurate cross section measurements at these energies for charged-particle-induced reactions, as they brutally decrease to values of nano- or pico-barns because of the Coulomb barrier penetration. Measurements are thus very challenging; the background is usually overwhelming, hence the need for extrapolation to the BBN energies. Neutron-induced reactions are instead complicated by the problems related to the production of neutron beams with sufficient intensity and energy precision to be helpful for astrophysical aims.

Extrapolation of the S(E) (the astrophysical factor) rather than the cross section is one of the means used to reach these very low energies because it keeps a nearly constant trend in cases of a non-resonant reaction. But the extrapolation cannot be a complete solution, as it does not solve cases with resonances and is not helpful in evaluating electron screening enhancement at ultra-low energies. Moreover, extrapolation can be source of a huge error because the presence and the effects of under-threshold resonances can be unknown.

Indirect measurements are complementary to the direct ones and have proven to always be more helpful in completing our knowledge on the astrophysically interesting yields. Among them, the Trojan Horse Method (THM) provides bare nucleus cross section without electron screening but mostly without suppression effects due to the Coulomb barrier (or centrifugal barrier in case of n-induced reactions), as discussed in detail in the review by Spitaleri et al. (2016, 2019).

The THM allows us to cover a wide energy range using only one beam energy (see for instance, Sergi et al., 2015; Cvetinović et al., 2018; Rapisarda et al., 2018). For this reason, the THM is used not only in contexts where light elements are present, as in the case of BBN scenario, but also for studying heavier species interaction, like ^{12}C + ^{12}C (Tumino et al., 2018), which are fundamental for stellar physics. Moreover, in recent years, it has been applied to measure n-induced reactions, bypassing all the problems related to the neutron beam production using deuterons as source of virtual neutrons (Lamia et al., 2008; Gulino et al., 2010; Guardo et al., 2017). On top of that, THM applications to radioactive ion beams (Cherubini et al., 2015; Pizzone et al., 2016) have paved the way to the unique possibility of studying the interaction between exotic beams and neutrons. We have also mentioned a recent measurement of the ^{3}He(α,γ)^{7}Be, by means of the ANC method, which has provided a new value of $S(E = 0 = 0.534 \pm 0.025$ keV·b (see reference Kiss et al., 2020 for details).

3. THM MEASUREMENTS FOR THE BBN SCENARIO

Some of the most influential reactions for SBBN (as an example see Cyburt et al., 2016), i.e., ^{2}H(d,p)^{3}H, ^{2}H(d,n)^{3}He, ^{3}He(d,p)^{4}He, ^{7}Li(p,α)^{4}He, ^{7}Be(n,α)^{4}He, have been investigated using the THM in the energy range of interest, and their measurements were performed in an experimental campaign that took place within the last decade (Pizzone et al., 2003; La Cognata et al., 2005; Tumino et al., 2011). We will not go into the details of the THM because this is done elsewhere (see Spitaleri et al., 2003; Spitaleri et al., 2016, 2019; Tumino et al., 2013 and references therein), but it is necessary to recall that the THM provides a bare S(E), i.e., an astrophysical factor that is lacking in screening and barrier effects (Coulomb or centrifugal), for the reaction under investigation after studying an appropriate three-body one in the quasi-free (QF) kinematical conditions. The basic idea of the THM is to get the cross section at low energies of a two-body reaction, which is interesting for astrophysical scenarios:

$$a + x \rightarrow c + C \tag{1}$$

extracting it by means of the QF mechanism of a proper three-body reaction

$$a + A \rightarrow s + c + C. \tag{2}$$

Consequently, we will measure the cross section of the a nucleus interacting with A, which is composed by the two clusters x, participating to the binary reaction in Equation (2), and s, namely the residual nucleus, or spectator, which will not take part in the binary reaction. The break-up of A is QF when s is emitted with the same momentum it had inside A.

Once the QF break up mechanism is disentangled from all other reaction mechanisms, and through the use of Plane Wave Impulse Approximation (PWIA), the three-body cross section can be factorized:

$$\frac{d^3\sigma}{d\Omega_c d\Omega_C dE_C} \propto KF|\phi(-\vec{p}_s)|^2 \left(\frac{d\sigma}{d\Omega}\right)_{Cc}^{HOES}. \tag{3}$$

where the kinematical factor KF generally comes from Monte Carlo simulation, which considers the detectors geometrical position, while $|\phi_{exp}(p_s)|^2$ is the momentum distribution of the spectator particle. From Equation (3) one can extract the HOES cross sections, $\frac{d\sigma}{d\Omega}{}_{Cc}^{HOES}$, and then normalize it to OES one above the Coulomb barrier to the directly measured data. This cross section for the binary reaction $a + x \rightarrow c + C$ can be obtained as a function of the relative energy E_{ax}, given by $E_{ax} = E_{Cc} - Q_{2b}$ (where Q_{2b} is the Q value of the binary reaction) from energy conservation. Indeed, in QF kinematics when $p_x = 0$, it results in the following:

$$E_{ax} = \frac{m_x}{m_x + m_a} E_a - B_{sx}. \tag{4}$$

This explains how the two-body reaction can be induced at such low energies, exploiting the compensation of the interaction energy for the TH nucleus binding energy.

Considering the temperatures of the universe at SBBN time, measurements of cross sections are interesting at energies of $10^{1\div2}$ keV. The possibility to investigate this energy range with a unique beam energy is allowed by measuring small deviations from QF conditions. This means that Equation (4) becomes the following:

$$E_{ax} = \frac{m_x}{m_x + m_a} E_a - \frac{p_s^2}{2\mu_{xs}} + \frac{\vec{k}_s \cdot \vec{k}_a}{m_x + m_a} - B_{sx}. \tag{5}$$

A small variation of the p_s value and/or of the θ_s (the angle where the spectator is emitted) thus makes it possible to scan most of the desired energy range.

For the examined reactions, the S(E) factors were normalized and then compared with those available from direct measurements in literature. They have showed to be in fair agreement in the energy region where screening effects are negligible.

3.1. R-Matrix Fit

Details of this fit procedure are given in Pizzone et al. (2014).

Here we just recall that these fits have been done by means of AZURE, the multilevel and multi-channel R-matrix public code (Azuma et al., 2010). We used direct data together with THM data in the energy range where they were available and used only direct data where not, to fit the R-matrix output of the reactions in section 3. The parameterization of these functions has considered n_R resonances, where E_j [MeV] are the resonance energies and Γ_j [MeV] the widths, which are the sum of polynomials and Breit-Wigner functions:

$$S_{fit}(E) = \sum_{i=1}^{6} b_i E^{i-1} + \sum_{j=1}^{n_R} \frac{c_j}{(E - E_j)^2 + \Gamma_j^2/4}, \qquad (6)$$

in [MeV · b]. We considered the ordinary χ^2 statistics, as explained in Pizzone et al. (2014).

3.2. ^{2}H(d,p)^{3}H

The $d + d$ reactions are among the most influential processes on the final abundance output, being at the base of the reaction chain that leads to the light element production. For this reason and for their interest in energy production with fusion, many measurements are available in the literature for each of the two mirror channels, ^{2}H(d,p)^{3}H and ^{2}H(d,n)^{3}He. We updated for each reaction the data sets from direct measurement to be compared with the THM one, to better estimate the impact of the indirect result. For the *pt* channel we have chosen data reported in Greife et al. (1995), Krauss et al. (1987), McNeill and Keyser (1951), Schulte et al. (1972), Brown and Jarmie (1990), Ganeev et al. (1957), Arnold et al. (1954), Raiola et al. (2002), Booth et al. (1956), Davenport et al. (1953), Von Engel and Goodyear (1961), Cook and Smith (1953), Moffatt et al. (1952), Tie-Shan et al. (2007), and Leonard et al. (2006).

The data set in Greife et al. (1995) shows an enhanced S-factor at very low energy values due to the electron screening effect. This effect has to be removed in order for us to use data sets for astrophysical applications. It is also noticeable that any data set is present at energies of 1 MeV, so the fitting procedure can hardly be reliable.

Experimental runs to extract the TH bare nucleus S-factor from three-body reaction ^{2}H(^{3}He,pt)H, with their data analysis started with an early work of Rinollo et al. (2005) and were followed by Tumino et al. (2011), Pizzone et al. (2013), and Tumino et al. (2014). In these latter works the energy range covered span from 2.6 keV up to 1.5 MeV with a 5% error. The TH result is shown in **Figure 1** (blue filled circles) together with the data sets by direct measurements (red circles), used for comparison. The R-matrix fit to both direct and indirect data is indicated by a solid line, with parameters for an equivalent polynomial fit, using Equation (6), listed in **Table 1**.

3.3. ^{2}H(d,n)^{3}He

The n^3He is the mirror channel of the previous reaction, and it is therefore not surprising that available literature measurements depict a state of the art before the THM measurement very similar to it, including that data sets are missing between 600 keV and 1 MeV. But, unlike the *pt* case, no experimental points in absolute units are present below 6 keV. We thus used data sets from Greife et al. (1995), Krauss et al. (1987), McNeill and Keyser (1951), Schulte et al. (1972), Brown and Jarmie (1990), Ganeev et al. (1957), Arnold et al. (1954), Raiola et al. (2002), Booth et al. (1956), Leonard et al. (2006), Davidenko et al. (1957), Hofstee et al. (2001), Preston et al. (1954), Belov et al. (1990), Ying et al. (1973), and Bystritsky et al. (2010).

TH bare nucleus S-factor obtained extracting the quasi-free mechanism from the ^{2}H(^{3}He,n^{3}He)H (Tumino et al., 2011, 2014) is shown in **Figure 2**, with a 5% experimental error on the whole data set, from 2.6 keV up to 1.5 MeV, as blue filled triangles and red filled triangles are direct measurements. Also in this case the solid lines are the R-matrix fits (to direct and indirect data), with parameters for an equivalent polynomial fit, using Equation (6), listed in **Table 1**.

3.4. ^{3}He(d,p)^{4}He

The ^{3}He(d,p)^{4}He fusion reaction is important in the ultra-low energy range for many different topic, e.g., Solar Physics,

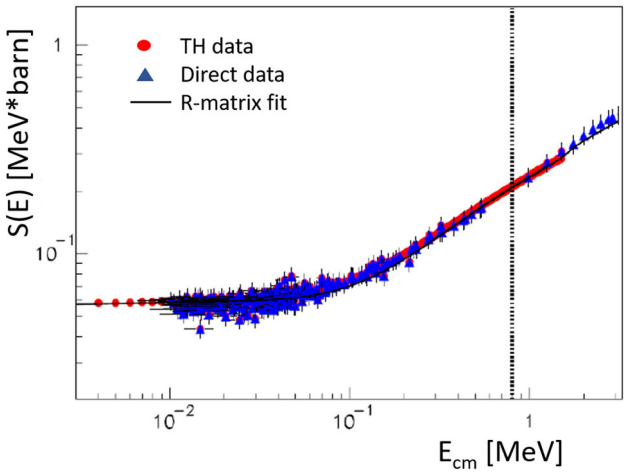

FIGURE 1 | Bare nucleus S-factor for the ^{2}H(d,p)^{3}H reaction obtained after putting together direct data (blue filled triangles) and with the THM ones (red filled circles) taken from (Tumino et al., 2014). The solid line is the R-matrix fit to direct and indirect sets, as in section 3.1. The resulting parameters of the equivalent fit (polynomial plus Breit-Wigner) are listed in **Table 1**. Energy range of interest for BBN is marked by the vertical dotted line. The figure is adapted from Pizzone et al. (2014).

TABLE 1 | Fit parameters for the S-factors of the reactions ^{2}H(d,p)^{3}H and ^{2}H(d,n)^{3}He measured in TH experiments using Equation (6).

Parameter	^{2}H(d,p)^{3}H	^{2}H(d,n)^{3}He
b_1	5.5325 $\times 10^{-2}$	5.8613 $\times 10^{-2}$
b_2	0.18293	0.18101
b_3	0.28256	0.44676
b_4	0.62121	0.8682
b_5	0.44865	0.61893
b_6	0.61893	0.15675

The coefficients b_i are given in appropriate units to express the astrophysical factor in MeV·barns.

cosmology, pure, and applied physics. Its cross section was measured in the Gamow energy region by several authors through direct methods. For the ^{3}He(d,p)^{4}He we used the direct data from Engstler et al. (1988), Krauss et al. (1987), Bonner et al. (1952), Zhichang et al. (1977), Geist et al. (1999), Möller and Besenbacher (1980), Erramli et al. (2005), Schroeder et al. (1989), and Aliotta et al. (2001). Together with other indirect methods, the THM also offered an alternative approach by means of a dedicated experiment which was performed using ^{6}Li as a Trojan Horse nucleus and extracting data from the quasi-free break-up channel to the ^{3}He(^{6}Li,pα)^{4}He reaction. The astrophysical factor was consequently measured for $E_{cm} = 0 \div 1$ MeV and fitted following Equation (6), as reported in La Cognata et al. (2005). The result is portrayed in **Figure 3** with red solid dots for THM data and full blue triangles for the direct data (Bonner et al., 1952; Krauss et al., 1987; Geist et al., 1999; Aliotta et al., 2001). The solid

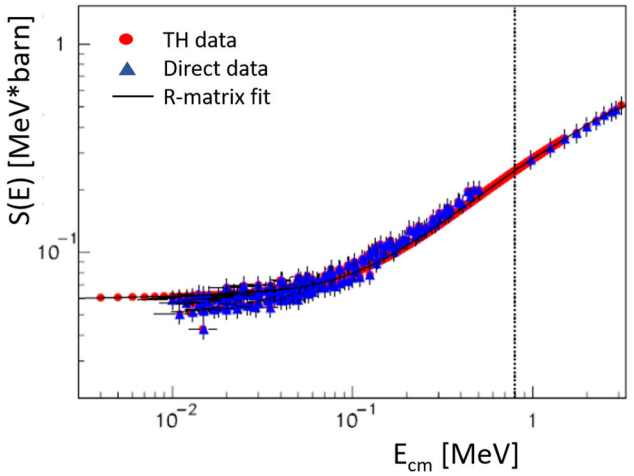

FIGURE 2 | Bare nucleus S-factor for the ^{2}H(d,n)^{3}He reaction obtained after putting together direct data (blue filled triangles) and with the THM ones (red filled circles) taken from Tumino et al. (2014). The solid line is the R-matrix fit to direct and indirect sets, as in section 3.1. The resulting parameters of the equivalent fit (polynomial plus Breit-Wigner) are listed in **Table 1**. Energy range of interest for BBN is marked by the vertical dotted line. The figure is adapted from Pizzone et al. (2014).

TABLE 2 | Table of fit parameters for the S-factors of the reactions ^{3}He(d,p)^{4}He and ^{7}Li(p,α)^{4}He measured in TH experiments using Equation (6).

Parameter	^{3}He(d,p)^{4}He	^{7}Li(p,α)^{4}He
b_1	1.7096	-2.8141×10^{-2}
b_2	−20.121	2.6584×10^{-2}
b_3	38.975	-2.7907×10^{-2}
b_4	−20.406	-1.9457×10^{-3}
b_5	–	9.4651×10^{-4}
b_6	–	-5.0471×10^{-4}
c_1	0.49562	0.3198
E_{R1}	0.24027	2.5765
Γ_{R1}	0.35011	1.1579
c_2	–	9.7244×10^{-2}
E_{R2}	–	5.0384
Γ_{R2}	–	0.79323
c_3	–	0.40377
E_{R3}	–	6.0159
Γ_{R3}	–	1.8935
c_4	–	1.9247
E_{R4}	–	8.0614
Γ_{R4}	–	4.0738

The coefficients b_i and c_i are given in appropriate units to express the astrophysical factor in MeV·barns. Energies and widths are in units of MeV.

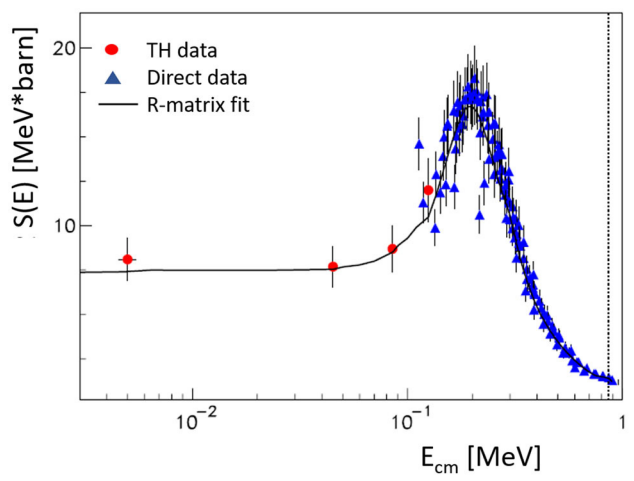

FIGURE 3 | Bare nucleus S(E)-factor for the ^{3}He(d,p)^{4}He process obtained with direct data (blue filled triangles) and with the THM (red filled dots) taken from La Cognata et al. (2005). Full description is reported in the text. The figure is adapted from Pizzone et al. (2014).

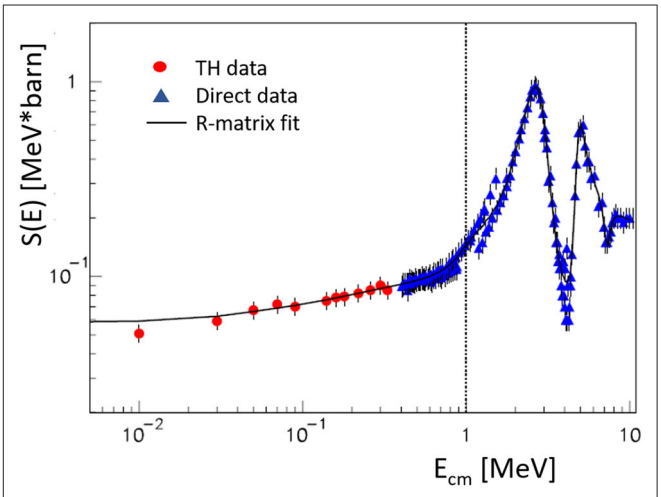

FIGURE 4 | Bare nucleus S(E)-factor for the ^{7}Li(p,α)^{4}He reaction obtained with direct data (blue triangles) and with the THM (red dots) taken from Lamia et al. (2012b). The solid line is an R-matrix fit to the overall direct and indirect data sets as discussed in the text. The figure is adapted from Pizzone et al. (2014).

line is an R-matrix fit to the direct and THM data, as described in section 3.1. The coefficients for the polynomial plus Breit-Wigner fit are reported in **Table 2**.

3.5. ^{7}Li(p,α)^{4}He

The process that contributes most to Li destruction in cosmic environments is the ^{7}Li(p,α)^{4}He. This is therefore the determinant in the challenging scenarios of both primordial and stellar lithium destruction. In the BBN the discrepancy of about a factor of three between its predictions and the observed Li abundances in halo stars represents the well-known and still debated "cosmological lithium problem." Many possible reasons for this discrepancy were suggested, from stellar depletion to non-standard Big Bang Nucleosynthesis models.

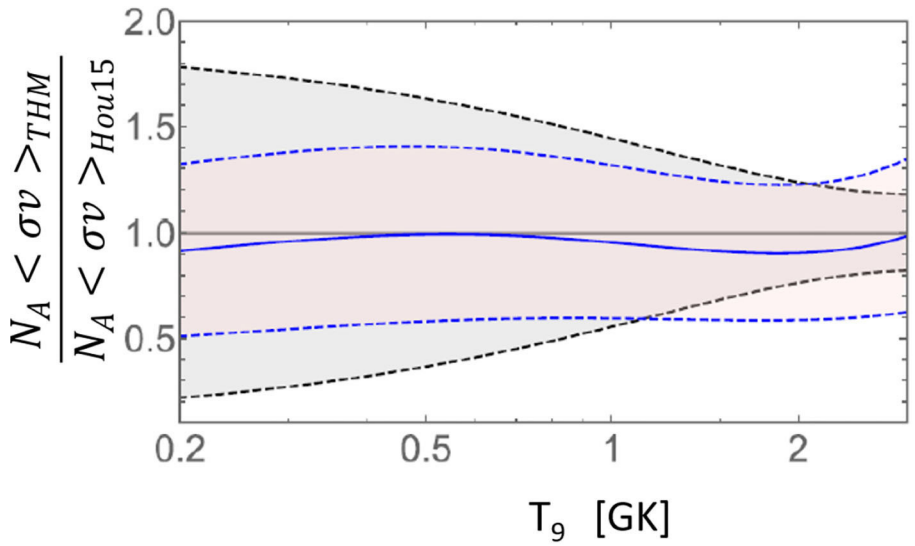

FIGURE 5 | Ratio of indirect (Lamia et al., 2019) on the direct (Hou et al., 2015) rates for ^{7}Be(n,α)^{4}He reaction, as a function of T_9. Rates are in agreement and the uncertainty is reduced thanks to the indirect measurement. The figure is adapted from Lamia et al. (2019).

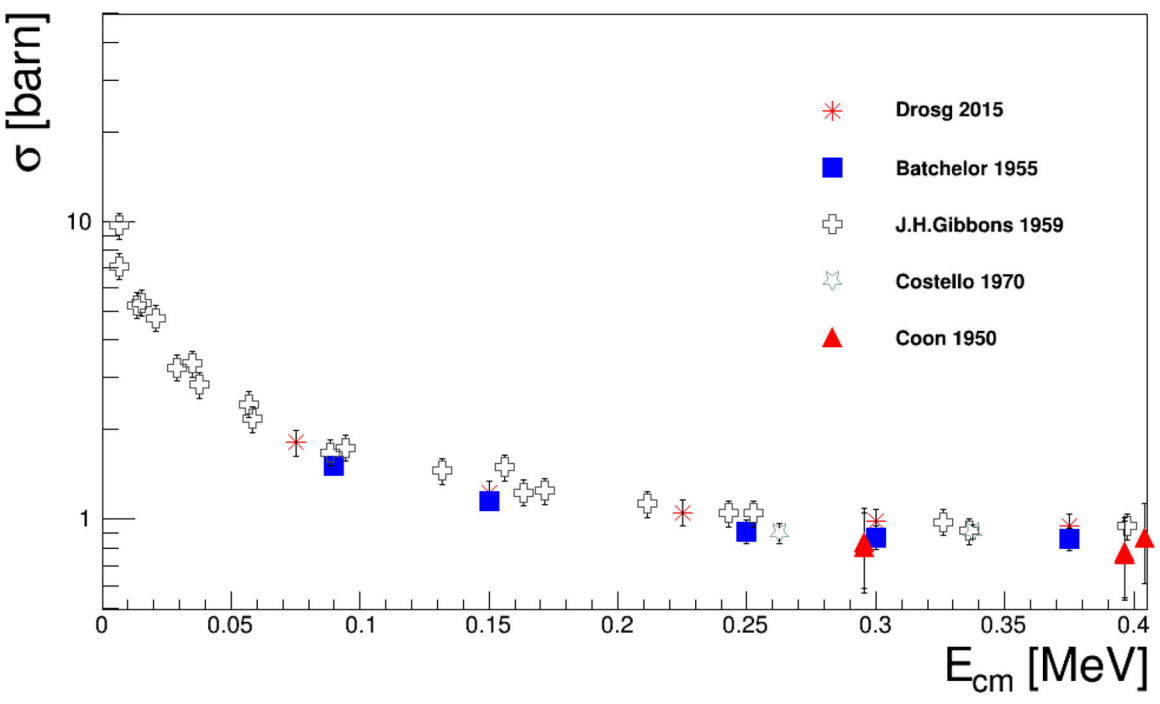

FIGURE 6 | Present day measurements of the ^{3}He(n,p)^{3}H cross section performed by different methods as reported in the text.

The ^{7}Li(p,α)^{4}He process was studied accurately in the last three decades either by means of direct methods (Engstler et al., 1988; Cruz et al., 2009) as well as by indirect ones (Aliotta et al., 2000; Lattuada et al., 2001; Pizzone et al., 2003; Lamia et al., 2012b), using the THM.

For this reaction we used data arising from the measurements performed by Schroeder et al. (1989), Mani et al. (1964), Cassagnou et al. (1962), Fiedler and Kunze (1967), Spinka et al. (1971), Rolfs and Kavanagh (1986), and Harmon (1989) as well as Engstler et al. (1992), Ciric et al. (1976), Spraker et al. (1999), Lee (1969), and Cruz et al. (2009). The most recent data set for the S(E) factor for this reaction, obtained with the THM after *d* quasi-free breakup, are plotted in **Figure 4** (Lamia et al., 2012a) as red dots while the direct ones are reported as blue triangles. The solid line represents a R-matrix fit to both direct and indirect data following the prescription in section 3.1. The parameters for an equivalent polynomial expansion are reported in **Table 2**.

3.6. ^{7}Be(n,α)^{4}He

The evaluation of this reaction rate has been the subject of many efforts, being one of the most influential on the ^{7}Li primordial abundance; it is simultaneously a difficult measurement, as it involves a neutron and a radioactive nucleus. For this reason literature data sets available are very few, and indirect methods have proved to be very helpful in this case (Hou et al., 2015; Kawabata et al., 2017). The use of the THM has led to a first reaction rate evaluation (Lamia et al., 2017) in which the cross section was derived from two measurements of ^{7}Li(p,α)^{4}He (described in section 3.5) using the charge symmetry hypothesis. Later, the S(E) of the ^{7}Be(n,α)^{4}He was obtained using the THM applied to the ^{2}H(^{7}Be,α ^{4}He)H measurement, performed at the EXOTIC facility, whose results are shown in Lamia et al. (2019). Here the experimental difficulties are partially overcome by the use of the deuteron target as a neutron virtual inducer, as already successfully tested in many other TH experiments (Lamia et al., 2008; Gulino et al., 2010; Spartá, 2016; Guardo et al., 2017).

TABLE 3 | Parameters of the reaction rates of Equation (7) for ^{2}H(d,p)^{3}H and ^{2}H(d,n)^{3}He evaluated from the S-factors from TH + direct measurements and from direct measurements.

a_i	^{2}H(d,p)^{3}H (TH + direct)	^{2}H(d,p)^{3}H (direct)	^{2}H(d,n)^{3}He (TH + direct)	^{2}H(d,n)^{3}He (direct)
a_1	14.996	20.255	16.1787	13.3209
a_2	−2.4127	−0.63670	−1.9372	−2.9254
a_3	2.8261×10^{-3}	7.7756×10^{-5}	2.0671×10^{-3}	4.0072×10^{-3}
a_4	−5.3256	−4.2722	−5.0226	−5.6687
a_5	6.6125	−1.0758	5.7866	10.1787
a_6	2.4656	2.3211	-2.039×10^{-2}	0.1550
a_7	−3.8702	−1.3062	−0.7935	−2.5764
a_8	1.6700	0.38274	0.2678	1.1967
a_9	−0.25851	-5.0848×10^{-2}	-3.1586×10^{-2}	−0.1807

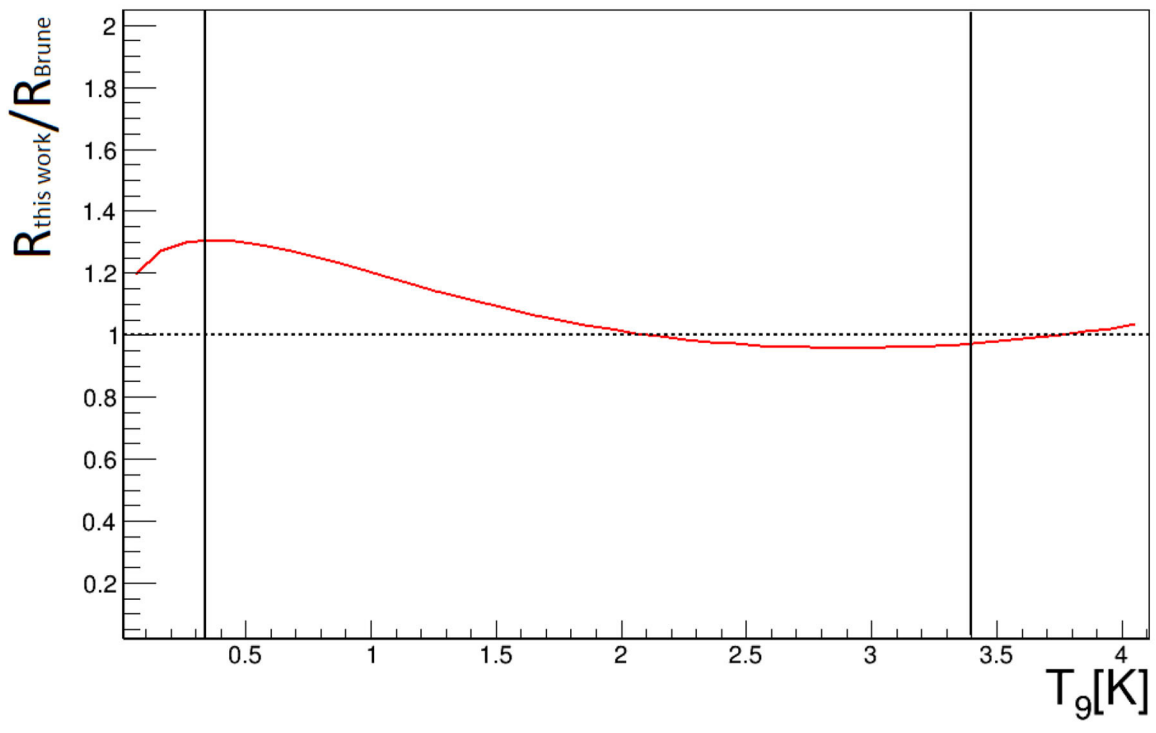

FIGURE 7 | Reaction rate for the ^{3}He(n,p)^{3}H calculated from THM data (red line) reported in Pizzone et al. (2020) compared with the calculations from Brune et al. (1999). The black vertical lines mark the temperature interval important for BBN.

The obtained reaction rate is shown in **Figure 5** as a ratio to the one obtained with the direct measurement of Hou et al. (2015), where they appear in fair agreement but the uncertainty is reduced in the indirect measurement.

3.7. ^{3}He(n,p)^{3}H

The ^{3}He(n,p)^{3}H reaction is one of the most important neutron-induced processes in BBN and has an important impact on the primordial ^{3}He and ^{7}Li abundances. At the temperatures important for predicting Big Bang yields, the reaction rate is determined by the cross section in the energy range $0.03 \leq E_{cm} \leq 0.3$ MeV. The first studies of this reaction were performed by Coon (1950) in the $0.1 \leq E_{cm} \leq 30$ MeV using a neutron beam. Errors turned out to be around 30%. Other measurements, more focused at lower energies, were conducted by Batchelor et al. (1955) (direct one, $0.1 \leq E_{cm} \leq 1$ MeV), Gibbons and Macklin (1959) (inverse measurement with larger uncertainties), and Costello et al. (1970) who measured directly in the range $0.3 \leq E_{cm} \leq 1.1$ MeV. The most recent data belong to Drosg and Otuka (2015) in a wide energy range. Reaction rates were then calculated for astrophysical applications by Brune et al. (1999) and Adahchour and Descouvemont (2003), which show a similar trend at temperatures of astrophysical interest while the reaction rate calculated by Caughlan and Fowler (1988) is sensitively higher. In the energy range of interest, the existing data are therefore sparse and mostly measured more than 50 years ago after facing tough experimental challenges, several times resulting in errors as high as 30%. This is clearly reported in **Figure 6**.

A measurement was recently performed by means of the THM with the same methodology reported for the other reactions. Data analysis is still in progress (Pizzone et al., 2020; Spampinato et al., 2020). A preliminary reaction rate, calculated upon

TABLE 4 | Parameters of the reaction rates of Equation (7) for ^{2}H(d,p)^{3}H and ^{2}H(d,n)^{3}He evaluated from the S-factors from TH + direct measurements and from direct measurements.

a_i	^{3}He(d,p)^{4}He (TH + direct)	^{3}He(d,p)^{4}He (direct)	^{7}Li(p,α)^{4}He (TH + direct)	^{7}Li(p,α)^{4}He (direct)
a_1	20.4005	38.9078	17.6686	17.5315
a_2	1.3850	5.9512	−1.1549	−1.397
a_3	-1.2982×10^{-2}	-1.6061×10^{-2}	-4.4059×10^{-4}	6.9425×10^{-4}
a_4	−4.1193	−2.1962	−8.5485	−8.7921
a_5	12.2954	−20.5983	4.6683	5.7430
a_6	−15.2114	1.5636	−0.7858	−2.4092
a_7	5.4147	0.7040	−2.3208	0.6434
a_8	−0.5048	−0.1877	2.0628	1.290
a_9	-4.3372×10^{-2}	2.9419×10^{-2}	−0.4747	−0.3467

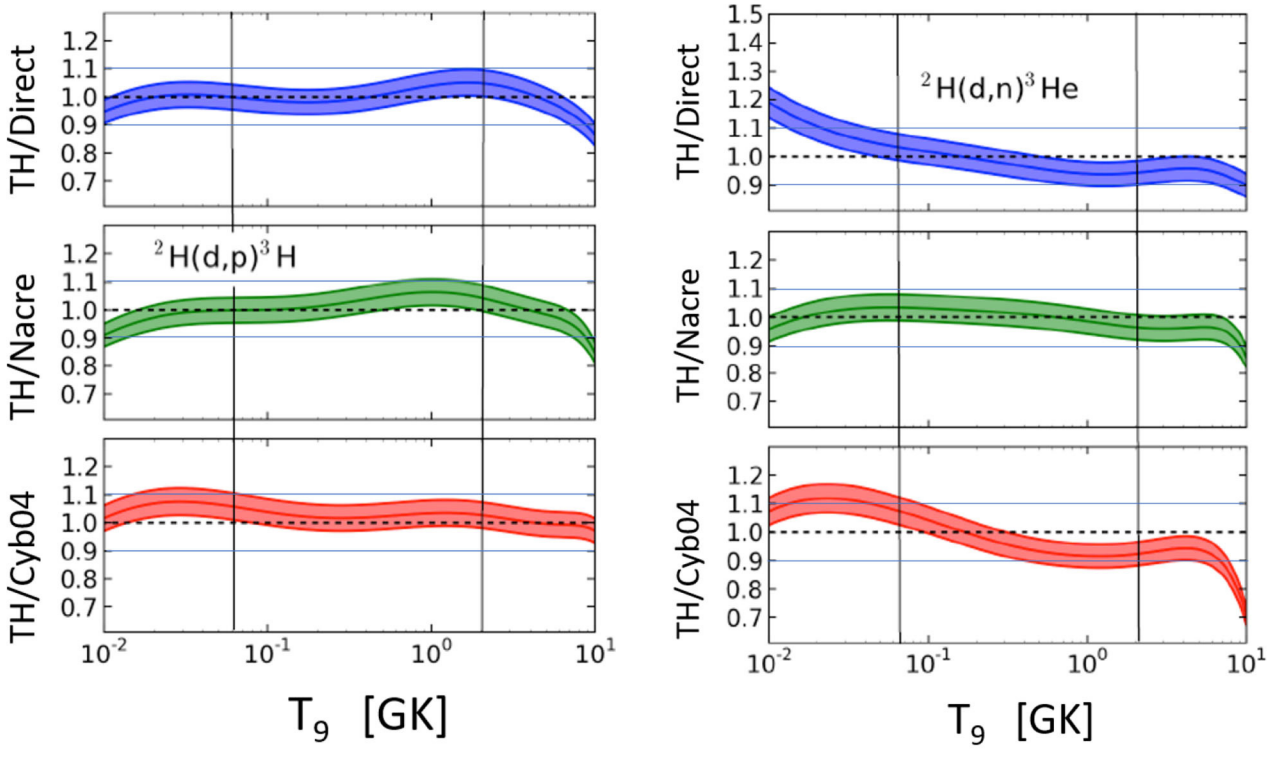

FIGURE 8 | (Left) Trojan Horse ^{2}H(d,p)^{3}H reaction rates as a ratio to the one obtained from direct data fit in the upper panel; the middle and lower panels show rates as a ratio to rates published in NACRE (Angulo et al., 1999; Cyburt, 2004). Lower and upper temperature of interest for BBN are marked by the vertical lines. Blue lines define the ±10% deviation from the unity. The figure is adapted from Pizzone et al. (2014). **(Right)** Same reaction rates ratios as in the left figure but for ^{2}H(d,n)^{3}He. The figure is adapted from Pizzone et al. (2014).

the data shown in Pizzone et al. (2020) is plotted in **Figure 7** with a comparison with the reaction rate published by Brune et al. (1999). In the energy region important for astrophysics a deviation up to 20% is present and will be investigated in future works.

3.8. From TH Data to Reaction Rates

These new compilation of direct and THM data has led to the numerical calculation of new reaction rates for the reactions in sections above, introducing the R-matrix fits in the reaction rate definition.

Then, these rates have been fitted with the Equation (7),

$$N_A \langle \sigma v \rangle = \exp\left[a_1 + a_2 \ln T_9 + \frac{a_3}{T_9} + a_4 T_9^{-1/3} + a_5 T_9^{1/3} + a_6 T_9^{2/3} + a_7 T_9 + a_8 T_9^{4/3} + a_9 T_9^{5/3}\right], \quad (7)$$

as it is the common procedure adopted in previous works (as for example Smith et al., 1993; Cyburt, 2004; Coc et al., 2012).

Equation (7) contains the relevant temperature dependence of the reaction rates during the BBN. Moreover, we also got the respective uncertainties in the rates including experimental errors in the calculations.

In **Table 3** the a_i coefficients for the ^{2}H(d,p)^{3}H and ^{2}H(d,n)^{3}He are listed, while the same are listed for ^{3}He(d,p)^{4}He and ^{7}Li(p,α)^{4}He in **Table 4**. The odd columns consider the rates coming from both THM and direct measurements, while the even ones consider the rates coming from the direct data sets (see next section for details).

TABLE 5 | Reaction rate table for ^{7}Be(n,α)^{4}He calculated from the TH measurement in Lamia et al. (2019) (*Adopted*) as a function of T_9 and expressed in $\frac{cm^3}{mol \cdot s}$.

T_9	Lower	Adopted	Upper
0.2	0.88×10^6	1.58×10^6	2.27×10^6
0.3	1.26×10^6	2.24×10^6	3.21×10^6
0.4	1.65×10^6	2.87×10^6	4.09×10^6
0.5	2.05×10^6	3.51×10^6	4.96×10^6
1	4.30×10^6	6.90×10^6	9.51×10^7
1.5	6.94×10^6	1.08×10^7	1.46×10^7
2	9.81×10^6	1.51×10^7	2.04×10^7
2.5	1.28×10^7	1.98×10^7	2.70×10^7
3	1.59×10^7	2.51×10^7	3.42×10^7

Lower *and* Upper *columns are the values obtained considering the error bars.*

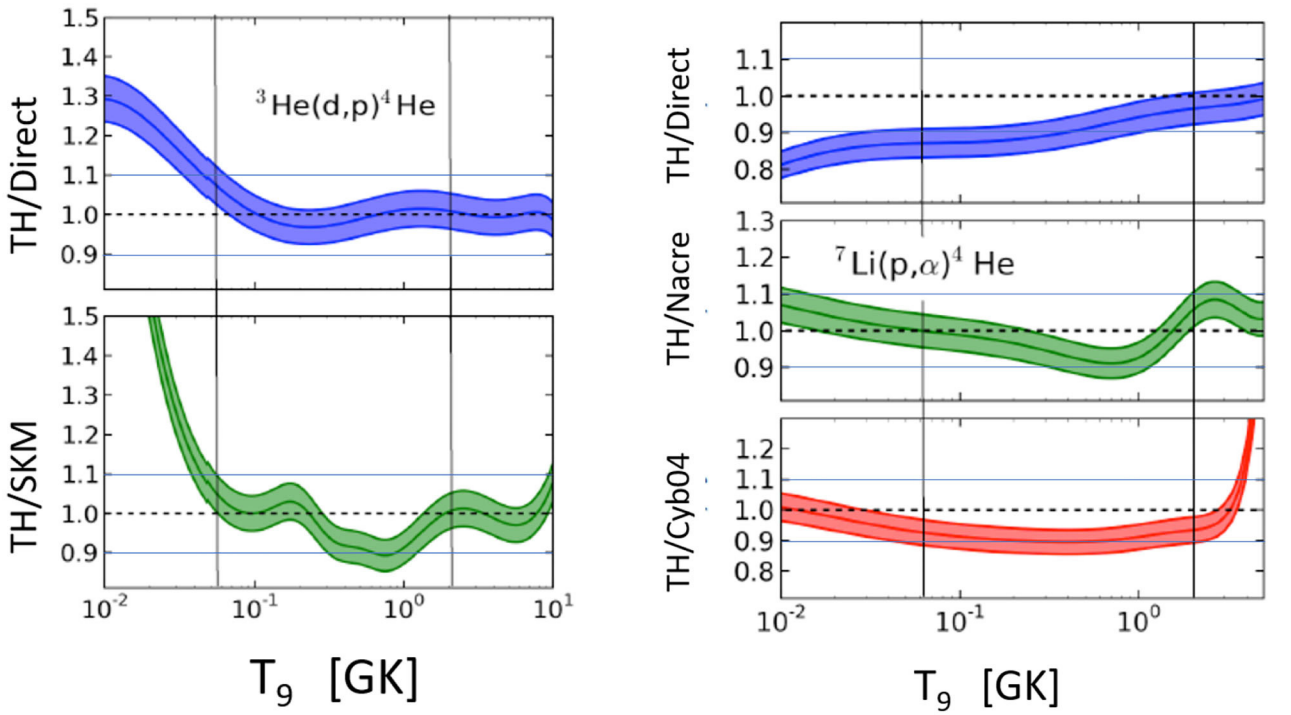

FIGURE 9 | (Left) Trojan Horse ^{3}He(d,p)^{4}He reaction rates as a ratio to the one obtained from direct data fit in the upper panel; the middle panel shows the same as a ratio to rate in Smith et al. (1993). Lower and upper temperature of interest for BBN are marked by the vertical lines. Blue lines define the ±10% deviation from the unity. The figure is adapted from Pizzone et al. (2014). **(Right)** ^{7}Li(p,α)^{4}He reaction rates ratios from THM to the one obtained from direct data (upper panel), while in the middle and lower panels there TH rates ratios with rates published in NACRE (Angulo et al., 1999; Cyburt, 2004). Lower and upper temperatures of interest for BBN are marked by the vertical lines. Blue lines define the ±10% deviation from the unity. The figure is adapted from Pizzone et al. (2014).

TABLE 6 | Primordial abundances as predicted by the Kawano code changing the reaction rate sets (described in the text) and compared with the observational results (last column).

Yields	Direct	^{2}H(d,p)^{3}H	^{2}H(d,n)^{3}He	^{3}He(d,p)^{4}He	^{7}Li(p,α)^{4}He	All	Observed
Y_p	0.249	$0.248^{+0.001}_{-0.001}$	$0.25^{+0.00}_{-0.00}$	$0.249^{+0.000}_{-0.000}$	$0.249^{+0.000}_{-0.000}$	$0.248^{+0.001}_{-0.002}$	0.256 ± 0.006
$\frac{D}{H}/10^{-5}$	2.645	$2.621^{+0.079}_{-0.046}$	$2.718^{+0.077}_{-0.036}$	$2.645^{+0.002}_{-0.007}$	$2.645^{+0.000}_{-0.000}$	$2.692^{+0.177}_{-0.070}$	2.82 ± 0.26
$\frac{^3He}{H}/10^{-6}$	9.748	$9.778^{+0.216}_{-0.076}$	$9.722^{+0.052}_{-0.092}$	$9.599^{+0.050}_{-0.003}$	$9.748^{+0.000}_{-0.000}$	$9.441^{+0.511}_{-0.466}$	$\geq 11. \pm 2.$
$\frac{^7Li}{H}/10^{-10}$	4.460	$4.460^{+0.001}_{-0.001}$	$4.470^{+0.010}_{-0.006}$	$4.441^{+0.190}_{-0.088}$	$4.701^{+0.119}_{-0.082}$	$4.683^{+0.335}_{-0.292}$	1.58 ± 0.31

TABLE 7 | Predicted primordial abundances of ^{7}Li, ^{7}Be, and their sum, inserting reaction rates from Pizzone et al. (2014) (**Table 6**) and the ^{7}Be(n,α)^{4}He from Hou et al. (2015) in the first line, Lamia et al. (2017) in the second, and Lamia et al. (2019) in the third.

Reaction rate	^{7}Li/H	^{7}Be/H	^{7}Li/H+^{7}Be/H
TH2014 + Hou15	2.840×10^{-11}	4.149×10^{-10}	4.433×10^{-10}
TH2014 + Lamia17	2.845×10^{-11}	4.156×10^{-10}	4.441×10^{-10}
TH2014 + Lamia19	2.670×10^{-11}	3.990×10^{-10}	4.260×10^{-10}

To avoid the enhancement due to the electron screening, it is worth noticing that direct data for ^{3}He(d,p)^{4}He and ^{7}Li(p,α)^{4}He were considered for energies above 100 keV and above 10 keV for ^{2}H(d,p)^{3}H and ^{2}H(d,n)^{3}He.

Figures 8, **9** show the ratio of the THM reaction rates ("TH") with those from other compilations, meaning our own fit to existing direct reaction capture data ("Direct"), the NACRE compilation (Angulo et al., 1999) ("Nacre"), from Smith et al. (1993) (SKM), and from Cyburt (2004) ("Cyb04"). Here the error bands are related to the error bars of the associated THM + direct S-factors.

For the four reactions considered, deviations up to 20% from previous compilations have been obtained, and for ^{7}Li(p,α)^{4}H above $T_9 \sim 4$, a very large discrepancy with the reaction rate by Cyburt (2004) was found.

The ^{7}Be(n,α)^{4}He rate, discussed in section 3.6, has been compared to the direct and recent one in Hou et al. (2015), with the ratio of the two rates is shown in **Figure 5**. The TH rate is reported in tabular form in **Table 5** as a function of T_9 and with the *Lower* and *Upper* values, which take into account the error bars.

4. RESULTS

The cross section measurements obtained with THM in the energy range of interest for BBN were used to evaluate the relative reaction rates; the parameters are listed in **Tables 3**–**5**. These have been put in a revised BBN code originally from Kawano and discussed in Pizzone et al. (2014).

The observational ^{4}He mass fraction, $Y_p = 0.2565 \pm 0.006$ is from Izotov and Thuan (2010). The deuterium abundance is the mean average equivalent to $\Omega \cdot h^2_{BBN} = 0.0213 \pm 0.0013$ from O'Meara et al. (2006). As for the ^{3}He, the abundance is adopted from Bania et al. (2002) as a lower limit to the primordial abundance; finally, ^{7}Li abundance is reported in Sbordone et al. (2010) from the observations of *lithium plateau* stars.

Primordial abundances are then calculated using different reaction rate sets: the first column of **Table 6** shows the results from our own fit to the world direct data, while in the second column direct data for ^{2}H(d,p)^{3}H has been replaced by TH data from Tumino et al. (2014) (in section 3.2).

The same holds for the other columns, adopting the reaction rate for ^{2}H(d,n)^{3}He (section 3.3), ^{3}He(d,p)^{4}He (section 3.4), and ^{7}Li(p,α)^{4}He (section 3.5), respectively, keeping the rest of the rates coming from direct measurements. The values in the column marked with *All* are obtained using the four TH reaction rates described in the sections mentioned above. These values from the code are affected by an uncertainty due to the propagation of the experimental errors. Finally, they can be compared to the last column, which reports the primordial abundances from observations.

Similar calculations have been carried out also for the ^{7}Be(n,α)^{4}He reaction in order to get the primordial values of lithium and beryllium abundances. **Table 7** reports results from different calculations. In particular, ^{7}Be(n,α)^4 rates from different sources have been included in the THM rates reported in Pizzone et al. (2014): from Hou et al. (2015) in the first line, from Lamia et al. (2017) the second line, and from Lamia et al. (2019) in the third line.

5. CONCLUSIONS

Primordial abundances in **Table 6** are obtained from direct and indirect reaction rates, while values in the last column refer to the observations. It can be seen that no relevant changes are obtained with these different sets of rates.

A similar result is the one proposed in **Table 7**, where it is worth noticing that all the three values calculated for lithium abundances are still larger than the one resulting from halo-stars observation in Sbordone et al. (2010) of $1.58^{+0.35}_{-0.28}$. This definitely leads to the idea that the cosmological lithium problem is not imputable to systematic errors in nuclear measurements, and no nuclear solution to the cosmological lithium problem can be foreseen. Proposed alternative ideas can be found in Bertulani (2019) or Mathews et al. (2020). Further measurements, such as the ^{7}Be(n,p)^{7}Li with THM, will probably be helpful to strengthen this result.

AUTHOR CONTRIBUTIONS

Nuclear data were collected, elaborated, and fitted by RS and RP. LL and SH took care of the ^{7}Be(n,p)^{7}Li data analysis and the relative reaction rate calculation. RP, AT, RS, and LL analyzed the THM data available in the present paper. CB and SH performed the primordial nucleosynthesis calculations. The paper was written by RS and corrected by all authors.

FUNDING

SH was supported by the National Natural Science Foundation of China under Grant No. 11705244 and the Youth Innovation Promotion Association of Chinese Academy of Sciences under Grant No. 2019406. CB was supported by U.S. DOE Grant No. DE-FG02-08ER41533 and the U.S. NSF Grant No. 1415656. This work has been partially supported by grant Finanziamenti di linea 2 and Starting grant 2020 by University of Catania.

REFERENCES

Adahchour, A., and Descouvemont, P. (2003). R-matrix analysis of the ^{3}He(n, p)^{3}H and ^{7}Be(n, p)^{7}Li reactions. *J. Phys. G Nucl. Phys.* 29, 395–403. doi: 10.1088/0954-3899/29/2/315

Aliotta, M., Raiola, F., Gyürky, G., Formicola, A., Bonetti, R., Broggini, C., et al. (2001). Electron screening effect in the reactions ^{3}He(d,p)^{4}He and d(^{3}He,p)^{4}He*. *Nucl. Phys. A* 690, 790–800. doi: 10.1016/S0375-9474(01)00366-9

Aliotta, M., Spitaleri, C., Lattuada, M., Musumarra, A., Pizzone, R. G., Tumino, A., et al. (2000). Improved information on electron screening in ^{7}Li(p,α)α using the Trojan-horse method. *Eur. Phys. J. A* 9, 435–437. doi: 10.1007/s100500070001

Angulo, C., Arnould, M., Rayet, M., Descouvemont, P., Baye, D., Leclercq-Willain, C., et al. (1999). A compilation of charged-particle induced thermonuclear reaction rates. *Nucl. Phys. A* 656, 3–183. doi: 10.1016/S0375-9474(99)00030-5

Arnold, W. R., Phillips, J. A., Sawyer, G. A., Stovall, E. J., and Tuck, J. L. (1954). Cross sections for the reactions D(d, p)T, D(d, n)He^{3}, T(d, n)He^{4}, and He^{3}(d, p)He^{4} below 120 keV. *Phys. Rev.* 93, 483–497. doi: 10.1103/PhysRev.93.483

Aver, E., Olive, K. A., and Skillman, E. D. (2015). The effects of He I λ10830 on helium abundance determinations. *J. Cosmol. Astropart. Phys.* 2015:011. doi: 10.1088/1475-7516/2015/07/011

Azuma, R. E., Uberseder, E., Simpson, E. C., Brune, C. R., Costantini, H., de Boer, R. J., et al. (2010). AZURE: an R-matrix code for nuclear astrophysics. *Phys. Rev. C* 81:045805. doi: 10.1103/PhysRevC.81.045805

Bania, T., Rood, R. T., and Balser, D. S. (2002). The cosmological density of baryons from observations of 3 He+ in the milky way. *Nature* 415, 54–57. doi: 10.1038/415054a

Batchelor, R., Aves, R., and Skyrme, T. H. R. (1955). Helium-3 filled proportional counter for neutron spectroscopy. *Rev. Sci. Instr.* 26, 1037–1047. doi: 10.1063/1.1715182

Belov, A. S., Kusik, V. E., and Ryabov, Y. V. (1990). The nuclear fusion for the reactions ^{2}H(d,n)^{3}He, ^{2}H(d,γ)^{4}He at low deuterons energy and cold nuclear fusion. *Il Nuovo Cim. A* 103, 1647–1650. doi: 10.1007/BF02820309

Bertulani, C. A. (2019). Big bang nucleosynthesis and the lithium problem. *J. Phys. Conf. Series* 1291:012002. doi: 10.1088/1742-6596/1291/1/012002

Boesgaard, A. M., McGrath, E. J., Lambert, D. L., and Cunha, K. (2004). Boron benchmarks for the galactic disk. *Astrophys. J.* 606, 306–318. doi: 10.1086/382672

Bonner, T. W., Conner, J. P., and Lillie, A. B. (1952). Cross section and angular distribution of the He3(d,p)He4 nuclear reaction. *Phys. Rev.* 88:473. doi: 10.1103/PhysRev.88.473

Booth, D. L., Preston, G., and Shaw, P. F. D. (1956). The cross section and angular distributions of the dd reactions between 40 and 90 keV. *Proc. Phys. Soc. A* 69:265. doi: 10.1088/0370-1298/69/3/309

Brown, R. E., and Jarmie, N. (1990). Differential cross sections at low energies for H2(d,p)3D and h2(d,n)^{3}He. *Phys. Rev. C* 41:1391. doi: 10.1103/PhysRevC.41.1391

Brune, C. R., Hahn, K. I., Kavanagh, R. W., and Wrean, P. R. (1999). Total cross section of the 3 H (p, n) 3 he reaction from threshold to 4.5 MeV. *Phys. Rev. C* 60:015801. doi: 10.1103/PhysRevC.60.015801

Bystritsky, V. M., Gerasimov, V. V., Krylov, A. R., Parzhitsktii, S. S., Il'guzin, D. A., Ananin, P. S., et al. (2010). Using a hall accelerator to investigate d(d,n)^{3}He and d(p,γ)^{3}He reactions in the astrophysical energy region. *Bull. Russ. Acad. Sci. Phys.* 74, 531–534. doi: 10.3103/S1062873810040234

Cassagnou, Y., Jeronymo, J. M. F., Mani, G. S., Sadeghi, A., and Forsyth, P. D. (1962). The li7(p,α)α reaction. *Nucl. Phys.* 33, 449–457. doi: 10.1016/0029-5582(62)90537-0

Caughlan, G. R., and Fowler, W. A. (1988). Thermonuclear reaction rates v. *Atomic Data Nucl. Data Tables* 40, 283–334. doi: 10.1016/0092-640X(88)90009-5

Cayrel, R., Spite, M., Spite, F., Vangioni-Flam, E., Cassé, M., and Audouze, J. (1999). New high S/N observations of the (^{6}Li)/(7) Li blend in HD 84937 and two other metal-poor stars. *arXiv* astro-ph/9901205.

Cherubini, S., Gulino, M., Spitaleri, C., Rapisarda, G. G., La Cognata, M., Lamia, L., et al. (2015). First application of the trojan horse method with a radioactive ion beam: Study of the 18f(p,α)15o reaction at astrophysical energies. *Phys. Rev. C* 92:015805. doi: 10.1103/PhysRevC.92.015805

Ciric, D. M., Popic, R. V., Zakula, R. B., Stepancic, B. Z., Aleksic, M. R., and Seytajcic, J. P. (1976). The interaction of ^{7}Li isotope with low energy proton and triton beams. *Rev. Sci. Res. Czech Rep.* 6:115.

Coc, A., Goriely, S., Xu, Y., Saimpert, M., and Vangioni, E. (2012). Standard big bang nucleosynthesis up to CNO with an improved extended nuclear network. *Astrophys. J.* 744:158. doi: 10.1088/0004-637X/744/2/158

Cook, C. F., and Smith, J. R. (1953). Cross section for the reaction D(d,p)H3. *Phys. Rev.* 89:785. doi: 10.1103/PhysRev.89.785

Cooke, R. J., Pettini, M., and Steidel, C. C. (2018). One percent determination of the primordial deuterium abundance. *Astrophys. J.* 855:102. doi: 10.3847/1538-4357/aaab53

Coon, J. H. (1950). Disintegration of he3 by fast neutrons. *Phys. Rev.* 80:488. doi: 10.1103/PhysRev.80.488

Costello, D. G., Friesenhahn, S. J., and Lopez, W. M. (1970). ^{3}He(n,p)t cross section from 0.3 to 1.16 MeV. *Nucl. Sci. Eng.* 39, 409–410. doi: 10.13182/NSE70-A20005

Cruz, J., Fonseca, M., Luis, H., Mateus, R., Marques, H., Jesus, A., et al. (2009). Production and characterization of thin ^{7}Li targets fabricated by ion implantation. *Nucl. Instr. Methods Phys. Res. B* 267, 478–481. doi: 10.1016/j.nimb.2008.11.028

Cvetinović, A., Spitaleri, C., Spartá, R., Rapisarda, G. G., Puglia, S. M. R., La Cognata, M., et al. (2018). Trojan horse measurement of the b 10 (p, α 0) be 7 cross section in the energy range from 3 keV to 2.2 MeV. *Phys. Rev. C* 97:065801. doi: 10.1103/PhysRevC.97.065801

Cyburt, R. H. (2004). Primordial nucleosynthesis for the new cosmology: determining uncertainties and examining concordance. *Phys. Rev. D* 70:023505. doi: 10.1103/PhysRevD.70.023505

Cyburt, R. H., Fields, B. D., Olive, K. A., and Yeh, T.-H. (2016). Big bang nucleosynthesis: present status. *Rev. Mod. Phys.* 88:015004. doi: 10.1103/RevModPhys.88.015004

Davenport, P. A., Jeffries, T. O., Owen, M. E., Price, F. V., and Roaf, D. (1953). The dd cross-section and angular distribution between 55 and 430 keV. *Proc. R. Soc. Lond. A Math. Phys. Sci.* 216, 66–71. doi: 10.1098/rspa.1953.0007

Davidenko, V. A., Kucher, A. M., Pogrebov, I. S., and u, F., T. J. (1957). Total cross section measurement of D(d,n)^{3}He reaction in energy range 20 to 220 keV. *Soviet Atomic Energy Suppl.* 5:7.

Drosg, M., and Otuka, N. (2015). *Evaluation of the Absolute Angle-Dependent Differential Neutron Production Cross Sections by the Reactions ^{3}H(p,n)^{3}He, ^{1}H(t, n)^{3}He, ^{2}H(d,n)^{3}He, ^{3}H(d,n)^{4}He, and ^{2}H(t,n)^{4}He and of the Cross Sections of Their Time-Reversed Counterparts Up to 30 MeV and Beyond.* INDC (AUS)-0019 (Vienna: International Atomic Energy Agency).

Engstler, S., Krauss, A., Neldner, K., Rolfs, C., Schröder, U., and Langanke, K. (1988). Effects of electron screening on the ^{3}He(d,p)^{4}He low-energy cross sections. *Phys. Lett. B* 202, 179–184. doi: 10.1016/0370-2693(88)90003-2

Engstler, S., Raimann, G., Angulo, C., Greife, U., Rolfs, C., Schröder, U., et al. (1992). Test for isotopic dependence of electron screening in fusion reactions. *Phys. Lett. B* 279, 20–24. doi: 10.1016/0370-2693(92)91833-U

Erramli, H., Sauvage, T., Rhazi, M., and Misdaq, M. A. (2005). Measurement of the ^{3}He(d,p)^{4}He nuclear reaction cross section by coincidence detection of alphas and protons: application to the determination of the ^{3}He desorption rate from helium bubbles in silicon. *Phys. Chem. News* 23, 67–72.

Fiedler, O., and Kunze, P. (1967). Wirkungsquerschnitte der kernreaktionen ^{6}Li(p,α)^{3}He und ^{7}Li(p,α)^{4}He bei kleinsten energien. *Nucl. Phys. A* 96, 513–520. doi: 10.1016/0375-9474(67)90601-X

Ganeev, A. S., Govorov, A. M., Osetinskii, G. M., Rakivnenko, A. N., Sizov, I. V., and S, S. V. (1957). The D-D reaction in the deuteron energy range 100–1000 keV. *Soviet Atomic Energy Suppl.* 5:21.

Geist, W. H., Brune, C. R., Karwowski, H. J., Ludwig, E. J., Veal, K. D., and Hale, G. M. (1999). The ^{3}He(d,p)^{4}He reaction at low energies. *Phys. Rev. C* 60:054003. doi: 10.1103/PhysRevC.60.054003

Gibbons, J. H., and Macklin, R. L. (1959). Total neutron yields from light elements under proton and alpha bombardment. *Phys. Rev.* 114:571. doi: 10.1103/PhysRev.114.571

Greife, U., Gorris, F., Junker, M., Rolfs, C., and Zahnow, D. (1995). Oppenheimer-phillips effect and electron screening in D + D fusion reactions. *Z. Phys. A Hadrons Nuclei* 351, 107–112. doi: 10.1007/BF01292792

Guardo, G. L., Spitaleri, C., Lamia, L., Gulino, M., La Cognata, M., Tang, X., et al. (2017). Assessing the near threshold cross section of the O17(n, α)C14 reaction by means of the trojan horse method. *Phys. Rev. C* 95:025807. doi: 10.1103/PhysRevC.95.025807

Gulino, M., Spitaleri, C., Cherubini, S., Crucillá, V., La Cognata, M., Lamia, L., et al. (2010). Study of the ^{6}Li(n,α)^{3}H reaction via the ^{2}H quasi-free break-up. *J. Phys. G Nucl. Part. Phys.* 37:125105. doi: 10.1088/0954-3899/37/12/125105

Harmon, J. F. (1989). Cross sections and astrophysical s factor for the ^{7}Li (p, α) reaction at low energies. *Nucl. Instr. Methods Phys. Res. B* 40, 507–509. doi: 10.1016/0168-583X(89)91033-1

Hofstee, M. A., Pallone, A. K., Cecil, F. E., McNeil, J. A., and Galovich, C. S. (2001). Measurement of low energy (d, n) reactions on light nuclei important to astrophysics. *Nucl. Phys. A* 688, 527–529. doi: 10.1016/S0375-9474(01)00777-1

Hou, S. Q., He, J. J., Kubono, S., and Chen, Y. S. (2015). Revised thermonuclear rate of Be7(n, α)He4 relevant to big-bang nucleosynthesis. *Phys. Rev. C* 91:055802. doi: 10.1103/PhysRevC.91.055802

Izotov, Y. I., and Thuan, T. X. (2010). The primordial abundance of ^{4}He: evidence for non-standard big bang nucleosynthesis. *Astrophys. J.* 710, L67–L71. doi: 10.1088/2041-8205/710/1/L67

Kawabata, T., Fujikawa, Y., Furuno, T., Goto, T., Hashimoto, T., Ichikawa, M., et al. (2017). Time-reversal measurement of the p-wave cross sections of the be 7(n, α)He4 reaction for the cosmological Li problem. *Phys. Rev. Lett.* 118:052701. doi: 10.1103/PhysRevLett.118.052701

Kiss, G. G., La Cognata, M., Spitaleri, C., Yarmukhamedov, R., Wiedenhöver, I., Baby, L. T., et al. (2020). Astrophysical s-factor for the ^{3}He(,)7Be reaction via the asymptotic normalization coefficient (ANC) method. *Phys. Lett. B* 807:135606. doi: 10.1016/j.physletb.2020.135606

Krauss, A., Becker, H. W., Trautvetter, H. P., Rolfs, C., and Brand, K. (1987). Low-energy fusion cross sections of D + D and D + ^{3}He reactions. *Nucl. Phys. A* 465, 150–172. doi: 10.1016/0375-9474(87)90302-2

La Cognata, M., Spitaleri, C., Tumino, A., Typel, S., Cherubini, S., Lamia, L., et al. (2005). Bare-nucleus astrophysical factor of the ^{3}He(d,p)^{4}He reaction via the "Trojan horse" method. *Phys. Rev. C* 72:065802. doi: 10.1103/PhysRevC.72.065802

Lamia, L., La Cognata, M., Spitaleri, C., Irgaziev, B., and Pizzone, R. G. (2012a). Influence of the d-state component of the deuteron wave function on the application of the Trojan horse method. *Phys. Rev. C* 85:025805. doi: 10.1103/PhysRevC.85.025805

Lamia, L., Mazzocco, M., Pizzone, R. G., Hayakawa, S., La Cognata, M., Spitaleri, C., et al. (2019). Cross-section measurement of the cosmologically relevant ^{7}Be(n,α)^{4}He reaction over a broad energy range in a single experiment. *Astrophys. J.* 879:23. doi: 10.3847/1538-4357/ab2234

Lamia, L., Spitaleri, C., Bertulani, C. A., Hou, S. Q., La Cognata, M., Pizzone, R. G., et al. (2017). On the determination of the ^{7}Be(n, α)^{4}He reaction cross section at BBN energies. *Astrophys. J.* 850:175. doi: 10.3847/1538-4357/aa965c

Lamia, L., Spitaleri, C., Carlin, N., Cherubini, S., Del Szanto, M. G., Gulino, M., et al. (2008). Indirect study of (p,α) and (n,α) reactions induced on boron isotopes. *Nuovo Cim. C Geophys. Space Phys. C* 31, 423–431. doi: 10.1393/ncc/i2009-10303-2

Lamia, L., Spitaleri, C., La Cognata, M., Palmerini, S., and Pizzone, R. G. (2012b). Recent evaluation of the ^{7}Li(p,α)^{4}He reaction rate at astrophysical energies via the Trojan Horse method. *Astron. Astrophys.* 541:A158. doi: 10.1051/0004-6361/201219014

Lattuada, M., Pizzone, R. G., Typel, S., Figuera, P., Miljanić, D., Musumarra, A., et al. (2001). The bare astrophysical S(E) factor of the ^{7}Li(p, α)α reaction. *Astrophys. J.* 562, 1076–1080. doi: 10.1086/323868

Lee, C. C. (1969). *A Study on the ^{7}Li+P and ^{6}Li+D Nuclear Reactions*. Technical report, Yonsei University, Seoul, South Korea.

Leonard, D. S., Karwowski, H., Brune, C., Fisher, B., and Ludwig, E. (2006). Precision measurements of H2(d,p)H3 and H2(d,n)He3 total cross sections at big bang nucleosynthesis energies. *Phys. Rev. C* 73:045801. doi: 10.1103/PhysRevC.73.045801

Mani, G. S., Freeman, R., Picard, F., Sadeghi, A., and Redon, D. (1964). Study of the reaction Li7(p,α)α up to 12 MeV proton energy. *Nucl. Phys.* 60, 588–592. doi: 10.1016/0029-5582(64)90095-1

Mathews, G. J., Kedia, A., Sasankan, N., Kusakabe, M., Luo, Y., Kajino, T., et al. (2020). "Cosmological solutions to the lithium problem," in *Proceedings of the 15th International Symposium on Origin of Matter and Evolution of Galaxies (OMEG15)* (Beijing), 011033. doi: 10.7566/JPSCP.31.011033

McNeill, K. G., and Keyser, G. M. (1951). The relative probabilities and absolute cross sections of the d-d reactions. *Phys. Rev.* 81:602. doi: 10.1103/PhysRev.81.602

Moffatt, J., Roaf, D., and Sanders, J. H. (1952). The D-D cross-section and angular distribution below 50 keV. *Proc. R. Soc. Lond. A* 212:220. doi: 10.1098/rspa.1952.0077

Möller, W., and Besenbacher, F. (1980). A note on the ^{3}He+ d nuclear-reaction cross section. *Nucl. Instr. Methods* 168, 111–114. doi: 10.1016/B978-1-4832-2889-1.50020-7

O'Meara, J. M., Burles, S., Prochaska, J. X., Prochter, G. E., Bernstein, R. A., and Burgess, K. M. (2006). The deuterium-to-hydrogen abundance ratio toward the QSO SDSS j155810.16-003120.0. *Astrophys. J. Lett.* 649:L61. doi: 10.1086/508348

Pinsonneault, M. (1997). Mixing in stars. *Annu. Rev. Astron. Astrophys.* 35, 557–605. doi: 10.1146/annurev.astro.35.1.557

Pitrou, C., Coc, A., Uzan, J.-P., and Vangioni, E. (2018). Precision big bang nucleosynthesis with improved helium-4 predictions. *Phys. Rep.* 754, 1–66. doi: 10.1016/j.physrep.2018.04.005

Pizzone, R. G., Roeder, B. T., McCleskey, M., Trache, L., Tribble, R. E., Spitaleri, C., et al. (2016). Trojan horse measurement of the ^{18}F(p,α)^{15}O astrophysical s(e)-factor. *Eur. Phys. J. A* 52:24. doi: 10.1140/epja/i2016-16024-3

Pizzone, R. G., Spampinato, C., Spartá, R., Couder, M., Tan, W., Burjan, V., et al. (2020). Indirect measurement of the ^{3}He(n,p)^{3}H reaction cross section at Big Bang energies. *Eur. Phys. J. A* 56:199. doi: 10.1140/epja/s10050-020-00212-x

Pizzone, R. G., Spartá, R., Bertulani, C. A., Spitaleri, C., La Cognata, M., Lalmansingh, J., et al. (2014). Big bang nucleosynthesis revisited via trojan horse method measurements. *Astrophys. J.* 786:112. doi: 10.1088/0004-637X/786/2/112

Pizzone, R. G., Spitaleri, C., Bertulani, C. A., Mukhamedzhanov, A. M., Blokhintsev, L., La Cognata, M., et al. (2013). Updated evidence of the trojan horse particle invariance for the ^{2}H(d,p)^{3}H reaction. *Phys. Rev. C* 87:025805. doi: 10.1103/PhysRevC.87.025805

Pizzone, R. G., Spitaleri, C., Lattuada, M., Cherubini, S., Musumarra, A., Pellegriti, M. G., et al. (2003). Proton-induced lithium destruction cross-section and its astrophysical implications. *Astron. Astrophys.* 398, 423–427. doi: 10.1051/0004-6361:20021700

Planck Collaboration, Aghanim, N., Akrami, Y., Ashdown, M., Aumont, J., Baccigalupi, C., et al. (2018). Planck 2018 results. VI. Cosmological parameters. *arXiv* 1807.06209.

Preston, G., Shaw, P. F. D., and Young, S. A. (1954). The cross-sections and angular distributions of the D1,0D reactions between 150 and 450 keV. *Proc. R. Soc. Lond. A* 226, 206–216. doi: 10.1098/rspa.1954.0249

Raiola, F., Migliardi, P., Gyürky, G., Aliotta, M., Formicola, A., Bonetti, R., et al. (2002). Enhanced electron screening in D(d,p)T for deuterated TA. *Eur. Phys. J. A Hadrons Nuclei* 13, 377–382. doi: 10.1007/s10050-002-8766-5

Rapisarda, G. G., Spitaleri, C., Cvetinović, A., Spartá, R., Cherubini, S., Guardo, G. L., et al. (2018). Study of the ^{10}B(p,α_1)^{7}Be reaction by means of the Trojan Horse method. *Eur. Phys. J. A* 54:189. doi: 10.1140/epja/i2018-12622-3

Rinollo, A., Romano, S., Spitaleri, C., Bonomo, C., Cherubini, S., Del Zoppo, A., et al. (2005). Measurement of cross section and astrophysical factor of the D(d, p)T reaction using the trojan horse method. *Nucl. Phys. A* 758, 146–149. doi: 10.1016/j.nuclphysa.2005.05.030

Rolfs, C., and Kavanagh, R. W. (1986). The ^{7}Li(p,α)^{4}He cross section at low energies. *Nucl. Phys. A* 455, 179–188. doi: 10.1016/0375-9474(86)90351-9

Sbordone, L., Bonifacio, P., Caffau, E., Ludwig, H.-G., Behara, N. T., Hernández, J. G., et al. (2010). The metal-poor end of the spite plateau-I. Stellar parameters, metallicities, and lithium abundances. *Astron. Astrophys*. 522:A26. doi: 10.1051/0004-6361/200913282

Schroeder, U., Engstler, S., Krauss, A., Neldner, K., Rolfs, C., Somorjai, E., et al. (1989). Search for electron screening of nuclear reactions at sub-coulomb energies. *Nucl. Instr. Methods Phys. Res. B* 40, 466–469. doi: 10.1016/0168-583X(89)91022-7

Schulte, R. L., Cosack, M., Obst, A. W., and Weil, J. L. (1972). ^{2}H+ reactions from 1.96 to 6.20 MeV. *Nucl. Phys. A* 192, 609–624. doi: 10.1016/0375-9474(72)90093-0

Sergi, M. L., Spitaleri, C., La Cognata, M., Lamia, L., Pizzone, R. G., Rapisarda, G. G., et al. (2015). Improvement of the high-accuracy ^{17}O(p,α)^{14}N reaction-rate measurement via the Trojan Horse method for application to ^{17}O nucleosynthesis. *Phys. Rev. C* 91:065803. doi: 10.1103/PhysRevC.91.065803

Smith, M. S., Kawano, L. H., and Malaney, R. A. (1993). Experimental, computational, and observational analysis of primordial nucleosynthesis. *Astrophys. J. Suppl. Series* 85, 219–247. doi: 10.1086/191763

Spampinato, C., Pizzone, R. G., Spartá, R., Couder, M., Tan, W., Burian, V., et al. (2020). Study of ^{3}He(n, p)^{3}H reaction at cosmological energies with trojan horse method. *EPJ Web Conf*. 227:02013. doi: 10.1051/epjconf/202022702013

Spartá, R. (2016). New measurement of the 10B(n, α)^{7}Li through the trojan horse method. *J. Phys. Conf. Series* 703:012026. doi: 10.1088/1742-6596/703/1/012026

Spinka, H., Tombrello, T., and Winkler, H. (1971). Low-energy cross sections for ^{7}Li(p,α)^{4}He and ^{6}Li(p,α)^{3}He. *Nucl. Phys. A* 164, 1–10. doi: 10.1016/0375-9474(71)90839-6

Spitaleri, C., Cherubini, S., del Zoppo, A., Di Pietro, A., Figuera, P., Gulino, M., et al. (2003). The Trojan Horse method in nuclear astrophysics. *Nucl. Phys. A* 719, C99–C106. doi: 10.1016/S0375-9474(03)00975-8

Spitaleri, C., La Cognata, M., Lamia, L., Mukhamedzhanov, A. M., and Pizzone, R. G. (2016). Nuclear astrophysics and the trojan horse method. *Eur. Phys. J. A* 52:77. doi: 10.1140/epja/i2016-16077-2

Spitaleri, C., La Cognata, M., Lamia, L., Pizzone, R. G., and Tumino, A. (2019). Astrophysics studies with the trojan horse method. *Eur. Phys. J. A* 55:161. doi: 10.1140/epja/i2019-12833-0

Spraker, M., Prior, R. M., Godwin, M. A., Rice, B. J., Wulf, E. A., Kelley, J. H., et al. (1999). Slope of the astrophysical s factor for the ^{7}Li(p, γ)^{8}Be reaction. *Phys. Rev. C* 61:015802. doi: 10.1103/PhysRevC.61.015802

Tanabashi, M., Hagiwara, K., Hikasa, K., Nakamura, K., Sumino, Y., Takahashi, F., et al. (2018). Review of particle physics. *Phys. Rev. D* 98:030001. doi: 10.1103/PhysRevD.98.030001

Tie-Shan, W., Zhen, Y., Yunemura, H., Nakagawa, A., Hui-Yi, L., v., et al. (2007). Measurement of D(d,p)T reaction cross sections in sm metal in low energy region ($10 \leq e_d \leq 20$ keV). *Chin. Phys. Lett*. 24:3103. doi: 10.1088/0256-307X/24/11/024

Tumino, A., Spartá, R., Spitaleri, C., Mukhamedzhanov, A. M., Typel, S., Pizzone, R. G., et al. (2014). New determination of the ^{2}H(d,p)^{3}H and ^{2}H(d,n)^{3}He reaction rates at astrophysical energies. *Astrophys. J*. 785:96. doi: 10.1088/0004-637X/785/2/96

Tumino, A., Spitaleri, C., Cherubini, S., Gulino, M., La Cognata, M., Lamia, L., et al. (2013). New advances in the trojan horse method as an indirect approach to nuclear astrophysics. *Few Body Syst*. 54, 745–753. doi: 10.1007/s00601-012-0407-1

Tumino, A., Spitaleri, C., La Cognata, M., Cherubini, S., Guardo, G. L., Gulino, M., et al. (2018). An increase in the ^{12}C + ^{12}C fusion rate from resonances at astrophysical energies. *Nature* 557, 687–690. doi: 10.1038/s41586-018-0149-4

Tumino, A., Spitaleri, C., Mukhamedzhanov, A. M., Typel, S., Aliotta, M., Burjan, V., et al. (2011). Low-energy D + D fusion reactions via the trojan horse method. *Phys. Lett. B* 700, 111–115. doi: 10.1016/j.physletb.2011.10.056

Von Engel, A., and Goodyear, C. (1961). Fusion cross-section measurements with deuterons of low energy. *Proc. R. Soc. Lond. A Math. Phys. Sci*. 264, 445–457. doi: 10.1098/rspa.1961.0210

Ying, N., Cox, B. B., Barnes, B. K., and Barrows, A. W. (1973). A study of the ^{2}H(d, p) ^{3}H and ^{2}H(d, n)^{3}He reactions and the excited state of ^{4}He at 23.9 MeV. *Nucl. Phys. A* 206, 481–497. doi: 10.1016/0375-9474(73)90080-8

Zhichang, L., Jingang, Y., and Xunliang, D. (1977). Measurement of He-3(d,p)He-4 reaction cross sections. *Chin. J. Sci. Tech*. 11:229.

Conflict of Interest: The authors declare that the research was conducted in the absence of any commercial or financial relationships that could be construed as a potential conflict of interest.

frontiers in Astronomy and Space Sciences

REVIEW
published: 02 November 2020
doi: 10.3389/fspas.2020.00060

Indirect Measurements of n- and p-Induced Reactions of Astrophysical Interest on Oxygen Isotopes

M. L. Sergi[1,2], G. L. Guardo[1,2], M. La Cognata[1], M. Gulino[1,3], J. Mrazek[4], S. Palmerini[5,6], C. Spitaleri[1,2] and M. Wiescher[7]*

[1] Laboratori Nazionali del Sud, Istituto Nazionale di Fisica Nucleare, Catania, Italy, [2] Dipartimento di Fisica e Astronomia "Ettore Majorana", Università degli Studi di Catania, Catania, Italy, [3] Facoltà di Ingegneria e Architettura, Università degli Studi di Enna Kore, Enna, Italy, [4] Nuclear Physics Institute (NPI) of the Czech Academy of Sciences, (CAS), Řež, Czechia, [5] Dipartimento di Fisica e Geologia, Università degli Studi di Perugia, Perugia, Italy, [6] Sezione di Perugia, Istituto Nazionale di Fisica Nucleare, Perugia, Italy, [7] Department of Physics, University of Notre Dame, Notre Dame, IN, United States

OPEN ACCESS

Edited by:
Scilla Degl'Innocenti, University of Pisa, Italy

Reviewed by:
Hidetoshi Yamaguchi, The University of Tokyo, Japan
Alain Coc, UMR9012 Laboratoire de Physique des 2 Infinis Iréne Joliot-Curie (IJCLab), France

***Correspondence:**
M. La Cognata
lacognata@lns.infn.it

Specialty section:
This article was submitted to Nuclear Physics, a section of the journal Frontiers in Astronomy and Space Sciences

Received: *10 June 2020*
Accepted: *31 July 2020*
Published: *02 November 2020*

Citation:
Sergi ML, Guardo GL, La Cognata M, Gulino M, Mrazek J, Palmerini S, Spitaleri C and Wiescher M (2020) Indirect Measurements of n- and p-Induced Reactions of Astrophysical Interest on Oxygen Isotopes. Front. Astron. Space Sci. 7:60. doi: 10.3389/fspas.2020.00060

Observations of abundances and isotopic ratio determinations in stars yield powerful constraints on stellar models. In particular, the oxygen isotopic ratios are of particular interest because they are affected not only by nucleosynthesis but also by mixing processes, which are not very well-understood yet. This review is focused on the measurements via the Trojan Horse Method (THM) that have been carried out to investigate the low-energy cross sections of proton and neutron-induced reactions on ^{17}O as well as the proton-induced reaction on ^{18}O, overcoming extrapolation procedures and enhancement effects due to electron screening. The (p,α) reactions induced on these oxygen isotopes are of paramount importance for the nucleosynthesis in a number of stellar sites, including red giants (RGs), asymptotic giant branch (AGB) stars, massive stars, and classical novae. In detail, the indirect measurement of the low-energy region of ^{17}O(p,α)^{14}N was performed. The strength of the narrow resonance at 65 keV was evaluated, and it was used to renormalize the corresponding resonance strength in the ^{17}O+p radiative capture channel. The reaction rate was then evaluated for both the ^{17}O(p,α)^{14}N and the ^{17}O(p,γ)^{18}F reactions, and significant differences of 30 and 20% with respect the literature data were found, respectively, in the temperature range relevant for RG, AGB, and massive stars nucleosynthesis. Regarding the ^{18}O(p,α)^{15}N reaction, the strength of the 20 keV resonance was extracted, which is the main contribution to the reaction rate for astrophysical applications. This approach has allowed us to improve the data accuracy of a factor 8.5, as it is based on the measured strength instead of educated guesses or spectroscopic measurements. Finally, the ^{17}O(n,α)^{14}C reaction was studied because of its role during the s-process nucleosynthesis as a possible neutron poison reaction. This study represents the extension of THM to resonant neutron-induced reactions. In this measurement, the subthreshold level centered at −7 keV in the center-of-mass system, corresponding to the 8.039 MeV ^{18}O excited level, was observed. Moreover, the THM measurements showed a clear agreement with the

available direct measurements and the additional contribution of the 8.121 MeV ^{18}O level, strongly suppressed in direct measurements because of its l = 3 angular momentum. The contributions of those levels to the total reaction rate were than evaluated for future astrophysical applications.

Keywords: nuclear reactions, nucleosynthesis, abundances, stars: abundances, direct reactions

1. INTRODUCTION

In recent years, the Trojan Horse Method (THM) has been used to investigate the low-energy cross sections of proton-induced reactions on A = 17 and A = 18 oxygen isotopes, overcoming extrapolation procedures and enhancement effects due to electron screening. The (p,α) reactions induced on these oxygen isotopes are, indeed, related to various open questions in astrophysics: the relative abundances of the oxygen isotopes have been observed at the surface of some Red Giant (RG) stars (Dearborn, 1992) and hundreds of presolar grains found in meteorites are composed of oxides with laboratory measured isotopic compositions (Zinner, 2014).

In particular, the ^{17}O+p reactions are of paramount importance for the nucleosynthesis in a number of stellar sites, including RGs, asymptotic giant branch (AGB) stars, massive stars, and classical novae. The ^{17}O(p,α)^{14}N and ^{17}O(p,γ)^{18}F reactions govern the destruction of ^{17}O and the formation of the short-lived radio-isotope ^{18}F, which is of special interest for gamma ray astronomy (Hernanz et al., 1999; José and Hernanz, 2007). At temperatures typical of the above-mentioned astrophysical scenario, T = 0.01–0.1 GK for RGs, AGB, and massive stars and T = 0.1–0.4 GK for classical nova explosions, the ^{17}O(p,α)^{14}N cross section is expected to be dominated by a resonance at $E_{c.m.}$ = 65 keV, corresponding to the $E_X(J^\pi)$ = 5.673 MeV (1^-) level in ^{18}F. A sub-threshold level at $E_X(J^\pi)$ = 5.605 MeV (1^-) could also play a significant role in the reaction rate both through its high-energy tail and because of possible interference effects with the 5.673 MeV level. Other states that could be involved in the stellar reaction rates are the $E_X(J^\pi)$ = 5.603 MeV (1^+) level, bound only by 3 keV against proton decay, and the $E_X(J^\pi)$ = 5.786 MeV (2^-) level for high-temperature processes, corresponding to the $E_{c.m.}$ = 183 keV resonance in the ^{17}O(p,α)^{14}N and ^{17}O(p,γ)^{14}N reactions (Hernanz et al., 1999; José and Hernanz, 2007).

Regarding the ^{18}O(p,α)^{15}N reaction, it is of primary importance to pin down the uncertainties affecting present-day models of AGB stars that are the observationally confirmed astrophysical scenarios for fluorine nucleosynthesis. The ^{18}O(p,α)^{15}N is the main ^{15}N production channel, which is then burnt to ^{19}F by means of the ^{15}N(α,γ)^{19}F radiative capture during thermal pulses that arise in the ^{4}He-rich intershell region of AGB stars at temperatures of the order of 10^8 K. However, the observed abundances of ^{19}F (Jorissen et al., 1992) are in clear discrepancy with the theoretical predictions because the largest ^{19}F abundances cannot be justified for the typical ^{12}C/^{16}O values (Lugaro et al., 2004). Nine resonances are present, at least, in the ^{18}O(p,α)^{15}N cross section in the 0–1 MeV energy range, which is the most relevant to astrophysics. However, only a few of them, those at 20, 144, and at 656 keV strongly influences the reaction rate (Angulo et al., 1999). Though these resonances have been directly studied by many authors (Mak et al., 1978; Lorenz-Wirzba et al., 1979) and have been subject of spectroscopic investigations (Yagi et al., 1962; Schmidt and Duhm, 1970; Wiescher et al., 1980; Champagne and Pitt, 1986), the reaction rate for the ^{18}O(p,α)^{15}N reaction is still affected a sizeable uncertainty (Angulo et al., 1999) at astrophysical energies. This is especially true for the 20 keV resonance, whose strength is known from spectroscopic studies carried out using the transfer reaction ^{18}O(^{3}He, d)^{19}F (Champagne and Pitt, 1986) and the radiative capture reaction ^{18}O(p,γ)^{19}F (Wiescher et al., 1980). Because of the experimental and optical potentials uncertainties, the deduced reaction rate is affected by unpredictable uncertainties, owing to the model dependence affecting the spectroscopic factors. Also, the error on the resonance energy is exponentially contributing to the uncertainty on the reaction rate, making the investigation of the 20 keV resonance of high importance (Champagne and Pitt, 1986). Regarding the other influential resonances, the one at 143.5 keV is fairly well-established (Lorenz-Wirzba et al., 1979). The broad resonance at 656 keV, which strongly contributes both at low and high temperatures, has, however, a total width that is not as well known (La Cognata et al., 2008b), and, consequently, a poorly known corresponding contribution to the reaction rate.

Finally, in the case of the ^{17}O(n,α)^{14}C reaction, its importance is two-fold, first in nuclear reactors and second in many astrophysical scenarios. With regards to the nuclear reactor, the neutron-induced reactions on ^{14}N or ^{17}O are the dominant sources of the radioactive isotope ^{14}C ($T_{1/2}$ = 5730 yr), thus constituting a dangerous possible contaminant for life, because it is carcinogenic (Yim and Caron, 2006). In massive stars (M>8$M_\odot$), it is considered as a neutron poison for the weak component of the s-process since it may reduce the total neutron flux (Käppeler et al., 2011). On the other hand, ^{17}O can experience also the (α,n) reaction, thus re-injecting the captured neutrons into the nucleosynthesis path. Therefore, it is of key importance to fix the (α,n) to (n,α) cross section ratios to determine the net neutron flux for the s-process. Direct measurements of ^{17}O(n,α)^{14}C reaction cross section have shown the population of the two excited states at energies 8,213 and 8,282 keV and the influence of the sub-threshold level at 8,038 keV, while no evidence for the 8,125 keV level is present. Indeed, as this resonance is populated in the f-wave, its contribution is suppressed by the centrifugal barrier penetrability (Ajzenberg-Selove, 1987).

In this paper we report on the indirect studies of the ^{17}O(p,α)^{14}N, ^{18}O(p,α)^{15}N, and ^{17}O(n,α)^{14}C reactions via the Trojan Horse method by applying the approach developed for extracting the strength of narrow resonances at ultra-low energies. Moreover, the strength of the 65 keV resonance in the ^{17}O(p,α)^{14}N reaction, measured by means of the THM, is used to renormalize the corresponding resonance strength in the ^{17}O+p radiative capture channel and in the ^{17}O(p,γ)^{18}F reaction-rate evaluation.

2. THE TROJAN HORSE METHOD

The THM is an indirect technique for determining bare nucleus cross sections of astrophysical interest. It allows the measurement of a binary reaction $a + x \rightarrow c + d$ of astrophysical interest for which direct measurements require the use of the extrapolation procedure to reach the relevant Gamow peak energy region (Spitaleri et al., 2011, 2016, 2019; Tribble et al., 2014) and references therein. In the last decades, the THM gave a relevant contribution to solve several problems, varying from pure nuclear physics to nuclear astrophysics. In recent past, an extension of the THM pointed out the ability of the method to overcome also the centrifugal barrier, measuring the bare nuclear cross section in neutron induced reactions (Gulino et al., 2010, 2013; Guardo et al., 2017, 2019). In addition, a brand new application of the method demonstrated the possibility to measure astrophysical relevant reaction cross section involving radioactive ion beams (Cherubini et al., 2015; Pizzone et al., 2016; La Cognata et al., 2017), with clear consequences in shedding light on research of neutron-induced reaction with unstable beams, usually tricky to perform with direct experiments (Lamia et al., 2019).

The direct reaction mechanism approach is the basic theory of the THM, having its background in the research of the Quasi Free (QF) reaction mechanism (Baur, 1986; Zadro et al., 1989; Calvi et al., 1990). Essentially, in this kind of direct reactions, an impinging nucleus may cause during the interaction a *break-up* of the target (or likewise of the projectile). A schematic description of the THM is reported in **Figure 1**, where choosing an opportune reaction $a + A \rightarrow c + d + s$ (with the target A characterized by a strong $x \oplus s$ cluster configuration) induced at energies well above the Coulomb barrier the selection of the QF contribution grants to measure the relevant $a(x,c)d$ two-body reaction cross section (Shapiro, 1967). The appropriate adopted energy allows to avoid Coulomb barrier, centrifugal barrier, and electron screening effects in the TH yield of the $a + x \rightarrow c + d$ reaction. A precise selection of peculiar kinematical conditions ensures that the QF process represents the dominant process, while other ones, such as re-scattering among the emerging products, can be neglected (Shapiro, 1967). In this framework (called pole approximation), the s-cluster of the nucleus A does not take part on the $a + x \rightarrow c + d$ virtual reaction, where the projectile a interacts only with the x-cluster (*participant*).

The prescriptions of the impulse approximation (IA) establish that the $a+A \rightarrow c+d+s$ reaction cross section is related to the $a+x \rightarrow c+d$ two-body one (Chew, 1952) and in particular, applying

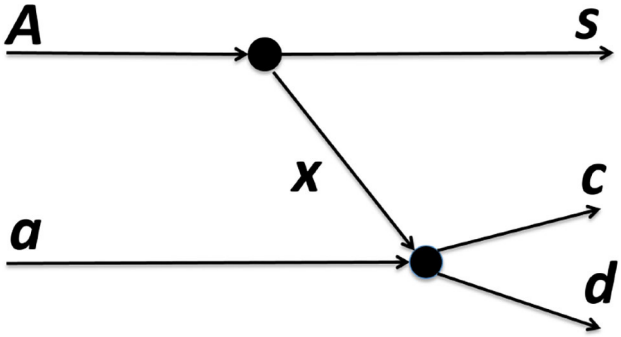

FIGURE 1 | The quasi-free (QF) $a + A \rightarrow c + d + s$ reaction described by a pole diagram (see text for details). The upper pole represents the breakup of the nucleus A into its cluster x and s. In this description, the x nucleus is called *participant* of the binary reaction $a(x,c)d$ (lower pole), while the s particle flies away without taking part to the reaction (*spectator*).

the simple Plane Wave Impulse Approximation (PWIA), it can be written as (Spitaleri et al., 2011):

$$\frac{d^3\sigma}{d\Omega_c d\Omega_d dE_c} \propto KF \cdot \mid \phi(\vec{p}_s) \mid^2 \cdot \left(\frac{d\sigma}{d\Omega}\right)^{HOES} \quad (1)$$

where:

- KF is a kinematical factor containing the final state phase-space factor, and it is a function of the masses, momenta, and emission angles of the two detected particles c and d;
- $\phi(\vec{p}_s)$ is the Fourier transform of the radial wave function $\chi(\vec{r}_{xs})$ of the $x - s$ inter-cluster motion;
- $\left(\frac{d\sigma}{d\Omega}\right)^{HOES}$ represents the half-off-energy-shell (HOES) differential cross section for the a(x,c)d reaction, referred to energy in the center-of-mass system E_{cm}. The latter can be expressed following the post-collision prescription by the relation

$$E_{cm} = E_{cd} - Q_{2b} \quad (2)$$

where Q_{2b} is the two-body reaction Q-value and E_{cd} indicates the c and d nuclei relative energy.

When the lower vertex of **Figure 1** proceeds via the $a + x \rightarrow F_i \rightarrow c + d$ process showing the population of the i^{th} resonant state of the F compound nucleus, the $a + A$ reaction can be described using a two steps approach: the stripping $a + A \rightarrow s + F$ to a resonant state in the compound system F_i, which later decays to the c+d channel (La Cognata et al., 2008a, 2010a; Mukhamedzhanov et al., 2008).

In this case, the TH double differential cross section is composed as reported in Dolinsky et al. (1973), Mukhamedzhanov et al. (2008), and La Cognata et al. (2008a) following the PWIA approach (Dolinsky et al., 1973) for stripping reactions to a resonant state (Dolinsky et al., 1973):

$$\frac{d^2\sigma^{TH}}{d\Omega_{\mathbf{k}_{sF}} dE_{cd}} = \frac{1}{2\pi} \frac{\Gamma_{cd}(E_{cd})}{(E_{cd} - E_{R_{cd}})^2 + \frac{1}{4}\Gamma^2(E_{cd})} \times \frac{d\sigma_{(a+A\rightarrow s+F)}}{d\Omega_{\mathbf{k}_{sF}}}, \quad (3)$$

where the differential cross section can be written as:

$$\frac{d\sigma_{(a+A\rightarrow s+F)}}{d\Omega_{Ok_{sF}}} = \frac{\mu_{sF}\,\mu_{aA}}{4\,\pi^2}\,\frac{k_{sF}}{k_{aA}}\,\frac{1}{\hat{J}_A\,\hat{J}_a} \times \sum_{M_F\,M_s\,M_A\,M_a} |M_{M_F\,M_s;M_A\,M_a}(\mathbf{k}_{sF},\mathbf{k}_{aA})|^2 \quad (4)$$

where J_j is the spin of the particle j and M_j its projection. Finally, the transfer reaction amplitude M results as

$$M_i \approx \phi(p_{xs})\; W_{xA}^{F_i}(\mathbf{p}_{xA})\,, \quad (5)$$

where $\phi(p_{xs})$ is the Fourier transform of the radial $x-s$ bound-state wave function, p_{xs} is the $x-s$ relative momentum, while

$$W_{xA}^{F_i}(\mathbf{p}_{xA}) = < I_{xA}^{F_i}|V_{xA}|\mathbf{p}_{xA} > \quad (6)$$

is the form factor for the $A+x\rightarrow F_i$ process.

The main advantage in the use of the THM is the presence of the transfer reaction amplitude $M_i(E)$ instead of the entrance channel partial resonance width $\Gamma_{(ax)_i}(E_{ax})$. As a consequence, the cross section of the three-body process can be connected to the one for the two-body reaction of interest by evaluating the transfer amplitude $M_i(E)$.

3. THE ^{17}O$(p,\alpha)^{14}$N REACTION

The cross section of the ^{17}O(p,α)^{14}N reaction has been the subject of several experimental investigations (Brown, 1962; Rolfs and Rodney, 1975; Berka et al., 1977; Kieser et al., 1979; Mak et al., 1980; Landre et al., 1989; Berheide et al., 1992; Blackmon et al., 1995; Angulo et al., 1999; Hannam and Thompson, 1999; Fox et al., 2004, 2005; Chafa et al., 2007; Moazen et al., 2007; Newton et al., 2007; Iliadis et al., 2010; Scott et al., 2012; Di Leva et al., 2014) in the last 50 years, mainly focusing on the 65 and 183 keV resonances showing up in the ^{17}O-p interaction at astrophysical energies. Although the resonance energy and strength of the 183 keV resonance have been extensively studied by direct measurements, several issues concern the 65 keV and the subthreshold resonances parameters. The direct measurements of low-lying resonance strengths such as of the 65 keV peak are, in fact, very difficult because of the Coulomb barrier. Therefore, large uncertainties are present in the available direct data (see Sergi et al., 2015 for more details). In 2006, we therefore started a campaign of measurements to investigate the contribution of the 65 keV resonance to the reaction rate of the ^{17}O(p,α)^{14}N by using the indirect THM. Recently, a new direct measurement (Bruno et al., 2016) of the 65 keV resonance strength performed at the Laboratory for Underground Nuclear Astrophysics (LUNA) accelerator has led to an value $\omega\gamma = 10.0 \pm 1.4_{stat} \pm 0.7_{syst}$ neV, a factor of three larger with respect to value obtained by using THM (Sergi et al., 2015). In the following sections we discuss the results of the indirect study of the ^{17}O(p,α)^{14}N reaction via the THM by applying the approach recently developed for extracting the strength of narrow resonances at ultra-low energies.

3.1. The Experiment and the Reaction Channel Selection

The experiment was performed at INFN-LNS in Catania (Italy) by using a 41 MeV ^{17}O beam that hit a 150 μg/cm^2 CD_2 target fixed orthogonally with respect to the beam axis. In addition, a detailed data analysis was also made on the ^{17}O+^{2}H experimental data belonging to the NSL experiment (University of Notre Dame, South Bend, Indiana, USA) for studying the ^{17}O(p,α)^{14}N reaction, although the NSL experiment was initially devoted to the ^{17}O(n,α)^{14}C study (described in detail in section five of the present paper). This approach allowed us to improve the statistics of the experimental data. The angles and the energies of the ejected α and ^{14}N were detected in coincidence by using an experimental setup, symmetric with respect to the beam axis, which consists of six single-area, resistive-readout position-sensitive silicon detectors (PSDs) with spatial resolution of 0.5 mm. Since the neutron was not detected in these experiments, and its energy and emission angle were reconstructed from the momenta of the detected particles. The PSDs covered the angular ranges (in the laboratory reference system) $5.1^\circ - 10.1^\circ$ ($PSD_{1,4}$), $13.8^\circ - 21.2^\circ$ ($PSD_{2,5}$) and $21.3^\circ - 28.7^\circ$ ($PSD_{3,6}$) in the LNS experiment, and $5.0^\circ - 10.0^\circ$ ($PSD_{1,4}$), $13.1^\circ - 18.1^\circ$ ($PSD_{2,5}$), and $23.8^\circ - 28.8^\circ$ ($PSD_{3,6}$), in the NSL experiment (**Figure 2**). The forward one (PSD 1) was optimized for ^{14}N detection, PSDs 2 and 3 were optimized instead for α-particles detection. The other three PSDs (4, 5, and 6) were placed on the opposite side with respect to the beam axis, at symmetrical angles. Two ionization chambers were used as ΔE detectors to discriminate nitrogen from carbon ions, thus allowing for the distinction between the ^{2}H(^{17}O,α^{14}N)n and ^{2}H(^{17}O,α^{14}C)p channels. After detectors calibration, the first step of the analysis was the identification of the events corresponding to the ^{2}H(^{17}O,α^{14}N)n TH reaction. In order to identify the channel of interest and to choose the kinematical conditions where the QF process is dominant, ^{14}N particles were selected using the standard ΔE-E technique. For these selected events, the experimental Q-value spectrum was reconstructed (**Figure 3**) and it results in good agreement with the theoretical one ($Q_{th} = -1.033$ MeV). The agreement, within the experimental uncertainties, is a signature of a good detector calibration. Events inside the experimental Q-value peak were selected for further analysis.

3.2. Reaction Mechanism Selection

After the three-body reaction selection, the identification of the different reaction mechanisms is a crucial step in the data analysis. In fact, the application of THM are possible only under the assumption that particle s, namely the neutron, acts as a spectator to the $A-x$ interaction (QF-condition). A standard way to investigate the reaction mechanisms is the study of the experimental momentum distribution, this quantity being very sensitive to the reaction mechanism. By selecting a narrow $E_{c.m.}$ relative energy window, $\Delta E = 100$ keV, at the top of the 183 keV resonant peak where the differential two-body cross section of the ^{17}O-p reaction can be considered to be almost constant (Spitaleri et al., 2004), the experimental neutron momentum distribution is

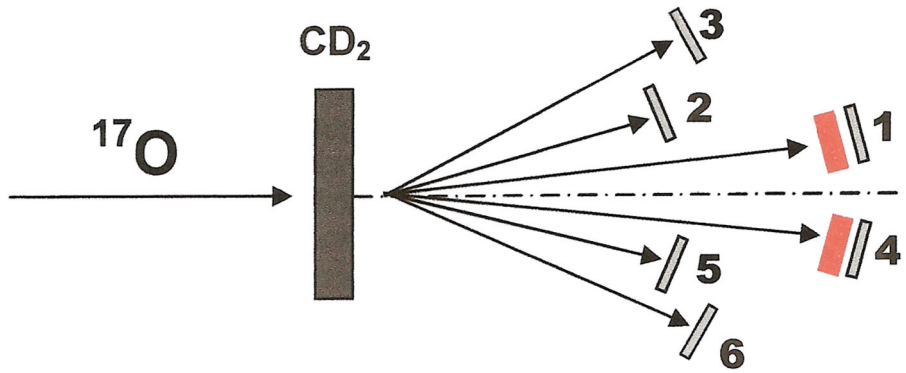

FIGURE 2 | Experimental set-up adopted for the study of the ^{2}H(^{17}O,α^{14}N)n reaction. The position of the detectors assures the covering of the QF angular region.

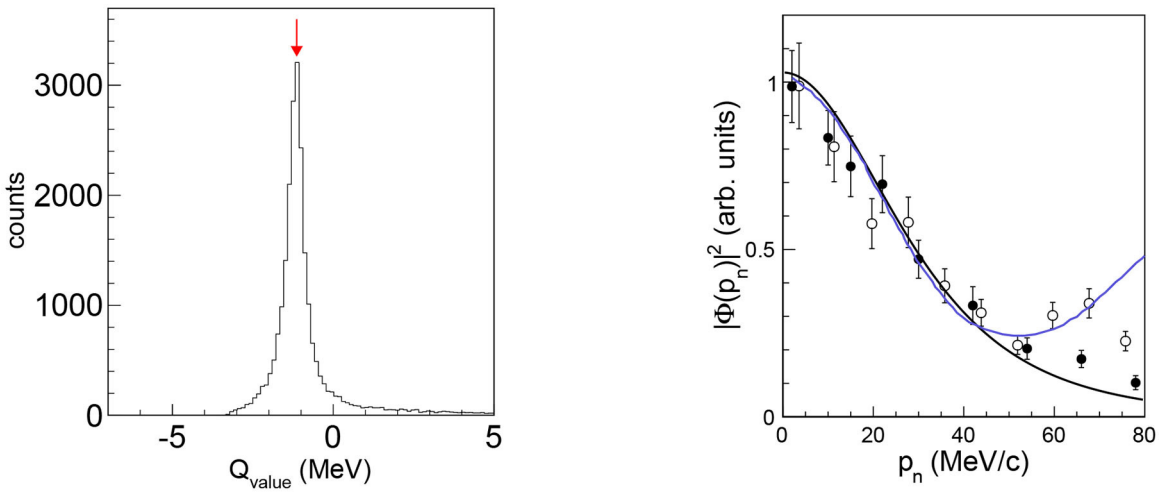

FIGURE 3 | (Left) Experimental *Q*-value spectrum for LNS experiment. A single peak shows up, centered at about −1.0 MeV, corresponding to the ^{2}H(^{17}O,α^{14}N)n channel. The red arrow corresponds to the theoretical Q-value, $Q_{th} = -1.033$ MeV. Similar spectrum was obtained for the ND experimental data. **(Right)** Experimental momentum distribution (full dots for LNS experiment and empty dots for NSL experiments) compared with the theoretical one given by the squared Hulthén wave function in momentum space (black line) and the one given in terms of a DWBA calculation performed via the FRESCO code (blue line). The error bars include only statistical errors.

obtained in arbitrary units by inverting Equation (1):

$$|\phi(\vec{p}_n)|^2 \propto \left[\frac{d^3\sigma}{d\Omega_\alpha d\Omega_{^{14}\mathrm{N}} dE_{c.m.}}\right] \cdot [KF]^{-1}, \qquad (7)$$

Figure 3 shows the experimental momentum distributions $|\phi(\vec{p}_n)|^2$ for the LNS data (solid black line) and for the NSL data (empty circle). The black line corresponds to the square of the Hulthén function in momentum space, representing the shape of the n-p momentum distribution inside the deuteron in the PWIA, while the blue line represents the DWBA distribution evaluated by means of the FRESCO code (Thompson, 1988). In DWBA calculation the optical potential parameters adjusted from the Perey and Perey compilation (Perey and Perey, 1976) were adopted. The good agreement, within $|\vec{p}_n| \leq 30$ MeV/c, between the two theoretical approaches and the experimental data, means that the QF mechanism is present and dominant in the considered $\vec{p}_n$ range. For this reason the narrower 0–30 MeV/c momentum range was chosen for the next analysis.

3.3. Results: Cross Section and Reaction Rate Evaluation

The resulting ^{2}H(^{17}O,α ^{14}N)n reaction cross section is shown in **Figure 4** as full dots for both the LNS (**Figure 4A**) and the NSL experiments (**Figure 4B**). The vertical error bars include only the statistical error (about 20%) while the horizontal ones the data bin width. The solid line represents the incoherent sum of the three Gaussian functions (dashed lines) used to fit the resonant behavior and of the first-order polynomial (dot-dashed straight line) used to fit the combinatorial background. The fits were performed to extract the parameters describing the resonance top values, the peak values N_i of the two resonances (N_1 for

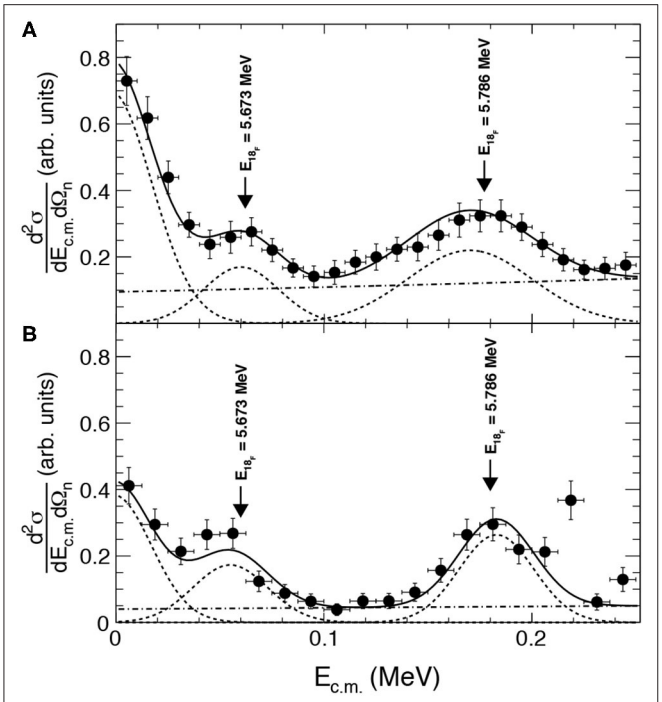

FIGURE 4 | Cross section of the ^{2}H(^{17}O, α^{14}N)n TH reaction (full circles) for the LNS **(A)** and NSL **(B)** experiments. See text for more details.

TABLE 1 | Summary table of the strengths of the low-energy resonances in the $^{17}O(p,\alpha)^{14}N$ astrophysical factor.

Resonance energy (keV)	J^π	$\omega\gamma$ (eV)	References
56	1^-	$8\times10^{-8,\star}$	Brown, 1962
62	1^-	$\leq1.3\times10^{-9,\star}$	Rolfs and Rodney, 1975
66.1 ± 0.3^a	1^-	$7.1^{+4.0}_{-5.7}\times10^{-8,\star}$	Landre et al., 1989
–	1^-	$22\pm3_{stat}\pm2_{target}{}^{+2}_{-1\ beam}\times10^{-9,\star}$	Blackmon et al., 1995
–	1^-	$\leq8\times10^{-10}$	Berheide et al., 1992
66.07	1^-	$(5.5^{+1.8}_{-1.0})\times10^{-9}$	Angulo et al., 1999
–	1^-	$21\pm2\times10^{-9,\star}$	Hannam and Thompson, 1999
–	1^-	$(4.7\pm0.8)\times10^{-9}$	Fox et al., 2004, 2005
–	1^-	$(19.0\pm3.2)\times10^{-9,\star}$	Iliadis et al., 2010
–	1^-	$(3.42\pm0.60)\times10^{-9}$	Sergi et al., 2015
–	1^-	$(10.0\pm1.4_{stat}\pm0.7_{syst})\times10^{-9}$	Bruno et al., 2016
179^b	2^-	$\leq1.4\times10^{-3,\star}$	Rolfs and Rodney, 1975
180 ± 2.4	2^-	$\leq2.8\times10^{-3,\star}$	Landre et al., 1989
180	2^-	$\leq2.8\times10^{-3,c,\star}$	Angulo et al., 1999
183.3 ± 0.3	2^-	$(1.6\pm0.2)\times10^{-3}$	Chafa et al., 2007**
–	2^-	$(1.66\pm0.17)\times10^{-3}$	Newton et al., 2007**
–	2^-	$(1.70\pm0.15)\times10^{-3}$	Moazen et al., 2007**
–	2^-	$(4.00\pm0.24)\times10^{-3,\star}$	Iliadis et al., 2010**

*For these references the partial widths Γ_p are reported as the corresponding resonance strength values are not available in the literature.

**The weighted average of these four resonance strengths was used for normalization of the THM results, as discussed in Sergi et al. (2015).

[a] Berka et al. (1977).

[b] Ajzenberg-Selove (1987).

[c] Landre et al. (1989).

the 65 keV resonance and N_2 for the 183 keV resonance) with their statistical errors. In case of narrow resonance, the N_i peak values are connected to the resonance strengths $(\omega\gamma)_i$ (Rolfs and Rodney, 1988) of the ^{18}F levels, which are the key parameters to evaluate the reaction rate for astrophysical applications.

$$(\omega\gamma)_i = \frac{1}{2\pi}\omega_i N_i \frac{\Gamma_{(p^{17}O)_i}(E_{R_i})}{\sigma_{R_i}(\theta)}, \tag{8}$$

where $\omega_i = (2J_{^{18}F_i}+1)/[(2J_{^{17}O}+1)(2J_p+1)]$ $(i=1,2)$ is the statistical factor, $\Gamma_{(p^{17}O)_i}(E_{R_i})$ is the partial widths for the $p + {}^{17}O \rightarrow {}^{18}F_i$ channel leading to the population of the ith excited state in ^{18}F and $\sigma_{R_i}(\theta)$ the direct transfer reaction cross section for the binary reaction ^{17}O + d$\rightarrow{}^{18}F_i + n$ populating the ith resonant state in ^{18}F with the resonance energyE_{R_i}. Since we did not measure the absolute value of the cross section, the absolute strength of the resonance at 65 keV $(\omega\gamma)_1$ was obtained from the ratio between the N_1 and N_2 peak values through the relation (La Cognata et al., 2010a; Sergi et al., 2010)

$$(\omega\gamma)_1 = \frac{\omega_1}{\omega_2}\frac{\Gamma_{(p^{17}O)_1}}{\sigma_{R_1}(\theta)}\frac{\sigma_{R_2}(\theta)}{\Gamma_{(p^{17}O)_2}}\frac{N_1}{N_2}(\omega\gamma)_2. \tag{9}$$

where $(\omega\gamma)_2$ is the strength of 183 keV resonance, which is well-known from the literature. In particular, the adopted value for $(\omega\gamma)_2$ is $(1.67\pm0.07)\times10^{-3}$ eV, obtained by the weighted average of the four strength values reported in literature (Chafa et al., 2007; Moazen et al., 2007; Newton et al., 2007; Iliadis et al., 2010). The resulting weighted average for the two measurements $(\overline{\omega\gamma})_1^{THM}=(3.42\pm0.60)\times10^{-9}$ eV is in good agreement with the strength given by NACRE, $(\omega\gamma)_N = (5.5^{+1.8}_{-1.5})\times10^{-9}$ eV (Angulo et al., 1999) and with the direct value, $(\omega\gamma)_D = (4.7\pm0.8)\times10^{-9}$ eV calculated by using the same Γ_p and Γ_α reported in Chafa et al. (2007) and Iliadis et al. (2010), namely, $\Gamma_\alpha = 130$ eV (Mak et al., 1980), and $\Gamma_p = 19\pm3$ neV (Hannam and Thompson, 1999; Fox et al., 2005). The results of the THM measurement and the strengths of the low-energy resonances are summarized in **Table 1**.

In the application of Equation (9), it is worth noting that the presence of the Γ/σ double ratio makes it possible to strongly reduce the model dependence of the THM resonance strength. This is due to a number of reasons: (i) since the same spectroscopic factor would appear in both the partial width and the transfer cross section, it cancels out so the corresponding single particle quantities can be used; (ii) the same $p+{}^{17}$O single particle wave function enters the calculation of both Γ and σ, so their ratio reduces the sensitivity on the potential well; (iii) the dependence on the other potentials used in the evaluation of the transfer cross sections is also reduced thanks to the normalization procedure, leading to the appearance of the ratio

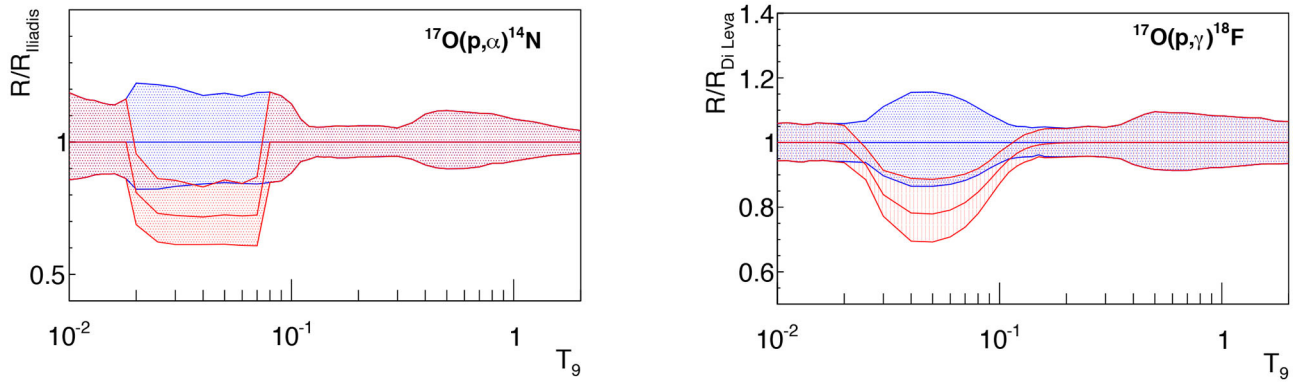

FIGURE 5 | (Left) Comparison of the THM reaction rate of the ^{17}O(p,α)^{14}N reaction with the direct one (Iliadis et al., 2010). See text for more details. **(Right)** Comparison of the THM reaction rate of the ^{17}O(p,γ)^{18}F reaction with the direct one (Di Leva et al., 2014). See text for more details.

of the transfer cross sections for two nearby resonances. A more detailed discussion can be found in La Cognata et al. (2010a).

In the calculation of the ^{17}O(p,α)^{14}N reaction rate, we followed the method based on Monte Carlo technique adopted in Iliadis et al. (2010). The interference effects between the 65 and the −1.64 keV and between the 183 and 1,202 keV were also evaluated, resulting smaller than 1% in the temperature range between 0.02 and 0.07 GK, where the ^{17}O(p,α)^{14}N reaction rate is dominated by the 65 keV resonance. Thus, the total reaction rate $N_A \langle \sigma v \rangle_{tot}^{THM}$ was calculated using the following equation:

$$N_A \langle \sigma v \rangle_{tot}^{THM} = N_A \langle \sigma v \rangle_{tot}^{Iliadis} - N_A \langle \sigma v \rangle_{65}^{Iliadis} + N_A \langle \sigma v \rangle_{65}^{THM}, \quad (10)$$

where $N_A \langle \sigma v \rangle_{tot}^{Iliadis}$ is the total reaction rate calculated in Iliadis et al. (2010).

Figure 5 (left panel) shows the ratio (red middle line) between the reaction rate R extracted here by Equation (10) and the reaction rate $R_{\rm Iliadis}$ (Iliadis et al., 2010). The red area of **Figure 5**, instead, marks the reaction-rate interval allowed by the experimental uncertainties on the 65 keV resonance strength only. The blue area is used to display the uncertainty range characterizing direct data (Iliadis et al., 2010). A significant variation (∼30%) can be seen in the range $T_9 = 0.02 - 0.07$, while no significant differences are present at higher temperatures.

The definition of the resonance strength (Equation 9) allows us to calculate a new value for the strength of the $E_R = 65$ keV resonance also in the ^{17}O(p,γ)^{18}F channel. By using the following formula

$$(\omega\gamma)_{p\gamma}^{THM} = (\omega\gamma)_{p\alpha}^{THM} \frac{\Gamma_\gamma}{\Gamma_\alpha}, \quad (11)$$

the 65 keV resonance strength in the (p,γ) channel has been evaluated equal to $(\omega\gamma)_{p\gamma}^{THM} = (1.18 \pm 0.21) \times 10^{-11}$ eV. This obtained value is 39% smaller than the value of $(1.6 \pm 0.3) \times 10^{-11}$ eV given in literature (Fox et al., 2005; Chafa et al., 2007) and in the most recent reviews (Iliadis et al., 2010; Adelberger et al., 2011). The Γ_γ and Γ_α values used in Equation (11) are those reported in Iliadis et al. (2010). The right panel of **Figure 5** shows the ratio (red middle line) of the THM reaction rate to reaction rate evaluation $R_{\rm DiLeva}$ of Di Leva et al. (2014) (blue line) for the ^{17}O(p,γ)^{18}F reaction. The red area marks the reaction-rate interval allowed by the experimental uncertainties on the 65 keV resonance strength only, while the blue area is used to display the uncertainty range characterizing direct data (Di Leva et al., 2014). Also in this case, a significant reduction (∼20%) of the reaction rate in the T_9=0.03 − 0.09 temperature range was obtained due to the THM measurement of the 65 keV resonance strength.

Finally, **Tables 2**, **3** contains the THM reaction rate together with the upper and lower limits allowed by experimental uncertainties of (p,α) and (p,γ) channels, respectively.

The discrepancy between THM results and the direct data is still under study, especially after the results published by LUNA (Bruno et al., 2016). However, as discussed in Sergi et al. (2015) a possible explanation for the discrepancies between direct and THM results in both (p,α) and (p,γ) channels could be attributable to the electron screening effect that affects direct measurements.

4. THE ^{18}O(p, α)^{15}N REACTION

As already widely discussed in section 1, even if the cross section of the ^{18}O$(p,\alpha)^{15}$N reaction has been the subject of several experimental investigations in the past, several issues concern the 20 keV resonance. Recently, the work of Bruno et al. (2019) supplied a new direct measurement of the ^{18}O$(p,\alpha)^{15}$N cross section. The authors used the thick target technique to come close to the energy region of astrophysical interest and perform the spectroscopy of ^{19}F. Though the 20 keV state could not be observed, the authors reported a factor of 10 larger strength for the 90 keV resonance reaching about 1.6 μeV, with respect to existing measurements (Lorenz-Wirzba et al., 1979; La Cognata et al., 2008a, 2010a). Their R-matrix analysis also seems to suggest the occurrence of a previously unaccounted, very broad resonance at about 106 keV ($\Gamma \sim 86$ keV). As a result, the reaction rate is enhanced up to a factor of about 2 at about

TABLE 2 | Rate of the $^{17}O(p,\alpha)^{14}N$ reaction.

Temperature (10^9 K)	Rate THM ($cm^3mol^{-1}s^{-1}$)		
	Lower	Adopted	Upper
0.010	$5.05\,10^{-25}$	$5.89\,10^{-25}$	$6.99\,10^{-25}$
0.011	$5.35\,10^{-24}$	$6.21\,10^{-24}$	$7.28\,10^{-24}$
0.012	$4.37\,10^{-23}$	$5.04\,10^{-23}$	$5.85\,10^{-23}$
0.013	$2.89\,10^{-22}$	$3.30\,10^{-22}$	$3.82\,10^{-22}$
0.014	$1.60\,10^{-21}$	$1.82\,10^{-21}$	$2.09\,10^{-21}$
0.015	$7.67\,10^{-21}$	$8.73\,10^{-21}$	$9.98\,10^{-21}$
0.016	$3.29\,10^{-20}$	$3.73\,10^{-20}$	$4.26\,10^{-20}$
0.018	$5.40\,10^{-19}$	$6.25\,10^{-19}$	$7.28\,10^{-19}$
0.020	$1.06\,10^{-17}$	$1.25\,10^{-17}$	$1.48\,10^{-17}$
0.025	$9.23\,10^{-15}$	$1.09\,10^{-14}$	$1.28\,10^{-14}$
0.030	$1.05\,10^{-12}$	$1.24\,10^{-12}$	$1.48\,10^{-12}$
0.040	$3.72\,10^{-10}$	$4.37\,10^{-10}$	$5.03\,10^{-10}$
0.050	$1.15\,10^{-8}$	$1.36\,10^{-8}$	$1.61\,10^{-8}$
0.060	$1.09\,10^{-7}$	$1.28\,10^{-7}$	$1.51\,10^{-7}$
0.070	$5.25\,10^{-7}$	$6.25\,10^{-7}$	$7.40\,10^{-7}$
0.080	$1.65\,10^{-6}$	$1.96\,10^{-6}$	$2.36\,10^{-6}$
0.090	$4.14\,10^{-6}$	$5.17\,10^{-6}$	$6.13\,10^{-6}$
0.100	$1.27\,10^{-5}$	$1.42\,10^{-5}$	$1.63\,10^{-5}$
0.110	$4.33\,10^{-5}$	$4.62\,10^{-5}$	$4.99\,10^{-5}$
0.120	$1.49\,10^{-4}$	$1.59\,10^{-4}$	$1.67\,10^{-4}$
0.130	$4.72\,10^{-4}$	$4.97\,10^{-4}$	$5.24\,10^{-4}$
0.140	$1.30\,10^{-3}$	$1.38\,10^{-3}$	$1.46\,10^{-3}$
0.150	$3.17\,10^{-3}$	$3.35\,10^{-3}$	$3.55\,10^{-3}$
0.160	$6.88\,10^{-3}$	$7.32\,10^{-3}$	$7.76\,10^{-3}$
0.180	$2.52\,10^{-2}$	$2.67\,10^{-2}$	$2.83\,10^{-2}$
0.200	$7.00\,10^{-2}$	$7.42\,10^{-2}$	$7.88\,10^{-2}$
0.250	$4.29\,10^{-1}$	$4.54\,10^{-1}$	$4.82\,10^{-1}$
0.300	1.59	1.68	1.77
0.350	5.87	6.28	6.74
0.400	$2.33\,10^{1}$	$2.55\,10^{1}$	$2.82\,10^{1}$
0.450	$8.24\,10^{1}$	$9.13\,10^{1}$	$1.02\,10^{2}$
0.500	$2.41\,10^{2}$	$2.68\,10^{2}$	$3.00\,10^{2}$
0.600	$1.26\,10^{3}$	$1.40\,10^{3}$	$1.56\,10^{3}$
0.700	$4.15\,10^{3}$	$4.58\,10^{3}$	$5.08\,10^{3}$
0.800	$1.03\,10^{4}$	$1.12\,10^{4}$	$1.24\,10^{4}$
0.900	$2.09\,10^{4}$	$2.27\,10^{4}$	$2.49\,10^{4}$
1.000	$3.74\,10^{4}$	$4.03\,10^{4}$	$4.38\,10^{4}$
1.250	$1.12\,10^{5}$	$1.19\,10^{5}$	$1.28\,10^{5}$
1.500	$2.51\,10^{5}$	$2.64\,10^{5}$	$2.80\,10^{5}$
1.750	$4.76\,10^{5}$	$4.99\,10^{5}$	$5.24\,10^{5}$
2.000	$8.03\,10^{5}$	$8.39\,10^{5}$	$8.76\,10^{5}$

TABLE 3 | Rate of the $^{17}O(p,\gamma)^{18}F$ reaction.

Temperature (10^9 K)	Rate THM ($cm^3mol^{-1}s^{-1}$)		
	Lower	Adopted	Upper
0.010	$3.34\,10^{-25}$	$3.54\,10^{-25}$	$3.75\,10^{-25}$
0.011	$3.55\,10^{-24}$	$3.76\,10^{-24}$	$3.99\,10^{-24}$
0.012	$2.87\,10^{-23}$	$3.05\,10^{-23}$	$3.23\,10^{-23}$
0.013	$1.86\,10^{-22}$	$1.98\,10^{-22}$	$2.09\,10^{-22}$
0.014	$1.01\,10^{-21}$	$1.07\,10^{-21}$	$1.13\,10^{-21}$
0.015	$4.65\,10^{-21}$	$4.93\,10^{-21}$	$5.23\,10^{-21}$
0.016	$1.89\,10^{-20}$	$2.00\,10^{-20}$	$2.12\,10^{-20}$
0.018	$2.25\,10^{-19}$	$2.39\,10^{-19}$	$2.53\,10^{-19}$
0.020	$1.93\,10^{-18}$	$2.04\,10^{-18}$	$2.16\,10^{-18}$
0.025	$1.72\,10^{-16}$	$1.81\,10^{-16}$	$1.91\,10^{-16}$
0.030	$7.43\,10^{-15}$	$8.08\,10^{-15}$	$8.80\,10^{-15}$
0.040	$1.74\,10^{-12}$	$1.96\,10^{-12}$	$2.23\,10^{-12}$
0.050	$5.36\,10^{-11}$	$6.03\,10^{-11}$	$6.86\,10^{-11}$
0.060	$5.47\,10^{-10}$	$6.11\,10^{-10}$	$6.90\,10^{-10}$
0.070	$3.08\,10^{-9}$	$3.39\,10^{-9}$	$3.76\,10^{-9}$
0.080	$1.24\,10^{-8}$	$1.34\,10^{-8}$	$1.46\,10^{-8}$
0.090	$4.13\,10^{-8}$	$4.40\,10^{-8}$	$4.70\,10^{-8}$
0.100	$1.23\,10^{-7}$	$1.29\,10^{-7}$	$1.37\,10^{-7}$
0.110	$3.39\,10^{-7}$	$3.54\,10^{-7}$	$3.71\,10^{-7}$
0.120	$8.74\,10^{-7}$	$9.11\,10^{-7}$	$9.51\,10^{-7}$
0.130	$2.10\,10^{-6}$	$2.20\,10^{-6}$	$2.29\,10^{-6}$
0.140	$4.75\,10^{-6}$	$4.96\,10^{-6}$	$5.18\,10^{-6}$
0.150	$1.00\,10^{-5}$	$1.04\,10^{-5}$	$1.09\,10^{-5}$
0.160	$1.97\,10^{-5}$	$2.06\,10^{-5}$	$2.16\,10^{-5}$
0.180	$6.43\,10^{-5}$	$6.73\,10^{-5}$	$7.03\,10^{-5}$
0.200	$1.73\,10^{-4}$	$1.81\,10^{-4}$	$1.89\,10^{-4}$
0.250	$1.14\,10^{-3}$	$1.19\,10^{-3}$	$1.25\,10^{-3}$
0.300	$4.86\,10^{-3}$	$5.09\,10^{-3}$	$5.33\,10^{-3}$
0.350	$1.90\,10^{-2}$	$2.00\,10^{-2}$	$2.11\,10^{-2}$
0.400	$7.54\,10^{-2}$	$8.09\,10^{-2}$	$8.68\,10^{-2}$
0.450	$2.74\,10^{-1}$	$2.97\,10^{-1}$	$3.23\,10^{2}$
0.500	$8.45\,10^{-1}$	$9.23\,10^{-1}$	1.01
0.600	4.97	5.44	5.94
0.700	$1.80\,10^{1}$	$1.97\,10^{1}$	$2.15\,10^{1}$
0.800	$4.73\,10^{1}$	$5.15\,10^{1}$	$5.60\,10^{1}$
0.900	$9.96\,10^{1}$	$1.08\,10^{2}$	$1.17\,10^{2}$
1.000	$1.79\,10^{2}$	$1.94\,10^{2}$	$2.10\,10^{2}$
1.250	$5.04\,10^{2}$	$5.43\,10^{2}$	$5.85\,10^{2}$
1.500	$9.80\,10^{2}$	$1.05\,10^{3}$	1.13 10

50 MK, with respect to the one in Iliadis et al. (2010). This makes astrophysical predictions far from conclusive and calls for alternative investigations aiming at reducing uncertainties on nuclear physics inputs. With this in mind, the THM offers the opportunity of an independent investigation right at astrophysical energies, devoid of the need of extrapolation. In detail, the cross section of the $^{18}O(p,\alpha)^{15}N$ reaction is deduced from the $^{2}H(^{18}O,\alpha^{15}N)n$ three-body process, performed in QF kinematics. The beam energy is chosen larger than the Coulomb barrier for the $d + {}^{18}O$ system, so the break-up of the *Trojan-horse* nucleus, d, takes place inside the ^{18}O nuclear field. So the $^{18}O(p,\alpha)^{15}N$ HOES process is not suppressed by the Coulomb interaction, and no electron screening is enhancing the astrophysical factor.

4.1. Experimental Investigation

The experiment was performed at Laboratori Nazionali del Sud, Catania (Italy), where the 15 MV Tandem Van de Graaff

accelerator delivered a ϕ = 1 mm, 54 MeV ^{18}O beam, with an average intensity of 5 enA. The experiment target was a 100-μg/cm^2-thick self-supported deuterated polyethylene foil (CD_2). The detection setup consisted of a telescope (A), to single out nitrogen isotopes, made up of an ionization chamber and a silicon position sensitive detector (PSD A). On the opposite side with respect to the beam direction, we placed three additional silicon PSD's (B, C, and D) optimized to detect α particles from the ^{2}H(^{18}O, α^{15}N)n reaction. The experimental setup is described in La Cognata et al. (2008a); here we underscore that the detector angles were chosen to span the whole QF angular region. After detector calibration, we carried out the reaction channel selection, to pick up the three-body reaction of interest among the several reactions which can take place in the target. Since no particle identification was performed in PSD's B, C, and D and no isotope discrimination was possible in telescope A, the reaction channel selection was performed from the kinematics of the events. Indeed, in a reaction with three particles in the exit channel the events pile up in a well-defined kinematical regions, fixed by the Q-value of the ^{2}H(^{18}O, α^{15}N)n reaction. A clear event selection was performed by means of the procedure described in Costanzo et al. (1990), after gating on the $\Delta E - E$ 2D spectra to select the nitrogen locus. The deduced kinematic locus of the ^{2}H(^{18}O,α^{15}N)n reaction was extracted and compared with the one simulated using a Monte Carlo simulation, showing no additional contribution besides the one of the ^{2}H(^{18}O, α^{15}N)n.

Next step was the selection of the QF process. Indeed, direct break-up (DBU) or sequential decay (SD) may populate the reaction channel, besides the QF break up. This was accomplished by studying the $E_{^{15}\mathrm{N}-n}$ and the $E_{\alpha-n}$ relative energy spectra, to deduce whether excited states from ^{16}N* and ^{5}He* contribute to the reaction yield. However, states in ^{19}F* could be fed through QF and SD reaction mechanisms, and the experimental neutron momentum distribution was therefore also evaluated. Indeed, a necessary condition for the occurrence of QF break-up is that the ejected neutron keeps the same momentum distribution as inside d, given by the squared Hulthén wave function in momentum space (Lamia et al., 2012). The inspection of the relative energy spectra and of the experimental momentum distribution, as extensively discussed in La Cognata et al. (2010a,c), shows that the QF reaction mechanism is present and dominant in the 0–50 MeV/c neutron momentum range and that the SD of ^{5}He, ^{16}N, and ^{19}F excited states is negligible in the energy range of astrophysical interest. Additionally, distortions due to the Coulomb interaction in the entrance channel, for instance, turned out to be negligible as in La Cognata et al. (2010b).

Gating on the 0–50 MeV/c neutron momentum range, we extracted the three-body cross section and integrated it over the whole ^{18}O$(p,\alpha)^{15}$N c.m. angular range (see La Cognata et al., 2010a,c for details). In this way, we deduced the ^{2}H(^{18}O, α^{15}N)n reaction cross section given in **Figure 6**. Horizontal error bars in the figure represent the integration bin while the vertical ones stand for statistical uncertainty. The dashed, dotted, and dot-dashed lines in the figure are Gaussian fitting of the resonances at E_{R_1} = 19.5 ± 1.1 keV, E_{R_2} = 96.6 ± 2.2 keV, and E_{R_3} = 145.5 ± 0.6 keV, in good agreement with the values reported in the literature (Angulo et al., 1999). The solid line is the sum of three Gaussian functions while the straight line is used to fit the non-resonant behavior. The fitting also allowed us to deduce the peak value of each resonance: N_1 = 138 ± 8, N_2 = 82 ± 9, and N_3 = 347 ± 8 (arbitrary units), which were used to derive the resonance strengths using the formula:

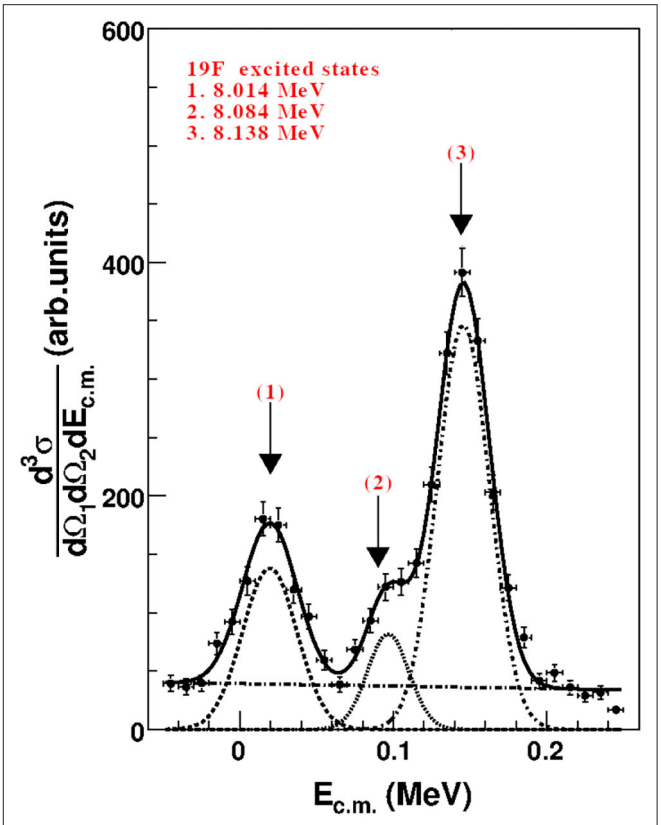

FIGURE 6 | Cross section of the ^{2}H(^{18}O, α^{15}N)n TH reaction. See text for details.

$$(\omega\gamma)_i = \frac{2J_{^{19}\mathrm{F}_i}+1}{(2J_{^{18}\mathrm{O}}+1)(2J_p+1)}\frac{\Gamma_{(p^{18}\mathrm{O})_i}\Gamma_{(\alpha^{15}\mathrm{N})_i}}{\Gamma_i}, \qquad (12)$$

through the equation (La Cognata et al., 2010a):

$$N_i = 4\,\frac{\Gamma_{\alpha_i}(E_{R_i})\,M_i^2(E_{R_i})}{\Gamma_i^2(E_{R_i})}, \qquad (13)$$

where $\Gamma_{(\alpha^{15}\mathrm{N})_i}(E) \equiv \Gamma_{\alpha_i}(E)$. In fact, the transfer amplitude is proportional to the entrance channel reduced width $\gamma_{(p^{18}\mathrm{O})_i}$, and the N_i factors thus represent the THM resonance strengths in arbitrary units and devoid of Coulomb suppression, the penetration factor $P_l(kr)$ does not appearing in Equation (13). Normalization is then achieved by scaling the THM resonance strengths, corrected to include the Coulomb effects, to the strength of a well-known resonance. Indeed, since the proton and alpha partial widths for the ∼ 144 keV resonance are well-known (Angulo et al., 1999), we can determine the absolute values of the

TABLE 4 | Summary table of the strengths of the low-energy resonances in the $^{18}O(p,\alpha)^{15}N$ astrophysical factor.

Resonance energy (keV)	J^π	$\omega\gamma$ (eV)	References
20 ± 1	$5/2^+$	$6^{+17}_{-5} \times 10^{-19}$	Angulo et al., 1999
19.5 ± 1.1	$5/2^+$	$8.3^{+3.8}_{-2.6} \times 10^{-19}$	La Cognata et al., 2010a
89 ± 3	$3/2^+$	$(0.16 \pm 0.05) \times 10^{-6}$	Lorenz-Wirzba et al., 1979
96.6 ± 2.2	$3/2^+$	$(0.18 \pm 0.03) \times 10^{-6}$	La Cognata et al., 2010a
90.3 ± 0.3	$3/2^+$	$(1.57 \pm 0.18) \times 10^{-6}$	Bruno et al., 2019
143.9 ± 0.9	$1/2^+$	0.17 ± 0.02	Lorenz-Wirzba et al., 1979
142.8 ± 0.1	$1/2^+$	0.167 ± 0.012	Becker et al., 1995[a]
143.2 ± 0.3	$1/2^+$	0.164 ± 0.012	Bruno et al., 2015

[a]*The strength of this resonance was used for normalization of the THM results, as discussed in La Cognata et al. (2010a).*

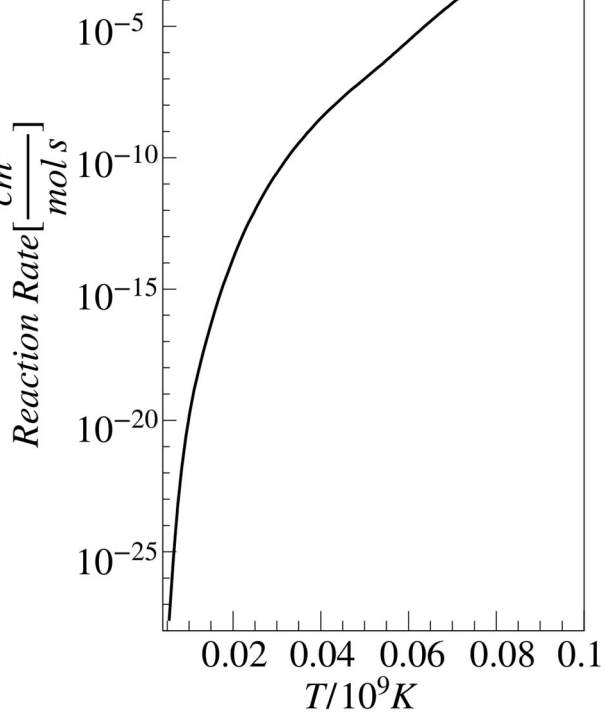

FIGURE 7 | Reaction rate of the $^{18}O(p,\alpha)^{15}N$ reaction.

strengths of the 20 and 90 keV resonances from normalization to the strength of the $\sim$ 144 keV peak, as discussed by La Cognata et al. (2008a). The normalization is accurate also because electron screening gives a negligible contribution close to 144 keV (4% maximum; Assenbaum et al., 1987). Taking $(\omega\gamma)_3$ from Becker et al. (1995), we got $(\omega\gamma)_1 = 8.3^{+3.8}_{-2.6} \times 10^{-19}$ eV, which is well within the confidence range established by NACRE, $6^{+17}_{-5} \times 10^{-19}$ eV (Angulo et al., 1999), with a much reduced uncertainty, because Angulo et al. (1999) value is based on spectroscopic data while the present result is obtained from experimental ones. The largest contribution to the error is due to the uncertainty on the resonance energy, while statistical and normalization errors sum up to about 9.5%. To cross check the method, we extracted the resonance strength of the 90 keV resonance, which turned out to be $(\omega\gamma)_2 = (1.76 \pm 0.33) \times 10^{-7}$ eV, in good agreement with the Angulo et al. (1999) strength, $(1.6 \pm 0.5) \times 10^{-7}$ eV. The results of the THM measurement and the strengths of the low-energy resonances are summarized in **Table 4**.

4.2. Extraction of the Reaction Rate

By using the narrow resonance approximation (Angulo et al., 1999), which is satisfied for these resonances at $\sim$ 20, $\sim$ 90, and $\sim$ 144 keV, we calculated the reaction rate for the $^{18}O(p,\alpha)^{15}N$ reaction using the equation:

$$N_A \langle \sigma v \rangle_{R_i} = N_A \left(\frac{2\pi}{\mu k_B}\right)^{3/2} \hbar^2 \sum_i (\omega\gamma)_i T^{-3/2} \exp\left(-E_{R_i}/k_B T\right) \quad (14)$$

where μ is the reduced mass for the projectile-target system, T is the temperature of the astrophysical site, and the index i runs over the relevant resonances. The resulting rate $R_{^{18}O(p,\alpha)^{15}N}$ is displayed in **Figure 7** as a function of the temperature given in units of $T_9 = T/10^9$ K. We also obtained the analytic expression of the reaction rate, with an accuracy of about 10%:

$$\begin{aligned} R_{^{18}O(p,\alpha)^{15}N} &= \frac{5.58\,10^{11}}{T_9^{2/3}} \exp\left(-\frac{16.732}{T_9^{1/3}} - \left(\frac{T_9}{0.51}\right)^2\right)(1 + 3.2\,T_9 + 21.8\,T_9^2) \\ &+ \frac{1.375\,10^{-13}}{T_9^{3/2}} \exp\left(-\frac{0.232}{T_9}\right) \\ &+ \frac{2.58\,10^4}{T_9^{3/2}} \exp\left(-\frac{1.665}{T_9}\right) \\ &+ \frac{3.24\,10^8}{T_9^{0.378}} \exp\left(-\frac{6.395}{T_9}\right) \end{aligned} \quad (15)$$

where the reaction rate $R_{^{18}O(p,\alpha)^{15}N}$ is expressed in $cm^3 mol^{-1} sec^{-1}$.

The next **Figure 8** shows the comparison of the present results with the one in the literature, reported in NACRE compilation (Angulo et al., 1999). Owing to the steep slope of the reaction rate, for sake of comparison the ratio of the THM rate to the NACRE one for the $^{18}O(p,\alpha)^{15}N$ is shown. In detail, the full black line is used to show the ratio of the recommended THM reaction rate to the NACRE one, while the dot-dashed and dotted black lines represent the upper and lower limits, respectively, in the same representation. Red lines are instead used, with the same meaning, for the Angulo et al. (1999) reaction rate.

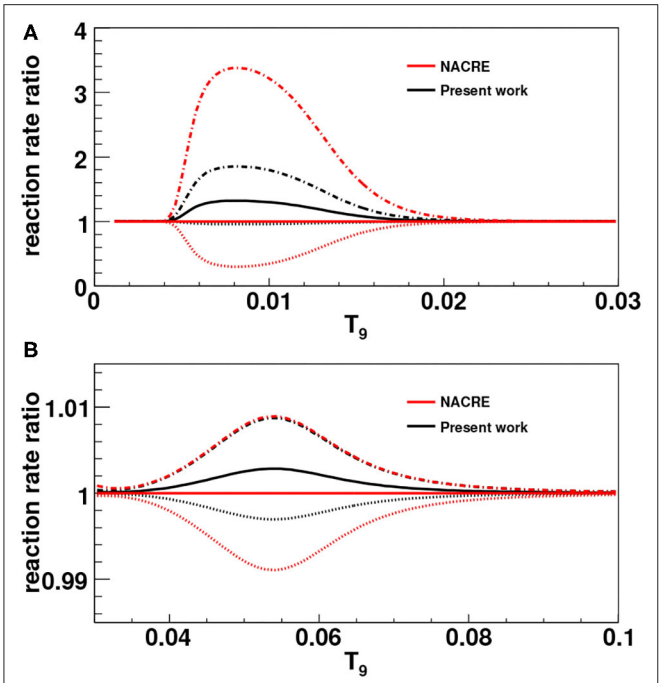

FIGURE 8 | Comparison of the reaction rate of the $^{18}O(p,\alpha)^{15}N$ reaction with the NACRE one (Angulo et al., 1999). In **(A)**, the contribution of the 20 keV resonance is shown; in **(B)**, the one of the 90 keV resonance (the upper limits for the NACRE and present-work rates overlap).

TABLE 5 | Rate of the $^{18}O(p,\alpha)^{15}N$ reaction.

Temperature (10^9 K)	Rate THM($cm^3mol^{-1}s^{-1}$)		
	Lower	Adopted	Upper
0.007	$8.12\,10^{-25}$	$1.11\,10^{-24}$	$1.54\,10^{-24}$
0.008	$4.02\,10^{-23}$	$5.55\,10^{-23}$	$7.79\,10^{-23}$
0.009	$8.60\,10^{-22}$	$1.18\,10^{-21}$	$1.65\,10^{-21}$
0.010	$1.03\,10^{-20}$	$1.39\,10^{-20}$	$1.92\,10^{-20}$
0.011	$8.15\,10^{-20}$	$1.07\,10^{-19}$	$1.45\,10^{-19}$
0.012	$4.90\,10^{-19}$	$6.22\,10^{-19}$	$8.14\,10^{-19}$
0.013	$2.45\,10^{-18}$	$2.96\,10^{-18}$	$3.72\,10^{-18}$
0.014	$1.07\,10^{-17}$	$1.24\,10^{-17}$	$1.48\,10^{-17}$
0.015	$4.30\,10^{-17}$	$4.75\,10^{-17}$	$5.40\,10^{-17}$
0.016	$1.58\,10^{-16}$	$1.69\,10^{-16}$	$1.85\,10^{-16}$
0.018	$1.72\,10^{-15}$	$1.76\,10^{-15}$	$1.83\,10^{-15}$
0.020	$1.41\,10^{-14}$	$1.42\,10^{-14}$	$1.44\,10^{-14}$
0.025	$1.00\,10^{-12}$	$1.01\,10^{-12}$	$1.01\,10^{-12}$
0.030	$2.64\,10^{-11}$	$2.64\,10^{-11}$	$2.64\,10^{-11}$
0.040	$3.12\,10^{-9}$	$3.12\,10^{-9}$	$3.12\,10^{-9}$
0.050	$1.01\,10^{-7}$	$1.01\,10^{-7}$	$1.01\,10^{-7}$
0.060	$2.81\,10^{-6}$	$2.81\,10^{-6}$	$2.81\,10^{-6}$
0.070	$7.52\,10^{-5}$	$7.52\,10^{-5}$	$7.52\,10^{-5}$
0.080	$1.10\,10^{-3}$	$1.10\,10^{-3}$	$1.10\,10^{-3}$
0.090	$9.07\,10^{-3}$	$9.07\,10^{-3}$	$9.07\,10^{-3}$
0.100	$4.88\,10^{-2}$	$4.88\,10^{-2}$	$4.88\,10^{-2}$

In the low temperature region (below $T_9 = 0.03$, see **Figure 8A**) the reaction rate was found to be about 35% larger than the one in NACRE, while the uncertainty is considerably reduced by a factor ≈ 8.5, taking into account the contribution of the 20 keV resonance only. The corresponding temperatures match with those typical of the bottom of the convective envelope, thus an increase of the reaction rate might influence the surface abundances resulting from the cool bottom process (Nollett et al., 2003) in AGB stars. Regarding the 90 keV resonance in the $^{18}O(p,\alpha)^{15}N$ reaction, we confirmed that its contribution is negligible since an increase of <1% was obtained due to the THM measurement, taking as reference the NACRE rate (**Figure 8B**). Finally, **Table 5** contains the THM reaction rate together with the upper and lower limits allowed by experimental uncertainties. In particular, in the inclusion of the uncertainties on the Angulo et al. (1999) reaction rate, it is assumed that the only source of error is coming from the 20 keV resonance.

5. THE $^{17}O(n,\alpha)^{14}C$ REACTION

The $^{17}O(n,\alpha)^{14}C$ reaction has been studied as an extension of the THM to the neutron-induced reactions. This investigation pointed out the ability of the THM to overcome the centrifugal barrier suppression effects in the entrance channel. This study demonstrates the effectiveness of the THM to emphasize the mere nuclear interaction, which avoids the centrifugal suppression or the electron screening effect, thus opening new perspectives in the use of the method for nuclear structure studies. Moreover, as regards the $^{17}O(n,\alpha)^{14}C$, only few direct measurements are reported in literature, showing discordance at neutron thermal energy range (Sanders, 1956; Koehler and Graff, 1991; Schatz et al., 1993; Wagemans et al., 2002).

In the following section, we discuss the main results of the $^{17}O(n,\alpha)^{14}C$ cross section measurement in the energy range from 0 up to a few hundred keV.

5.1. The Experiment

The $^{17}O(n,\alpha)^{14}C$ reaction has been studied via the three-body $^2H(^{17}O, \alpha^{14}C)p$ reaction. The experiment has been performed at NSL of the University of Notre Dame (South Bend, Indiana, USA) using the JN Tandem Van der Graaff. The ^{17}O beam impinged on a deuterated polyethylene target (CD_2) with an energy of 43.5 MeV. The target thickness was about 150 $\mu g/cm^2$, and the target itself has been placed at 90° with respect to the beam direction. A sketch of the used experimental setup is shown in **Figure 9**, chosen accordingly with a preliminary study that pointed out the phase-space region where a strong contribution of the QF reaction mechanism is expected.

The detection setup consists of two telescopes, made up of a ionization chamber (IC) as ΔE and a 1,000μm PSD (A1 and B1 in **Figure 9**) as E stage. The telescopes have been placed at $d_{A1} = 46.4$ cm and $d_{B1} = 49.5$ cm from the target covering and angular range 7.5±2.5°. The ICs have been filled with about 50 mbar isobutane gas allowing to an energy resolution of ∼10%, which was enough to discriminate particles by their charge but

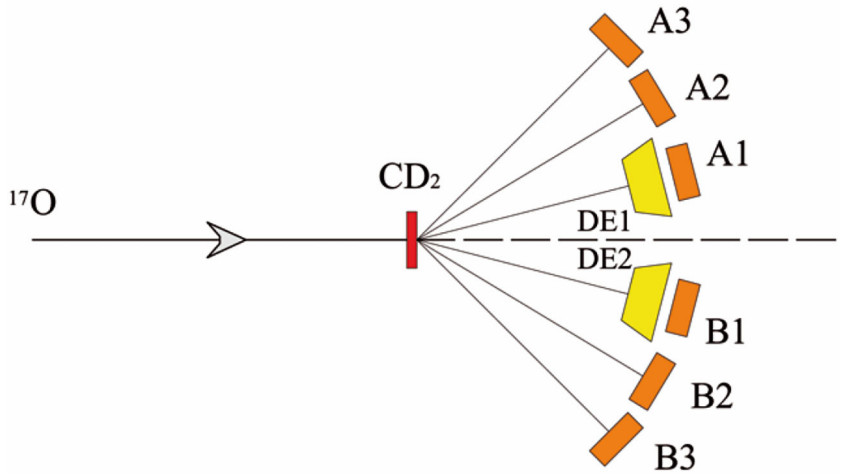

FIGURE 9 | Sketch of the experimental setup. The ^{17}O beam was impinging on a CD_2 target. The emitted particles were detected by four PSDs (A2, A3, B2, and B3) and by two ΔE-E telescopes (DE1-A1 and DE2-B1).

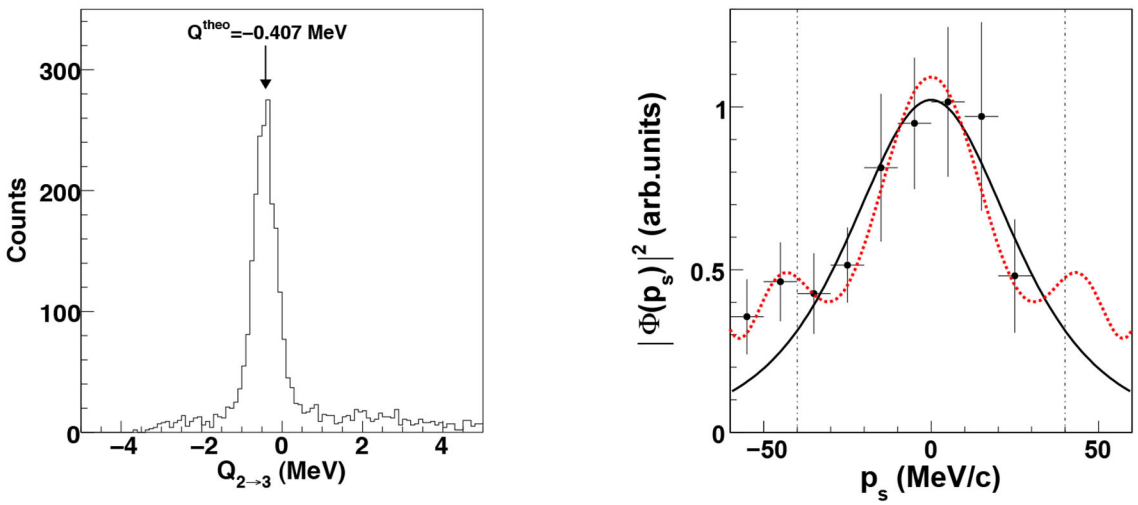

FIGURE 10 | (Left) Reconstructed *Q*-value spectrum. The theoretical value of −0.407 MeV for the ^{2}H(^{17}O,α^{14}C)^{1}H reaction is reported with the black arrow and it is in good agreement with the experimental peak. **(Right)** Experimental momentum distribution (full dots) compared with theoretical ones, given by the square of the Hulthén wave function in momentum space (black solid line) and by the DWBA momentum distribution evaluated by means of the FRESCO code (red dotter lines). The agreement is a necessary condition for the presence of the QF-mechanism in the data.

not their mass. Entrance and exit windows of ICs consist of two thin mylar foils, respectively of 0.9 and 1.5 μm in order to minimize the angular straggling. In addition, four 500μm thick PSDs referred to as A2, A3, B2, and B3 have been employed, placed at a distance $d_{A2} = 47.6$ cm, $d_{A3} = 38.1$ cm, $d_{B2} = 49.4$ cm, and $d_{B3} = 40.5$ cm from the target, covering the angular ranges 17.5°±2.5° for A2 and B2 while 27.3°±3.5° for A3 and B3. The telescopes have been optimized for C detection while the other PSDs for alpha particles.

Moreover, since the required kinematical conditions are very similar, the presence of the ^{17}O(n,α)^{14}C reaction channel was also checked in the LNS experiment optimized for the measurement of the ^{17}O(p,α)^{14}N reaction (described in section three of the present paper) (Gulino et al., 2013; Guardo et al., 2017). The good agreement between the two THM measurements, within the experimental uncertainties, allow us to average the two data sets, weighting the respective errors, in order to improve the statistics and data quality.

5.2. Reaction Channel Selection

After detector calibration, the three-body ^{2}H(^{17}O,α^{14}C)p reaction channel of interest has been selected. This separation has been accomplished by studying the coincidence events corresponding to a carbon particle detected in one of the two $\Delta E - E$ telescopes with any particles on opposite PSDs. The kinematic of the undetected emerging proton has been deduced

TABLE 6 | Summary table of the ^{18}O resonance parameters observed in Guardo et al. (2017).

Resonance energy (keV)	J^{π}	Γ_{tot} (eV)	References
−6	1^-	$2,400 \pm 300$	Guardo et al., 2017
		2,400	Wagemans et al., 2002
		$2,000 \pm 700$	Avila et al., 2014
75	5^-	36 ± 5	Guardo et al., 2017
178	2^+	$2,260 \pm 300$	Guardo et al., 2017
		$2,258 \pm 135$	Wagemans et al., 2002[a]
		$1,900 \pm 200$	Avila et al., 2014
244	3^-	$14,700 \pm 3,800$	Guardo et al., 2017
		$14,739 \pm 590$	Wagemans et al., 2002[a]
		$8,500 \pm 900$	Avila et al., 2014

For comparison, resonance parameters from Wagemans et al. (2002) and from Avila et al. (2014) are also reported.

[a]*The n and α partial widths of this resonance were used for normalization of the THM results, as discussed in Guardo et al. (2017), since the strengths are not available in literature.*

by means of momentum and energy conservation laws. In left panel of **Figure 10**, the experimental Q-value spectrum for the selected events is plotted showing a prominent peak, centered at about −0.4 MeV, in good agreement with the expected value of −0.407 MeV, marked by the black vertical arrow. The very low background (≤7% with respect the total statistics) clearly demonstrates that no other reaction channels influence the one of interest. This result represents a signature of a good calibration and a precise selection of the ^{2}H(^{17}O,α^{14}C)p reaction channel.

5.3. Selection of the QF Reaction Mechanism

The next essential step for a precise selection of the TH data is a detailed study of the momentum distribution for the $p-n$ intercluster motion in the deuteron. By using the same procedure already described in section 3.2, the experimental proton momentum distribution has been obtained. The comparison between the experimental momentum distribution (black dots) and the theoretical one (black solid line) is shown in the right panel of **Figure 10**. The present distribution returns an FWHM value of 58±11 MeV/c, in good agreement with the theoretical one of ∼60 MeV/c.

Moreover, the experimental data are also compared with the DWBA distribution (red dashed line in **Figure 10**) evaluated via the FRESCO code (Thompson, 1988) in order to check if the simple PWIA approach gives an accurate description of the $p-n$ momentum distribution. For this calculation, optical potential parameters adjusted from the Perey and Perey (1976) compilation have been adopted. The good agreement, within $|\vec{p}_s| \leq 40$ MeV/c, between DWBA, PWIA, and the experimental data makes us confident that the QF mechanism gives the main contribution to the reaction in the considered p_s range. Finally, the vertical dot-dashed lines mark the position of the selected events for which the TH has been applied.

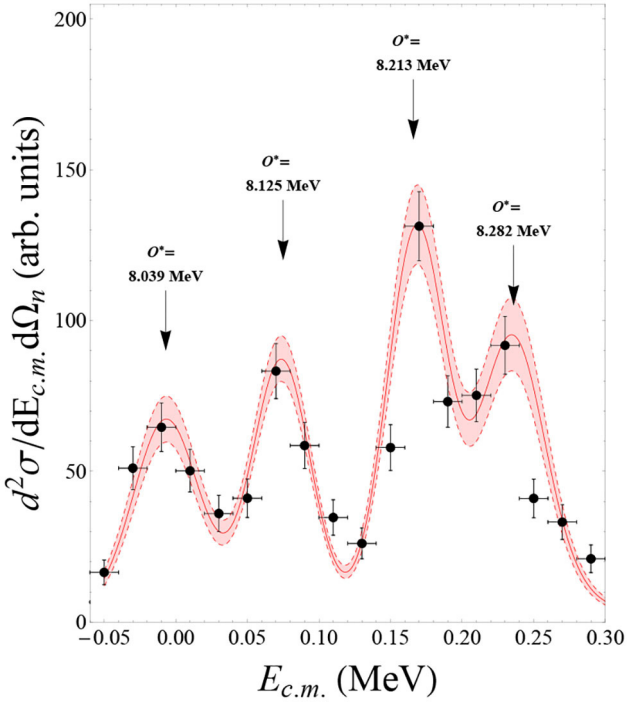

FIGURE 11 | Integrated QF two-body cross section for the ^{17}O(n,α)^{14}C reaction in arbitrary units. Experimental data are displayed with black points. The n-^{17}O relative energy binning are reported with the horizontal error bars, while the vertical ones represent the statistical and integration uncertainties. The red line is the best fit to the data calculated with the modified R-matrix approach.

5.4. Extraction of the Reaction Rate

Now that the presence of the QF process is completely ascertained and following the prescription of Equation (1), the two-body cross section can be extracted by dividing the experimental three-body one by the product of the momentum distribution of the spectator inside the Trojan Horse nucleus and the kinematic factor. The result has been corrected for the penetration factor (described in this case in terms of the spherical Bessel and Neumann functions) in order to be compared with direct data and to perform the normalization at high energies, namely, to the well-known resonances at 8,213 and 8,282 keV reported in Wagemans et al. (2002) (see **Table 6**). This extracted $(d\sigma/d\Omega)^{HOES}$ as a function of E_{cm} integrated over the whole θ_{cm} range (for further information see Gulino et al., 2013) is reported in **Figure 11** with black points. The error bars take into account the statistical and angular distribution integration uncertainties. The arrows in **Figure 11** indicate four resonances corresponding to ^{18}O states at 8.039, 8.125, 8.213, and 8.282 MeV (Ajzenberg-Selove, 1987) clearly present in the THM cross section. It is important to underline the presence of the 8,125 keV level ($J^{\pi} = 5^-$) since its population occurs via f-wave ^{17}O-n relative motion and consequently is strongly suppressed in the available direct measurements (Wagemans et al., 2002). Hence, this experimental result shows the power of THM for n-induced

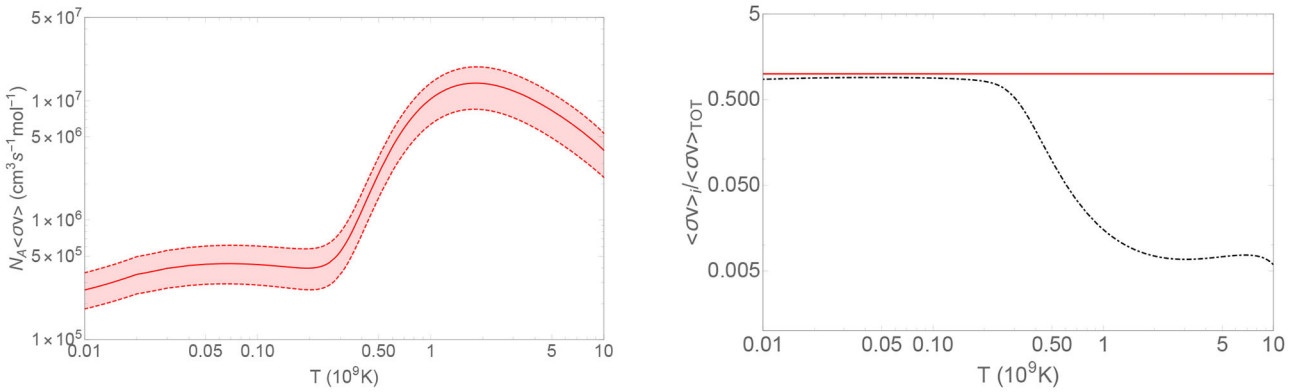

FIGURE 12 | (Left) The experimental TH reaction rate (red line). The red band represents the statistical and normalization errors. **(Right)** Contribution of the subthreshold resonant state to the total reaction rate.

reactions to extrapolate information about resonant levels that are suppressed in direct measurements due to the presence of the centrifugal barrier. Finally, the experimental data have been fitted following the modified R-matrix approach. The result, for which a reduced χ^2 of $\tilde{\chi} = 0.8$ has been found, is displayed in **Figure 11** with the solid red line, while the red band accounts for the error introduced by the normalization procedure, evaluated here at about 15% [for a detailed procedure see Guardo et al. (2017) and references therein].

Figure 12 (left panel) shows the astrophysical rate, calculated from the cross section according to the usual definition (Iliadis et al., 2010). The red band highlights the region allowed by uncertainties (statistical and normalization). The values of the astrophysical rate calculated here is reported in **Table 7**. In addition, the application of the THM allowed for the first time to excite and disentangle the contribution of the subthreshold level centered at −7 keV in the center-of-mass system. This result is fundamental to determine the total reaction rate at low energies and may change significantly the abundance ratios of the elements involved in the nucleosynthesis network of the weak component of the s-process (Wagemans et al., 2002; Guardo et al., 2017). Indeed, in the right panel of **Figure 12**, the contribution of the −7 keV resonance state to the total reaction rate is disentangled showing its pivotal importance at astrophysical relevant temperatures (Guardo et al., 2017).

TABLE 7 | Rate of the $^{17}O(n,\alpha)^{14}C$ reaction.

Temperature	Rate THM ($cm^3mol^{-1}s^{-1}$)		
(10^9 K)	Lower	Adopted	Upper
0.01	$0.22\,10^6$	$0.26\,10^6$	$0.30\,10^6$
0.02	$0.30\,10^6$	$0.35\,10^6$	$0.40\,10^6$
0.03	$0.33\,10^6$	$0.39\,10^6$	$0.45\,10^6$
0.04	$0.35\,10^6$	$0.41\,10^6$	$0.47\,10^6$
0.05	$0.36\,10^6$	$0.42\,10^6$	$0.48\,10^6$
0.1	$0.36\,10^6$	$0.42\,10^6$	$0.48\,10^6$
0.15	$0.34\,10^6$	$0.40\,10^6$	$0.46\,10^6$
0.2	$0.32\,10^6$	$0.38\,10^6$	$0.44\,10^6$
0.3	$0.40\,10^6$	$0.47\,10^6$	$0.54\,10^6$
0.4	$0.77\,10^6$	$0.90\,10^6$	$1.04\,10^6$
0.5	$1.45\,10^6$	$1.71\,10^6$	$1.97\,10^6$
0.6	$2.35\,10^6$	$2.76\,10^6$	$3.17\,10^6$
0.8	$4.19\,10^6$	$4.93\,10^6$	$5.67\,10^6$
1.	$5.64\,10^6$	$6.64\,10^6$	$7.64\,10^6$
1.5	$7.34\,10^6$	$8.64\,10^6$	$9.94\,10^6$
2.	$7.46\,10^6$	$8.78\,10^6$	$1.01\,10^7$
2.5	$7.03\,10^6$	$8.27\,10^6$	$9.51\,10^6$
3.	$6.44\,10^6$	$7.58\,10^6$	$8.72\,10^6$
3.5	$5.85\,10^6$	$6.88\,10^6$	$7.91\,10^6$
4.	$5.31\,10^6$	$6.25\,10^6$	$7.19\,10^6$
5.	$4.40\,10^6$	$5.18\,10^6$	$5.96\,10^6$
6.	$3.71\,10^6$	$4.36\,10^6$	$5.01\,10^6$
7.	$3.16\,10^6$	$3.72\,10^6$	$4.28\,10^6$
8.	$2.70\,10^6$	$3.18\,10^6$	$3.66\,10^6$
9.	$2.35\,10^6$	$2.77\,10^6$	$3.18\,10^6$
10.	$2.05\,10^6$	$2.41\,10^6$	$2.77\,10^6$

6. FINAL REMARKS

In this paper we have discussed the influence of the neutron and proton induced reactions on the stable, neutron-rich oxygen isotopes, ^{17}O and ^{18}O.

In detail, we reported on the application of the THM to the QF $^2H(^{17}O,\alpha^{14}N)n$ reaction for extracting the $^{17}O(p,\alpha)^{14}N$ cross section and reaction rate, by using the approach for the resonant case discussed in La Cognata et al. (2010a). Two measurements were carried out, at LNS and at NSL, with the main aim of extracting the strength of the 65 keV resonance, laying right at astrophysical energies. By normalizing to the strength of the well-known 183 keV resonance, the THM measurements led to a recommended value of $\omega\gamma = 3.42 \pm 0.60 \times 10^{-9}$ eV, from the weighted average of the results of the two experiments. Such strength was then used to calculate the $^{17}O(p,\alpha)^{14}N$ reaction

rate, resulting in an increase of $\sim$ 30% with respect the data in the literature at the temperatures typical of RGs, AGB stars and massive stars (Iliadis et al., 2010). From such result we could also provide a revised value for the strength of the 65 keV resonance in the $^{17}O(p,\gamma)^{18}F$ reaction, leading to an increase of about 20% with respect to the literature (Di Leva et al., 2014).

In the case of the $^{18}O(p,\alpha)^{15}N$ reaction, we underscore that, for the first time, the strength of the low-lying 20 keV resonance was experimentally determined thanks to the use of the THM. Thanks to this result, the reaction rate was calculated, which turned out to be about 35% larger than the NACRE rate (Angulo et al., 1999) in the temperature region where the effect of the 20 keV resonance is dominant. Since no spectroscopic factor was needed to fix the strength of this state, the reaction rate was determined with high accuracy, reducing the uncertainty due to the modest knowledge of the resonance parameters by a factor $\sim$ 8.5. Moreover, the THM result is not affected by the electron screening, which can enhance the astrophysical factor by a factor larger than about 2.4 at 20 keV (Assenbaum et al., 1987), making any direct measurement of the nuclear cross section presently impossible.

Finally, the same QF reaction, under slightly different kinematic conditions, made also possible to measure the $^{17}O(n,\alpha)^{14}C$ with no need of neutron beams. In detail, it was possible to observe the subthreshold level centered at -7 keV in the center-of-mass system corresponding to the ^{18}O level at 8.039 MeV, that strongly affects the total reaction rate. Also, since the THM approach allows us to bypass the Coulomb and centrifugal barriers, we could observe the 8.121 MeV ^{18}O level that, having a spin parity $J^{\pi}=5^{-}$ is suppressed in direct measurements because of it is populated in f-wave. Therefore, we could obtain an accurate experimental trend of the $^{17}O(n,\alpha)^{14}C$ cross section over the whole range of astrophysical interest, up to about 250 keV, in good agreement with the results available in the literature (where present). Then the recommended reaction rate was calculated, combining the results of the THM measurement and the direct data of Wagemans et al. (2002) above $\sim$ 100 keV, leading to an increase of the rate over the whole temperature range of interest, with potential consequences for the weak component of the s-process.

AUTHOR CONTRIBUTIONS

Nuclear data of $^{17}O(p,\alpha)^{14}N$ and $^{18}O(p,\alpha)^{15}N$ were analyzed by MS and ML, respectively, and GG and MG took care of the $^{17}O(n,\alpha)^{14}C$ data analysis. All the listed authors contributed to the writing of the paper.

FUNDING

This work has been partially supported by the Italian Ministry of University MIUR under Grants No. RFBR082838 (FIRB2008), LNS-Astrofisica Nucleare (fondi premiali). It has been partially supported also by Grants No. LC 07050 of the Czech MSMT, No. M10480902 of the Czech Academy of Science, No. LH1101 of the AMVIS project, and of the GAČR Project under Grant No. P203/10/0310. The Notre Dame collaborators were supported by Grant No. PHY-1713857 and JINA-CEE Grant No. PHY-1430152.

ACKNOWLEDGMENTS

The authors acknowledge Alain Coc for his suggestions about the topics discussed in the present article and also Programma ricerca di ateneo UNICT 2020-22 linea2 by University of Catania.

REFERENCES

Adelberger, E. G., García, A., Robertson, R. G. H., Snover, K. A., Balantekin, A. B., Heeger, K., et al. (2011). Solar fusion cross sections. II. The pp chain and CNO cycles. *Rev. Modern Phys.* 83, 195–246. doi: 10.1103/RevModPhys.83.195

Ajzenberg-Selove, F. (1987). Energy levels of light nuclei A = 18-20. *Nucl. Phys. A* 475, 1–198. doi: 10.1016/0375-9474(87)90205-3

Angulo, C., Arnould, M., Rayet, M., Descouvemont, P., Baye, D., Leclercq-Willain, C., et al. (1999). A compilation of charged-particle induced thermonuclear reaction rates. *Nucl. Phys. A* 656, 3–183. doi: 10.1016/S0375-9474(99)00030-5

Assenbaum, H. J., Langanke, K., and Rolfs, C. (1987). Effects of electron screening on low-energy fusion cross sections. *Z. Phys. A Hadron. Nuclei* 327, 461–468. doi: 10.1007/BF01289572

Avila, M. L., Rogachev, G. V., Goldberg, V. Z., Johnson, E. D., Kemper, K. W., Tchuvil'sky, Y. M., et al. (2014). α-cluster structure of O18. *Phys. Rev. C* 90:024327. doi: 10.1103/PhysRevC.90.024327

Baur, G. (1986). Breakup reactions as an indirect method to investigate low-energy charged-particle reactions relevant for nuclear astrophysics. *Phys. Lett. B* 178, 135–138. doi: 10.1016/0370-2693(86)91483-8

Becker, H. W., Bahr, M., Berheide, M., Borucki, L., Buschmann, M., Rolfs, C., et al. (1995). Hydrogen depth profiling using^{18}O ions. *Z. Phys. A Hadron. Nuclei* 351, 453–465. doi: 10.1007/BF01291151

Berheide, M., Rolfs, C., Schröder, U., and Trautvetter, H. P. (1992). Search for the 70 keV resonance in$^{17}O(p,\alpha)^{14}N$. *Z. Phys. A Hadron. Nuclei* 343, 483–487. doi: 10.1007/BF01289827

Berka, I., Jackson, K. P., Rolfs, C., Charlesworth, A. M., and Azuma, R. E. (1977). Isospin mixing of the 5605 and 5668 keV states in ^{18}F in the light of a new state at 5603 keV. *Nucl. Phys. A* 288, 317–333. doi: 10.1016/0375-9474(77)90138-5

Blackmon, J. C., Champagne, A. E., Hofstee, M. A., Smith, M. S., Downing, R. G., and Lamaze, G. P. (1995). Measurement of the $^{17}O(p,\alpha)^{14}N$ cross section at stellar energies. *Phys. Rev. Lett.* 74, 2642–2645. doi: 10.1103/PhysRevLett.74.2642

Brown, R. E. (1962). Experimental study of the $^{17}O(p,\alpha)^{14}N$ reaction and a calculation of the rate of this reaction in the CNO cycle in stars. *Phys. Rev.* 125, 347–358. doi: 10.1103/PhysRev.125.347

Bruno, C. G., Aliotta, M., Descouvemont, P., Best, A., Davinson, T., Bemmerer, D., et al. (2019). Improved astrophysical rate for the $^{18}O(p,\alpha)^{15}N$ reaction by underground measurements. *Phys. Lett. B* 790, 237–242. doi: 10.1016/j.physletb.2019.01.017

Bruno, C. G., Scott, D. A., Aliotta, M., Formicola, A., Best, A., Boeltzig, A., et al. (2016). Improved direct measurement of the 64.5 kev resonance strength in the $^{17}O(p,\alpha)^{14}N$ reaction at luna. *Phys. Rev. Lett.* 117:142502. doi: 10.1103/PhysRevLett.117.142502

Bruno, C. G., Scott, D. A., Formicola, A., Aliotta, M., Davinson, T., Anders, M., et al. (2015). Resonance strengths in the $^{17,18}O(p,\alpha)^{14,15}N$ reactions and background suppression underground. Commissioning of a

new setup for charged-particle detection at LUNA. *Eur. Phys. J. A* 51:94. doi: 10.1140/epja/i2015-15094-y

Calvi, G., Lattuada, M., Miljanić, D., Riggi, F., Spitaleri, C., and Zadro, M. (1990). Quasi-free reaction mechanism in ^{2}H(^{6}Li,^{3}He α)n at E_0 = 21.6-33.6 MeV. *Phys. Rev. C* 41, 1848–1850. doi: 10.1103/PhysRevC.41.1848

Chafa, A., Tatischeff, V., Aguer, P., Barhoumi, S., Coc, A., Garrido, F., et al. (2007). Experimental determination of the ^{17}O(p, α)^{14}N and ^{17}O(p, γ)^{18}F reaction rates. *Phys. Rev. C* 75:035810. doi: 10.1103/PhysRevC.75.035810

Champagne, A. E., and Pitt, M. L. (1986). The destruction of ^{18}O in red giants. A search for a sub-threshold resonance in the ^{18}O + p system. *Nucl. Phys. A* 457, 367–374. doi: 10.1016/0375-9474(86)90384-2

Cherubini, S., Gulino, M., Spitaleri, C., Rapisarda, G. G., La Cognata, M., Lamia, L., et al. (2015). First application of the Trojan horse method with a radioactive ion beam: study of the ^{18}F(p,α)^{15}O reaction at astrophysical energies. *Phys. Rev. C* 92:015805. doi: 10.1103/PhysRevC.92.015805

Chew, G. F. (1952). The impulse approximation. *Phys. Rev* 85:636. doi: 10.1103/PhysRev.85.636

Costanzo, E., Lattuada, M., Romano, S., Vinciguerra, D., and Zadro, M. (1990). A procedure for the analysis of the data of a three body nuclear reaction. *Nucl. Instrum. Methods Phys. Res. A* 295, 373–376. doi: 10.1016/0168-9002(90)90715-I

Dearborn, D. S. P. (1992). Diagnostics of stellar evolution: the oxygen isotopes. *Phys. Rep*. 210, 367–382. doi: 10.1016/0370-1573(92)90080-J

Di Leva, A., Scott, D. A., Caciolli, A., Formicola, A., Strieder, F., Aliotta, M., et al. (2014). Underground study of the ^{17}O(p,γ)^{18}F reaction relevant for explosive hydrogen burning. *Phys. Rev. C* 89:015803. doi: 10.1103/PhysRevC.90.019902

Dolinsky, E. I., Dzhamalov, P. O., and Mukhamedzhanov, A. M. (1973). Peripheral-model approach to stripping into resonant states. *Nucl. Phys. A* 202, 97–122. doi: 10.1016/0375-9474(73)90244-3

Fox, C., Iliadis, C., Champagne, A. E., Coc, A., José, J., Longland, R., et al. (2004). Explosive hydrogen burning of ^{17}O in classical novae. *Phys. Rev. Lett*. 93:081102. doi: 10.1103/PhysRevLett.93.081102

Fox, C., Iliadis, C., Champagne, A. E., Fitzgerald, R. P., Longland, R., Newton, J., et al. (2005). Thermonuclear reaction rate of ^{17}O(p, γ)^{18}F. *Phys. Rev. C* 71:055801. doi: 10.1103/PhysRevC.71.055801

Guardo, G. L., Spitaleri, C., Lamia, L., Gulino, M., La Cognata, M., Tang, X., et al. (2017). Assessing the near threshold cross section of the ^{17}O(n, α)^{14}C reaction by means of the Trojan horse method. *Phys. Rev. C* 95:025807. doi: 10.1103/PhysRevC.95.025807

Guardo, G. L., Spitaleri, C., Lamia, L., Spartá, R., Carlin, N., Cherubini, S., et al. (2019). The ^{10}B(n,α)^{7}Li cross sections at ultra-low energy through the Trojan Horse Method applied to the ^{2}H(^{10}B,α^{7}Li)^{1}H. *Eur. Phys. J. A* 55:211. doi: 10.1140/epja/i2019-12914-0

Gulino, M., Spitaleri, C., Cherubini, S., Crucillá, V., La Cognata, M., Lamia, L., et al. (2010). Study of the ^{6}Li(n, α)^{3}H reaction via the ^{2}H quasi-free break-up. *J. Phys. G Nucl. Phys*. 37:125105. doi: 10.1088/0954-3899/37/12/125105

Gulino, M., Spitaleri, C., Tang, X. D., Guardo, G. L., Lamia, L., Cherubini, S., et al. (2013). Suppression of the centrifugal barrier effects in the off-energy-shell neutron +^{17}O interaction. *Phys. Rev. C* 87:012801. doi: 10.1103/PhysRevC.87.012801

Hannam, M. D., and Thompson, W. J. (1999). Estimating small signals by using maximum likelihood and Poisson statistics. *Nucl. Instrum. Methods Phys. Res. A* 431, 239–251. doi: 10.1016/S0168-9002(99)00269-7

Hernanz, M., José, J., Coc, A., Gómez-Gomar, J., and Isern, J. (1999). Gamma-ray emission from novae related to positron annihilation: constraints on its observability posed by new experimental nuclear data. *Astrophys. J.* 526, L97–L100. doi: 10.1086/312372

Iliadis, C., Longland, R., Champagne, A. E., Coc, A., and Fitzgerald, R. (2010). Charged-particle thermonuclear reaction rates: II. Tables and graphs of reaction rates and probability density functions. *Nucl. Phys. A* 841, 31–250. doi: 10.1016/j.nuclphysa.2010.04.009

Jorissen, A., Smith, V. V., and Lambert, D. L. (1992). Fluorine in red giant stars: evidence for nucleosynthesis. *Astron. Astrophys*. 261, 164–187.

José, J., and Hernanz, M. (2007). Nucleosynthesis in classical nova explosions. *J. Phys. G* 34, R431–R458. doi: 10.1088/0954-3899/34/12/R01

Käppeler, F., Gallino, R., Bisterzo, S., and Aoki, W. (2011). The s process: nuclear physics, stellar models, and observations. *Rev. Modern Phys*. 83, 157–194. doi: 10.1103/RevModPhys.83.157

Kieser, W. E., Azuma, R. E., and Jackson, K. P. (1979). The ^{17}O(p,α)^{14}N reaction: physics and astrophysics. *Nucl. Phys. A*, 331, 155–179. doi: 10.1016/0375-9474(79)90307-5

Koehler, P. E., and Graff, S. M. (1991). ^{17}O(n,α)^{14}C cross section from 25 meV to approximately 1 MeV. *Phys. Rev. C* 44, 2788–2793. doi: 10.1103/PhysRevC.44.2788

La Cognata, M., Pizzone, R. G., José, J., Hernanz, M., Cherubini, S., Gulino, M., et al. (2017). A Trojan horse approach to the production of ^{18}F in novae. *AstroPhys. J.* 846:65. doi: 10.3847/1538-4357/aa845f

La Cognata, M., Spitaleri, C., Mukhamedzhanov, A., Banu, A., Cherubini, S., Coc, A., et al. (2010a). A novel approach to measure the cross section of the ^{18}O(p, α)^{15}N resonant reaction in the 0-200 keV energy range. *Astrophys. J.* 708, 796–811. doi: 10.1088/0004-637X/708/1/796

La Cognata, M., Spitaleri, C., Mukhamedzhanov, A., Goldberg, V., Irgaziev, B., Lamia, L., et al. (2010b). DWBA momentum distribution and its effect on THM. *Nucl. Phys. A* 834, 658–660. doi: 10.1016/j.nuclphysa.2010.01.116

La Cognata, M., Spitaleri, C., and Mukhamedzhanov, A. M. (2010c). Effect of high-energy resonances on the ^{18}O(p, α)^{15}N reaction rate at AGB and post-AGB relevant temperatures. *Astrophys. J.* 723, 1512–1522. doi: 10.1088/0004-637X/723/2/1512

La Cognata, M., Spitaleri, C., Mukhamedzhanov, A. M., Irgaziev, B., Tribble, R. E., Banu, A., et al. (2008a). Measurement of the 20 and 90keV resonances in the ^{18}O(p,α)^{15}N reaction via the Trojan horse method. *Phys. Rev. Lett*. 101:152501. doi: 10.1103/PhysRevLett.101.152501

La Cognata, M., Spitaleri, C., Tribble, R. E., Al-Abdullah, T., Banu, A., Cherubini, S., et al. (2008b). Indirect measurement of the ^{18}O(p, α)^{15}N reaction rate through the THM. *J. Phys. G Nucl. Phys*. 35:014014. doi: 10.1088/0954-3899/35/1/014014

Lamia, L., La Cognata, M., Spitaleri, C., Irgaziev, B., and Pizzone, R. G. (2012). Influence of the d-state component of the deuteron wave function on the application of the Trojan horse method. *Phys. Rev. C* 85:025805. doi: 10.1103/PhysRevC.85.025805

Lamia, L., Mazzocco, M., Pizzone, R. G., Hayakawa, S., La Cognata, M., Spitaleri, C., et al. (2019). Cross-section measurement of the cosmologically relevant ^{7}Be(n, α)^{4}He reaction over a broad energy range in a single experiment. *Astrophys. J.* 879:23. doi: 10.3847/1538-4357/ab2234

Landre, V., Aguer, P., Bogaert, G., Lefebvre, A., Thibaud, J. P., Fortier, S., et al. (1989). ^{17}O(^{3}He,d)^{18}F reaction and its implication in the ^{17}O destruction in the CNO cycle in stars. *Phys. Rev. C* 40, 1972–1984. doi: 10.1103/PhysRevC.40.1972

Lorenz-Wirzba, H., Schmalbrock, P., Trautvetter, H. P., Wiescher, M., Rolfs, C., and Rodney, W. S. (1979). The ^{18}O(p, α)^{15}N reaction at stellar energies. *Nucl. Phys. A* 313, 346–362. doi: 10.1016/0375-9474(79)90505-0

Lugaro, M., Ugalde, C., Karakas, A. I., Görres, J., Wiescher, M., Lattanzio, J. C., et al. (2004). Reaction rate uncertainties and the production of ^{19}F in asymptotic giant branch stars. *Astrophys. J.* 615, 934–946. doi: 10.1086/424559

Mak, H. B., Evans, H. C., Ewan, G. T., and Macarthur, J. D. (1978). The ^{18}O(p,α)^{15}N cross section at low energies. *Nucl. Phys. A* 304, 210–220. doi: 10.1016/0375-9474(78)90104-5

Mak, H. B., Ewan, G. T., Evans, H. C., MacArthur, J. D., McLatchie, W., and Azuma, R. E. (1980). The alpha widths of the 5603, 5605 and 5668 keV states in ^{18}F. *Nucl. Phys. A* 343, 79–90. doi: 10.1016/0375-9474(80)90641-7

Moazen, B. H., Bardayan, D. W., Blackmon, J. C., Chae, K. Y., Chipps, K., Domizioli, C. P., et al. (2007). Measurement of the 183 keV resonance in ^{17}O(p,α)^{14}N using a novel technique. *Phys. Rev. C* 75:065801. doi: 10.1103/PhysRevC.75.065801

Mukhamedzhanov, A. M., Blokhintsev, L. D., Irgaziev, B. F., Kadyrov, A. S., La Cognata, M., Spitaleri, C., et al. (2008). Trojan Horse as an indirect technique in nuclear astrophysics. *J. Phys. G Nucl. Phys*. 35:014016. doi: 10.1088/0954-3899/35/1/014016

Newton, J. R., Iliadis, C., Champagne, A. E., Longland, R., and Ugalde, C. (2007). Remeasurement of the 193 keV resonance in ^{17}O(p,α)^{14}N. *Phys. Rev. C* 75:055808. doi: 10.1103/PhysRevC.75.055808

Nollett, K. M., Busso, M., and Wasserburg, G. J. (2003). Cool bottom processes on the thermally pulsing asymptotic giant branch and the isotopic composition of circumstellar dust grains. *Astrophys. J.* 582, 1036–1058. doi: 10.1086/344817

Perey, C. M., and Perey, F. G. (1976). Compilation of phenomenological optical-model parameters 1954-1975. *Atom. Data Nucl. Data Tables* 17:1. doi: 10.1016/0092-640X(76)90007-3

Pizzone, R. G., Roeder, B. T., McCleskey, M., Trache, L., Tribble, R. E., Spitaleri, C., et al. (2016). Trojan Horse measurement of the ^{18}F(p,α)^{15}O astrophysical S(E)-factor. *Eur. Phys. J. A* 52:24. doi: 10.1140/epja/i2016-16024-3

Rolfs, C., and Rodney, W. (1988). *Cauldrons in the Cosmos*. Chicago, IL: The University of Chicago Press.

Rolfs, C., and Rodney, W. S. (1975). Hydrogen burning of ^{17}O in the CNO cycle. *Nucl. Phys. A* 250, 295–308. doi: 10.1016/0375-9474(75)90260-2

Sanders, R. M. (1956). Study of the ^{14}C(p, n)^{14}N and ^{14}C(α, n)^{17}O reactions. *Phys. Rev. C* 104, 1434–1440. doi: 10.1103/PhysRev.104.1434

Schatz, H., Kaeppeler, F., Koehler, P. E., Wiescher, M., and Trautvetter, H. P. (1993). ^{17}O(n, α)^{14}C: closure of a primordial CNO Bi-Cycle? *AstroPhys. J.* 413:750. doi: 10.1086/173042

Schmidt, C., and Duhm, H. H. (1970). The ^{18}O(^{3}He,d)^{19}F reaction at E_3He = 16 MeV. *Nucl. Phys. A* 155, 644–658. doi: 10.1016/0375-9474(70)90918-8

Scott, D. A., Caciolli, A., Di Leva, A., Formicola, A., Aliotta, M., Anders, M., et al. (2012). First direct measurement of the ^{17}O(p,γ)^{18}F reaction cross section at gamow energies for classical novae. *Phys. Rev. Lett.* 109:202501. doi: 10.1103/PhysRevLett.109.202501

Sergi, M. L., Spitaleri, C., La Cognata, M., Coc, A., Mukhamedzhanov, A., Burjan, S. V., et al.. (2010). New high accuracy measurement of the ^{17}O(p,α)^{14}N reaction rate at astrophysical temperatures. *Phys. Rev. C* 82:032801. doi: 10.1103/PhysRevC.82.032801

Sergi, M. L., Spitaleri, C., La Cognata, M., Lamia, L., Pizzone, R. G., Rapisarda, G. G., et al. (2015). Improvement of the high-accuracy ^{17}O(p, α)^{14}N reaction-rate measurement via the Trojan horse method for application to ^{17}O nucleosynthesis. *Phys. Rev. C* 91:065803. doi: 10.1103/PhysRevC.91.065803

Shapiro, I. S. (1967). *Interaction of High-Energy Particles with Nuclei*. New York, NY: Academic Press.

Spitaleri, C., La Cognata, M., Lamia, L., Mukhamedzhanov, A. M., and Pizzone, R. G. (2016). Nuclear astrophysics and the Trojan horse method. *Eur. Phys. J. A* 52:77. doi: 10.1140/epja/i2016-16077-2

Spitaleri, C., La Cognata, M., Lamia, L., Pizzone, R. G., and Tumino, A. (2019). Astrophysics studies with the Trojan Horse method. *Eur. Phys. J. A* 55:161. doi: 10.1140/epja/i2019-12833-0

Spitaleri, C., Lamia, L., Tumino, A., Pizzone, R. G., Cherubini, S., del Zoppo, A., et al. (2004). The ^{11}B(p,α_0)^{8}Be reaction at sub-Coulomb energies via the Trojan-horse method. *Phys. Rev. C* 69:055806. doi: 10.1103/PhysRevC.69.055806

Spitaleri, C., Mukhamedzhanov, A. M., Blokhintsev, L. D., La Cognata, M., Pizzone, R. G., and Tumino, A. (2011). The Trojan horse method in nuclear astrophysics. *Phys. Atom. Nucl.* 74, 1725–1739. doi: 10.1134/S1063778811110184

Thompson, I. J. (1988). Coupled reaction channels calculations in nuclear physics. *Comput. Phys. Rep*. 7, 167–212. doi: 10.1016/0167-7977(88)90005-6

Tribble, R. E., Bertulani, C. A., La Cognata, M., Mukhamedzhanov, A. M., and Spitaleri, C. (2014). Indirect techniques in nuclear astrophysics: a review. *Rep. Prog. Phys*. 77:106901. doi: 10.1088/0034-4885/77/10/106901

Wagemans, J., Wagemans, C., Goeminne, G., Serot, O., Loiselet, M., and Gaelens, M. (2002). The ^{17}O(n,α)^{14}C reaction from subthermal up to approximately 350 keV neutron energy. *Phys. Rev. C* 65:034614. doi: 10.1103/PhysRevC.65.034614

Wiescher, M., Becker, H. W., Görres, J., Kettner, K. U., Trautvetter, H. P., Kieser, W. E., et al. (1980). Nuclear and astrophysical aspects of ^{18}O(p,γ)^{19}F. *Nucl. Phys. A* 349, 165–216. doi: 10.1016/0375-9474(80)90451-0

Yagi, K., Katori, K., Ohnuma, H., Hashimoto, Y., and Nogami, Y. (1962). Experiment on elastic scattering of protons by ^{18}O. *J. Phys. Soc. Jpn*. 17, 595–603. doi: 10.1143/JPSJ.17.595

Yim, M.-S., and Caron, F. (2006). Life cycle and management of carbon-14 from nuclear power generation. *Prog. Nucl. Energy* 48, 2–36. doi: 10.1016/j.pnucene.2005.04.002

Zadro, M., Miljanić, D., Spitaleri, C., Calvi, G., Lattuada, M., and Riggi, F. (1989). Excitation function of the quasifree contribution in the ^{2}H(^{7}Li,$\alpha\alpha$)n reaction at E_0 = 28-48 MeV. *Phys. Rev. C* 40, 181–185. doi: 10.1103/PhysRevC.40.181

Zinner, E. (2014). Presolar grains. 1, 181–213. doi: 10.1016/B978-0-08-095975-7.00101-7

Conflict of Interest: The authors declare that the research was conducted in the absence of any commercial or financial relationships that could be construed as a potential conflict of interest.

frontiers in Astronomy and Space Sciences

REVIEW
published: 10 November 2020
doi: 10.3389/fspas.2020.562466

ANC From Experimental Perspective

Vaclav Burjan, Jaromir Mrazek and Giuseppe D'Agata*

Nuclear Physics Institute of the Czech Academy of Sciences, Prague, Czechia

In this article, we review the activities of the application of the Asymptotic Normalization Coefficients (ANC) method for the determination of the cross-sections and astrophysical S-factors of the radiative (p, γ) captures, on stable and radioactive nuclei. A number of experiments were conducted at the Nuclear Physics Institute of the Czech Academy of Sciences, in cooperation with Texas A&M University and the Istituto Nazionale di Fisica Nucleare - Laboratori Nazionali del Sud (Catania, Italy). These measurements were performed using solid state detectors and a magnetic spectrometer. This method was introduced in the last decade of the twentieth century and was, at first, used to contribute to the intensively studied topic of solar neutrinos. Later its use was extended from the Li, Be, and B element region to the CNO cycle and above. The obtained results were found (where other measurements were available) to be compatible with other indirect methods and even with direct measurements. While the capacities of direct measurements constantly improve, the advantage of the ANC and other indirect methods in general is still crucial in determining the astrophysical S-factors where short living isotopes participate, e.g., in ^{11}C(p, γ)^{12}N, ^{12}N(p, γ)^{13}O, and ^{13}N(p, γ)^{14}O. The ANC method can also provide predictions for reactions with mirror nuclei. Other uses of ANCs are also discussed.

Keywords: nuclear physics, direct reactions, asymptotic normalization coefficient, astrophysical S-factor, CNO-cycle

OPEN ACCESS

Edited by:
Scilla Degl'Innocenti, University of Pisa, Italy

Reviewed by:
Pierre Descouvemont, Université libre de Bruxelles, Belgium
Andrea Celentano, Universities and Research, Italy
Juan Pablo Fernández García, Universidad de Sevilla, Spain

****Correspondence:***
Jaromir Mrazek
mrazek@ujf.cas.cz

Specialty section:
This article was submitted to Nuclear Physics, a section of the journal Frontiers in Astronomy and Space Sciences

Received: *15 May 2020*
Accepted: *25 August 2020*
Published: *10 November 2020*

Citation:
Burjan V, Mrazek J and D'Agata G (2020) ANC From Experimental Perspective. Front. Astron. Space Sci. 7:562466. doi: 10.3389/fspas.2020.562466

1. INTRODUCTION

One of the important tasks of nuclear astrophysics is the precise determination of cross-sections of nuclear reactions. This knowledge enables determining reaction rates, which influence or determine the evolution of complex systems in astrophysical scenarios. When we consider quiescent (non-explosive) processes—their typical location is a star interior and the temperatures correspond to energies only about tens of keV. Radiative captures—such as (p, γ), (n, γ), (α, γ)—typically appear in such environments.

Direct measurements in laboratory conditions at such low energies pose a great technical challenge and the analyses may still require the use of extrapolations to lower energies. The cross-sections are strongly reduced due to the presence of the Coulomb barrier (units of MeV) in case of charged particles. Neutron radiative capture measurements depend on the availability of the neutron beams at suitable energies and targets. Measurements with radioactive nuclei create another technological challenge. Indirect methods present useful tools, which do not completely replace the direct measurements, but they can add important pieces of independent information to deduce the desired cross-sections at energy regions of interest.

Nowadays, two indirect methods are used for radiative captures. (1) The Coulomb dissociation method (Baur et al., 1986) uses the reverse process of the radiative capture—the photodissociation reaction. The radiative capture process cross-section is then deduced from the detailed balance

principle. The experimental feasibility of this method depends on a combination of several factors (see more in Baur and Rebel, 1996). (2) The other method is based on Asymptotic Normalization Coefficients.

1.1. ANC

The physics foundation of the method stems from the consideration that the direct radiative captures at low energies, proceed at large distances. Their cross-sections thus depend mostly on wave function tails, which have a known behavior and their amplitudes are given by a normalization coefficient. The Asymptotic normalization coefficients (ANC) method was developed in the last decade of the twentieth century (Xu et al., 1994). This method was used, in particular, to study the nuclear processes in stars (the p-p chain, CNO cycles, and cycles with heavier elements) and to investigate the Big Bang Nucleosynthesis (BBN). The interactions in these processes predominantly have a surface character. The peripheral character is also typical for direct nuclear reactions (DR), that are thus, predetermined as a tool to study the radiative captures. It appears that cross-sections of direct transfer reactions contain the same elements—vertex constants—that determine the direct radiative capture. These elements are closely related to the amplitudes of asymptotic tails of the (radial overlap) wave functions of the participating nuclei. These amplitudes are called asymptotic normalization coefficients (ANC).

The ANC method provides an accurate tool to determine the direct capture cross-section using experimental information from peripheral nucleon transfers.

1.2. Strengths and Weaknesses of ANC

Transfer reactions can be studied at larger energies than those typical for nucleosynthesis and even with radioactive beams. Their cross-sections are usually orders of a magnitude larger than direct radiative captures at astrophysically low energies.

Uncertainties of the ANC method are related to the well-known model dependence of Distorted Wave Born Approximation (DWBA) calculations: on the choice of the optical model potential (OMP) and the transferred single particle wave function. By choosing appropriate reactions and beam energies, the peripheral mechanism can be selected and thus the uncertainty associated with the choice of optical model potentials can be minimized.

The application of the ANC method in nuclear astrophysics is based on these assumptions:

- The final state is weakly bound
- The absence of resonances

Under these conditions, the direct radiative capture cross section is crucial [e.g., ^{7}Be(p,γ)^{8}B]. States present around the threshold (at higher masses, larger binding energies) render the resonant capture more dominant. The contribution of the direct capture may fall orders of a magnitude below the total capture.

Nevertheless, the ANCs can

- Play an important role, where resonances are narrow and distant from the energy region of interest,
- Influence the interference of resonant contributions (^{15}N(p,γ)^{16}O),
- Still play a significant role in the cross-section at low energies in case of a sub-threshold resonance (^{20}Ne(p,γ)^{21}Na),
- Be used to deduce the width of the resonance in the mirror nucleus (^{26}Mg(n,γ)^{27}Mg).

After each reaction, we assess the applicability of the ANC method.

1.3. Paper Organization

The paper is organized into five sections:

- Section 1 - is the introduction,
- In section 2, we describe principles of the ANC method,
- In section 3, selected reactions with ANC application are presented,
- In section 4, ANC applications for mirror nuclei and nuclear radii are briefly described,
- Section 5 - we provide a summary.

1.4. Aim of the Paper

Several reviews concerning ANC were recently published:

Huang et al. (2010) presented calculated ANC values within the simplified two-body model and consideration of single-particle states. Comparison to available experimental values works well for many cases.

Timofeyuk (2013) used a source term approach (STA) with shell model wave functions to calculate ANCs within a $0-p$ shell. It is an update of the previous review of Timofeyuk (2010).

The aim of the paper is to review the experimental cases, where the authors have a deeper experimental insight, as they were part of the experimental team. The selection of reactions follows a chronological order, to show connections (where present) between experiments.

2. THE METHOD OF ASYMPTOTIC NORMALIZATION COEFFICIENTS

In case of low energy reactions of astrophysical interest, we usually express the cross-section for charged particles by the astrophysical S-factor to eliminate the Coulomb dependence of the cross-section at low energies. Without loss of generality we can consider a proton radiative capture

$$A + p \rightarrow B + \gamma.$$

Then the astrophysical S-factor is expressed as

$$S(E) = Ee^{2\pi\eta}\sigma(E),$$

where E is the center of mass energy of the relative motion of the nucleus A and proton, η is the Sommerfeld parameter $\eta = Z_A Z_p e^2/\hbar v$ (Z_A being the charge of the nucleus A, Z_p=1 and v the relative velocity) and $\sigma(E)$ is proportional to the square of the transition matrix element for the direct capture (see e.g., Xu et al., 1994):

$$\sigma(E) \approx |\langle \psi_B \mid \hat{O}^{(XL)} \mid \psi_A \psi_p \chi^{(+)} \rangle|^2 \quad (1)$$

$$\approx |\langle I^B_{Ap} \mid \hat{O}^{(XL)} \mid \chi^{(+)} \rangle|^2, \quad (2)$$

where ψ_A and ψ_p are the wave functions of the nucleus A and proton, $\chi_A^{(+)}$ is the distorted wave function in the entrance channel, ψ_B is the wave function of the nucleus B, and $\hat{O}^{(XL)}$ the electromagnetic operator, where (XL) refers to the electric or magnetic multipole, frequently $E1$. The overlap integral $\mathrm{I}^B_{Ap}(\vec{r})$ between the initial and final state can be written as:

$$\mathrm{I}^B_{Ap}(\vec{r}) = \sum_{l_B m_{l_B} j_B m_{j_B}} i^{l_B} \langle J_A M_A J_p M_p \mid j_B m_{j_B}\rangle \langle j_B m_{j_B} l_B m_B \mid J_B M_B\rangle \times I^B_{Apl_Bj_B}(r) Y_{l_B m_{l_B}}(\vec{r}).$$

The radial part of the overlap function can be approximated by a model wave function $\phi_{nlj}(r)$ of the proton bound state $B = (Ap)$

$$I^B_{Apl_Bj_B}(r) = S^{1/2}_{Apl_Bj_B}\phi_{n_Bl_Bj_B}(r),$$

where S is the spectroscopic factor.

The tail of the nuclear overlap function contributes to the matrix element, especially at low energies. The shape of this tail has a well-known asymptotic behavior and its amplitude alone gives the rate of the *direct* part of the capture reaction. The asymptotic behavior of the radial overlap function is expressed by the Whittaker function W (see Mukhamedzhanov et al., 1997)

$$I^B_{Ap}(r_{Ap}) \overset{r_{Ap}>R_B}{=} C^B_{Ap}\frac{W_{l_A+1/2}(2k_{Ap}r_{Ap})}{r_{Ap}}. \quad (3)$$

Here, the asymptotic normalization coefficient C^B_{Ap} for the system $A + p \rightarrow B$ specifies the amplitude of the proton tail of the wave function for nucleus B, for distances larger than the nuclear radius R_B and k is the wave number. This normalization coefficient determines the corresponding direct capture cross-section.

The asymptotic behavior of the model wave function $\phi_{n_Bl_Bj_B}(r)$ of the proton bound state can be written as

$$\phi_{n_Bl_Bj_B}(r_{Ap}) \overset{r_{Ap}>R_B}{=} b_{Ap}\frac{W_{l_A+1/2}(2k_{Ap}r_{Ap})}{r_{Ap}}. \quad (4)$$

The quantity b_{Ap} represents the single-particle ANC (SPANC) and defines the amplitude of the tail of the radial single-particle bound-state wave function.

For peripheral reactions, the differential cross-section calculated in DWBA approximation can be replaced by an integral over the external region, where the bound state is replaced by the Whittaker function, multiplied by the ANC. The cross-section of the direct (p,γ) can be finally expressed using ANC and SPANC from Equations (3) and (4) as in (Bertulani, 2003):

$$\sigma(E) = \sum \frac{(C^B_{Apl_Bj_B})^2}{(b_{Apl_Bj_B})^2}\sigma^{(\mathrm{cap})}_{l_Bj_B}(E), \quad (5)$$

where $\sigma^{(\mathrm{cap})}_{l_Bj_B}(E)$ is the cross-section for the electromagnetic transition to the final state l_Bj_B.

The same asymptotic normalization coefficient C^B_{Ap} as that in the radiative capture can be obtained from the direct transfer reactions. In the DWBA theory for the A(a,b)B reaction, where $a = p + b$, B = A + p, and p being the transferred proton, the transition amplitude is

$$M = \sum_{M_a}\langle \chi^{(-)}_f \psi_B\varphi_b \mid \Delta V \mid \varphi_a\psi_A\chi^{(+)}_i\rangle, \quad (6)$$

where $\chi^{(+)}_i, \chi^{(-)}_f$ are distorted wave functions in input and output channels, ψ_A, ψ_B are wave functions describing inner states of A, B nuclei, φ_a, φ_b are wave functions of particles a, and b. The transition operator ΔV has a shape $V_{bp} + U_{bA} - U_\beta$ for post form, where U_β is the optical potential in final channel. The transition amplitude M can be expressed as

$$M = \langle \chi^{(-)}_f I^B_{Ap} \mid \Delta V \mid I^a_{bp}\chi^{(+)}_i\rangle, \quad (7)$$

where $I^B_{Ap} = S^{1/2}\phi_{nlj}(r_{Ap})$ is the above mentioned overlap integral and I^a_{pb} is the overlap integral of a and b particles, in analogy with I^B_{Ap}. The experimental cross-section for the transfer proton reaction can be expressed at the asymptotic region larger than the nuclear radius R_B in this way (Mukhamedzhanov et al., 1997)

$$\frac{d\sigma(\theta)}{d\Omega} = \sum \frac{(C^B_{Apl_Bj_B})^2(C^a_{pbl_aj_a})^2}{(b_{Apl_Bj_B})^2(b_{pbl_aj_a})^2}\sigma^{DW}_{l_Bj_Bl_aj_a}(\theta). \quad (8)$$

Here, $(C^B_{Apl_Bj_B})^2$ and $(C^a_{pbl_aj_a})^2$ are ANCs of the systems $A + p$ and $p + b$, j_i and l_i are the total and orbital angular momenta of the transferred proton, respectively. Coefficients b are the single-particle ANCs, defining the amplitude of the tail of the radial proton bound-state wave function. $\sigma^{DW}_{l_Bj_Bl_aj_a}(\theta)$ is the deduced DWBA cross-section. Using the above expression, it is possible to express the cross-section of the direct proton capture at very low energies by the relation (5) where the normalization factor $(C^B_{Apl_Bj_B})^2$ is known from the transfer reaction (a,b).

For peripheral reaction, where only the outer region of the nuclear radial integrals contributes to the cross-section, the ratio

$$R(b_{Apl_Bj_B}, b_{pbl_aj_a}) = \frac{\sigma^{DW(max)}_{l_Bj_Bl_aj_a}(\theta)}{(b_{Apl_Bj_B})^2(b_{pbl_aj_a})^2}, \quad (9)$$

should not depend on the single particle ANCs b_{Ap} and b_{bp}. The $\sigma^{DW(max)}(\theta)$ is the DWBA differential cross-section at the main maximum of the angular distribution.

The stability of this ratio represents an important peripherality check of the transfer reaction.

3. SELECTED EXPERIMENTAL CASES

In the following section, we introduce several experimental cases, where the ANCs were determined.

At first, we illustrate in detail the experimental investigation of the direct capture of ^{7}Be(p, γ)^{8}B. This reaction is in the center of the so-called solar neutrino problem. There was a discrepancy between the prediction of the high energy solar neutrino flux and the measured values (Bahcall, 1985). The measured values of the neutrino flux represented one third of the predicted flux. These neutrinos are mainly products of the decaying ^{8}B from the radiative capture ^{7}Be(p, γ)^{8}B. The determination of astrophysical S-factor $S_{17}(0)$ for this capture seems to be the key to the problem.

Nowadays, the discrepancy between measured and produced flux of solar neutrinos is explained by neutrino oscillations (Ahmad et al., 2001; Bellerive et al., 2016—SNO collaboration) however, the independently and indirectly measured S-factor remains important for stellar models.

The suitable proton transfer reaction to study the direct capture ^{7}Be(p, γ)^{8}B by ANC method would be ^{8}B(^{7}Be, ^{8}B)^{7}Be. This reaction, due to the symmetry, contains the same ANC value twice and thus, the determination would not be affected by other ANCs. However, both reaction participants are radioactive nuclei, so, the other transfer reactions were selected: ^{10}B(^{7}Be, ^{8}B)^{9}Be and ^{14}N(^{7}Be, ^{8}B)^{13}C. These reactions both contain two different ANC values. The ANCs for the virtual decay $^{10}\mathrm{B} \rightarrow {}^{9}\mathrm{Be} + p$ and $^{14}\mathrm{N} \rightarrow {}^{13}\mathrm{C} + p$ had to be deduced. The techniques are described in more detail for the first reaction, and the details will not be repeated in the following experiments.

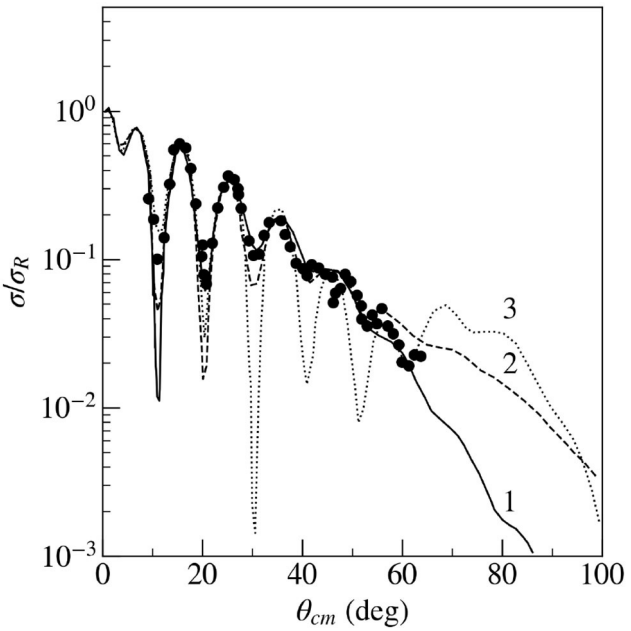

FIGURE 1 | The elastic scattering cross-section of the ^{10}B ions on the ^{9}Be target, fitted by optical model calculations with potentials 1—solid line, potential 2—dashed line, and potential 3—dotted line, the depths of the real part of these three optical model potentials were 64.2, 131.2, and 203.2 MeV, respectively, see details in Mukhamedzhanov et al. (1997). Ratio to Rutherford scattering is on the y-axis.

3.1. ^{9}Be(p, γ)^{10}B

The determination of ANC for the ^{9}Be(p, γ)^{10}B radiative capture was one of the problems when the method of ANCs was first applied by Mukhamedzhanov et al. (1997). A suitable transfer reaction is ^{9}Be(^{10}B, ^{9}Be)^{10}B, as it is symmetric in ANCs. At first, we measured the elastic scattering $^{10}\mathrm{B} + {}^{9}\mathrm{Be} \rightarrow {}^{10}\mathrm{B} + {}^{9}\mathrm{Be}$ to find the corresponding optical model parameters. Then, these parameters were used for the analysis of the proton transfer reaction ^{9}Be(^{10}B, ^{9}Be)^{10}B. The measurement was performed at the Cyclotron Institute of the Texas A&M University using 100 MeV beam of ^{10}B. ^{9}Be targets with thicknesses between 200 and 300 μg/cm^{2} were prepared by evaporation. The targets were located in the focal plane of the Multipole magnetic spectrometer (MDM). The magnetic spectrometer was tuned to measure either elastically scattered ^{10}B ions or ^{9}Be ions from the proton transfer reaction. The measurement of specific energy loss in the ionization chamber was used for particle identification and the residual energy was measured by a NE102A plastic scintillator located behind the exit window of the detector. The entrance and exit windows of the detector was made of 1.8 and 7.2 mg/cm^{2} thick Kapton foils, respectively. The ionization chamber was filled with pure isobutane at a pressure of 30 mbar. Outgoing ^{9}Be nuclei at forward angles are kinematically equivalent to ^{10}B elastically scattered in the backward hemisphere. The experimental elastic scattering was fitted with three optical model potentials, that differed mainly in depths of the real part of the OM potential (Mukhamedzhanov et al., 1997, see in **Figure 1**). Resulting fits are plotted in **Figure 1**. The potential 3 gave substantially worse χ^{2} and therefore, it was rejected for further analysis. With these optical model parameters, the angular distribution for the proton transfers to different final states of the ^{10}B were calculated by means of the PTOLEMY (Rhoades-Brown et al., 1983) code. The example of the fitted experimental angular distribution of the proton transfer to the ground state of ^{10}B is given in **Figure 2**. ANCs for the proton transfer reaction from the calculation with parameters of the optical models 1 and 2 are given in the **Table 1**. Several tests were made to prove the applicability of the ANC method. The peripheral character of the ^{9}Be(^{10}B, ^{9}Be)^{10}B reaction was verified. The ANC method is applicable, when the transfer process is peripheral. The peripherality can be demonstrated by showing that the cross-section does not depend on the inner part of the reaction region. Calculation of DWBA angular distribution with different cut-off radii did not reveal significant variations, when using values lower that 5 fm. This allows replacing the bound state function with the Whittaker asymptotic form. A next check was performed for the R function (Equation 9). This function should be constant in a region ($1.1 \leq r_0 \leq 1.3$ fm and $0.5 \leq a \leq 0.7$ fm), where r_0 and a are bound state potential well parameters. Then the dependence on the selection of a potential is weak. In the presented case, these differences are small (see **Table 1**, where they are included in uncertainties of ANCs). By changing parameters r_0 and a it is possible to demonstrate that the dependence of the spectroscopic factor on the single particle ANC b_{lj} is strong, it varies by factor

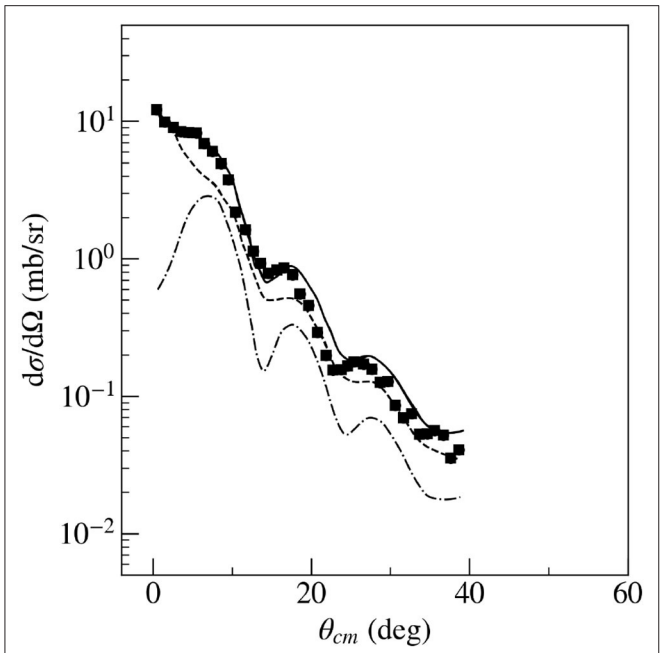

FIGURE 2 | The calculated angular distributions of the reaction ^{9}Be(^{10}B, ^{9}Be)^{10}B (g.s.) compared with the experimental data (black points). The DWBA fits for individual contributions of l = 0, 1, and 2 are represented by dashed, dotted, and dash-dotted lines, respectively. Calculations are performed with the optical potential 1 and the optical potential 2 gives the same fit.

TABLE 1 | The extracted ANCs(C^2) for the ^{9}Be(p, γ)^{10}B capture from the ^{9}Be(^{10}B, ^{9}Be)^{10}B reaction.

E^*(*MeV*)	j_p	C_1^2(*fm*$^{-1}$)	C_2^2(*fm*$^{-1}$)	C^2(*fm*$^{-1}$)
0.0	3/2	4.91(19)	5.35(21)	5.06(46)
0.718	1/2	1.23(15)	1.34(16)	1.27(21)
	3/2	3.33(17)	3.63(19)	3.43(42)
1.740	3/2	4.22(33)	4.60(36)	4.35(59)
2.154	1/2	0.28(5)	0.30(5)	0.29(6)
	3/2	0.80(8)	0.87(9)	0.82(12)

C_1^2 and C_2^2 are deduced ANCs using optical potentials 1 and 2, respectively, and the bound state potential with r_0 = 1.20 fm and a = 0.60 fm. The third C^2 is the adopted average value and uncertainty.

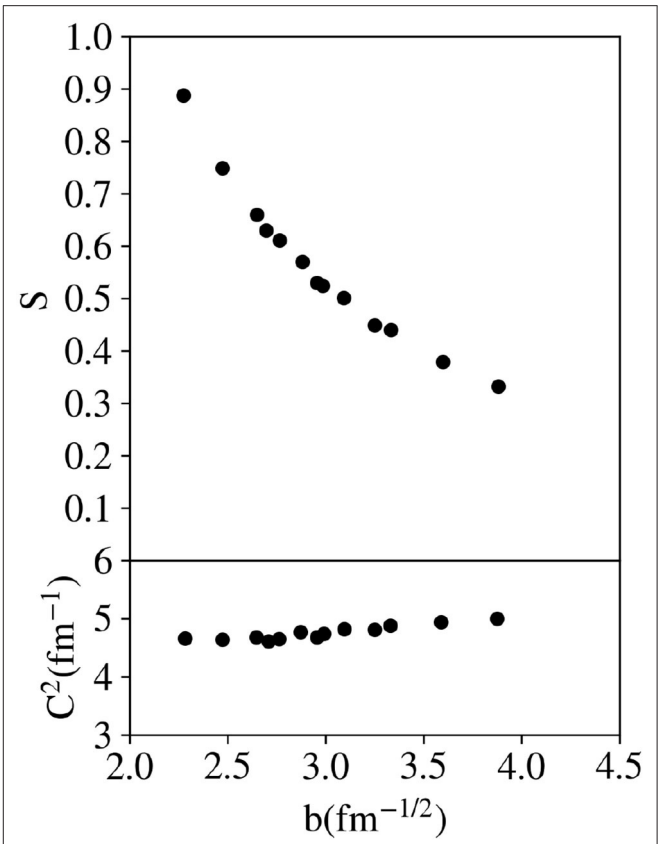

FIGURE 3 | The dependence of the spectroscopic factor **(upper)** and ANC (C^2) **(lower)** on the geometry of the bound state potential of the state ^{9}Be($3/2^-$) + $p(j_p = 3/2^-)$ in ^{10}B(*g.s.*). The geometry is expressed by the different single particle ANCs (value *b*, see Equation 4), i.e., achieved by changing the parameters r_0 and *a* of the bound state potential in some intervals.

3 (**Figure 3**), while C^2 changes in the considered region by only about 10%.

The extracted ANCs from **Table 1** were then used for the analysis of the proton transfer reaction ^{10}B(^{7}Be, ^{8}B)^{9}Be which is suitable in determining the normalization of the cross-section for the direct proton capture ^{7}Be(p, γ)^{8}B at low astrophysical energies.

The ANC of ^{9}Be(p, γ)^{10}B reaction, due to the applicability conditions, was only used for the analysis of ^{7}Be(p, γ)^{8}B capture.

3.2. ^{16}O(p, γ)^{17}F

Prior to the application of ANC method on ^{7}Be(p, γ)^{8}B, the ANC method was tested on the ^{16}O(p, γ)^{17}F capture. The direct measurement data at low energies (Chow et al., 1975; Morlock et al., 1997) were available for comparison. Two separate measurements were performed for the transfer reaction ^{16}O(^{3}He, d)^{17}F (Gagliardi et al., 1999).

One measurement was performed at the Nuclear Physics Institute of the Czech Academy of Sciences, Řež, (NPI CAS), using a 27.7 MeV ^{3}He beam. The absolute differential cross-section for the process was measured between 6.5° and 25° in the laboratory system. Products of the reaction on the mylar target ($C_{10}H_8O_4$) with a thickness of 134 μg/cm^2 were detected by solid state dE-E telescopes with thicknesses 150 and 2,000 μm.

The second measurement was realized at the Texas A&M University K500 superconducting cyclotron with a 29.71 MeV ^{3}He beam, with the mylar target (thickness 540 μg/cm^2) at small angles between 1° and 11°. A Multipole Dipole Multipole magnetic spectrometer (MDM) was used for the detection of reaction products. A gas ionization chamber (50 cm long) was placed at the MDM focal plane and was followed by NE102A plastic scintillator, where the residual energy was measured.

Theoretical analysis was performed using the code PTOLEMY with seven different parameter sets for the entrance

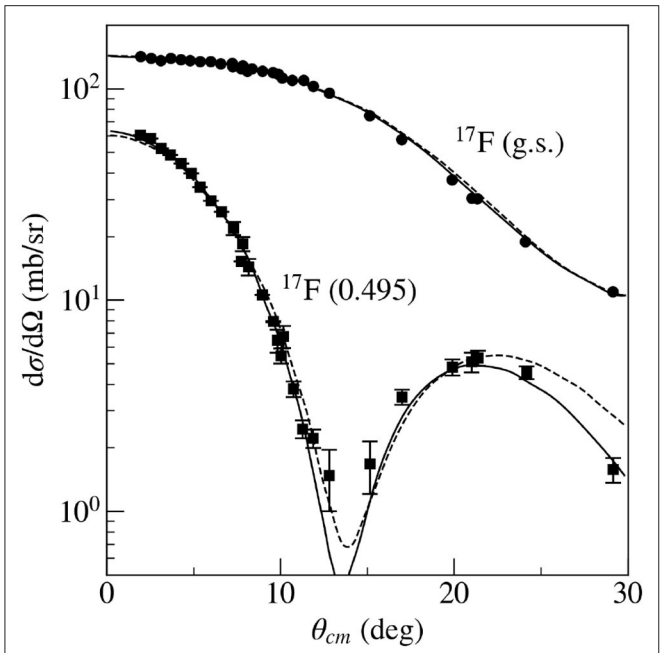

FIGURE 4 | Angular distributions for the ground and first excited states of ^{17}F from the ^{16}O(^{3}He, d)^{17}F reaction. The dashed and solid curves are DWBA fits using two optical model potential parameter sets (Gagliardi et al., 1999).

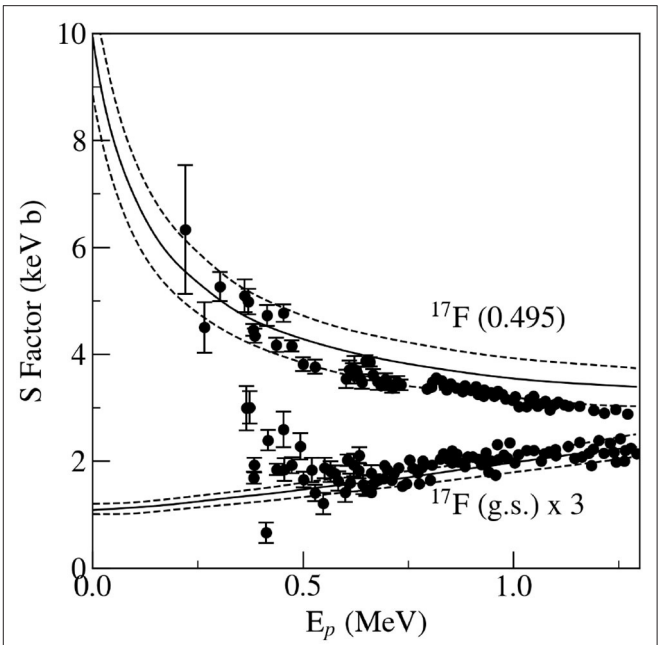

FIGURE 5 | The experimental S-factors and S-factors determined from the ANCs of the ^{16}O(^{3}He, d)^{17}F reaction (Gagliardi et al., 1999). The solid data points are from Morlock et al. (1997), and the open boxes are from Chow et al. (1975). The solid lines indicate the calculated S-factors, and the dashed lines correspond to the $\pm 1\sigma$ error bands.

channel and five parameter sets for the exit channel. The experimental angular distributions corresponding to the ground and first excited state of ^{17}F together with the best fits of OMP parameters are given in **Figure 4**. The conditions of peripherality were verified by changing the radius r_{cutoff}. Angular distributions were changing very slightly within limits from 0 to 3 fm (inner part of ^{16}O). Similarly, the change of the shape of the potential well of the captured proton did not change the corresponding angular distribution too much and consequently also C^2 (see **Figure 4**). The value of $C^2_{^3\mathrm{He},d}$ = 3.90 ± 0.06 fm^{-1} was used from Mukhamedzhanov et al. (1995), where it was determined by a careful analysis based on hundreds of experimental measurements. Final derived results of ANCs gave the value $C^2_{d_{5/2}}$ = 1.08 ± 0.10 fm^{-1} for the ground state, and the value $C^2_{s_{1/2}}$ = 6,490 ± 680 fm^{-1} for the first excited state. With these ANC values, the astrophysical S-factors for the ground and first excited state of ^{17}F were calculated and theoretical curves with the experimental values of S-factors are given in **Figure 5**. The agreement between experimental values of S-factors and direct measurements are very good for the interval below 1 MeV. For higher energies the agreement for the first excited state is worse because of the increasing role of the nuclear interior.

The assumptions of applicability of the ANC method are satisfied for the ^{16}O(p, γ)^{17}F reaction and the method was shown to work in real cases.

3.3. ^{7}Be(p, γ)^{8}B, ^{13}C(p, γ)^{14}N

The importance of the proton radiative capture p + ^{7}Be was discussed in the previous section. Two suitable reactions for the indirect determination of ^{7}Be were chosen: the reaction ^{10}B(^{7}Be, ^{8}B)^{9}Be which was discussed above and also the transfer reaction ^{14}N(^{7}Be, ^{8}B)^{13}C. Measurements of angular distributions of elastic scattering of ^{7}Be ions and also, of transfer reactions with these ions on the ^{10}B and ^{14}N targets were carried out on the K500 superconducting cyclotron at Texas A&M University (Azhari et al., 1999, 2001).

The beam of radioactive ^{7}Be ions was produced in the ^{1}H(^{7}Li, ^{7}Be)n reaction using ^{7}Li primary beam of 135 MeV energy. The ^{7}Li beam was striking on the liquid nitrogen cooled gas cell containing hydrogen with pressure about 1 atm. Windows of the gas cell were made from Havar foil with a 42 mg/cm^2 thickness. ^{7}Be ions from the gas cell were separated by the Momentum Achromat Recoil Spectrometer (MARS) and hit the target with a rate below 10^5 pps. The self-supported ^{10}B target was prepared from a mixture of pulverized ^{10}B and varnish deposited on a Ta backing from which the target layer was removed in distilled water. As the ^{14}N target the evaporated melamine ($C_3N_6H_6$) on a 20 μg/cm^2 layer of C and a 20 μg/cm^2 layer of collodion was used. The average thicknesses of the targets were 1.96 mg/cm^2 and 1.50 mg/cm^2 for the ^{10}B and ^{14}N targets. Reaction products were measured and identified by the telescope configuration consisting of a 100 μm silicon strip detector, backed by a 1,000 μm 5 × 5 cm^2 Si detector. Data from the telescope were then analyzed to deduce angular distributions of the elastic scattering of ^{7}Be and the studied transfer reactions. The angular distribution of elastic scattering was used for determination of optical model parameters. The parameters were obtained from

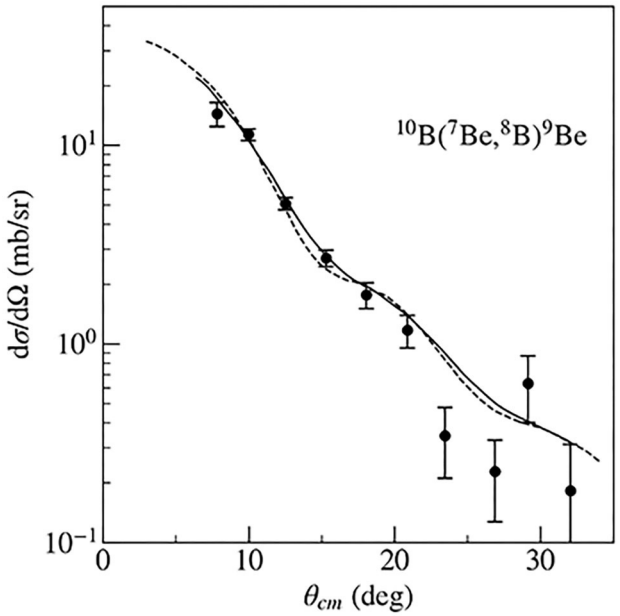

FIGURE 6 | Experimental angular distribution from the ^{10}B(^{7}Be, ^{8}B)^{9}Be reaction for the outgoing ions ^{7}Be. The dashed line corresponds to the predicted angular distribution and the solid line is corrected to finite angular distribution (Azhari et al., 1999).

double folding model calculations according to JLM effective interaction (Jeukenne et al., 1977).

Having the optical model parameters for the input channel and exit channels ^{10}B + ^{7}Be and ^{8}B + ^{9}Be, it was possible to calculate the differential cross-section for the transfer reaction. Similarly for the transfer reaction ^{14}N(^{7}Be, ^{8}B)^{13}C, where model parameters for the input channel ^{7}Be + ^{14}N and the exit channel ^{8}B + ^{13}C were needed. The experimental angular distribution for the outgoing ^{8}B of the ^{10}B(^{7}Be, ^{8}B)^{9}Be reaction ($Q \leq 28$ MeV) is shown in **Figure 6**. The calculations of theoretical angular distributions were performed by the code PTOLEMY. The peripheral character of both transfer reactions ^{10}B(^{7}Be, ^{8}B)^{9}Be and ^{14}N(^{7}Be, ^{8}B)^{13}C was tested using variations of radius and diffuseness values of the single-particle Woods-Saxon potential. The changes in deduced ANCs were only ±3.5%. The deduced value $C^2_{^{13}C+p,g.s.}$ = 19.5 ± 2.5 fm^{-1}, values for other states are shown in Trache et al. (1998), **Table 2**. The ANC value for ^{7}Be+p reaction is $C^2_{^{7}Be+p}$ = 0.388 ± 0.039 fm^{-1}. Using the ANCs from both transfer reactions ^{10}B(^{7}Be, ^{8}B)^{9}Be and ^{14}N(^{7}Be, ^{8}B)^{13}C, astrophysical S-factors $S_{17}(0)$ = 18.4 ± 2.5 eV b and $S_{17}(0)$ = 16.9 ± 1.9 eV b was obtained. The weighted average value $S_{17}(0)$ = 17.3 ± 1.8 eV b is included in the **Figure 7** (Azhari et al., 2001). This is in good agreement with the current accepted value $S_{17}(0) = 19^{+4}_{-2}$ eV b.

Solid targets, such as ^{14}N in the previous section, are available in the form of compounds and/or with other element backings. This may substantially complicate an analysis, due to peak overlap in spectra and different kinematical shifts for isotopes with different mass numbers. One of the experimental challenges was ANC measurement with pure isotopic gas targets.

The assumptions of applicability of the ANC method are satisfied for the ^{7}Be(p,γ)^{8}B reaction. The ANC of ^{13}C(p,γ)^{14}N reaction, due to the applicability conditions, was only used for the analysis of ^{7}Be(p, γ)^{8}B and other captures (see below).

3.4. ^{20}Ne(p,γ)^{21}Na

The ^{20}Ne(p,γ)^{21}Na capture reaction is a part of the so-called NeNa-cycle, which takes place in stars larger than the Sun. This cycle produces ^{21}Na, ^{21}Ne, ^{22}Na, and ^{22}Ne nuclei, while consuming hydrogen. The ^{20}Ne(^{3}He, d)^{21}Na reaction leads to four bound states of ^{21}Na. The highest lying state with excitation energy of 2.425 MeV is only a few keV below threshold The capture to this subthreshold state dominates the value of astrophysical S-factor.

The measurement was realized on the beam of the isochronous cyclotron U120M of NPI CAS. The ^{3}He beam with energy 25.83 MeV impinged the target gas cell filled with high purity ^{20}Ne. The input and output windows were made of 3.05 μm Havar foils. The working pressure was kept at 195 mbar and was continuously monitored together with the gas temperature. The detection system consisted of a pair of dE-E Si(Li) surface barrier detectors of thicknesses 220 μm and 4 mm, respectively. The effective thickness of the gas target seen by the telescopes was obtained from a simulation. One telescope at a fixed angle served as a monitor and the second telescope was movable in the angular interval from 6.5° to 70°. The obtained energy resolution ranged from 100 to 120 keV, depending on the measured angle.

The experimental angular distributions of emitted deuterons from the ^{20}Ne(^{3}He, d)^{21}Na reaction were analyzed within the DWBA theory. At first the angular distribution of elastic scattering of ^{3}He was fitted by means of the code ECIS79 (Raynal, 1981) to obtain optical model parameters for the input channel. The optical model parameters for the exit channel were adopted from global formulas in works by Daehnick et al. (1980) and Vernotte et al. (1994). In **Figure 8** we present, as an example, the experimental angular distribution fits for the state 2.425 MeV calculated by the code DWUCK5. The peripheral character of the reaction was verified using different cut-off radii of the integration over the radial part of interaction. The stability check of the function $R(b)$ (9) was checked and its behavior was almost flat. To deduce ANCs for the direct capture ^{20}Ne(p, γ)^{21}Na from the transfer reaction ^{20}Ne(^{3}He, d)^{21}Na, knowledge of ANC for the decay ^{3}He → d + p is necessary. For further analysis we used the value $(C^{^{3}He}_{dp})^2$ = 3.90 ± 0.06 fm^{-1} (Mukhamedzhanov et al., 1995).

Total uncertainties of ANC for the direct capture ^{20}Ne(p, γ)^{21}Na were estimated from 14% for the 2.425 MeV state to 28% for the 1.716 MeV state. The sources were mainly (1) the ambiguity of optical model parameters and (2) the uncertainty of absolute values of the cross-sections. R-matrix theory was used to determine S-factor, where the normalization of the direct capture amplitude was given by the ANC of the final bound state according the procedure used by Tang et al. (2003). The

TABLE 2 | Squared ANC values (in units of [fm^{-1}]) for selected reactions discussed in this paper (column C_1^2).

(A-1)	A	C^{2}_{HBG}	C^{2}_{Tim}	C^{2}_{1}	References$_1$	C^{2}_{rec}
^{7}Be(p,γ)	^{8}B(2^{+})	0.52	0.441	0.388	Azhari et al., 2001	0.544[a]
^{9}Be(p,γ)	^{10}B(3^{+})	11.8	3.53	5.06(46)	Mukhamedzhanov et al., 1997	
	^{10}B(1^{+})		5.28	4.7(60)		
	^{10}B(0^{+})		5.53	4.35(59)		
^{11}C(p,γ)	^{12}N(1^{+})	0.88	1.69	1.73(25)	Tang et al., 2003	1.83(27)[b]
^{12}N(p,γ)	^{13}O(3/2^{-})		3.07	2.53(30)[#]	Banu et al., 2009	3.92(147)[c]
^{13}C(p,γ)	^{14}N(1^{+})	9.3	14.5	18.7(13)	Bém et al., 2000	
	^{14}N(0^{+})		11.9	16.0(11)		
	^{14}N(1$^{+}_{2}$)		2.0	2.91(20)		
^{13}N(p,γ)	^{14}O(0^{+})	29.6	25.0	29.0(43)	Tang et al., 2004	30.4(71)[d]
^{14}C(n,γ)	^{15}C(1/2^{+})	1.82		1.64(26)	Mukhamedzhanov et al., 2011	
	^{15}C(5/2^{+})			0.0036(4)		
^{14}N(p,γ)	^{15}O(1/2^{-})	26.9	43.9	54(6)	Mukhamedzhanov et al., 2003	
	^{15}O(1/2^{+})					
	^{15}C(5/2^{+})			0.11(1)		
	^{15}C(3/2^{-})		0.49	0.50(6)		
^{15}N(p,γ)	^{16}O(0^{+})	186	197	192(26)	Mukhamedzhanov et al., 2008	
	^{16}O(3^{-})			3.52(44)		
^{16}O(p,γ)	^{17}F(5/2^{+})	0.83		1.08(10)	Gagliardi et al., 1999	
	^{17}F(1/2^{+})	5961		6490(680)		
^{18}O(p,γ)	^{19}F(1/2^{+})			71(14)	Burjan et al., 2019	
	^{19}F(5/2^{+})			14.8(30)		
^{18}O(n,γ)	^{19}O(5/2^{+})	0.56		0.42(4)	Burjan et al., 2014	
	^{19}O(3/2^{+})	0.008				
	^{19}O(1/2^{+})	5.11		5.2(10)		
^{20}Ne(p,γ)	^{21}Na(3/2^{+})			0.21(4)	Mukhamedzhanov et al., 2006	
	^{21}Na(0.332)	4.7		2.78(43)		
	^{21}Na(2.42)	11.3		6.14(83) $\times$ 10^{33}**		
^{2}H(p,γ)	^{3}He(1/2^{+})	2.43		3.90*	Mukhamedzhanov et al., 1995	4.2*,[e]

C^2_{HBG} contains calculated values within simplified two-body model from the review of Huang et al. (2010). In column C^2_{Tim} calculated values within source term approach from the review of Timofeyuk (2013) are shown. C^2_{rec} column contains more recent experimental values, where available.

[a] *From Trache et al. (2003).*

[b] *From Lee et al. (2011).*

[c] *From Guo et al. (2013).*

[d] *From Bing and Zhi-Hong (2007), determined from the mirror reaction.*

[e] *From Yarmukhamedov and Blokhintsev (2018).*

[#] *Only $C^2_{p1/2}$ was published in Banu et al. (2009) and it agrees with $C^2_{p1/2,Tim}$= 2.60 of.*

**Determined theoretically (values were/are used in deduction of the other ANCs).*

***Value for the subthreshold resonance is extremely high and sensitive to binding energy, however, its product with Whittaker function $|C|^2$ W^2 has a reasonable value and is stable. A reason for the discrepancy with the model is uncertain (Huang et al., 2010).*

S-factor for direct capture to the subthreshold state was found to be S(0) = 68.30 ± 9.30 keV b. The direct capture to the ground state is very weak. The capture to the ground state is dominated by the resonant capture through the subthreshold state. It was determined as S(0)= 5,870.0 ± 1,200 keV b. The R-matrix calculations were performed with the channel radius r = 5 fm. The calculated total S(E) consists of the sum of the direct capture to the subthreshold state and the capture by the subthreshold resonance to the ground state. We have thus S(0) = 5,900 ± 1,200 keV b (**Figure 9**). Contributions to the total S-factor from captures to other remaining states are negligible. The newly obtained S(0) factor is higher than the value given in Rolfs and Rodney (1988).

The proton partial width of the resonance, dominating the radiative capture of the ^{20}Ne(p,γ)^{21}Na reaction was deduced from the measured ANC.

3.5. ^{18}O(n,γ)^{19}O

The ANC method can be used not only for charged particle direct captures, but also, for a direct radiative neutron captures (Imai et al., 2001). However, the peripherality of the process must be ensured by a presence of a centrifugal barrier. The ^{18}O(n,γ)^{19}O capture is given as an example.

The inhomogeneous Big Bang models (IBBN) seemed to contain a solution for the problems of BBN. Nuclei with A > 12, in neutron-rich environments, could be formed in

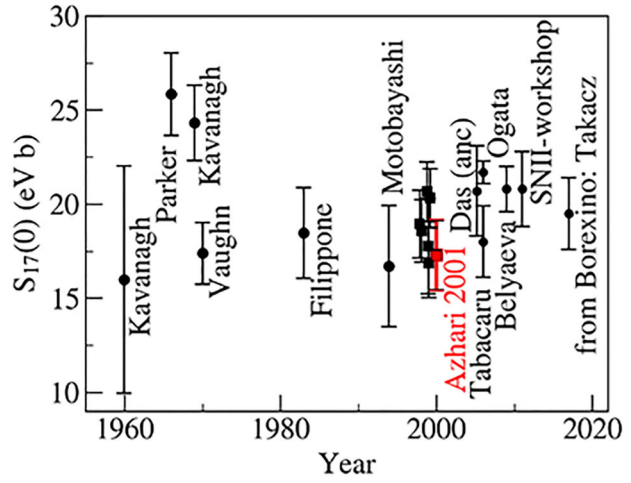

FIGURE 7 | History of the determination of astrophysical $S_{17}(0)$. The value measured in the experiment, discussed in the text, is in red and labeled "Azhari 2001." For details see (Azhari et al., 2001).

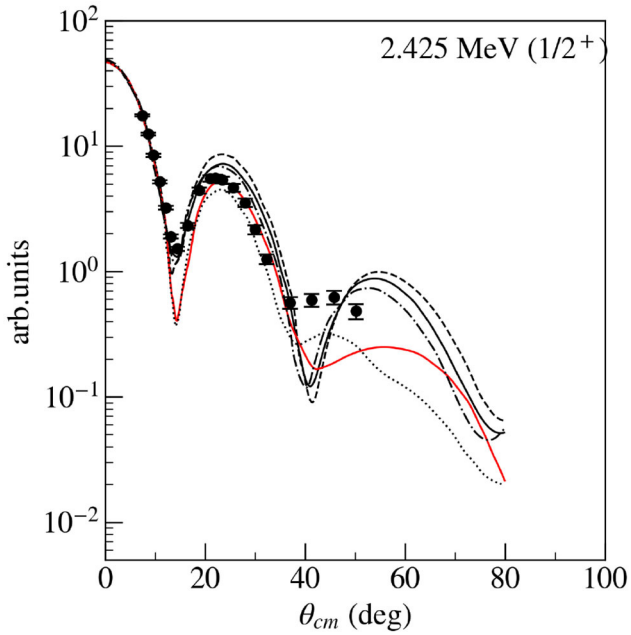

FIGURE 8 | The angular distribution of the ^{20}Ne(^{3}He, d)^{21}Na reaction corresponding to the transition to the subthreshold state of ^{21}Na fitted by combinations of different optical model parameters for input and output channels. OM parameters for input and output channels taken from earlier works produce the black solid curve. The black dashed and dash-dotted curves use the same output channel OM parameters, but the input channel OM parameters were obtained from a fit of the elastic scattering data with two different seeds. Black dotted and red curves are produced as the two previous curves, but with a different OM parameter set for the output channel. For details see (Mukhamedzhanov et al., 2006).

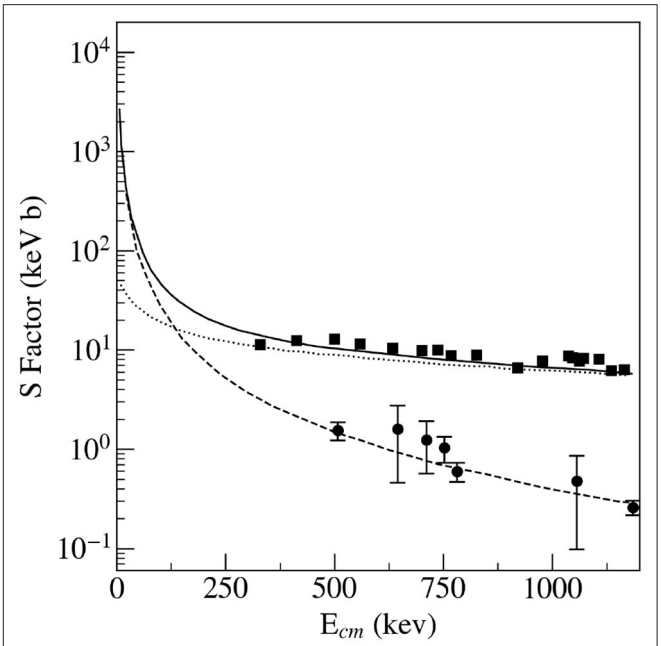

FIGURE 9 | The astrophysical S-factor for the direct ^{20}Ne(p, γ)^{21}Na capture. The solid squares and dotted curve are experimental data points from Rolfs et al. (1975) and results of Mukhamedzhanov et al. (2006) for direct capture to the subthreshold state, respectively. Similarly, for the capture to the ground state the open squares and dashed curve correspond to the experimental data points and to results for the direct capture. The determined total astrophysical S-factor is given by the solid curve.

the reaction sequence (Wiescher et al., 1990) ^{14}C$(n,\gamma)^{15}$C(β^-) ^{15}N(n,γ) ^{16}N(β^-) ^{16}O(n,γ) ^{17}O(n,γ) ^{18}O(n,γ) ^{19}O, where the reaction ^{18}O(n, γ) ^{19}O opens the path to elements with higher mass numbers (Wiescher et al., 1990). The neutron radiative capture ^{18}O(n, γ)^{19}O also has a significance for the estimation of reaction rates of stellar helium burning in massive red stars and AGB stars. To determine the direct (n,γ) cross-section, a precise measurement of (d, p) differential cross-section on ^{18}O target at forward angles (where the stripping mechanism is more pronounced) was required. Although, the transfer to higher excited states was also of interest (Herndl et al., 1999), not all were possible to resolve. The experiment was performed on the isochronous cyclotron U-120M of the NPI CAS (Burjan et al., 2013). A momentum analyzed 16.3 MeV deuteron beam impinged on an oxygen gas target. The gas chamber target was filled with a high purity ^{18}O isotope (99.9%). The working pressure was maintained at 150 mbar. Eight dE-E telescopes [250 μm and 5 mm thick Si(Li) surface barrier detectors] were used to register the reaction products. DWBA analysis of experimental angular distributions of the transfer reaction ^{18}O(d, p)^{19}O was performed to extract ANCs. The phenomenological optical potential of Kunz (1990) has been used for the analysis of the angular distributions. Input channel parameters were obtained by the fit of the experimental angular distribution of elastically scattered deuterons. For this purpose, the code ECIS79 of Raynal (1979) was used. Optical model parameter sets of Perey and Perey (1976) and others (Duke, 1963; Watson et al., 1969) were used for the proton exit channel. The experimental angular distributions ^{18}O(d, p)^{19}O

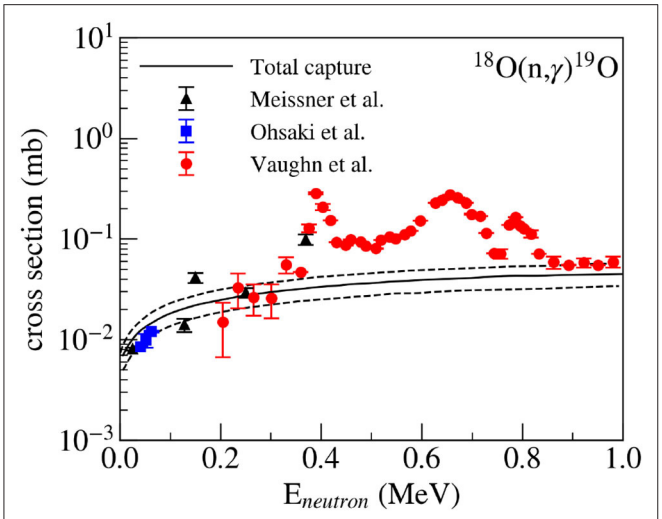

FIGURE 10 | Comparison of the cross-section of the direct radiative neutron capture ^{18}O(n, γ)^{19}O determined by the ANC method from the ^{18}O(d, p)^{19}O reaction with experimental data of Vaughn et al. (1965), Meissner et al. (1996), and Ohsaki et al. (2008). Dashed lines show the uncertainty band 22%.

were fitted within the DWBA theory using the DWUCK5 code (by Kunz, 1990). As in the above cases, two overlap integrals and two ANCs are contained in the DWBA description of this reaction. The ANC value for the virtual decay $d \rightarrow p + n$ is C^2_{pn} = 0.77 fm^{-1}, based on considerations about spectroscopic factor S = 1 and SPANC values at an asymptotic distance (Mukhamedzhanov et al., 2011).

For transferred neutral particle, instead of the Whittaker function, the Hankel function is used in the overlap integral in the asymptotic region. For the application of the ANC method, the condition of the weak cross-section dependence on the cut-off radius should be fulfilled. The difference of the cross-section at the maximum of the angular distribution was 13% between the case with 3 fm cut-off and no cut-off for the transfer to the ground state. Changes were negligible (2%) for other transitions. The obtained values C^2_{Anlj} for the transitions to five states of ^{19}O (g. s., 1.471, 3.153, 3.231, and 3.944 MeV) were used to estimate the direct neutron capture contribution by ^{18}O (see in Burjan et al., 2013). The FRESCO code (Thompson, 1988) was used for these (n,γ) calculations. In the calculations, the channel radius 3.3 fm was used and the *E*1 multipolarity was assumed in all cases. The largest contribution (black solid line in **Figure 10**) is from transition to the 1.471 MeV state ($2s_{1/2}$). The results were compared with available experimental data (**Figure 10**). Data points from Meissner et al. (1996) and Ohsaki et al. (2008) for the transitions to the ground state and 1.471 MeV state are shown. The larger energy interval was measured by Vaughn et al. (1965) (transitions to the g. s. and 1.471 MeV state). The direct part of the experimental data is quite consistent with the ANC method results for this neutron capture by ^{18}O.

The necessity of the centrifugal barrier allowed studying the p-wave direct capture contribution with the ANC method. Direct measurements show that it dominates in the energies bellow 100 keV.

3.6. ^{18}O(*p*, γ)^{19}F

A study of the radiative capture reaction ^{18}O(p, γ)^{19}F helps in better understanding the processes in AGB stars (i. e. stars several times heavier than our Sun). The hydrogen burning of ^{18}O via the (p, γ) in these stars is competing with the ^{18}O(p, α)^{19}F reaction (Lorenz-Wirzba et al., 1979). The (p, γ) capture causes the escape of ^{19}F from CNO cycles, while the (p, α) reaction (with a rate of about 3 orders higher at solar energies) returns the ^{19}F back. The ratio ^{18}O/^{16}O represents an important parameter that is characteristic for different nucleosynthesis locations and that can help to determine the origin of e.g., presolar grains (Abia et al., 2017; Palmerini et al., 2017). While the direct part of the ^{18}O(p, γ) process is not the major contribution to radiative capture, it may play a role in the total S-factor, via interferences with resonant states. A measurement of the ^{18}O(p, γ)^{19}F in the energy range E_p = 0.08–2.2 MeV was performed by Wiescher et al. (1980), where the direct part of the (p, γ) capture was determined experimentally and also calculated theoretically. Later, Buckner et al. (2012) investigated reaction rates of ^{18}O(p, γ)^{19}F and determined the direct part of this capture using different capture models. However, there is a substantial difference between the astrophysical S-factor of Wiescher et al. and of Buckner et al. at low energies. The energy dependence of values of Wiescher et al. decreases while that of Buckner et al. is increases. Also, their absolute values differ considerably. We therefore, decided to determine the astrophysical S-factor of the direct capture ^{18}O(p, γ)^{19}F by the ANC method. The differential cross-section of the ^{18}O(^{3}He, d)^{19}F transfer reaction was measured (Burjan et al., 2019). 24.6 MeV ^{3}He beam from the isochronous cyclotron U-120M at NPI CAS was used. High purity ^{18}O oxygen (99.9%) gas target was used as in the above experiment. Eight dE-E telescopes [250 μm and 5 mm thick Si(Li) surface barrier detectors] were used for detection of the reaction products. The geometry of detectors was very similar to the geometry used in the (d, p) experiment. Twelve deuteron peaks corresponding to the bound states of the ^{19}F were observed and analyzed. Other ^{19}F levels were populated weakly and were not considered further. The phenomenological optical potential was used for the analysis of the measured angular distributions. The input channel OM parameter sets were deduced from the fit of the angular distribution of elastic scattering ^{3}He + ^{18}O. The output channel OM parameters for deuterons were adopted from the global formula of Perey and Perey (1976). The FRESCO code (Thompson, 1988) was used to calculate the theoretical angular distributions of the ^{18}O(^{3}He, d)^{19}F transfer reaction. The transitions with the largest ANCs are to the ground state and to the 0.197 and 1.554 MeV levels of ^{19}F, $C^2_{^{18}O+p,\ g.s.}$ = 71.1 ± 14 fm^{-1}, $C^2_{^{18}O+p,\ 0.197}$ = 14.8 ± 3 fm^{-1}. The derived ANCs were used to deduce the direct capture cross-section $\sigma(E)_{cap}$ by the FRESCO code The dependence of the differential cross-section on the cut-off radius was tested to verify the surface character of the transfer reaction. E1 multipole electromagnetic operator was considered in the calculations. Woods-Saxon potential was used

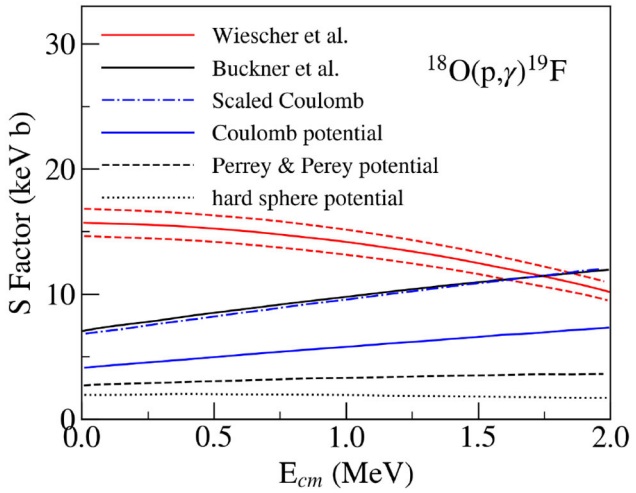

FIGURE 11 | S-factor of the total direct proton capture ^{18}O(p, γ)^{19}F determined from the transfer reaction. The red solid decreasing curve is based on the measurement of the direct contribution (p, γ) by Wiescher et al. (1980) with uncertainty about 7% (dashed red curves).

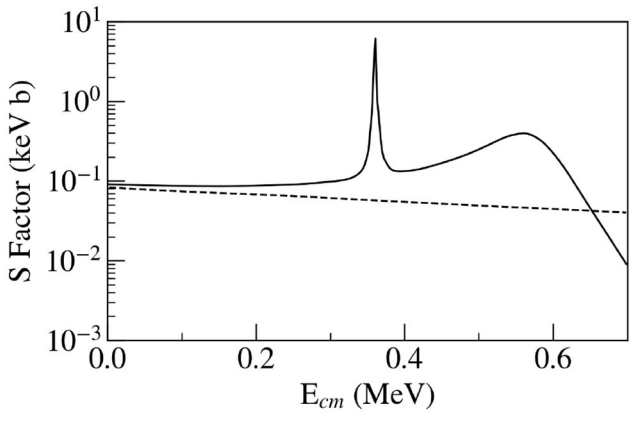

FIGURE 12 | The astrophysical S-factor for ^{11}C(p, γ)^{12}N, the total S-factor (solid line) and the direct contribution alone (dotted line).

for calculation of the bound state wave functions (Wiescher et al., 1980). Three kinds of potentials for scattered wave functions of incoming protons were: (1) the complex optical potential of Perey and Perey (1976), (2) the Coulomb potential only (which plays a major role at low proton energies) and (3) the hard sphere potential ($V = -300$ MeV) simulating a repulsive potential. The total direct S-factors for all three potentials are shown in **Figure 11**. The capture to the ground and 0.197 MeV states dominates the total direct S-factor (60% contribution). These S-factors were compared with calculations of ^{18}O(p, γ)^{19}F by Buckner et al. (2012) and with the direct measurement by Wiescher et al. (1980) at the low-energy region. It appears that the direct hard sphere potential S(E)-factor is almost constant (2 keV b), while the others have the tendency to rise slowly in the interval between 0 and 2 MeV, in agreement with Buckner et al. ($(S(E) = 7.06 + 2.98 \times 10^{-3}E - 2.6 \times 10^{-7}E^2$ [keV b]) and in disagreement with Wiescher et al. ($(S(E) = 15.7 - 0.34 \times 10^{-3}E - 1.21 \times 10^{-6}E^2$ [keV b]) The calculation of the direct S-factor with the Coulomb potential when normalized to the measured direct capture cross-section at $E_{c.m.}$ = 1751.9 keV by Wiescher et al. (1980) is in a good agreement with the result of Buckner et al. The total direct astrophysical S-factor calculated with three different interaction potentials show a tendency similar to that of Buckner et al. For the Coulomb interaction potential, the calculations reproduce these data very well, after normalization. Without normalization, they are lower than the values of Buckner et al. at least about 35%.

Due to the large number of resonances, the applicability conditions are not satisfied. The ANC value of ^{18}O$(p, \gamma)^{19}$F reaction can be compared with the different calculations used for determination of the direct S-factor.

3.7. ^{11}C$(p, \gamma)^{12}$N

The reaction ^{14}N(^{11}C, ^{12}N)^{13}C can provide ANC for the ^{12}N → ^{11}C + γ decay and the direct capture rate for ^{11}C(p, γ)^{12}N at astrophysical energies. This reaction is a part of the hot pp-chain (^{7}Be(α, γ)^{11}C). It may open a possibility for super-massive, low-metallicity stars to produce CNO nuclei (avoiding the three-alpha process) (Wiescher et al., 1989). The ^{11}C radioactive beam, at an intensity of 4.2 × 10^5 particles/s and energy 10 MeV/u, bombarded a 1.5 mg/cm^2 melamine target ($C_3N_6H_6$) (Gagliardi et al., 2002). This radioactive beam was produced in the reaction ^{1}H(^{11}B, ^{11}C)n and purified by the Momentum Achromat Recoil Spectrometer (MARS). S-factor for direct ^{11}C(p, γ)^{12}N was deduced (Gagliardi et al., 2001) using the R-matrix calculation that includes effects of two low-lying resonances and the determined ANC factor ($C^2_{^{11}\mathrm{C}+p}$=1.73 ± 0.25 fm^{-1}) (Tang et al., 2003). Results are shown in **Figure 12**. The values of S-factor are more than 10 times larger than previously given (Lefebvre et al., 1995).

Non-resonant capture is thought to dominate the ^{11}C$(p, \gamma)^{12}$N reaction at low energies (Lefebvre et al., 1995; Huang et al., 2010), ANC is an important component for the R-matrix analysis.

3.8. ^{12}N$(p, \gamma)^{13}$O

The new experimental information on the ^{12}N(p, γ)^{13}O capture is important for Population II stars with lower masses, modeling a nucleosynthesis and their evolution. This capture reaction was studied by the ANCs indirect method using the peripheral proton-transfer reaction ^{14}N(^{12}N, ^{13}O)^{13}C (Banu et al., 2009). The radioactive beam ^{12}N was produced from a primary beam of ^{12}C at 23 A MeV with an intensity of 150 pnA (particle nA) striking on a LN2-cooled H_2 gas cell. To reduce the ^{12}C energy to 12 A MeV where the reaction is peripheral a 250-μm-thick Al foil was put behind the gas cell. For the DWBA analysis of the transfer reaction ^{14}N(^{12}N, ^{13}O)^{13}C, the parameters of the optical model potential for both the entrance channel (^{12}N − ^{14}N) and exit channel (^{13}O − ^{13}C) were needed to calculate the distorted scattering wave functions. Analysis of the elastic scattering data was done with the help of semi-microscopic double-folding optical potentials. The calculated angular distribution of the

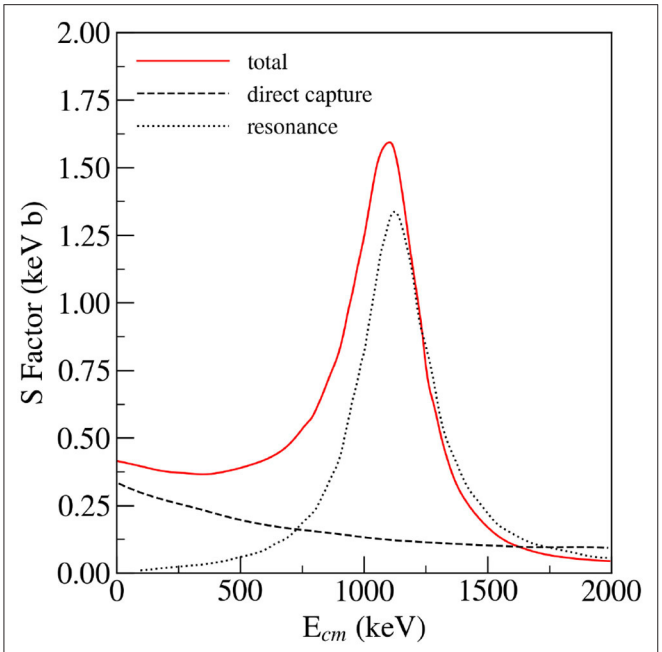

FIGURE 13 | The astrophysical S-factor for the ^{12}N(p, γ)^{13}O capture as a function of the energy. The solid red line shows results for the total S-factor, dashed line is the direct component of the S-factor and the dotted line is the resonant component.

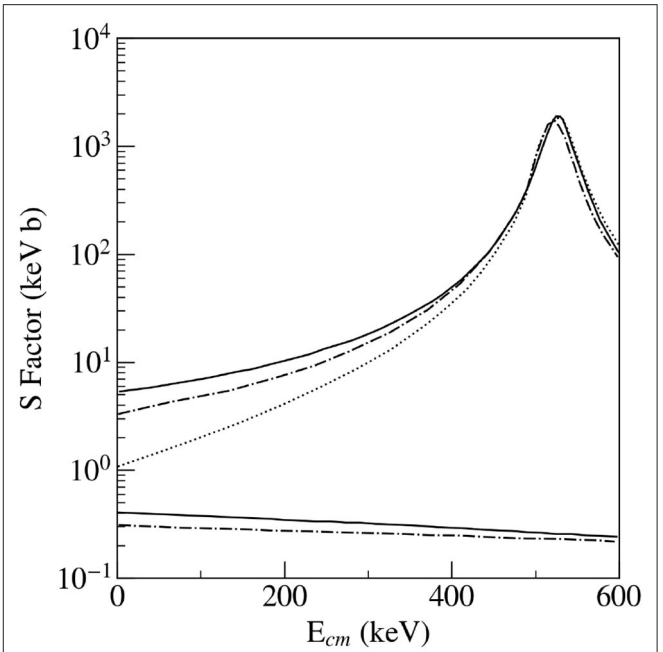

FIGURE 14 | The astrophysical S-factor for the ^{13}N(p, γ)^{14}O capture. The relatively flat solid line is the direct capture contribution determined from the ANC. This result is higher than that obtained by Decrock et al. (1993) (lowest dash-dotted line). Based on constructive interference, this updated result for the total S-factor, the top solid line, is about 38% higher than the previous result (upper dash-dotted line). For the sake of completeness, the result with destructive interference is shown (the dotted line).

transfer reaction ^{14}N(^{12}N, ^{13}O)^{13}C by the finite-range DWBA code PTOLEMY was used for the fit of the experimental angular distribution. From the comparison of theoretical and experimental angular distributions, the ANC was determined to be $C^2_{p_{1/2}}(^{13}\mathrm{O}) = 2.53 \pm 0.30$ fm^{-1}. This value of $C^2_{p_{1/2}}(^{13}\mathrm{O})$ then leads to S(0) = 0.33(4) keV b for the direct capture component. However, the resonant capture via the first excited state and the direct capture to the ground state interfere, which leads to a further increase of S-factor giving $S_{tot}(0)$ = 0.42(6) keV b (see **Figure 13**). This value is 2 orders lower than the theoretical value used by Wiescher et al. (1989). It is compatible with the analysis by Zhi-Hong (2006), who deduced the ANC from the shell-model. Later, Timofeyuk (2013) used the source term approach using shell model wave functions and it agreed with the measured value of ANC.

Non-resonant capture dominates the ^{12}N(p, γ)^{13}O reaction at low energies, where the ANC brings important information for the R-matrix analysis.

3.9. ^{13}N(p, γ)^{14}O

The ^{13}N(p, γ)^{14}O capture is one of the important reactions in the hot CNO cycle. The rate of this reaction is dominated by the resonant capture through the first excited state of ^{14}O (E_r=0.528 MeV). The transfer reaction used in this case was ^{14}N(^{13}N,^{14} O)^{13}C (Tang et al., 2004). The ^{13}N radioactive beam needed for the determination of the S-factor of this capture was produced by the ^{1}H(^{13}C, ^{13}N)n reaction (Tang et al., 2004). The ^{13}C beam of ~600 enA (electrical nA) at 15 A MeV from the K500 superconducting cyclotron bombarded a 10-cm-long, LN_2-cooled, cryogenic H_2 gas cell with havar windows. Recoiled ^{13}N nuclei were then separated by the magnetic spectrometer MARS at 0° and focused on a target consisting of 1.5 mg/cm^2 melamine $C_3N_6H_6$ with 20 μg/cm^2 carbon backing. The reaction products from the ^{13}N secondary beam bombarding the target were recorded by two detector telescopes, each consisted of a 5×5 cm 16-strip position-sensitive Si detector, with a thickness of 60 μm, backed by a 500 μm Si detector. Three sets of elastic scattering data on ^{14}N, ^{12}C, and ^{1}H were obtained.

The optical-model parameters were obtained from double-folding-model calculations for ^{13}N ions scattered on the melamine target (Trache et al., 2000).

After fitting the experimental angular distribution of the transfer reaction ^{14}N(^{13}N,^{14} O)^{13}C by theoretical calculations, the value of the ANC for $^{14}\mathrm{O} \rightarrow {}^{13}\mathrm{N} + \mathrm{p}$ was found to be $C^2_{p_{1/2}} = 29.0 \pm 4.3$ fm^{-1}.

The S-factor was deduced from the R-matrix approach (Tang et al., 2003), where the measured ANC and the experimental resonance parameters of the (broad) first excited state was used. Parameters of Magnus et al. (1994) ($E_R^{c.m.}$ = 527.9 ± 1.7 keV, γ_{total} = 37.3 ± 0.9 keV, and γ_γ = 3.36 ± 0.72 eV) were used for the first resonance. The total astrophysical S-factor including the constructive interference with the direct part is shown in **Figure 14**. This result is about 38% higher than the previous value of Decrock et al. (1993), obtained from the calculation.

Although the applicability conditions for ANC method are not fulfilled in $^{13}N(p,\gamma)^{14}O$ reaction, the direct capture part influences the total S-factor via the interference.

4. FURTHER USAGE OF ANCS

The properties of ANCs have a broader potential in nuclear physics. In the next section, we briefly outline a few examples.

4.1. Mirror Nuclei

From theoretical calculations performed over several 0*p* nuclei (Timofeyuk et al., 2003) it was found that the proton and neutron ANCs for mirror pairs $|C_p|^2$ and $|C_n|^2$ vary by a factor of two for different potentials used, while the ratio $R = |C_p/C_n|^2$ depends weakly on the used potential (less than 4%) (Timofeyuk et al., 2003 and references therein). This effect is connected to the fact that the Coulomb potential does not vary much inside the nucleus over the nuclear volume and thus, can be replaced by a constant equal to the energy difference between the separation energies for a proton and neutron. Hence, (see Timofeyuk et al., 2003) the bound-state wave function can be written in terms of the regular Coulomb and the Bessel functions of $l^{th}-$order:

$$\varphi_l(r) = \frac{F_l\left(ik_pR_N\right)}{k_pR_Nj_l\left(ik_nR_N\right)}j_l\left(ik_nr\right), \quad r \le R_N \tag{10}$$

where F_l is the regular Coulomb function at momentum k_p, j_l are the Bessel functions at momentum k_n and R_N is the nuclear radius. k_p and k_n are defined by the proton and neutron separation energies. Assuming that the difference between the wave functions for mirror pairs can be neglected, the ratio will be equal to:

$$R \approx R_0 = \left|\frac{F_l\left(ik_pR_N\right)}{k_pR_Nj_l\left(ik_nR_N\right)}\right|^2 \tag{11}$$

Considering the relation $C_{n(p)} = \sqrt{S_{n(p)}}b_{n(p)}$, where $b_{n(p)}$ is the single-particle ANC (SPANC), the equation 11 will become equal to $|b_{n(p)}/b_{p(n)}|^2$. Assuming that – for *p* and *n* – both the nuclear single-particle potentials and the single-particle wave functions in the interior are the same, the ratio will be weakly dependent from the chosen potentials.

Approaching the limits of (proton) stability, the separation energy for a neutron decreases and excited states may correspond to resonances for the proton-plus-core mirror system. In such a case, the connection between the width γ_p for the resonance and the mirror ANC C_n can be expressed (see Timofeyuk et al., 2003) as

$$R_\gamma = \frac{\Gamma_P}{|C_n|^2} \approx \frac{k_p}{\mu}\left|\frac{F_l\left(k_pR_N\right)}{k_pR_Nj_l\left(ik_nR_N\right)}\right|^2 \tag{12}$$

This ratio can be approximated by the single-particle ratio $R_\gamma^{s.p.} = \Gamma_P^{S.P.}/b_n^2$ if the single-particle potentials and spectroscopic factors for mirror pairs are considered equal. These relations were presented in Timofeyuk et al. (2003), where a number of mirror cases were theoretically tested, and the results were compared with the available experimental values of ANCs.

Reactions with mirror nuclei can be a solution to study reactions that involve a radioactive participant. This method was applied e.g., for $^7Be(p,\gamma)^8B$ (Trache et al., 2003), deduced from $^8Li \rightarrow ^7Li + n$ using $^{13}C(^7Li,^8Li)^{12}C$ reaction. Other cases in which the mirror nuclei procedure have been used are $^{20}Mg(p,\gamma)^{21}Al$ (Timofeyuk et al., 2012) from $^{20}O(n,\gamma)^{21}O$ using reaction 20O(d,p) 21O, $^{22}Mg(n,\gamma)^{23}Mg$ (Al-Abdullah et al., 2010) capture from $^{22}Ne(p,\gamma)^{23}Na$ using $^{13}C(^{22}Ne,^{23}Ne)^{12}C$.

Using mirror reactions to study the direct (p,γ) captures proved to be an important tool, especially for radioactive nuclei. However, this technique has some potential constraints:

- Demand on peripherality of (n,γ) capture. Without the presence of Coulomb barrier the peripherality must arise from the centrifugal barrier.
- Proper treatment of (d,p) reactions, see more in a recent discussion on the role of high internal momentum of *d* and proper application of DWBA, FR-DWBA, and CDCC (Timofeyuk et al., 2008; Gómez-Ramos and Timofeyuk, 2018).
- Mirror symmetry breaking may play a role (effect of 18% was determined for ^{27}Mg-^{27}P in Timofeyuk et al., 2008) and it should be treated on a case by case basis.

4.2. *Ab-initio* Methods

Recently, with the developments in *ab initio* methods, several techniques appeared feasible to perform ANC calculations. Despite the difficulties—convergence to long-asymptotics, sampling the tails (in Monte-Carlo methods)—the calculations can nowadays offer predictions consistent with experimental measurements for light (LiBeB) elements (Nollett and Wiringa, 2011).

4.3. Nuclear Radii

ANC being the normalization of the asymptotic wave function, it can naturally contain the information on nuclear halo/skin composed of the last peripheral nucleon. The possibility to access a nuclear radius, from a knowledge of overlap integrals between states with A and (A-1), was used by Timofeyuk (1998). The simple way to correlate the halo radius to ANC was used by Carstoiu et al. (2001) for the case of ^8B, where it was shown that the rms radius of the last proton can be determined and the proton is localized (in average) at the distance two times the core radius.

The ANC deduced from peripheral transfer reactions was used to determine the rms radii for ^{12}B, ^{13}C by Liu et al. (2001), for ^{13}C and ^{11}Be by Belyaeva et al. (2014), for ^{12}B by Belyaeva et al. (2018). Rms radii of valence neutron was studied in ^{16}N by Li et al. (2016) for several excited states. $^{9,11}Be$, ^{13}C and alpha cluster states were studied by Ogloblin et al. (2016).

As remarked by the above authors, the determination of the rms radius by ANC brings an independent approach, that increases reliability and is a test of other methods.

4.4. References to Computer Codes

Different computer codes were used in the above. They are listed here with the references and web sites:

- ECIS79 - Raynal, 1979, 1981,
- DWUCK5 - Kunz, 1990,
- FRESCO - Thompson, 1988,
- PTOLEMY - Rhoades-Brown et al., 1983,
- RADCAP - Bertulani, 2003

5. SUMMARY

The ANC method is used for determination of the astrophysical S-factor at low astrophysical energies of participating particles, where the cross-section is very low, and it is extremely difficult to measure it directly. Where the experimental effort is challenging and the case is favorable, mirror symmetry is/can be used to deduce the ANCs of bound states or properties of resonances.

We have illustrated the usefulness, but also limitations of the indirect ANC method in several examples with an astrophysical interest. They include experiments with solid or isotopic gas targets with stable beams and also experiments in inverse kinematics with radioactive beams.

The ANC method was successfully tested in number of reactions, found compatible with theory predictions as shown in the summarizing (**Table 2**). ANCs are also frequently deduced from R-matrix fits. These values are also generally in agreement with independently found ANCs.

An important region of ANC method application are measurements with radioactive beams. The reactions with the short-lived isotopes are still not accessible to direct measurements. Nuclei distant from the valley of stability have lower separation energies and thus the level density around threshold may be smaller. This is favorable to the direct radiative capture contribution to the total astrophysical S-factor. Reactions with radioactive beams, however, always need more development both in the experimental techniques (quality of elastic scattering data, resolutions) and in theoretical analysis (reliable OMP, reaction codes). This is discussed in more detail in the remarks to ECT* workshop by Trache and Carstoiu (2019).

AUTHOR CONTRIBUTIONS

All the listed authors contributed to the writing of the paper. VB worked on all experiments in section 3, JM has worked on ^{14}C(n,γ)^{15}C, ^{15}N(p,γ)^{16}O, and ^{18}O(p, γ)^{19}F.

FUNDING

We would like to thank for the support to the MEYS project SPIRAL2-CZ, EF16-013/0001679.

ACKNOWLEDGMENTS

Authors want to thank to all our colleagues from the Cyclotron Institute, Texas A&M University, College Station, Texas, colleagues from Istituto Nazionale di Fisica Nucleare, Laboratori Nazionali del Sud, Italia, Sicilia, Catania, and colleagues from the Nuclear Physics Institute of the Czech Academy of Sciences with whom we were happy to collaborate on topics included in this review. Authors are also indebted to referees, whose insightful suggestions and comments importantly improved the original text. The figures are adapted from the papers referred in each reaction.

REFERENCES

Abia, C., Hedrosa, R. P., Domínguez, I., and Straniero, O. (2017). The puzzle of the CNO isotope ratios in asymptotic giant branch carbon stars. *Astron. Astrophys.* 599:A39. doi: 10.1051/0004-6361/201629969

Ahmad, Q. R., Allen, R. C., Andersen, T. C., Anglin, J. D., Bühler, G., Barton, J. C., et al. (2001). Measurement of the rate of $\nu_e + d \rightarrow p + p + e^-$ interactions produced by ^{8}B solar neutrinos at the sudbury neutrino observatory. *Phys. Rev. Lett.* 87:071301. doi: 10.1103/PhysRevLett.87.071301

Al-Abdullah, T., Carstoiu, F., Chen, X., Clark, H. L., Fu, C., Gagliardi, C. A., et al. (2010). Stellar reaction rate for ^{22}Mg+p $\rightarrow$ ^{23}Al from the asymptotic normalization coefficient in the mirror nuclear system ^{22}Ne+n $\rightarrow$ ^{23}Ne. *Phys. Rev. C* 81:035802. doi: 10.1103/PhysRevC.81.035802

Azhari, A., Burjan, V., Carstoiu, F., Dejbakhsh, H., Gagliardi, C. A., Kroha, V., et al. (1999). The ^{10}B(^{7}Be,^{8}B)^{9}Be reaction and the ^{7}Be(p, γ)^{8}B S factor. *Phys. Rev. Lett.* 82, 3960–3963.

Azhari, A., Burjan, V., Carstoiu, F., Gagliardi, C. A., Kroha, V., Mukhamedzhanov, A. M., et al. (2001). Asymptotic normalization coefficients and the ^{7}Be(p, γ)^{8}B astrophysical S factor. *Phys. Rev. C* 63:055803. doi: 10.1103/PhysRevC.63.055803

Bahcall, J. N. (1985). The solar neutrino problem. *Solar Phys.* 100, 53–63.

Banu, A., Al-Abdullah, T., Fu, C., Gagliardi, C. A., McCleskey, M., Mukhamedzhanov, A. M., et al. (2009). Astrophysical S factor for the radiative capture ^{12}N(p, γ)^{13}O determined from the ^{14}N(^{12}N, ^{13}O)^{13}C proton transfer reaction. *Phys. Rev. C* 79:025805. doi: 10.1103/PhysRevC.79.025805

Baur, G., Bertulani, C. A., and Rebel, H. (1986). Coulomb dissociation as a source of information on radiative capture processes of astrophysical interest. *Nuclear Phys. A* 458, 188–204.

Baur, G., and Rebel, H. (1996). Coulomb breakup of nuclei—applications to Astrophysics. *Annu. Rev. Nuclear Part. Sci.* 46, 321–350.

Bellerive, A., Klein, J. R., McDonald, A. B., Noble, A. J., and Poon, A. W. P. (2016). The Sudbury Neutrino observatory. *Nuclear Phys. B* 908, 30–51. doi: 10.1016/j.nuclphysb.2016.04.035

Belyaeva, T. L., Goncharov, S. A., Demyanova, A. S., Ogloblin, A. A., Danilov, A. N., Maslov, V. A., et al. (2018). Neutron halos in the excited states of ^{12}B. *Phys. Rev. C* 98:034602. doi: 10.1103/PhysRevC.98.034602

Belyaeva, T. L., Perez-Torres, R., Ogloblin, A. A., Demyanova, A. S., Ershov, S. N., and Goncharov, S. A. (2014). Determination of neutron halo radii in the first excited states of ^{13}C and ^{11}Be with the asymptotic normalization coefficients method. *Phys. Rev. C* 90:064610. doi: 10.1103/PhysRevC.90.064610

Bém, P., Burjan, V., Kroha, V., Novák, J., Piskor, S., Šimečková, E., et al. (2000). Asymptotic normalization coefficients for ^{14}N$\leftrightarrow^{13}$C + p from ^{13}C(^{3}He, d)^{14}N. *Phys. Rev. C* 62:024320. doi: 10.1103/PhysRevC.62.024320

Bertulani, C. A. (2003). RADCAP: A potential model tool for direct capture reactions. *Comput. Phys. Commun.* 156, 123–141. doi: 10.1016/S0010-4655(03)00441-7

Bing, G., and Zhi-Hong, L. (2007). Determination of astrophysical ^{13}N(p, γ) ^{14}O S-factors from the asymptotic normalization coefficient of ^{14}C $\rightarrow^{13}$ C + n. *Chin. Phys. Lett.* 24, 65–68. doi: 10.1088/0256-307X/24/1/018

Buckner, M. Q., Iliadis, C., Cesaratto, J. M., Howard, C., Clegg, T. B., Champagne, A. E., et al. (2012). Thermonuclear reaction rate of ^{18}O(p, γ)^{19}F. *Phys. Rev. C* 86:065804. doi: 10.1103/PhysRevC.86.065804

Burjan, V., Hons, Z., Kroha, V., Mrázek, J., Piskor, S., Mukhamedzhanov, A. M., et al. (2013). Experimental study of the ^{18}O(d, p)^{19}O reaction and the ANC method. *J. Phys. Conf. Ser.* 420:012142. doi: 10.1088/1742-6596/420/1/012142

Burjan, V., Hons, Z., Kroha, V., Mrázek, J., Piskor, S., Mukhamedzhanov, A. M., et al. (2014). The ^{18}O(d, p)^{19}O reaction and the ANC method. *AIP Conf. Proc.* 1595, 163–167. doi: 10.1063/1.4875304

Burjan, V., Hons, Z., Kroha, V., Mrazek, J., Piskor, S., Mukhamedzhanov, A. M., et al. (2019). The determination of the astrophysical S-factor of the direct ^{18}O(p, γ)^{19}F capture by the ANC method. *Eur. Phys. J. A* 55:114. doi: 10.1140/epja/i2019-12801-8

Carstoiu, F., Trache, L., Gagliardi, C. A., Tribble, R. E., and Mukhamedzhanov, A. M. (2001). Radius of ^{8}B halo from the asymptotic normalization coefficient. *Phys. Rev. C* 63:054310. doi: 10.1103/PhysRevC.63.054310

Chow, H. C., Griffiths, G. M., and Hall, T. H. (1975). The ^{16}O(p, γ)^{17}F direct capture cross section with an extrapolation to astrophysical energies. *Can. J. Phys.* 53, 1672–1686. doi: 10.1139/p75-213

Daehnick, W. W., Childs, J. D., and Vrcelj, Z. (1980). Global optical model potential for elastic deuteron scattering from 12 to 90 MeV. *Phys. Rev. C* 21, 2253–2274. doi: 10.1103/PhysRevC.21.2253

Decrock, P., Gaelens, M., Huyse, M., Reusen, G., Vancraeynest, G., Van Duppen, P., et al. (1993). Study of the ^{13}N(d, n)^{14}O reaction cross section and its astrophysical implications for the ^{13}N proton capture reaction. *Phys. Rev. C* 48, 2057–2067. doi: 10.1103/PhysRevC.48.2057

Duke, C. B. (1963). Optical-model analysis of elastic scattering of protons on oxygen at intermediate energies. *Phys. Rev.* 129, 681–691. doi: 10.1103/PhysRev.129.681

Gagliardi, C., Azhari, A., Burjan, V., Carstoiu, F., Kroha, V., Mukhamedzhanov, A., et al. (2002). Asymptotic normalization coefficients and astrophysical direct capture rates. *Eur. Phys. J. A* 13, 227–232. doi: 10.1140/epja1339-38

Gagliardi, C. A., Azhari, A., Bem, P., Burjan, V., Carstoiu, F., Cejpek, J., et al. (2001). Asymptotic normalization coefficients from direct transfer reactions and astrophysical S factors. *Nuclear Phys. A* 682, 369–374. doi: 10.1016/S0375-9474(00)00662-X

Gagliardi, C. A., Tribble, R. E., Azhari, A., Clark, H. L., Lui, Y.-W., Mukhamedzhanov, A. M., et al. (1999). Tests of transfer reaction determinations of astrophysical S factors. *Phys. Rev. C* 59, 1149–1153. doi: 10.1103/PhysRevC.59.1149

Gómez-Ramos, M., and Timofeyuk, N. K. (2018). Reduced sensitivity of the (d, p) cross sections to the deuteron model beyond the adiabatic approximation. *Phys. Rev. C* 98:011601. doi: 10.1103/PhysRevC.98.011601

Guo, B., Su, J., Li, Z. H., Wang, Y. B., Yan, S. Q., Li, Y. J., et al. (2013). Determination of the astrophysical ^{12}N(p, γ)^{13}O reaction rate from the ^{2}H(^{12}N, ^{13}O)n reaction and its astrophysical implications. *Phys. Rev. C* 87:015803. doi: 10.1103/PhysRevC.87.015803

Herndl, H., Hofinger, R., Jank, J., Oberhummer, H., Görres, J., Wiescher, M., et al. (1999). Reaction rates for neutron capture reactions to C, N, and O isotopes to the neutron rich side of stability. *Phys. Rev. C* 60:064614. doi: 10.1103/PhysRevC.60.064614

Huang, J. T., Bertulani, C. A., and Guimarães, V. (2010). Radiative capture of nucleons at astrophysical energies with single-particle states. *Atom Data Nuclear Data Tables* 96, 824–847. doi: 10.1016/j.adt.2010.06.004

Imai, N., Aoi, N., Kubono, S., Beaumel, D., Abe, K., Kato, S., et al. (2001). Test of the ANC method via (d,p) reaction. *Nuclear Phys. A* 688, 281–284. doi: 10.1016/S0375-9474(01)00715-1

Jeukenne, J.-P., Lejeune, A., and Mahaux, C. (1977). Optical-model potential in finite nuclei from Reid's hard core interaction. *Phys. Rev. C* 16, 80–96. doi: 10.1103/PhysRevC.16.80

Kunz, P. (1990). DWUCK5: computer code DWUCK5: distorted wave Born approximation. Available online at: http://www.oecd-nea.org/tools/abstract/detail/nesc9872/

Lee, D. W., Powell, J., Perajarvi, K., Guo, F. Q., Moltz, D. M., and Cerny, J. (2011). Study of the ^{11}C(p, γ) reaction via the indirect d(^{11}C, ^{12}N)n transfer reaction. *J. Phys. G Nuclear Part. Phys.* 38:075201. doi: 10.1088/0954-3899/38/7/075201

Lefebvre, A., Aguer, P., Kiener, J., Bogaert, G., Coc, A., de Oliveira, F., et al. (1995). Astrophysical rate of the ^{11}C + p reaction from the coulomb break-up of a ^{12}N radioactive beam. *Nuclear Phys. A* 592, 69–88. doi: 10.1016/0375-9474(95)00291-8

Li, E. T., Guo, B., Li, Z. H., Wang, Y. B., Li, Y. J., Wu, Z. D., et al. (2016). Radii of the bound states in ^{16}N from the asymptotic normalization coefficients. *Chin. Phys. C* 40:114104. doi: 10.1088/1674-1137/40/11/114104

Liu, Z. H., Lin, C. J., Zhang, H. Q., Li, Z. C., Zhang, J. S., Wu, Y. W., et al. (2001). Asymptotic normalization coefficients and neutron halo of the excited states in ^{12}B and ^{13}C. *Phys. Rev. C* 64:034312. doi: 10.1103/PhysRevC.64.034312

Lorenz-Wirzba, H., Schmalbrock, P., Trautvetter, H. P., Wiescher, M., Rolfs, C., and Rodney, W. S. (1979). The ^{18}O(p, α)^{15}N reaction at stellar energies. *Nuclear Phys. A* 313, 346–362. doi: 10.1016/0375-9474(79)90505-0

Magnus, P. V., Adelberger, E. G., and Garcia, A. (1994). The "hot CNO cycle" ^{13}N(p, γ) resonance energy and the ^{18}Ne mass. *Phys. Rev. C* 49, R1755–R1758. doi: 10.1103/PhysRevC.49.R1755

Meissner, J., Schatz, H., Görres, J., Herndl, H., Wiescher, M., Beer, H., et al. (1996). Neutron capture cross section of ^{18}O and its astrophysical implications. *Phys. Rev. C* 53, 459–468. doi: 10.1103/PhysRevC.53.459

Morlock, R., Kunz, R., Mayer, A., Jaeger, M., Müller, A., Hammer, J. W., et al. (1997). Halo properties of the first $1/2^{+}$ state in ^{17}F from the ^{16}O(p, γ)^{17}F reaction. *Phys. Rev. Lett.* 79, 3837–3840. doi: 10.1103/PhysRevLett.79.3837

Mukhamedzhanov, A., Burjan, V., Gulino, M., Hons, Z., Kroha, V., McCleskey, M., et al. (2011). Asymptotic normalization coefficients from the ^{14}C(d, p)^{15}C reaction. *Phys. Rev. C* 84:024616. doi: 10.1103/PhysRevC.84.024616

Mukhamedzhanov, A. M., Bém, P., Brown, B. A., Burjan, V., Gagliardi, C. A., Kroha, V., et al. (2003). Asymptotic normalization coefficients for ^{14}N + p $\rightarrow$ ^{15}O and the astrophysical S factor for ^{14}N(p, γ)^{15}O. *Phys. Rev. C* 67:065804. doi: 10.1103/PhysRevC.68.019901

Mukhamedzhanov, A. M., Bém, P., Burjan, V., Gagliardi, C. A., Goldberg, V. Z., Hons, Z., et al. (2008). New astrophysical S factor for the ^{15}N(p, γ)^{16}O reaction via the asymptotic normalization coefficient (ANC) method. *Phys. Rev. C* 78:015804. doi: 10.1103/PhysRevC.78.015804

Mukhamedzhanov, A. M., Bém, P., Burjan, V., Gagliardi, C. A., Irgaziev, B. F., Kroha, V., et al. (2006). Asymptotic normalization coefficients from the ^{20}Ne(^{3}He, d)^{21}Na reaction and astrophysical factor for ^{20}Ne(p, γ)^{21}Na. *Phys. Rev. C* 73:035806. doi: 10.1103/PhysRevC.73.035806

Mukhamedzhanov, A. M., Clark, H. L., Gagliardi, C. A., Lui, Y.-W., Trache, L., Tribble, R. E., et al. (1997). Asymptotic normalization coefficients for ^{10}B$\rightarrow$^{9}Be + p. *Phys. Rev. C* 56, 1302–1312. doi: 10.1103/PhysRevC.56.1302

Mukhamedzhanov, A. M., Tribble, R. E., and Timofeyuk, N. K. (1995). Possibility to determine the astrophysical S factor for the ^{7}Be(p, γ)^{8}B radiative capture from analysis of the ^{7}Be(^{3}He, d)^{8}B reaction. *Phys. Rev. C* 51, 3472–3478. doi: 10.1103/PhysRevC.51.3472

Nollett, K. M., and Wiringa, R. B. (2011). Asymptotic normalization coefficients from *ab initio* calculations. *Phys. Rev. C* 83:041001. doi: 10.1103/PhysRevC.83.041001

Ogloblin, A. A., Demyanova, A. S., Danilov, A. N., Belyaeva, T. L., Goncharov, S. A., and Trzaska, W. (2016). Nuclear states with anomalously large radius (size isomers). *Phys. Atom. Nuclei* 79, 514–524. doi: 10.1134/S1063778816040177

Ohsaki, T., Igashira, M., Nagai, Y., Segawa, M., and Muto, K. (2008). Role of multiparticle-multihole states of ^{18,19}O in ^{18}O(n, γ)^{19}O reactions at keV energy. *Phys. Rev. C* 77:051303. doi: 10.1103/PhysRevC.77.051303

Palmerini, S., Trippella, O., and Busso, M. (2017). A deep mixing solution to the aluminum and oxygen isotope puzzles in pre-solar grains. *Monthly Notice R Astron. Soc.* 467, 1193–1201. doi: 10.1093/mnras/stx137

Perey, C. M., and Perey, F. G. (1976). Compilation of phenomenological optical-model parameters 1954–1975. *Atomic Data Nuclear Data Tables* 17, 1–101. doi: 10.1016/0092-640X(76)90007-3

Raynal, J. (1979). *Code ECIS79*. Available online at: https://www.oecd-nea.org/tools/abstract/detail/nea-0850; https://people.nscl.msu.edu/~brown/reaction-codes/

Raynal, J. (1981). Recurrence relations for distorted-wave Born approximation Coulomb excitation integrals and their use in coupled channel calculations. *Phys. Rev. C* 23, 2571–2585. doi: 10.1103/PhysRevC.23.2571

Rhoades-Brown M., Steven, P., and McFarlane M. (1983). Ptolemy: a program for heavy-ion direct-reaction calculations. Available online at: https://inis.iaea.org/search/searchsinglerecord.aspx?recordsFor=SingleRecord&RN=9416330

Rolfs, C., Rodney, W. S., Shapiro, M. H., and Winkler, H. (1975). Hydrogen burning of ^{20}Ne and ^{22}Ne in stars. *Nuclear Phys. A* 241, 460–486. doi: 10.1016/0375-9474(75)90398-X

Rolfs, C. E., and Rodney, W. S. (1988). *Cauldrons in the Cosmos: Nuclear Astrophysics*. Chicago, IL: University of Chicago Press.

Tang, X., Azhari, A., Fu, C., Gagliardi, C. A., Mukhamedzhanov, A. M., Pirlepesov, F., et al. (2004). Determination of the direct capture contribution for ^{13}N(p,γ)^{14}O from the ^{14}O $\rightarrow$ ^{13}N + p asymptotic normalization coefficient. *Phys. Rev. C* 69:055807. doi: 10.1103/PhysRevC.69.055807

Tang, X., Azhari, A., Gagliardi, C. A., Mukhamedzhanov, A. M., Pirlepesov, F., Trache, L., et al. (2003). Determination of the astrophysical S factor for ^{11}C(p,γ)^{12}N from the ^{12}N $\rightarrow$ ^{11}C+p asymptotic normalization coefficient. *Phys. Rev. C* 67:015804. doi: 10.1103/PhysRevC.67.015804

Thompson, I. J. (1988). Coupled reaction channels calculations in nuclear physics. *Comp. Phys. Rep.* 7, 167–212. doi: 10.1016/0167-7977(88)90005-6

Timofeyuk, N. K. (1998). One nucleon overlap integrals for light nuclei. *Nuclear Phys. A* 632, 19–38. doi: 10.1016/S0375-9474(98)00810-0

Timofeyuk, N. K. (2010). Overlap functions, spectroscopic factors, and asymptotic normalization coefficients generated by a shell-model source term. *Phys. Rev. C* 81:064306. doi: 10.1103/PhysRevC.81.064306

Timofeyuk, N. K. (2013). Spectroscopic factors and asymptotic normalization coefficients for 0p-shell nuclei: recent updates. *Phys. Rev. C* 88:044315. doi: 10.1103/PhysRevC.88.044315

Timofeyuk, N. K., Descouvemont, P., and Thompson, I. J. (2008). Threshold effects in the ^{27}P($\frac{3}{2}^+$) $\rightarrow$ ^{26}Si + p and ^{27}Mg($\frac{3}{2}^+$) $\rightarrow$ ^{26}Mg + n mirror decays and the stellar reaction ^{26}Si(p, γ)^{27}P. *Phys. Rev. C* 78:044323. doi: 10.1103/PhysRevC.78.044323

Timofeyuk, N. K., Fernández-Domínguez, B., Descouvemont, P., Catford, W. N., Delaunay, F., and Thomas, J. S. (2012). Core excitations and narrow states beyond the proton dripline: the exotic nucleus ^{21}Al. *Phys. Rev. C* 86:034305. doi: 10.1103/PhysRevC.86.034305

Timofeyuk, N. K., Johnson, R. C., and Mukhamedzhanov, A. M. (2003). Relation between proton and neutron asymptotic normalization coefficients for light mirror nuclei and its relevance to nuclear astrophysics. *Phys. Rev. Lett.* 91:232501. doi: 10.1103/PhysRevLett.91.232501

Trache, L., Azhari, A., Carstoiu, F., Clark, H. L., Gagliardi, C. A., Lui, Y.-W., et al. (2003). Asymptotic normalization coefficients for ^{8}B$\rightarrow^7$Be + p from a study of ^{8}Li$\rightarrow^7$Li + n. *Phys. Rev. C* 67:062801. doi: 10.1103/PhysRevC.67.062801

Trache, L., Azhari, A., Clark, H. L., Gagliardi, C. A., Lui, Y.-W., Mukhamedzhanov, A. M., et al. (1998). Asymptotic normalization coefficients for ^{13}C + p $\rightarrow$ ^{14}N. *Phys. Rev. C* 58, 2715–2719. doi: 10.1103/PhysRevC.58.2715

Trache, L., Azhari, A., Clark, H. L., Gagliardi, C. A., Lui, Y.-W., Mukhamedzhanov, A. M., et al. (2000). Optical model potentials involving loosely bound p-shell nuclei around 10 MeV/nucleon. *Phys. Rev. C* 61:024612. doi: 10.1103/PhysRevC.61.024612

Trache, L., and Carstoiu, F. (2019). Indirect methods in nuclear astrophysics. *arXiv preprint arXiv:1911.06077*. Available online at: http://arxiv.org/abs/1911.06077

Vaughn, F. J., Grench, H. A., Imhof, W. L., Rowland, J. H., and Walt, M. (1965). The total neutron cross section of O18 from 0.14 to 2.47 MeV. *Nuclear Phys.* 64, 336–342. doi: 10.1016/0029-5582(65)90361-5

Vernotte, J., Berrier-Ronsin, G., Kalifa, J., Tamisier, R., and Wildenthal, B. H. (1994). Spectroscopic factors from one-proton stripping reactions on sd-shell nuclei: Experimental measurements and shell-model calculations. *Nuclear Phys. A* 571, 1–42. doi: 10.1016/0375-9474(94)90339-5

Watson, B. A., Singh, P. P., and Segel, R. E. (1969). Optical-model analysis of nucleon scattering from 1p-shell nuclei between 10 and 50 meV. *Phys. Rev.* 182, 977–989. doi: 10.1103/PhysRev.182.977

Wiescher, M., Becker, H. W., Görres, J., Kettner, K. U., Trautvetter, H. P., Kieser, W. E., et al. (1980). Nuclear and astrophysical aspects of 18O(p, γ)19F. *Nuclear Phys. A* 349, 165–216. doi: 10.1016/0375-9474(80)90451-0

Wiescher, M., Gorres, J., Graff, S., Buchmann, L., and Thielemann, F.-K. (1989). The hot proton-proton chains in low-metallicity objects. *Astrophys. J.* 343, 352–364. doi: 10.1086/167709

Wiescher, M., Gorres, J., and Thielemann, F.-K. (1990). Capture reactions on C-14 in nonstandard big bang nucleosynthesis. *Astrophys. J.* 363, 340–343. doi: 10.1086/169348

Xu, H. M., Gagliardi, C. A., Tribble, R. E., Mukhamedzhanov, A. M., and Timofeyuk, N. K. (1994). Overall normalization of the astrophysical S factor and the nuclear vertex constant for ^{7}Be(p, γ)^{8}B reactions. *Phys. Rev. Lett.* 73, 2027–2030. doi: 10.1103/PhysRevLett.73.2027

Yarmukhamedov, R., and Blokhintsev, L. D. (2018). Asymptotic normalization coefficients (nuclear vertex constants), three-body asymptotic normalization functions (on-shell vertex functions) and nuclear astrophysics. *Phys. Atom. Nuclei* 81, 616–629. doi: 10.1134/S1063778818050198

Zhi-Hong, L. (2006). Astrophysical rates for ^{12}N(p, γ)^{13}O direct capture reaction. *Chin. Phys. Lett.* 23, 3219–3221. doi: 10.1088/0256-307X/23/12/027

Conflict of Interest: The authors declare that the research was conducted in the absence of any commercial or financial relationships that could be construed as a potential conflict of interest.

frontiers in Astronomy and Space Sciences

REVIEW
published: 25 January 2021
doi: 10.3389/fspas.2020.609460

Mergers of Binary Neutron Star Systems: A Multimessenger Revolution

Elena Pian *

INAF, Astrophysics and Space Science Observatory, Bologna, Italy

On August 17, 2017, less than two years after the direct detection of gravitational radiation from the merger of two ~30 $M_{\odot}$ black holes, a binary neutron star merger was identified as the source of a gravitational wave signal of ~100 s duration that occurred at less than 50 Mpc from Earth. A short gamma-ray burst was independently identified in the same sky area by the *Fermi* and *INTEGRAL* satellites for high energy astrophysics, which turned out to be associated with the gravitational event. Prompt follow-up observations at all wavelengths led first to the detection of an optical and infrared source located in the spheroidal Galaxy NGC4993 and, with a delay of ~10 days, to the detection of radio and X-ray signals. This article revisits these observations and focusses on the early optical/infrared source, which was thermal in nature and powered by the radioactive decay of the unstable isotopes of elements synthesized via rapid neutron capture during the merger and in the phases immediately following it. The far-reaching consequences of this event for cosmic nucleosynthesis and for the history of heavy elements formation in the Universe are also illustrated.

Keywords: gamma-ray burst, gravitational waves, neutron star, nucleosynthesis, r-process, kilonova

OPEN ACCESS

Edited by:
Livio Lamia,
University of Catania, Italy

Reviewed by:
Toshitaka Kajino,
The University of Tokyo, Japan
Fiorella Burgio,
Ministry of Education, Universities and Research, Italy

***Correspondence:**
Elena Pian
elena.pian@inaf.it

Specialty section:
This article was submitted to Nuclear Physics, a section of the journal Frontiers in Astronomy and Space Sciences

Received: *23 September 2020*
Accepted: *02 December 2020*
Published: *25 January 2021*

Citation:
Pian E (2021) Mergers of Binary Neutron Star Systems: A Multimessenger Revolution. Front. Astron. Space Sci. 7:609460. doi: 10.3389/fspas.2020.609460

1 INTRODUCTION

Although the birth of "multimessenger" astronomy dates back to the detection of the first solar neutrinos in the 1960s and was rejuvenated by the report of MeV neutrinos from SN 1987A in the Large Magellanic Cloud, the detection of gravitational radiation from the binary neutron star merger on August 17, 2017 (GW170817A), marks the transition to maturity of this approach to observational astrophysics, as it is expected to open an effective window into the study of astrophysical sources which is not limited to exceptionally close (the Sun) or rare (Galactic supernova) events. GW170817 is a textbook case for gravitational physics, because, with its accompanying short gamma-ray burst (GRB) and afterglow and its thermal aftermath "kilonova", it has epitomized the different epiphanies of the coalescence of a binary system of neutron stars and finally allowed us to unify them.

Owing its name to a typical peak luminosity of $\sim 10^{42}$ erg s^{-1}, i.e., 1000 times larger than that of a typical nova outburst, kilonova is the characteristic optical and infrared source accompanying a binary neutron star merger due to the radioactive decay of the many unstable isotopes of large atomic weight elements synthesized via rapid neutron capture in the promptly formed dynamical ejecta and in the delayed postmerger ejecta. Its evolution, as well as that of the GRB afterglow, was recorded with exquisite detail, thanks to its closeness (40 Mpc). The scope of this article is to review the electromagnetic multiwavelength observations of GW170817 with particular attention to the kilonova phenomenon.

The outline of the review is as follows: **Section 2** sets the context of binary systems of neutrons stars and describes the predicted outcomes of their coalescences; **Section 3** presents the case of GW170817, the only so far confirmed example of double neutron star merger and the multiwavelength features of its electromagnetic counterpart (short GRB and kilonova); **Section 4** focusses on the kilonova, elaborates on its observed optical and near-infrared light curves and spectra, draws the link with nucleosynthesis of heavy elements, and outlines the theoretical framework that is necessary to describe the kilonova properties and implications; **Section 5** summarizes the results and provides an outlook of this line of research in the near future.

2 BINARY NEUTRON STAR MERGERS

Neutron stars are the endpoints of massive stars evolution and therefore ubiquitous in the Universe: on average, they represent about 0.1% of the total stellar content of a Galaxy. Since massive stars are mostly in binary systems (Sana et al., 2012), neutron star binaries should form readily, if the supernova explosion of either progenitor massive star does not disrupt the system (Renzo et al., 2019). Alternatively, binary neutron star systems can form dynamically in dense environments like stellar clusters (see Ye et al., 2020 and references therein). Binary systems composed by a neutron star and a black hole are also viable, but rare (Pfahl et al., 2005), which may account for the fact that none has so far been detected in our Galaxy.

The prototype binary neutron star system in our Galaxy is PSR B1913 + 16, where one member was detected as a pulsar in a radio survey carried out at the Arecibo Observatory (Hulse and Taylor, 1974), and the presence of its companion was inferred from the periodic changes in the observed pulsation period of 59 ms (Hulse and Taylor, 1975). Among various tests of strong general relativity enabled by the radio monitoring of this binary system, which earned the Nobel Prize for Physics to the discoverers in 1993, was the measurement of the shrinking of the binary system orbit, signaled by the secular decrease of the 7.75 h orbital period, that could be entirely attributed to energy loss via gravitational radiation (Taylor and Weisberg, 1982; Weisberg and Huang, 2016 and references therein).

With an orbital decay rate of $\dot{P} = -2.4 \times 10^{-12}$ s s^{-1}, the merging time of the PSR B1913 + 16 system is ∼300 Myr. Following the detection of PSR B1913 + 16, another dozen of binary neutron stars systems were detected in our Galaxy (e.g., Wolszczan, 1991; Burgay et al., 2003; Tauris et al., 2017; Martinez et al., 2017). Almost half of these have estimated merging times significantly shorter than a Hubble time. The campaigns conducted by the LIGO interferometers in Sep 2015-Jan 2016 (first observing run) and, together with Virgo, in Nov 2016-Aug 2017 (second observing run), the latter leading to the first detection of gravitational waves from a merging double neutron star system (see **Section 3**), constrained the local merger rate density to be 110–3,840 Gpc^{-3} yr^{-1} (Abbott et al., 2019). This is consistent with previous estimates (see, e.g., Burgay et al., 2003), and, under a series of assumptions, marginally consistent with independent estimates based on double neutron star system formation in the classical binary evolution scenario (Chruslinska et al., 2018). Ye et al. (2020) have estimated that the fraction of merging binary neutron stars that have formed dynamically in globular clusters is negligible. Under the assumption that the event detected by LIGO on April 25, 2019, was produced by a binary neutron star coalescence, the local rate of neutron star mergers would be updated to 250 – 2810 Gpc^{-3} yr^{-1} (Abbott et al., 2020a).

The merger of a binary neutron star system has four predicted outcomes: (1) a gravitational wave signal that is mildly isotropic, with a stronger intensity in the polar direction than in the equatorial plane; (2) a relativistic outflow, which is highly anisotropic and can produce an observable high energy transient; (3) a thermal, radioactive source emitting most of its energy at ultraviolet, optical, and near-infrared wavelengths; and (4) a burst of MeV neutrinos (Eichler et al., 1989; Rosswog and Liebendörfer, 2003) following the formation of the central remnant and possibly of high-energy (>GeV) neutrinos from hadronic interactions within the relativistic jet (Fang and Metzger, 2017; Kimura et al., 2018). While neutrinos are extremely elusive and detectable only from very small distances with present instrumentation (see **Section 5**), the first three observables have been now all detected, as detailed in the next three subsections.

2.1 Gravitational Waves

Coalescing binary systems of degenerate stars and stellar mass black holes are optimal candidates for the generation of gravitational waves detectable from ground-based interferometers as the strong gravity conditions lead to huge velocities and energy losses (Shapiro and Teukolsky, 1983), and the frequency of the emitted gravitational waves reaches several kHz, where the sensitivity of the advanced LIGO, Virgo, and KAGRA interferometers is designed to be maximal (Abbott et al., 2018).

The time behavior of binary systems of compact stars consists of three phases: a first inspiral phase in a close orbit that shrinks as gravitational radiation of frequency proportional to the orbital frequency is emitted, a merger phase where a remnant compact body is produced as a result of the coalescence of the two stars, and a postmerger, or ringdown, phase where the remnant still emits gravitational radiation while settling to its new stable configuration. During the inspiral, the amplitude of the sinusoidal gravitational signal rapidly increases as the distance between the two bodies decreases and the frequency increases (chirp), while in the ringdown phase the signal is an exponentially damped sinusoid. This final phase may encode critical information on the equation of state of the newly formed remnant (a black hole or, in the case of light neutron stars, a massive neutron star or metastable supramassive neutron star). The mathematical tool that is used to describe this evolution is the waveform model that aims at reproducing the dynamics of the system through the application of post-Newtonian corrections of increasing order and at providing the essential parameters that can then be compared with the interferometric observations (Blanchet, 2014; Nakano et al., 2019).

Since the amplitude of gravitational waves depends on the masses of the binary member stars, the signal will be louder and thus detectable from larger distances, for binary systems that involve black holes than those with neutron stars. The current horizon for binary neutron star merger detection with LIGO is ∼ 200 Mpc, and 25–30% smaller with Virgo and KAGRA (Abbott et al., 2018). The dependence of the gravitational waves amplitude on the physical parameters of the system implies that gravitational wave sources are standard sirens (Schutz, 1986), provided account is taken of the correlation between the luminosity distance and the inclination of the orbital plane with respect to the line of sight (Nissanke et al., 2010; Abbott et al., 2016).

2.2 Short Gamma-Ray Bursts

GRBs, flashes of radiation of 100–1,000 keV that outshine the entire Universe in this band, have durations between a fraction of a second and hundreds or even thousands of seconds. However, the duration distribution is bimodal, with a peak around 0.2 s (short or subsecond GRBs) and one around 20 s (long GRBs; Kouveliotou et al., 1993). This bimodality is reflected in the spectral hardness, which is on average larger in short GRBs, and in a physical difference between the two groups. While most long GRBs are associated with core-collapse supernovae (Galama et al., 1998; Woosley and Bloom, 2006; Levan et al., 2016), subsecond GRBs are produced by the merger of two neutron stars or a neutron star and a black hole, as long predicted based on circumstantial evidence (Blinnikov et al., 1984; Eichler et al., 1989; Fong et al., 2010; Berger et al., 2013; Tanvir et al., 2013) and then proven by the detection of GW170817 and of its high energy counterpart GRB170817A (**Section 3**). The observed relative ratio of long vs. short GRBs depends on the detector sensitivity and effective energy band (e.g., Burns et al., 2016). However, the duration overlap of the two populations is very large, so that the minimum of the distribution has to be regarded as a rather vaguely defined value (Bromberg et al., 2013).

About 140 short GRBs were localized so far to a precision that is better than 10 arc-minutes[1]; of these, ∼100, ∼40, and ∼10 have a detected afterglow in X-rays, optical, and radio wavelengths, respectively, and ∼30 have measured redshifts (these range between $z = 0.111$ and $z = 2.211$, excluding the nearby GRB170817A, see **Section 3.1.1**, and GRB090426, $z = 2.61$, whose identification as a short GRB is not robust, Antonelli et al., 2009). Short GRBs are located at projected distances of a fraction of, to several kiloparsecs from, the centers of their host galaxies, which are of both early and late type, reflecting the long time delay between the formation of the short GRB progenitor binary systems and their mergers (Berger, 2014).

According to the classical fireball model, both prompt event and multiwavelength afterglow of short GRBs are produced in a highly relativistic jet directed at a small angle with respect to the line of sight, whose aperture can be derived from the achromatic steepening (or "jet break") of the observed afterglow light curve (Nakar, 2007). In principle, this could be used to reconstruct the collimation-corrected rate of short GRBs, to be compared with predictions of binary neutron star merger rates. However, these estimates proved to be very uncertain, owing to the difficulty of measuring accurately the jet breaks in short GRB afterglows (Wanajo et al., 2002; Fong et al., 2015; Jin et al., 2018; Lamb et al., 2019; Pandey et al., 2019).

2.3 R-process Nucleosynthesis

Elements heavier than iron cannot form via stellar nucleosynthesis, as no enough neutrons are available for the formation of nuclei and temperatures are not sufficiently high to overcome the repulsive Coulomb barrier that prevents acquisition of further baryons into nuclei (Burbidge et al., 1957). Supernovae (especially the thermonuclear ones) produce large amounts of iron via decay (through ^{56}Co.) of radioactive ^{56}Ni synthesized in the explosion. Heavier nuclei form via four neutron capture processes (Thielemann et al., 2011), the dominant ones being slow and rapid neutron capture, in brief s- and r-process, respectively, where "slow" and "rapid" refer to the timescale of neutron accretion into the nucleus with respect to that of the competing process of β^- decay. In the s-process, neutron captures occur with timescales of hundreds to thousands of years, making β^- decay highly probable, while r-process neutron capture occurs on a timescale of ∼0.01 s, leading to acquisition of many neutrons before β^- decay can set on. As a consequence, the s-process produces less unstable, longer-lived isotopes, close to the so-called valley of β-stability (the decay time of a radioactive nucleus correlates inversely with its number of neutrons), while the r-process produces the heaviest, neutron-richest, and most unstable isotopes of heavy nuclei, up to uranium (Sneden et al., 2008; Mennekens and Vanbeveren, 2014; Thielemann et al., 2017; Côté et al., 2018; Horowitz et al., 2019; Kajino et al., 2019; Cowan et al., 2020). Among both s-process and r-process elements, some are particularly stable owing to their larger binding energies per nucleon, which causes their abundances to be relatively higher than others. In the abundances distribution in the solar neighborhood, these are seen as maxima "peaks" centered around atomic numbers $Z = 39$ (Sr-Y-Zr), 57 (Ba-La-Ce-Nd), and 82 (Pb) for the s-process and, correspondingly somewhat lower atomic numbers $Z = 35$ (Se-Br-Kr), 53 (Te-I-Xe), and 78 (Ir-Pt-Au) for the r-process (e.g., Cowan et al., 2020).

Both s-process and r-process naturally occur in environments that are adequately supplied with large neutron fluxes. For the s-process, these are eminently asymptotic giant branch stars, where neutron captures are driven by the ^{13}C (α, n)^{16}O and ^{22}Ne (α, n)^{25}Mg reactions (Busso et al., 1999). The r-process requires much higher energy and neutron densities, which are only realized in most physically extreme environments. While it can be excluded that big-bang nucleosynthesis can accommodate heavy elements formation in any significant amount (Rauscher et al., 1994), there is currently no consensus on the relative amounts of nucleosynthetic yields in the prime r-process candidate sites: core-collapse supernovae and mergers of binary systems composed by neutron stars or a neutron star and a black hole.

[1]http://www.mpe.mpg.de/jcg/grbgen.html

Core-collapse supernovae have been proposed starting many decades ago as sites of r-process nucleosynthesis through various mechanisms and in different parts of the explosion, including dynamical ejecta of prompt explosions of O-Ne-Mg cores (Hillebrandt et al., 1976; Wheeler et al., 1998; Wanajo et al., 2002); C + O layer of O-Ne-Mg-core supernovae (Ning et al., 2007); He-shell exposed to intense neutrino flux (Epstein et al., 1988; Banerjee et al., 2011); re-ejection of fallback material (Fryer et al., 2006); neutrino-driven wind from protoneutron stars (Takahashi et al., 1994; Woosley et al., 1994); and magnetohydrodynamic jets of rare core-collapse SNe (Nishimura et al., 2006; Winteler et al., 2012). Similarly old is the first proposal that the tidal disruption of neutron stars by black holes in close binaries (Lattimer and Schramm, 1974, 1976; Symbalisty and Schramm, 1982; Davies et al., 1994) and coalescences of binary neutron star systems (Eichler et al., 1989) could be at the origin of r-process nucleosynthesis. This should manifest as a thermal optical-infrared source of radioactive nature of much lower luminosity (a factor of 1,000) and shorter duration (rise time of a few days) than supernova (Li & Paczyński, 1998).

The models for r-process elements production in core-collapse supernova all have problems inherent in their physics (mostly related to energy budget and neutron flux density). On the other hand, the binary compact star merger origin may fail to explain observed r-process element abundances in very low metallicities stars, i.e., at very early cosmological epochs, owing to the nonnegligible binary evolution times (see Cowan et al., 2020 for an accurate review of all arguments in favor and against either channel). While the event of August 17, 2017 (**Section 3**), has now provided incontrovertible evidence that binary neutron star mergers host r-process nucleosynthesis, the role of core-collapse supernovae cannot be dismissed although their relative contribution with respect to the binary compact star channel must be assessed (Ramirez-Ruiz et al., 2015; Ji et al., 2016; Shibagaki et al., 2016; Côté et al., 2019; Safarzadeh et al., 2019; Simonetti et al., 2019). It cannot be excluded that both "weak" and "strong" r-process nucleosyntheses take place, with the former occurring mainly in supernova and possibly failing to produce atoms up to the third peak of r-process elemental abundance distribution (Cowan et al., 2020). The hint that heavy elements may be produced in low-rate events with high yields (Sneden et al., 2008; Wallner et al., 2015; Macias and Ramirez-Ruiz, 2019) points to binary compact star mergers or very energetic (i.e., expansion velocities larger than 20,000 km s^{-1}) core-collapse supernovae as progenitors, rather than regular core-collapse supernovae. Along these lines, it has been proposed that accretion disks of collapsars (the powerful core-collapse supernovae that accompany long GRBs, Woosley and Bloom, 2006) produce neutron-rich outflows that synthesize heavy r-process nuclei (Nakamura et al., 2013; Kajino et al., 2014; Nakamura et al., 2015). Siegel et al. (2019) calculated that collapsars may supply more than 80% of the r-process content and computed synthetic spectra for models of r-process-enriched supernovae corresponding to an MHD supernova and a collapsar disk outflow scenario.

Neutrons are tightly packed together in neutrons stars, but during coalescence of a binary neutron star system the tidal forces disrupt them and the released material forms promptly a disk-like rotating structure (dynamical ejecta, Rosswog et al., 1999; Shibata and Hotokezaka, 2019) where the neutron density rapidly drops to optimal values for r-process occurrence ($\sim 10^{24-32}$ neutrons cm^{-3}, Freiburghaus et al., 1999) and for copious formation of neutron-rich stable and unstable isotopes of large atomic number elements (Fernández and Metzger, 2016; Tanaka, 2016; Tanaka et al., 2018; Wollaeger et al., 2018; Metzger, 2019).

3 THE BINARY NEUTRON STAR MERGER OF 17 AUGUST, 2017

On August 17, 2017, the LIGO and Virgo interferometers detected for the first time a gravitational signal that corresponds to the final inspiral and coalescence of a binary neutron star system (Abbott et al., 2017a). The sky uncertainty area associated with the event was 28 square degrees, in principle too large for a uniform search for an electromagnetic counterpart with ground-based and orbiting telescopes. However, its small distance (40^{+8}_{-14} Mpc), estimated via the "standard siren" property of gravitational wave signals associated with binary neutron star mergers, suggested that the aftermath could be rather bright and motivated a large-scale campaign at all wavelengths from radio to very high energy gamma-rays, which was promptly and largely rewarded by success and then timely followed by a long and intensive monitoring (Abbott et al., 2017b; Abbott et al., 2017c), as described in **Section 3.1**. Searches of MeV-to-EeV neutrinos directionally coincident with the source using data from the Super-Kamiokande, ANTARES, IceCube, and Pierre Auger Observatories between 500 s before and 14 days after the merger returned no detections (Albert et al., 2017; Abe et al., 2018).

Based on the detection of electromagnetic radiation, Bauswein et al. (2017) have argued that the merger remnant may not be a black hole or at least the postmerger collapse to a black hole may be delayed. Since the postmerger phase "ring-down" signal of GW170817 was not detected (Abbott et al., 2017e), this hypothesis cannot be tested directly with gravitational data. Bauswein et al. (2017) also derived lower limits on the radii of the neutron stars.

Notably, while the gravitational data made it possible to set an upper limit on the tidal-deformability parameter of the binary neutron stars ($\tilde{\Lambda} \lesssim 800$, Abbott et al., 2017a), the optical observation of kilonova ejecta limited the same parameter from below ($\tilde{\Lambda} \gtrsim 400$, Radice et al., 2018), based on the consideration that for smaller values of $\tilde{\Lambda}$ a long-lived remnant would not be favored, contradicting the result of Bauswein et al. (2017). The limits on the $\tilde{\Lambda}$ parameter constrain the neutron star radius to the range 11.8 km $\lesssim R_{1.5} \lesssim$ 13.1 km, where $R_{1.5}$ refers to a 1.5 $M_{\odot}$ neutron star (Burgio et al., 2018), and in turn confine the possible ensemble of viable equations of state (Annala et al., 2018; Lim and Holt, 2018), a fundamental, yet poorly known, descriptor of neutron star physics (Özel and Freire, 2016). Furthermore, by circumscribing the number of equations of state of the compact stars, their exploration can be brought beyond nucleonic matter and extended to scenarios of matter presenting a phase transition

(Burgio et al., 2018; Most et al., 2018). The results on the tidal deformability of the neutron star progenitors of GW170817 and on the behavior of the remnant thus provide a brilliant confirmation of the added value of a multimessenger approach over separate observations of individual carriers of information.

3.1 The Electromagnetic Counterpart of GW170817

Independent of LIGO-Virgo detection of the gravitational wave signal, the Gamma-ray Burst Monitor (GBM) onboard the NASA *Fermi* satellite and the Anticoincidence Shield for the gamma-ray Spectrometer (SPI) of the *International Gamma-Ray Astrophysics Laboratory* (*INTEGRAL*) satellite were triggered by a faint short GRB (duration of $\sim$2 s), named GRB170817A (Abbott et al., 2017b; Goldstein et al., 2017; Savchenko et al., 2017). This gamma-ray transient, whose large error box was compatible with that determined by LIGO-Virgo, lags the gravitational merger by 1.7 s, a delay that may be dominated by the propagation time of the jet to the gamma-ray production site (Beniamini et al., 2020; see however Salafia et al., 2018). The preliminary estimate of the source distance provided a crucial constraint on the maximum distance of the Galaxy that could plausibly have hosted the merger, so that the searching strategy was based on targeting galaxies within a $\sim$50 Mpc cosmic volume (see, e.g., Gehrels et al., 2016) with telescopes equipped with large (i.e., several square degrees) field-of-view cameras.

About 70 ground-based optical telescopes participated in the hunt and each of them adopted a different pointing sequence. This systematic approach enabled many groups to identify the optical counterpart candidate in a timely manner (with optical magnitude $V \simeq 17$), i.e., within $\sim$12 h of the merger (Arcavi et al., 2017; Lipunov et al., 2017; Soares-Santos et al., 2017; Valenti et al., 2017; Tominaga et al., 2018). Coulter et al. (2017) were the first to report a detection with the optical 1 m telescope Swope at Las Campanas Observatory. The optical source lies at 10 arc-seconds angular separation, corresponding to a projected distance of $\sim$2 kpc, from the center of the spheroidal Galaxy NGC 4993 at 40 Mpc (Blanchard et al., 2017; Im et al., 2017; Levan et al., 2017; Pan et al., 2017; Tanvir et al., 2017).

Rapid follow-up of the gravitational wave and GRB signal in X-rays did not show any source comparable to, or brighter than, a typical afterglow of a short GRB. Since both the gravitational data and the faintness of the prompt GRB emission suggested a jet viewed significantly off axis, this could be expected, as the afterglows from misaligned GRB jets have longer rise times than those of jets observed at small viewing angles (Van Eerten and MacFadyen, 2011). Therefore, X-ray monitoring with *Swift*/XRT, *Chandra,* and *Nustar* continued, and $\sim$10 days after merger led to the detection with *Chandra* of a faint source ($L_X \simeq 10^{40}$ erg s^{-1}) (Evans et al., 2017; Margutti et al., 2017; Troja et al., 2017), whose intensity continued to rise up to $\sim$100 days (D'Avanzo et al., 2018; Troja et al., 2020). Similarly, observations of cm and mm wavelengths at various arrays, including VLA and ALMA, failed to detect the source before $\sim$16 days after the gravitational signal, which was interpreted as evidence that a jetted source accompanying the binary neutron star merger must be directed at a significant angle ($\geq$20°) with respect to the line of sight (Alexander et al., 2017; Andreoni et al., 2017; Hallinan et al., 2017; Kim et al., 2017; Pozanenko et al., 2018).

The *Fermi* Large Area Telescope covered the sky region of GW170817 starting only 20 min after the merger and did not detect any emission in the energy range 0.1–1 GeV to a limiting flux of 4.5×10^{-10} erg s^{-1} cm^{-2} in the interval 1,153–2027 s after the merger (Ajello et al., 2018). Follow-up observation with the atmospheric Cherenkov experiment H.E.S.S. (0.3–8 TeV) from a few hours to $\sim$5 days after merger returned no detection to a limit of a few 10^{-12} erg s^{-1} cm^{-2} (Abdalla et al., 2017). A summary of the results of the multiwavelength observing campaign within the first month of gravitational wave signal detection is reported in Abbott et al. (2017c).

While the radio and X-ray detections are attributed to the afterglow of the short GRB, the ultraviolet, optical, and near-infrared data are dominated by the kilonova at early epochs (with a possible contribution at $\lesssim$ 4 days at blue wavelengths from cooling of shock-heated material around the neutron star merger, Piro and Kollmeier, 2018) and later on by the afterglow, as described in the next two sections.

3.1.1 The Gamma-Ray Burst and Its Multiwavelength Afterglow

The short GRB170817A, with an energy output of $\sim 10^{46}$ erg, was orders of magnitude dimmer than most short GRBs (Berger, 2014). Together with a viewing angle of $\sim$30 deg estimated from the gravitational wave signal (Abbott et al., 2017a), this led to the hypothesis that the GRB was produced by a relativistic jet viewed at a comparable angle. However, the early light curve of the radio afterglow is not consistent with the behavior predicted for an off-axis collimated jet and rather suggests a quasispherical geometry, possibly with two components, a more collimated one and a nearly isotropic and mildly relativistic one, which is responsible also for producing the gamma-rays (Mooley et al., 2018a). This confirms numerous predictions whereby the shocked cloud surrounding a binary neutron star merger forms a mildly relativistic cocoon that carries an energy comparable to that of the jet and is responsible for the prompt emission and the early multiwavelength afterglow (Lazzati et al., 2017a; Lazzati et al., 2017b; Nakar and Piran, 2017; Bromberg et al., 2018; Xie et al., 2018) and is supported by detailed numerical simulations (Gottlieb et al., 2018; Lazzati et al., 2018).

Using milliarcsecond resolution radio VLBI observations at 75 and 230 days, Mooley et al. (2018b) detected superluminal motion with $\beta = 3 - 5$, while Ghirlanda et al. (2019) determined that, at 207 days, the source is still angularly smaller than two milliarcseconds at the 90% confidence, which excludes that a nearly isotropic, mildly relativistic outflow is responsible for the radio emission, as in this case the source apparent size, after more than six months of expansion, should be significantly larger and resolved by the VLBI observation. These observations point to a structured jet as the source of GRB170817A, with a narrow opening angle ($\theta_{op} \simeq 3.4$ degrees) and an energetic core ($\sim 3 \times 10^{52}$ erg) seen under a viewing angle of $\sim$15° (Ghirlanda et al., 2019). This is further confirmed by later

radio observations, extending up to 300 days after merger, that show a sharp downturn of the radio light curve, suggestive of a jet rather than a spherical source (Mooley et al., 2018c).

The optical/near-infrared kilonova component subsided rapidly (see **Section 3.1.2**) leaving room to the afterglow emission: the HST observations at ~100 days after the explosion show a much brighter source than inferred from the extrapolation of the early kilonova curve to that epoch (Lyman et al., 2018). This late-epoch flux is thus not consistent with kilonova emission and is rather due to the afterglow produced within an off-axis structured jet (Fong et al., 2019). At X-ray energies, the GRB counterpart is still detected with *Chandra* three years after explosion (Troja et al., 2020), but its decay is not fully compatible with a structured jet, indicating that the physical conditions have changed or that an extra component is possibly emerging (e.g., a nonthermal aftermath of the kilonova ejecta; see next section).

3.1.2 The Kilonova

The early ground-based optical and near-infrared and space-based (with *Swift*/UVOT) near-ultraviolet follow-up observations started immediately after identification of the optical counterpart of GW170817, detecting a rapid rise (~1 day timescale, Arcavi et al., 2017) and wavelength-dependent time decay, quicker at shorter wavelengths (Andreoni et al., 2017; Cowperthwaite et al., 2017; Díaz et al., 2017; Drout et al., 2017; Evans et al., 2017; McCully et al., 2017; Nicholl et al., 2017; Tanvir et al., 2017; Utsumi et al., 2017; Villar et al., 2017). The optical light is polarized at the very low level of (0.50 ± 0.07)% at 1.46 days, consistent with intrinsically unpolarized emission scattered by Galactic dust, indicating that no significant alignment effect in the emission or geometric preferential direction is present in the source at this epoch, consistent with expectation for kilonova emission (Covino et al., 2017).

Starting the same night when the optical counterpart was detected, low resolution spectroscopy was carried out at the Magellan telescope (Shappee et al., 2017). This spectrum shows that the source is not yet transparent as it is emitting black body radiation, whose maximum lies however blueward of the sampled wavelength range, suggesting that the initial temperature may have been larger than ~10,000 K. The following night (1.5 days after merger) the spectrum is still described by an almost perfect black body law whose maximum at ~5000 K was fully resolved by spectroscopy at the Very Large Telescope (VLT) with the X-Shooter spectrograph over the wavelength range 3,500–24,000 Å (Pian et al., 2017). At this epoch, the expansion velocity of the expelled ejecta, whose total mass was estimated to be 0.02–0.05 $M_\odot$ (Pian et al., 2017; Smartt et al., 2017; Waxman et al., 2018), was ~20% of the light speed, which is only mildly relativistic and therefore much less extreme than the ultrarelativistic kinematic regime of the GRB and of its early afterglow, analogous to the observed difference between the afterglows and the supernovae accompanying long GRBs. At 2.5 days after merger, the spectrum starts deviating from a black body as the ejecta become increasingly transparent and absorption lines are being imprinted on the spectral continuum by the atomic species present in the ejecta (Chornock et al., 2017; Pian et al., 2017; Smartt et al., 2017). In the following days these features become prominent and they evolve as the ejecta decelerate and the photosphere recedes (**Figure 1**).

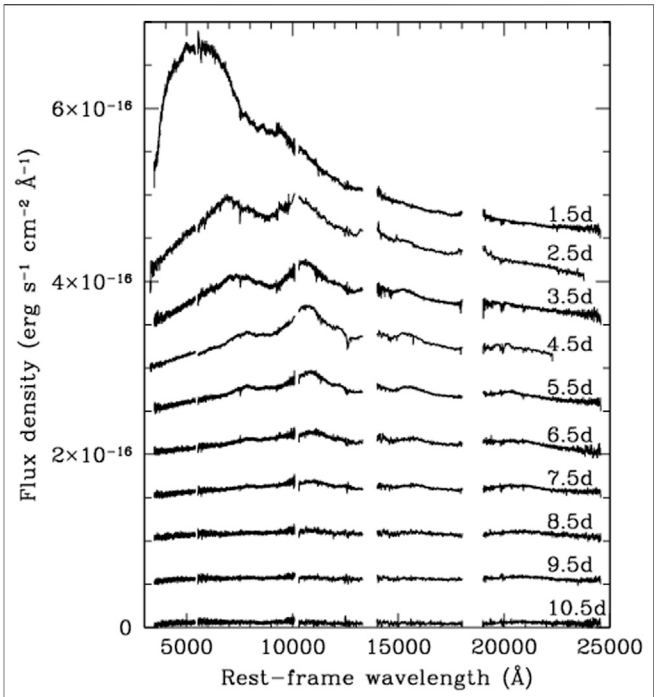

FIGURE 1 | ESO VLT X-Shooter spectra of the counterpart of GW170817 from Pian et al. (2017) and Smartt et al. (2017), at phases indicated in days after merger time, corrected for Galactic extinction E (B-V) = 0.1 mag, deredshifted, and offset in flux by multiples of a 5×10^{-17} erg s^{-1} cm^{-2} $Å^{-1}$ additive constant with respect to the 10.5-day spectrum. Wavelength ranges of poor atmospheric transmission were blanked out. The spectra of the 19th (2.5 days) and the 21st (4.5 days) of August 2017 have been recalibrated with respect to the originally published version, courtesy of J. Gillanders, J. Selsing, and S. Smartt.

In particular, in the spectrum at day 1.5 an absorption feature extending from ~7,000 to ~8,100 Å is detected, so that Smartt et al. (2017) preliminarily identified atomic transitions occurring in neutral Cs and Te, broadened and blueshifted by ~0.2*c*, consistent with the expansion velocity of the photosphere. In the second spectrum (2.5 days) the Cs I and Te I lines are still detected at somewhat larger wavelengths, compatibly with a reduced photospheric expansion speed. These lines were however later disproved on account of the fact that, at the temperature of the ejecta immediately below the photosphere (~3700 K), numerous transitions of other lanthanide elements of higher ionization potential should be observed besides Cs and Te, but are not (Watson et al., 2019). Watson et al. (2019) reanalyzed the absorption feature observed at 7,000–8,100 Å and an absorption feature at ~3,500 Å with the aid of local thermodynamic equilibrium models with abundances from a solar-scaled r-process and from metal-poor stars and determined that the absorption features can be identified with Sr II. In the spectra at the successive epochs the line at the longer wavelength is still detected and develops a P Cygni profile.

Strontium is a very abundant element and is produced close to the first r-process peak. Its possible detection makes it important to consider lighter r-process elements in addition to the lanthanides in shaping the kilonova emission spectrum (Watson et al., 2019).

At ∼10 days after merger, the kilonova spectrum fades out of the reach of the largest telescopes. The radioactive source could still be monitored photometrically for another week in optical and near-infrared (Cowperthwaite et al., 2017; Drout et al., 2017; Kasliwal et al., 2017; Pian et al., 2017; Smartt et al., 2017; Tanvir et al., 2017); it was last detected at 4.5 μm with the *Spitzer* satellite 74 days after merger (Villar et al., 2018). The kilonova ejecta are also expected to interact with the circum-binary medium and produce low-level radio and X-ray emission that peaks years after the merger (Kathirgamaraju et al., 2019). The search for this component has not returned (yet) a detection at radio wavelengths (Hajela et al., 2019), but it may start to be revealed at X-rays (Troja et al., 2020).

3.1.3 The Host Galaxy of GW170817

HST and *Chandra* images, combined with VLT MUSE integral field spectroscopy of the optical counterpart of GW170817, show that its host Galaxy, NGC 4993, is a lenticular (S0) Galaxy at z = 0.009783 that has undergone a recent (∼1 Gyr) galactic merger (Levan et al., 2017; Palmese et al., 2017). This merger may be responsible for igniting weak nuclear activity. No globular or young stellar cluster is detected at the location of GW170817, with a limit of a few thousand solar masses for any young system. The population in the vicinity is predominantly old and the extinction from local interstellar medium is low. Based on these data, the distance of NGC4993 was determined to be 41.0 ± 3.1 Mpc (Hjorth et al., 2017). The HST imaging made it also possible to establish the distance of NGC4993 through the surface brightness fluctuation method with an uncertainty of ∼ 6% (40.7 ± 1.4 ± 1.9 Mpc, random and systematic errors, respectively), making it the most precise distance measurement for this Galaxy (Cantiello et al., 2018). Combining this with the recession velocity measured from optical spectroscopy of the Galaxy, corrected for peculiar motions, returns a Hubble constant $H_0 = 71.9 \pm 7.1$ km s^{-1} Mpc^{-1}.

Based only on the gravitational data and the standard siren argument and assuming that the optical counterpart represents the true sky location of the gravitational-wave source instead of marginalizing over a range of potential sky locations, Abbott et al. (2017d) determined a "gravitational" distance of $43.8^{+2.9}_{-6.9}$ Mpc that is refined with respect to the one previously reported in Abbott et al. (2017a). Together with the corrected recession velocity of NGC4993, this yields a Hubble constant $H_0 = 70^{+12}_{-8}$ km s^{-1} Mpc^{-1}, comparable to, but less precise than, that obtained from the superluminal motion of the radio counterpart core, $H_0 = 70.3^{+5.3}_{-5.0}$ km s^{-1} Mpc^{-1} (Hotokezaka et al., 2019).

4 KILONOVA LIGHT CURVE AND SPECTRUM

The unstable isotopes formed during coalescence of a binary neutron star system decay radioactively and the emitted gamma-ray photons are downscattered to the ultraviolet, optical, and infrared thermal radiation that constitutes the kilonova source (**Section 3.1.2**). Its time decline is determined by the convolution of radioactive decay chain curves of all present unstable nuclei. This is analogous to the supernova phenomenon, where however the vastly dominant radioactive chain is ^{56}Ni decaying into ^{56}Co. and then into ^{56}Fe.

While radioactive nuclei decay, atoms recombine, as the source is cooling, and absorption features are imprinted in the kilonova spectra. Among neutron-rich nuclei, the lanthanides (atomic numbers 57–71) series have full f-shells and therefore numerous atomic transitions that suppress the spectrum at shorter wavelengths ($\lesssim$ 8,000 Å). Spectra of dynamical ejecta of kilonova may therefore be heavily intrinsically reddened, depending on the relative abundance of lanthanides (Barnes and Kasen, 2013; Kasen et al., 2013; Tanaka and Hotokezaka, 2013). Prior to the clear detection of kilonova accompanying GW170817 (**Section 3**), such a source may have been detected in HST images in near-infrared H band of the afterglow of GRB130603B (Berger et al., 2013; Tanvir et al., 2013). Successive claims for association with short GRBs and kilonova radiation were similarly uncertain (Jin et al., 2015; Jin et al., 2016).

If the neutron stars coalescence does not produce instantaneously a black hole and a hypermassive neutron star is formed as a transitory remnant, a neutrino wind is emitted that may inhibit the formation of neutrons and reduce the amount of neutron-rich elements (Fernández and Metzger, 2013; Kajino et al., 2014; Kiuchi et al., 2014; Metzger and Fernández, 2014; Perego et al., 2014; Kasen et al., 2015; Lippuner et al., 2017). This "postmerger" kilonova component, of preferentially polar direction, is thus relatively poor in lanthanides and gives rise to a less reddened spectrum (Kasen et al., 2017; Tanaka et al., 2017).

The optical/near-infrared spectral behavior of kilonova is analogous to that of supernovae with the largest kinetic energies (>10^{52} erg), like those associated with GRBs: the large photospheric velocities broaden the absorption lines and blueshift them in the direction of the observer. Furthermore, broadening causes the lines to blend, which makes it difficult to isolate and identify individual atomic species (Iwamoto et al., 1998; Mazzali et al., 2000; Nakamura et al., 2001). While these effects can be controlled and deconvolved with the aid of a radiation transport model as it has been done for supernovae of all types (Mazzali et al., 2016; Hoeflich et al., 2017; Ergon et al., 2018; Hillier and Dessart, 2019; Ashall and Mazzali, 2020; Shingles et al., 2020), a more fundamental hurdle in modeling kilonova spectra consists in the much larger number of electronic transitions occurring in r-process element atoms than in the lighter ones that populate supernova ejecta, and in our extremely limited knowledge of individual atomic opacities of these neutron-rich elements, owing to the lack of suitable atomic data. First systematic atomic structure calculations for lanthanides and for all r-process elements were presented by Fontes et al. (2020) and Tanaka et al. (2020), respectively.

5 SUMMARY AND FUTURE PROSPECTS

The gravitational and electromagnetic event of August 17, 2017, provided the long-awaited confirmation that binary neutron star

mergers are responsible for well identifiable gravitational signals at kHz frequencies, for short GRBs, and for thermal sources, a. k.a. kilonovae or macronovae, produced by the radioactive decay of unstable heavy elements synthesized via r-process during the coalescence. The intensive and long-term electromagnetic monitoring from ground and space allowed clear detection of the counterpart at all wavelengths. Brief (~2 s) gamma-ray emission, peaking at ~200 keV and lagging the gravitational signal by 1.7 s, is consistent with a weak short GRB. At ultraviolet-to-near-infrared wavelengths, the kilonova component—never before detected to this level of accuracy and robustness—dominates during the first 10 days and decays rapidly under detection threshold thereafter, while an afterglow component emerges around day ~100. Up to the most recent epochs of observation (day ~1,000 at X-rays), the kilonova does not add significantly to the bright radio and X-ray afterglow component. Multiepoch VLBI observations measured—for the first time in a GRB—superluminal motion of the radio source, thus providing evidence of late-epoch emergence of a collimated off-axis relativistic jet.

Doubtlessly, this series of breakthroughs were made possible by the closeness of the source (40 Mpc), almost unprecedented for GRBs, and by the availability of first-class ground-based and space-borne instruments. The many findings and exceptional new physical insight afforded by GW170817/GRB170817A make it a *rosetta stone* for future similar events. When a sizable group of sources with good gravitational and electromagnetic detections will be available, the properties of binary systems containing at least one neutron star, of their mergers and their aftermaths, can be mapped. It will then become possible to clarify how the dynamically ejected mass depends on the binary system parameters, mass asymmetry, and neutron stars equation of state (Ruffert and Janka, 2001; Hotokezaka et al., 2013), how the jet forms and evolves, which kinematic regimes and geometry it takes up in time, and how the GRB and afterglow observed phenomenologies can help distinguish the intrinsic properties from viewing angle effects (Janka et al., 2006; Lamb and Kobayashi, 2018; Ioka and Nakamura, 2019), what the detailed chemical content of kilonova ejecta is and how the r-process abundance pattern inferred from kilonova spectra compares with the history of heavy elements cosmic enrichment (Rosswog et al., 2018), how kilonovae can help constrain the binary neutron star rates and how the parent population of short GRBs evolves (Guetta and Stella, 2009; Yang et al., 2017; Belczynski et al., 2018; Artale et al., 2019; Matsumoto and Piran, 2020), and how gravitational and electromagnetic data can be used jointly to determine the cosmological parameters (Schutz, 1986; Del Pozzo, 2012; Abbott et al., 2017d), to mention only some fundamental open problems. Comparison of the optical and near-infrared light curves of GW170817 kilonova with those of short GRBs with known redshift suggests infact significant diversity in the kilonova component luminosities (Gompertz et al., 2018; Rossi et al., 2020).

Regrettably, short GRBs viewed at random angles, and not pole on, are relativistically beamed away from the observer direction and kilonovae are intrinsically weak. These circumstances make electromagnetic detections very difficult if the sources lie at more than ~100 Mpc, as proven during the third and latest observing run (Apr 2019–Mar 2020) of the gravitational interferometers network. In this observing period, two merger events possibly involving neutron stars were reported by the LIGO-Virgo consortium: GW190425, caused by the coalescence of two compact objects of masses each in the range 1.12–2.52 $M_\odot$, at ~160 Mpc (Abbott et al., 2020a), and GW190814, caused by a 23 $M_\odot$ black hole merging with a compact object of 2.6 $M_\odot$ at ~240 Mpc (Abbott et al., 2020b). In neither case did the search for an optical or infrared counterpart return a positive result (Coughlin et al., 2019; Gomez et al., 2019; Ackley et al., 2020; Andreoni et al., 2020; Antier et al., 2020; Kasliwal, 2020), owing presumably to the large distance and sky error areas, although a short GRB may have been detected by the *INTEGRAL* SPI-ACS simultaneously with GW190425 (Pozanenko et al., 2019). Note that all coalescing stars may have been black holes, as the neutron star nature of the binary members lighter than 3 $M_\odot$ could not be confirmed.

The search for electromagnetic counterparts of gravitational radiation signals is currently thwarted primarily by the large uncertainty of their localization in the sky, which is usually no more accurate than several dozens of square degrees. Much smaller error boxes are expected to be available when the KAGRA (which had already joined LIGO-Virgo in the last months of the 2019–2020 observing run) and the INDIGO interferometers will operate at full regime as part of the network during the next observing run (Abbott et al., 2018). Observing modes, strategies, and simulations are being implemented to optimize the electromagnetic multiwavelength search and follow-up (Bartos et al., 2016; Patricelli et al., 2018; Cowperthwaite et al., 2019; Graham et al., 2019; Artale et al., 2020), and new dedicated space-based facilities are designed with critical capabilities of large sky area coverage and rapid turnaround (e.g., *ULTRASAT*, Sagiv et al., 2014; *THESEUS*, Amati et al., 2018, Stratta et al., 2018; *DORADO*, Cenko, 2019), to maximize the chance of detection of dim, fast-declining transients.

Finally, the possible detection of elusive MeV and >GeV neutrinos associated with the kilonova (Kyutoku and Kashiyama, 2018) and with the GRB (Bartos et al., 2019; Aartsen et al., 2020), respectively, will bring an extra carrier of information into play and thus complete the multimessenger picture associated with the binary neutron star merger phenomenon. Gravitational waves from binary neutron star inspirals and mergers; gamma-ray photons—downscattered to UV/optical/infrared light—from radioactive decay of unstable nuclides of heavy elements, freshly formed after the merger; multiwavelength photons from nonthermal mechanisms in the relativistic jet powered by the merger remnant; and thermal and high-energy neutrinos accompanying the remnant cooling and hadronic processes in the jet, respectively, all collectively underpin the role of the four physical interactions. This fundamental role of compact star merger phenomenology thus points to the formidable opportunity offered by a multimessenger approach: bringing the communities of astrophysicists and nuclear physicists closer will foster that cross-fertilization and interdisciplinary coordination that is not only beneficial but also essential for progress in this field.

AUTHOR CONTRIBUTIONS

The author confirms being the sole contributor of this work and has approved it for publication.

ACKNOWLEDGMENTS

The author is indebted to T. Belloni, S. Cristallo, Th. Janka, P. Mazzali, A. Possenti, M. Tanaka, and F. Thielemann for discussion. She acknowledges hospitality from Liverpool John Moores University, Weizmann Institute of Science, Rehovot, and the Hebrew University of Jerusalem, Israel; National Astronomical Observatory of Japan, Tokyo; Beihang University, Beijing; Yunnan National Astronomical Observatory, Kunming, China; and Max-Planck Institute for Astrophysics and Munich Institute for Astro- and Particle Physics, Garching, Germany, where part of this work was accomplished.

REFERENCES

Aartsen, M. G., Ackermann, M., Adams, J., Aguilar, J. A., Ahlers, M., Ahrens, M., et al. (2020). IceCube search for neutrinos coincident with compact binary mergers from LIGO-virgo's first gravitational-wave transient catalog. *Astrophys. J.* 898, L10. doi:10.3847/2041-8213/ab9d24

Abbott, B. P., Abbott, R., Abbott, T. D., Abernathy, M. R., Acernese, F., Ackley, K., et al. (2016). Properties of the binary black hole merger GW150914. *Phys. Rev. Lett.* 116, 241102. doi:10.1103/PhysRevLett.116.241102

Abbott, B. P., Abbott, R., Abbott, T. D., Acernese, F., Ackley, K., Adams, C., et al. (2017a). GW170817: observation of gravitational waves from a binary neutron star inspiral. *Phys. Rev. Lett.* 119, 161101. doi:10.1103/PhysRevLett.119.161101

Abbott, B. P., Abbott, R., Abbott, T. D., Acernese, F., Ackley, K., Adams, C., et al. (2017b). Gravitational waves and gamma-rays from a binary neutron star merger: GW170817 and GRB 170817A. *Astrophys. J.* 848, L13. doi:10.3847/2041-8213/aa920c

Abbott, B. P., Abbott, R., Abbott, T. D., Acernese, F., Ackley, K., Adams, C., et al. (2017c). Multi-messenger observations of a binary neutron star merger. *Astrophys. J.* 848, L12. doi:10.3847/2041-8213/aa91c9

Abbott, B. P., Abbott, R., Abbott, T. D., Acernese, F., Ackley, K., Adams, C., et al. (2017d). A gravitational-wave standard siren measurement of the Hubble constant. *Nature* 551, 85. doi:10.1038/nature24471

Abbott, B. P., Abbott, R., Abbott, T. D., Acernese, F., Ackley, K., Adams, C., et al. (2017e). Search for post-merger gravitational waves from the remnant of the binary neutron star merger GW170817. *Astrophys. J.* 851, L16. doi:10.3847/2041-8213/aa9a35

Abbott, B. P., Abbott, R., Abbott, T. D., Abernathy, M. R., Acernese, F., Ackley, K., et al. (2018). Prospects for observing and localizing gravitational-wave transients with Advanced LIGO, Advanced Virgo and KAGRA. *Living Rev. Relat.* 21, 3. doi:10.1007/s41114-018-0012-9

Abbott, B. P., Abbott, R., Abbott, T. D., Abraham, S., Acernese, F., Ackley, K., et al. (2019). GWTC-1: a gravitational-wave transient catalog of compact binary mergers observed by LIGO and Virgo during the first and second observing runs. *Phys. Rev. X* 9, 031040. doi:10.1103/PhysRevX.9.031040

Abbott, B. P., Abbott, R., Abbott, T. D., Abraham, S., Acernese, F., Ackley, K., et al. (2020a). Observation of a compact binary coalescence with total mass ~ 3.4 $M_{\odot}$. *Astrophys. J.* 892, L3. doi:10.3847/2041-8213/ab75f5

Abbott, B. P., Abbott, T. D., Abraham, S., Acernese, F., Ackley, K., Adams, C., et al. (2020b). GW190814: gravitational waves from the coalescence of a 23 solar mass black hole with a 2.6 solar mass compact object. *Astrophys. J.* 896, L44. doi:10.3847/2041-8213/ab960f

Abdalla, H., Abramowski, A., Aharonian, F., Ait Benkhali, F., Angüner, E. O., Arakawa, M., et al. (2017). TeV gamma-ray observations of the binary neutron star merger GW170817 with H. E.S.S.. *Astrophys. J.* 850, L22. doi:10.3847/2041-8213/aa97d2

Abe, K., Bronner, C., Hayato, Y., Ikeda, M., Iyogi, K., and Kameda, J. (2018). Search for neutrinos in super-kamiokande associated with the GW170817 neutron-star merger. *Astrophys. J.* 857, L4. doi:10.3847/2041-8213/aabaca

Ackley, K., Amati, L., Barbieri, C., Bauer, F. E., Benetti, S., and Bernardini, M. G., (Forthcoming 2020). Observational constraints on the optical and near-infrared emission from the neutron star-black hole binary merger S190814bv. *Astr. Astrophys* Available at: https://arxiv.org/abs/2002.01950 (Accessed February 5, 2020).

Ajello, M., Allafort, A., Axelsson, M., Baldini, L., Barbiellini, G., Baring, M. G., et al. (2018). Fermi-LAT observations of LIGO/Virgo event GW170817. *Astrophys. J.* 861, 85. doi:10.3847/1538-4357/aac515

Albert, A., Andre, M., Anghinolfi, M., Ardid, M., Aubert, J.-J., Aublin, J., et al. (2017). Search for high-energy neutrinos from binary neutron star merger GW170817 with ANTARES, IceCube, and the Pierre auger observatory. *Astrophys. J.* 850, L35. doi:10.3847/2041-8213/aa9aed

Alexander, K. D., Berger, E., Fong, W., Williams, P. K. G., Guidorzi, C., Margutti, R., et al. (2017). The electromagnetic counterpart of the binary neutron star merger LIGO/Virgo GW170817. VI. Radio constraints on a relativistic jet and predictions for late-time emission from the kilonova ejecta. *Astrophys. J.* 848, L21. doi:10.3847/2041-8213/aa905d

Amati, L., O'Brien, P., Götz, D., Bozzo, E., Tenzer, C., Frontera, F., et al. (2018). The THESEUS space mission concept: science case, design and expected performances. *Adv. Space Res.* 62, 191. doi:10.1016/j.asr.2018.03.010

Andreoni, I., Ackley, K., Cooke, J., Acharyya, A., Allison, J. R., Anderson, G. E., et al. (2017). Follow up of GW170817 and its electromagnetic counterpart by Australian-led observing programmes. *Pub. Astron. Soc. Au.* 34, 69. doi:10.1017/pasa.2017.65

Andreoni, I., Goldstein, D. A., Kasliwal, M. M., Nugent, P. E., Zhou, R., Newman, J. A., et al. (2020). GROWTH on S190814bv: deep synoptic limits on the optical/near-infrared counterpart to a neutron star-black hole merger. *Astrophys. J.* 890, 131. doi:10.3847/1538-4357/ab6a1b

Annala, E., Gorda, T., Kurkela, A., and Vuorinen, A. (2018). Gravitational-wave constraints on the neutron-star-matter equation of state. *Phys. Rev. Lett.* 120, 172703. doi:10.1103/PhysRevLett.120.172703

Antier, S., Agayeva, S., Almualla, M., Awiphan, S., Baransky, K., Barynova, S., et al. (2020). GRANDMA observations of advanced LIGO's and advanced Virgo's third observational campaign. *Mon. Not. Roy. Astron. Soc.* 497, 5518. doi:10.1093/mnras/staa1846

Antonelli, L. A., D'Avanzo, P., Perna, R., Amati, L., Covino, S., Cutini, S., et al. (2009). Grb 090426: the farthest short gamma-ray burst? *Astron. Astrophys.* 507, L45. doi:10.1051/0004-6361/200913062

Arcavi, I., Hosseinzadeh, G., Andrew Howell, D., McCully, C., Poznanski, D., Kasen, D., et al. (2017). Optical emission from a kilonova following a gravitational-wave-detected neutron-star merger. *Nature* 551, 64. doi:10.1038/nature24291

Artale, M. C., Michela, M., Nicola, G., Sabha, N. B., Mario, S., Santoliquido, F., et al. (2019). Host galaxies of merging compact objects: mass, star formation rate, metallicity, and colours. *Mon. Not. Roy. Astron. Soc.* 487, 1675. doi:10.1093/mnras/stz1382

Artale, M. C., Bouffanais, Y., Mapelli, M., Giacobbo, N., Sabha, N. B., Santoliquido, F., et al. (2020). An astrophysically motivated ranking criterion for low-latency electromagnetic follow-up of gravitational wave events. *Mon. Not. Roy. Astron. Soc.* 495, 1841. doi:10.1093/mnras/staa1252

Ashall, C., and Mazzali, P. (2020). Extracting high-level information from gamma-ray burst supernova spectra. *Mon. Not. Roy. Astron. Soc.* 492, 5956. doi:10.1093/mnras/staa212

Banerjee, P., Haxton, W. C., and Qian, Y.-Z. (2011). Long, cold, early r process? Neutrino-Induced nucleosynthesis in He shells revisited. *Phys. Rev. Lett.* 106, 201104. doi:10.1103/PhysRevLett.106.201104

Barnes, J., and Kasen, D. (2013). Effect of a high opacity on the light curves of radioactively powered transients from compact. object mergers. *Astrophys. J.* 775, 18. doi:10.1088/0004-637X/775/1/18

Bartos, I., Huard, T. L., and Márka, S. (2016). James webb space telescope can detect kilonovae in gravitational wave follow-up search. *Astrophys. J.* 816, 61. doi:10.3847/0004-637X/816/2/61

Bartos, I., Veske, D., Keivani, A., Marka, Z., Countryman, S., Blaufuss, E., et al. (2019). Bayesian multimessenger search method for common sources of gravitational waves and high-energy neutrinos. *Phys. Rev. D* 100, 083017. doi:10.1103/PhysRevD.100.083017

Bauswein, A., Just, O., Janka, H.-J., and Stergioulas, N. (2017). Neutron-star radius constraints from GW170817 and future detections. *Astrophys. J.* 850, L34. doi:10.3847/2041-8213/aa9994

Belczynski, K., Askar, A., Arca-Sedda, M., Chruslinska, M., Donnari, M., Giersz, M., et al. (2018). The origin of the first neutron star - neutron star merger. *Astron. Astrophys.* 615, A91. doi:10.1051/0004-6361/201732428

Beniamini, P., Duran, R. B., Petropoulou, M., and Giannios, D. (2020). Ready, set, launch: time interval between a binary neutron star merger and short gamma-ray burst jet formation. *Astrophys. J.* 895, L33. doi:10.3847/2041-8213/ab9223

Berger, E., Fong, W., and Chornock, R. (2013). An r-process kilonova associated with the short-hard GRB 130603B. *Astrophys. J.* 774, L23. doi:10.1088/2041-8205/774/2/L23

Berger, E. (2014). Short-duration gamma-ray bursts. *Annu. Rev. Astron. Astrophys.* 52, 43. doi:10.1146/annurev-astro-081913-035926

Blanchard, P. K., Berger, E., Fong, W., Nicholl, M., Leja, J., Conroy, C., et al. (2017). The electromagnetic counterpart of the binary neutron star merger LIGO/Virgo GW170817. VII. Properties of the host galaxy and constraints on the merger timescale. *Astrophys. J.* 848, L22. doi:10.3847/2041-8213/aa9055

Blanchet, L. (2014). Gravitational radiation from post-Newtonian sources and inspiralling compact binaries. *Living Rev. Relat.* 17, 2. doi:10.12942/lrr-2014-2

Blinnikov, S. I., Novikov, I. D., Perevodchikova, T. V., and Polnarev, A. G. (1984). Exploding neutron stars in close binaries. *Sov. Astron. Lett.* 10, 177.

Bromberg, O., Nakar, E., Piran, T., and Sari, R. (2018). The γ-rays that accompanied GW170817 and the observational signature of a magnetic jet breaking out of NS merger ejecta. *Mon. Not. Roy. Astron. Soc.* 475, 2971. doi:10.1093/mnras/stx3316

Bromberg, O., Nakar, E., Piran, T., and Sari, R. (2013). Short versus long and collapsars versus non-collapsars: a quantitative classification of gamma-ray bursts. *Astrophys. J.* 764, 179. doi:10.1088/0004-637X/764/2/179

Burbidge, E. M., Burbidge, G. R., Fowler, W. A., and Hoyle, F. (1957). Synthesis of the elements in stars. *Rev. Mod. Phys.* 29, 547. doi:10.1103/RevModPhys.29.547

Burgay, M., D'Amico, N., Possenti, A., Manchester, R. N., Lyne, A. G., and Joshi, B. C. (2003). An increased estimate of the merger rate of double neutron stars from observations of a highly relativistic system. *Nature*. 426, 531. doi:10.1038/nature02124

Burgio, G. F., Drago, A., Pagliara, G., Schulze, H.-J., and Wei, J.-B. (2018). Are small radii of compact stars ruled out by GW170817/AT2017gfo?. *Astrophys. J.* 860, 139. doi:10.3847/1538-4357/aac6ee

Burns, E., Connaughton, V., Zhang, B.-B., Lien, A., Briggs, M. S., Goldstein, A., et al. (2016). Do the Fermi gamma-ray burst monitor and Swift burst alert telescope see the same short gamma-ray bursts?. *Astrophys. J.* 818, 110. doi:10.3847/0004-637X/818/2/110

Busso, M., Gallino, R., and Wasserburg, G. J. (1999). Nucleosynthesis in asymptotic giant branch stars: relevance for galactic enrichment and solar system formation. *Annu. Rev. Astron. Astrophys.* 37, 239. doi:10.1146/annurev.astro.37.1.239

Cantiello, M., Jensen, J. B., Blakeslee, J. P., Berger, E., Levan, A. J., Tanvir, N. R., et al. (2018). A precise distance to the host galaxy of the binary neutron star merger GW170817 using surface brightness fluctuations. *Astrophys. J.* 854, L31. doi:10.3847/2041-8213/aaad64

Cenko, S. B. (2019). The gravitational-wave ultraviolet counterpart imager (GUCI) network. *American Astronomical Society Meeting Abstracts* 234, 212.

Chornock, R., Berger, E., Kasen, D., Cowperthwaite, P. S., Nicholl, M., Villar, V. A., et al. (2017). The electromagnetic counterpart of the binary neutron star merger LIGO/Virgo GW170817. IV. Detection of near-infrared signatures of r-process nucleosynthesis with gemini-south. *Astrophys. J.* 848, L19. doi:10.3847/2041-8213/aa905c

Chruslinska, M., Belczynski, K., Klencki, J., and Benacquista, M. (2018). Double neutron stars: merger rates revisited. *Mon. Not. Roy. Astron. Soc.* 474, 2937. doi:10.1093/mnras/stx2923

Côté, B., Fryer, C. L., Belczynski, K., Korobkin, O., Chruślińska, M., Vassh, N., et al. (2018). The origin of r-process elements in the milky way. *Astrophys. J.* 855, 99. doi:10.3847/1538-4357/aaad67

Côté, B., Eichler, M., Arcones, A., Hansen, C. J., Simonetti, P., Frebel, A., et al. (2019). Neutron star mergers might not Be the only source of r-process elements in the milky way. *Astrophys. J.* 875, 106. doi:10.3847/1538-4357/ab10db

Coughlin, M. W., Ahumada, T., Anand, S., De, K., Hankins, M. J., Kasliwal, M. M., et al. (2019). GROWTH on S190425z: searching thousands of square degrees to identify an optical or infrared counterpart to a binary neutron star merger with the zwicky transient facility and palomar gattini-IR. *Astrophys. J.* 885, L19. doi:10.3847/2041-8213/ab4ad8

Coulter, D. A., Foley, R. J., Kilpatrick, C. D., Drout, M. R., Piro, A. L., Shappee, B. J., et al. (2017). Swope Supernova Survey 2017a (SSS17a), the optical counterpart to a gravitational wave source. *Science* 358, 1556. doi:10.1126/science.aap9811

Covino, S., Wiersema, K., Fan, Y. Z., Toma, K., Higgins, A. B., Melandri, A., et al. (2017). The unpolarized macronova associated with the gravitational wave event GW 170817. *Nature Astr* 1, 791. doi:10.1038/s41550-017-0285-z

Cowan, J. J., Sneden, C., Lawler, J. E., Aprahamian, A., Weischer, M., Langanke, M., et al. (Forthcoming 2020). Origin of the heaviest elements: the rapid neutron-capture process. *Rev. Mod. Phys* Available at: https://arxiv.org/abs/1901.01410 (Accessed January 5, 2020).

Cowperthwaite, P. S., Berger, E., Villar, V. A., Metzger, B. D., Nicholl, M., Chornock, R., et al. (2017). The electromagnetic counterpart of the binary neutron star merger LIGO/Virgo GW170817. II. UV, optical, and near-infrared light curves and comparison to kilonova models. *Astrophys. J.* 848, L17. doi:10.3847/2041-8213/aa8fc7

Cowperthwaite, P. S., Villar, V. A., Scolnic, D. M., and Berger, E. (2019). LSST target-of-opportunity observations of gravitational-wave events: essential and efficient. *Astrophys. J.* 874, 88. doi:10.3847/1538-4357/ab07b6

D'Avanzo, P., Campana, S., Salafia, O. S., Ghirlanda, G., Ghisellini, G., Melandri, A., et al. (2018). The evolution of the X-ray afterglow emission of GW 170817/GRB 170817A in XMM-Newton observations. *Astron. Astrophys.* 613, L1. doi:10.1051/0004-6361/201832664

Davies, M. B., Benz, W., Piran, T., and Thielemann, F. K. (1994). Merging neutron stars. I. Initial results for coalescence of noncorotating systems. *Astrophys. J.* 431, 742. doi:10.1086/174525

Del Pozzo, W. (2012). Inference of the cosmological parameters from gravitational waves: application to second generation interferometers. *Phys. Rev. D* 86, 043011. doi:10.1103/PhysRevD.86.043011

Díaz, M. C., Macri, L. M., Garcia Lambas, D., Mendes de Oliveira, C., Nilo Castellon, L., Ribeiro, T., et al. (2017). Observations of the first electromagnetic counterpart to a gravitational-wave source by the TOROS collaboration. *Astrophys. J.* 848, L29. doi:10.3847/2041-8213/aa9060

Drout, M. R., Piro, A. L., Shappee, B. J., Kilpatrick, C. D., Simon, J. D., Contreras, C., et al. (2017). Light curves of the neutron star merger GW170817/SSS17a: implications for r-process nucleosynthesis. *Science*. 358, 1570. doi:10.1126/science.aaq0049

Eichler, D., Livio, M., Piran, T., and Schramm, D. N. (1989). Nucleosynthesis, neutrino bursts and gamma-rays from coalescing neutron stars. *Nature* 340, 126. doi:10.1038/340126a0

Epstein, R. I., Colgate, S. A., and Haxton, W. C. (1988). Neutrino-induced r-process nucleosynthesis. *Phys. Rev. Lett.* 61, 2038. doi:10.1103/PhysRevLett.61.2038

Ergon, M., Fransson, C., Jerkstrand, A., Kozma, C., Kromer, M., and Spricer, K. (2018). Monte-Carlo methods for NLTE spectral synthesis of supernovae. *Astron. Astrophys.* 620, A156. doi:10.1051/0004-6361/201833043

Evans, P. A., Cenko, S. B., Kennea, J. A., Emrey, S. W. K., Kuin, N. P. M., Korobkin, O., et al. (2017). Swift and NuSTAR observations of GW170817: detection of a blue kilonova. *Science*. 358, 1565. doi:10.1126/science.aap9580

Fang, K., and Metzger, B. D. (2017). High-energy neutrinos from millisecond magnetars formed from the merger of binary neutron stars. *Astrophys. J* 849, 153. doi:10.3847/1538-4357/aa8b6a

Fernández, R., and Metzger, B. D. (2013). Delayed outflows from black hole accretion tori following neutron star binary coalescence. *Mon. Not. Roy. Astron. Soc.* 435, 502. doi:10.1093/mnras/stt1312

Fernández, R., and Metzger, B. D. (2016). Electromagnetic signatures of neutron star mergers in the advanced LIGO era. *Annu. Rev. Nucl. Part Sci.* 66, 23. doi:10.1146/annurev-nucl-102115-044819

Fong, W., Berger, E., and Fox, D. B. (2010). Hubble space telescope observations of short gamma-ray burst host galaxies: morphologies, offsets, and local environments. *Astrophys. J.* 708, 9. doi:10.1088/0004-637X/708/1/9

Fong, W., Berger, E., Margutti, R., and Zauderer, B. A. (2015). A decade of short-duration gamma-ray burst broadband Afterglows: energetics, circumburst densities, and jet opening angles. *Astrophys. J.* 815, 102. doi:10.1088/0004-637X/815/2/102

Fong, W., Blanchard, P. K., Alexander, K. D., Strader, J., Margutti, R., Hajela, A., et al. (2019). The optical afterglow of GW170817: an off-axis structured jet and

deep constraints on a globular cluster origin. *Astrophys. J.* 883, L1. doi:10.3847/2041-8213/ab3d9e

Fontes, C. J., Fryer, C. L., Hungerford, A. L., Wollaeger, R. T., and Korobkin, O. (2020). A line-binned treatment of opacities for the spectra and light curves from neutron star mergers. *Mon. Not. Roy. Astron. Soc.* 493, 4143. doi:10.1093/mnras/staa485

Freiburghaus, C., Rosswog, S., and Thielemann, F. (1999). R-process in neutron star mergers. *Astrophys. J.* 525, L121. doi:10.1086/312343

Fryer, C. L., Herwig, F., Hungerford, A., and Timmes, F. X. (2006). Supernova fallback: a possible site for the r-process. *Astrophys. J.* 646, L131. doi:10.1086/507071

Galama, T. J., Vreeswjik, P. M., van Paradijs, J., Kouveliotou, C., Augusteijn, T., and Bohnhardt, H. (1998). An unusual supernova in the error box of the γ-ray burst of 25 April 1998. *Nature* 395, 670. doi:10.1038/27150

Gehrels, N., Cannizzo, J. K., Kanner, J., Kasliwal, M. M., Nissanke, S., and Singer, L. P. (2016). Galaxy strategy for LIGO-virgo gravitational wave counterpart searches. *Astrophys. J.* 820, 136. doi:10.3847/0004-637X/820/2/136

Ghirlanda, G., Salafia, O. S., Paragi, Z., Giroletti, M., Yang, J., Marcote, B., et al. (2019). Compact radio emission indicates a structured jet was produced by a binary neutron star merger. *Science*. 363, 968. doi:10.1126/science.aau8815

Goldstein, A., Veres, P., Burns, E., Briggs, M. S., Hamburg, R., Kocevski, D., et al. (2017). An ordinary short gamma-ray burst with extraordinary implications: fermi-GBM detection of GRB 170817A. *Astrophys. J.* 848, L14. doi:10.3847/2041-8213/aa8f41

Gomez, S., Hosseinzadeh, G., Cowperthwaite, P. S., Villar, V. A., Berger, E., Gardner, T., et al. (2019). A galaxy-targeted search for the optical counterpart of the candidate NS-BH merger S190814bv with magellan. *Astrophys. J.* 884, L55. doi:10.3847/2041-8213/ab4ad5

Gompertz, B. P., Levan, A. J., Tanvir, N. R., Hjorth, J., Covino, S., Evans, P. A., et al. (2018). The diversity of kilonova emission in short gamma-ray bursts. *Astrophys. J.* 860, 62. doi:10.3847/1538-4357/aac206

Gottlieb, O., Nakar, E., Piran, T., and Hotokezaka, K. (2018). A cocoon shock breakout as the origin of the γ-ray emission in GW170817. *Mon. Not. Roy. Astron. Soc.* 479, 588. doi:10.1093/mnras/sty1462

Graham, M. J., Kulkarni, S. R., Bellm, E. C., Adams, S. M., Barbarino, C., Blagorodnova, N., et al. (2019). The zwicky transient facility: science objectives. *Publ. Astron. Soc. Pac.* 131, 078001. doi:10.1088/1538-3873/ab006c

Guetta, D., and Stella, L. (2009). Short γ-ray bursts and gravitational waves from dynamically formed merging binaries. *Astron. Astrophys*. 498, 329. doi:10.1051/0004-6361:200810493

Hajela, A., Margutti, R., Alexander, K. D., Kathirgamaraju, A., Baldeschi, A., Guidorzi, C., et al. (2019). Two years of nonthermal emission from the binary neutron star merger GW170817: rapid fading of the jet afterglow and first constraints on the kilonova fastest ejecta. *Astrophys. J.* 886, L17. doi:10.3847/2041-8213/ab5226

Hallinan, G., Corsi, A., Mooley, K. P., Hotokezaka, K., Nakar, E., Kasliwal, M. M., et al. (2017). A radio counterpart to a neutron star merger. *Science* 358, 1579. doi:10.1126/science.aap9855

Hillebrandt, W., Takahaski, K., and Kodama, T. (1976). R-process nucleosynthesis: a dynamical model. *Astron. Astrophys*. 52, 63.

Hillier, D. J., and Dessart, L. (2019). Photometric and spectroscopic diversity of Type II supernovae. *Astron. Astrophys*. 631, A8. doi:10.1051/0004-6361/201935100

Hjorth, J., Levan, A. J., Tanvir, N. R., Lyman, J. D., Wojtak, R., Schrøder, S. L., et al. (2017). The distance to NGC 4993: the host galaxy of the gravitational-wave event GW170817. *Astrophys. J.* 848, L31. doi:10.3847/2041-8213/aa9110

Hoeflich, P., Hsiao, E. Y., Ashall, C., Burns, C. R., Diamond, T. R., Phillips, M. M., et al. (2017). Light and color curve properties of type ia supernovae: theory versus observations. *Astrophys. J.* 846, 58. doi:10.3847/1538-4357/aa84b2

Horowitz, C. J., Arcones, A., Côté, B., Dillmann, I., Nazarewicz, W., Roederer, I. U., et al. (2019). R-process nucleosynthesis: connecting rare-isotope beam facilities with the cosmos. *J. Phys. G Nucl. Part. Phys.* 46, 083001. doi:10.1088/1361-6471/ab0849

Hotokezaka, K., Kuichi, K., Kyutoku, K., Okawa, H., Sekiguchi, Y.-i., Shibata, M., et al. (2013). Mass ejection from the merger of binary neutron stars. *Phys. Rev. D* 87, 024001. doi:10.1103/PhysRevD.87.024001

Hotokezaka, K., Nakar, E., Gottlieb, O., Nissanke, S., Masuda, K., Hallinan, G., et al. (2019). A Hubble constant measurement from superluminal motion of the jet in GW170817. *Nature Astr* 3, 940. doi:10.1038/s41550-019-0820-1

Hulse, R. A., and Taylor, J. H. (1974). A high-sensitivity pulsar survey. *Astrophys. J.* 191, L59. doi:10.1086/181548

Hulse, R. A., and Taylor, J. H. (1975). Discovery of a pulsar in a binary system. *Astrophys. J.* 195, L51. doi:10.1086/181708

Im, M., Yoon, Y., Lee, S. J., Lee, H. M., Kim, J., Lee, C.-U., et al. (2017). Distance and properties of NGC 4993 as the host galaxy of the gravitational-wave source GW170817. *Astrophys. J.* 849, L16. doi:10.3847/2041-8213/aa9367

Ioka, K., and Nakamura, T. (2019). Spectral puzzle of the off-axis gamma-ray burst in GW170817. *Mon. Not. Roy. Astron. Soc* 487, 4884. doi:10.1093/mnras/stz1650

Iwamoto, K., Mazzali, P. A., Nomoto, K., Umeda, H., Nakamura, T., Patat, F., et al. (1998). A hypernova model for the supernova associated with the γ-ray burst of 25 April 1998. *Nature*. 395, 672. doi:10.1038/27155

Janka, H. -Th., Aloy, M.-A., Mazzali, P. A., and Pian, E. (2006). Off-Axis properties of short gamma-ray bursts. *Astrophys. J.* 645, 1305. doi:10.1086/504580

Ji, A. P., Frebel, A., Chiti, A., and Simon, J. D. (2016). R-process enrichment from a single event in an ancient dwarf galaxy. *Nature* 531, 610. doi:10.1038/nature17425

Jin, Z.-P., Li, X., Cano, Z., Covino, S., Fan, Y.-Z., Wei, D.-M., et al. (2015). The light curve of the macronova associated with the long-short burst GRB 060614. *Astrophys. J.* 811, L22. doi:10.1088/2041-8205/811/2/L22

Jin, Z.-P., Hotokezaka, K., Li, X., Tanaka, M., D'Avanzo, P., Fan, Y.-Z., et al. (2016). The Macronova in GRB 050709 and the GRB-macronova connection. *Nat. Commun*. 7, 12898. doi:10.1038/ncomms12898

Jin, Z.-P., Xiang, L., Hao, W., Yuan, Z.-W., Hao, N.-H., Yuan, Q., et al. (2018). Short GRBs: opening angles, local neutron star merger rate, and off-axis events for GRB/GW association. *Astrophys. J.* 857, 128. doi:10.3847/1538-4357/aab76d

Kajino, T., Grant, J. M., and Takehito, H. (2014). Neutrinos in core-collapse supernovae and nucleosynthesis. *J. Phys. G Nucl. Phys*. 41, 044007. doi:10.1088/0954-3899/41/4/044007

Kajino, T., Aoki, W., Balantekin, A. B., Diehl, R., Famiano, M. A., Mathews, G J., et al. (2019). Current status of r-process nucleosynthesis. *Prog. Part. Nucl. Phys*. 107, 109. doi:10.1016/j.ppnp.2019.02.008

Kasen, D., Badnell, N. R., and Barnes, J. (2013). Opacities and spectra of the r-process ejecta from neutron star mergers. *Astrophys. J.* 774, 25. doi:10.1088/0004-637X/774/1/25

Kasen, D., Rodrigo, F., and Brian, D. M. (2015). Kilonova light curves from the disc wind outflows of compact object mergers. *Mon. Not. Roy. Astron. Soc*. 450, 1777. doi:10.1093/mnras/stv721

Kasen, D., Metzger, B., Barnes, J., Quataeart, E., and Ramirez-Ruiz, E. (2017). Origin of the heavy elements in binary neutron-star mergers from a gravitational-wave event. *Nature* 551, 80. doi:10.1038/nature24453

Kasliwal, M. M., Nakar, E., Singer, L. P., Kaplan, D. L., Cook, D. O., Van Sistine, A., et al. (2017). Illuminating gravitational waves: a concordant picture of photons from a neutron star merger. *Science* 358, 1559. doi:10.1126/science.aap9455

Kasliwal, M. M., Anand, S., Ahumada, T., Stein, R., Carracedo, A. S., Andreoni, I., et al. (Forthcoming 2020). Kilonova luminosity function constraints based on zwicky transient facility searches for 13 neutron star mergers. *Astrophys. J* Available at: https://arxiv.org/abs/2006.11306 (Accessed June 19, 2020).

Kathirgamaraju, A., Giannios, D., and Beniamini, P. (2019). Observable features of GW170817 kilonova afterglow. *Mon. Not. Roy. Astron. Soc*. 487, 3914. doi:10.1093/mnras/stz1564

Kim, S., Schulze, S., Resmi, L., González-López, J., Higgins, A. B., Ishwara-Chandra, C. H., et al. (2017). ALMA and GMRT constraints on the off-axis gamma-ray burst 170817A from the binary neutron star merger GW170817. *Astrophys. J.* 850, L21. doi:10.3847/2041-8213/aa970b

Kimura, S. S., Murase, K., Bartos, I., Ioka, K., Heng, I. S., and Mészáros, P. (2018). Transejecta high-energy neutrino emission from binary neutron star mergers. *Phys. Rev. D* 98, 043020. doi:10.1103/PhysRevD.98.043020

Kiuchi, K., Kyutoku, K., Sekiduchi, Y., Shibata, M., and Wada, T. (2014). High resolution numerical relativity simulations for the merger of binary magnetized neutron stars. *Phys. Rev. D*. 90, 041502. doi:10.1103/PhysRevD.90.041502

Kouveliotou, C., Meegan, C. A., Fishman, G. J., Bhat, N. P., Briggs, M. S., Koshut, T. M., et al. (1993). Identification of two classes of gamma-ray bursts. *Astrophys. J.* 413, L101. doi:10.1086/186969

Kyutoku, K., and Kashiyama, K. (2018). Detectability of thermal neutrinos from binary neutron-star mergers and implications for neutrino physics. *Phys. Rev. D* 97, 103001. doi:10.1103/PhysRevD.97.103001

Lamb, G. P., and Kobayashi, S. (2018). GRB 170817A as a jet counterpart to gravitational wave triggerGW 170817. *Mon. Not. Roy. Astron. Soc.* 478, 733. doi:10.1093/mnras/sty1108

Lamb, G. P., Tanvir, N., Levan, A., Postigo, A. d. U., Kawaguchi, K., Corsi, A., et al. (2019). Short GRB 160821B: a reverse shock, a refreshed shock, and a well-sampled kilonova. *Astrophys. J.* 883, 48. doi:10.3847/1538-4357/ab38bb

Lattimer, J. M., and Schramm, D. N. (1974). Black-hole-neutron-star collisions. *Astrophys. J.* 192, L145. doi:10.1086/181612

Lattimer, J. M., and Schramm, D. N. (1976). The tidal disruption of neutron stars by black holes in close binaries. *Astrophys. J.* 210, 549. doi:10.1086/154860

Lazzati, D., Deich, A., Morsony, B. J., and Workman, J. C. (2017a). Off-axis emission of short gamma-ray bursts and the detectability of electromagnetic counterparts of gravitational-wave-detected binary mergers. *Mon. Not. Roy. Astron. Soc.* 471, 1652. doi:10.1093/mnras/stx1683

Lazzati, D., Lopez-Camara, D., Cantiello, M., Morsony, B. J., Perna, R., and Workman, J. C. (2017b). Off-axis prompt X-ray transients from the cocoon of short gamma-ray bursts. *Astrophys. J.* 848, L6. doi:10.3847/2041-8213/aa8f3d

Lazzati, D., Perna, R., Morsony, B. J., Lopez-Camara, D., Cantiello, M., Ciolfi, R., et al. (2018). Late time afterglow observations reveal a collimated relativistic jet in the ejecta of the binary neutron star merger GW170817. *Phys. Rev. Lett.* 120, 241103. doi:10.1103/PhysRevLett.120.241103

Levan, A., Crowther, P., Grijs, R. d., Langer, N., Xu, D., and Yoon, S.-C. (2016). Gamma-ray burst progenitors. *Space Sci. Rev.* 202, 33. doi:10.1007/s11214-016-0312-x

Levan, A., Lyman, J. D., Tanvir, N. R., Hjorth, J., Mandel, I., Stanway, E. R., et al. (2017). The environment of the binary neutron star merger GW170817. *Astrophys. J.* 848, L28. doi:10.3847/2041-8213/aa905f

Li, L.-X., and Paczyński, B. (1998). Transient events from neutron star mergers. *Astrophys. J.* 507, L59. doi:10.1086/311680

Lim, Y., and Holt, J. W. (2018). Neutron star tidal deformabilities constrained by nuclear theory and experiment. *Phys. Rev. Lett.* 121, 062701. doi:10.1103/PhysRevLett.121.062701

Lippuner, J., Fernandez, R., Roberts, L. F., Foucart, F., Rasen, D., Metzger, B. D., et al. (2017). Signatures of hypermassive neutron star lifetimes on r-process nucleosynthesis in the disc ejecta from neutron star mergers. *Mon. Not. Roy. Astron. Soc.* 472, 904. doi:10.1093/mnras/stx1987

Lipunov, V. M., Gorbovskoy, E., Kornilov, V. G., Tyurina, N., Balanutsa, P., Kuznetsov, A., et al. (2017). MASTER optical detection of the first LIGO/Virgo neutron star binary merger GW170817. *Astrophys. J.* 850, L1. doi:10.3847/2041-8213/aa92c0

Lyman, J. D., Lamb, G. P., Levan, A. J., Mandel, I., Tanvir, N. R., Kobayashi, S., et al. (2018). The optical afterglow of the short gamma-ray burst associated with GW170817. *Nature Astr* 2, 751. doi:10.1038/s41550-018-0511-3

Macias, P., and Ramirez-Ruiz, E. (2019). Constraining collapsar r-process models through stellar abundances. *Astrophys. J.* 877, L24. doi:10.3847/2041-8213/ab2049

Margutti, R., Berger, E., Fong, W., Guidorzi, C., Alexander, K. D., Metzger, B. D., et al. (2017). The electromagnetic counterpart of the binary neutron star merger LIGO/Virgo GW170817. V. Rising X-ray emission from an off-axis jet. *Astrophys. J.* 848, L20. doi:10.3847/2041-8213/aa9057

Martinez, J. G., Stovall, K., Freire, P. C. C., Deneva, J. S., Tauris, T. M., Ridolfi, A., et al. (2017). Pulsar J1411+2551: a low-mass double neutron star system. *Astrophys. J.* 851, L29. doi:10.3847/2041-8213/aa9d87

Matsumoto, T., and Piran, T. (2020). On short GRBs similar to GRB 170817A detected by Fermi-GBM. *Mon. Not. Roy. Astron. Soc.* 492, 4283. doi:10.1093/mnras/staa050

Mazzali, P. A., Iwamoto, K., and Nomoto, K. (2000). A spectroscopic analysis of the energetic type ic hypernova SN 1997ef. *Astrophys. J.* 545, 407. doi:10.1086/317808

Mazzali, P. A., Sullivan, M., Pian, E., Greiner, J., and Kann, D. A. (2016). Spectrum formation in superluminous supernovae (Type I). *Mon. Not. Roy. Astron. Soc.* 458, 3455. doi:10.1093/mnras/stw512

McCully, C., Hiramatsu, D., Howell, D. A., Hosseinzadeh, G., Arcavi, I., Kasen, D., et al. (2017). The rapid reddening and featureless optical spectra of the optical counterpart of GW170817, at 2017gfo, during the first four days. *Astrophys. J.* 848, L32. doi:10.3847/2041-8213/aa9111

Mennekens, N., and Vanbeveren, D. (2014). Massive double compact object mergers: gravitational wave sources and r-process element production sites. *Astron. Astrophys.* 564, A134. doi:10.1051/0004-6361/201322198

Metzger, B. D., and Fernández, R. (2014). Red or blue? A potential kilonova imprint of the delay until black hole formation following a neutron star merger. *Mon. Not. Roy. Astron. Soc.* 441, 3444. doi:10.1093/mnras/stu802

Metzger, B. D. (2019). Kilonovae. *Living Reviews in Relativity*. 23, 1. doi:10.1007/s41114-019-0024-0

Mooley, K., Nakar, E., Hotokezaka, K., Hallinan, G., Corsi, A., Frail, D. A., et al. (2018a). A mildly relativistic wide-angle outflow in the neutron-star merger event GW170817. *Nature* 554, 207. doi:10.1038/nature25452

Mooley, K., Deller, A. T., Gottlieb, O., Nakar, E., Hallinan, G., Bourke, S., et al. (2018b). Superluminal motion of a relativistic jet in the neutron-star merger GW170817. *Nature* 561, 355. doi:10.1038/s41586-018-0486-3

Mooley, K., Frail, D. A., Dobie, D., Lenc, E., Corsi, A., De, K., et al. (2018c). A strong jet signature in the late-time light curve of GW170817. *Astrophys. J.* 868, L11. doi:10.3847/2041-8213/aaeda7

Most, E. R., Lukas, R. W., Rezzolla, L., and Schaffner-Bielich, J. (2018). New constraints on radii and tidal deformabilities of neutron stars from GW170817. *Phys. Rev. Lett.* 120, 261103. doi:10.1103/PhysRevLett.120.261103

Nakamura, T., Mazzali, P. A., Nomoto, K., and Iwamoto, K. (2001). Light curve and spectral models for the hypernova SN 1998BW associated with GRB 980425. *Astrophys. J.* 550, 991. doi:10.1086/319784

Nakamura, K., Kajino, T., Mathews, G. J., Sato, S., and Harikae, S. (2013). A review of R-PROCESS nucleosynthesis in the collapsar jet. *Int. J. Mod. Phys. E.* 22, 1330022. doi:10.1142/S0218301313300221

Nakamura, K., Kajino, T., Mathews, G. J., Sato, S., and Harikae, A. (2015). r-process nucleosynthesis in the MHD+neutrino-heated collapsar jet. *Astron. Astrophys.* 582, A34. doi:10.1051/0004-6361/201526110

Nakano, H., Narikawa, T., Oohara, K.-I., Sakai, K., Shinkai, H.-A., Takahashi, H., et al. (2019). Comparison of various methods to extract ringdown frequency from gravitational wave data. *Phys. Rev. D* 99, 124032. doi:10.1103/PhysRevD.99.124032

Nakar, E., and Piran, T. (2017). The observable signatures of GRB cocoons. *Astrophys. J.* 834, 28. doi:10.3847/1538-4357/834/1/28

Nakar, E. (2007). Short-hard gamma-ray bursts. *Phys. Rep.* 442, 166. doi:10.1016/j.physrep.2007.02.005

Nicholl, M., Berger, E., Kasen, D., Metzger, B. D., Elias, J., Briceno, C., et al. (2017). The electromagnetic counterpart of the binary neutron star merger LIGO/Virgo GW170817. III. Optical and UV spectra of a blue kilonova from fast polar ejecta. *Astrophys. J.* 848, L18. doi:10.3847/2041-8213/aa9029

Ning, H., Qian, Y.-Z., and Meyer, B. S. (2007). R-Process nucleosynthesis in shocked surface layers of O-Ne-Mg cores. *Astrophys. J.* 667, L159. doi:10.1086/522372

Nishimura, S., Kotake, K., Hashimoto, M.-A., Yamada, S., Nishimura, N., Fujimoto, S., et al. (2006). R-Process nucleosynthesis in magnetohydrodynamic jet explosions of core-collapse supernovae. *Astrophys. J.* 642, 410. doi:10.1086/500786

Nissanke, S., Holz, D. E., Hughes, S. A., Dalal, N., and Sievers, J. L. (2010). Exploring short gamma-ray bursts as gravitational-wave standard sirens. *Astrophys. J.* 725, 496. doi:10.1088/0004-637X/725/1/496

Özel, F., and Freire, P. (2016). Masses, radii, and the equation of state of neutron stars. *Annu. Rev. Astron. Astrophys.* 54, 401. doi:10.1146/annurev-astro-081915-023322

Palmese, A., Hartley, W., Tarsitano, F., Conselice, C., Lahav, O., Allam, S. S., et al. (2017). Evidence for dynamically driven formation of the GW170817 neutron star binary in NGC 4993. *Astrophys. J.* 849, L34. doi:10.3847/2041-8213/aa9660

Pan, Y. -C., Kilpatrick, C. D., Simon, J. D., Xhakaj, E., Boutsia, K., Coulter, D.A., et al. (2017). The old host-galaxy environment of SSS17a, the first electromagnetic counterpart to a gravitational-wave source. *Astrophys. J* 848, L30. doi:10.3847/2041-8213/aa9116

Pandey, S. B., Hu, Y., Tirado, A. J. C., Pozanenko, A. S., Sanchez-Ramirez, R., Gorosabel, J., et al. (2019). A multiwavelength analysis of a collection of short-duration GRBs observed between 2012 and 2015. *Mon. Not. Roy. Astron. Soc.* 485, 5294. doi:10.1093/mnras/stz530

Patricelli, B., Stamerra, A., Razzano, M., Pian, E., and Cella, G. (2018). Searching for gamma-ray counterparts to gravitational waves from merging binary neutron stars with the Cherenkov Telescope Array. *J. Cosmol. Astropart. Phys.* 5, 056. doi:10.1088/1475-7516/2018/05/056

Perego, A., Rosswog, S., Cabezon, R., Korobkin, O., Kaeppeli, R., Arcones, A., et al. (2014). Neutrino-driven winds from neutron star merger remnants. *Mon. Not. Roy. Astron. Soc.* 443, 3134. doi:10.1093/mnras/stu1352

Pfahl, E., Podsiadlowski, P., and Rappaport, S. (2005). Relativistic binary pulsars with black hole companions. *Astrophys. J.* 628, 343. doi:10.1086/430515

Pian, E., D'Avanzo, P., Benetti, S., Branchesi, M., Brocato, E., Campana, S., et al. (2017). Spectroscopic identification of r-process nucleosynthesis in a double neutron-star merger. *Nature*. 551, 67. doi:10.1038/nature24298

Piro, A. L., and Kollmeier, J. A. (2018). Evidence for cocoon emission from the early light curve of SSS17a. *Astrophys. J.* 855, 103. doi:10.3847/1538-4357/aaaab3

Pozanenko, A. S., Barkov, M. V., Minaev, P. V., Volnova, A. A., Mazaeva, E. D., Moskvitin, A. S., et al. (2018). GRB 170817A associated with GW170817: multi-frequency observations and modeling of prompt gamma-ray emission. *Astrophys. J.* 852, L30. doi:10.3847/2041-8213/aaa2f6

Pozanenko, A. S., Minaev, P. Y., Grebenev, S. A., and Chelovekov, I. V. (2019). Observation of the second LIGO/Virgo event connected with a binary neutron star merger S190425z in the gamma-ray range. *Astrophys. Lett.* 45, 710. doi:10.1134/S1063773719110057

Radice, D., Perego, A., Zappa, F., and Bernuzzi, S. (2018). GW170817: joint constraint on the neutron star equation of state from multimessenger observations. *Astrophys. J.* 852, L29. doi:10.3847/2041-8213/aaa402

Ramirez-Ruiz, E., Trenti, M., Macleod, M., Roberts, L. F., Lee, W. H., Saladino-Rosas, M. I., et al. (2015). Compact stellar binary assembly in the first nuclear star clusters and r-process synthesis in the early Universe. *Astrophys. J.* 802, L22. doi:10.1088/2041-8205/802/2/L22

Rauscher, T., Applegate, J. M., Cowan, J. J., and Weischer, M. (1994). Production of heavy elements in inhomogeneous cosmologies. *Astrophys. J.* 429, 499. doi:10.1086/174339

Renzo, M., Zapartas, E., de Mink, S. E., Gotberg, Y., Justham, S., Farmer, R. J., et al. (2019). Massive runaway and walkaway stars. A study of the kinematical imprints of the physical processes governing the evolution and explosion of their binary progenitors. *Astron. Astrophys*. 624, A66. doi:10.1051/0004-6361/201833297

Rossi, A., Stratta, G., Maiorano, E., Spighi, D., Masetti, N., Palazzi, E., et al. (2020). A comparison between short GRB afterglows and kilonova AT2017gfo: shedding light on kilonovae properties. *Mon. Not. Roy. Astron. Soc.* 493, 3379. doi:10.1093/mnras/staa4794

Rosswog, S., and Liebendörfer, M. (2003). High-resolution calculations of merging neutron stars - II. Neutrino emission. *Mon. Not. Roy. Astron. Soc.* 342, 673. doi:10.1046/j.1365-8711.2003.06579.x

Rosswog, S., Liebendorfer, M., Thielemann, F.-K., Davies, M. B., Benz, W., and Piran, T. (1999). Mass ejection in neutron star mergers. *Astron. Astrophys*. 341, 499.

Rosswog, S., Sollerman, J., Feindt, U., Goobar, A., Korobkin, O., Wollaeger, R., et al. (2018). The first direct double neutron star merger detection: implications for cosmic nucleosynthesis. *Astron. Astrophys*. 615, A132. doi:10.1051/0004-6361/201732117

Ruffert, M., and Janka, H. -Th. (2001). Coalescing neutron stars - a step towards physical models. III. Improved numerics and different neutron star masses and spins. *Astron. Astrophys*. 380, 544. doi:10.1051/0004-6361:20011453

Safarzadeh, M., Sarmento, R., and Scannapieco, E. (2019). On neutron star mergers as the source of r-process-enhanced metal-poor stars in the milky way. *Astrophys. J.* 876, 28. doi:10.1088/2041-8205/802/2/L22

Sagiv, I., Gal-Yam, A., Ofek, E. O., Waxman, E., Aharonson, O., Kulkarni, S. R., et al. (2014). Science with a wide-field UV transient explorer. *Astrophys. J.* 147, 79. doi:10.1088/0004-6256/147/4/79

Salafia, O. S., Ghisellini, G., Ghirlanda, G., and Colpi, M. (2018). Interpreting GRB170817A as a giant flare from a jet-less double neutron star merger. *Astron. Astrophys*. 619, A18. doi:10.1051/0004-6361/201732259

Sana, H., Mink, S. E. d., Koter, A. d., Langer, N., Evans, C. J., Geiles, M., et al. (2012). Binary interaction dominates the evolution of massive stars. *Science*. 337, 444. doi:10.1126/science.1223344

Savchenko, V., Ferrigno, C., Kuulkers, E., Bazzano, A., Bozzo, E., Brandt, S., et al. (2017). Integral detection of the first prompt gamma-ray signal coincident with the gravitational-wave event GW170817. *Astrophys. J.* 848, L15. doi:10.3847/2041-8213/aa8f94

Schutz, B. F. (1986). Determining the Hubble constant from gravitational wave observations. *Nature* 323, 310. doi:10.1038/323310a0

Shapiro, S. L., and Teukolsky, S. A. (1983). Black holes, white dwarfs, and neutron stars. *The Physics of Compact Objects*. doi:10.1002/9783527617661

Shappee, B. J., Simon, J. D., Drout, M. R., Piro, A. L., Morrell, N., Prieto, J. L., et al. (2017). Early spectra of the gravitational wave source GW170817: evolution of a neutron star merger. *Science* 358, 1574. doi:10.1126/science.aaq0186

Shibagaki, S., Kajino, T., Mathews, G. J., Chiba, S., Nishimura, S., Lorusso, G., et al. (2016). Relative contributions of the weak, main, and fission-recycling r-process. *Astrophys. J.* 816, 79. doi:10.3847/0004-637X/816/2/79

Shibata, M., and Hotokezaka, K. (2019). Neutron star collisions and the r-process. *Annu. Rev. Nucl. Part Sci*. 69, 41. doi:10.1146/annurev-nucl-101918-023625

Shingles, L. J., Sim, S. A., Kromer, M., Maguire, K., Bulla, M., Collins, C., et al. (2020). Monte Carlo radiative transfer for the nebular phase of Type Ia supernovae. *Mon. Not. Roy. Astron. Soc*. 492, 2029. doi:10.1093/mnras/stz3412

Siegel, D. M., Barnes, J., and Metzger, B. D. (2019). Collapsars as a major source of r-process elements. *Nature*. 569, 241. doi:10.1038/s41586-019-1136-0

Simonetti, P., Matteucci, F., Greggio, L., and Cescutti, G. (2019). A new delay time distribution for merging neutron stars tested against Galactic and cosmic data. *Mon. Not. Roy. Astron. Soc*. 486, 2896. doi:10.1093/mnras/stz991

Smartt, S. J., Chen, T.-W., Jerkstrand, A., Coughlin, M., Kankare, E., Sim, S. A., et al. (2017). A kilonova as the electromagnetic counterpart to a gravitational-wave source. *Nature*. 551, 75. doi:10.1038/nature24303

Sneden, C., Cowan, J. J., and Gallino, R. (2008). Neutron-capture elements in the early galaxy. *Annu. Rev. Astron. Astrophys*. 46, 241. doi:10.1146/annurev.astro.46.060407.145207

Soares-Santos, M., Holz, D. E., Annis, J., Chornock, R., Herner, K., Berger, E., et al. (2017). The electromagnetic counterpart of the binary neutron star merger LIGO/Virgo GW170817. I. Discovery of the optical counterpart using the dark energy camera. *Astrophys. J.* 848, L16. doi:10.3847/2041-8213/aa9059

Stratta, G., Ciolfi, R., Amati, L., Bozzo, E., Ghirlanda, G., Maiorano, E., et al. (2018). Theseus: a key space mission concept for Multi-Messenger Astrophysics. *Adv. Space Res*. 62, 662. doi:10.1016/j.asr.2018.04.013

Symbalisty, E., and Schramm, D. N. (1982). Neutron star collisions and the r-process. *Astrophys. Lett*. 22, 143.

Takahashi, K., Witti, J., and Janka, H.-T. (1994). Nucleosynthesis in neutrino-driven winds from protoneutron stars II. The r-process. *Astron. Astrophys*. 286, 857.

Tanaka, M., and Hotokezaka, K. (2013). Radiative transfer simulations of neutron star merger ejecta. *Astrophys. J.* 775, 113. doi:10.1088/0004-637X/775/2/113

Tanaka, M., Utsumi, Y., Mazzali, P. A., Tominaga, N., Yoshida, M., Sekiguchi, Y., et al. (2017). Kilonova from post-merger ejecta as an optical and near-Infrared counterpart of GW170817. *Publ. Astron. Soc. Jpn.* 69, 102. doi:10.1093/pasj/psx121

Tanaka, M., Kato, D., Gaigalas, G., Rynkun, P., Radziute, L., Wanajo, S., et al. (2018). Properties of kilonovae from dynamical and post-merger ejecta of neutron star mergers. *Astrophys. J.* 852, 109. doi:10.3847/1538-4357/aaa0cb

Tanaka, M., Kato, D., Gaigalas, G., and Kawaguchi, K. (2020). Systematic opacity calculations for kilonovae. *Mon. Not. Roy. Astron. Soc*. 496, 1369. doi:10.1093/mnras/staa1576

Tanaka, M. (2016). Kilonova/Macronova emission from compact binary mergers. *Advances in Astronomy*, 634197. doi:10.1155/2016/6341974

Tanvir, N. R., Levan, A. J., Fruchter, A. S., Hjorth, J., Hounsell, R. A., Weirsema, K., et al. (2013). A "kilonova" associated with the short-duration γ-ray burst GRB 130603B. *Nature*. 500, 547. doi:10.1038/nature12505

Tanvir, N. R., Levan, A. J., Gonzalez-Fernandez, C., Korobkin, O., Mandel, I., Rosswog, S., et al. (2017). The emergence of a lanthanide-rich kilonova following the merger of two neutron stars. *Astrophys. J.* 848, L27. doi:10.3847/2041-8213/aa90b6

Tauris, M. T., Kramer, M., Freire, P. C. C., Wex, N., Janka, H.-T., Langer, N., et al. (2017). Formation of double neutron star systems. *Astrophys. J.* 846, 170. doi:10.3847/1538-4357/aa7e89

Taylor, J. H., and Weisberg, J. M. (1982). A new test of general relativity - gravitational radiation and the binary pulsar PSR 1913+16. *Astrophys. J.* 253, 908. doi:10.1086/159690

Thielemann, F.-K., Arcones, A., Kappeli, R., Liebendorfer, M., Rauscher, T., Winteler, C., et al. (2011). What are the astrophysical sites for the r-process and the production of heavy elements? *Prog. Part. Nucl. Phys*. 66, 346. doi:10.1016/j.ppnp.2011.01.032

Thielemann, F.-K., Eichler, M., Panov, I. V., and Wehmeyer, B. (2017). Neutron star mergers and nucleosynthesis of heavy elements. *Annu. Rev. Nucl. Part Sci*. 67, 253. doi:10.1146/annurev-nucl-101916-123246

Tominaga, N., Tanaka, M., Morokuma, T., Utsumi, Y., Yamaguchi, M. S., Yasuda, N., et al. (2018). Subaru hyper suprime-cam survey for an optical counterpart of GW170817. *Publ. Astron. Soc. Jpn*. 70, 28. doi:10.1093/pasj/psy007

Troja, E., Piro, L., van Eerten, H., Wollaeger, R. T., Im, M., Fox, O. D., et al. (2017). The X-ray counterpart to the gravitational-wave event GW170817. *Nature* 551, 71. doi:10.1038/nature24290

Troja, E., van Eerten, H., Zhang, B., Ryan, G., Piro, L., Ricci, R., et al. (Forthcoming 2020). A thousand days after the merger: continued X-ray emission from GW170817. *Mon. Not. Roy. Astron. Soc* Available at: https://arxiv.org/abs/2006.01150 (Accessed June 1, 2020).

Utsumi, Y., Tanaka, M., Tominaga, N., Yoshida, M., Barway, S., Nagayama, T., et al. (2017). J-GEM observations of an electromagnetic counterpart to the neutron star merger GW170817. *Publ. Astron. Soc. Jpn*. 69, 101. doi:10.1093/pasj/psx118

Valenti, S., David, J. S., Yang, S., Cappellaro, E., Tartaglia, L., Corsi, A., et al. (2017). The discovery of the electromagnetic counterpart of GW170817: kilonova at 2017gfo/DLT17ck. *Astrophys. J.* 848, L24. doi:10.3847/2041-8213/aa8edf

van Eerten, H. J., and MacFadyen, A. I. (2011). Synthetic off-axis light curves for low-energy gamma-ray bursts. *Astrophys. J.* 733, L37. doi:10.1088/2041-8205/733/2/L37

Villar, V. A., Guillochon, J., Berger, E., Metzger, B. D., Cowperthwaite, P. S., Nicholl, M., et al. (2017). The combined ultraviolet, optical, and near-infrared light curves of the kilonova associated with the binary neutron star merger GW170817: unified data set, analytic models, and physical implications. *Astrophys. J.* 851, L21. doi:10.3847/2041-8213/aa9c84

Villar, V. A., Cowperthwaite, P. S., Berger, E., Blanchard, P. K., Gomez, S., Alexander, K. D., et al. (2018). Spitzer space telescope infrared observations of the binary neutron star merger GW170817. *Astrophys. J.* 862, L11. doi:10.3847/2041-8213/aad281

Wallner, A., Faestermann, T., Feige, J., Feldstein, C., Knie, K., Korschinek, G., et al. (2015). Abundance of live Pu in deep-sea reservoirs on Earth points to rarity of actinide nucleosynthesis. *Nat. Commun*. 6, 5956. doi:10.1086/ncomms6956

Wanajo, S., Itoh, N., Ishimaru, Y., Nozawa, S., and Beers, T. C. (2002). The r-process in the neutrino winds of core-collapse supernovae and U-Th cosmochronology. *Astrophys. J.* 577, 853. doi:10.1086/342230

Wang, X.-G., Zhang, B., Liang, E.-W., Lu, R.-J., Lin, D.-B., Li, J., et al. (2018). Gamma-ray burst jet breaks revisited. *Astrophys. J.* 859, 160. doi:10.3847/1538-4357/aabc13

Watson, D., Hansen, C. J., Selsing, J., Koch, A., Malesani, D. B., Anderson, A. C., et al. (2019). Identification of strontium in the merger of two neutron stars. *Nature* 574, 497. doi:10.1038/s41586-019-1676-3

Waxman, E., Ofek, E. O., Doron, K., and Avishay, G.-Y. (2018). Constraints on the ejecta of the GW170817 neutron star merger from its electromagnetic emission. *Mon. Not. Roy. Astron. Soc*. 481, 3423. doi:10.1093/mnras/sty2441

Weisberg, J. M., and Huang, Y. (2016). Relativistic measurements from timing the binary pulsar PSR B1913+16. *Astrophys. J.* 829, 55. doi:10.3847/0004-637X/829/1/55

Wheeler, J. C., Cowan, J. J., and Hillebrandt, W. (1998). The r-process in collapsing O/Ne/Mg cores. *Astrophys. J.* 493, L101. doi:10.1086/311133

Winteler, C., Kappeli, R., Perego, A., Arcones, A., Vasset, N., Nishimura, N., et al. (2012). Magnetorotationally driven supernovae as the origin of early galaxy r-process elements? *Astrophys. J.* 750, L22. doi:10.1088/2041-8205/750/1/L22

Wollaeger, R. T., Korobkin, O., Fontes, C. J., Rosswog, S. K., Even, W. P., Fryer, C. L., et al. (2018). Impact of ejecta morphology and composition on the electromagnetic signatures of neutron star mergers. *Mon. Not. Roy. Astron. Soc*. 478, 3298. doi:10.1093/mnras/sty1018

Wolszczan, A. (1991). A nearby 37.9-ms radio pulsar in a relativistic binary system. *Nature* 350, 688. doi:10.1038/350688a0

Woosley, S. E., and Bloom, J. S. (2006). The supernova gamma-ray burst connection. *Annu. Rev. Astron. Astrophys*. 44, 507. doi:10.1146/annurev.astro.43.072103.150558

Woosley, S. E., Wilson, J. R., Mathews, G. J., Hoffman, R. D., and Meyer, B. S. (1994). The r-process and neutrino-heated supernova ejecta. *Astrophys. J.* 433, 229. doi:10.1086/174638

Xie, X., Zrake, J., and MacFadyen, A. (2018). Numerical simulations of the jet dynamics and synchrotron radiation of binary neutron star merger event GW170817/GRB 170817A. *Astrophys. J.* 863, 58. doi:10.3847/1538-4357/aacf9c

Yang, S., Valenti, S., Cappellaro, E., Sand, D. J., Tartaglia, L., Corsi, A., et al. (2017). An empirical limit on the kilonova rate from the DLT40 one day cadence supernova survey. *Astrophys. J.* 851, L48. doi:10.3847/2041-8213/aaa07d

Yaron, O., and Gal-Yam, A. (2012). WISeREP—an interactive supernova data repository. *Publ. Astr. Soc. Pacific* 124, 668. doi:10.1086/666656

Ye, C. S., Fong, W.-F., Kremer, K., Rodriguez, C. L., Chatterjee, S., Fragione, G., et al. (2020). On the rate of neutron star binary mergers from globular clusters. *Astrophys. J.* 888, L10. doi:10.3847/2041-8213/ab5dc5

Conflict of Interest: The author declares that the research was conducted in the absence of any commercial or financial relationships that could be construed as a potential conflict of interest.

frontiers in Astronomy and Space Sciences

REVIEW
published: 02 February 2021
doi: 10.3389/fspas.2020.589240

Experimental Nuclear Astrophysics With the Light Elements Li, Be and B: A Review

G.G. Rapisarda[1], L. Lamia[1,2,3], A. Caciolli[4,5], Chengbo Li[6,7], S. Degl'Innocenti[8,9], R. Depalo[4,5], S. Palmerini[10,11], R.G. Pizzone[1], S. Romano[1,2,3], C. Spitaleri[1], E. Tognelli[8,9] and Qungang Wen[12]*

[1]Laboratori Nazionali del Sud, INFN-LNS, Catania, Italy, [2]Dipartimento di Fisica e Astronomia "E. Majorana", Univ. di Catania, Catania, Italy, [3]CSFNSM-Centro Siciliano di Fisica Nucleare e Struttura della Materia, Catania, Italy, [4]Physics and Astronomy Department, University of Padova, Padova, Italy, [5]INFN Section of Padova, Padova, Italy, [6]Key Laboratory of Beam Technology of Ministry of Education, Beijing Radiation Center, Beijing Academy of Science and Technology, Beijing 100875, China, [7]College of Nuclear Science and Technology, Beijing Normal University, Beijing 100875, China, [8]INFN, Section of Pisa, Pisa, Italy, [9]Department of Physics "E.Fermi", University of Pisa, Pisa, Italy, [10]Dipartimento di Fisica e Geologia, University of Perugia, Perugia, Italy, [11]INFN sezione di Perugia, Perugia, Italy, [12]School of Physics and Materials Science, Anhui University, Hefei, China

OPEN ACCESS

Edited by:
Douglas Weadon Higinbotham, Thomas Jefferson National Accelerator Facility, United States

Reviewed by:
Roelof Bijker, Universidad Nacional Autónoma de México, Mexico
Pierre Descouvemont, Université libre de Bruxelles, Belgium

***Correspondence:**
L. Lamia
llamia@lns.infn.it

Specialty section:
This article was submitted to Nuclear Physics, a section of the journal Frontiers in Astronomy and Space Sciences

Received: *30 July 2020*
Accepted: *23 September 2020*
Published: *02 February 2021*

Citation:
Rapisarda GG, Lamia L, Caciolli A, Li C, Degl'Innocenti S, Depalo R, Palmerini S, Pizzone RG, Romano S, Spitaleri C, Tognelli E and Wen Q (2021) Experimental Nuclear Astrophysics With the Light Elements Li, Be and B: A Review. Front. Astron. Space Sci. 7:589240. doi: 10.3389/fspas.2020.589240

Light elements offer a unique opportunity for studying several astrophysical scenarios from Big Bang Nucleosynthesis to stellar physics. Understanding the stellar abundances of light elements is key to obtaining information on internal stellar structures and mixing phenomena in different evolutionary phases, such as the pre-main-sequence, main-sequence or red-giant branch. In such a case, light elements, i.e., lithium, beryllium and boron, are usually burnt at temperatures of the order of 2–5 × 10^6 K. Consequently, the astrophysical S(E)-factor and the reaction rate of the nuclear reactions responsible for the burning of such elements must be measured and evaluated at ultra-low energies (between 0 and 10 keV). The Trojan Horse Method (THM) is an experimental technique that allows us to perform this kind of measurements avoiding uncertainties due to the extrapolation and electron screening effects on direct data. A long Trojan Horse Method research program has been devoted to the measurement of light element burning cross sections at astrophysical energies. In addition, dedicated direct measurements have been performed using both in-beam spectroscopy and the activation technique. In this review we will report the details of these experimental measurements and the results in terms of S(E)-factor, reaction rate and electron screening potential. A comparison between astrophysical reaction rates evaluated here and the literature will also be given.

Keywords: nuclear astrophysics, nuclear reactions, activation method, reaction rate, nucleosynthesis, electron screening effect

1 INTRODUCTION

Lithium, beryllium and boron (hereafter LiBeB, for simplicity) are carriers of important information in several domain of astrophysics, from primordial Big Bang Nucleosynthesis (BBN) to cosmic ray nucleosyntheis (GCR nucleosynthesis) and stellar nucleosynthesis (both for quiescent and explosive scenarios).

Primordial nucleosynthesis is one of the three pillars of the Big Bang theory together with Hubble expansion and the relic Cosmic Microwave Background (CMB) radiation. Although a strong agreement exists between BBN theoretical predictions for ^{2}H and ^{3,4}He abundances, the long-standing debate about the cosmological Li-problem is far from solved (Pitrou et al., 2018). The primordial lithium abundances (Li)[1] are derived from metal-poor main sequence halo star observations. These stars show a remarkably constant value of Li/H since the metallicity [Fe/H] varies (for [Fe/H] < −1.5 and $T_{\rm eff}$ above ~5,900 K), leading to the so called Spite plateau [see, e.g., (Spite and Spite, 1982; Meléndez et al., 2010; Sbordone et al., 2010), and references therein]. An averaged value of $(\mathrm{Li/H})_{obs} = (1.58^{+0.35}_{-0.28}) \times 10^{-10}$ is currently accepted, as reported in (Sbordone et al., 2010). By comparing $(\mathrm{Li/H})_{obs}$ with the most recent inferred lithium abundances $(\mathrm{Li/H})_{BBN} \sim (5.623) \times 10^{-10}$ (Pitrou et al., 2018), we can find a discrepancy of a factor of ~3.6. Several efforts have been made within pure nuclear physics in the recent years to alleviate this deviation, as in the case of the recent cross section measurements of the ^{7}Be(n,p) ^{7}Li and ^{7}Be(n,α) ^{4}He neutron-induced reactions (Barbagallo et al., 2016; Lamia et al., 2017; Damone et al., 2018; Lamia et al., 2019), which affect the total ^{7}Li primordial abundance. Despite these efforts or new physics in BBN models [see e.g. (Fields, 2011; Goudelis et al., 2016; Coc and Vangioni, 2017)] or possible stellar depletion mechanisms [diffusion, mass-loss, accretion (Vauclair and Charbonnel, 1995; Richard et al., 2005; Fu et al., 2015; Tognelli et al., 2020)], the Li-problem seems to be far from the solution. For completeness, the BBN calculations of (Coc et al., 2012) allow us to get the primordial abundances of boron (^{11}B), $N(^{11}B)/N(H) \approx 3 \times 10^{-16}$ and beryllium $N(^{9}Be)/N(H) \approx 3 \times 10^{-18}$ at very low values with respect the ones observed up to now in halo-stars (Tan et al., 2009; Primas, 2010; Boesgaard et al., 2011).

Galactic cosmic ray (GCR) nucleosynthesis is responsible for the production of most cosmic ^{9}Be through spallation reactions induced by the interaction of high-energy particles with CNO nuclei in the interstellar medium (Lemoine et al., 1998; Fields and Olive, 1999). Additionally, GCR nucleosynthesis allows one to explain LiBeB abundances and isotopic ratios, although only in the late 90s was it made clear that additional sources for the production of ^{7}Li and ^{11}B were needed. An indisputable "signature" of the GCR action is the increase of Be and B abundances with the metallicity (Fields and Olive, 1999; Prantzos, 2012; Prantzos et al., 2017). For Milky Way disc stars with [Fe/H] larger than about −1.5, [Li/H] increases with [Fe/H] from the Spite plateau value up to its solar value (Lambert and Reddy, 2004). Nevertheless, it is widely recognized that GCR nucleosyntesis cannot account for the total lithium abundance observed in the galactic disc, and stellar nucleosynthesis contributes significantly (Prantzos et al., 2017).

Stellar burning effectively depletes LiBeB at stellar depths where temperatures of few 10^{6} K are reached, ranging from T ≈ 2 × 10^{6} K for ^{6}Li to T ≈ 4–5 × 10^{6} K for boron isotopes. Their surface abundances are strongly influenced by the nuclear burnings as well as by the extension of the convective envelope (see e.g., Deliyannis et al., 2000; Jeffries, 2006). The prediction of light element abundances in stars still represents an unsolved and challenging task for astrophysics since it strongly depends on the adopted input physics in theoretical models e.g., nuclear reaction rates, opacity of the stellar matter, equation of state, efficiency of microscopic diffusion, etc. (see e.g., Piau and Turck-Chièze, 2002; D'Antona and Montalbán, 2003; Montalbán and D'Antona, 2006; Tognelli et al., 2012) as well as on the assumed external convection efficiency. In addition, since the first observational evidences from Li abundances in Hyades (~600 My) and Pleiades (~70 My) open clusters (Spite and Spite, 1986), the light elements LiBeB problem has also been confirmed by the existence of a less-pronounced Be-dip connected with Li-dip, by the Li–Be and Be–B correlation and by the (nearly) constant B abundances in the open clusters (Boesgaard et al., 2004; Boesgaard et al., 2005; Boesgaard et al., 2019). Astronomical observations suggest that lithium and beryllium are depleted in F-type MS stars in middle-aged clusters (such as those detected in the Hyades or Praesepe, ~600 My). On the other hand, there is no evidence of this depletion in F-type PMS stars, as revealed by observations of young open clusters [for ages ≤150–200 My (Boesgaard et al., 2004; Sestito and Randich, 2005)]. The discrepancies between astronomical observations and stellar models could be overcome if non-standard stellar mixing, mainly induced by stellar rotation, is taken into account (Stephens et al., 1997; Boesgaard et al., 2016). In addition, explosive scenario could significantly contribute to the light element abundances, particularly ^{7}Li ones. Carbon-oxygen (CO) novae have been recently studied as possible contributors for galactic lithium-7 production in the work of Starrfield et al. (2019) thanks to the large contribution of ^{7}Be present in the ejected material of a Nova explosion, which later decays into ^{7}Li. Lithium and boron abundances could also be used to constrain neutrino driven nucleosynthesis, as recently suggested by Kusakabe et al. (2019).

2 THE ROLE OF THE TROJAN HORSE METHOD IN NUCLEAR ASTROPHYSICS

LiBeB are easily burnt by proton capture reactions at temperatures of few million Kelvin. At such temperatures, the (p,α) channel dominates the total proton-capture cross section. In order to evaluate the energy range at which such processes occur, the general formula of the Gamow window could be applied (Rolfs and Rodney, 1988):

$$E_0 = 1.22\left(Z_x^2 Z_X^2 \mu T_6^2\right)^{\frac{1}{3}} \text{ keV}$$

$$\Delta E_0 = 0.749\left(Z_x^2 Z_X^2 \mu T_6^5\right)^{\frac{1}{6}} \text{ keV},$$

[1]Here, *Li* is the sum of lithium-6 and lithium-7 abundances. BBN predicts ^{6}Li abundances lower that the ^{7}Li ones. Metal-poor main sequence stars exhibit a negligible amount of ^{6}Li compared to the ^{7}Li ones (Lind et al., 2013).

where E_0 is the central energy and ΔE_0 the Gamow window's width, Z_x and Z_X are the atomic numbers of the two interacting particles, μ their reduced mass and T_6 the temperature of the stellar plasma in million degrees Kelvin. **Table 1** summarizes the value of E_0 and ΔE_0 for the proton induced reactions on LiBeB of interest for the stellar burning conditions as given in **Section 1**.

At such energies, the direct measurement of a charged-particle-induced reaction cross section is hindered by the Coulomb barrier penetration probability, which suppresses nuclear cross sections to the nano or picobarn scale. Moreover, a further difficulty in performing ultra-low energy cross section measurements is related to the presence of the electron screening effect due to the electronic cloud surrounding the interacting particles in a terrestrial laboratory measurement (Rolfs and Rodney, 1988). Indeed, nuclear reaction cross sections measured in the laboratory exhibit an enhancement, with respect to the bare-nucleus ones, given by (Rolfs and Rodney, 1988)

$$f_{enh} = \frac{\sigma_{sh}}{\sigma_b} \approx \exp\left(\pi\eta \frac{U_e}{E}\right), \tag{1}$$

σ_{sh} being the shielded nuclear cross section measured in the laboratory, σ_b the bare-nucleus cross section, η the Sommerfeld parameter (Rolfs and Rodney, 1988) and U_e the electron screening potential in the laboratory. The combined effects of Coulomb barrier penetration and electron screening make it difficult to access the Gamow energy window, leaving extrapolation as the most common way to extract the S(E)-factor

$$S(E) = E\sigma(E)exp(2\pi\eta) \tag{2}$$

down to the relevant energies.

The knowledge of the $S(E)$-factor allows us to evaluate the reaction rate through the following formula:

$$N_A\langle\sigma v\rangle = \left(\frac{8}{\pi\mu}\right)^{\frac{1}{2}} \frac{N_A}{(kT)^{\frac{3}{2}}} \int_0^\infty S(E) e^{-2\pi\eta - \frac{E}{kT}} dE \tag{3}$$

where E is the center-of-mass energy.

Extrapolation procedures are difficult to perform, as the electron screening phenomenon is far from completely understood. Indeed, large deviations are present when comparing the electron screening potential U_e values intervening in Eq. 1, as deduced in the laboratory alongside the ones predicted by theoretical models. Such a deviation inevitably makes extrapolation procedures difficult, as the enhanced cross section values measured in a laboratory cannot properly be revealed from any electron screening potential value known *a priori* (Adelberger et al., 2011).

Thanks to the development of experimental techniques and the improvement of devoted theoretical formalism, several indirect methods have been proposed in the last years to access the astrophysically relevant energy region without the use of any extrapolation procedure (Tribble et al., 2014). Among them, the Trojan Horse Method is a powerful tool for measuring the bare-nucleus cross section of a binary reaction of interest for astrophysics at Gamow energies without the influence of Coulomb suppression or electron screening phenomena.

THM allows us to extract the cross section of an astrophysically relevant $A(x, c)C$ reaction by selecting the quasi-free (QF) component of a suitable $2 \rightarrow 3$ body reaction $a(A, cC)s$ (Baur, 1986; Spitaleri, 1991; Spitaleri et al., 2003; Spitaleri et al., 2004; Tribble et al., 2014; Spitaleri et al., 2016; Spitaleri et al., 2019). Nucleus a, called the "Trojan-horse (TH) nucleus", exhibits a dominant $a = x \oplus s$ cluster configuration probability with a low $x - s$ binding energy. In addition, the radial wave function for the $x - s$ configuration is known from independent studies. The $2 \rightarrow 3$ body reaction occurs at energies higher than the $A + a$ Coulomb barrier, thus causing the breakup of a into its components x and s directly in the nuclear field. In the quasi-free conditions, the "spectator" s maintains in the exit channel the same momentum distribution it had in a before the occurrence of the break-up, i.e., only x takes part to the binary reaction as "participant". The role of the $x - s$ binding energy is of primary importance since it allows for compensating the energy of the incoming projectile down to astrophysical energies (Tribble et al., 2014; Spitaleri et al., 2016; Spitaleri et al., 2019). Thus, THM data will be not affected by Coulomb barrier penetration effects or screening phenomena (Assenbaum et al., 1987) since the interaction $A - x$ switches on in the nuclear field.

Taking advantage of the Plane Wave Impulse Approximation (PWIA), it is possible to relate the $a(A,cC)s$ reaction cross section to the $A(x,c)C$ one through the relation (Tribble et al., 2014; Spitaleri et al., 2016; Spitaleri et al., 2019):

$$\frac{d^3\sigma}{dE_c d\Omega_c d\Omega_C} \propto \mathrm{KF} \cdot \left|\Phi\left(\overrightarrow{p_{xs}}\right)\right|^2 \cdot \left.\frac{d\sigma}{d\Omega}\right|_{cm}^{HOES} \tag{4}$$

where:

- the kinematical factor KF is function of masses, momenta and angles of the outgoing particles;
- $\left|\Phi\left(\overrightarrow{p_{xs}}\right)\right|^2$ is the squared modulus of the Fourier transform of the radial wave function for the $x - s$ motion. Depending on the selected TH-nucleus, it can be described through the Hulthén, Hänkel or Eckart functions;
- $d\sigma/d\Omega|_{cm}^{HOES}$ is the half-off-energy-shell (HOES) $A(x,c)C$ differential cross section at the center of mass energy $E_{cm} = E_{cC} - Q$. Q is the $A(x,c)C$ Q-value while E_{cC} is the relative c–C energy measured in laboratory. This quantity is the HOES

TABLE 1 | Central energy and width of the Gamow windows for the proton-induced reactions on LiBeB at temperatures, typical of their stellar burning as discussed in **Section 1**, expressed in millions of Kelvin.

Isotope	T (MK)	E_0 (keV)	ΔE_0 (keV)
^{6}Li	2.5	4.44	2.26
^{7}Li	2.5	4.47	2.27
^{9}Be	3.5	6.84	3.32
^{10}B	5	10.10	4.82
^{11}B	5	10.13	4.83

since the transferred particle x, with mass m_x, is *virtual*; the corresponding energy and momentum do not obey the mass-shell equation $E_x = k_x^2/(2m_x)$. In QF conditions, the relative $A - x$ energy is given by $E_{Ax} = p_{Ax}^2/(2\mu_{Ax}) - \epsilon_{sx}$, being ϵ_{sx} the binding energy of the TH-nucleus. Since the outgoing c–C particles are "real", the energy-momentum relation is restored in the exit channel (Tribble et al., 2014).

More advanced techniques have also been developed for resonant reactions (see for instance Sergi et al., 2015) together with the modified R-matrix approach of Mukhamedzhanov et al. (2008), La Cognata et al. (2011) for multiresonant reactions (Guardo et al., 2017; Indelicato et al., 2017; Tumino et al., 2018). Recently, an extension to RIB's induced reactions has been also provided, as discussed in Cherubini et al. (2015), Pizzone et al. (2016), Lamia et al. (2019).

3 STUDY CASES: LiBeB BURNING REACTIONS

The THM has largely been applied to shed light on cross section measurements for the light element burning processes. In the following, some of the most important results concerning the study of the ^{6,7}Li(p,α)^{3,4}He, ^{9}Be(p,α)^{6}Li and ^{10,11}B(p,α)^{7,8}Be reactions will be reported.

3.1 The ^{6}Li(p,α)^{3}He Burning Reaction

3.1.1 Direct Measurement

The ^{6}Li(p,α)^{3}He reaction has been studied at low energies (<1 MeV) by several groups. Among them, the direct measurement of Engstler et al. (1992) covers the energy range between 10 and 500 keV and provides an extrapolated S(E)-factor to zero energy $S(0) = 3.09 \pm 1.23$ MeV barns, where the 40% error accounts for the uncertainty on the absolute cross section. Concerning the electron screening potential, the authors derived a value of $U_e = 470 \pm 150$ eV (by considering cross section measurements on atomic lithium targets) and $U_e = 440 \pm 150$ eV (by considering cross section measurements on molecular lithium targets). The direct measurements by Cruz et al. (2005), Cruz et al. (2008) provide the most recent direct study of the ^{6}Li(p,α)^{3}He reaction. The energy ranges spanned 30–100 keV and 90–1740 keV, respectively, using different lithium-implanted targets. The extrapolated zero-energy S(E)-factor was $S(0) = 3.52 \pm 0.08$ MeV barns, while the extracted electron screening potential was $U_e = 237 \pm 111$ eV (Li_2WO_4 target) (Cruz et al., 2008).

The theoretical value provided by the adiabatic limit is $U_e^{ad} = 175$ eV.

3.1.2 Trojan Horse Method Measurement

The THM low-energy investigation of the ^{6}Li(p,α)^{3}He reaction was performed in two different measurements. In Tumino et al. (2003), the ^{6}Li(p,α)^{3}He reaction was studied by means of THM applied to the ^{2}H(^{6}Li,α^{3}He)n QF reaction. The experiment was performed at Laboratori Nazionali del Sud in Catania by means of a 25 MeV ^{6}Li beam provided by the SMP Tandem van de Graaff accelerator, which was delivered on a 250 μg/cm^2-thick deuterated polyethylene CD_2 target. Beam energy and angular displacement of the detection setup were selected following the standard procedure for THM experiments, as discussed in Spitaleri et al. (2016).

Silicon position-sensitive detectors (PSD) were placed inside the CAMERA2000 scattering chamber to cover the phase space region where the quasi-free reaction mechanism is expected to be dominant. Kinematical conditions allowed us to measure the excitation function in a center-of-mass energy range from 2 MeV down to 40 keV. In order to get the ^{6}Li(p,α)^{3}He reaction cross section in absolute units, TH data have been normalized to direct data from Engstler et al. (1992). The zero-energy S(E)-factor obtained was $S(0) = 3.00 \pm 0.19$ MeV barns. The error is only statistical, while an additional ~11% error was due to the normalization procedure.

The second THM study (Tumino et al., 2004) was performed at the 4 MV Tandem accelerator of the Dynamitron Tandem Laboratorium in Bochum with the aim of exploring lower energies with respect the measurement of Tumino et al. (2003). For such a purpose, a 14 MeV ^{6}Li beam was used, allowing us to investigate down to about 10 keV in the center-of-mass energy. The simultaneous fit of the two THM data sets confirmed a zero energy S(E)-factor $S(0) = 3.00 \pm 0.19$ MeV barns (Tumino et al., 2003; Tumino et al., 2004). Moreover, an estimation of electron screening potential was provided: $U_e = 450 \pm 100$ eV. More details regarding the TH measurements can be found in Tumino et al. (2003) and Tumino et al. (2004). Pizzone et al. (2005) evaluated the reaction rate, taking into account TH bare-nucleus cross section and evaluating its impact on the lithium abundance during the PMS phase.

In Lamia et al. (2013) a new evaluation of the ^{6}Li(p,α)^{3}He S(E)-factor was performed due to the recent availability of direct data. In detail, the direct measurements of Cruz et al. (2008) were included in the data set necessary for THM normalization together with the ones available in the NACRE compilation (Angulo et al., 1999). A new normalization procedure was consequently made for the THM data (Tumino et al., 2004) with the advantage of the small uncertainties on the new set of direct data (Cruz et al., 2008). The final result of the investigation made in Lamia et al. (2013) is reported in **Figure 1** as red squares, while black dots represent TH data from Tumino et al. (2003). The two TH data set have been fitted with a third-order polynomial function (black line in **Figure 1**) with the aim of extracting the zero-energy S(E)-factor:

$$S(E) = 3.44 - 3.50E + 1.74E^2 + 0.23E^3 \ \text{MeV barns} \quad (5)$$

The obtained value was $S(0) = 3.44 \pm 0.35$ MeV barns, where the quoted error accounts for the statistical error on the TH experimental points (~7% an average) and on the direct data as well (~7% an average), while a ~3% uncertainty was due to the normalization procedure.

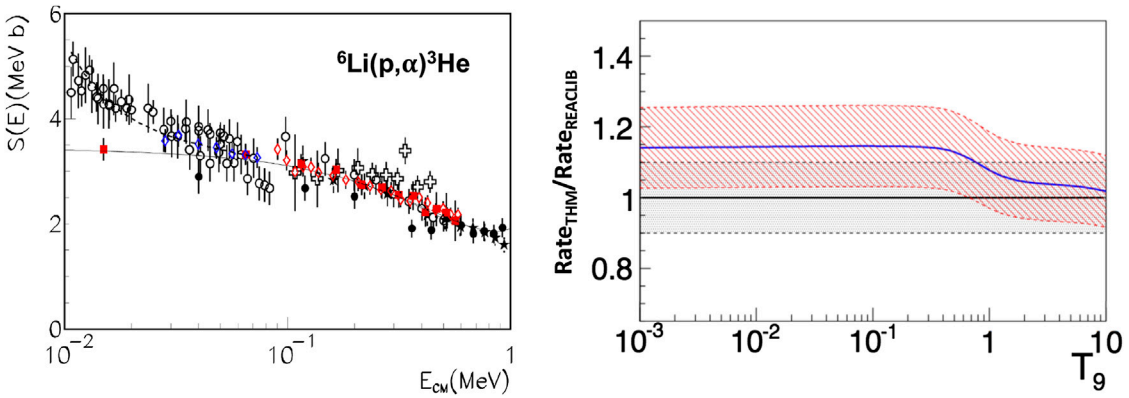

FIGURE 1 | Left panel S(E)-factor for the ^{6}Li(p,α)^{3}He reaction. TH data from Lamia et al. (2013) (red squares) normalized to the available direct measurements of Elwyn et al. (1979), Kwon et al. (1989), Cruz et al. (2008). Black dots represent TH data from Tumino et al. (2003). The full line is the result of the polynomial fit of TH data. Dashed line is the result of the fit of Engstler et al. (1992) and Cruz et al. (2005) data to extract the electron screening potential. Right panel The ratio between the THM reaction rate of Lamia et al. (2013) compared with the one reported in Cyburt et al. (2010) [Figures adapted from Lamia et al. (2013)].

The electron screening potential was then extracted following the standard procedure adopted for these kinds of measurements so far, i.e., by fitting the low-energy (<70 keV) data of Engstler et al. (1992) and Cruz et al. (2005) via Eq. 1, considering the bare-nucleus cross section given by Eq. 5 and leaving U_e as the only free parameter. This led to the value of U_e = 355 ± 100 eV, where the error takes into account a ~12% related to the uncertainties in the low-energy direct data of Engstler et al. (1992) (more details in Lamia et al., 2013). The result of the fit is shown in **Figure 1** (left side) as dashed line.

Lamia et al. (2013) provide also a new evaluation of the ^{6}Li(p,α)^{3}He reaction rate at astrophysical energies, deduced via Eq. (3). The reaction rate given in Lamia et al. (2013) was then compared with the one reported in the JINA-REACLIB compilation (Cyburt et al., 2010), as reported in the left panel of **Figure 1**. The TH result deviates at low temperatures from the one of Cyburt et al. (2010), showing an increase of about ~5–15% as the temperature decreases from 1 down to 10^{-3} T$_9$.

The astrophysical impact of the TH reaction rate (with respect to the one from the widely used NACRE compilation) was evaluated by Lamia et al. (2013) in which the focus was on PMS stellar models by use of the FRANEC stellar evolution code (Degl'Innocenti et al., 2008; Dell'Omodarme et al., 2012; Tognelli et al., 2012). The greatest differences are present for those stars that efficiently burn ^{6}Li, which correspond to stars in the mass interval 0.6–1.2M$_\odot$; in this case, the adoption of the recent TH reaction rate reduces the lithium abundance by ~15%. However, the current ^{6}Li reaction rate and its estimated uncertainty introduce variations on the surface lithium abundance in stellar models that are less important than those caused by the uncertainties on other physics input and parameters used in stellar evolutionary codes, such as the uncertainty on the radiative opacity, equation of state, outer boundary conditions, convection efficiency and initial chemical composition (see, e.g., Tognelli et al., 2012).

3.2 The ^{7}Li(p,α)^{4}He Burning Reaction

3.2.1 Direct Measurements

Several direct cross section measurements were dedicated to the study of the ^{7}Li(p,α)^{4}He reaction. A thorough list is reported in Lamia et al. (2012a) together with the results in terms of S(E)-factor and electron screening potential. In particular, Engstler et al. (1992) measured the ^{7}Li(p,α)^{4}He reaction over the c.m. energy range from ~1 MeV down to ~30 keV. The extrapolated zero-energy S(E)-factor was $S(0)$ = 59 ± 23 keV barns, where the error is derived from the absolute cross-section determination, while the obtained electron screening potential values were U_e = 300 ± 280 eV for atomic lithium target and U_e = 300 ± 160 eV for molecular lithium target. The experimental results in Engstler et al. (1992) are included in the NACRE compilation (Angulo et al., 1999). The latest direct measurements are discussed in Cruz et al. (2005) and Cruz et al. (2008). The two measurements covered the following c. m. energy range 30–100 keV and 90–1740 keV respectively, providing a data set with lower uncertainties with respect previous measurements. To extract the zero-energy S(E)-factor, data have been fitted by an R-matrix calculation, obtaining $S(0) = 55.6^{+0.8}_{-1.7}$ keV barns. The measured electron screening potential was $U_e = 237^{+133}_{-77}$ eV. For completeness, we report the theoretical value U_e^{ad} = 175 eV provided by the adiabatic limit.

3.2.2 Trojan Horse Method Measurements

A number of THM experiments have been dedicated to the study of the ^{7}Li(p,α)^{4}He reaction. In particular, the TH measurement of the low-energy ^{7}Li(p,α)^{4}He bare-nucleus S(E)-factor was reported in Aliotta et al. (2000), Lattuada et al. (2001) while an extended measurement also at higher energies (i.e., up to ~3 MeV in center of mass) was reported in Tumino et al. (2006). In both the experimental works Aliotta et al. (2000) and Lattuada et al. (2001), the deuteron was used as the TH nucleus because of its p⊕n structure. In Tumino et al. (2006), ^{3}He was instead used because of its p⊕d structure. The agreement between the two

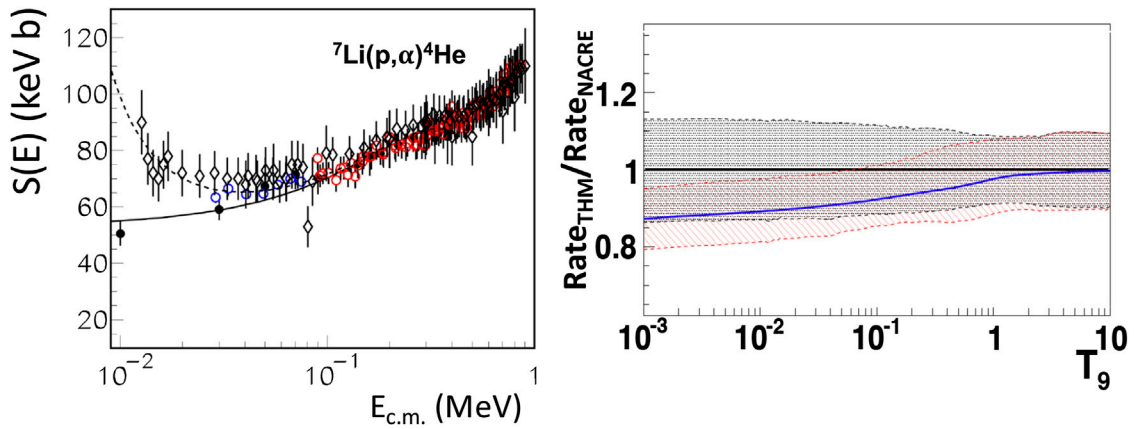

FIGURE 2 | Left panel S(E)-factor for the ^{7}Li(p,α)^{4}He reaction. Black dots are TH data after the new normalization to Cruz et al. (2008). Red and blue circles represent data from Cruz et al. (2005) and Cruz et al. (2008), respectively. Open diamonds represent Engstler et al. (1992) data. The full line is the result of the polynomial fit of TH data, while the dashed line is the fit to the low-energy (<60 keV) direct data of Engstler et al. (1992) and Cruz et al. (2005). Right panel The ratio between the THM reaction rate of Lamia et al. (2012a) and the one of NACRE (Angulo et al., 1993) [This figure has been adapted from the ones of Lamia et al. (2012a)].

different THM measurements, where different TH-nuclei were adopted, was the experimental confirmation of the so-called "polar-invariance" of THM measurements, as extensively discussed in Pizzone et al. (2011), Pizzone et al. (2013).

Focusing on the work by Lattuada et al. (2001), the ^{7}Li(p,α)^{4}He cross section measurement was performed by applying the THM to the QF ^{2}H(^{7}Li,$\alpha\alpha$)n reaction. The experiment was performed at Laboratori Nazionali del Sud (Catania, Italy) using a ^{7}Li beam at three different energies: 19.0, 19.5 and 20.0 MeV delivered onto a 250 μg/cm^2-thick CD_2 target. The outgoing α particles were detected by means of PSD displaced in order to cover the kinematic region at which a strong contribution from the QF reaction mechanism is expected. The excitation function for the ^{7}Li(p,α)^{4}He reaction was measured in the energy range 10–400 keV. More details about the experimental setup and data analysis can be found in Lattuada et al. (2001).

To obtain the zero-energy S(E)-factor, TH data were normalized to the direct ones of Engstler et al. (1992) and then fitted via a second-order polynomial. This procedure leads to a value of S(0) = 55 ± 3 keV barns, where the error is only statistical. The data also suffer from a systematic error of ~10% caused by the normalization procedure to the direct data (Engstler et al., 1992).

The THM results were included in a review paper regarding solar fusion cross sections (Adelberger et al., 2011), where the recommended value is S(0) = 55 ± 6 keV barns.

TH data were then used to evaluate the astrophysical impact in the framework of the solar lithium problem and primordial nucleosynthesis (Pizzone et al., 2003). The obtained solar lithium abundance agree, within 5%, with the ones based on NACRE compilation (Angulo et al., 1993).

Lamia et al. (2012a) provided a new THM investigation by adopting the more recent direct measurements (Cruz et al., 2008) for re-normalizing the TH data of Lattuada et al. (2001). The improved TH S(E)-factor was fitted via a second order polynomial obtaining to the following function:

$$S(E) = 53 + 213E - 336E^2 \text{ keV barns} \quad (6)$$

being E the energy in the c.m. system. The TH S(E)-factor is reported on the left-hand side of **Figure 2** as black dots, and the figure also shows direct data from Cruz et al. (2005) and Cruz et al. (2008) (red and blue circles, respectively) and the result of the fit (Eq. 6, black line).

The obtained value for the bare-nucleus zero-energy S(E)-factor was S(0) = 53 ± 5 keV barns, where the error takes into account a ~4% related to the normalization procedure, a ~6% due to the statistics of the TH data and to an error of ~6% related to the uncertainty of the direct data average (Cruz et al., 2008), as discussed in details in Lamia et al. (2012a).

Thanks to the low-energy behavior of the ^{7}Li(p,α)^{4}He bare-nucleus cross section given by Eq. 6, the electron screening potential was determined by fitting the low-energy (<60 keV) direct data of Engstler et al. (1992) and Cruz et al. (2005) with Eq. (1). The obtained value for the electron screening potential was U_e = 425 ± 60 eV, where the error is mainly due to the ~14% uncertainty on data from Engstler et al. (1992). The resulting fitting curve is shown in **Figure 2** (left side) as a dashed line, while open diamonds represent (Engstler et al., 1992) data.

In order to evaluate the astrophysical impact of the new ^{7}Li(p,α)^{4}He S(E)-factor, the reaction rate was then calculated in the temperature range ~0.01 < T_9 < ~2. The reaction rate deviates from ~5 to ~13% as the temperature decreases from T_9 = 1 down to $T_9 = 10^{-3}$ with respect the NACRE one (see right panel of **Figure 2**). This called for further evaluations on astrophysical sites. In particular, the impact of the TH reaction rate was evaluated on a solar-metallicity RGB star. The authors found no significant variations of lithium abundance (Lamia et al., 2012a). In the case of primordial BBN, ^{7}Li is mainly burnt

TABLE 2 | List of the extracted S(0) factor and the electron screening potential U_e value of different direct measurements of ^{9}Be destroyed reactions.

References	Energy range	$S(0)\|^{(p,\alpha)}$	$S(0)\|^{(p,d)}$	U_e
	keV	MeV barns	MeV barns	eV
Sierk and Tombrello (1973)	28–697	17^{+25}_{-7}	17^{+25}_{-7}	
Zahnow et al. (1997)	16–390	16.1 ± 0.5	14.5 ± 0.5	900 ± 0.5
Brune et al. (1998)	77–321	16.9	15.1	806
Kaihong et al. (2018)	18–100	16.2 ± 1.8	17.4	545 ± 98
Zhang et al. (2020)	18–100	17.3 ± 2.1	13.9 ± 1.8	512 ± 77

through its (p,α) destruction channel while ^{7}Be come into play for its production. The role of ^{7}Li(p,α)^{4}He has been thus also taken into account in the work of Pizzone et al. (2014), and, more recently, the neutron-induced reactions on ^{7}Be have also been evaluated (Barbagallo et al., 2016; Damone et al., 2018; Lamia et al., 2019). Such studies conclude that it is unlikely that the solution of ^{7}Li cosmological problem could be related to these nuclear physics processes.

3.3 The ^{9}Be(p,α)^{6}Li Burning Reaction

3.3.1 Direct Measurements

In astrophysical environments, ^{9}Be is mainly depleted by proton capture via the ^{9}Be(p,α)^{6}Li and ^{9}Be(p,d)^{8}Be reactions within a Gamow energy (E_G) ranging from about 3 keV (for stellar nucleosynthesis) to 100 keV (for primordial nucleosynthesis), which makes it an exquisite probe of depletion mechanisms in stellar evolution and inhomogeneous BBN.

In order to accurately calculate the depletion of ^{9}Be, the cross sections for these reactions must be known at Gamow energies. Several direct measurements of the ^{9}Be(p,α)^{6}Li and ^{9}Be(p,d)^{8}Be reactions at low energies have been reported (Sierk and Tombrello, 1973; Zahnow et al., 1997; Brune et al., 1998; Kaihong et al., 2018; Zhang et al., 2020), as listed in **Table 2**. However, reaction rates for the ^{9}Be destruction channels still come with large uncertainties owing to large errors induced by extrapolation to the low energy of astrophysical interest.

3.3.2 Trojan Horse Method Measurements

The THM has been used in order to extract the bare-nucleus S(E)-factor of the ^{9}Be(p,α)^{6}Li reaction at astrophysical energies avoiding extrapolations free of Coulomb suppression and electron screening effect.

The first indirect measurement of the ^{9}Be(p,α)^{6}Li S(E)-factor was carried out at INFN-LNS in Catania (Romano et al., 2006), using THM by properly selecting the QF-contribution of the three-body reaction ^{2}H(^{9}Be,α^6Li)n. Deuterons were used as TH nuclei because of the obvious $d = (p \oplus n)$ structure with a weak binding energy of 2.225 MeV and the $p - n$ relative motion mainly occurring in s-wave. The experiment was performed by using a 22 MeV, 2–5 pnA ^{9}Be beam impinging onto a 190 μg/cm^2-thick deuterated polyethylene target CD_2. Particle detection was performed by using two silicon ΔE – E telescopes in coincidence, with a PSD as the E stage. Angular distributions were investigated, thus allowing us to study the resonant contribution at ~250 keV (^{9}Be-p c.m. energy) due to the population of the 6.87 MeV ^{10}B ($J^\pi = 1^-$) excited level. The preliminary astrophysical S(E)-factor was then extracted and compared to direct data, although the poor energy resolution (~90 keV) prevented us from accessing the S(0)-factor and determining the electron screening potential. More details about the adopted experimental setup and data analysis can be found in Romano et al. (2006).

To completely study the reaction, and thanks to both experimental and theoretical improvements to the method, a further THM experiment has been performed at the CIAE (China Institute of Atomic Energy, Beijing, China) (Wen et al., 2008; Wen et al., 2011; Wen et al., 2016). The ^{9}Be beam energy was 22.35 MeV. A strip CD_2 target of about 155 μg/cm^2 in thickness and 1.5 mm in width was used in order to limit the beam spot size and decrease the angle uncertainty.

Here, experimental results reported in Wen et al. (2008) are discussed. For the first time, an intermediate process, $^9Be + {}^2H \rightarrow {}^9Be + p + n$, was considered as one criterion of the QF condition. As a result, most of the sequential decay processes were eliminated by using the new QF-selection, as seen in **Figure 3**. In order to obtain the astrophysical S(E)-factor, the experimental TH data have then been normalized to the direct ones (Zahnow et al., 1997), thus allowing us to get a zero-energy S(E)-factor $S(0)$ = 21.0 ± 0.8 MeV barns. The THM S(E)-factor is reported in **Figure 4** as red points. From the comparison with low-energy data of Zahnow et al. (1997), the electron screening potential energy U_e = 676 ± 86 eV was extracted. This value is significantly higher than that predicted by current theoretical models (U_e^{ad} = 240 eV), whereas it is lower than U_e = 900 eV or U_e = 830 eV (Zahnow et al., 1997), being the second value extracted from direct measurements with inclusion of the −26 keV subthreshold resonance due to the 6.56 MeV ^{10}B level (Zahnow et al., 1997).

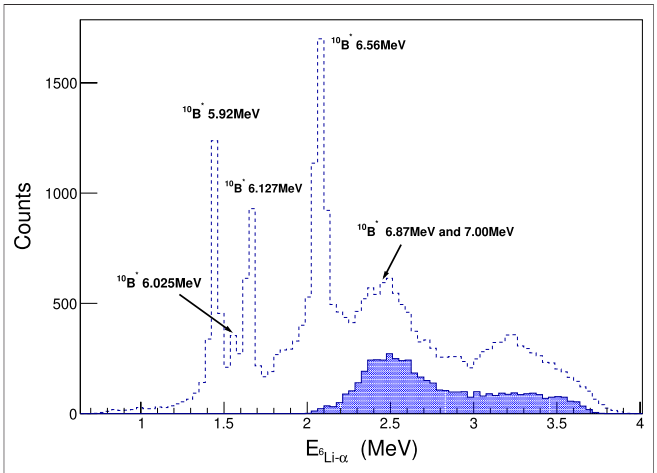

FIGURE 3 | The spectrum of $E_{^6Li-\alpha}$ with QF-cut. The filled solid histogram is restricted by the condition that the assumed intermediate breakup process ^{9}Be + ^{2}H → ^{9}Be + p + n is one criterion of the QF process. Without this restriction, the energy region of the QF process overlaps with that of the sequential decay via the 5.92, 6.025, 6.127, 6.56, 6.87 and 7.00 MeV ^{10}B levels (dashed histogram). The picture is adapted from ref. Wen et al. (2008).

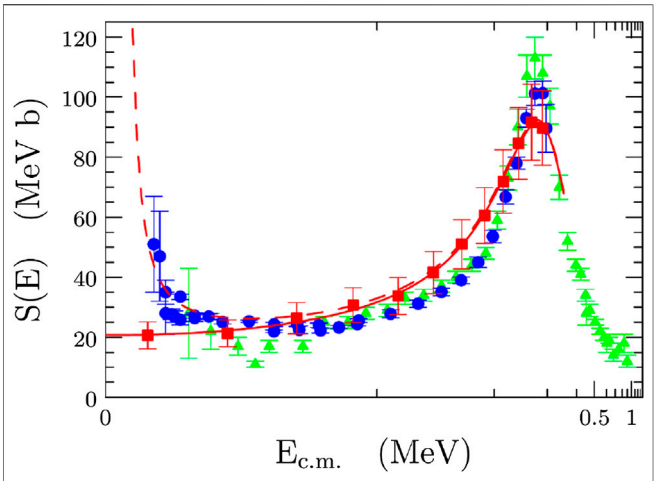

FIGURE 4 | The S(E)-factor of ^{9}Be(p,α)^{6}Li via THM (red points) compared to the direct data (green and blue points). The solid red curve describes the fit of the bare-nucleus THM data, leading to $S(0)$ = 21.0 ± 0.8 MeV barns. The red dashed line describes the enhancing caused by electron screening effects with a fitted value of U_e = 676 ± 86 eV, as given in Wen et al. (2008).

The U_e value is sensitive to low energy points; if compared with another set of direct data from Kaihong et al. (2018), the extracted U_e will be about 500 eV.

The measured THM zero-energy S(E)-factor deviates by a factor 1.23 from the one of the NACRE compilation, which adopts a low-energy extrapolation, leading to $S(0) = 17^{+25}_{-7}$ MeV barns. In Lamia et al. (2015) the astrophysical impact of THM S(E)-factor is evaluated. The reaction rate at astrophysical energies has been deduced via Eq. 3 by using the p + ^{9}Be bare-nucleus S(E)-factor of Wen et al. (2008) integrated from 200 keV down to about 10 keV. An analytical form of the thermonuclear reaction rate was derived as the following:

$$N_A\langle\sigma v\rangle = \exp\left[a_1 + \frac{a_2}{T_9} + \frac{a_3}{T_9^{1/3}} + a_4 \times T_9^{1/3} + a_5 \times T_9 + a_6 \times T_9^{5/3} + a_7 \times \ln T_9\right] \quad (7)$$

where the a_i coefficients have been left as free parameters for the ^{9}Be(p,α)^{6}Li reaction. The temperature T_9 is expressed in units of 10^9 K and the final reaction rate given in (cm^{3}mol^{-1}s^{-1}). The resulting a_i coefficients are listed in Lamia et al. (2015). As discussed in Lamia et al. (2015), at temperatures lower than 10^8 K, the THM S(E)-factor reduces the reaction rate uncertainties from 70–90% (Angulo et al., 1999) to about 20%.

The impact of such a variation on the surface beryllium abundance of PMS stars was investigated in Lamia et al. (2015). In stars, beryllium is destroyed by two reactions, 1) ^{9}Be(p,α)^{6}Li (R_1) and 2) ^{9}Be(p,2α)^{2}H (R_2). At temperatures typical of ^{9}Be burning, the reaction rates have a ratio $R_1/R_2 \approx 1.2$, and the two channels are thus both important to correctly follow the temporal evolution of ^{9}Be abundance. The impact of upgrading only the first channel is thus partially masked by the fact that the second is unmodified. The total expected variation of the resulting ^{9}Be destruction rate due to only the upgrade of R_1 is thus smaller than the actual relative change of R_1. With respect to NACRE, the TH reaction rate is about 25% larger but, for what we just discussed, the net effect on beryllium destruction rate is expected to be of the order of 14%. As expected, the adoption of TH reaction rate reduces the level of Be destruction in stars at a given age. The effect depends on the stellar mass, and only in the case of stars that show a large Be depletion ($0.10 \leq M/M_{\odot} \leq 0.45$), the reaction rate upgrade significantly affects surface ^{9}Be abundance up to a difference of 0.3–0.4 dex in the surface logarithmic abundances.

3.4 The ^{10}B(p,α)^{7}Be Burning Reaction

3.4.1 Direct Measurements

Because of the presence of a $l = 0$ resonance at 10 keV (^{10}B–p c.m. system energy), the experimental measurement of the ^{10}B(p,α)^{7}Be reaction S(E)-factor at energies of astrophysical interest is very important to the avoidance of possible uncertainties caused by the extrapolation procedure. This resonance, due to the 8.699 MeV $J^{\pi} = 5^{+}/2$ of ^{11}C, rises exactly at the Gamow energy for typical boron quiescent burning (see **Table 1**). The ^{10}B(p,α)^{7}Be reaction has been studied by many groups in the past, but only two direct measurements (Youn et al., 1991; Angulo et al., 1993) have provided an estimation of the S(E)-factor at the Gamow energy by means of an extrapolation procedure from data at higher energy. In particular, Angulo et al. (1993) declared for the S(E)-factor at the resonance energy the value of S(10) = 2,870 ± 500 MeV barns. Regarding the electron screening potential, the adopted value is U_e = 430 ± 80 eV, deduced from the direct measurement of the ^{11}B(p,α)^{8}Be S(E)-factor under the hypothesis of no isotopic dependence of U_e (Assenbaum et al., 1987). The theoretical value provided by the adiabatic limit is U_e^{ad} = 340 eV.

The ^{10}B(p,α)^{7} Be astrophysical S(E)-factor is enhanced both by the presence of the 10 keV resonance and by the effect of electron screening. In this framework, indirect low-energy measurements of the ^{10}B(p,α)^{7}Be cross section performed with the THM are pivotal to disentangling the two components and avoiding possible uncertainty due to the extrapolation procedure. Unfortunately, high-energy data available in literature until recently did not provide a reliable reference for normalization. Indeed, the energy range between 200 keV and 2 MeV was poorly explored, and there was some tension between the two existing data sets (see **Figure 6**). Moreover, direct data from Youn et al. (1991), between 200 and 500 keV, were scaled by a factor of 1.83 to obtain a better agreement with lower-energy data.

3.4.2 ^{10}B(p,α)^{7}Be Cross Section Measurements via Activation Method at Legnaro National Laboratories

To solve the discrepancies existing in the intermediate energy range, a number of new measurements have been performed recently at different facilities, including one experiment at the Legnaro National Laboratories (Italy).

At stellar energies, the ^{10}B(p,α)^{7}Be reaction proceeds through two different transitions: it can either populate the ground state of

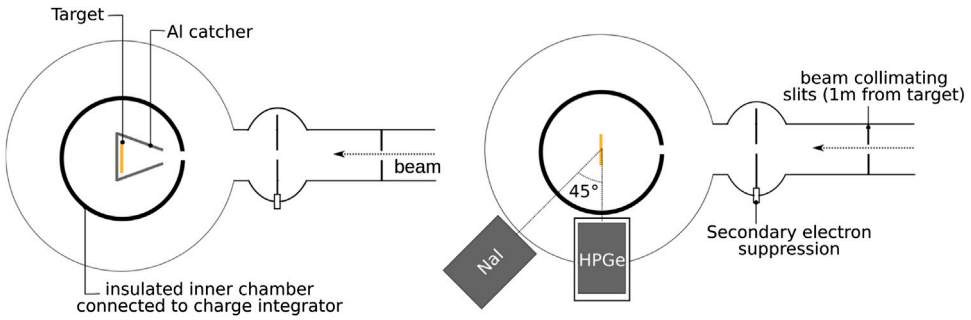

FIGURE 5 | Sketch of the experimental setup used for the study of the ^{10}B(p,α)^{7}Be reaction at LNL with the activation technique **(left)** and with prompt-gamma spectroscopy **(right)**.

^{7}Be (hereafter called the α_0 channel) or leave ^{7}Be in its first excited state (hereafter called α_1 channel), which then de-excites emitting a γ ray of E_γ = 429 keV. Subsequently, ^{7}Be decays to ^{7}Li via electron capture with a half life of 53.22 days. Then, 10.44% of these decays in turn populate the first excited state of ^{7}Li, which then goes to the ground state by the emission of a E_γ = 477.6 keV γ ray.

Because of the properties outlined above, the ^{10}B(p,α)^{7}Be reaction can be investigated with different, complementary approaches, involving the detection of α particles, gamma rays or with the activation technique (Iliadis, 2007). The latter allows us to derive the number of ^{7}Be nuclei produced by the reaction through off-beam gamma spectroscopy, detecting the 477.6 keV γ rays emitted in ^{7}Be decay. The activation technique offers the advantage of being free of beam-induced background. Moreover, counting facilities are often equipped with passive shields around the gamma detectors in order to suppress environmental radioactivity and increase the sensitivity to small cross sections. On the other hand, when counting ^{7}Be nuclei with the activation method it is not possible to disentangle the α_0 and α_1 channels. Though the α_0 channel dominates the total cross section at low energies, its contribution to the total cross section is of the order of 10% at 1 MeV.

The ^{10}B(p,α_1)^{7}Be cross section is also not well constrained at energies between 500 keV and 2 MeV. In this energy range, the dominant contribution to the cross section comes from a resonance at 1,500 keV. Two pioneering experiments performed in the 1950s (Brown et al., 1951; Day and Huus, 1954) provided contradictory results on the value of the cross section on top of the resonance. As a consequence (Day and Huus, 1954), adopted the average cross section at the peak to normalize its data. Following experiments made the picture even more complicated, finding cross sections up to a factor of two lower (Hunt et al., 1957).

Given the discrepancies existing in the literature, both in the α_0 and α_1 channel, two separate experiments were performed at the AN2000 accelerator of the INFN National Laboratories of Legnaro: the first exploited the activation method (using the formalism discussed in Scott et al. (2012), Di Leva et al. (2014) for the total cross section (Caciolli et al., 2016) and the second was devoted to detecting only the prompt γ rays produced by the α_1 channel (Caciolli et al., 2019).

The AN2000 accelerator was installed at the INFN-LNL in 1971 and can provide proton and α beams in an energy range from 250 keV up to 2.2 MeV. A sketch of the experimental setups is shown in **Figure 5**, while a detailed description of the chamber and the beam current measurement can be found in Caciolli et al. (2016), Caciolli et al. (2019).

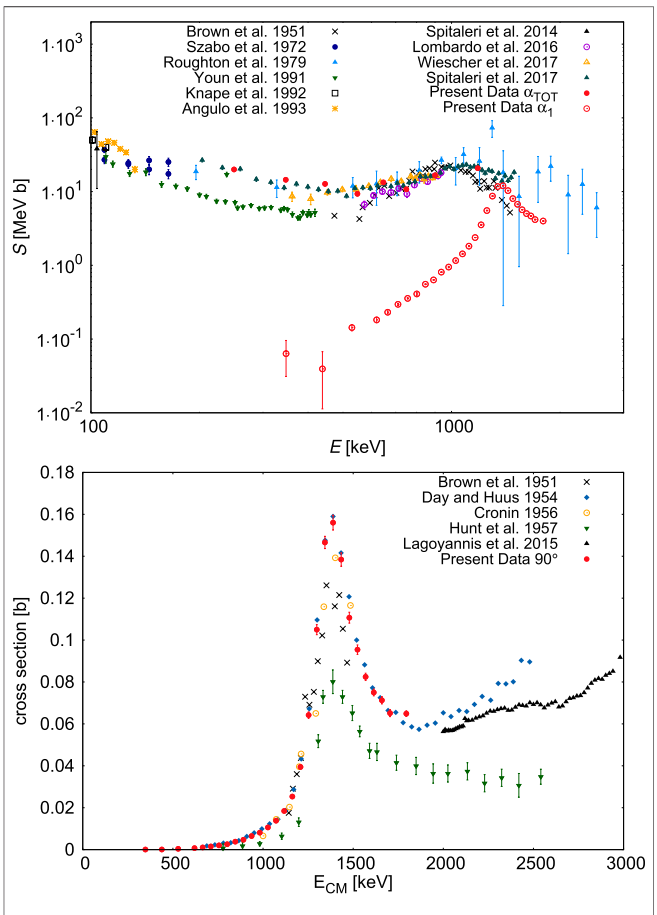

FIGURE 6 | Upper panel: Total astrophysical S(E)-factor for the ^{10}B(p,α)^{7}Be reaction. Lower panel: Cross section for the ^{10}B(p,α1)^{7}Be reaction channel.

For the measurement with the activation technique, no detectors were needed during the irradiation, and the ^{7}Be decays were counted in a dedicated low counting level facility (Caciolli et al., 2012; Xhixha et al., 2013) after removing the sample from the beamline. For the measurement of the α_1 cross section, two gamma-ray detectors were placed around the scattering chamber: a high-purity germanium detector at 90° and a sodium iodide detector at 45°.

Results from the two experiments are summarized in **Figure 6**, together with literature cross sections. ^{10}B(p,α)^{7}Be total cross section data cover the energy range $E_{c.m.}$ = 249–1,182 keV, providing a link between literature data sets in an energy region that was poorly explored. ^{10}B(p,α_1)^{7}Be data span the range $E_{c.m.}$ = 348–1795 keV and cover the resonance at 1,400 keV.

The new total cross section data are in good agreement with old data from Roughton et al. (1979), but error bars are greatly reduced. There is also a fair agreement with data from Lombardo et al. (2016), published concurrently. Present data confirm the destructive interference pattern between the 10 keV and the 500 keV resonances. This results in a decrease in the astrophysical factor above 500 keV. Below 500 keV, some tension still exists between present data and more recent results published in Wiescher et al. (2017). Further investigations will be needed to address this issue. Moreover, in order to obtain a reliable and consistent R-matrix fit of all data sets, new data extending up to 3 MeV are needed to better constraint the four resonances dominating the cross section.

3.4.3 Trojan Horse Method Measurements

A first attempt of studying the ^{10}B(p,α_0)^{7}Be reaction at stellar energies through THM was discussed in Lamia et al. (2007). Starting from that, an improved THM measurement was performed by Spitaleri et al. (2014), applying THM to the ^{2}H(^{10}B,$\alpha_0{}^{7}$Be)n three-body reaction. The experiment was carried out at LNS by means of a 24.5 MeV ^{10}B beam delivered on a 200 μg/cm^2 thick CD_2 target. The deuteron was thus used as the TH nucleus. Thanks to the devoted experimental setup, an energy resolution of ~30 keV in the ^{10}B + p c.m. system was reached, thus allowing the proper separation of the 8.699 MeV resonance of interest from the sub-threshold peak due to the population of the 8.654 MeV $J^{\pi} = 7^{+}/2$ level of ^{11}C (Spitaleri et al., 2014). By means of the standard procedure and by following the factorization reported in Eq. 4, the spectator momentum distribution and half-off energy shell cross section were deduced via the PWIA formalism. In order to extract the S(E)-factor in absolute units, TH data have been normalized to direct ones available in literature at that time (Youn et al., 1991; Angulo et al., 1993) in an energy range of 50–100 keV, where the electron screening effect is negligible. Due to the experimental resolution affecting TH data, the normalization procedure is not straightforward. The detailed procedure is described in Spitaleri et al. (2014). Authors highlighted a possible presence of systematic effects in the energy region where the two direct data sets overlap, underlining the need of a new direct measurement in this energy range (Spitaleri et al., 2014) (see also **Section 3.4**). The measured TH bare-nucleus S(E)-factor at the Gamow energy peak was S(10 keV) = 3,127 ± 583 Mev barns.

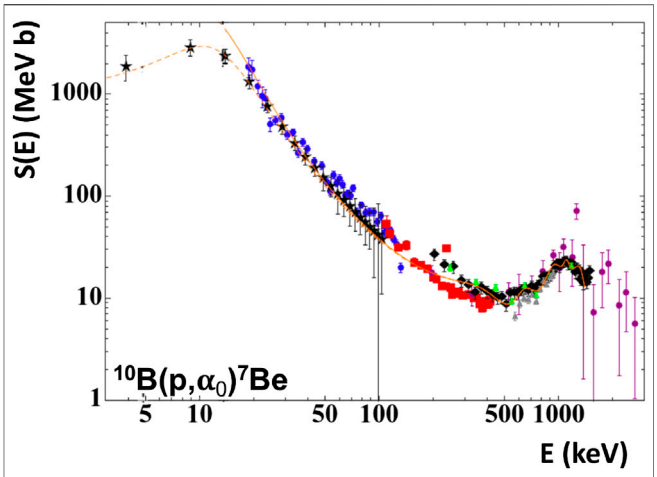

FIGURE 7 | S(E)-factor for the ^{10}B(p,α_0)^{7}Be reaction. The following data set are reported: TH data from Spitaleri et al. (2017) (black diamonds) and from Spitaleri et al. (2014) (black stars) and direct data from Caciolli et al. (2016) (green triangles), Lombardo et al. (2016) (grey triangles), Roughton et al. (1979) (purple circles), Angulo et al. (1999) (blue circles) and Youn et al. (1991) (red squares). The dashed line represent the R-matrix fit performed on TH data (Spitaleri et al., 2017). [Figure adapted from Spitaleri et al. (2017)].

As extensively described in Spitaleri et al. (2014), the effect of experimental resolution has been removed from the obtained results and the quoted error accounts for statistical, sub-threshold subtraction, normalization and channel radius uncertainties.

The THM study provided the first independent measurement of the electron screening U_e for the ^{10}B(p,α_0)^{7}Be reaction since the adopted value derived from applying the so-called isotopic independence hypothesis for electron screening. The obtained result was U_e = 240 ± 200 eV where the error derives from the uncertainties affecting TH S(E)-factor.

Thanks to the broad-energy range direct measurements of Lombardo et al. (2016), Caciolli et al. (2016) (see **Section 3.4.2**) and Wiescher et al. (2017), a further THM S(E)-factor determination was performed by Spitaleri et al. (2017). The ^{2}H(^{10}B,$\alpha_0{}^{7}$Be)n reaction measurement was performed at the Pelletron–Linac laboratory - Departamento de Fisica Nuclear (DFN) in São Paolo, Brazil. The Tandem accelerator provided a 27 MeV ^{10}B beam sent on a 200 μg/cm^2-thick CD_2 target. For the first time the astrophysical factor of the ^{10}B(p,α_0)^{7}Be reaction has been measured over a wide energy range, from 5 keV to 1.5 MeV, in a single experiment and with a reduction of the normalization error from ~18–20% to ~4%. In **Figure 7** TH data has been reported (black diamonds) together with TH data from Spitaleri et al. (2014) (black stars) and direct data from Caciolli et al. (2016) (green triangles) Lombardo et al. (2016), (grey triangles) Roughton et al. (1979), (purple circles) (Angulo et al. (1999), (blue circles) and Youn et al. (1991) (red squares). A very good agreement was found between the direct data and the TH ones. The investigation of the ^{10}B(p,α_0)^{7}Be reaction in a wide energy range suggested the performance of a devoted R-matrix fit of the deduced S(E) TH data (dashed line in **Figure 7**). The details of this calculation, together with the interesting spectroscopic implication on ^{11}C levels, are described in Spitaleri et al.

(2017). Consequently, a more accurate evaluation of the S(E)-factor was provided S(10 keV) = 2,942 ± 398 MeV barns [relative error 13.5% with respect to 18.6% in Spitaleri et al. (2014)] as well as of the electron screening potential, U_e = 240 ± 50 eV [relative error 20.8% with respect to 83.3% in Spitaleri et al. (2014)].

The latest THM study is discussed in Cvetinović et al., 2018. The experiment was performed at LNS applying THM to the ^{2}H(^{10}B,$\alpha_0{}^7$Be)n three-body reaction. Particular attention has been paid to the improvement of the experimental resolution. In particular, thanks to the reduction of the CD_2 target thickness, set at 56 μg/cm^2 (Rapisarda et al., 2018), an energy resolution of 17 keV in the ^{10}B + p c.m. system has been obtained, allowing for a better separation between the 10 keV resonance and the subthreshold level. Moreover, the experimental resolution allowed for the first time in a THM study the separation and the independent study of the α_0 (Cvetinović et al., 2018) and α_1 channel (Rapisarda et al., 2018). As a further improvement, the experimental setup allowed for a measurement of the S(E)-factor in a wide energy range from 3 keV up to 2.2 MeV expanding the explored energy range with respect to the previous THM measurement (Spitaleri et al., 2017). In this way, TH data have been normalized to the R-matrix calculation provided in Spitaleri et al. (2017) in a wide energy range, reducing the normalization error to about 2.8%. The obtained value for S(E)-factor is S(10 keV) = 2,950 ± 291 MeV barns, which is in agreement with the previous results but with a reduced relative error of 9.9%. The declared electron screening potential value is U_e = 391 ± 74 eV relative error 18.9%.

Lamia et al. (2015) provided an evaluation of the reaction rate for the ^{10}B(p,α)^{7}Be reaction based on the TH S(E)-factor from Spitaleri et al. (2014), resulting in the analytical form already given by Eq. 3 with the corresponding coefficients listed in Lamia et al. (2015). The TH reaction rate has been compared with the NACRE compilation (Angulo et al., 1999) and with the more recent NACREII (Xu et al., 2013). A first result concerned the reduction of reaction rate uncertainties at lower temperatures, that is, close to the Gamow peak typical of quiescent boron burning. Moreover, at temperatures of 2–5 × 10^6 K, the TH reaction rate deviated with respect to the NACRE one, being ~25–30% lower.

Astrophysical implications of the evaluated ^{10}B(p,α)^{7}Be burning rate on surface abundances of pre-MS stars are exhaustively discussed in Lamia et al. (2015). The reduction of the reaction rate by about 25–30% in the temperature range characteristic of the ^{10}B stellar destruction is especially relevant for stars with masses between about 0.1–0.3M$_\odot$. The TH reaction rate significantly reduces the level of ^{10}B depletion, with a logarithmic abundance variation up to 0.9–1 dex for those stars that undergo a strong surface ^{10}B depletion, as discussed in detail in Lamia et al. (2015). Unfortunately, at the moment, it is difficult to observe ^{10}B in cool stars where the largest impact of the reaction rate is expected but only few data are available to test the models predictions.

3.5 The ^{11}B(p,α)^{8}Be Burning Reaction

3.5.1 Direct Measurements

At low energies the ^{11}B(p,α)^{8}Be astrophysical S(E)-factor is characterized by the presence of two resonances that rise at about ~150 keV and ~600 keV (^{11}B – p center of mass energy) due to the formation of the 16.106 MeV ($J^\pi = 2^+$) and 16.570 MeV ($J^\pi = 2^-$) ^{12}C excited levels. In particular, the α_0 channel S(E)-factor is characterized by the presence of the l = 1 ~150 keV level superimposed on a non-resonant contribution, while the ~600 keV resonance is excluded because of spin-parity selection rules. On the other hand, both levels contribute to the reaction yield of the α_1 channel.

The direct measurements of the ^{11}B(p,α)^{8}Be reaction cross section at energy of astrophysical interest are reported in Segel et al. (1965), Davidson et al. (1979), Becker et al. (1987), Angulo et al. (1993). In particular, the extrapolated astrophysical S(E)-factor was provided in Becker et al. (1987) for α_0 and α_1 channels. The obtained values are $S(0)$ = 2.1 MeV barns (α_0) and $S(0)$ = 195 MeV barns (α_1). No evaluation of the electron screening potential was provided in Becker et al. (1987). A further measurement of the astrophysical S(E)-factor (α_0 + α_1 channels) in the energy range from E$_{cm}$ = 132 keV down to E$_{cm}$ = 18.73 keV was given in Angulo et al. (1993). In this paper, the authors declared an electron screening potential of U_e = 430 ± 80 eV. This value turns out to be higher than the upper limit provided by the adiabatic model U_e^{ad} = 340 eV, confirming the systematic discrepancy between experimental and theoretical values of the electron screening potential. All the direct measurements are above the Gamow energy and both $S(0)$ and U_e are obtained with extrapolation procedures.

3.5.2 Trojan Horse Method Measurements

The first measurement of the ^{11}B(p,α_0)^{8}Be reaction cross section covering the whole energy region of astrophysical interest was reported in Spitaleri et al. (2004). THM was applied to the three-body reaction ^{2}H(^{11}B,$\alpha_0{}^8$Be)n using a 27 MeV ^{11}B beam impinging on a CD_2 target where the deuteron provide the virtual proton. This study represented an important validity test for THM since it showed the possibility to measure resonances at low energy, below the Coulomb barrier of the interacting nuclei. The poor experimental resolution suffered by the discussed THM measurement pushed to proceed further in the experimental work, as shown in Lamia et al. (2008), Lamia et al. (2012b). THM was again applied to the ^{2}H(^{11}B,$\alpha_0{}^8$Be)n three-body reaction, and a 27 MeV ^{11}B beam was delivered on a CD_2 target about 170 μg/cm^2 thick. The detection setup allowed the detection of α particles in coincidence with ^{8}Be. α particles coming from the three-body reaction were detected by PSDs. ^{8}Be events were reconstructed following the procedure described in Spitaleri et al. (2004) and in Lamia et al. (2008) using a Dual Position Sensitive Detector made up of two PSDs mounted one above the other, and this guaranteed the coincident detection of the two α particles coming from the ^{8}Be decay. More details on the experimental setup are provided in Lamia et al. (2012b). In order to improve the experimental resolution, significant efforts were made on the selection of the quasi-free events, disentangling the events of interest from those produced by sequential mechanism (Lamia et al., 2012b). Additionally, a devoted study was performed on the neutron momentum distribution. In more detail, the

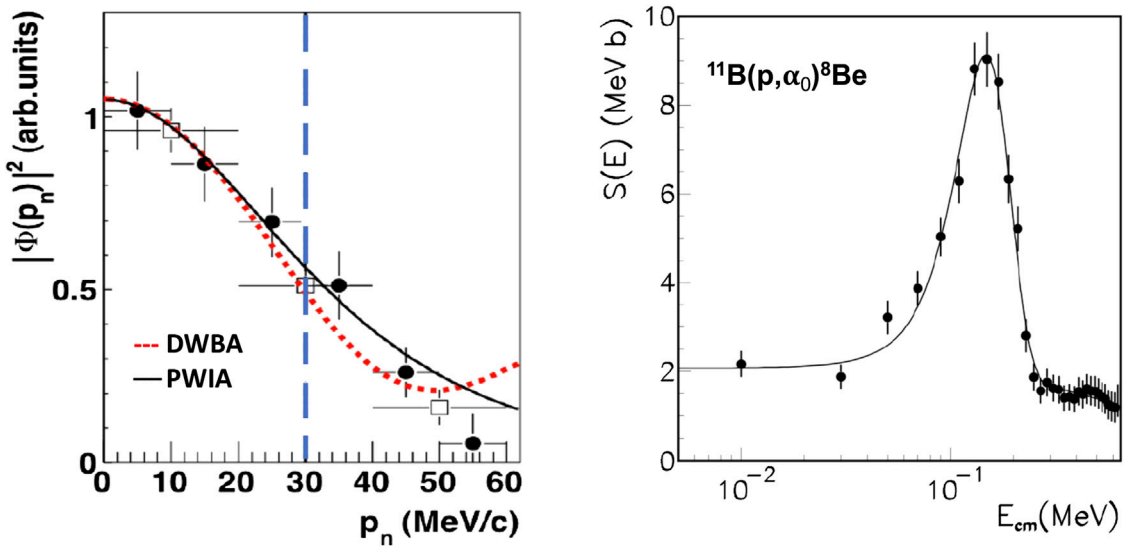

FIGURE 8 | Left panel Experimental momentum distribution of the neutron *spectator* (black and open points) compared with the Hulthén wave function in momentum space (black curve) and the DWBA calculation (red dashed). Only the data with momenta lower than 30 MeV/c were considered for the analysis. Right panel S(E)-factor for the ^{11}B(p,α_0)^{8}Be reaction. Black points represent the THM data while the solid line represents the fit given in terms of Eq. 8 [Figures adapted from Lamia et al. (2012b)].

experimental momentum distribution (black points of **Figure 8**) was compared with both PWIA (black line) and DWBA calculations (dashed line). For DWBA calculations, the FRESCO code was adopted by using optical potential parameters adjusted from those of Perey and Perey (1976), as performed in several THM papers such as La Cognata et al. (2010a), La Cognata et al. (2010b), Sergi et al. (2010). In the FRESCO calculation, optical potentials are used for the following systems: ^{2}H-^{11}B and n-^{12}C (for distorted waves evaluation in both entrance and exit channel, respectively), n-p and p-^{11}B (to calculate the bound state wave functions) and the core–core potential n-^{11}B. In total, the calculation involves several parameters besides a normalization factor, fixed by scaling the theoretical distribution to the experimental one (black dots of **Figure 8**). Both calculations agree nicely at low-neutron momenta (below 30 MeV/c for the present case), i.e., at those values of interest for THM application. This shows once more the goodness of the approach via the most simple PWIA factorization of Eq. 4 (see Lamia et al., 2012b for details).

The extracted excitation function can be described by the resonance contribution due to the resonance at E_{cm} = 150 keV (l = 1), superimposed onto a non-resonant contribution (l = 0). TH data have been normalized to direct data provided by Becker et al. (1987) after a spread-out procedure to take into account the THM experimental resolution (~40 keV). In particular the non-resonant contribution has been normalized in an energy range between 400 and 600 keV, while for the resonant part areas under the peak have been equalized. TH data have been fitted with a function given by the incoherent sum of a second order polynomial and a Gauss function in order to take in to account the non-resonant and resonant contributions to the reaction cross section, obtaining the following function:

$$S(E)_{\alpha_0}^{THM} = 2.04 - 1.37E + 0.12E^2 + 7.28 \times \exp\left[-0.5\left(\frac{E-0.148}{0.044}\right)^2\right] \text{ MeV barns} \quad (8)$$

The obtained bare-nucleus TH zero-energy S(E)-factor for ^{11}B(p,α_0)^{8}Be reaction is $S(0)$ = 2.07 ± 0.41 MeV barns, where the total error takes into account the following: the statistical error on the experimental points (~10%), the uncertainties on the normalization procedure (~10%) and the systematic

TABLE 3 | Overview of THM astrophysical S(E)-factor and electron screening potential for the discussed reactions. Theoretical values for electron screening potential according to the adiabatic approximation U_e^{ad} are reported for completeness.

Reaction	$S(0)$	U_e	U_e^{ad}	References
	MeV barns	eV	eV	
^{6}Li(p,α)^{3}He	3.00 ± 0.19	450 ± 100	175	Tumino et al. (2003), Tumino et al. (2004)
	3.44 ± 0.35	355 ± 100		Lamia et al. (2013)
^{7}Li(p,α)^{4}He	55 ± 3[a]		175	Lattuada et al. (2001)
	53 ± 5[a]	425 ± 60		Lamia et al. (2012a)
^{9}Be(p,α)^{6}Li	21.0 ± 0.8	676 ± 86	240	Wen et al. (2008)
^{10}B(p,α)^{7}Be	3,127 ± 583[b]	240 ± 200	340	Spitaleri et al. (2014)
	2,942 ± 398[b]	240 ± 50		Spitaleri et al. (2017)
	2,950 ± 291[b]	391 ± 74		Cvetinović et al. (2018)
^{11}B(p,α)^{8}Be	2.07 ± 0.41	472 ± 160	340	Lamia et al. (2012b)

[a] *keV barns*
[b] *S(E)-factor evaluated at 10 keV.*

uncertainties due to the choice of the cut-off radius in the Coulomb penetrability function (~14%). The TH $S(0)$ value and the one extrapolated from direct measurement are in agreement within the experimental errors. In the right panel of **Figure 8**, the TH S(E)-factor evaluated in Lamia et al. (2012b) is shown (black points) together with the fit obtained from Eq. 8. Taking advantage of direct data reported in Angulo et al. (1993) and of the bare-nucleus TH S(E)-factor the electron screening potential U_e has been evaluated. The extracted value U_e = 472 ± 160 eV is in agreement with the value provided in Angulo et al. (1993) U_e = 430 ± 80 eV and higher than the upper limit predicted by the adiabatic limit U_e = 340 eV (Lamia et al., 2012b).

4 CONCLUSIONS

This paper has provided a review on the experimental studies performed through the application of the Trojan Horse Method and devoted to the measurement of the light elements LiBeB burning cross section at the low energies of interest for astrophysics. Moreover, experimental results obtained by means of the activation technique have been discussed as well. For each (p,α) channel of interest in the LiBeB problem, we discussed the S(E)-factor evaluation, the determination of the electron screening potential and the reaction rate evaluation together with the comparison with the most recent direct data available in literature. **Table 3** provides an overview of the zero-energy S(E)-factor and electron screening potential values of the discussed reactions, as obtained via THM.

Despite the efforts made, open issues are still present. In addition to the nuclear astrophysics field, the study of the ^{11}B(p,α)^{8}Be is of interest also for the plasma fusion community since the ^{11}B+p process is considered one of the best candidates for the aneutronic fusion. In this framework, detailed information is needed also on the ^{11}B(p,α_1)^{8}Be reaction, whose cross section is about two orders of magnitude higher than the α_0 channel. A dedicated THM study will provide more information on the contribution of the α_1 channel (Lamia et al., 2012b).

Moreover, natural boron fuel used for aneutronic fusion is composed by ~19% of ^{10}B, whose interaction with protons produces ^{7}Be a radioactive isotope ($T_{1/2}$ = 53.22 ± 0.06 days). In order to evaluate a safe ^{11}B enrichment level to avoid radioprotection issues, an accurate measurement of the ^{10}B(p,α)^{7}Be cross-section is necessary for both α_0 and α_1 channels. In this framework, starting from the results obtained by Rapisarda et al. (2018), a new THM study will be dedicated to the ^{10}B(p,α_1)^{7}Be in a wide energy range, including the low energy of astrophysical interest.

AUTHOR CONTRIBUTIONS

Nuclear data were analyzed by G.G.R., L.L., R.D., A.C., C.L., R.G.P., S.R., C.S. and Q.W. S.D.I., E.T. and S.P. took care of the astrophysical impact of these data. All the listed authors contributed to the writing of the paper.

ACKNOWLEDGMENTS

The authors acknowledge "Programma ricerca di ateneo UNICT 2020-22 linea2" and "Starting grant 2020" of University of Catania. CL and QW acknowledge the partial support of National Natural Science Foundation of China (10575132, 11075218, 12075031). RD acknowledges funding from Italian Ministry of Education, University and Research (MIUR) through the "Dipartimenti di eccellenza" project Science of the Universe.

REFERENCES

Adelberger, E. G., García, A., Robertson, R. G. H., Snover, K. A., Balantekin, A. B., Heeger, K., et al. (2011). Solar fusion cross sections. II. The pp chain and CNO cycles. *Rev. Mod. Phys.* 83, 195–246. doi:10.1103/RevModPhys.83.195

Aliotta, M., Spitaleri, C., Lattuada, M., Musumarra, A., Pizzone, R. G., Tumino, A., et al. (2000). Improved information on electron screening in ^{7}Li(p,α)α using the Trojan-horse method. *Eur. Phys. J. A.* 9, 435–437. doi:10.1007/s100500070001

Angulo, C., Arnould, M., Rayet, M., Descouvemont, P., Baye, D., Leclercq-Willain, C., et al. (1999). A compilation of charged-particle induced thermonuclear reaction rates. *Nucl. Phys.* 656, 3–183. doi:10.1016/S0375-9474(99)00030-5

Angulo, C., Engstler, S., Raimann, G., Rolfs, C., Schulte, W. H., and Somorjai, E. (1993). The effects of electron screening and resonances in (p,α) reactions on ^{10}B and ^{11}B at thermal energies. *Zeitschrift fur Physik A Hadrons and Nuclei.* 345, 231–242. doi:10.1007/BF01293350

Assenbaum, H. J., Langanke, K., and Rolfs, C. (1987). Effects of electron screening on low-energy fusion cross sections. *Zeitschrift fur Physik A Hadrons and Nuclei.* 327, 461–468.

Barbagallo, M., Musumarra, A., Cosentino, L., Maugeri, E., Heinitz, S., Mengoni, A., et al. (2016). ^{7}Be(n,α)^{4}He reaction and the cosmological lithium problem: measurement of the cross section in a wide energy range at n_TOF at CERN. *Phys. Rev. Lett.* 117, 152701. doi:10.1103/PhysRevLett.117.152701

Baur, G. (1986). Breakup reactions as an indirect method to investigate low-energy charged-particle reactions relevant for nuclear astrophysics. *Phys. Lett. B.* 178, 135–138. doi:10.1016/0370-2693(86)91483-8

Becker, H. W., Rolfs, C., and Trautvetter, H. P. (1987). Low-energy cross sections for ^{11}B(p, 3α). *Zeitschrift fur Physik A Hadrons and Nuclei.* 327, 341–355.

Boesgaard, A. M., Armengaud, E., and King, J. R. (2004). Beryllium abundances in F and G Dwarfs in Praesepe and other young clusters from Keck HIRES observations. *Astrophys. J.* 605, 864–873. doi:10.1086/382943

Boesgaard, A. M., Deliyannis, C. P., and Steinhauer, A. (2005). Boron depletion in F and G Dwarf stars and the beryllium-boron correlation. *Astrophys. J.* 621, 991–998. doi:10.1086/427687

Boesgaard, A. M., Lum, M. G., and Deliyannis, C. P. (2019). *Correlated depletion and dilution of lithium and beryllium revealed by subgiants in M 67.* arXiv e-printsarXiv:1910.07656

Boesgaard, A. M., Lum, M. G., Deliyannis, C. P., King, J. R., Pinsonneault, M. H., and Somers, G. (2016). Boron abundances across the "Li-Be dip" in the Hyades cluster. *Astrophys. J.* 830, 49. doi:10.3847/0004-637X/830/1/49

Boesgaard, A. M., Rich, J. A., Levesque, E. M., and Bowler, B. P. (2011). Beryllium and Alpha-element abundances in a large sample of metal-poor stars. *Astrophys. J.* 743, 140. doi:10.1088/0004-637X/743/2/140

Brown, A., Snyder, C., Fowler, W., and Lauritsen, C. (1951). *Phys. Rev.* 82, 159.

Brune, C., Geist, W., Karwowski, H., Ludwig, E., and Veal, K. (1998). ^{11}B(p,α)^{8}Be and ^{9}Be(p,α)^{6}Li and reactions at low energies. *Phys.* Rev. C. 57, 3437–3446.

Caciolli, A., Baldoncini, M., Bezzon, G., Broggini, C., Buso, G., Callegari, I., et al. (2012). A new fsa approach for *in situ* γ ray spectroscopy. *Sci. Total Environ.* 414, 639–645. doi:10.1016/j.scitotenv.2011.10.071

Caciolli, A., Depalo, R., Broggini, C., La Cognata, M., Lamia, L., Menegazzo, R., et al. (2016). A new study of ^{10}B(p,α)^{7}Be reaction at low energies. *Eur. Phys. J. A.* 52, 136. doi:10.1140/epja/i2016-16136-8

Caciolli, A., Depalo, R., and Rigato, V. (2019). A new study of the ^{10}B(p,α_1)^{7}Be reaction from 0.35 to 1.8 MeV. *Eur. Phys. J. A.* 55, 171. doi:10.1140/epja/i2019-12859-2

Cherubini, S., Gulino, M., Spitaleri, C., Rapisarda, G. G., La Cognata, M., Lamia, L., et al. (2015). First application of the Trojan horse method with a radioactive ion beam: study of the ^{19}F (p,α)^{14}O reaction at astrophysical energies. *Phys. Rev. C.* 92, 015805. doi:10.1103/PhysRevC.92.015805

Coc, A., Goriely, S., Xu, Y., Saimpert, M., and Vangioni, E. (2012). Standard big bang nucleosynthesis up to CNO with an improved extended nuclear network. *Astrophys. J.* 744, 158. doi:10.1088/0004-637X/744/2/158

Coc, A., and Vangioni, E. (2017). Primordial nucleosynthesis. *Int. J. Mod. Phys. E.* 26, 1741002. doi:10.1142/S0218301317410026

Cruz, J., Fülöp, Z., Gyürky, G., Raiola, F., di Leva, A., Limata, B., et al. (2005). Electron screening in ^{7}Li(p,α)α and ^{6}Li(p, α)^{3}He for different environments. *Phys. Lett. B.* 624, 181–185. doi:10.1016/j.physletb.2005.08.036

Cruz, J., Luis, H., Fonseca, M., Fülöp, Z., Gyürky, G., Raiola, F., et al. (2008). Experimental study of proton-induced nuclear reactions in Li. *J. Phys. G Nucl. Phys.* 35, 014004. doi:10.1088/0954-3899/35/1/014004

Cvetinović, A., Spitaleri, C., Spartá, R., Rapisarda, G. G., Puglia, S. M. R., La Cognata, M., et al. (2018). Trojan horse measurement of the 10B(p,α^0)^{7}Be cross section in the energy range from 3 keV to 2.2 MeV. *Phys. Rev. C.* 97, 065801. doi:10.1103/PhysRevC.97.065801

Cyburt, R. H., Amthor, A. M., Ferguson, R., Meisel, Z., Smith, K., Warren, S., et al. (2010). The JINA REACLIB Database: its recent updates and impact on type-I X-ray bursts. *Astrophys. J. Suppl.* 189, 240–252. doi:10.1088/0067-0049/189/1/240

Damone, L., Barbagallo, M., Mastromarco, M., Mengoni, A., Cosentino, L., Maugeri, E., et al. (2018). ^{7}Be(n,p)^{7}Li reaction and the cosmological lithium problem: measurement of the cross section in a wide energy range at n_TOF at CERN. *Phys. Rev. Lett.* 121, 042701. doi:10.1103/PhysRevLett.121.042701

Davidson, J. M., Berg, H. L., Lowry, M. M., Dwarakanath, M. R., Sierk, A. J., and Batay-Csorba, P. (1979). Low energy cross sections for ^{10}B(p, 3α). *Nucl. Phys.* 315, 253–268. doi:10.1016/0375-9474(79)90647-X

Day, R. B., and Huus, T. (1954). Gamma radiation from bombarded by protons. *Phys. Rev.* 95, 1003–1006. doi:10.1103/PhysRev.95.1003

Degl'Innocenti, S., Prada Moroni, P. G., Marconi, M., and Ruoppo, A. (2008). The FRANEC stellar evolutionary code. *Astrophys. Space Sci.* 316, 25–30. doi:10.1007/s10509-007-9560-2

Deliyannis, C. P., Pinsonneault, M. H., and Charbonnel, C. (2000). "Sinks of light elements in stars - Part I (invited paper)," in *The light elements and their evolution*. Editors L da Silva, R de Medeiros, and M Spite (IAU Symposium), 198, 61.

Dell'Omodarme, M., Valle, G., Degl'Innocenti, S., and Prada Moroni, P. G. (2012). The Pisa stellar evolution data base for low-mass stars. *Astron. Astrophys.* 540, A26. doi:10.1051/0004-6361/201118632

Di Leva, A., Scott, D. A., Caciolli, A., Formicola, A., Strieder, F., Aliotta, M., et al. (2014). Underground study of the ^{17}O(p,γ)^{19}F reaction relevant for explosive hydrogen burning. *Phys. Rev. C.* 89, 015803. doi:10.1103/PhysRevC.89.015803

D'Antona, F., and Montalbán, J. (2003). Efficiency of convection and Pre-Main Sequence lithium depletion. *Astron. Astrophys.* 412, 213–218. doi:10.1051/0004-6361:20031410

Elwyn, A. J., Holland, R. E., Davids, C. N., Meyer-Schützmeister, L., Mooring, F. P., and Ray, J. W. (1979). Cross sections for the ^{7}Li(p,He)^{3}He reaction at energies between 0.1 and 3.0 MeV. *Phys. Rev. C.* 20, 1984. doi:10.1103/PhysRevC.20.1984

Engstler, S., Raimann, G., Angulo, C., Greife, U., Rolfs, C., Schröder, U., et al. (1992). Isotopic dependence of electron screening in fusion reactions. *Zeitschrift fur Physik A Hadrons and Nuclei.* 342, 471–482. doi:10.1007/BF01294958

Fields, B. D., and Olive, K. A. (1999). The revival of galactic cosmic-ray nucleosynthesis?. *Astrophys. J.* 516, 797–810. doi:10.1086/307145

Fields, B. D. (2011). The primordial lithium problem. *Annu. Rev. Nucl. Part Sci.* 61, 47–68. doi:10.1146/annurev-nucl-102010-130445

Fu, X., Bressan, A., Molaro, P., and Marigo, P. (2015). Lithium evolution in metal-poor stars: from pre-main sequence to the Spite plateau. *Monthly Notices of the RAS.* 452, 3256–3265. doi:10.1093/mnras/stv1384

Goudelis, A., Pospelov, M., and Pradler, J. (2016). Light particle solution to the cosmic lithium problem. *Phys. Rev. Lett.* 116, 211303. doi:10.1103/PhysRevLett.116.211303

Guardo, G. L., Spitaleri, C., Lamia, L., Gulino, M., La Cognata, M., Tang, X., et al. (2017). Assessing the near threshold cross section of the ^{17}O(n,α)^{14}C reaction by means of the Trojan horse method. *Phys. Rev. C.* 95, 025807. doi:10.1103/PhysRevC.95.025807

Hunt, S. E., Pope, R. A., and Evans, W. W. (1957). Investigation of the gamma radiation produced by irradiating with protons in the energy range 0.7 to 3.0 mev. *Phys. Rev.* 106, 1012–1015. doi:10.1103/PhysRev.106.1012

Iliadis, C. (2007). *Nuclear physics of stars*. New York: Wiley

Indelicato, I., La Cognata, M., Spitaleri, C., Burjan, V., Cherubini, S., Gulino, M., et al. (2017). New improved indirect measurement of the ^{18}F(p,α)^{15}O reaction at energies of astrophysical relevance. *Astrophys. J.* 845, 19. doi:10.3847/1538-4357/aa7de7

Jeffries, R. D. (2006). *Pre-main-sequence lithium depletion (Chemical abundances and mixing in stars in the Milky Way and its satellites.*, 163. New York, NY: Springer, 163. 978-3-540-34135-2

Kaihong, F., Qian, Z., Bingjun, C., Zhengwei, Z., Qiang, W., Tieshan, W., et al. (2018). Direct measurement of astrophysical factor S(E) and screening potential for reaction at low energy. *P*hys. Lett. B. 785, 262–267

Kusakabe, M., Cheoun, M. K., Kim, K. S., Hashimoto, Ma., Ono, M., Nomoto, K., et al. (2019). Supernova neutrino process of ^{10}Li and ^{11}B revisited. *Astrophys. J.* 872, 164. doi:10.3847/1538-4357/aafc35

Kwon, J. U., Kim, J. C., and Sung, B. N. (1989). Low-energy cross sections for the ^{10}Li(p, He)^{3}He reaction. *Nucl. Phys.* 493, 112–123. doi:10.1016/0375-9474(89)90535-6

La Cognata, M., Mukhamedzhanov, A. M., Spitaleri, C., Indelicato, I., Aliotta, M., Burjan, V., et al. (2011). The fluorine destruction in stars: first experimental study of the ^{19}F(p, α^0)^{16}O reaction at astrophysical energies. *Astrophys. J. Lett.* 739, L54. doi:10.1088/2041-8205/739/2/L54

La Cognata, M., Spitaleri, C., Mukhamedzhanov, A., Banu, A., Cherubini, S., Coc, A., et al. (2010a). A novel approach to measure the cross section of the ^{17}O(p, α)^{14}N resonant reaction in the 0-200 keV energy range. *Astrophys. J.* 708, 796–811. doi:10.1088/0004-637X/708/1/796

La Cognata, M., Spitaleri, C., Mukhamedzhanov, A., Goldberg, V., Irgaziev, B., Lamia, L., et al. (2010b). DWBA momentum distribution and its effect on. *THM. Nucl. Phys. A.* 834, 658–660. doi:10.1016/j.nuclphysa.2010.01.116

Lambert, D. L., and Reddy, B. E. (2004). Lithium abundances of the local thin disc stars. *Month. Notices RAS.* 349, 757–767. doi:10.1111/j.1365-2966.2004.07557.x

Lamia, L., Mazzocco, M., Pizzone, R. G., Hayakawa, S., La Cognata, M., Spitaleri, C., et al. (2019). Cross-section measurement of the cosmologically relevant ^{7}Be(n,α)^{4}He reaction over a broad energy range in a single experiment. *Astrophys. J.* 879, 23. doi:10.3847/1538-4357/ab2234

Lamia, L., Romano, S., Carlin, N., Cherubini, S., Crucillà, V., de Moura, M. M., et al. (2007). Boron depletion: indirect measurement of the ^{11}B(p,α)^{4}Be S(E)-factor. *Nucl. Phys.* 787, 309–314. doi:10.1016/j.nuclphysa.2006.12.049

Lamia, L., Spitaleri, C., Bertulani, C. A., Hou, S. Q., La Cognata, M., Pizzone, R. G., et al. (2017). On the determination of the ^{7}Be(n,α)^{4}He reaction cross section at BBN energies. *Astrophys. J.* 850, 175. doi:10.3847/1538-4357/aa965c

Lamia, L., Spitaleri, C., Burjan, V., Carlin, N., Cherubini, S., Crucillà, V., et al. (2012b). New measurement of the ^{11}B(p,α)^{4}Be bare-nucleus S(E) factor via the Trojan horse method. *J. Phys. G Nucl. Phys.* 39, 015106. doi:10.1088/0954-3899/39/1/015106

Lamia, L., Spitaleri, C., Carlin, N., Cherubini, S., Del Szanto, M. G., Gulino, M., et al. (2008). Indirect study of (p,ant) and (n,ant) reactions induced on boron isotopes. *Nuovo Cimento C Geophys. Space Phys. C.* 31, 423–431. doi:10.1393/ncc/i2009-10303-2

Lamia, L., Spitaleri, C., La Cognata, M., Palmerini, S., and Pizzone, R. G. (2012a). Recent evaluation of the ^{10}Li(p, α)^{4}He reaction rate at astrophysical energies via the Trojan Horse method. *Astron. Astrophys.* 541, A158. doi:10.1051/0004-6361/201219014

Lamia, L., Spitaleri, C., Pizzone, R. G., Tognelli, E., Tumino, A., Degl'Innocenti, S., et al. (2013). An updated ^{10}Li(p, α)^{4}He reaction rate at astrophysical energies with the Trojan Horse method. *Astrophys. J.* 768, 65. doi:10.1088/0004-637X/768/1/65

Lamia, L., Spitaleri, C., Tognelli, E., Degl'Innocenti, S., Pizzone, R. G., and Prada Moroni, P. G. (2015). Astrophysical impact of the updated ^{4}Be(p,α)^{11}Li and ^{10}B(p,α)^{3}Be reaction rates as deduced by THM. *Astrophys. J.* 811, 99. doi:10.1088/0004-637X/811/2/99

Lattuada, M., Pizzone, R. G., Typel, S., Figuera, P., Miljanić, D., Musumarra, A., et al. (2001). The bare astrophysical S(E) factor of the ^{11}Li(p, α)α reaction. *Astrophys. J.* 562, 1076–1080. doi:10.1086/323868

Lemoine, M., Vangioni-Flam, E., and Cassé, M. (1998). Galactic cosmic rays and the evolution of light elements. *Astrophys. J.* 499, 735–745. doi:10.1086/305650

Lind, K., Melendez, J., Asplund, M., Collet, R., and Magic, Z. (2013). The lithium isotopic ratio in very metal-poor stars. *Astron. Astrophys.* 554, A96. doi:10.1051/0004-6361/201321406

Lombardo, I., Dell'Aquila, D., Conte, F., Francalanza, L., La Cognata, M., Lamia, L., et al. (2016). New investigations of the ^{11}B(p,α)^{4}Be reaction at bombarding energies between 0.6 and 1 MeV. *J. Phys. G Nucl. Phys.* 43, 045109. doi:10.1088/0954-3899/43/4/045109

Meléndez, J., Casagrande, L., Ramírez, I., Asplund, M., and Schuster, W. J. (2010). Observational evidence for a broken Li Spite plateau and mass-dependent Li depletion. *Astron. Astrophys.* 515, L3. doi:10.1051/0004-6361/200913047

Montalbán, J., and D'Antona, F. (2006). New light on the old problem of lithium pre-main sequence depletion: models with 2D radiative-hydrodynamical convection. *Monthly Notices of the RAS.* 370, 1823–1828. doi:10.1111/j.1365-2966.2006.10600.x

Mukhamedzhanov, A. M., Blokhintsev, L. D., Irgaziev, B. F., Kadyrov, A. S., La Cognata, M., Spitaleri, C., et al. (2008). Trojan Horse as an indirect technique in nuclear astrophysics. *J. Phys. G Nucl. Phys.* 35, 014016. doi:10.1088/0954-3899/35/1/014016

Perey, C. M., and Perey, F. G. (1976). Compilation of Phenomenological optical-model parameters 1954-1975. *Atomic Data Nucl. Data Tables.* 17, 1. doi:10.1016/0092-640X(76)90007-3

Piau, L., and Turck-Chièze, S. (2002). Lithium depletion in pre-main-sequence solar-like stars. *Astrophys. J.* 566, 419–434. doi:10.1086/324277

Pitrou, C., Coc, A., Uzan, J. P., and Vangioni, E. (2018). Precision big bang nucleosynthesis with improved Helium-4 predictions. *Phys. Rep.* 754, 1–66. doi:10.1016/j.physrep.2018.04.005

Pizzone, R. G., Roeder, B. T., McCleskey, M., Trache, L., Tribble, R. E., Spitaleri, C., et al. (2016). Trojan Horse measurement of the ^{18}F(p,α)^{15}O astrophysical S(E)-factor. *Eur. Phys. J. A.* 52, 24. doi:10.1140/epja/i2016-16024-3

Pizzone, R. G., Spartá, R., Bertulani, C. A., Spitaleri, C., La Cognata, M., Lalmansingh, J., et al. (2014). Big bang nucleosynthesis revisited via Trojan Horse method measurements. *Astrophys. J.* 786, 112. doi:10.1088/0004-637X/786/2/112

Pizzone, R. G., Spitaleri, C., Bertulani, C. A., Mukhamedzhanov, A. M., Blokhintsev, L., La Cognata, M., et al. (2013). Updated evidence of the Trojan horse particle invariance for the ^{2}H(d, p)^{3}H reaction. *Phys. Rev. C.* 87, 025805. doi:10.1103/PhysRevC.87.025805

Pizzone, R. G., Spitaleri, C., Lamia, L., Bertulani, C., Mukhamedzhanov, A., Blokhintsev, L., et al. (2011). Trojan horse particle invariance studied with the Li6(d,α)He4 and Li7(p,α)He4 reactions. *Phys. Rev. C.* 83, 045801. doi:10.1103/PhysRevC.83.045801

Pizzone, R. G., Spitaleri, C., Lattuada, M., Cherubini, S., Musumarra, A., Pellegriti, M. G., et al. (2003). Proton-induced lithium destruction cross-section and its astrophysical implications. *Astron. Astrophys.* 398, 423–427. doi:10.1051/0004-6361:20021700

Pizzone, R. G., Tumino, A., degl'Innocenti, S., Spitaleri, C., Cherubini, S., Musumarra, A., et al. (2005). Trojan Horse estimate of bare nucleus astrophysical S(E)-factor for the ^{6}Li(p,α)^{3}He reaction and its astrophysical implications. *Astron. Astrophys.* 438, 779–784. doi:10.1051/0004-6361:20052863

Prantzos, N., de Laverny, P., Guiglion, G., Recio-Blanco, A., and Worley, C. C. (2017). The AMBRE project: a study of Li evolution in the Galactic thin and thick discs. *Astron. Astrophys.* 606, A132. doi:10.1051/0004-6361/201731188

Prantzos, N. (2012). Production and evolution of Li, Be, and B isotopes in the Galaxy. *Astron. Astrophys.* 542, A67. doi:10.1051/0004-6361/201219043

Primas, F. (2010). "Beryllium and boron in metal-poor stars," in *Light elements in the Universe.* Editors C Charbonnel, M Tosi, F Primas, and C Chiappini (IAU Symposium), 268, 221–230. doi:10.1017/S1743921310004163

Rapisarda, G. G., Spitaleri, C., Cvetinović, A., Spartà, R., Cherubini, S., Guardo, G. L., et al. (2018). Study of the ^{11}B(p,α)^{4}Be reaction by means of the Trojan Horse method. *Eur. Phys. J. A.* 54, 189. doi:10.1140/epja/i2018-12622-3

Richard, O., Michaud, G., and Richer, J. (2005). Implications of WMAP observations on Li abundance and stellar evolution models. *Astrophys. J.* 619, 538–548. doi:10.1086/426470

Rolfs, C., and Rodney, W. (1988). *Book Review: Cauldrons in the cosmos: nuclear astrophysics.*, 42. Chicago: U Chicago Press, 71. doi:10.1063/1.2811016

Romano, S., Lamia, L., Spitaleri, C., Li, C., Cherubini, S., Gulino, M., et al. (2006). Study of the ^{9}Be(p,α)^{6}Li reaction via the Trojan Horse method. *Eur. Phys. J. A Hadrons Nucl.* 27, 221–225

Roughton, N. A., Fritts, M. R., Peterson, R. J., Zaidins, C. S., and Hansen, C. J. (1979). Thick-target measurements and astrophysical thermonuclear reaction rates: proton-induced reactions. *Atom. Data Nucl. Data Tables.* 23, 177. doi:10.1016/0092-640X(79)90004-4

Sbordone, L., Bonifacio, P., Caffau, E., Ludwig, H. G., Behara, N. T., González Hernández, J. I., et al. (2010). The metal-poor end of the Spite plateau. I. Stellar parameters, metallicities, and lithium abundances. *Astron. Astrophys.* 522, A26. doi:10.1051/0004-6361/200913282

Scott, D. A., Caciolli, A., Di Leva, A., Formicola, A., Aliotta, M., Anders, M., et al. (2012). First direct measurement of the O(p,γ)F reaction cross section at Gamow energies for classical novae. *Phys. Rev. Lett.* 109, 202501. doi:10.1103/PhysRevLett.109.202501

Segel, R. E., Hanna, S. S., and Allas, R. G. (1965). States in C Between 16.4 and 19.6 MeV. *Phys. Rev.* 139, 818–830. doi:10.1103/PhysRev.139.B818

Sergi, M. L., Spitaleri, C., La Cognata, M., Coc, A., Mukhamedzhanov, A., Burjan, S. V., et al. (2010). New high accuracy measurement of the O^{17}(p,α)N^{14} reaction rate at astrophysical temperatures. *Phys. Rev. C.* 82, 032801. doi:10.1103/PhysRevC.82.032801

Sergi, M. L., Spitaleri, C., La Cognata, M., Lamia, L., Pizzone, R. G., Rapisarda, G. G., et al. (2015). Improvement of the high-accuracy ^{17}O(p,α)^{14}N reaction-rate measurement via the Trojan Horse method for application to ^{17}O nucleosynthesis. *Phys. Rev. C.* 91, 065803. doi:10.1103/PhysRevC.91.065803

Sestito, P., and Randich, S. (2005). Time scales of Li evolution: a homogeneous analysis of open clusters from ZAMS to late-MS. *Astron. Astrophys.* 442, 615–627. doi:10.1051/0004-6361:20053482

Sierk, A. J., and Tombrello, T. A. (1973). The ^{9}Be(p,α) and (p, d) cross sections at low energies. *Nucl. Phys.* 210, 341–354

Spitaleri, C., Cherubini, S., del Zoppo, A., di Pietro, A., Figuera, P., Gulino, M., et al. (2003). The Trojan Horse method in nuclear astrophysics. *Nucl. Phys.* 719, C99. doi:10.1016/S0375-9474(03)00975-8

Spitaleri, C., La Cognata, M., Lamia, L., Mukhamedzhanov, A. M., and Pizzone, R. G. (2016). Nuclear astrophysics and the Trojan Horse method. European Physical Journal A. 52, 77. doi:10.1140/epja/i2016-16077-2

Spitaleri, C., La Cognata, M., Lamia, L., Pizzone, R. G., and Tumino, A. (2019). Astrophysics studies with the Trojan Horse method. *Eur. Phys. J. A.* 55, 161. doi:10.1140/epja/i2019-12833-0

Spitaleri, C., Lamia, L., Puglia, S. M. R., Romano, S., La Cognata, M., Crucillà, V., et al. (2014). Measurement of the 10 keV resonance in the B^{10}(p,α)Be^{7} reaction via the Trojan Horse method. *Phys. Rev. C.* 90, 035801. doi:10.1103/PhysRevC.90.035801

Spitaleri, C., Lamia, L., Tumino, A., Pizzone, R. G., Cherubini, S., del Zoppo, A., et al. (2004). The ^{11}B(p,α)^{8}Be reaction at sub-Coulomb energies via the Trojan-horse method. *Phys. Rev. C.* 69, 055806. doi:10.1103/PhysRevC.69.055806

Spitaleri, C. (1991). Problems of fundamental modern Physics, II. *Proceedings.* 28, 21–36

Spitaleri, C., Puglia, S. M. R., La Cognata, M., Lamia, L., Cherubini, S., Cvetinović, A., et al. (2017). Measurement of the ^{11}B(p,α)^{8}Be cross section from 5 keV to 1.5 MeV in a single experiment using the Trojan horse method. *Phys. Rev. C.* 95, 035801. doi:10.1103/PhysRevC.95.035801

Spite, F., and Spite, M. (1982). Abundance of lithium in unevolved halo stars and old disk stars - interpretation and consequences. *Astron. Astrophys.* 115, 357–366

Spite, M., and Spite, M. (1986). *Astron. Astrophys.* 115, 357

Starrfield, S., Bose, M., Iliadis, C., Hix, W. R., Woodward, C. E., and Wagner, R. M. (2019). *Carbon-oxygen classical novae are galactic li producers as well as potential supernova ia progenitors.* .arXiv e-printsarXiv:1910.00575

Stephens, A., Boesgaard, A. M., King, J. R., and Deliyannis, C. P. (1997). Beryllium in lithium-deficient F and G stars. *Astrophys. J.* 491, 339–358. doi:10.1086/304933

Tan, K. F., Shi, J. R., and Zhao, G. (2009). Beryllium abundances in metal-poor stars. *Monthly Notices of the RAS.* 392, 205–215. doi:10.1111/j.1365-2966.2008.14027.x

Tognelli, E., Degl'Innocenti, S., and Prada Moroni, P. G. (2012). ^{7}Li surface abundance in pre-main sequence stars. Testing theory against clusters and binary systems. *Astron. Astrophys.* 548, A41. doi:10.1051/0004-6361/201219111

Tognelli, E., Prada Moroni, P. G., Degl'Innocenti, S., Salaris, M., and Cassisi, S. (2020). *Protostellar accretion in low mass metal poor stars and the cosmological lithium problem.* arXiv e-printsarXiv:2004.14857

Tribble, R. E., Bertulani, C. A., La Cognata, M., Mukhamedzhanov, A. M., and Spitaleri, C. (2014). Indirect techniques in nuclear astrophysics: a review. *Rep. Prog. Phys.* 77, 106901. doi:10.1088/0034-4885/77/10/106901

Tumino, A., Spitaleri, C., di Pietro, A., Figuera, P., Lattuada, M., Musumarra, A., et al. (2003). Validity test of the "Trojan horse" method applied to the ^{7}Li(p,α) ^{4}He reaction. *Phys. Rev. C.* 67, 065803. doi:10.1103/PhysRevC.67.065803

Tumino, A., Spitaleri, C., La Cognata, M., Cherubini, S., Guardo, G. L., Gulino, M., et al. (2018). An increase in the ^{12}C + ^{12}C fusion rate from resonances at astrophysical energies. *Nature.* 557, 687–690. doi:10.1038/s41586-018-0149-4

Tumino, A., Spitaleri, C., Pappalardo, L., Cherubini, S., Zoppo, A. D., La Cognata, M., et al. (2004). Indirect study of the astrophysically relevant ^{7}Li(p, α)^{3}He reaction by means of the Trojan Horse method. *Prog. Theor. Phys. Suppl.* 154, 341–348. doi:10.1143/PTPS.154.341

Tumino, A., Spitaleri, C., Sergi, M. L., Kroha, V., Burjan, V., Cherubini, S., et al. (2006). Validity test of the Trojan Horse Method applied to the ^{7}Li + p → α + α reaction via the ^{3}He break-up. *Eur. Phys. J. A.* 27, 243–248. doi:10.1140/epja/i2006-08-038-1

Vauclair, S., and Charbonnel, C. (1995). Influence of a stellar wind on the lithium depletion in halo stars: a new step towards the lithium primordial abundance. *Astron. Astrophys.* 295, 715

Wen, Q. G., Li, C. B., Zhou, S. H., Irgaziev, B., Fu, Y. Y., Spitaleri, C., et al. (2016). Experimental study to explore the ^{9}Be-induced nuclear reaction via the Trojan horse method. *Phys. Rev. C.* 93, 035803

Wen, Q. G., Li, C. B., Zhou, S. H., Meng, Q. Y., Spitaleri, C., Tumino, A., et al. (2011). A new approach to select the quasifree mechanism in the Trojan horse method. *J. Phys. G Nucl. Part. Phys.* 38, 085103

Wen, Q. G., Li, C. B., Zhou, S. H., Meng, Q. Y., Zhou, J., Li, X. M., et al. (2008). Trojan horse method applied to ^{9}Be(p,α)^{6}Li at astrophysical energies. *Phys. Rev. C.* 78, 035805

Wiescher, M., deBoer, R. J., Görres, J., and Azuma, R. E. (2017). Low energy measurements of the ^{10}B(p,α)^{7}Be reaction. *Phys. Rev. C.* 95, 044617. doi:10.1103/PhysRevC.95.044617

Xhixha, G., Bezzon, G. P., Broggini, C., Buso, G. P., Caciolli, A., Callegari, I., et al. (2013). The worldwide norm production and a fully automated gamma-ray spectrometer for their characterization. *J. Radioanal. Nucl. Chem.* 295, 445–457. doi:10.1007/s10967-012-1791-1

Xu, Y., Takahashi, K., Goriely, S., Arnould, M., Ohta, M., and Utsunomiya, H. (2013). NACRE II: an update of the NACRE compilation of charged-particle-induced thermonuclear reaction rates for nuclei with mass number A<16. *Nucl. Phys.* 918, 61–169. doi:10.1016/j.nuclphysa.2013.09.007

Youn, M., Chung, H. T., Kim, J. C., Bhang, H. C., and Chung, K. H. (1991). The ^{10}B(p, α)^{4}Be reaction in the thermonuclear energy region. *Nucl. Phys.* 533, 321–332. doi:10.1016/0375-9474(91)90493-P

Zahnow, D., Rolfs, C., Schmidt, S., and Trautvetter, H. P. (1997). Low-energy S(E) factor of ^{9}Be(p,α)^{6}Li and .^{11}B(p,α)^{8}Be. *Zeitschrift fur Physik A Hadrons Nucl.* 359, 211–218. doi:10.1007/s002180050389

Zhang, Q., Huang, Z., Hu, J., Chen, B., and Fang, K. (2020). Astrophysical S(E) for the ^{11}B(p,d)^{6}Li and ^{11}B(p,α)^{8}Be reactions by direct measurement. *Astrophys. J.* 893, 126

Conflict of Interest: The authors declare that the research was conducted in the absence of any commercial or financial relationships that could be construed as a potential conflict of interest.

frontiers in Astronomy and Space Sciences

REVIEW
published: 15 February 2021
doi: 10.3389/fspas.2020.607245

Low Mass Stars or Intermediate Mass Stars? The Stellar Origin of Presolar Oxide Grains Revealed by Their Isotopic Composition

S. Palmerini[1,2]*, *S. Cristallo*[2,3], *M. Busso*[1,2], *M. La Cognata*[4], *M. L. Sergi*[4,5] *and D. Vescovi*[2,3,6]

[1]Dipartimento di Fisica e Geologia, Università degli Studi di Perugia, Perugia, Italy, [2]INFN, Sezione di Perugia, via A. Pascoli snc, Perugia, Italy, [3]INAF, Observatorio d'Abruzzo, via Mentore Maggini snc, Teramo, Italy, [4]INFN LNS, via Santa Sofia 62, Catania, Italy, [5]Dipartimento di Fisica e Astronomia, Università degli Studi di Catania, Catania, Italy, [6]Gran Sasso Science Institute, viale Francesco Crispi, L'Aquila, Italy

Among presolar grains, oxide ones are made of oxygen, aluminum, and a small fraction of magnesium, produced by the ^{26}Al decay. The largest part of presolar oxide grains belong to the so-called group 1 and 2, which have been suggested to form in Red Giant Branch (RGB) and Asymptotic Giant Branch (AGB) stars, respectively. However, standard stellar nucleosynthesis models cannot account for the ^{17}O/^{16}O, ^{18}O/^{16}O, and ^{26}Al/^{27}Al values recorded in those grains. Hence, for more than 20 years, the occurrence of mixing phenomena coupled with stellar nucleosynthesis have been suggested to account for this peculiar isotopic mix. Nowadays, models of massive AGB stars experiencing Hot Bottom Burning or low mass AGB stars where Cool Bottom Process, or another kind of extra-mixing, is at play, nicely fit the oxygen isotopic mix of group 2 oxide grains. The largest values of the ^{26}Al/^{27}Al ratio seem somewhat more difficult to account for.

Keywords: AGB stars, presolar grains, nucleosynthesis–stars: abundances, reaction rates, isotopic abundances

OPEN ACCESS

Edited by:
Scilla Degl'Innocenti, University of Pisa, Italy

Reviewed by:
Flavia Dell'Agli, Astronomical Observatory of Rome (INAF), Italy
Santi Cassisi, Astronomical Observatory of Abruzzo (INAF), Italy

***Correspondence:**
S. Palmerini
sara.palmerini@pg.infn.it

Specialty section:
This article was submitted to Nuclear Physics, a section of the journal Frontiers in Astronomy and Space Sciences

Received: *16 September 2020*
Accepted: *18 November 2020*
Published: *15 February 2021*

Citation:
Palmerini S, Cristallo S, Busso M, La Cognata M, Sergi ML and Vescovi D (2021) Low Mass Stars or Intermediate Mass Stars? The Stellar Origin of Presolar Oxide Grains Revealed by Their Isotopic Composition. Front. Astron. Space Sci. 7:607245. doi: 10.3389/fspas.2020.607245

INTRODUCTION

Dust is an alternative probe, with respect to direct astronomical observations, to explore stars and their nucleosynthesis. In particular, presolar grains are tiny refractory particles formed in the envelopes of evolved stars; they come to us as inclusions in pristine meteorites, once spread in the interstellar medium by stellar winds. Even if they were involved in the formation of the Solar System, presolar grains preserved the chemical and isotopic composition of the stellar environments where they condensed. They can therefore provide information about the nucleosynthesis of the progenitor stars with an accuracy often higher than direct stellar observations.

The evolutionary phase of the progenitor star is easily recognizable for some types of presolar grains. For example, this is the case of the MainStream SiC grains in which the presence of s-elements is the fingerprint of their origin in Asymptotic Giant Branch (AGB) stars. Instead, oxide grains do not carry any exotic trace hinting to the type of star in which they were formed. Being essentially made only of oxygen and aluminum, oxide grains are classified into four groups according to their oxygen isotopic compositions, as shown in **Figure 1** (Nittler et al., 1997; Zinner, 2014).

- Grains with $^{17}O/^{16}O \geq 3.82 \cdot 10^{-4}$ (solar value) and $10^{-3} \leq {}^{18}O/^{16}O \leq 2.01 \cdot 10^{-3}$ (solar value) belong to group 1 and have oxygen isotopic ratios similar to those observed in Red Giant

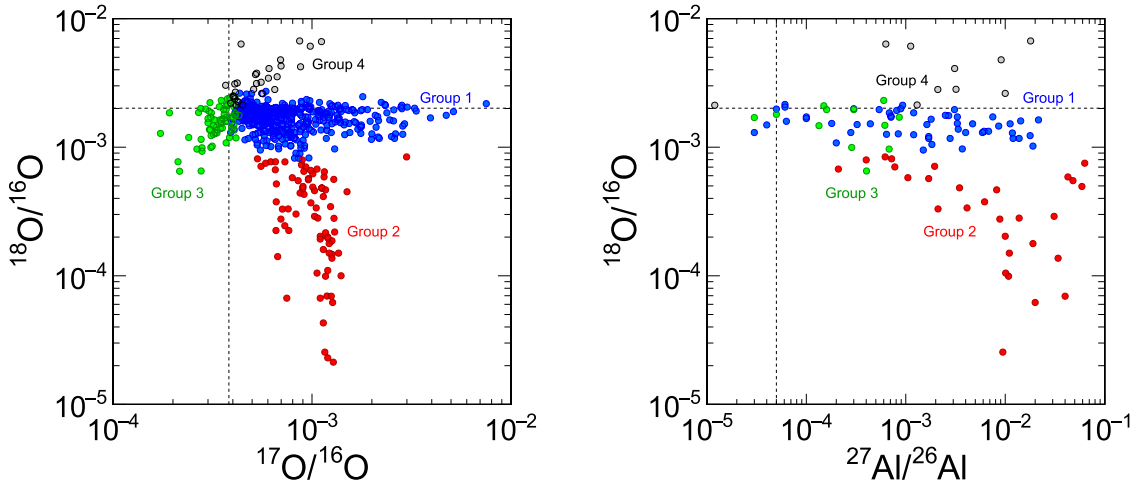

FIGURE 1 | Left panel: oxygen isotopic ratios in presolar oxide grains. Different colors identify grains belonging to different groups as defined by Nittler et al. (1997) and indicated by the labels. **Right panel:** $^{18}O/^{16}O$ and $^{26}Al/^{27}Al$ isotopic ratios in presolar oxide grains. Group 2 grains generally show significant $^{18}O/^{16}O$ depletion and higher values of $^{26}Al/^{27}Al$ even if there is no simple correlation between the two isotopic ratios. Grain data in this figure as well as in all the figures of this paper are from the Presolar Grain database of the Laboratory for Space Sciences at the Washington University in Saint Louis (Hynes and Gyngard, 2009). Dashed lines mark solar isotopic values.

Branch (RGB) stars (Harris and Lambert, 1984; Abia et al., 2012), and they have therefore been suggested as progenitors of those grains.

- Grains belonging to group 2 show $^{17}O/^{16}O$ larger than the solar value and large ^{18}O depletions ($^{18}O/^{17}O \leq 0.001$). Such isotopic mix cannot be reproduced by standard stellar nucleosynthesis; for this reason, several authors have suggested that mixing mechanisms coupled with H-burning nucleosynthesis of low mass red giant stars can account for this grain composition. We will discuss this point in detail in this paper.
- Group 3 grains, with both $^{17}O/^{16}O$ and $^{18}O/^{16}O$ ratios smaller than solar ones, might come from low mass stars with lower-than-solar metallicity. The oxygen isotopic ratios of group 3 grains are supposed to reflect the evolution of the oxygen isotope abundances in the Galaxy. They have actually been used to obtain an estimate of the age of the Milky Way (Nittler, 2009).
- Group 4 grains show excesses of both $^{17}O/^{16}O$ and $^{18}O/^{16}O$ ratios, and they likely form in supernovae when ^{18}O-rich material from the He/C zone can be admixed to material from oxygen-rich zones (Choi et al., 1998). However, up to now, only three oxide grains with evidence of SN origins (very rich in ^{16}O) have been identified (Hynes and Gyngard, 2009). It has been suggested that such a paucity of SN grains is related to the fact that oxide grains from supernovae are smaller than those from red giant stars and, as such, are difficult to spot in meteorite samples (Zinner, 2014).

Notably, some oxide grains show traces of ^{26}Mg, hinting at the initial presence of ^{26}Al ($t_{1/2} = 7.16{\cdot}10^5$ years, see the right panel of **Figure 1**). This aspect is important to identify the grain stellar progenitor, but it is also puzzling. Indeed, excluding massive stars (the main contributors to galactic ^{26}Al), grains with ^{26}Al must have formed in AGB stars, as their hydrogen-burning shells are efficient ^{26}Al producers. However, isotopic abundances of oxygen and aluminum in grains have values that can be found in the hydrogen burning shell when the temperature is higher than some 10^7 K (e.g., to achieve $^{26}Al/^{27}Al$ ratios $\geq 3{\cdot}10^{-3}$, the H-shell has to burn at $T \geq 4{\cdot}10^7$ K): how could material so rich in ^{26}Al be present in the envelopes of evolved stars with mass smaller than 2 $M_\odot$?

The stellar structure of an AGB star is made of a CO unburning core surrounded by a He- and a H-rich shell. The latter burns radiatively below the convective envelope for most of the evolutionary phase, supplying energy to the star. The H-burning is periodically interrupted by convective episodes due to the activation of the He-burning shell, called thermal pulses. The abundances of CNO isotopes, and light nuclei in general, in the envelope of Red Giant Stars (namely the candidate progenitor of group 1 and 2 grains) are set by the first dredge-up[1] (hereafter FDU). A second dredge-up (SDU) occurs in the very early AGB phase in objects with masses larger than $\sim 4\ M_\odot$ (Boothroyd and Sackmann, 1999). Furthermore, at the exhaustion of each thermal pulse, the convective envelope penetrates down to the He-rich layers and enriches the stellar surface with the products of the He-burning and the s-process[2] nucleosynthesis. This mixing episode is called third dredge-up

[1]The convective mixing episode that affects stars at the beginning of the RGB and enriches the stellar surface with the product of core H-burning nucleosynthesis.
[2]The slow neutron capture nucleosynthesis process typical of AGB stars and responsible for the production of many elements heavier than Fe in the Galaxy.

(hereafter TDU), and, unlike the other two, it occurs numerous times during the AGB phase.

Firstly, Wasserburg et al. (1995) suggested the existence of a nonstandard mixing mechanism (namely, other than FDU, SDU, and TDU) coupled with AGB star nucleosynthesis to explain the oxygen isotopic abundances found in oxide grains (in particular of those that a few years later were identified by Nittler et al., 1997 as belonging to the group 1 and 2). A C/O ratio smaller than 1, together with $^{17}O/^{16}O$ larger than the solar value, $^{18}O/^{16}O$ much lower than the solar reference, and $^{26}Al/^{27}A$ suitable to account for abundances recorded in group 2 oxide grains can be obtained in the envelopes of AGB stars in two possible scenarios: objects with initial mass smaller than 1.5–1.7 $M_{\odot}$ affected by cool bottom process (CBP) or more massive stars ($M > 4\,M_{\odot}$) in which hot bottom burning (HBB) is at play.

CBP is a non-convective mixing phenomenon operated by conveyor belts, which, from the cool bottom of the convective envelope, drag material toward the inner region of the star and, once they reach the area near the hydrogen burning shell, they collect the fresh nucleosynthesis products and drag those ashes upwards, pouring them into the stellar envelope. It turns out that the surface stellar abundances are modified and assume values similar (if not equal) to those of the H-burning regions. CBP and similar mixing phenomena (also called extra-mixing or non-convective mixing), as well as their possible physical causes, have been investigated by several authors (e.g., Nollett et al., 2003; Eggleton et al., 2006; Palacios et al., 2006; Denissenkov et al., 2009; Busso et al., 2010; Palmerini et al., 2011a). In particular, Nollett et al. (2003), Busso et al. (2010) and Palmerini et al. (2011a) have shown that extra-mixing is able to reproduce the oxygen isotopic mix in group 1 and group 2 oxide grains, eventually preventing stars from becoming carbon stars. However, the higher $^{26}Al/^{27}A$ ratios recorded in some group 2 grains (up to a few 10^{-2}) can be accounted for by just a few extra-mixing models, such as that proposed by Palmerini et al. (2017). In this scenario, the advection into the envelope of magnetic bubbles, formed just above the H-burning shell, allows for effective enrichment of ^{26}Al due to a bottom-up mixing mechanism. This mixing is different from the classic CBP, because the relatively fast up-flow of the magnetic bubbles triggers a diffusive down flow of material (Trippella et al., 2016; Vescovi et al., 2020), hence there is not a real circulation nor the transported matter has time to experience further low temperature proton captures. As it is, instead, in the semianalytic CBP calculation model presented by Nollett et al., 2003, which can account for the highest $^{26}Al/^{27}Al$ values found in "extreme oxide grains" if the mass circulation reaches the most energetic layers of the H-burning shell; in this case, however, the CBP feedback on the stellar energy balance is not negligible (Palmerini et al., 2011a).

To reproduce the oxygen and aluminum isotopic ratios recorded in group 2 grains, an extra-mixing mechanism has to efficiently pauperize in ^{18}O the stellar envelope as well as efficiently enrich it in ^{26}Al. The mixed material must therefore experience temperatures higher than $4–5{\cdot}10^7$ K. This fact rules out the thermohaline mixing (for details see e.g., Eggleton et al., 2008; Lagarde et al., 2012; Lattanzio et al., 2015) as being responsible for the changes in the envelope composition necessary to reproduce the composition of those grains. It is actually not deep enough because the average molecular weight inversion, which is due to the burning of the $^3He(^3He,2p)^4He$ reaction and triggers this diffusive mixing, occurs in relatively superficial layers of the H-shell where the temperature never exceeds $3–3.5{\cdot}10^7$ K (Busso et al., 2010; Palmerini et al., 2011b).

An alternative explanation comes from HBB in more massive ($M > 4\,M_{\odot}$) AGB stars (Iben, 1975; Boothroyd and Sackmann, 1992; D'Antona and Mazzitelli, 1996; Ventura and D'Antona, 2005). In this case, the temperature at the base of the convective envelope is high enough to allow the local burning of some proton capture reactions. As a matter of fact, HBB efficiently modifies the distribution of light isotopes, enhancing the abundances of some of them (^{13}C, ^{14}N, ^{26}Al) and efficiently destroying others (^{12}C, ^{18}O). In massive AGBs (in particular at metallicities lower than solar), two competing mechanisms are at work: TDU (which carries carbon to the surface) and HBB (which destroys it). Presolar SiC grains (formed in C-rich environments) may thus grow depending on which of the two above-mentioned mechanisms is dominating. Iliadis et al. (2008) suggested that, in the light of a new measurement of the $^{16}O(p,\gamma)^{17}F$ reaction rate, ^{16}O could not be destroyed, even partially, by red giant stars (also of intermediate mass), and group 2 oxide grains therefore have to form in low-mass AGB stars. The situation took a different turn when Lugaro et al. (2017) showed that massive AGB star models are able to reproduce the oxygen isotopic composition of group 2 grains if the $^{17}O(p,\alpha)^{14}N$ reaction rate measured by Bruno et al. (2016) is used. However, in this case, grains with $^{26}Al/^{27}Al > 0.06$ cannot be reproduced by those models. In this paper, we review the possibility of reproducing the isotopic abundances of oxygen and aluminum recorded in group 2 grains with low and intermediate mass AGB models by adopting the $^{17}O+p$ reaction rates proposed by different authors.

To provide the reader with a better comparison of the discussed mixing models, we report in **Figure 2** a scheme of the three mentioned mechanisms: the conveyor belt CBP, the magnetic induce extra-mixing, and the HBB. Before analyzing in detail their effects on the oxygen and aluminum isotopic mix in the envelopes of AGB stars, in the next section, we discuss how reaction rates affect the oxygen isotope nucleosynthesis during H-burning.

SENSITIVITY OF $^{17}O/^{16}O$ RATIO TO THE H-BURNING TEMPERATURE AND THE NUCLEAR REACTION RATES

The nucleosynthesis of ^{17}O and ^{26}Al is so sensitive to the temperature that their abundances can be used as a thermometer for the H-burning of the stellar layers where they form. In the case of ^{26}Al, the higher the temperature the larger is the abundance. This is valid also for the $^{26}Al/^{27}Al$ isotopic ratio, being the proton capture on ^{27}Al less efficient than that on ^{26}Al. On the other side, the situation is a bit more complicate for ^{17}O. Indeed, the ^{16}O is efficiently consumed by the

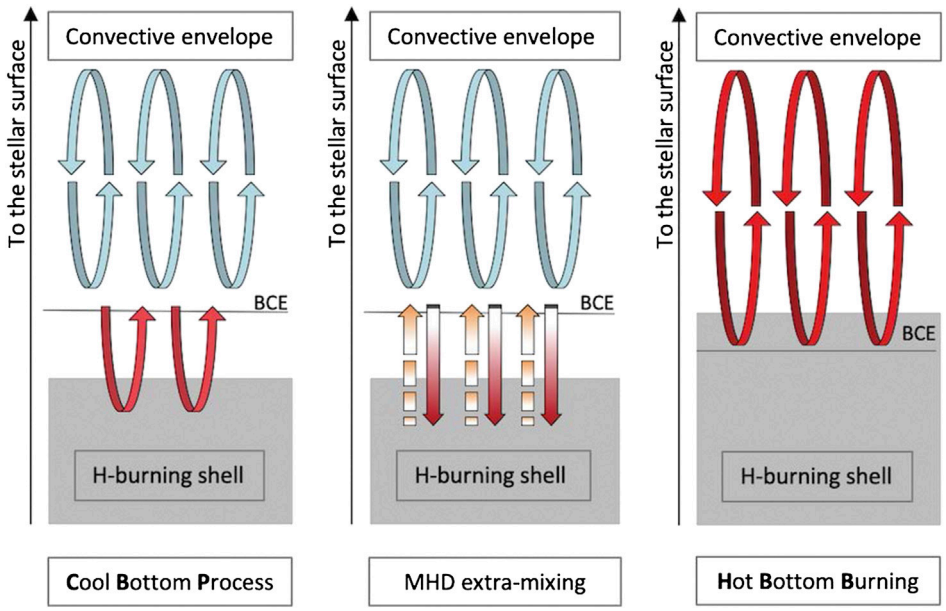

FIGURE 2 | Scheme of the mixing phenomena that coupled with the stellar nucleosynthesis might account for the oxygen and aluminum isotopic ratios recorded in group 2 oxide grains. **Left panel:** the classic CBP operated by a conveyor-belt-like mechanism that starts from the bottom of the convective envelope (BCE, as thought and presented by Wasserburg et al., 1995; Nollett et al., 2003). **Central panel:** the magnetic induced extra-mixing, the stellar magnetic fields induce a bottom-up mixing triggered by the up-flow of "bubbles" according to Nucci and Busso (2014); Trippella et al. (2016) and Palmerini et al. (2017). **Right panel:** the HBB that takes place when the temperature above the BCE is high enough to allow the further occurrence of some proton capture reactions. The gray areas in the three panels show the stellar region where temperatures are sufficiently high to burn H. Figures are not to scale.

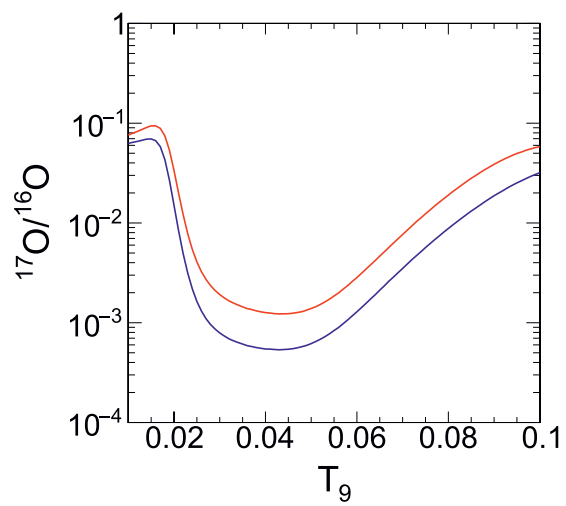

FIGURE 3 | $^{17}O/^{16}O$ equilibrium values as a function of temperature computed by using reaction rates of set A (red line) and set B (blue line). See **Table 1** and the text for more details. Only results obtained for recommended values of the reaction rates are shown because nucleosynthesis calculations have been run employing only recommended values.

$^{16}O(p,\gamma)^{17}F$ reaction only in the inner and hotter layers of the H-burning shell, while the $^{17}O+p$ reaction rate has not a linear or monotonic dependence with temperature. It turns out that in the temperature range typical of H-burning in red giants, the equilibrium value of the $^{17}O/^{16}O$ as a function of the temperature has the trend shown in **Figure 3**. Such a value is uniquely determined by the proton capture reactions. From this competition, the temporal evolution of the ^{17}O abundance is described by the equation

$$\frac{dY(^{17}O)}{dt} = Y(p)Y(^{16}O)\rho\langle\sigma\nu\rangle_{^{16}O(p,\gamma)} - Y(p)Y(^{17}O)\rho\left(\langle\sigma\nu\rangle_{^{17}O(p,\gamma)} + \langle\sigma\nu\rangle_{^{17}O(p,\alpha)}\right) \quad (1)$$

and then in equilibrium condition

$$\frac{Y(^{17}O)}{Y(^{16}O)} = \frac{\langle\sigma\nu\rangle_{^{16}O(p,\gamma)}}{\langle\sigma\nu\rangle_{^{17}O(p,\gamma)} + \langle\sigma\nu\rangle_{^{17}O(p,\alpha)}}. \quad (2)$$

From **Eq. 2**, it is clear that if the reaction rates are well known, the isotopic ratio $^{17}O/^{16}O$ can reveal the temperature of the stellar envelope where the nucleosynthesis took place as well as the maximum temperature experienced by the materials reversed into the stellar envelope by convective or non-convective mixing phenomena. In this way, the ^{17}O abundance can be a valuable probe to investigate stars and their interiors. For example, Abia et al. (2012) have suggested an estimation of the stellar mass of α–*Boo* and α–*Tau*, with a precision of 1/10 of the solar mass, on the basis of the $^{17}O/^{16}O$ surface abundances observed for the two red giants. However, this scenario is affected by a very strong criticality: each new measurement of a nuclear reaction rate might

lead to significant changes in the nucleosynthesis predictions and their agreement, or disagreement, with the observational constraints. This is exactly the case of the puzzling isotopic composition of the presolar oxide grains, which has been gradually understood over the years as new measures have allowed us to increase the accuracy of nuclear physics inputs in stellar nucleosynthesis models. An extended discussion on the state of the art of measurements and uncertainty estimations on the $^{17}O + p$ reaction rate is presented in review paper by Sergi et al. (2020).

As mentioned in the previous section, the envelope abundances of oxygen isotopes of red giant stars are set by the FDU (or in a few cases the SDU) and they will remain unchanged until CBP or HBB takes place. The $^{17}O/^{16}O$ ratio with which a star approaches the AGB phase is thus determined by the H-burning temperature in its interior and the stellar mass. Firstly, Boothroyd et al. (1994) and Wasserburg et al. (1995) pointed out that just the narrow range of $10^{-3} \leq {}^{17}O/^{16}O \leq 2.2\ 10^{-3}$ was accessible to stars with mass smaller than 2 $M_{\odot}$, while more massive objects (up to 7 $M_{\odot}$) were suggested to be the progenitor of grains showing larger values of $^{17}O/^{16}O$. In any case, CBP (in low mass stars) and HBB (in more massive ones) were needed to reduce the $^{18}O/^{16}O$ isotopic ratio from values around 0.0015 (the average value set by FDU and SDU) down to a few 10^{-4}, as recorded in the first presolar grains analyzed. Moreover, in the $^{18}O/^{16}O$ vs. $^{17}O/^{16}O$ plane, a *forbidden* region was found at $^{17}O/^{16}O < 0.0005$ and $^{18}O/^{16}O < 0.0015$. This portion of the plane, even if occupied by several oxide grains, was not accessible by HBB nor CBP models.

A few years later, Nollett et al. (2003), in examining the effects of CBP on the C, N, O, and Al isotopic ratios in AGB star nucleosynthesis, demonstrated that oxide grain isotopic ratios could be accounted for by the conveyor belt mixing model. This is so because ^{17}O can produced or destroyed according to the mixing depth, the ^{18}O depleted, and the ^{26}Al efficiently synthesized. However, the region accessible to low-mass star nucleosynthesis remained limited to $5.\ 10^{-4} \leq {}^{17}O/^{16}O \leq 2.2.\ 10^{-3}$.

The situation was improved by a new measurement of the bottleneck reaction of the CNO cycle: the $^{14}N(p,\gamma)^{15}O$. Indeed, the reaction rate was found to be the 50% smaller and this requires the CNO burning to take place at higher densities and temperatures (25% and the 10%, respectively) in the H-shell during the RGB phase as well as inside the stellar core during the main sequence (see Palmerini et al., 2011a, for an extended discussion). This induces small but effective changes not only in the nucleosynthesis but also in the stellar structure and, as a consequence, the surface $^{17}O/^{16}O$ abundance of a 2 $M_{\odot}$ star after the FDU moves from $2{\cdot}10^{-3}$ to $5.14{\cdot}10^{-3}$ and the whole range of the $^{17}O/^{16}O$ values recorded in group 1 oxide grains is covered by RGB stars with mass $\leq$2 $M_{\odot}$. Palmerini et al., 2011a have shown that in stars with mass smaller than 2.2 $M_{\odot}$ CBP can be at play also during the RGB phase, and, if so, it might account for subsolar values of the $^{18}O/^{16}O$ isotopic ratio recorded in group 1 grains. The mixing model in the quoted paper is a parametric one and the authors assume CBP during the RGB phase to have both the mixing rate and the mixing depth smaller than during the AGB phase. However, even assuming the same CBP parameters assumed for the AGB phase, the temperature of the H-burning shell of a low mass RGB star is not high enough to allow a $^{18}O/^{16}O$ depletion below $7{\cdot}10^{4}$, which is the upper limit of the isotopic ratio recorded in group 2 grains. For the same reason (low temperature) also the ^{26}Al enrichment due to CBP in the RGB phase is limited to $^{26}Al/^{27}Al \leq 10^{-4}$. The temperatures of the H-burning during the AGB phase are higher than in the previous RGB phase, and, as a consequence, CBP or a similar extra-mixing phenomenon at play during the AGB phase in a star with mass $\leq$1.5 $M_{\odot}$ leads the surface abundance of ^{17}O and ^{18}O to the values typical of group 2 grains. Finally, updates of the proton capture cross sections on ^{17}O and ^{18}O (La Cognata et al., 2010; Palmerini et al., 2013) allowed the nucleosynthesis models to cross the *forbidden* region.

In 2013, after the cited updates in the nuclear physics data, the scenario was roughly the same as shown by the blue curves of **Figure 4** (panel A). In the light of the agreement between models and oxygen isotopic mix of grains, it would be possible to state that group 1 dust might form in RGB stars with mass smaller than 2 $M_{\odot}$ and that group 2 grains form in AGB of 1.2–1.5 $M_{\odot}$ being an extra-mixing mechanism at play. All the stars being of solar metallicity. Despite this nice agreement between observational constraints and theory for oxygen isotopes, there was a problem: the $^{26}Al/^{27}Al$ values larger than a few 10^{-3} could not be reached by extra-mixing models. This was a severe limit for the extra-mixing models because the composition of group 2 grains, and especially those rich in $^{26}Al/^{27}Al$, necessarily requires relatively high temperatures to be reproduced. However, mixing mechanisms cannot push the mixed materials beyond a certain depth of H-burning shell to avoid a luminosity feedback due to extra energy provided by the burning of the mixed material.

As mentioned in the introduction and shown by Palmerini et al. (2017), the sole low mass AGB nucleosynthesis model able to simultaneously reproduce the $^{17}O/^{16}O$, the $^{18}O/^{16}O$ and the $^{26}Al/^{27}Al$ ratios measured in group 2 oxide grains is the one based on the theory by Nucci and Busso (2014). In this scenario the natural expansion of magnetic structures from above the H-burning shell induces a bottom-up mixing that reverses in the stellar envelope materials relatively hot and rich enough in ^{26}Al to reproduce also the highest value of the Al isotopic ratio recorded in group 2 oxide grains. In the same year, Lugaro et al. (2017) suggested that group 2 oxide grains condensate in the envelope of more massive AGB stars (4.5–6 $M_{\odot}$) of solar metallicity. Their HBB models well reproduce the oxygen isotopic mix shown by those grains and also the $^{26}Al/^{27}Al$ isotopic ratio when smaller than 0.06. This paper has brought attention back to the hypothesis that oxide grains might have formed in intermediate mass stars due to the presence of HBB: a scenario that had been cast aside in the last years.

Beside the stellar models, the papers by Palmerini et al. (2017) and Lugaro et al. (2017) differ for the nuclear physics inputs employed: the first study mainly uses reaction rates (for proton captures on oxygen isotopes) measured with the Trojan Horse Method by the AsFiN collaboration (Tribble et al., 2014, set A in **Table 1**), while the second uses reaction rates directly measured

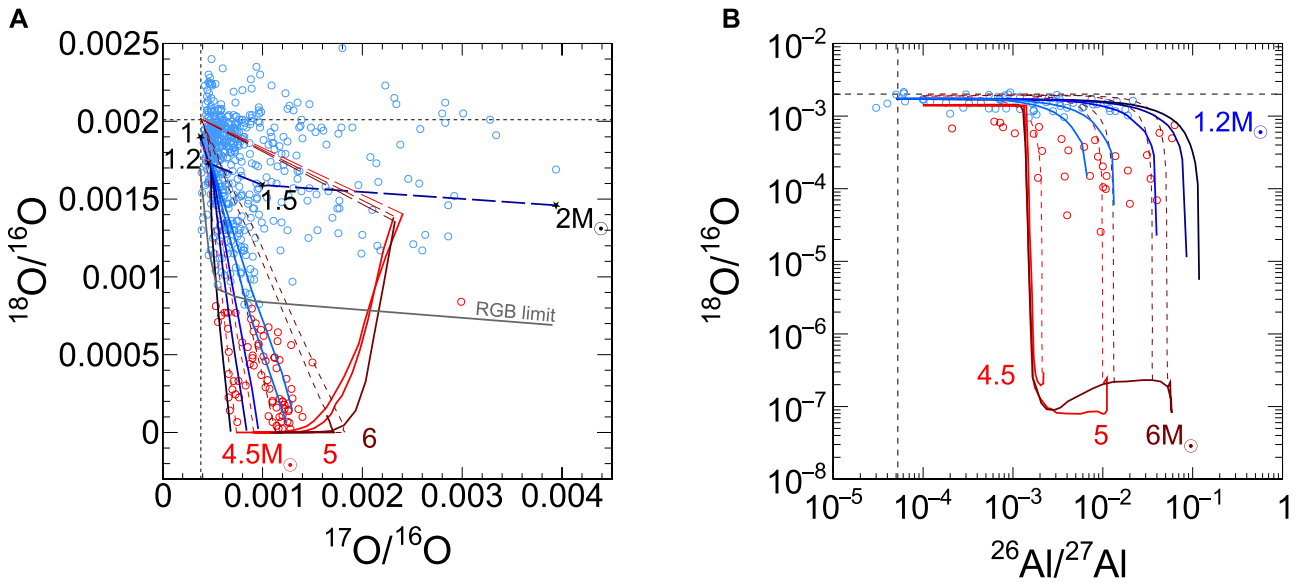

FIGURE 4 | Panel (A). Evolution of the $^{17}O/^{16}O$ and $^{18}O/^{16}O$ isotopic ratios in the envelope of low mass and intermediate mass AGB stars of solar metallicity due to magnetic mixing (blu curves) and HBB (red curves). Star markers along the blue dashed line indicate the post-FDU composition of stars with mass from 1 to 2 $M_\odot$ as indicated by the labels. Open blue circles are group 1 oxide grains while red ones are those of group 2. The descending blue lines refer to magnetic mixing model results for a 1.2 $M_\odot$ AGB star for different values of *k*, computed employing reaction rates from set A (see the text for details). The maximum modification of the envelope composition that can be produced by the mixing during the RGB phase is indicated by the gray curve. Red curves deal with the evolution of $^{17}O/^{16}O$ and $^{18}O/^{16}O$ isotopic ratio in the envelope of a 4.5, a 5, and a 6 $M_\odot$ star affected by HBB, as reported by Lugaro et al. (2017), which runs calculations with reaction rates of set B. The long dashed red lines indicate the evolution of the oxygen isotopic ratio in the stellar evolution before the AGB phase, while the short dashed red curves show effects of diluting the stellar wind with early solar system materials (see the text for details). The two gray dashed lines mark the $^{17}O/^{16}O$ and $^{18}O/^{16}O$ solar values. **Panel (B)**. Same models and grain data of plot in **panel (A)**, but dealing with the $^{18}O/^{16}O$ isotopic ratio vs. the $^{26}Al/^{27}Al$ one. The horizontal dashed line shows the $^{18}O/^{16}O$ solar value while the vertical one the estimate value of the $^{26}Al/^{27}A$ in the early solar system as reported by Vescovi et al. (2018).

TABLE 1 | The 2 sets of reaction rates employed in our nucleosynthesis calculations.

Reaction	Set A	Set B
$^{16}O(p,\gamma)^{17}F$	Iliadis et al. (2010)	Iliadis et al. (2010)
$^{17}O(p,\alpha)^{14}N$	Sergi et al. (2015)	Bruno et al. (2016)
$^{17}O(p,\gamma)^{18}F$	Sergi et al. (2015)	Di Leva et al. (2014)
$^{18}O(p,\alpha)^{15}N$	La Cognata et al. (2010)	Iliadis et al. (2010)
$^{18}O(p,\gamma)^{19}F$	Iliadis et al. (2010)	Iliadis et al. (2010)
$^{25}Mg(p,\gamma)^{26}Al$	Straniero et al. (2013)	Straniero et al. (2013)
$^{26}Al(p,\gamma)^{27}Si$	Iliadis et al. (2010)	Iliadis et al. (2010)

by the LUNA collaboration (Broggini et al., 2018, set B in **Table 1**).

MAGNETIC INDUCED MIXING IN LOW MASS AGB STARS

The occurrence of mixing mechanisms during the AGB phase is one of the most critical issue in the stellar modeling; they have been invoked to explain both the superficial anomalies of light element/isotope abundances and the formation of a reservoir of ^{13}C in the He-rich layers below the H-burning shell, which provides the necessary neutrons for the s-process in low mass AGBs ($M \leq 3\ M_\odot$). Single and coupled effects of stellar rotation, magnetic fields, inversion of the average molecular weight, gravity waves, overshooting, and many other phenomena have been extensively studied over the decades to explain the peculiarities observed in the nucleosynthesis of red giant stars (for an extended discussion see the reviews by Lattanzio, 2019; El Eid, 2016; Nomoto et al., 2013; Herwig, 2005, and references therein). We concentrate on the mixing induce by stellar magnetic fields that, as demonstrated in Nucci and Busso (2014), might trigger the formation and the expansion of bubbles of magnetized materials in the radiative regions of low mass red giant stars. Trippella et al. (2016) have shown that such a mechanism can induce the formation of a ^{13}C-pocket suitable to address the observational constrains to s-process nucleosynthesis in low mass AGB stars, but our interest in the magnetic induced mixing is due to the possibility of reproducing the isotopic composition recorded in both SiC and oxide presolar grains of AGB origin (Palmerini et al., 2017, Palmerini et al., 2018).

According to Nucci and Busso (2014) the velocity $v(r)$ by which the bubbles of magnetized material expand from above the H-burning shell of AGB stars to the base of the convective envelope is describe by the following equation:

$$v(r) = v(r_k)\left(\frac{r_k}{r}\right)^{k+1}, \quad (3)$$

where r is the position along the stellar radius, k is the index of the power law $\rho \propto r^k$, which deals with the density distributions of the stellar plasma in the region of our interest, and r_k and $v(r_k)$ are the mixing starting depth and starting velocity, respectively. In AGBs with M ≤ 2 $M_\odot$, when the H-shell is active, k is consistently equal to -3 for most of the radiative region, from the base of the envelope to the stellar interior layers, and it suddenly drops to very small values, $\ll -10$, in close proximity to the H-shell layers that are burning and producing the most of the energy. From this point and beyond the analytical solutions of the MHD equations found by Nucci and Busso (2014) are not held. The deepest layer in the radiative region from which k keeps to be constant (and ~ −3 in our case) can thus be choosen as the deepest layer from which the magnetic mixing starts, namely, where magnetic bubbles start their expansion (see **Figure 1B** in Palmerini et al., 2017, and the text for more details). Moreover, the quoted authors assume that the bubble will cross the border between the radiative region and the convective envelope with a velocity a bit smaller than the velocity of the deepest convective layer (e.g., $v(r_e) \sim 10^4$ cm s^{-1}), so that the bubbles are rapidly destroyed releasing the trapped mass. If it so $v(r_k)$ turns to be of the order of a few tenths cm s^{-1}. To complete the extra-mixing model, the mixing rate is estimated as discussed by Trippella et al. (2016), where

$$\dot{M} = 4\pi\rho_e^2 v(r_e) f_1 f_2, \quad (4)$$

being ρ_e the density of the radiative layers just below the border of the convective envelope. The factors $f_1 \sim (0.01 \div 0.02)$ and $f_1 \sim 0.01$ represent the fraction of the stellar surface covered by the magnetized bubbles and their filling factor, respectively. These values are assumed, following the hypothesis that (i) the fraction of stellar surface covered by the bubbles (which are portions of magnetic flux tubes) at the base of convective should be less than 1/100 Nucci and Busso (2014), and ii) the mass in flux tubes is concentrated in thin current sheets of about 1/100 of the tube section (Hirayama, 1992). As mentioned at the beginning of this section, this magnetic mixing scenario has been demonstrated to account for both the anomalies in light element abundances and the formation of the ^{13}C-pocket responsible for the typical s-process nucleosynthesis in low mass AGB stars by adopting the same choices for the free parameters of the mixing model (as the reader can infer from Trippella et al., 2016; Palmerini et al., 2017, Palmerini et al., 2018). To be efficient enough, the mixing has to be triggered by a magnetic field of a few 10^5 G. Such a value is in perfect agreement with the intensity of internal magnetic fields estimated with asteroseismology studies for many low mass red giants by the Kepler Observatory (Fuller et al., 2015).

The magnetic extra-mixing model, once applied to a 1.2 $M_\odot$ AGB star with solar metallicity, modifies the oxygen isotopic ratios in the stellar envelopes as reported in **Figure 4**. Panel A shows nucleosynthesis calculations run by Palmerini et al. (2017) with nuclear reaction rates from set A. The descending blue curves show the evolution of the oxygen isotopic mix due to magnetic buoyancy during the RGB and AGB phase, starting from the surface composition left by the FDU and adopting different values of k (−3.5, −3.4, −3.3, −3.2, and −3.1). The smaller the value of k, the darker the curve. In the same way, panel B of **Figure 4** shows the evolution of the surface abundance of $^{18}O/^{16}O$ as a function of the $^{26}Al/^{27}Al$ ratio for the same models. Oxide grains of group 1 (open blue circles) and group 2 (open red circles) are reported **Figure 4** for comparison with model predictions. The various choices of k, for the reported models, correspond to various depth of the mixing starting layers and define a zone thick enough to host different abundances and temperatures. For this reason models with a smaller k are more efficient in destroying ^{18}O and enriching the stellar envelope in ^{26}Al. The dependence of the final values of the $^{17}O/^{16}O$ isotopic ratio to the adopted k is instead a bit more complicated because the trend of the equilibrium value of this isotopic ratio as a function of the temperature is not linear (see **Figure 3**). From panel A of **Figure 4**, one can observe that magnetic mixing calculations for the 1.2 $M_\odot$ AGB well accounts for the majority of the grains, with small changes in the value of the parameter k. In same way, panel B of the Figure shows that the 1.2 $M_\odot$ AGB model is also a valuable candidates to be progenitors of group 2 grains because the whole range of the $^{26}Al/^{27}Al$ isotopic ratio recorded in the grains is covered by the lines dealing with the surface abundance evolution due to the magnetic mixing. In the figures we only report the models that better match the oxygen isotopic mix of the grains, but even if the agreement between predictions and observations is slightly worse for the oxygen isotopes, the 1.5 $M_\odot$ model in Palmerini et al. (2017) also results in being a possible candidate as a progenitor of at least group 2 oxide grains with $^{17}O/^{16}O > 0.001$.

It has to be pointed out that in AGB stars ^{26}Al is produced and destroyed through its decay and through neutron and/or proton captures. However, the products of neutron capture reactions are visible on the surface of an AGB star only after some TDU episodes. The low mass star considered here is characterized by a low number of TDUs. We can therefore safely conclude that, in the study of presolar oxide grains, the contribution of (n,γ) reactions on ^{26}Al nucleosynthesis is almost negligible.

HOT BOTTOM BURNING AND ALUMINA DUST PRODUCTION IN INTERMEDIATE MASS STARS

The detection of an Al_2O_3 dust shell in several oxygen-rich AGB stars (through mid-infrared interferometric observations at VLTI/MIDI, Karovicova et al., 2013), as long with the detection of a rotational line emission of AlO in the wind of a few stars of the same kind (De Beck et al., 2017), proves that O-rich AGB stars are the main source of alumina dust in the Galaxy, as suggested by several authors starting from Onaka et al. (1986). It is without doubt that more massive objects reverse a major amount of dust in the interstellar medium and that the mass of the Al_2O_3 grains produced increases with metallicity; intermediate-mass AGB stars, namely, those with a mass up to 7–8 $M_\odot$ and those with solar metallicity, or higher, affected by HBB, are reliable progenitors of presolar oxide grains (Ventura et al., 2020, and references therein). Moreover, the thesis of the production of alumina dust in AGB stars experiencing HBB is so

strong and shared that the aluminum abundance in grains has been suggested as an indicator of the mass and of the evolutionary stage of the stellar progenitor (Dell'Agli et al., 2014). Even if several authors discuss the elemental abundances of Al and O in AGB dust, only a few papers in the literature show nucleosynthesis calculations with predictions for oxygen and aluminum isotopic abundances to be compared with the ratios recorded in presolar oxide grains and those of group 2 in particular. Such a lack of data might be due to our still partial knowledge of the physical processes at play and the related computational limitations strongly limits the predictive power of intermediate mass AGB models. The modeling of those stars is actually far from being completely understood and is dependent on many theoretical aspects:

- first, the mixing scheme adopted is extremely important. The use of instantaneous convective mixing (Iben 1973) leads to different (wrong) abundances with respect to the adoption of a time-dependent convective algorithm (Sackmann and Boothroyd, 1992).
- second, the presence of a strong mass-loss hampers the core mass growth, strongly limiting the increase of the HBB efficiency (Mazzitelli et al., 1999).
- last but not least, the resulting nucleosynthesis distribution of light isotopes depends on the degree of coupling between the different physical processes at work at the base of the envelope of massive AGB, particularly the one between mixing and burning (Ventura and D'Antona, 2005).

As already highlighted in the text, the delicate balance between TDU and HBB establishes the production of presolar oxide and SiC grains in massive AGBs, and Lugaro et al. (2017) show that AGB stellar models with mass between 4.5 and 6 $M_{\odot}$ (and solar metallicity) and HBB at play might account for the oxygen isotopic ratios observed in group 2 oxide grains. Such agreement is possible thanks to the increased rate of $^{17}O(p,\alpha)^{14}N$ reaction rate measured by Bruno et al. (2016), while data grains are not reproduced by the same nucleosynthesis models run with a different reaction rate, such as the one reported by Iliadis et al. (2010). The comparison of the model predictions with grain isotopic mix is shown by the red curves in **Figure 4**, where the darker the color the more massive the star is. The red solid lines deal with the evolution in the stellar envelopes of the $^{18}O/^{16}O$ isotopic ratio as a function of the $^{17}O/^{16}O$ and the $^{26}Al/^{27}Al$ (in panel A and B, respectively). The stellar models are supposed to approach the AGB phase with $^{17}O/^{16}O \geq 0.0023$, $^{18}O/^{16}O \leq 0.0014$ (see the corner points of the curves in panel A) and $^{26}Al/^{27}Al \geq 0.005$; beyond these values, the HBB is at play. A careful inspection of **Figure 4** might lead to the conclusion that intermediate mass models are not compatible to the oxygen ratios measured in oxide grains because the solid curves are too rich in $^{17}O/^{16}O$ to match the grains area for most of the grains in panel A. Moreover, the models reach a range of $^{26}Al/^{27}Al$ values of the grains when the $^{18}O/^{16}O$ is two or three orders of magnitude smaller than the observed ones (panel B). However, Lugaro et al. (2017) highlighted the possibility that material coming from ancient AGB stars may have been diluted with solar-system material, as illustrated by the dashed lines in **Figure 4** that nicely cross the plot areas occupied by grains. If real, such a dilution should be applied to isotopes that are mainly destroyed by HBB, such as ^{18}O, but it should have a comparatively minor effect on those isotopes which are mainly produced in AGBs, as ^{17}O and ^{26}Al.

CONCLUSION

At the state of the art, low mass AGB stars with a bottom-up extra-mixing (as the magnetic induced one) are likely candidates to be progenitors of group 2 presolar oxide grains. This conclusion is based on the comparison between nucleosynthesis prediction and the isotopic mix recorded in the grains. On the other hand, intermediate mass AGB stars, where HBB is at play, are recognized to be the main sources of alumina dust in the galaxy, but the nucleosynthesis models of those stars are able to reproduce the O and Al isotopic abundances of the grain sample only, 1) assuming a dilution of the stellar wind of the progenitor star with solar-system material and 2) employing in calculations the nuclear data set B (and the $^{17}O(p,\alpha)^{14}N$ reaction rate by Bruno et al., 2016 in particular). These are two factors that weaken the likelihood of this second hypothesis.

To definitively answer the question whether the progenitors of group 2 oxide grains are low mass AGB with a bottom-up mixing or intermediate mass AGB affected by HBB, a study of the sensitivity of those two scenarios to the nuclear physics inputs should be carried out. A possible way is recomputing the nucleosynthesis of both low mass and intermediate mass AGB stars with the two sets of nuclear reaction rates reported in **Table 1**. The results of this former analysis will be presented in a future paper (Palmerini et al., *in preparation*).

AUTHOR CONTRIBUTIONS

SP, SC, MB and DV run the stellar models for nucleosynthesis calculations. MC and LS took care of the nuclear physics data employed in calculations. All the authors collaborated in writing the paper.

REFERENCES

Abia, C., Palmerini, S., Busso, M., and Cristallo, S. (2012). Carbon and oxygen isotopic ratios in Arcturus and Aldebaran. *Astron. Astrophys.* 548, A55. doi:10.1051/0004-6361/201220148

Boothroyd, A. I., and Sackmann, I.-J. (1992). Breakdown of the core mass-luminosity relation at high luminosities on the asymptotic giant branch. *Astrophys. J.* 393, L21. doi:10.1086/186441

Boothroyd, A. I., Sackmann, I.-J., and Wasserburg, G. J. (1994). Predictions of oxygen isotope ratios in stars and of oxygen-rich interstellar grains in meteorites. *Astrophys. J.* 430, L77. doi:10.1086/187442

Boothroyd, A. I., and Sackmann, I. J. (1999). The CNO isotopes: deep circulation in red giants and first and second dredge-up. *Astrophys. J.* 510, 232–250. doi:10.1086/306546

Broggini, C., Bemmerer, D., Caciolli, A., and Trezzi, D. (2018). LUNA: status and prospects. *Prog. Part. Nucl. Phys.* 98, 55–84. doi:10.1016/j.ppnp.2017.09.002

Bruno, C. G., Scott, D. A., Aliotta, M., Formicola, A., Best, A., Boeltzig, A., et al. (2016). Improved direct measurement of the 64.5 keV resonance strength in the ˆ{17}O(p,α){14}N reaction at LUNA. *Phys. Rev. Lett.* 117, 142502. doi:10.1103/PhysRevLett.117.142502

Busso, M., Palmerini, S., Maiorca, E., Cristallo, S., Straniero, O., Abia, C., et al. (2010). On the need for deep-mixing in asymptotic giant branch stars of low mass. *Astrophys. J.* 717, L47. doi:10.1088/2041-8205/717/1/L47

Choi, B. G., Huss, G. R., Wasserburg, G. J., and Gallino, R. (1998). Presolar corundum and spinel in ordinary chondrites: origins from AGB stars and a supernova. *Science* 282, 1284. doi:10.1126/science.282.5392.1284

Cognata, M. L., Spitaleri, C., and Mukhamedzhanov, A. M. (2010). Effect of high-energy resonances on the $^{18}O(p,\alpha)^{15}N$ reaction rate at AGB and post-AGB relevant temperatures. *Astrophys. J.* 723, 1512–1522. doi:10.1088/0004-637X/723/2/1512

De Beck, E., Decin, L., Ramstedt, S., Olofsson, H., Menten, K. M., Patel, N. A., et al. (2017). Search for aluminium monoxide in the winds of oxygen-rich AGB stars. *Astron. Astrophys.* 598, A53. doi:10.1051/0004-6361/201628928

Dell'Agli, F., García-Hernández, D. A., Rossi, C., Ventura, P., Di Criscienzo, M., and Schneider, R. (2014). On the alumina dust production in the winds of O-rich asymptotic giant branch stars. *Mon. Not. Roy. Astron. Soc.* 441, 1115–1125. doi:10.1093/mnras/stu647

Denissenkov, P. A., Pinsonneault, M., and MacGregor, K. B. (2009). Magneto-thermohaline mixing in red giants. *Astrophys. J.* 696, 1823–1833. doi:10.1088/0004-637X/696/2/1823

Di Leva, A., Scott, D. A., Caciolli, A., Formicola, A., Strieder, F., Aliotta, M., et al. (2014). Underground study of the $O^{17}(p,\gamma)F^{18}$ reaction relevant for explosive hydrogen burning. *Phys. Rev. C* 89, 015803. doi:10.1103/PhysRevC.89.015803

D'Antona, F., and Mazzitelli, I. (1996). Hot bottom burning in asymptotic giant branch stars and the turbulent convection model. *Astrophys. J.* 470, 1093. doi:10.1086/177933

Eggleton, P. P., Dearborn, D. S., and Lattanzio, J. C. (2006). Deep mixing of 3He: reconciling Big Bang and stellar nucleosynthesis. *Science* 314, 1580. doi:10.1126/science.1133065

Eggleton, P. P., Dearborn, D. S. P., and Lattanzio, J. C. (2008). Compulsory deep mixing of 3He and CNO isotopes in the envelopes of low-mass red giants. *Astrophys. J.* 677, 581–592. doi:10.1086/529024

El Eid, M. F. (2016). Introduction to asymptotic giant branch stars. *J. Phys. Conf. Ser.* 703, 012005. doi:10.1088/1742-6596/703/1/012005

Fuller, J., Cantiello, M., Stello, D., Garcia, R. A., and Bildsten, L. (2015). Asteroseismology can reveal strong internal magnetic fields in red giant stars. *Science* 350, 423–426. doi:10.1126/science.aac6933

Harris, M. J., and Lambert, D. L. (1984). Oxygen isotopic abundances in the atmospheres of seven red giant stars. *Astrophys. J.* 285, 674–682. doi:10.1086/162544

Herwig, F. (2005). Evolution of asymptotic giant branch stars. *Annu. Rev. Astron. Astrophys.* 43, 435–479. doi:10.1146/annurev.astro.43.072103.150600

Hirayama, T. (1992). The current sheet and joule heating of a slender magnetic tube in the upper photosphere. *Sol. Phys.* 137, 33–50. doi:10.1007/BF00146574

Hynes, K. M., and Gyngard, F. (2009). The Presolar Grain Database: http://presolar.wustl.edu. In Lunar and Planetary Science Conference, Woodlands, TX, March 23–27, 2009, 1198.

Iben, I. J. (1973). On the abundance of lithium in red giants of intermediate mass. *Astrophys. J.* 185, 209–212. doi:10.1086/152409

Iben, I. J. (1975). Thermal pulses; p-capture, alpha-capture, s-process nucleosynthesis; and convective mixing in a star of intermediate mass. *Astrophys. J.* 196, 525–547. doi:10.1086/153433

Iliadis, C., Angulo, C., Descouvemont, P., Lugaro, M., and Mohr, P. (2008). New reaction rate for $16O(p,\gamma)17F$ and its influence on the oxygen isotopic ratios in massive AGB stars. *Phys. Rev. C* 77, 045802. doi:10.1103/PhysRevC.77.045802

Iliadis, C., Longland, R., Champagne, A. E., Coc, A., and Fitzgerald, R. (2010). Charged-particle thermonuclear reaction rates: II. Tables and graphs of reaction rates and probability density functions. *Nucl. Phys.* 841, 31–250. doi:10.1016/j.nuclphysa.2010.04.009

Karovicova, I., Wittkowski, M., Ohnaka, K., Boboltz, D. A., Fossat, E., and Scholz, M. (2013). New insights into the dust formation of oxygen-rich AGB stars. *Astron. Astrophys.* 560, A75. doi:10.1051/0004-6361/201322376

La Cognata, M., Spitaleri, C., and Mukhamedzhanov, A. M. (2010). Effect of High-energy Resonances on the 18O(p, α)15N Reaction Rate at AGB and Post-AGB Relevant Temperatures. *Astrophys. J.* 723, 1512–1522. doi:10.1088/0004-637X/723/2/1512

Lagarde, N., Decressin, T., Charbonnel, C., Eggenberger, P., Ekström, S., and Palacios, A. (2012). Thermohaline instability and rotation-induced mixing. *Astron. Astrophys.* 543, A108. doi:10.1051/0004-6361/201118331

Lattanzio, J. (2019). AGB stars: remaining problems. *Proc. IAU* 14, 3–8. doi:10.1017/S1743921318007019

Lattanzio, J. C., Siess, L., Church, R. P., Angelou, G., Stancliffe, R. J., Doherty, C. L., et al. (2015). On the numerical treatment and dependence of thermohaline mixing in red giants. *Mon. Not. Roy. Astron. Soc.* 446, 2673–2688. doi:10.1093/mnras/stu2238

Lugaro, M., Karakas, A. I., Bruno, C. G., Aliotta, M., Nittler, L. R., Bemmerer, D., et al. (2017). Origin of meteoritic stardust unveiled by a revised proton-capture rate of 17O. *Nat Astron* 1, 0027. doi:10.1038/s41550-016-0027

Mazzitelli, I., D'Antona, F., and Ventura, P. (1999). Full spectrum of turbulence convective mixing. II. Lithium production in AGB stars. *Astron. Astrophys.* 348, 846–860.

Nittler, L. R., Alexander, C. M. O. D., Gao, X., Walker, R. M., and Zinner, E. (1997). Stellar sapphires: the properties and origins of presolar Al2O3in meteorites. *Astrophys. J.* 483, 475–495. doi:10.1086/304234

Nittler, L. R. (2009). On the mass and metallicity distributions of the parent AGB stars of O-rich presolar stardust grains, *Publ. Astron. Soc. Aust.*, 26, 271–277. doi:10.1071/AS08071

Nollett, K. M., Busso, M., and Wasserburg, G. J. (2003). Cool bottom processes on the thermally pulsing asymptotic giant branch and the isotopic composition of circumstellar dust grains. *Astrophys. J.* 582, 1036–1058. doi:10.1086/344817

Nomoto, K. i., Kobayashi, C., and Tominaga, N. (2013). Nucleosynthesis in stars and the chemical enrichment of galaxies. *Annu. Rev. Astron. Astrophys.* 51, 457–509. doi:10.1146/annurev-astro-082812-140956

Nucci, M. C., and Busso, M. (2014). Magnetohydrodynamics and deep mixing in evolved stars. I. Two- and three-dimensional analytical models for the asymptotic giant branch. *Astrophys. J.* 787, 141. doi:10.1088/0004-637X/787/2/141

Onaka, T., Nakada, Y., Tanabe, T., Sakata, A., and Wada, S. (1986). A Quenched Carbonaceous Composite/QCC/Grain model for the interstellar 220-NM extinction hump. *Astrophys. Space Sci.*, 118, 411. doi:10.1007/BF00651159

Palacios, A., Charbonnel, C., Talon, S., and Siess, L. (2006). Rotational mixing in low-mass stars. *Astron. Astrophys.* 453, 261–278. doi:10.1051/0004-6361:20053065

Palmerini, S., La Cognata, M., Cristallo, S., and Busso, M. (2011a). Deep mixing in evolved stars. I. The effect of reaction rate revisions from C to Al. *Astrophys. J.* 729, 3. doi:10.1088/0004-637X/729/1/3

Palmerini, S., Cristallo, S., Busso, M., Abia, C., Uttenthaler, S., Gialanella, L., et al. (2011b). Deep mixing in evolved stars. II. interpreting Li abundances in red giant branch and asymptotic giant branch stars. *Astrophys. J.*, 741, 26. doi:10.1088/0004-637X/741/1/26

Palmerini, S., Sergi, M. L., La Cognata, M., Lamia, L., Pizzone, R. G., and Spitaleri, C. (2013). The RGB and AGB star nucleosynthesis in light of the recent $^{17}O(p,\alpha)^{14}N$ and $^{18}O(p,\alpha)^{15}N$ reaction-rate determinations. *Astrophys. J.* 764, 128. doi:10.1088/0004-637X/764/2/128

Palmerini, S., Trippella, O., and Busso, M. (2017). A deep mixing solution to the aluminum and oxygen isotope puzzles in presolar grains. *Mon. Not. Roy. Astron. Soc.* 467, stx137–1201. doi:10.1093/mnras/stx137

Palmerini, S., Trippella, O., Busso, M., Vescovi, D., Petrelli, M., Zucchini, A., et al. (2018). s-Processing from MHD-induced mixing and isotopic abundances in presolar SiC grains. *Geochem. Cosmochim. Acta* 221, 21–36. doi:10.1016/j.gca.2017.05.030

Sackmann, I.-J., and Boothroyd, A. I. (1992). The creation of superrich lithium giants. *Astrophys. J.* 392, L71. doi:10.1086/186428

Sergi, M. L., La Cognata, M., Guardo, G. L., Gulino, M., Mrazek, J., Palmerini, S., et al. (2020). Indirect measurements of oxygen burning reactions of astrophysical interest. *Front. Astron. Space Sci.*, 60, 7. doi:10.3389/fspas.2020.00060

Sergi, M. L., Spitaleri, C., La Cognata, M., Lamia, L., Pizzone, R. G., Rapisarda, G. G., et al. (2015). Improvement of the high-accuracy $^{17}O(p,\alpha)^{14}N$ reaction-rate measurement via the Trojan Horse method for application to O nucleosynthesis. *Phys. Rev. C* 91, 065803. doi:10.1103/PhysRevC.91.065803

Straniero, O., Imbriani, G., Strieder, F., Bemmerer, D., Broggini, C., Caciolli, A., et al. (2013). Impact of a revised $^{25}Mg(p, \gamma)^{26}Al$ reaction rate on the operation of the Mg-Al cycle. *Astrophys. J.* 763, 100. doi:10.1088/0004-637X/763/2/100

Tribble, R. E., Bertulani, C. A., Cognata, M., Mukhamedzhanov, A. M., and Spitaleri, C. (2014). Indirect techniques in nuclear astrophysics: a review. *Rep. Prog. Phys.* 77, 106901. doi:10.1088/0034-4885/77/10/106901

Trippella, O., Busso, M., Palmerini, S., Maiorca, E., and Nucci, M. C. (2016). s-Processing in AGB stars revisited. ii. enhanced13c production through MHD-induced mixing. *Astrophys. J.* 818, 125. doi:10.3847/0004-637X/818/2/125

Ventura, P., and D'Antona, F. (2005). Full computation of massive AGB evolution. *Astron. Astrophys.* 431, 279–288. doi:10.1051/0004-6361:20041917

Ventura, P., Dell'Agli, F., Lugaro, M., Romano, D., Tailo, M., and Yagüe, A. (2020). Gas and dust from metal-rich AGB stars. *Astron. Astrophys.* 641, A103. doi:10.1051/0004-6361/202038289

Vescovi, D., Busso, M., Palmerini, S., Trippella, O., Cristallo, S., Piersanti, L., et al. (2018). On the origin of early solar system radioactivities: problems with the asymptotic giant branch and massive star scenarios. *Astrophys. J.* 863, 115. doi:10.3847/1538-4357/aad191

Vescovi, D., Cristallo, S., Busso, M., and Liu, N. (2020). Magnetic-buoyancy-induced mixing in AGB stars: presolar SiC grains. *Astrophys. J.* 897, L25. doi:10.3847/2041-8213/ab9fa1

Wasserburg, G. J., Boothroyd, A. I., and Sackmann, I.-J. (1995). Deep circulation in red giant stars: a solution to the carbon and oxygen isotope puzzles? *Astrophys. J. Lett.* 447, L37. doi:10.1086/309555

Zinner, E. (2014). "Presolar Grains," in: *Meteorites and cosmochemical processes*. Editors Davis and M. Andrew, Vol. 1, 181–213. Available at: https://ui.adsabs.harvard.edu/abs/2014mcp..book..181Z. Provided by the SAO/NASA Astrophysics Data System.

Conflict of Interest: The authors declare that the research was conducted in the absence of any commercial or financial relationships that could be construed as a potential conflict of interest.

The reviewer SC declared a shared affiliation with the authors, DV and SC, to the handling editor at time of review.

frontiers in Astronomy and Space Sciences

REVIEW
published: 02 March 2021
doi: 10.3389/fspas.2020.618356

The Relevance of Nuclear Reactions for Standard Solar Models Construction

Francesco L. Villante[1,2]* *and Aldo Serenelli*[3,4]

[1]*Dipartimento di Scienze Fisiche e Chimiche, Università degli Studi dell'Aquila, L'Aquila, Italy,* [2]*Laboratori Nazionali del Gran Sasso (LNGS), Istituto Nazionale di Fisica Nucleare (INFN), Assergi, Italy,* [3]*Institute of Space Sciences (ICE, CSIC), Barcelona, Spain,* [4]*Institut D'Estudis Espacials de Catalunya (IEEC), Barcelona, Spain*

The fundamental processes by which nuclear energy is generated in the Sun have been known for many years. However, continuous progress in areas such as neutrino experiments, stellar spectroscopy and helioseismic data and techniques requires ever more accurate and precise determination of nuclear reaction cross sections, a fundamental physical input for solar models. In this work, we review the current status of (standard) solar models and present a complete discussion on the relevance of nuclear reactions for detailed predictions of solar properties. In addition, we also provide an analytical model that helps understanding the relation between nuclear cross sections, neutrino fluxes and the possibility they offer for determining physical characteristics of the solar interior. The latter is of particular relevance in the context of the conundrum posed by the solar composition, the solar abundance problem, and in the light of the first ever direct detection of solar CN neutrinos recently obtained by the Borexino collaboration. Finally, we present a short list of wishes about the precision with which nuclear reaction rates should be determined to allow for further progress in our understanding of the Sun.

Keywords: solar physics, solar models, nuclear reactions, nuclear astrophysics, solar neutrino fluxes

OPEN ACCESS

Edited by:
Scilla Degl'Innocenti, University of Pisa, Italy

Reviewed by:
Sarbani Basu, Yale University, United States
Wick Haxton, University of California, Berkeley, United States

***Correspondence:**
Francesco L. Villante
villante@lngs.infn.it

Specialty section:
This article was submitted to Nuclear Physics, a section of the journal Frontiers in Astronomy and Space Sciences

Received: *16 October 2020*
Accepted: *11 December 2020*
Published: *02 March 2021*

Citation:
Villante FL and Serenelli A (2021) The Relevance of Nuclear Reactions for Standard Solar Models Construction. Front. Astron. Space Sci. 7:618356. doi: 10.3389/fspas.2020.618356

1 INTRODUCTION

The history of solar models, or standard solar models (SSMs) to be more precise, is formed by three large chapters related to the type of observational and experimental data about the solar interior that existed at any given time. The first part of this history comprises the period over which only neutrino data were available, and it spans about 20 years, from the mid 60 s to the early 80 s of the past century. During that period, the solar neutrino problem was seen by many as having an origin in the complexities involved in building accurate and precise SSMs, a fundamental part of which is determined by the nuclear reaction rates involved in the generation of the solar nuclear energy. Around the end of that era, the precision of nuclear reaction rates involved in the chains of reactions leading to the production of the different solar neutrino fluxes were on the order to 20–30%. These uncertainties may seem large for present day standards. However, if some faith was put in their accuracy, these uncertainties were small enough that associating the solar neutrino problem to nuclear cross section measurements was highly unlikely (Bahcall et al., 1982).

In the mid 80s helioseismology, the study of solar oscillations, evolved into a precision branch of solar physics. The sensitivity of the frequency spectrum of these global pressure waves to the details of the interior solar structure allowed their reconstruction by means of inversion methods (see e.g., Deubner and Gough (1984); Christensen-Dalsgaard et al. (1985)), in particular of the solar interior

sound speed. This (r)evolution peaked during the second half of the 1990s with the establishment of the Global Oscillation Network Group (GONG), a network of six instruments established around the world that carried out resolved radial velocity measurements of the solar surface (Harvey et al., 1996) and with the launch of the SoHO satellite, both of which provided rich helioseismic datasets. In turn, this led to determination of the solar interior properties with precision of better than 1% (and in some cases even an order of magnitude better) (Gough et al., 1996). These results led to the appearance of a new generation of SSMs (Bahcall et al., 1995; Christensen-Dalsgaard et al., 1996), which were successful in satisfying the tight observational constraints imposed by helioseismology, leaving little room for an astrophysical solution to the solar neutrino problem, as had originally been suggested a few years earlier (Elsworth et al., 1990). Simultaneously, Super-Kamiokande (Fukuda, 1998; Fukuda et al., 2001) led to the precise measurement of ^{8}B neutrino flux which, in combination with the results of radiochemical experiments Homestake (Cleveland et al., 1998), Gallex (Hampel et al., 1999) and SAGE (Abdurashitov et al., 1999) strongly hinted at the existence of solar neutrino oscillations, result confirmed just a few years later by SNO results (Ahmad et al., 2001; Ahmad et al., 2002). The needs of refined nuclear reaction rates imposed by the type and quality of the new observational and experimental data led to famous revisions of nuclear reaction rates such as NACRE (Angulo et al., 1999) and in particular that of Solar Fusion I (Adelberger, 1998). In the latter, a critical analysis of the accumulated experimental and theoretical data was performed and consensus values were provided for all relevant nuclear reactions affecting energy generation and neutrino production in the Sun. The improvement in the uncertainties, in particular, was about a factor of to 2, leading to typical errors around 10%. Simultaneously, several authors used helioseismic inversion of the solar sound speed to determine, or at least set constraints, on the proton-proton reaction rate, showing that its value had to be within about 15% of its theoretically determined value (degl'Innocenti et al., 1998; Schlattl et al., 1999; Antia and Chitre, 1999; Turck-chièze et al., 2001; Antia and Chitre, 2002).

The combination of helioseismic constraints and the discovery of neutrino oscillations changed the focus of interest of SSMs. In particular, the accurate and precise determination of neutrino fluxes from individual reactions started playing a fundamental role in the determination of the neutrino oscillation parameters. SSMs became a fundamental source of information, a reference, not just for astrophysics, but for particle physics as well. In 2007, the final and present chapter in this history started when Borexino presented the first measurement of the ^{7}Be neutrinos (Arpesella et al., 2008), originating from a subdominant branch of reactions, the so-called pp-II branch of the pp-chain that accounts for about 10% of the energy generation of the Sun. Further work by Borexino led to an almost complete characterization of the spectrum of neutrinos from the pp-chain (Agostini et al., 2018). Together with the very precise measurement of the ^{8}B flux from SNO (Aharmim, 2013) and Super-Kamiokande (Abe, 2016), we have come full circle and results from solar neutrino experiments can now be used to learn about the properties of the Sun. This is timely. There is a lingering dispute about which is the detailed chemical composition of the Sun, the solar abundance problem (**Section 2.1**), that is intimately linked to the uncertainties in our knowledge of radiative opacities in the solar interior. Solar neutrino data can in principle be used to disentangle this problem (Haxton and Serenelli, 2008; Serenelli et al., 2013; Villante et al., 2014), in particular if the promising results by Borexino on solar CN neutrinos (Agostini et al., 2020a) can be further improved. But progress along this line depends crucially on the accuracy and precision with which nuclear reaction rates are known. The latest compilation, Solar Fusion II (Adelberger, 2011), and subsequent work on specific reactions (**Section 2**), show on average a factor of two improvement with respect to the status 10–15 years ago, and 5% uncertainties are nowadays typical. But further work is still needed; uncertainties from nuclear reactions still have a non negligible role in the overall SSMs error budget.

In **Section 2** we summarize the current status of SSMs, review the solar abundance problem, the SSM predictions on the solar neutrino spectrum and the status of nuclear reaction rates affecting model predictions. **Section 3** presents an analytical formation of the relation between nuclear reaction rates and solar model properties both for reactions from the pp-chains and CNO-cycles. **Section 4** reviews results from numerical SSM calculations, including a detailed assessment of uncertainties and highlighting where progress is most needed, and revises the possibility of using future CN neutrino measurements to determine the solar core C + N abundance.

2 STANDARD SOLAR MODELS

SSMs are a snapshot in the evolution of a 1 $M_\odot$ star, calibrated to match present-day surface properties of the Sun. Two basic assumptions in SSM calculations are: 1) after the phase of star formation the Sun was chemically homogenized as a result of the fully convective phase during its contracting along the Hayashi track and before nuclear reactions start altering its initial composition and, 2) at all moments during its evolution up to the present solar age $\tau_\odot = 4.57$ Gyr mass loss is negligible. The calibration is done by adjusting the mixing length parameter ($\alpha_{\rm MLT}$) and the initial helium and metal mass fractions ($Y_{\rm ini}$ and $Z_{\rm ini}$, respectively), in order to satisfy the constraints imposed by the present-day solar luminosity $L_\odot = 3.8418 \times 10^{33}\,{\rm erg\,s^{-1}}$, radius $R_\odot = 6.9598 \times 10^{10}$cm (Bahcall et al., 2006), and surface metal to hydrogen abundance ratio $(Z/X)_\odot$, see **section 2.1**. As a result of this procedure, SSM has no free parameters and completely determines the physical properties of the Sun. It can be then validated (or falsified) by other observational constraints, in particular by those provided by solar neutrino fluxes measurements and helioseismic frequencies determinations.

The physics input in the SSM is rather simple and it accounts for: convective and radiative transport of energy, chemical evolution driven by nuclear reactions, microscopic diffusion of elements which comprises different processes but among which gravitational settling dominates. Over more than 25 years, since

TABLE 1 | Solar photospheric composition through time and authors for most relevant metals in solar modeling. Abundances are given in the standard astronomical scale $\epsilon_i = \log_{10}(n_i/n_H) + 12$, where n_i is the number density of a given atomic species.

El	GN93	GS98	AGSS09	C11	AGSS15
C	8.55	8.52	8.43	8.50	—
N	7.97	7.92	7.83	7.86	—
O	8.87	8.83	8.69	8.76	—
Ne	8.08	8.08	7.93	8.05	7.93
Mg	7.58	7.58	7.60	7.54	7.59
Si	7.55	7.55	7.51	7.52	7.51
S	7.33	7.33	7.13	7.16	7.13
Fe	7.50	7.50	7.50	7.52	7.47
$(Z/X)_\odot$	0.0245	0.0230	0.0180	0.0209	—

TABLE 2 | The two canonical HZ and LZ solar mixtures given as $\epsilon_i = \log_{10}(n_i/n_H) + 12$. The two compilations are obtained by using the photospheric (volatiles) + meteoritic (refractories) abundances from GS98 and AGSS09 respectively, and correpond to the admixture labeled as GS98 and AGSS09met in Vinyoles et al. (2017).

El	High-Z (HZ)	Low-Z (LZ)	δz_i
C	8.52 ± 0.06	8.43 ± 0.05	0.23
N	7.92 ± 0.06	7.83 ± 0.05	0.23
O	8.83 ± 0.06	8.69 ± 0.05	0.38
Ne	8.08 ± 0.06	7.93 ± 0.10	0.41
Mg	7.58 ± 0.01	7.53 ± 0.01	0.12
Si	7.56 ± 0.01	7.51 ± 0.01	0.12
S	7.20 ± 0.06	7.15 ± 0.02	0.12
Ar	6.40 ± 0.06	6.40 ± 0.13	0.00
Fe	7.50 ± 0.01	7.45 ± 0.01	0.12
$(Z/X)_\odot$	0.02292	0.01780	0.29

TABLE 3 | Main characteristics of SSMs with different surface composition (Vinyoles et al., 2017). The observational values for Y_s and R_{CZ} are taken from Basu and Antia (2004) and Basu and Antia (1997), respectively. The quantity $\delta c/c = (c_\odot - c_{mod})/c_{mod}$ is the fractional difference between sound speed helioseismic determination and model prediction.

Qnt	B16-HZ	B16-LZ	Solar
Y_s	0.2426 ± 0.0059	0.2317 ± 0.0059	0.2485 ± 0.0035
$R_{CZ}/R_\odot$	0.7116 ± 0.0048	0.7223 ± 0.0053	0.713 ± 0.001
$\langle \delta c/c \rangle$	$0.0005^{+0.0006}_{-0.0002}$	0.0021 ± 0.001	–
α_{MLT}	2.18 ± 0.05	2.11 ± 0.05	–
Y_{ini}	0.2718 ± 0.0056	0.2613 ± 0.0055	–
Z_{ini}	0.0187 ± 0.0013	0.0149 ± 0.0009	–
Z_s	0.0170 ± 0.0012	0.0134 ± 0.0008	–
Y_c	0.6328 ± 0.0053	0.6217 ± 0.0062	–
Z_c	0.0200 ± 0.0014	0.0159 ± 0.0010	–

the modern version of the SSM was established with the inclusion of microscopic diffusion (Bahcall and Pinsonneault, 1992; Christensen-Dalsgaard et al., 1993), the continuous improvement of the constitutive physics has brought about the changes and the evolution of SSMs. In particular, a lot of effort has gone into experimental and theoretical work on nuclear reaction rates. But changes in radiative opacities and the equation of state were also relevant. We take here as a reference the results of recent SSM calculations by Vinyoles et al. (2017), the so-called Barcelona 2016 (B16, for short) SSMs, which are based on the following state of the art ingredients. The equation of state is calculated consistently for each of the compositions used in the solar calibrations by using FreeEOS (Cassisi et al., 2003). Atomic radiative opacities are from the Opacity Project (OP) (Badnell et al., 2005), complemented at low temperatures with molecular opacities from Ferguson et al. (2005). Nuclear reaction rates for the pp-chain and CNO-bicycle, which are described in more details in the following section, are from the Solar Fusion II compilation (Adelberger, 2011) with important updates for the rates of $p(p, e^+\nu_e)d$ (Marcucci et al., 2013; Tognelli et al., 2015; Acharya et al., 2016), $^7Be(p,\gamma)^8B$ (Zhang et al., 2015) and $^{14}N(p,\gamma)^{15}O$ (Marta, 2011) reactions. Microscopic diffusion coefficients are computed as described in Thoul et al. (1994). Convection is treated according to the mixing length theory (Kippenhahn and Weigert, 1990). The atmosphere is gray and modeled according to a Krishna-Swamy $T - \tau$ relationship (Krishna Swamy, 1966).

2.1 The Solar Composition Problem

The solar surface composition, determined with spectroscopic techniques, is a fundamental input in the construction of SSMs. The development of three dimensional hydrodynamic models of the solar atmosphere, of techniques to study line formation under non-local thermodynamic conditions and the improvement in atomic properties (e.g., transition strengths) have led since 2001 to a complete revision of solar abundances. **Table 1** lists the abundances determined by different authors for the most relevant metals in solar modeling: GN93 (Grevesse and Noels, 1993), GS98 (Grevesse and Sauval, 1998), AGSS09 (Asplund et al., 2009), C11 (Caffau et al., 2011) and AGSS15 (Scott et al., 2015a; Scott et al., 2015b; Grevesse et al., 2015). Note that only abundances relative to hydrogen can be obtained from spectroscopy because the intensity of spectroscopic lines is measured relative to a continuum that is determined by the hydrogen abundance in the solar atmosphere. The last row in the table gives the total photospheric present-day metal-to-hydrogen ratio $(Z/X)_\odot$ and it is the quantity used as observational constraint to construct a solar model. In fact, the solar composition set used in solar models determines not only $(Z/X)_\odot$ but also the relative abundances of metals in the models. In this sense, Z_{ini} acts as a normalization factor that, together with Y_{ini} and the relation $X_{ini} + Y_{ini} + Z_{ini} = 1$, determines completely the initial composition of the model.

There is no complete agreement among authors, and some controversy still remains as to what the best values for the new spectroscopic abundances are. However, there is consensus in that all determinations of the solar metallicity based on the new generation of spectroscopic studies yield a solar metallicity lower than older spectroscopic results (Grevesse and Noels, 1993; Grevesse and Sauval, 1998), in particular for the volatile and most abundant C, N, and O. For refractories elements, like Fe, Si, Mg and S that have important role in solar modeling being important contributors to the radiative opacity, meteorites offer a very valuable alternative method (see e.g., Lodders et al. (2009))

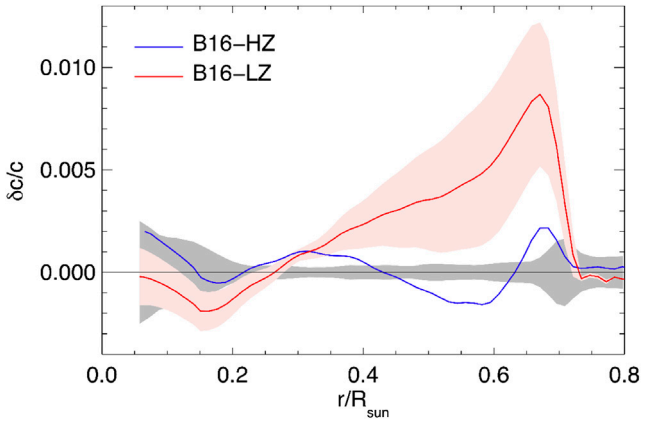

FIGURE 1 | Fractional sound speed difference in the sense $\delta c/c = (c_\odot - c_{mod})/c_{mod}$. Gray shaded regions corresponds to errors from helioseismic inversion procedure. Red shaded region corresponds to uncertainties in SSM predictions which we chose to plot around the B16-LZ central value (solid red line). An equivalent relative error band holds around the central value of the B16-HZ central value (solid blue line) which we do not plot for the sake of clarity.

and, in fact, elemental abundances determined from meteorites have been historically more robust than spectroscopic ones.

Considering that uncertainties in element abundances are difficult to quantify, it has become customary to consider two canonical sets of abundances to which we refer to as high metallicity (HZ) and low metallicity (LZ) solar admixtures, see e.g., Serenelli et al. (2011); Vinyoles et al. (2017) as reference assumptions for SSM calculations. These are obtained by using the photospheric (volatiles) + meteoritic (refractories) abundances from GS98 and AGSS09 respectively, and are reported in **Table 2**. In the last column, we give the fractional differences $\delta z_i \equiv z_i^{HZ}/z_i^{LZ} - 1$ where $z_i \equiv Z_i/X$ is the ratio of the i–element abundance with that of hydrogen, to facilitate comparison among the two admixtures. Even if GS98 abundances are presumably surpassed by the more recent determinations, they are still considered as a valid option to construct solar models because they lead to a temperature stratification that well reproduces the helioseismic constraints.

This can be better appreciated by considering **Table 3** and **Figure 1** where we compare theoretical predictions of SSMs implementing HZ and LZ surface composition with helioseismic determinations of the surface helium abundance Y_s, of the convective envelope depth R_{CZ} and the solar sound speed $c_\odot(r)$. We see that solar models implementing the LZ abundances fail to reproduce all helioseismic probes of solar properties. This disagreement constitutes the so-called *solar abundance problem* (Basu and Antia, 2004; Bahcall et al., 2005a; Delahaye and Pinsonneault, 2006) that has defied a complete solution. All proposed modifications to physical processes in SSMs offer, at best, only partial improvements in some helioseismic probes (e.g. Guzik et al. (2005); Castro et al. (2007); Basu and Antia (2008); Guzik and Mussack (2010); Serenelli et al. (2011)). An alternative possibility is to consider modifications to the physical inputs of SSMs at the level of the constitutive physics, radiative opacities in particular. The effective opacity profile in the solar interior results from the combination of the reigning thermodynamic conditions, including composition, and the atomic opacity calculations at hand. Early works (Montalban et al., 2004; Bahcall et al., 2005b) already suggested that a localized increase in opacities could solve or, at least, alleviate the disagreement of low-Z solar models with helioseismology. Refs. (Christensen-Dalsgaard et al., 2009; Villante, 2010) have concluded that a tilted increase in radiative opacities, with a few percent increase in the solar core and a larger (15–20%) increase at the base of the convective envelope could lead to low-Z SSMs that would satisfy helioseismic probes equally as well as SSMs based on the older, higher, metallicities.

Recent years have seen a surge of activity in theoretical calculations of atomic radiative opacities. Updated calculations (Badnell et al., 2005) by the Opacity Project have led the way, followed by OPAS (Blancard et al., 2012; Mondet et al., 2015), STAR (Krief et al., 2016b) and a new version of OPLIB, the opacities from Los Alamos (Colgan et al., 2016). For conditions in solar interiors, all theoretical opacities agree with each other within few %. Interestingly Bailey et al. (2015), have presented the first ever measurement of opacity under conditions very close to those at the bottom of the solar convective envelope. While the experiment has been carried out only for iron, their conclusion is that all theoretical calculations predict a too low Rosseland mean opacity, at a level of 7 ± 4%, for the temperature and density combinations realized in the experiment. Further experimental work on chromium and nickel opacities was carried out (Nagayama et al., 2019) to help evaluate discrepancies between experimental and theoretical resuls on iron opacity. Results point toward a shortcomings that affect models, particularly in the case of open electronic L-shell configurations such as is present in iron at the base of the convective envelope. Also, the disagreement between theoretical and measured line shapes for the three elements indicates shortcomings in the theoretical understanding of atomic interaction with the plasma. On the other hand, the results also indicated that the quasicontinuum opacity determined experimentally agrees well with the chromium and nickel experiments, contrary to results from the iron experiment. However, the chromium and nickel experiments were carried out at lower temperatures than those used in the original iron experiment, which suggests that the problem of missing quasicontinuum opacity might have an unknown temperature dependence, or that a systematic error affected the high temperature iron measurements. Moreover, Ref. (Krief et al., 2016a) in a recent theoretical analysis of line broadening modeling in opacity calculations, have found that uncertainties linked to this are larger at the base of the convective envelope than in the core. These arguments suggest that opacity calculations are more accurate in the solar core than in the region around the base of the convective envelope. To take this into account, opacity uncertainty was modeled in B16-SSM calculations in terms of two parameters, κ_a and κ_b, that can change both the scale and the temperature dependence of

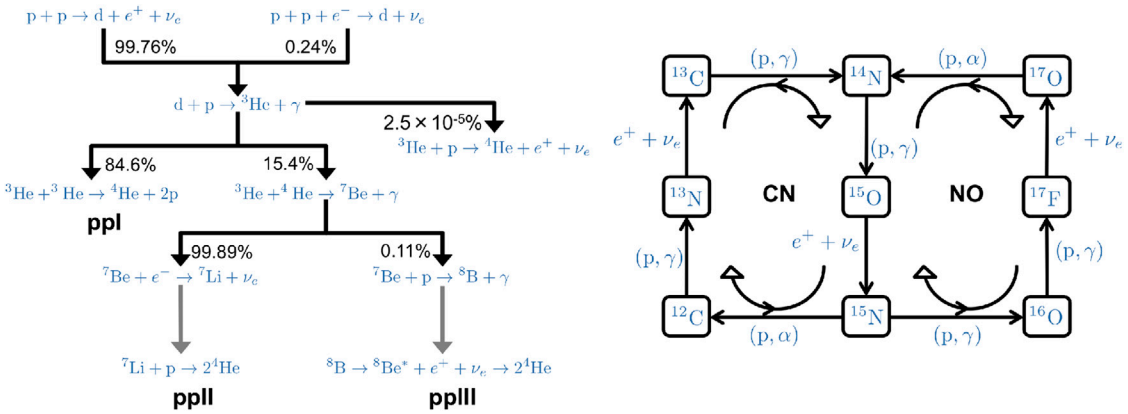

FIGURE 2 | Left Panel: The pp-chain; **Right Panel:** The CNO-bicycle.

opacity according to $\delta k(T) = \kappa_a + (\kappa_b/\Delta)\log(T/T_c)$, where $\delta\kappa$ is the fractional opacity variation, $\Delta = \log(T_c/T_{CZ})$, $T_c = 15.6 \times 10^6$ K and $T_{CZ} = 2.3 \times 10^6$ K are the temperatures at the solar center and at the bottom of the convective zone, respectively. The parameters κ_a and κ_b have been treated as independent random variables with mean equal to zero and dispersions $\sigma_a = 2\%$ and $\sigma_b = 6.7\%$, corresponding to opacity uncertainty $\sigma_{in} = \sigma_a = 2\%$ at the solar center and $\sigma_{out} = (\sigma_a^2 + \sigma_b^2)^{1/2} = 7\%$ at the base of the convective region.

2.2 Nuclear Reactions in the Sun

The overall effect of nuclear reactions in the Sun, as in any other star in hydrogen burning stage, is the conversion:

$$4\,\mathrm{p} + 2\,e^- \rightarrow {}^4\mathrm{He} + 2\,\nu_e \qquad (1)$$

with the production of a fixed amount of energy $Q = 4\,m_p + 2m_e - m_{^4\mathrm{He}} = 26.7$ MeV per synthesized ^{4}He nucleus. Most of this energy is released in the solar plasma and slowly diffuses toward the solar surface supporting the radiative luminosity of the Sun. A small fraction of it, that depends on the specific channel by which hydrogen burning proceeds, is emitted in neutrinos. According to SSM calculations, the two neutrinos carry away about 0.6 MeV on the average.

The SSM predicts that most of the solar energy (> 99%) is produced by the pp-chain, i.e. the hydrogen fusion reaction chain displayed in the left panel of **Figure 2**. The pp-chain is mostly initiated by $\mathrm{p}(\mathrm{p}, e^+\nu_e)\mathrm{d}$ reaction and, to a minor extent, by electron capture reaction $\mathrm{p}(\mathrm{p}e^-, \nu_e)\mathrm{d}$ and has several possible terminations that depend on the specific mechanism by which helium-3 nuclei, which are produced by $\mathrm{d}(\mathrm{p},\gamma)^3\mathrm{He}$ reaction, are converted to heavier elements. In the Sun, the dominant mechanism is $^3\mathrm{He}(^3\mathrm{He}, 2p)^4\mathrm{He}$ that corresponds to the so-called pp-I termination of the pp-chain. Alternatively, helium-3 can undergo $^3\mathrm{He}(^4\mathrm{He},\gamma)^7\mathrm{Be}$ reaction with the effect of producing beryllium-7. Depending on the destiny of ^{7}Be, that can be processed either by the electron capture $^7\mathrm{Be}(e^-, \nu_e)^7\mathrm{Li}$ or by the (largely sub-dominant) proton capture reaction $^7\mathrm{Be}(\mathrm{p},\gamma)^8\mathrm{B}$, one obtains the pp-II or the pp-III terminations of the chain. Finally, a very small amount of helium-4 nuclei is produced by $^3\mathrm{He}(\mathrm{p}, e^+\nu_e)^4\mathrm{He}$ reaction. The relative importance of the different branches of the pp-chain depends primarily on the core temperature of the Sun and on the cross section of specific reactions, as will be discussed in next section. The numbers given in **Figure 2** show the branching ratios in the present Sun. According to SSM calculations, the central temperature and density of the present Sun are $T_c \simeq 15.6 \times 10^6$ K and $\rho_c \simeq 150$ g cm^{-3} and they decrease as a function of the solar radius as it is shown in **Figure 3**. Most of the solar luminosity is produced in the region $r \lesssim 0.2\,R_\odot$ that contains about 30% of the total mass of the Sun. In this region we observe a relevant increase (decrease) of the helium-4 (hydrogen) mass fraction Y (X), as a result of hydrogen burning during the Sun lifetime. The helium-3 mass fraction (X_3) has a non monotonic behavior, explained by the fact that ^{3}He burning time is larger than the age of the Sun for $r \gtrsim 0.3R_\odot$ and thus helium-3 accumulates proportionally to the efficiency of $\mathrm{d}(\mathrm{p},\gamma)^3\mathrm{He}$ reaction. In the energy-producing core, however, ^{3}He nuclei are efficiently converted to heavier elements by nuclear processes (mainly by $^3\mathrm{He}(^3\mathrm{He}, 2p)^4\mathrm{He}$), and the abundance X_3 is equal to the equilibrium value.

An alternative hydrogen burning mechanism is provided by the CNO-bicycle that is displayed in the right panel of **Figure 2**. The CNO-bicycle uses carbon, nitrogen and oxygen nuclei that are present in the core of the Sun as catalysts for hydrogen fusion. It is composed by two different branches, i.e. the CN-cycle and the NO-cycle, whose relative importance depends on the outcome of proton capture reaction on nitrogen-15. In the Sun, the $^{15}\mathrm{N}(\mathrm{p},\alpha)^{12}\mathrm{C}$ channel is largely dominant and so, in practice, the CNO-bicycle is reduced to the CN-cycle with a marginal contribution by the NO-cycle. Note that the CN-cycle conserves the total number of ^{12}C and ^{14}N nuclei in the core of the Sun, but alters their distribution as it burns into equilibrium, eventually achieving equilibrium abundances proportional to the inverse of the respective rates, see right panel of **Figure 3**. The reactions controlling conversion of ^{12}C and ^{14}N in the solar core and the approach to equilibrium are $^{12}\mathrm{C}(\mathrm{p},\gamma)^{13}\mathrm{N}$ and $^{14}\mathrm{N}(\mathrm{p},\gamma)^{15}\mathrm{O}$: these are the next-to-slowest and slowest rates in the CN-cycle, respectively. The temperature above which the ^{12}C burning time through $^{12}\mathrm{C}(\mathrm{p},\gamma)^{13}\mathrm{N}$ is smaller than the Sun's lifetime is $T \sim 10^7$ K. In the SSM, the entire energy-producing core,

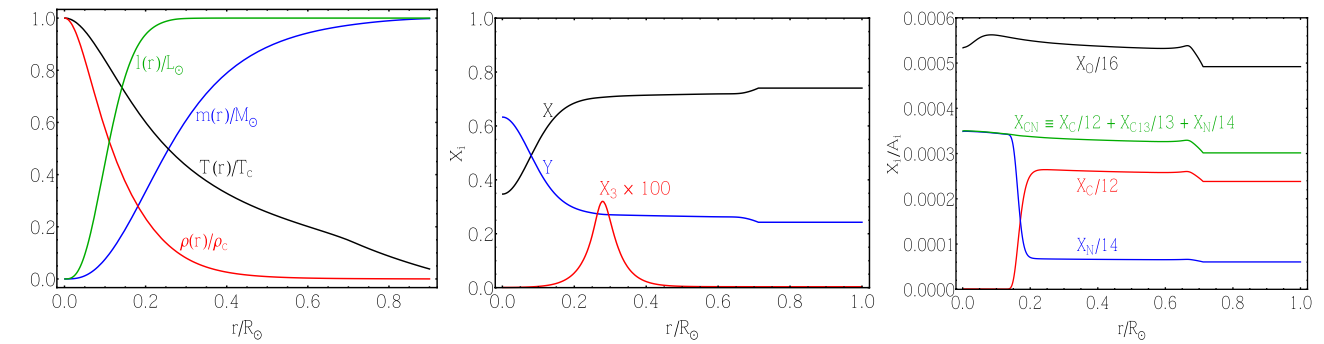

FIGURE 3 | Left Panel: The behavior of temperature T and density ρ (scaled to central values T_c and ρ_c) and of mass m and luminosity l (scaled to total mass $M_\odot$ and luminosity $L_\odot$) as a function of the solar radius. **Middle Panel:** The abundances of hydrogen (X), helium-4 (Y) and helium-3 (X_3) in the present Sun; **Right Panel:** The abundances of CNO elements in the present Sun.

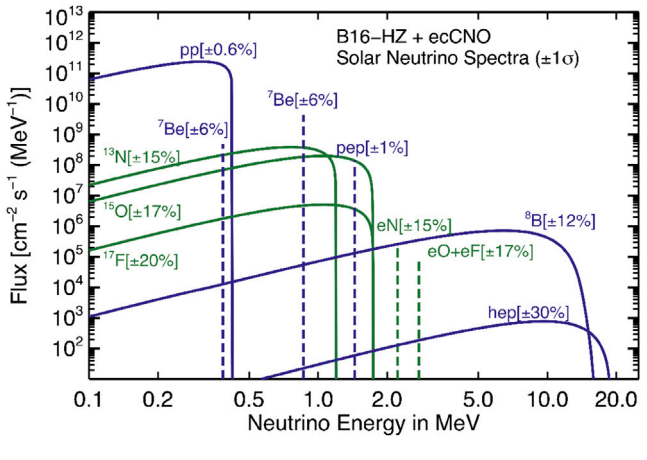

FIGURE 4 | The solar neutrino spectrum.

TABLE 4 | Solar neutrino fluxes predicted by SSMs with different surface composition (Vinyoles et al., 2017). Units are: 10^{10} (pp), 10^9 (^{7}Be), 10^8 (pep, ^{13}N, ^{15}O), 10^6 (^{8}B,^{17}F), 10^5 (eN, eO) and 10^3 (hep, eF) cm^{-2}s^{-1}.

Flux	B16-HZ	B16-LZ
Φ(pp)	5.98(1 ± 0.006)	6.03(1 ± 0.005)
Φ(pep)	1.44(1 ± 0.01)	1.46(1 ± 0.009)
Φ(hep)	7.98(1 ± 0.30)	8.25(1 ± 0.30)
Φ(^{7}Be)	4.93(1 ± 0.06)	4.50(1 ± 0.06)
Φ(^{8}B)	5.46(1 ± 0.12)	4.50(1 ± 0.12)
Φ(^{13}N)	2.78(1 ± 0.15)	2.04(1 ± 0.14)
Φ(^{15}O)	2.05(1 ± 0.17)	1.44(1 ± 0.16)
Φ(^{17}F)	5.29(1 ± 0.20)	3.26(1 ± 0.18)
Φ(eN)	2.20(1 ± 0.15)	1.61(1 ± 0.14)
Φ(eO)	0.81(1 ± 0.17)	0.57(1 ± 0.16)
Φ(eF)	3.11(1 ± 0.20)	1.91(1 ± 0.18)

$r \lesssim 0.2R_\odot$ and $m \lesssim 0.3M_\odot$ is at temperature larger than this value, so that nearly all of the core's carbon-12 is converted to nitrogen-14. The slower ^{14}N(p, γ)^{15}O: reaction determines whether equilibrium is achieved. The ^{14}N burning time is shorter than the age of the Sun for $T \gtrsim 1.3 \times 10^7$ K. Therefore equilibrium for the CN cycle is reached only for $R \lesssim 0.1R_\odot$, corresponding to the central 7% of the Sun by mass. Consequently, over a significant portion of the outer core, ^{12}C is converted to ^{14}N, but further reactions are inhibited by the ^{14}N(p, γ)^{15}O bottleneck.

A very effective tool to investigate nuclear energy generation in the Sun is provided by neutrinos which are necessarily produced along with ^{4}He nuclei during hydrogen burning, in order to satisfy lepton number conservation. Neutrinos free stream in the solar plasma and reach the Earth in about 8 min where they can be detected by solar neutrino experiments. While the total amount of neutrinos produced in the Sun can be easily estimated from the solar luminosity constraint, i.e., the assumption that the luminosity radiated from the surface of the Sun is exactly counterbalanced by the amount of energy produced by hydrogen fusion reactions in the solar core (see e.g., Bahcall (2002); Degl'Innocenti et al. (1997); Vissani (2019) for a detailed discussion), the evaluation of their spectrum requires the knowledge of the individual rates of neutrino producing reactions and thus the construction of a complete solar model. We report in **Figure 4** and **Table 4**, the SSM predictions for the different components of the solar neutrino flux, named according to the specific reaction by which they are produced (Vinyoles et al., 2017). We also include, for completeness, ecCNO neutrinos, i.e. neutrinos produced by electron capture reaction in the CNO-bicycle (in addition to the "standard" CNO neutrinos produced by β decays of ^{13}N, ^{15}O and ^{17}F) that were originally calculated in Bahcall (1990); Stonehill et al. (2004) and recently reevaluated in Villante (2015)[a]. The two columns "B16-HZ" and "B16-LZ" reported in **Table 4** are obtained by considering two different options for the solar surface composition, as it discussed in **Section 2.1**. During the last few decades, solar neutrino

[a]In order to take into account the new inputs in B16-SSM calculations, the ecCNO fluxes given in **Table 4** have been scaled with respect to the values quoted in Villante (2015) proportionally to the corresponding β-decay fluxes. This follows from the assumption that the ratio of electron capture and beta decay processes in the Sun is equal to what evaluated in Villante (2015).

experiments have allowed us to determine with great accuracy most of the components of the solar flux. As an example, ^{7}Be and B8 neutrino fluxes are measured with accuracy better than $\sim 3\%$ by Borexino (Agostini et al., 2018), Super-Kamiokande (Abe, 2016) and SNO (Aharmim, 2013). The pp and pep-neutrino flux can be determined with $\lesssim 1\%$ accuracy by assuming the solar luminosity constraint, see e.g., Bergstrom et al. (2016). These fluxes, however, have been also directly measured by Borexino (Bellini et al., 2012; Bellini, 2014; Agostini et al., 2018) with $\sim 10\%$ and $\sim 17\%$ accuracy, respectively. Finally, Borexino has recently obtained the experimental identification of CNO neutrinos (Agostini et al., 2020a), providing the first direct evidence that CNO-bicycle is active in the Sun.

2.3 Nuclear Reaction Rates

The cross sections of nuclear reaction in pp-chain and in CNO-bicycle are fundamental inputs for SSM calculations. Even if the focus of this work is on the role of nuclear rates for solar modeling (more than on reviewing the present situation for cross section measurements and calculations), we believe that it is useful to briefly discuss the adopted assumptions for the B16-SSM (Vinyoles et al., 2017). whose results have been previously discussed. The nuclear rates adopted for these models are from the Solar Fusion II compilation (Adelberger, 2011) with few relevant changes summarized in the following.

- $\mathbf{p(p,e^+\nu_e)d}$: The astrophysical factor $S_{11}(E)$ has been recalculated in Marcucci et al. (2013) by using chiral effective field theory framework, including the P-wave contribution that had been previously neglected. For the leading order they obtain $S_{11}(0) = (4.03 \pm 0.006) \cdot 10^{-25}$ MeV b. More recently, and also using chiral effective field theory, $S_{11}(E)$ was calculated by Acharya et al. (2016), resulting in $S_{11}(0) = 4.047^{+0.024}_{-0.032} \cdot 10^{-25}$ MeV b. This is in very good agreement with result from Marcucci et al. (2013). Ref. Acharya et al. (2016) have performed a more thorough assessment of uncertainty sources leading to an estimated error of 0.7%, much closer to the 1% uncertainty which was obtained by Adelberger (2011). In B16-SSM calculations, the astrophysical factor $S_{11}(E)$ is taken from Marcucci et al. (2013) with a conservative 1% error estimate Vinyoles et al. (2017).
- $^7\mathbf{Be(p,\gamma)^8B}$: Solar Fusion II recommended value is $S_{17}(0) = (2.08 \pm 0.07 \pm 0.14) \cdot 10^{-5}$ MeV b (Adelberger, 2011), where the first error term comes from uncertainties in the different experimental results and the second one from considering different theoretical models employed for the low-energy extrapolation of the rate. Ref. (Zhang et al., 2015) presented a new low-energy extrapolation $S_{17}(0) = (2.13 \pm 0.07) \cdot 10^{-5}$ MeV b, based on Halo Effective Field Theory, which allows for a continuous parametric evaluation of all low-energy models. Marginalization over the family of continuous parameters then amounts to marginalizing the results over the different low-energy models. In B16-SSM calculations, it was conservatively adopted an intermediate error between those from Zhang et al. (2015) and Adelberger (2011). The adopted value is $S_{17}(0) = (2.13 \pm 0.1) \cdot 10^{-5}$ MeV b. The derivatives of the astrophysical factor were updated by using the recommended values in Zhang et al. (2015).
- $^{14}\mathbf{N(p,\gamma)^{15}O}$: Ref. (Marta, 2011) presented cross-section data for this reaction obtained at the Laboratory for Underground Nuclear Astrophysics (LUNA) experiment. With the new data and using R-matrix analysis they recommend the value for the ground-state capture of $S_{GS}(0) = (0.20 \pm 0.05) \cdot 10^{-3}$MeV b. Combined with other transitions (see Table XI in that work) this leads to $S_{114}(0) = (1.59 \cdot 10^{-3})$MeV b, about 4% lower than the previous recommended value in Ref. (Adelberger, 2011). The derivatives and the errors remain unchanged.
- $^3\mathbf{He}(^4\mathbf{He},\gamma)^7\mathbf{Be}$: Two recent analyses (deBoer et al., 2014; Iliadis et al., 2016) have provided determinations of the astrophysical factor that differs by about 6% (to be compared with a claimed accuracy equal to 4% and 2% for deBoer et al. (2014) and Iliadis et al. (2016), respectively). Considering that the results from deBoer et al. (2014) and Iliadis et al. (2016) bracket the previously adopted value from Adelberger (2011), the latter was considered as preferred choice in Vinyoles et al. (2017).

Finally, Salpeter's formulation of weak screening (Salpeter, 1954) is adopted. The validity of this formulation for solar conditions, where electrons are only weakly degenerate, has been discussed in detail in Gruzinov and Bahcall (1998), where a more sophisticated approach was shown to lead, to within differences of about 1%, to Salpeter's result. Other proposed deviations from this formulation have been discussed at length in Bahcall et al. (2002), including different approaches to dynamic screening, and shown to be flawed or not well physically motivated. More recent calculations of dynamic screening (Mao et al., 2009; Mussack and Dappen, 2011) still leave, however, some room for discussion on this topic. In the weak screening limit, and in conditions under which screening is not numerically large, the dominant scaling is with the product of the charge of the two reacting nuclei. In the solar core, screening enhancement is about 5% for $p(p,e^+\nu_e)d$, 20% for $^3He(^4He,\gamma)^7Be$ and $^7Be(p,\gamma)^8B$, and 40% for $^{14}N(p,\gamma)^{15}O$.

3 THE ROLE OF NUCLEAR REACTIONS

In the following, we discuss the role of nuclear reactions in SSM construction. Among nuclear processes, the $p(p,e^+\nu_e)d$ reaction is the only one that can affect the temperature stratification of the Sun. Indeed, this process determines the global efficiency of hydrogen burning in the Sun. The other reactions in the pp-chain and in the CNO-cycle have a minor importance in this

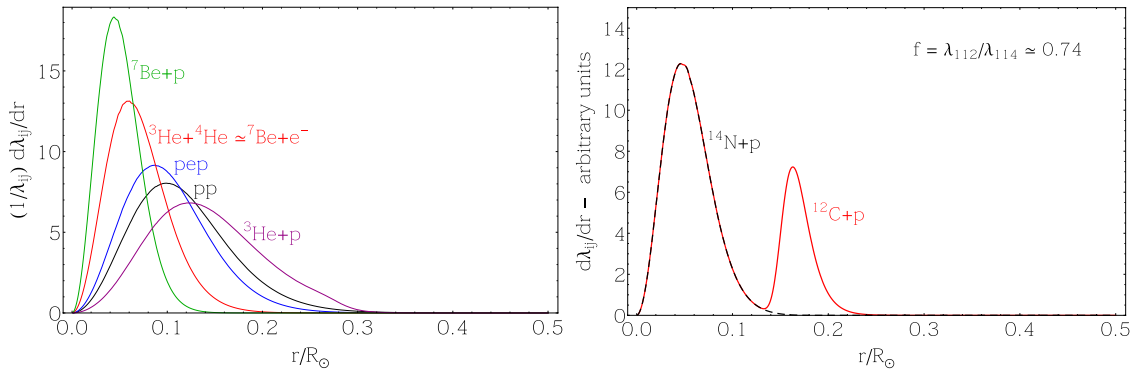

FIGURE 5 | The differential rates for nuclear reactions in the pp-chain **(Left Panel)** and CN-cycle **(Right Panel)**. The curves in the left panel have been normalized to one to facilitate comparison among them. The curves in the right panel are not normalized to emphasize that reactions $^{12}C(p,\gamma)^{13}N$ and $^{14}N(p,\gamma)^{15}O$ have the same rate in the equilibrium region.

respect. However, they have a crucial role in determining the relative rates of the different pp-chain terminations and the efficiency of the CNO-cycle, thus affecting the predictions for the different components of the solar neutrino spectrum.

3.1 The pp-Reaction Rate and the Central Temperature of the Sun

In SSM calculations, where the Sun is assumed to be in thermal equilibrium, the rate of the pp-reaction is basically determined by the solar luminosity. Indeed, by considering that helium-4 is mainly produced by $^3He(^3He,2p)^4He$, we arrive at the conclusion that the integrated pp-rate in the Sun is $\lambda_{11} \sim 2L_\odot/Q_I$, where $Q_I = Q - 2\langle E_\nu\rangle_{pp} \sim 26.2\,MeV$ is the energy released in the solar plasma when ^4He is synthesized through pp-I termination. In the previous expression, we considered that the average energy of neutrinos produced by $p(p,e^+\nu_e)d$ is $\langle E_\nu\rangle_{pp} = 0.265\,MeV$ and we took into account that, at equilibrium, the pp-I termination involves twice the pp-reaction in order to feed the process $^3He(^3He,2p)^4He$.

Being the reaction rate fixed by the observed luminosity, the cross section of $p(p,e^+\nu_e)d$ determines the central temperature of the Sun, as it is explained in the following. The rate λ_{11} can be expressed as:

$$\lambda_{11} = \int d^3r\,\frac{\rho^2}{m_u^2}\,\frac{X^2}{2}\,\langle\sigma v\rangle_{11} \tag{2}$$

where ρ is the density, m_u is the atomic mass unit, X is the hydrogen mass fraction and $\langle\sigma v\rangle_{11}$ is the reaction rate per particle pair of the $p(p,e^+\nu_e)d$ reaction. The above integral involves, in principle, the entire solar structure but it gets a non-vanishing contribution only from the inner core of the Sun at $r \le 0.3\,R_\odot$. This can be appreciated by looking at **Figure 5** where we show the differential rates $(1/\lambda_{ij})\,(d\lambda_{ij}/dr)$ for the $p(p,e^+\nu_e)d$ (black), $p(pe^-,\nu_e)d$ (blue), $^3He(^4He,\gamma)^7Be$ (red), $^7Be(p,\gamma)^8B$ (green) and $^3He(p,e^+\nu_e)^4He$ (purple) reactions as a function of the solar radius. The different curves are all normalized to one in order to facilitate comparison among them. These curves also corresponds to the normalized production rates of pp, pep, ^7Be, ^8B and hep neutrinos, respectively[b].

Taking into account that $p(p,e^+\nu_e)d$ reaction is active in a narrow region of the Sun at $r_0 \simeq 0.1R_\odot$ whose physical conditions are similar to those at the solar center, we write the approximate scaling law:

$$\lambda_{11} \propto \rho_c^2\,X_c^2\,S_{11}\,T_c^{\gamma_{11}} \tag{3}$$

where the notation Q_c indicates that the generic quantity Q is evaluated at the center of the Sun, S_{11} is the astrophysical factor of the pp-reaction and we considered that $\langle\sigma v\rangle_{11} \propto S_{11}\,T_c^{\gamma_{11}}$ with $\gamma_{11} \simeq 4$. **Eq. 3** implies the following linearized relationship:

$$\delta\lambda_{11} \simeq 2\delta\rho_c + 2\delta X_c + \gamma_{11}\,\delta T_c + \delta S_{11}\,, \tag{3.1}$$

where δQ indicates the fractional variation of the quantity Q with respect to the reference SSM value. The above expression contains input parameters for solar model construction, i.e. the astrophysical factor S_{11}, and structural parameters, like e.g., the temperature, density and hydrogen abundance in the core of the Sun which are the result of solar model self-calibrated calculations. In principle, a modification of S_{11} induces a change of the solar structure and, thus, the different terms in the r.h.s of **Eq. 3.1** are correlated. In order to keep $\delta\lambda_{11} \simeq 0$, an increase of the astrophysical factor $\delta S_{11} \ge 0$ has to be counterbalanced by an opposite contribution $2\delta\rho_c + 2\delta X_c + \gamma_{11}\,\delta T_c \le 0$. This is achieved by varying the initial helium and metal abundance of the Sun according to $\delta Y_{ini} = 0.6\,\delta S_{11}$ and $\delta Z_{ini} \simeq -0.10\,\delta S_{11}$ with the effect of obtaining a (slightly) colder solar core. We obtain numerically:

$$\delta T_c \sim -0.13\,\delta S_{11} \tag{4}$$

that will be useful in the following to understand the effects of S_{11} variations on the various components of the solar neutrino spectrum. In **Figure 6**, we show the effect of a 10% increase of

[b]Note that the rate of $^3He(^4He,\gamma)^7Be$ is basically equal to that of the neutrino producing reaction $^7Be(e^-,\nu_e)^7Li$

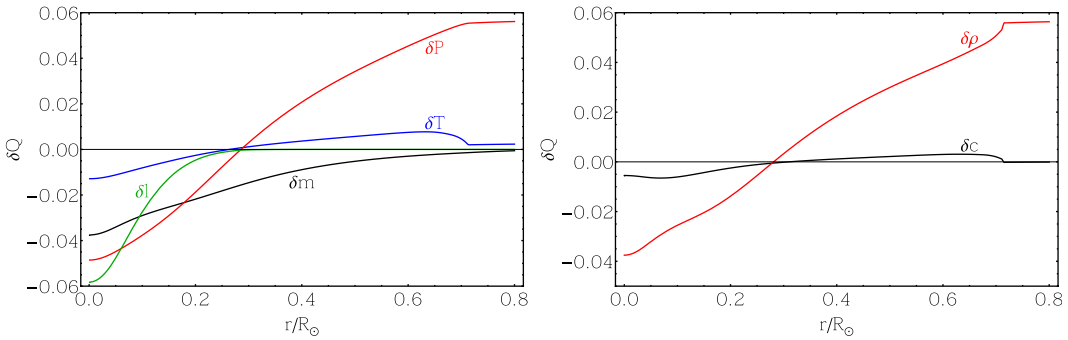

FIGURE 6 | The effects of a 10% increase of the astropysical factor of $p(p,e^+\nu_e)d$ reaction on the physical properties of the Sun **(left Panel)** and on helioseismic observable quantities $\delta c(r)$ and $\delta\rho(r)$ **(right Panel)**. The fractional variations δQ are calculated with respect to the reference SSM predictions.

S_{11} on the temperature profile of SSMs and on the helioseismic observable quantities $\delta c(r)$ and $\delta\rho(r)$.

3.2 The Dependence of Neutrino Fluxes on the Central Temperature of the Sun and on Nuclear Reaction Cross Sections

Even a small modification of the central temperature of the Sun reflects into large variations of solar neutrino fluxes. By considering the arguments discussed in Bahcall and Ulmer (1996); Degl'Innocenti et al. (1997), we discuss the dependence of solar neutrino fluxes on the core temperature of the Sun, highlighting the role of nuclear reactions for determining the branching ratios of the different pp-chain terminations and the efficiency of the CNO-bicycle.

3.2.1 PP-Chain Neutrino Fluxes

The pp-neutrino flux:

The vast majority of the solar neutrino emission is due to pp-neutrinos whose flux $\Phi(pp)$ is directly linked to λ_{11} being $\Phi(pp) = \lambda_{11}/(4\pi D^2)$ where $D = 1$ A.U. is the Sun-Earth distance. According to discussion in the previous Section, the rate λ_{11} is directly fixed by solar luminosity and thus $\Phi(pp)$ is expected to be independent from the central temperature of the Sun and nuclear reaction cross sections. This result is obtained by assuming that pp-I is the only mechanism for helium-4 production by nuclear reaction in the Sun. A more accurate description can be obtained by taking into account the contribution the secondary branches of the pp-chain (namely, the pp-II termination) initiated by the $^3He(^3He,\gamma)^7Be$ which provides an alternative ^3He burning mechanism to the most common $^3He(^3He,2p)^4He$. In this assumption, we have:

$$L_\odot = Q_I\,\lambda_{33} + Q_{II}\,\lambda_{34} \tag{5}$$

where λ_{33} and λ_{34} are the integrated rate of the $^3He(^3He,2p)^4He$ and $^3He(^4He,\gamma)^7Be$ reactions, while $Q_I = 26.20$ MeV and $Q_{II} = 25.65$ MeV give the amount of energy, corrected for neutrino emission, delivered in the plasma when ^4He is produced through pp-I and pp-II termination, respectively. By considering that $\lambda_{11} = 2\lambda_{33} + \lambda_{34}$ at equilibrium, we arrive at the conclusion that (Bahcall and Ulmer, 1996):

$$\Phi(pp) = \frac{1}{4\pi D^2}\left(\frac{2L_\odot}{Q_I} - \lambda_{34}\right) \tag{6}$$

where we considered that $Q_I \simeq Q_{II}$. While the first term in the r.h.s of the above equation is constant, the rate λ_{34} depends on the temperature of the plasma and on nuclear reaction cross sections. If we take into account that $\lambda_{34} \propto S_{34}\cdot(S_{11}/S_{33})^{1/2}\cdot T_c^{\beta_{Be}}$ with $\beta_{Be} \sim 11$, as motivated later in this section, we obtain the following relationship

$$\delta\Phi(pp) = -\eta\,\delta S_{34} - \frac{\eta}{2}(\delta S_{11} - \delta S_{33}) + \beta_{pp}\,\delta T_c \tag{7}$$

that gives the fractional variation of the flux $\delta\Phi(pp)$ as a function of fractional variation of the core temperature δT_c and of the astrophysical factors δS_{ij}. The coefficients in the above equation correspond to the logarithmic derivatives of $\Phi(pp)$ with respect to these quantities and are given by $\eta = \lambda_{34}/\lambda_{11} \simeq \Phi(^7Be)/\Phi(pp) \simeq 0.08$ and $\beta_{pp} = -\eta\beta_{Be} \simeq -0.9$, showing that the pp-neutrino flux is a decreasing function of the central temperature of the Sun.

The pep-neutrino flux:

The pep-neutrinos are produced by electron capture reaction $p(pe^-,\nu_e)d$ which is linked to the β-decay process $p(p,e^+\nu_e)d$ by well-known nuclear physics. Since the two processes depend on the same allowed nuclear matrix element, the ratio between their rates is determined by the available reaction phase spaces and by the electron density n_e of the solar plasma only. It can be determined with ~1% precision for the conditions of the solar interior and is mildly dependent on the properties of the solar plasma, being roughly proportional to $T_c^{-1/2}\,n_e$ (see e.g., Adelberger (2011) for a review). We can thus assume $\Phi(pep) \propto T_c^{1/2}\,\Phi(pp)$, allowing us to conclude:

$$\delta\Phi(pep) = -\eta\,\delta S_{34} - \frac{\eta}{2}(\delta S_{11} - \delta S_{33}) + \beta_{pep}\,\delta T_c \tag{8}$$

where $\beta_{pep} = \beta_{pp} - 1/2 \simeq -1.4$, and we neglected effects related to possible density and chemical composition variations in the solar core.

The ^{7}Be-neutrino flux:

The formation of beryllium-7 through $^3He(^4He,\gamma)^7Be$ leads to neutrino production through the electron capture reaction

^{7}Be$(e^-, \nu_e)^7$Li. This process largely dominates over the competing proton-capture reaction whose effects are discussed in the following paragraph. Taking this into account, the Be-neutrino flux can be directly estimated from the rate of the ^{3}He$(^4$He$, \gamma)^7$Be reaction by using $\Phi(^7\text{Be}) = \lambda_{34}/(4\pi D^2)$. The rate λ_{34} is given by:

$$\lambda_{34} = \int d^3r \, \frac{\rho^2}{m_u^2} \, \frac{X_3 \, Y}{12} \, \langle \sigma v \rangle_{34} \tag{9}$$

where Y (X_3) is the helium-4 (helium-3) mass fraction and $\langle \sigma v \rangle_{34}$ is the reaction rate per particle pair of ^{3}He$(^3$He$, \gamma)^7$Be. The amount of helium-4 nuclei in the present Sun is determined by the assumed initial abundance $Y_{\rm ini}$ and by nuclear processes that have converted hydrogen into helium during the Sun evolution. We may thus expect that Y depends on nuclear cross sections, in particular on S_{11} that determines the global efficiency of hydrogen burning. This dependence is however marginal because the product $L_\odot \tau_\odot$ essentially provides an observational determination of the integrated solar luminosity (and thus of the total amount of helium synthesized by nuclear reactions during the Sun lifetime). The helium-3 abundance in the solar core depends instead on the temperature T_c and on the cross sections of the p(p, $e^+\nu_e$)d and ^{3}He$(^3$He$, 2p)^4$He reactions. It can be indeed calculated by using the equilibrium condition

$$X_3 \simeq X_{3,\rm eq} = 3\,X \sqrt{\frac{\langle \sigma v \rangle_{11}}{2 \langle \sigma v \rangle_{33}}} \tag{10}$$

where X is the hydrogen mass fraction. Considering that $\langle \sigma v \rangle_{ij} \propto S_{ij} \, T_c^{\gamma_{ij}}$, this can be rewritten as $X_{3,c} \propto (S_{11}/S_{33})^{1/2} \cdot T_c^{(\gamma_{11}-\gamma_{33})/2}$ where we neglected effects related to possible hydrogen abundance variations[c]. This expression, combined with **Eq. 9**, allows us to conclude that:

$$\Phi(^7\text{Be}) \propto S_{34} \cdot (S_{11}/S_{33})^{1/2} \cdot T_c^{\beta_{\rm Be}} \tag{11}$$

or, equivalently,

$$\delta\Phi(^7\text{Be}) = \delta S_{34} + \frac{1}{2}(\delta S_{11} - \delta S_{33}) + \beta_{\rm Be}\,\delta T_c \tag{12}$$

where $\beta_{\rm Be} = \gamma_{34} + (\gamma_{11} - \gamma_{33})/2 \sim 11$. Note that the ^{7}Be-neutrino flux does not depends on the cross section of ^{7}Be$(e^-, \nu_e)^7$Li, due to the fact that (almost) the totality of beryllium-7 nuclei produced by ^{3}He$(^4$He$, \gamma)^7$Be are expected to decay through this reaction.

The ^{8}B-neutrino flux:

The ^{8}B neutrinos constitute a largely subdominant component of the solar flux which is produced when ^{7}Be nuclei capture a proton (instead of an electron) producing ^{8}B (instead of ^{7}Li). The ^{8}B-neutrino flux is thus given by $\Phi(^8\text{B}) = r\,\Phi(^7\text{Be})$ where $r \equiv \lambda_{17}/\lambda_{e7}$ is the ratio between proton and electron capture rates on beryllium-7. The parameter r scales as $r \propto (S_{17}/S_{e7}) \cdot T_c^\alpha$ where $\alpha = \gamma_{17} + (1/2)$ and we have considered that $\langle \sigma v \rangle_{e7} \propto S_{e7}\, T_c^{-1/2}$ for electron capture reaction. Taking this into account, we obtain the following scaling law:

$$\Phi(^8\text{B}) \propto (S_{17}/S_{e7}) \cdot S_{34} \cdot (S_{11}/S_{33})^{1/2} \cdot T_c^{\beta_B} \tag{13}$$

that also corresponds to:

$$\delta\Phi(^8\text{B}) = (\delta S_{17} - \delta S_{e7}) + \delta S_{34} + \frac{1}{2}(\delta S_{11} - \delta S_{33}) + \beta_{\rm B}\,\delta T_c \tag{14}$$

with $\beta_{\rm B} = \beta_{\rm Be} + \gamma_{17} + 1/2 \simeq 24$. The large value of $\beta_{\rm B}$ indicates that ^{8}B neutrinos are a very sensitive probe of the core temperature of the Sun.

3.2.2 The CNO Neutrino Fluxes

The neutrino fluxes produced in the CN-cycle by β-decay (and electron capture reactions) of ^{13}N and ^{15}O nuclei, besides depending on the solar central temperature, are approximately proportional to the stellar-core number abundance of CN elements. This dependence is relevant to understand the role of cross section for CNO-neutrino production. Moreover, as it is discussed in Haxton and Serenelli (2008); Haxton et al. (2013), it permits us to use CNO neutrinos, in combination with other neutrino fluxes, to directly probe the chemical composition of the Sun.

The ^{15}O-neutrino flux:

This component of the solar neutrino spectrum is determined by the production rate of oxygen-15 by ^{14}N(p, $\gamma)^{15}$O reaction in the core of the Sun. It can be calculated as $\Phi(^{15}\text{O}) = \lambda_{114}/(4\pi D^2)$ where the rate λ_{114}, given by:

$$\lambda_{114} = \int d^3r \, \frac{\rho^2}{m_u^2} \, \frac{X\,X_{14}}{14} \, \langle \sigma v \rangle_{114} \tag{15}$$

is proportional to the nitrogen-14 mass fraction X_{14} in the solar core (see **Figure 3**) and to the reaction rate per particle pair $\langle \sigma v \rangle_{114}$ of the ^{14}N (p,$\gamma)^{15}$O reaction. The above integral get a non vanishing contribution from a narrow region at $r \lesssim 0.1 R_\odot$ whose conditions are similar to that at the solar center, see **Figure 5**. We thus write the approximate scaling law:

$$\Phi(^{15}\text{O}) \propto \lambda_{114} \propto X_{14,c}\, S_{114}\, T_c^{\beta_O} \tag{16}$$

where S_{114} is the astrophysical factor of the ^{14}N (p,$\gamma)^{15}$O reaction, we considered that $\langle \sigma v \rangle_{114} \propto S_{114}\, T_c^{\gamma_{114}}$ and we defined $\beta_O = \gamma_{114} \simeq 20$. **Eq. 16** implies the following linearized relationship:

$$\delta\Phi(^{15}\text{O}) = \delta X_{14,c} + \delta S_{114} + \beta_O\,\delta T_c \tag{17}$$

In the above expressions, we neglected effect related to possible variations of the density and of the hydrogen abundance in the solar core, since these are expected to be small. We instead explicitly considered the dependence of $\Phi(O^{15})$ on the central abundance of nitrogen-14 which is essentially determined, as it is explained in the following, by the total abundances of CN elements in the solar core. It is useful to remark that, being the CNO cycle sub-dominant, a modification of its efficiency does not alter the solar luminosity and does not require a readjustement of the central temperature. Moreover, carbon and nitrogen give a marginal contribution to the opacity of the solar plasma and thus a variation of their abundances do not alter the temperature stratification. As a result of this, we can consider the different terms in **Eq. 17** as independent.

[c]We evaluate the exponents γ_{ij} by using $\gamma_{ij} \simeq (E_0)_{ij} - 2/3$ where $(E_0)_{ij}$ is the Gamov peak energy of the considered reaction, see e.g., Bahcall and Ulmer (1996).

The ^{13}N-neutrino flux:

The flux of ^{13}N-neutrinos can be calculated $\Phi(^{13}\mathrm{N}) = \lambda_{112}/(4\pi D^2)$ where λ_{112} is the total rate of the $^{12}\mathrm{C}(\mathrm{p},\gamma)^{13}\mathrm{N}$ reaction in the Sun. This is given by:

$$\lambda_{112} = \int d^3r \, \frac{\rho^2}{m_u^2} \, \frac{X X_{12}}{12} \, \langle \sigma v \rangle_{112} \tag{18}$$

where X_{12} is the carbon-12 mass fraction and $\langle \sigma v \rangle_{112}$ is the reaction rate per particle pair of $^{12}\mathrm{C}$ $(\mathrm{p},\gamma)^{13}\mathrm{N}$. We can write:

$$\lambda_{112} = \lambda_{114} + \lambda_{112}^{(\mathrm{ne})} \tag{19}$$

where the quantity:

$$\lambda_{112}^{(\mathrm{ne})} = \int d^3r \, \frac{\rho^2}{m_u^2} \, X \left[\frac{X_{12}}{12} \, \langle \sigma v \rangle_{112} - \frac{X_{14}}{14} \, \langle \sigma v \rangle_{114} \right] \tag{20}$$

gives the contribution to the total rate produced in the region of the Sun where the CN-cycle is incomplete. The above integral vanishes indeed for $r \leq 0.13 R_\odot$ where the equilibrium condition for the CN-cycle ensures that $(X_{12}/12)\,\langle \sigma v \rangle_{112} - (X_{14}/14)\,\langle \sigma v \rangle_{114} = 0$. This can be appreciated in the right panel of **Figure 5** where we show the differential rate $d\lambda_{114}/dr$ and $d\lambda_{112}/dr$ of $^{14}\mathrm{N}(\mathrm{p},\gamma)^{15}\mathrm{O}$ (black) and $^{12}\mathrm{C}(\mathrm{p},\gamma)^{13}\mathrm{N}$ (red) reactions as a function of the solar radius r.

Eq. 19 implies that $\Phi(^{13}\mathrm{N})$ can be decomposed as the sum:

$$\Phi(^{13}\mathrm{N}) = \Phi(^{15}\mathrm{O}) + \Phi(^{13}\mathrm{N})^{(\mathrm{ne})} \tag{21}$$

where the quantity $\Phi(^{13}\mathrm{N})^{(\mathrm{ne})} \equiv \lambda_{112}^{(\mathrm{ne})}/(4\pi D^2)$ represents the neutrino flux produced in the region $0.13 \lesssim r/R_\odot \lesssim 0.25$, where $^{14}\mathrm{N}(\mathrm{p},\gamma)^{15}\mathrm{O}$ reaction is not effective. This component of the flux scales as:

$$\Phi(^{13}\mathrm{N})^{(\mathrm{ne})} \propto X_{12}(r_{\mathrm{ne}}) \, S_{112} \, T_c^{\gamma_{114}} \tag{22}$$

where we considered that $\langle \sigma v \rangle_{112} \propto S_{112} \, T_c^{\gamma_{112}}$ with $\gamma_{112} \simeq 18$ and we neglected effects related to possible variations of density and hydrogen abundance. Note that the carbon-12 mass fraction in **Eq. 22** is evaluated at $r_{\mathrm{ne}} \simeq 0.16\, R_\odot$ where the out-of-equilibrium ^{13}N-neutrino production rate is maximal, see **Figures 3**, **5**. In principle, the temperature should be also evaluated at this position. However, we can take the central value T_c as representative for the entire energy producing region, motivated by the fact that $T(r)$ (differently from $X_{12}(r)$) is slowly varying in the solar core. **Eq. 22** implies the following relationship:

$$\delta\Phi(^{13}\mathrm{N})^{(\mathrm{ne})} = \delta X_{12}(r_{\mathrm{ne}}) + \delta S_{112} + \gamma_{112}\, \delta T_c \tag{23}$$

that combined with **Eq. 17** gives:

$$\delta\Phi(^{13}\mathrm{N}) = f\left[\delta X_{14,c} + \delta S_{114} + \gamma_{114}\, \delta T_c\right] + (1-f)\left[\delta X_{12}(r_{\mathrm{ne}}) + \delta S_{112} + \gamma_{112}\, \delta T_c\right] \tag{24}$$

where $f = \Phi(^{15}\mathrm{O})/\Phi(^{13}\mathrm{N}) = 0.74$ is the ratio between ^{15}O and ^{13}N neutrino fluxes in SSMs (Vinyoles et al., 2017).

The abundance of carbon and nitrogen in the core of the Sun.

Eqs. 17, **24** describe the dependence of the CN-neutrino fluxes from the abundances of nitrogen $X_{14,c}$ and carbon $X_{12}(r_{\mathrm{ne}})$ at the center of the Sun and close to $r_{\mathrm{ne}} = 0.16 R_\odot$, respectively. These abundances are determined by the formation and chemical evolution history of the Sun, i.e. by the initial solar composition and by the subsequent action of nuclear reactions and elemental diffusion, as it is described in the following. Let us first consider that the CN-cycle conserves the total number of CN-nuclei in the core of the Sun. This is shown in **Figure 3** by the behavior of the quantity:

$$\mathcal{N} \equiv X_{12}/12 + X_{13}/13 + X_{14}/14 \tag{25}$$

which is proportional to the total carbon + nitrogen number density (X_{13} represents the carbon-13 mass abundance) and it is nearly constant in the solar core despite the action of nuclear reactions. In the SSM paradigm, the radial dependence of $\mathcal{N}$ is only due to elemental diffusion so that we can write:

$$\mathcal{N}(r) = \mathcal{N}_{\mathrm{ini}}[1 + \Delta(r)] \tag{26}$$

where $\mathcal{N}_{\mathrm{ini}}$ is the initial carbon + nitrogen abundance that is assumed to be uniform in the solar structure while the function $\Delta(r)$ describes the effects of gravitational settling. It takes the value $\Delta_c = 0.06$ at the center of the Sun that can be considered also representative for $r_{\mathrm{ne}} = 0.16 R_\odot$, and $\Delta_s = -0.09$ in external convective envelope according to SSM calculations (Vinyoles et al., 2017). It is useful to connect the core composition to photospheric abundances since these are observationally constrained by spectroscopic measurements. We thus write:

$$\mathcal{N}_c = \mathcal{N}_s\left[1 + \Delta^{(\mathrm{cs})}\right] \tag{27}$$

where $\mathcal{N}_s$ ($\mathcal{N}_c$) is the carbon + nitrogen abundance in the external convective envelope (at the center) of the Sun while $\Delta^{(\mathrm{cs})} = (\Delta_c - \Delta_s)/(1 + \Delta_s) = 0.16$ represents the fractional difference between core and surface abundances.

The abundance $X_{14,c}$ that controls the equilibrium production of CN-neutrinos is directly related to total abundance of carbon and nitrogen in the core of the Sun. Indeed, for $r \lesssim 0.1 R_\odot$ the CN-cycle is complete and all available carbon is essentially transformed into nitrogen, giving $X_{14,c} \simeq 14\, \mathcal{N}_c$ (see **Figure 3**). We thus obtain the relation $\delta X_{14,c} = \delta \mathcal{N}_c$ that, by taking advantage of **Eqs. 25**, **27**), can be rewritten as:

$$\delta X_{14,c} = a\, \delta X_{14,s} + (1-a)\, \delta X_{12,s} + b\, (\Delta^{(\mathrm{cs})} - 0.16) \tag{28}$$

where $b = 1/(1 + 0.16) = 0.86$, $a = 6\xi/(6\xi + 7) \simeq 0.20$ and $\xi = (X_{N,s}/X_{C,s}) \simeq 0.30$ is the surface nitrogen-to-carbon ratio in SSM. The first two terms of the r.h.s in the above equation describe the effects produced by a variation of the surface composition. A modification of the chemical composition profile that is instead produced either "primordially" (e.g., by assuming that the Sun was not born chemical homogenous) or during the evolution (e.g., by anomalous diffusion) on time scales longer than carbon and nitrogen burning time at the solar center, is instead described in terms of a variation of $\Delta^{(\mathrm{cs})}$ from the SSM value, i.e., by assuming $\Delta^{(\mathrm{cs})} - 0.016 \neq 0$.

TABLE 5 | The logarithmic derivatives $\alpha(Q,I)$ of the solar neutrino fluxes with respect to nuclear input parameters calculated in B16-HZ SSMs.

	S_{11}	S_{33}	S_{34}	S_{e7}	S_{17}	S_{hep}	S_{114}	S_{116}
Φ(pp)	0.101	0.034	−0.066	0.000	0.000	0.000	−0.006	−0.000
Φ(pep)	−0.222	0.049	−0.095	0.000	0.000	0.000	−0.010	0.000
Φ(hep)	−0.104	−0.463	−0.081	0.000	0.000	1.000	−0.006	−0.000
$\Phi(^{7}\mathrm{Be})$	−1.035	−0.440	0.874	0.002	−0.001	0.000	−0.001	0.000
$\Phi(^{8}\mathrm{B})$	−2.665	−0.419	0.831	−0.998	1.028	0.000	0.007	0.000
$\Phi(^{13}\mathrm{N})$	−2.114	0.030	−0.061	0.001	0.000	0.000	0.762	0.001
$\Phi(^{15}\mathrm{O})$	−2.916	0.023	−0.050	0.001	0.000	0.000	1.051	0.001
$\Phi(^{17}\mathrm{F})$	−3.072	0.021	−0.046	0.001	0.000	0.000	0.007	1.158
Y_s	0.131	−0.005	0.010	0.000	0.000	0.000	0.001	0.000
R_{CZ}	−0.059	0.002	−0.004	0.000	0.000	0.000	0.000	0.000

A slightly more involved expression is obtained for the abundance $X_{12}(r_{ne})$ that controls the non-equilibrium production of ^{13}N-neutrinos. In the relevant region $0.13 \lesssim r/R_\odot \lesssim 0.25$, the carbon-12 abundance differs from the surface value $X_{12,s}$ due to the action of elemental diffusion and $^{12}\mathrm{C}(\mathrm{p},\gamma)^{13}\mathrm{N}$ reaction only, since further reactions are inhibited by the bottleneck. It can be approximately described as

$$X_{12}(r_{ne}) \simeq X_{12,s}\left[1+\Delta^{(cs)}\right]\exp\left(-\overline{\mathcal{D}}_{112}(r_{ne})\,t_\odot\right) \tag{29}$$

where the quantity $\overline{\mathcal{D}}_{112}$ represents the carbon-12 burning rate

$$\mathcal{D}_{112} = \frac{\rho X}{m_u}\langle\sigma v\rangle_{112} \tag{30}$$

averaged over the Sun lifetime, see Appendix for details. The maximal neutrino production is achieved at $r_{ne} \simeq 0.16\,R_\odot$ where the integrated burning rate is $\overline{\mathcal{D}}_{112}(r_{ne})\,t_\odot \simeq 1$. Indeed, in the inner core where $\overline{\mathcal{D}}_{112}\,t_\odot \gg 1$, carbon-12 abundance is too low to efficiently feed $^{12}\mathrm{C}(\mathrm{p},\gamma)^{13}\mathrm{N}$ reaction. On the other hand, the carbon-12 burning time is much larger than solar age (and thus $^{12}\mathrm{C}(\mathrm{p},\gamma)^{13}\mathrm{N}$ reaction is not effective) in more external regions where $\overline{\mathcal{D}}_{112} \ll (1/t_\odot)$, as can be understood by considering that $\mathcal{D}_{112} \simeq \overline{\mathcal{D}}_{112}$. Taking this into account, we obtain the following relation:

$$\delta X_{12}(r_{ne}) = \delta X_{12,s} + b\left(\Delta^{(cs)} - 0.16\right) - \delta S_{112} - \gamma_{112}\,\delta T_c \tag{31}$$

where we considered that $\overline{\mathcal{D}}_{112}(r_{ne}) \propto S_{112}\,T_c^{\gamma_{112}}$.

The final expressions the CN neutrino fluxes.

By using the above equations, we are able to calculate the dependence of neutrino fluxes produced in the CN-cycle on the properties of the Sun. By using **Eqs. 28**, **31** into **Eqs. 17**, **24**, we obtain:

$$\begin{aligned}\delta\Phi(^{15}\mathrm{O}) &= \beta_O\,\delta T_c + (1-a)\,\delta X_{12,s} + a\,\delta X_{14,s} + b\left(\Delta^{(cs)} - 0.16\right) + \delta S_{114}\\ \delta\Phi(^{13}\mathrm{N}) &= \beta_N\,\delta T_c + (1-a')\,\delta X_{12,s} + a'\,\delta X_{14,s} + b\left(\Delta^{(cs)} - 0.16\right) + f\,\delta S_{114}\end{aligned} \tag{32}$$

with $\beta_O = 20$, $f = 0.74$, $a = 0.2$, $b = 0.86$, $\beta_N \equiv f\,\beta_O = 15$ and $a' \equiv f\,a = 0.15$. Note that, in the derivation of the second equation, we took into account that the third and the fourth terms in the r.h.s of **Eq. 31** cancels the dependence of $\Phi(^{13}\mathrm{N})^{(ne)}$ on S_{112} and T_c expressed in **Eq. 23**. This is due to the fact that, as far as the ^{13}N-neutrino (non equilibrium) production rate is concerned, the effect of $^{12}\mathrm{C}(\mathrm{p},\gamma)^{13}\mathrm{N}$ cross section enhancement is compensated by the reduction of residual carbon-12 abundance due the more efficient carbon burning.

4 NUMERICAL RESULTS AND NUCLEAR UNCERTAINTIES

The expressions obtained for the neutrino fluxes can be compared with the results of SSMs calculations. In particular, the numerical coefficients in **Eqs. 7**, **8**, **12**, **14** , **32** should reproduce the logarithmic derivatives of the neutrino fluxes with respect to the astrophysical factors of the relevant nuclear cross sections reported in **Table 5**. We see that a good agreement exists, indicating that all the major physical effects are included in our discussion and correctly described. In the case of S_{11}, we have to take into account that the role of this parameter is twofold; indeed, besides altering the efficiency of pp-reaction (at fixed temperature), this parameter also induces a variation of the central temperature of the Sun as described by **Eq. 4**. This effect, combined with the strong temperature dependence of the fluxes, allow us to understand the large values for logarithmic derivatives reported in the first column of **Table 5**.

For completeness, we also discuss in the last two rows of **Table 5** the dependence of the helioseismic observable quantities Y_s (surface helium abundance) and R_{CZ} (depth of the convective envelope) on nuclear reactions cross sections. We see that S_{11} is the only nuclear parameter that affects the predictions for these quantities. The effects of S_{11} modifications on sound speed and density profiles are shown in the right panel of **Figure 6**. Finally, **Table 6** gives the logarithmic derivatives of neutrino fluxes and helioseismic quantities on other input parameters (beside nuclear cross sections) which are necessary to construct SSMs. These are: the solar age (age), luminosity (lumi) and the diffusion coefficients (diffu); the opacity of solar plasma whose uncertainty is described in terms of two parameters κ_a and κ_b defined in **Section 2.1**; the surface abundances of key elements (C, N, O, Ne, Mg, Si, S, Ar, Fe) which are determined through spectroscopic measurements as discussed in **Section 2.1**. We can see that the logarithmic derivatives of the CN-neutrino fluxes with respect to the surface carbon and nitrogen abundances are correctly predicted by **Eq. 32**.

TABLE 6 | The logarithmic derivatives $\alpha(Q,I)$ of the solar neutrino fluxes with respect to solar properties that produce environmental effects and chemical composition parameters calculated in B16-HZ SSMs.

	Age	Diffu	Lumi	κ_a	κ_b	C	N	O	Ne	Mg	Si	S	Ar	Fe
Φ(pp)	−0.085	−0.013	0.773	−0.084	−0.019	−0.007	−0.001	−0.005	−0.005	−0.003	−0.009	−0.006	−0.001	−0.019
Φ(pep)	−0.003	−0.018	0.999	−0.270	−0.001	−0.014	−0.002	−0.011	−0.005	−0.003	−0.012	−0.013	−0.004	−0.060
Φ(hep)	−0.125	−0.039	0.149	−0.395	−0.107	−0.008	−0.002	−0.024	−0.018	−0.016	−0.036	−0.027	−0.006	−0.066
$\Phi(^7\mathrm{Be})$	0.753	0.132	3.466	1.332	0.380	−0.000	0.002	0.057	0.053	0.052	0.106	0.075	0.018	0.209
$\Phi(^8\mathrm{B})$	1.319	0.278	6.966	2.863	0.658	0.022	0.007	0.128	0.102	0.092	0.198	0.138	0.034	0.498
$\Phi(^{13}\mathrm{N})$	0.863	0.345	4.446	1.592	0.314	0.864	0.154	0.073	0.051	0.047	0.110	0.078	0.020	0.272
$\Phi(^{15}\mathrm{O})$	1.328	0.395	5.960	2.220	0.456	0.819	0.209	0.104	0.075	0.068	0.153	0.107	0.027	0.388
$\Phi(^{17}\mathrm{F})$	1.424	0.418	6.401	2.427	0.503	0.026	0.007	1.112	0.082	0.074	0.167	0.116	0.029	0.424
Y_s	−0.195	−0.077	0.351	0.608	0.255	−0.008	−0.001	0.019	0.032	0.032	0.062	0.042	0.010	0.084
R_{CZ}	−0.081	−0.018	−0.016	0.008	−0.079	−0.003	−0.003	−0.024	−0.012	−0.004	0.003	0.005	0.001	−0.008

TABLE 7 | The fractional uncertainties of enviromental and nuclear input parameters in SSM construction.

Age	Diffu	Lum	κ_a	κ_b	S_{11}	S_{33}	S_{34}	S_{17}	S_{e7}	S_{114}	S_{116}	S_{hep}
0.0044	0.15	0.004	0.02	0.067	0.01	0.052	0.052	0.047	0.02	0.075	0.076	0.30

TABLE 8 | Dominant theoretical error sources for neutrino fluxes and for the main characteristics of the SSM.

Quant	Dominant theoretical error sources in %			
Φ(pp)	$L_\odot$: 0.3	S_{34}: 0.3	κ: 0.2	Diff: 0.2
Φ(pep)	κ: 0.5	$L_\odot$: 0.4	S_{34}: 0.4	S_{11}: 0.2
Φ(hep)	S_{hep}: 30.2	S_{33}: 2.4	κ: 1.1	Diff: 0.5
$\Phi(^7\mathrm{Be})$	S_{34}: 4.1	κ: 3.8	S_{33}: 2.3	Diff: 1.9
$\Phi(^8\mathrm{B})$	κ: 7.3	S_{17}: 4.8	Diff: 4.0	S_{34}: 3.9
$\Phi(^{13}\mathrm{N})$	C: 10.0	S_{114}: 5.4	Diff: 4.8	κ: 3.9
$\Phi(^{15}\mathrm{O})$	C: 9.4	S_{114}: 7.9	Diff: 5.6	κ: 5.5
$\Phi(^{17}\mathrm{F})$	O: 12.6	S_{116}: 8.8	κ: 6.0	Diff: 6.0
Y_s	κ: 2.2	Diff: 1.1	Ne: 0.6	O: 0.3
R_{CZ}	κ: 0.6	O: 0.3	Diff: 0.3	Ne: 0.2

The uncertainties in solar properties leading to environmental effects and chemical composition parameters, together with uncertainties in nuclear reaction cross sections propagate to SSM predictions which are affected by a *theoretical* (or *model*) error that can be estimated by Monte-Carlo techniques and/or linear propagation. By using this approach, the fractional error σ_Q on a generic SSM prediction Q can be obtained as the sum (in quadrature) of different contributions, according to:

$$\sigma_Q^2 = \sum_I [\alpha(Q,I)]^2 \sigma_I^2 \tag{33}$$

where $I = age, lumi, \ldots$ indicates a specific input, σ_I represents its fractional uncertainty and $\alpha(Q,I) \equiv d\ln Q/d\ln I$ is the logarithmic derivative of Q with respect to I. **Table 7** contains the uncertainties σ_I that have been considered for the construction of B16-SSMs (the surface composition errors are reported in **Table 2**), see Vinyoles et al. (2017) for details. By using these values, one is able to estimate the contribution $\delta Q_I \equiv \alpha(Q,I)\sigma_I$ of each input parameter to the total error budget of Q. The dominant error sources for solar neutrino fluxes and helioseismic quantities are given in **Table 8**.[d]

Focusing on nuclear reactions, we note that, despite the progress in the field, they are still an important uncertainty source for neutrino fluxes. In particular, the error contributions from S_{34} and S_{17} are comparable to or larger than the uncertainties in the experimental determinations of $\Phi(^8\mathrm{B})$ and $\Phi(^7\mathrm{Be})$. As discussed in Vinyoles et al. (2017), the ability of solar neutrinos produced in the pp-chain to play a significant role in constraining physical conditions in the solar interior depends, although it is not the only factor, on pinning down errors of nuclear reaction rates to just $\sim 2\%$. For CN fluxes, we see that S_{114} is the dominant error source if composition is left aside. This is particularly relevant, especially in consideration of the fact that Borexino has just opened the era of CNO neutrino detection, obtaining for the first time $\sim 5\sigma$ direct experimental evidence for a non vanishing flux from the Sun (Agostini et al., 2020a).

For a correct evaluation of the importance of nuclear cross section, it should be remarked that, while neutrino fluxes generally change with variation in any of the input parameters, SSM predictions are strongly correlated with a single output parameter, the core temperature T_c (Bahcall and Ulmer, 1996; Degl'Innocenti et al., 1997; Haxton and Serenelli, 2008; Serenelli et al., 2013). As a consequence, a multi-dimensional set of variations of enviromental and chemical composition parameters $\{\delta I\}$ often collapses to a one-dimensional dependence on δT_c, where δT_c is an implicit function of the variations $\{\delta I\}$. The dominance of T_c as the

[d]The total error due to opacity is obtained by combining in quadrature the contributions from κ_a and κ_b.

controlling parameter for neutrino fluxes can be exploited to cancel out uncertainties in the analysis of solar neutrino data. One can indeed form weighted ratios $\Phi(\nu_1)/\Phi(\nu_2)^{x_{12}}$, or equivalently weighted fractional differences $\delta\Phi(\nu_1) - x_{12}\,\delta\Phi(\nu_2)$ with respect to SSM predictions that are nearly independent of T_c and thus marginally affected by environmental effects and chemical composition, using the residual dependence on selected parameters to learn something about them.

In Haxton and Serenelli (2008); Serenelli et al. (2013), it was suggested to combine the CN-neutrino fluxes with the boron neutrino flux that, due to the exquisite precision of current experimental results and the large temperature sensitivity can be efficiently used as solar thermometer. As can be understood by considering **Eqs. 14**, **32**, the following combinations can be formed:

$$\delta\Phi(^{15}\mathrm{O}) - x\,\delta\Phi(^{8}\mathrm{B}) = (1-a)\,\delta X_{12,\mathrm{s}} + a\,\delta X_{14,\mathrm{s}} + b\,\left(\Delta^{(\mathrm{cs})} - 0.16\right) + \delta S_{114} - x\left(\frac{\delta S_{11}}{2} - \frac{\delta S_{33}}{2} + \delta S_{34} + \delta S_{17} - \delta S_{e7}\right) \tag{34}$$

$$\delta\Phi(^{13}\mathrm{N}) - x'\,\delta\Phi(^{8}\mathrm{B}) = (1-a')\,\delta X_{12,\mathrm{s}} + a'\,\delta X_{14,\mathrm{s}} + b\,\left(\Delta^{(\mathrm{cs})} - 0.16\right) + \delta S_{114} - x'\left(\frac{\delta S_{11}}{2} - \frac{\delta S_{33}}{2} + \delta S_{34} + \delta S_{17} - \delta S_{e7}\right) \tag{35}$$

where $x = \beta_O/\beta_B \simeq 0.8$ and $x' = f\,x \simeq 0.6$, that are independent from δT_c. This possibility is extremely important because it allows us to cancels out the dependence on the radiative opacity (implicit in δT_c). The uncertainty of available opacity calculations is indeed not easily quantified and may be potentially underestimated. Moreover, it breaks the degeneracy between composition and opacity effects on solar observable properties. Indeed, the considered flux combinations only depend on the carbon and nitrogen abundance in the solar core allowing us to test the chemical composition and evolution of the Sun. The first two terms in the r.h.s of **Eqs. 34**, **35** quantify the effects of a variation of the surface C and N abundances. A change of the diffusion efficiency is instead described in terms of a variation of $\Delta^{(\mathrm{cs})}$ from the SSM value, i.e., by assuming $\Delta^{(\mathrm{cs})} - 0.016 \neq 0$. It should be remarked that the ability to probe solar composition by using this approach is only limited by experimental accuracy of flux determinations and by nuclear cross section uncertainties.

While the above relationships are based on the simplified arguments discussed in the previous section, the optimal combinations $\delta\Phi(\nu_1) - x_{12}\delta\Phi(\nu_2)$, or equivalently weighted ratios $\Phi(\nu_1)/\Phi(\nu_2)^{x_{12}}$, can be determined by using the power-law coefficients from Vinyoles et al. (2017) given in **Table 6**. The parameter x_{12} is obtained by minimizing the residual

$$\rho = \sum_{I=1}^{N} \left[\alpha(\nu_1, I) - x_{12}\,\alpha(\nu_2, I)\right]^2 \sigma_I^2 \tag{36}$$

where the sum extends to the N input parameters whose dependence we want to cancel out and σ_I are the corresponding uncertainties. The minimal value for ρ gives the intrinsic error in the considered approach. This method, originally proposed by Haxton and Serenelli (2008); Serenelli et al. (2013), has been recently adapted to Borexino (Agostini et al., 2020b). By taking into account that the measured CNO neutrino signal in Borexino is basically probing $\delta\phi^{\mathrm{BX}}_{\mathrm{CNO}} \equiv \xi\,\delta\Phi(^{15}\mathrm{O}) + (1-\xi)\,\delta\Phi(^{13}\mathrm{N})$ with $\xi = 0.764$, it was concluded that the surface composition of the Sun can be probed by the combination:

$$\delta R^{\mathrm{BX}}_{\mathrm{CNO}} - 0.716\,\delta\Phi(^{8}\mathrm{B}) = 0.814\,\delta X_{12,\mathrm{s}} + 0.191\,\delta X_{14,\mathrm{s}} \pm 0.5\%\ (\mathrm{env}) \pm 9.1\%\ (\mathrm{nucl}) \pm 2.8\%\ (\mathrm{diff}) \tag{37}$$

where $\delta R^{\mathrm{BX}}_{\mathrm{CNO}}$ is the fractional difference of the observed CNO signal with respect to SSM expectations and the quoted uncertainties are obtained by propagating errors of SSM input parameters. The error budget is presently dominated by the uncertainty of the CNO signal Borexino measurement. However, a relevant error ($\sim 10\%$) is also provided by nuclear reactions, with the largest contributions coming from S_{114} (7.6%), S_{34} (3.4%), and S_{17} (3.5%). In the perspective of future improvements of the CNO signal determination, it is evidently important to have reliable and accurate determinations of these cross sections.

5 CONCLUDING REMARKS

A fundamental part in solar model calculations is the knowledge of the rates of nuclear reactions involved in the generation of solar nuclear energy. During the last decades, we experienced a substantial progress in the accuracy of SSM calculations that was made possible, among the other ingredients, by the continuous improvements of nuclear cross sections that are now typically determined with $\sim 5\%$ accuracy. However, SSMs have now to challenge new puzzles, like e.g., the solar composition problems. Moreover, SSM neutrino flux predictions, which are directly affected to nuclear cross sections uncertainties, have to be compared against very accurate observational determinations, having errors at few % level or better e.g., for $\Phi(^{7}\mathrm{Be})$ and $\Phi(^{8}\mathrm{B})$.

As a consequence, further work is needed on the side of nuclear reactions. Indeed, nuclear uncertainties have a non negligible role in SSMs error budget. As an example, the error contributions from S_{34} and S_{17} are about a factor 2 larger than the uncertainties in the experimental determinations of $\Phi(^{7}\mathrm{Be})$ and $\Phi(^{8}\mathrm{B})$. As it is discussed in Vinyoles et al. (2017), the few percent systematics in the determination of these reaction rates is still a relevant source of difficulty in using neutrino fluxes as constraints to solar model properties. The astrophysical factor S_{114} is morevoer a relevant error source for CN neutrino fluxes. This last point is particularly important after Borexino opened the era of CNO neutrino detection, obtaining the first ever direct

evidence of a non vanishing CN neutrino signal from the Sun. In the perspective of future and more accurate measurements, nuclear uncertainties can become a limiting factor in the possibility to use the CN-neutrinos, in combination with ^{8}B neutrinos, to directly probe the solar composition, thus addressing the solar composition problem. At the moment, the nuclear error contribution to CN-core abundance uncertainty is $\sim 10\%$, see **Eq. 37**. This is comparable to the error in CN-surface abundance determinations (0.05 dex in LZ composition) and only a factor ~ 2 smaller than the difference between HZ and LZ results, which can be regarded as an estimate of the systematic shift in the surface abundances produced by advances in stellar spectroscopy during the last 20 years. We remark that a high accuracy determination of the solar core composition could be used not only to discriminate among different solar surface admixtures but also to test the chemical evolution scheme employed by SSMs, e.g., by verifying the effect of elemental diffusion according to which core abundances are expected to be $\sim 15\%$ larger than surface values.

In conclusion, it would be desirable to further improve our knowledge of nuclear cross sections, in particular for $^3\mathrm{He}(^4\mathrm{He},\gamma)^7\mathrm{Be}$, $^7\mathrm{Be}(\mathrm{p},\gamma)^8\mathrm{B}$ and $^{14}\mathrm{N}(\mathrm{p},\gamma)^{15}\mathrm{O}$ reactions. As we discussed in the introduction, the history of SSMs appears to be formed by three large chapters, during which the knowledge of nuclear rates improved at each stage by about a factor two with respect to the previous period, up to the present situation in which the leading cross section in pp-chain and CN-cycle are typically determined with $\sim 5\%$ accuracy. The ambitious goal for the next stage could be a further factor ~ 2 reduction, in such a way that nuclear reactions uncertainties will not represent a limiting factor in constraining the physical conditions of solar interior.

AUTHOR CONTRIBITIONS

All authors listed have made a substantial, direct, and intellectual contribution to the work and approved it for publication.

FUNDING

FV acknowledges support by 'Neutrino and Astroparticle Theory Network' under the program PRIN 2017 funded by the Italian Ministry of Education, University and Research (MIUR) and INFN Iniziativa Specifica TAsP. AS acknowledges support by the Spanish Government through the MICINN grant PRPPID 2019–108709GB-I00.

REFERENCES

Abdurashitov, J., Gavrin, V. N., Girin, S. V., Gorbachev, V. V., Ibragimova, T. V., Kalikhov, A. V., et al. (1999). Measurement of the solar neutrino capture rate with gallium metal. *Phys. Rev. C* 60, 055801. doi:10.1103/PhysRevC.60.055801

Abe, K. (2016). Solar neutrino measurements in super-kamiokande-IV. *Phys. Rev. D* 94, 052010. doi:10.1103/PhysRevD.94.052010

Acharya, B., Carlsson, B. D., Ekström, A., Forssén, C., and Platter, L. (2016). Uncertainty quantification for proton-proton fusion in chiral effective field theory. *Phys. Lett.* B7 60, 584–589. doi:10.1016/j.physletb.2016.07.032

Adelberger, E. G. (2011). Solar fusion cross sections II: the pp chain and CNO cycles. *Rev. Mod. Phys.* 83, 195. doi:10.1103/RevModPhys.83.195

Adelberger, E. G. (1998). Solar fusion cross-sections. *Rev. Mod. Phys.* 70, 1265–1292. doi:10.1103/RevModPhys.70.1265

Agostini, M., Altenmüller, K., and The Borexino Collaboration. (2018). Comprehensive measurement of -chain solar neutrinos. *Nature* 562, 505–510. doi:10.1038/s41586-018-0624-y

Agostini, M., Altenmüller, K., and The Borexino Collaboration. (2020a). First direct experimental evidence of CNO neutrinos. *Nature* 587, 577–582. doi:10.1038/s41586-020-2934-0

Agostini, M., Altenmüller, K., and The Borexino Collaboration. (2020b). Sensitivity to neutrinos from the solar CNO cycle in Borexino. *Eur. Phys. J. C* 80. doi:10.1140/epjc/s10052-020-08534-2

Aharmim, B. (2013). Combined analysis of all three phases of solar neutrino data from the sudbury neutrino observatory. *Phys. Rev. C* 88, 025501. doi:10.1103/PhysRevC.88.025501

Ahmad, Q., Allen, R C., Andersen, T C., Anglin, J D., Barton, J C., Beier, E W., et al. (2002). Direct evidence for neutrino flavor transformation from neutral current interactions in the Sudbury Neutrino Observatory. *Phys. Rev. Lett.* 89, 011301. doi:10.1103/PhysRevLett.89.011301

Ahmad, Q., Allen, R C., Andersen, T C., Anglin, J D., Barton, J C., Beier, E W., et al. (2001). Measurement of the rate of interactions produced by solar neutrinos at the Sudbury Neutrino Observatory. *Phys. Rev. Lett.* 87, 071301. doi:10.1103/PhysRevLett.87.071301

Angulo, C., Arnould, M., Rayet, M., Descouvemont, P., Baye, D., Leclercq-Willain, C., et al. (1999). A compilation of charged-particle induced thermonuclear reaction rates. *Nucl. Phys.* 656, 3–183. doi:10.1016/S0375-9474(99)00030-5

Antia, H. M., and Chitre, S. M. (2002). Helioseismic limit on heavy element abundance. *Astron. Astrophys.* 393, L95–L98. doi:10.1051/0004-6361:20021253

Antia, H. M., and Chitre, S. M. (1999). Limits on the proton-proton reaction cross-section from helioseismology. *Astron. Astrophys.* 347, 1000–1004.

Arpesella, C., Back, H. O., Bellini, G. B., Balata, M., Benzinger, J., Leclercq-Willain, C., et al. (2008). Direct measurement of the Be-7 solar neutrino flux with 192 Days of Borexino data. *Phys. Rev. Lett.* 101, 091302. doi:10.1103/PhysRevLett.101.091302

Asplund, M., Grevesse, N., Sauval, A. J., and Scott, P. (2009). The chemical composition of the Sun. *Annu. Rev. Astron. Astrophys.* 47, 481–522. doi:10.1146/annurev.astro.46.060407.145222

Badnell, N. R., Bautista, M. A., Butler, K., Delahaye, F., Mendoza, C., Palmeri, P., et al. (2005). Up-dated opacities from the opacity Project. *Mon. Not. Roy. Astron. Soc.* 360, 458–464. doi:10.1111/j.1365-2966.2005.08991.x

Bahcall, J. N., Basu, S., Pinsonneault, M., and Serenelli, A. M. (2005a). Helioseismological implications of recent solar abundance determinations. *Astrophys. J.* 618, 1049–1056. doi:10.1086/426070

Bahcall, J. N., Brown, L. S., Gruzinov, A., and Sawyer, R. (2002). The Salpeter plasma correction for solar fusion reactions. *Astron. Astrophys.* 383, 291–295. doi:10.1051/0004-6361:20011715

Bahcall, J. N., Huebner, W. F., Lubow, S. H., Parker, P. D., and Ulrich, R. K. (1982). Standard solar models and the uncertainties in predicted capture rates of solar neutrinos. *Rev. Mod. Phys.* 54, 767–799. doi:10.1103/RevModPhys.54.767

Bahcall, J. N. (1990). Line versus continuum solar neutrinos. *Phys. Rev.* D41, 2964. doi:10.1103/PhysRevD.41.2964

Bahcall, J. N., and Pinsonneault, M. H. (1992). Standard solar models, with and without helium diffusion, and the solar neutrino problem. *Rev. Mod. Phys.* 64, 885–926. doi:10.1103/RevModPhys.64.885

Bahcall, J. N., Pinsonneault, M. H., and Wasserburg, G. J. (1995). Solar models with helium and heavy-element diffusion. *Rev. Mod. Phys.* 67, 781–808. doi:10.1103/RevModPhys.67.781

Bahcall, J. N., Serenelli, A. M., and Basu, S. (2006). 10,000 standard solar models: a Monte Carlo simulation. *Astrophys. J. Suppl.* 165, 400–431. doi:10.1086/504043

Bahcall, J. N., Serenelli, A. M., and Basu, S. (2005b). New solar opacities, abundances, helioseismology, and neutrino fluxes. *Astrophys. J. Lett.* 621, L85–L88. doi:10.1086/428929

Bahcall, J. N. (2002). The Luminosity constraint on solar neutrino fluxes. *Phys. Rev.* C65, 025801. doi:10.1103/PhysRevC.65.025801

Bahcall, J. N., and Ulmer, A. (1996). The Temperature dependence of solar neutrino fluxes. *Phys. Rev.* D53, 4202–4210. doi:10.1103/PhysRevD.53.4202

Bailey, J. E., Nagayama, T., Loisel, G. P., Rochau, G. A., Blancard, C., Colgan, J., et al. (2015). A higher-than-predicted measurement of iron opacity at solar interior temperatures. *Nature* 517, 56–59. doi:10.1038/nature14048

Basu, S., and Antia, H. M. (2004). Constraining solar abundances using helioseismology. *Astrophys. J.* 606, L85. doi:10.1086/421110

Basu, S., and Antia, H. M. (2008). Helioseismology and solar abundances. *Phys. Rep.* 457, 217–283. doi:10.1016/j.physrep.2007.12.002

Basu, S., and Antia, H. M. (1997). Seismic measurement of the depth of the solar convection zone. *Mon. Not. Roy. Astron. Soc.* 287, 189–198. doi:10.1093/mnras/287.1.189

Bellini, G., Benziger, J., Bick, D., Bonetti, S., Bonfini, G., Bravo, D., et al. (2012). First evidence of pep solar neutrinos by direct detection in Borexino. *Phys. Rev. Lett.* 108, 051302. doi:10.1103/PhysRevLett.108.051302

Bellini, G. (2014). Neutrinos from the primary proton-proton fusion process in the Sun. *Nature* 512, 383–386. doi:10.1038/nature13702

Bergstrom, J., Gonzalez-Garcia, M. C., Maltoni, M., Pena-Garay, C., Serenelli, A. M., and Song, N. (2016). Updated determination of the solar neutrino fluxes from solar neutrino data. *JHEP* 03, 132. doi:10.1007/JHEP03(2016)132

Blancard, C., Cossé, P., and Faussurier, G. (2012). Solar mixture opacity calculations using detailed configuration and level accounting treatments. *Astrophys. J.* 745, 10. doi:10.1088/0004-637X/745/1/10

Caffau, E., Ludwig, H.-G., Steffen, M., Freytag, B., and Bonifacio, P. (2011). Solar chemical abundances determined with a CO5BOLD 3D model atmosphere. *Sol. Phys.* 268, 255. doi:10.1007/s11207-010-9541-4

Cassisi, S., Salaris, M., and Irwin, A. W. (2003). The initial helium content of galactic globular cluster stars from the r-parameter: comparison with the cmb constraint. *Astrophys. J.* 588, 862. doi:10.1086/374218

Castro, M., Vauclair, S., and Richard, O. (2007). Low abundances of heavy elements in the solar outer layers: comparisons of solar models with helioseismic inversions. *Astron. Astrophys.* 463, 755–758. doi:10.1051/0004-6361:20066327

Christensen-Dalsgaard, J., Dappen, W., Ajukov, S. V., Anderson, E. R., Antia, H. M., Basu, S., et al. (1996). The current state of solar modeling. *Science* 272, 1286–1292. doi:10.1126/science.272.5266.1286

Christensen-Dalsgaard, J., Di Mauro, M. P., Houdek, G., and Pijpers, F. (2009). On the opacity change required to compensate for the revised solar composition. *Astron. Astrophys.* 494, 205. doi:10.1051/0004-6361:200810170

Christensen-Dalsgaard, J., Duvall, J., T. L.Gough, D. O., Harvey, J. W., Rhodes, J., et al. (1985). Speed of sound in the solar interior. *Nature* 315, 378–382. doi:10.1038/315378a0

Christensen-Dalsgaard, J., Proffitt, C. R., and Thompson, M. J. (1993). Effects of diffusion on solar models and their oscillation frequencies. *Astrophys. J. Lett.* 403, L75. doi:10.1086/186725

Cleveland, B., Daily, T., Davis, J., Raymond, Distel, J. R., Lande, K., Lee, C., et al. (1998). Measurement of the solar electron neutrino flux with the Homestake chlorine detector. *Astrophys. J.* 496, 505–526. doi:10.1086/305343

Colgan, J., Kilcrease, D. P., Magee, N. H., Sherrill, M. E., Abdallah, J., J., Hakel, P., et al. (2016). A new generation of Los Alamos opacity tables. *Astrophys. J.* 817, 116. doi:10.3847/0004-637X/817/2/116

deBoer, R. J., Görres, J., Smith, K., Uberseder, E., Wiescher, M., Kontos, A., et al. (2014). Monte Carlo uncertainty of the He3(alpha,gamma)Be7 reaction rate. *Phys. Rev.* C90, 035804. doi:10.1103/PhysRevC.90.035804

Degl'Innocenti, S., Dziembowski, W. A., Fiorentini, G., and Ricci, B. (1997). Helioseismology and standard solar models. *Astropart. Phys.* 7, 77–95. doi:10.1016/S0927-6505(97)00004-2

degl'Innocenti, S., Fiorentini, G., and Ricci, B. (1998). Helioseismology and p+p → d + e^+ ν_e in the sun. *Phys. Lett. B* 416, 365–368. doi:10.1016/S0370-2693(97)01197-0

Delahaye, F., and Pinsonneault, M. (2006). The solar heavy element abundances. 1. constraints from stellar interiors. *Astrophys. J.* 649, 529–540. doi:10.1086/505260

Deubner, F.-L., and Gough, D. (1984). Helioseismology: oscillations as a diagnostic of the solar interior. *Annu. Rev. Astron. Astrophys.* 22, 593–619. doi:10.1146/annurev.aa.22.090184.003113

Elsworth, Y., Howe, R., Isaak, G. R., McLeod, C. P., and New, R. (1990). Evidence from solar seismology against non-standard solar-core models. *Nature* 347, 536–539. doi:10.1038/347536a0

Ferguson, J. W., Alexander, D. R., Allard, F., Barman, T., Bodnarik, J. G., Hauschildt, P. H., et al. (2005). Low temperature opacities. *Astrophys. J.* 623, 585–596. doi:10.1086/428642

Fukuda, S., Fukuda, Y., Ishitsuka, M., Itow, Y., Kajita, T., Kameda, J., et al. (2001). Solar B-8 and hep neutrino measurements from 1258 days of Super-Kamiokande data. *Phys. Rev. Lett.* 86, 5651–5655. doi:10.1103/PhysRevLett.86.5651

Fukuda, Y. (1998). Measurements of the solar neutrino flux from Super-Kamiokande's first 300 days. *Phys. Rev. Lett.* 81, 1158–1162. doi:10.1103/PhysRevLett.81.1158

Gough, D. O., Kosovichev, A. G., Toomre, J., Anderson, E., Antia, H. M., Basu, S., et al. (1996). The seismic structure of the sun. *Science* 272, 1296–1300. doi:10.1126/science.272.5266.1296

Grevesse, N., and Noels, A. (1993). "Cosmic abundances of the elements,". *Origin and evolution of the elements*. Editors N. Prantzos, E. Vangioni-Flam, and M. Casse (Tokyo, Japan: Cambridge University Press), 15–25.

Grevesse, N., and Sauval, A. J. (1998). Standard solar composition. *Space Sci. Rev.* 85, 161–174. doi:10.1023/A:1005161325181

Grevesse, N., Scott, P., Asplund, M., and Sauval, A. J. (2015). The elemental composition of the Sun III. The heavy elements Cu to Th. *Astron. Astrophys.* 573, A27. doi:10.1051/0004-6361/201424111

Gruzinov, A. V., and Bahcall, J. N. (1998). Screening in thermonuclear reaction rates in the sun. *Astrophys. J.* 504, 996–1001. doi:10.1086/306116

Guzik, J. A., and Mussack, K. (2010). Exploring mass loss, low-Z accretion, and convective overshoot in solar models to mitigate the solar abundance problem. *Astrophys. J.* 713, 1108–1119. doi:10.1088/0004-637X/713/2/1108

Guzik, J. A., Watson, L., and Cox, A. N. (2005). Can enhanced diffusion improve helioseismic agreement for solar models with revised abundances?. *Astrophys. J.* 627, 1049–1056. doi:10.1086/430438

Hampel, W., Handt, J., Heusser, G., Kiko, J., Kirsten, T., Laubenstein, M., et al. (1999). GALLEX solar neutrino observations: results for GALLEX IV. *Phys. Lett. B* 447, 127–133. doi:10.1016/S0370-2693(98)01579-2

Harvey, J. W., Hill, F., Hubbard, R. P., Kennedy, J. R., Leibacher, J. W., Pintar, J. A., et al. (1996). The global oscillation network group (GONG) Project. *Science* 272, 1284–1286. doi:10.1126/science.272.5266.1284

Haxton, W. C., Hamish Robertson, R. G., and Serenelli, A. M. (2013). Solar neutrinos: status and prospects. *Annu. Rev. Astron. Astrophys.* 51, 21–61. doi:10.1146/annurev-astro-081811-125539

Haxton, W. C., and Serenelli, A. M. (2008). CN-cycle solar neutrinos and Sun's primordial core metalicity. *Astrophys. J.* 687, 678–691. doi:10.1086/591787

Iliadis, C., Anderson, K., Coc, A., Timmes, F., and Starrfield, S. (2016). Bayesian estimation of thermonuclear reaction rates. *Astrophys. J.* 831, 107. doi:10.3847/0004-637X/831/1/107

Kippenhahn, R., and Weigert, A. (1990). *Stellar structure and evolution*. Berlin Heidelberg, New York: Springer, 606.

Krief, M., Feigel, A., and Gazit, D. (2016a). Line broadening and the solar opacity problem. *Astrophys. J.* 824, 98. doi:10.3847/0004-637X/824/2/98

Krief, M., Feigel, A., and Gazit, D. (2016b). Solar opacity calculations using the super-transition-array method. *Astrophys. J.* 821, 45. doi:10.3847/0004-637X/821/1/45

Krishna Swamy, K. S. (1966). Profiles of strong lines in K-dwarfs. *Astrophys. J.* 145, 174. doi:10.1086/148752

Lodders, K., Palme, H., and Gail, H.-P. (2009). Abundances of the elements in the solar system. *Landolt Börnstein*, 712. doi:10.1007/978-3-540-88055-43410.1007/978-3-540-88055-4_34

Mao, D., Mussack, K., and Dappen, W. (2009). Dynamic screening in solar plasma. *Astrophys. J.* 701, 1204–1208. doi:10.1088/0004-637X/701/2/1204

Marcucci, L. E., Schiavilla, R., and Viviani, M. (2013). Proton-proton weak capture in chiral effective field theory. *Phys. Rev. Lett.* 110, 192503. doi:10.1103/PhysRevLett.110.192503

Marta, M. (2011). The 14N(p,gamma)15O reaction studied with a composite germanium detector. *Phys. Rev.* C83, 045804. doi:10.1103/PhysRevC.83.045804

Mondet, G., Blancard, C., Cossé, P., and Faussurier, G. (2015). Opacity calculations for solar mixtures. *Astrophys. J. Supp.* 220, 2. doi:10.1088/0067-0049/220/1/2

Montalban, J., Miglio, A., Noels, A., Grevesse, N., and Di Mauro, M. (2004). Solar model with CNO revised abundances. *ESA Spec. Publ.* 559, 574

Mussack, K., and Dappen, W. (2011). Dynamic screening correction for solar p-p reaction rates. *Astrophys. J.* 729, 96. doi:10.1088/0004-637X/729/2/96

Nagayama, T., Bailey, J. E., Loisel, G. P., Dunham, G. S., Rochau, G. A., Blancard, C., et al. (2019). Systematic study of L -shell opacity at stellar interior temperatures. *Phys. Rev. Lett.* 122, 235001. doi:10.1103/PhysRevLett.122.235001

Salpeter, E. (1954). Electron screening and thermonuclear reactions. *Austral. J. Phys.* 7, 373–388. doi:10.1071/PH540373

Schlattl, H., Bonanno, A., and Paternò, L. (1999). Signatures of the efficiency of solar nuclear reactions in the neutrino experiments. *Phys. Rev. D* 60, 113002. doi:10.1103/PhysRevD.60.113002

Scott, P., Asplund, M., Grevesse, N., Bergemann, M., and Sauval, A. J. (2015a). The elemental composition of the Sun II. The iron group elements Sc to Ni. *Astron. Astrophys.* 573, A26. doi:10.1051/0004-6361/201424110

Scott, P., Grevesse, N., Asplund, M., Sauval, A. J., Lind, K., Takeda, Y., et al. (2015b). The elemental composition of the Sun I. The intermediate mass elements Na to Ca. *Astron. Astrophys.* 573, A25. doi:10.1051/0004-6361/201424109

Serenelli, A. M., Haxton, W. C., and Pena-Garay, C. (2011). Solar models with accretion. I. Application to the solar abundance problem. *Astrophys. J.* 743, 24. doi:10.1088/0004-637X/743/1/24

Serenelli, A., Peña-Garay, C., and Haxton, W. C. (2013). Using the standard solar model to constrain solar composition and nuclear reaction S factors. *Phys. Rev.* D 87, 043001. doi:10.1103/PhysRevD.87.043001

Stonehill, L. C., Formaggio, J. A., and Robertson, R. G. H. (2004). Solar neutrinos from CNO electron capture. *Phys. Rev.* C 69, 015801. doi:10.1103/PhysRevC.69.015801

Thoul, A. A., Bahcall, J. N., and Loeb, A. (1994). Element diffusion in the solar interior. *Astrophys. J.* 421, 828–842. doi:10.1086/173695

Tognelli, E., Degl'Innocenti, S., Marcucci, L. E., and Prada Moroni, P. G. (2015). Astrophysical implications of the proton-proton cross section updates. *Phys. Lett.* B 742, 189–194. doi:10.1016/j.physletb.2015.01.033

Turck-chièze, S., Nghiem, P., Couvidat, S., and Turcotte, S. (2001). Solar internal composition and nuclear reaction rates in the light of helioseismology. *Sol. Phys.* 200, 323–342. doi:10.1023/A:1010365125791

Villante, F. L. (2010). Constraints on the opacity profile of the sun from helioseismic observables and solar neutrino flux measurements. *Astrophys. J.* 724, 98–110. doi:10.1088/0004-637X/724/1/98

Villante, F. L. (2015). ecCNO solar neutrinos: a challenge for gigantic ultra-pure liquid scintillator detectors. *Phys. Lett.* B 742, 279–284. doi:10.1016/j.physletb.2015.01.043

Villante, F. L., Serenelli, A. M., Delahaye, F., and Pinsonneault, M. H. (2014). The chemical composition of the Sun from helioseismic and solar neutrino data. *Astrophys. J.* 787, 13. doi:10.1088/0004-637X/787/1/13

Vinyoles, N., Serenelli, A. M., Villante, F. L., Basu, S., Bergström, J., Gonzalez-Garcia, M. C., et al. (2017). A new generation of standard solar models. *Astrophys. J.* 835, 202. doi:10.3847/1538-4357/835/2/202

Vissani, F. (2019). "Luminosity constraint and entangled solar neutrino signals," in Solar Neutrinos. Editors M. Meyer and K. Zuber. 121–141.

Zhang, X., Nollett, K. M., and Phillips, D. R. (2015). Halo effective field theory constrains the solar ^{7}Be + p $\rightarrow ^{8}$B + gamma rate. *Phys. Lett.* B 751, 535–540. doi:10.1016/j.physletb.2015.11.005

Conflict of Interest: The authors declare that the research was conducted in the absence of any commercial or financial relationships that could be construed as a potential conflict of interest.

APPENDIX: THE ^{12}C ABUNDANCE IN NON-EQUILIBRIUM REGION

In the region $0.13 \lesssim r/R_\odot \lesssim 0.25$, the CN-cycle is incomplete; carbon-12 is partially burned by $^{12}\mathrm{C}(\mathrm{p},\gamma)^{13}\mathrm{N}$ while nitrogen-14 is not effectively processed by $^{14}\mathrm{N}(\mathrm{p},\gamma)^{15}\mathrm{O}$ reaction. If we neglect elemental diffusion, the equation that describes the time evolution of carbon-12 is (in lagrangian coordinates):

$$\frac{\partial X_{12}}{\partial t} = -X_{12}\,\mathcal{D}_{112} \tag{38}$$

where the carbon-12 burning rate $\mathcal{D}_{112}$ is given by:

$$\mathcal{D}_{112} = \frac{\rho X}{m_u}\langle\sigma v\rangle_{112} \tag{39}$$

The solution of **Eq. 38** is:

$$X_{12} = X_{12,\mathrm{ini}}\exp\Big(-\overline{\mathcal{D}}_{112}\,t_\odot\Big) \tag{40}$$

where $X_{12,\mathrm{ini}}$ is the initial abundance and $\overline{\mathcal{D}}_{112}$ is given by:

$$\overline{\mathcal{D}}_{112} \equiv \frac{1}{t_\odot}\int_0^{t_\odot} dt\,\mathcal{D}_{112}\,. \tag{41}$$

We include *a-posteriori* the effecs of elemental diffusion by replacing $X_{12,\mathrm{ini}} \to X_{12,\mathrm{ini}}\,(1+\Delta(r))$ with the function $\Delta(r)$ defined in **Eq. 26**. We can then recast in terms of the surface carbon abundance, obtaining:

$$X_{12} = X_{12,\mathrm{s}}\left[1+\Delta^{(\mathrm{cs})}\right]\exp\Big(-\overline{\mathcal{D}}_{112}\,t_\odot\Big). \tag{42}$$

where $\Delta^{(\mathrm{cs})} = 0.16$ is the fractional difference between core and surface abundances induced by elemental diffusion.

frontiers in Astronomy and Space Sciences

REVIEW
published: 08 March 2021
doi: 10.3389/fspas.2020.617946

The Study of Key Reactions Shaping the Post-Main Sequence Evolution of Massive Stars in Underground Facilities

F. Ferraro[1], *G. F. Ciani*[2,3], *A. Boeltzig*[3], *F. Cavanna*[4] *and S. Zavatarelli*[1]*

[1]Università Degli Studi di Genova and INFN, Sezione di Genova, Genova, Italy, [2]Dipartimento di Matematica e Fisica, Università della Campania L. Vanvitelli, Caserta, Italy, [3]INFN, Laboratori Nazionali del Gran Sasso (LNGS), Assergi, Italy, [4]INFN, Sezione di Torino, Torino, Italy

The chemical evolution of the Universe and several phases of stellar life are regulated by minute nuclear reactions. The key point for each of these reactions is the value of cross-sections at the energies at which they take place in stellar environments. Direct cross-section measurements are mainly hampered by the very low counting rate and by cosmic background; nevertheless, they have become possible by combining the best experimental techniques with the cosmic silence of an underground laboratory. In the nineties, the LUNA (Laboratory for Underground Nuclear Astrophysics) collaboration opened the era of underground nuclear astrophysics, installing first a homemade 50 kV and, later on, a second 400 kV accelerator under the Gran Sasso mountain in Italy: in 25 years of experimental activity, important reactions responsible for hydrogen burning could have been studied down to the relevant energies thanks to the high current proton and helium beams provided by the machines. The interest in the next and warmer stages of star evolution (i.e., post-main sequence and helium and carbon burning) drove a new project based on an ion accelerator in the MV range called LUNA-MV, able to deliver proton, helium, and carbon beams. The present contribution is aimed to discuss the state of the art for some selected key processes of post-main sequence stellar phases: $^{12}C(\alpha,\gamma)^{16}O$ and $^{12}C+^{12}C$ are fundamental for helium and carbon burning phases, and $^{13}C(\alpha,n)^{16}O$ and $^{22}Ne(\alpha,n)^{25}Mg$ are relevant to the synthesis of heavy elements in AGB stars. The perspectives opened by an underground MV facility will be highlighted.

Keywords: helium burning, gamma spectroscopy, neutron spectroscopy, underground nuclear astrophysics, carbon burning

OPEN ACCESS

Edited by:
Scilla Degl'Innocenti, University of Pisa, Italy

Reviewed by:
Aurora Tumino, Kore University of Enna, Italy
Marco La Cognata, Laboratori Nazionali del Sud (INFN), Italy

***Correspondence:**
S. Zavatarelli
sandra.zavatarelli@ge.infn.it

Specialty section:
This article was submitted to Nuclear Physics, a section of the journal Frontiers in Astronomy and Space Sciences

Received: *15 October 2020*
Accepted: *31 December 2020*
Published: *08 March 2021*

Citation:
Ferraro F, Ciani GF, Boeltzig A, Cavanna F and Zavatarelli S (2021) The Study of Key Reactions Shaping the Post-Main Sequence Evolution of Massive Stars in Underground Facilities. Front. Astron. Space Sci. 7:617946. doi: 10.3389/fspas.2020.617946

INTRODUCTION

The hypothesis that the energy which powers the Sun comes from thermonuclear reactions seems to be mainly due to Eddington (1920) and Aston. After the discovery of nuclear reactions by Rutherford in the twenties, it became clear that only the enormous amount of energy stored in the nuclei and released during fusion reactions was able to support the Sun luminosity for a time period compatible with the geological datings (von Weizsäcker, 1938; Bethe and Critchfield, 1938): by fact, in order to properly understand the chemical evolution and the stellar energy engine, it is fundamental to precisely know how light nuclei are converted to heavier ones.

According to current theories, the first nuclei were formed through a network of nuclear reactions in the Big Bang nucleosynthesis (BBN), a few minutes after the Big Bang. BBN left our Universe containing about 75% hydrogen and 24% helium by mass, with some traces of lithium and deuterium. The composition of the present Universe is not very different from the primordial one, with the total mass elements heavier than hydrogen and helium ("metals" according to the astronomers) at the level of a few percent. Stars fuse light elements to heavier ones in their cores, up to iron and nickel in the more massive stars.

The most important stellar properties that determine the evolutionary fate of a star are its mass and its composition (Rolfs and Rodney, 1988; Iliadis, 2015): the larger the mass, the larger the temperature in the core. The star composition influences which reactions dominate the burning processes.

When a low-mass star like the Sun runs out of hydrogen in the core, it becomes a red giant star, fusing H to He via the CNO cycle in a shell surrounding an inert He core. When the core temperature reaches 100 million K, the He nuclei in the core have sufficient kinetic energy to fuse to C (helium burning), forming ^{12}C in a two-stage process. Subsequent fusion with another helium nucleus produces ^{16}O nuclei. This process, in symbols $^{12}C(\alpha,\gamma)^{16}O$, is the main source of the carbon and oxygen found in the Universe, including that in our bodies, and represents by fact the "Holy Grail" of nuclear astrophysics since the C/O ratio at the end of helium burning greatly affects the subsequent evolution of the star. At some point, when He in the core is exhausted, the stars start to burn He in a shell surrounding the inert C/O core, in addition to burning H to He in a shell surrounding the He-burning region. This phase, referred to as the asymptotic giant branch (AGB), is characterized by thermal instabilities: at a given time, the burning shells extinguish and the low-mass star will end its existence as a white dwarf, consisting mainly of C and O and supported by electron degeneracy pressure.

Massive stars evolve very differently from low-mass stars. After the end of a burning phase, the core contracts gravitationally, and the temperature increase can be sufficient to ignite the next and heavier nuclear fuel. In the case of masses larger than $11M_{\odot}$, after undergoing He burning, the core experiences further burning episodes referred to as C, Ne, O, and Si burning. The duration of each subsequent nuclear burning phase decreases significantly. There are two main reasons: the first is that each burning phase releases by far less energy per unit mass with respect to the previous phase; the second that an increasing fraction of energy is radiated away by neutrinos. Therefore, while H burning may continue for many million years, C burning typically lasts hundreds of days and Si burning may run out in just one day. After the last advanced burning stage (Si burning), the core consists mainly of iron isotopes: no more energy can be generated through fusion reactions. The core contracts and when it exceeds the Chandrasekhar mass limit, it collapses until the density of nuclear matter is reached. As a consequence of the neutron degeneracy pressure, the core rebounds and produces an outgoing shock wave. The wave heats and compresses the overlying layers of the star, consisting of successive shells of Si, O, Ne, and C; thus, more episodes of nucleosynthesis, referred to as explosive Si, O, Ne, and C burning, take place.

The creation of elements heavier than iron occurs mainly through neutron-capture processes, eventually followed by beta-decays in the so-called slow process (*s*-process) (Käppeler et al., 2011) and rapid process (*r*-process). The *r*-process dominates in environments with higher free neutrons fluxes and it produces heavier elements and more neutron-rich isotopes than the *s*-process. Supernovae explosions and neutron star mergers are potential sites for the *r*-process. The *s*-process is slow in the sense that there is enough time for beta-decays to occur before another neutron is captured: a network of reactions produces stable isotopes by moving along the valley of beta-decay stable isobars. This process primarily occurs within ordinary stars, particularly AGB stars, where the neutron flux is sufficient to cause neutron captures to recur every 10–100 years, much slower than for the *r*-process, which requires 100 captures per second.

The key point for each of these reactions is the value of cross-sections at the energies at which they take place in stellar environments. For most stellar scenarios, the changes in the system are slower than the collision time between the ions or atoms inside the stars; thus, the temperature profile is well-defined: the thermonuclear reaction rate depends on the Maxwell–Boltzmann velocity distribution and on the cross-section σ(E) energy dependence (Rolfs and Rodney, 1988). Typical stellar temperatures for main sequence low-mass stars correspond to peak energies of the Maxwell–Boltzmann distribution of $k_{\mathrm{B}}T \sim 0.9 - 90$ keV. In the case of more massive stars during advanced burning stages, peak energies can be as high as a few MeV. For charged particles induced reactions, these energies are typically well below the Coulomb barrier due to the nuclei electrostatic repulsion and the nuclear reactions proceed via tunnel effect. As a consequence, the low values of the cross-sections, ranging from picobarn to femtobarn and even lower, prevent their measurements in a laboratory at the Earth's surface where the signal-to-background ratio is too small mainly because of cosmic rays. The observed energy dependence of the cross-section at high energies is extrapolated to astrophysically relevant energies leading to substantial uncertainties. In particular, the reaction mechanism might change, or there might be the contribution of unknown resonances that could completely dominate the reaction rate at the stellar energies.

In the nineties, the LUNA collaboration proved that the installation of the experiments in a deep underground laboratory, the Gran Sasso National Laboratory, is a successful approach: for the first time, nuclear astrophysics measurements with very low counting rates down to few events per month became a reality.

The high current hydrogen and helium beams provided by the 50 kV (Greife et al., 1994) and, later on, by the LUNA-400 kV accelerators (Formicola et al., 2003) allowed for the investigation, for the first time at stellar energies, of the most important reactions responsible for the hydrogen burning in the Sun, such as $^{3}\mathrm{He}(^{3}\mathrm{He}, 2p)^{4}\mathrm{He}$ (Bonetti et al., 1999), and for the BBN such as $^{2}\mathrm{H}(\mathrm{p},\gamma)^{3}\mathrm{He}$ (Casella et al., 2002; Mossa et al., 2020).

Full descriptions of LUNA and of several results obtained in 25 years of experimental activity can be found in recent review articles (Broggini et al., 2018; Cavanna and Prati, 2018; Broggini et al., 2019).

Such achievements have motivated two proposals for similar facilities in China (Liu et al., 2016) and in the United States (Robertson et al., 2016).

The importance of extending such precise studies to the processes relevant to the late and warmer stages of star evolution (post-main sequence phases and helium and carbon burning) has motivated the LUNA collaboration to acquire a new and more powerful 3.5 MV single-ended accelerator. The new machine will deliver ion beams of H^+, $^4He^+$, $^{12}C^+$, and $^{12}C^{++}$ in the energy range from 0.350 to 7 MeV with 100 μA–1 mA intensity currents, depending on the ion species and on the energy value.

In the following sections, first, we will focus on the technical aspects, which are important for an underground nuclear astrophysics experiment. Then, the state of the art and the expected improvements from underground measurements are presented for some selected key processes of post-main sequence stellar phases: in detail, $^{13}C(\alpha,n)^{16}O$ and $^{22}Ne(\alpha,n)^{25}Mg$ are sources of neutrons for the s-process in AGB stars and during hydrostatic evolution of massive stars and the $^{12}C(\alpha,\gamma)^{16}O$ and the $^{12}C+^{12}C$ reactions are key processes of helium and carbon burning, respectively.

In conclusion, the commissioning phase of the new accelerator will be detailed, together with highlights about the exciting perspectives opened by the new facility in a larger time window scenario.

THE MV FACILITY AT GRAN SASSO

The MV facility will be hosted in the north side of Hall B in the Gran Sasso Laboratory and will consist of an accelerator room with concrete walls and a multistory building housing the control room and technical facilities. The concrete walls and ceiling (thickness of 80 cm) of the accelerator room will act as neutron shielding.

Nuclear astrophysics experiments require both high beam currents and a well-defined and stable beam energy: to perform reliable energy scans of the targets, the accelerator terminal voltage must be stable to <1 keV over many hours and to <0.1 keV over 1 h. A precise energy value is mandatory because of the almost exponential energy dependence of the cross-section induced by the tunnel effect probability: a small fluctuation of the beam energy would cause a large uncertainty in the measured cross-section value. Since, for some reactions, long data taking times are expected, the ion source must be able to run stably overnight without human intervention.

A 3.5 MV linear DC accelerator was specifically developed by High Voltage Engineering to meet the stringent requirements on beam intensity and stability (Sen et al., 2019). The machine will deliver ion beams into two different beamlines via a 35° switching analyzing magnet. Two independent target stations for solid and gas targets will be located at a 2 m distance from the analyzing magnet. The LUNA-MV accelerator is single-ended; i.e., it has an ion source and an injector block located inside the accelerator tank in the high-voltage terminal.

TABLE 1 | Beam intensity on target.

Ion species	Current (eμA)
	TV range: 3.5–0.5 MV (0.5–0.3 MV)
$^1H^+$	1,000 (500)
$^4He^+$	500 (300)
$^{12}C^+$	150 (100)
$^{12}C^{++}$	100 (60)

The need for high-intensity protons and carbon ions in the 2^+ charge state were the reasons to prefer an electron cyclotron resonance (ECR) ion source for the accelerator.

The accelerator operates at a terminal voltage (TV) range of 300 kV–3.5 MV, while the ion source can operate at 30 kV–40 kV. In the present system, high-intensity beam currents should be maintained over a large dynamic range: by considering a 1 mA current capability in the case of a proton beam, the beam power can be as high as 3.5 kW. To guarantee voltage stability for longer time periods (>1 h), a high-precision, low-temperature coefficient (<5 ppm°C) resistor chain is used to measure the TV. Beam intensities on target for H, He, and C ions are reported in **Table 1**. Compared to previous Singletron accelerators, the LUNA-MV has improved specifications for TV stability and ripple (10^{-5}). Beam energy reproducibility is in the order of 10^{-4}. A detailed description can be found in Sen et al. (2019).

For practical considerations, targets for direct measurements of nuclear cross-sections on stable nuclides are typically in either solid or gaseous state. The basic aspects of such targets are similar for experiments underground and on the surface, but certain requirements are emphasized for experiments deep underground to fully embrace the advantages of the location. In the case of a solid target, the beam energy loss occurs in a relatively small volume. The resulting power density, up to the order of 10^2–10^3 W/cm^2 at LUNA 400 if the beam is stopped in the target, requires the target to be cooled to avoid an increase of temperature that would damage the target or accelerate beam-induced target degradation. For targets on inert backing material, such as those produced by evaporation, sputtering, or implantation, water cooling behind the target is often used to dissipate the heat. The maximal power densities attainable on target will increase with the next generation of underground accelerators, either because of higher beam energies at comparable intensities (such as the MV facility at Gran Sasso) or due to further increased beam intensities (cf. JUNA Liu et al. 2016) compared to LUNA 400. Efforts are underway to adopt and advance techniques from surface experiments, such as cooling for high-powered targets (Wolfgang Hammer et al., 1986) or large-area reaction targets (Chen et al., 2020), to overcome thermal limitations on the beam intensity in future underground experiments. Even with best efforts in cooling, the performance of solid targets degrades under the beam, which

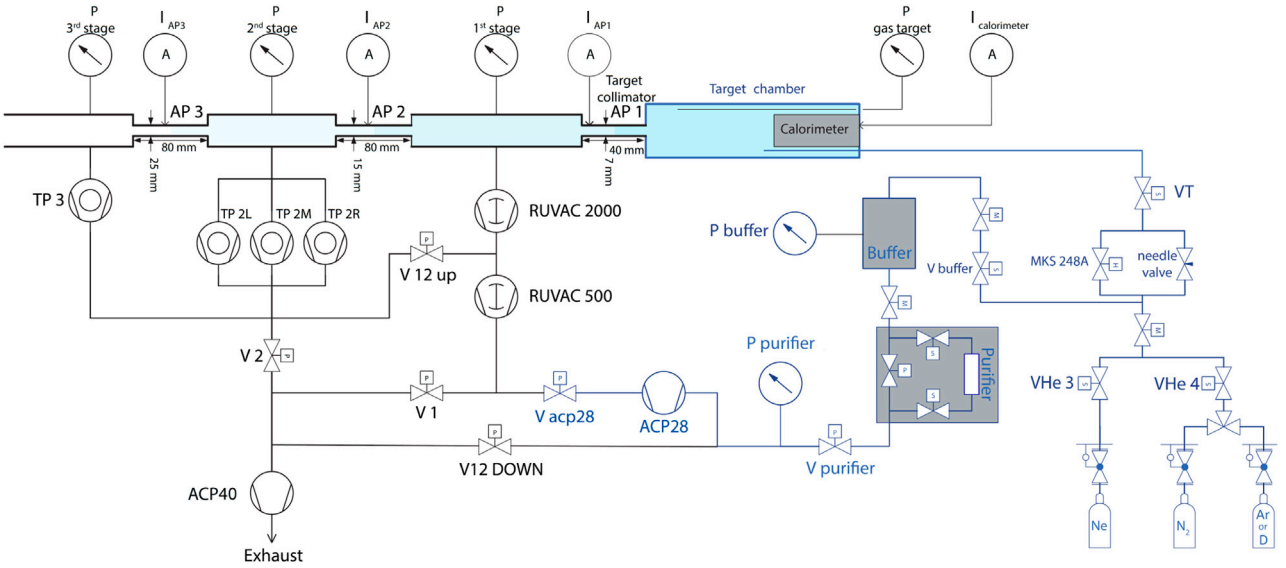

FIGURE 1 | Differential pumping system schematic. The beam comes from the accelerator on the left, passes through the apertures AP3, AP2, and AP1, enters the target chamber, and stops on the calorimeter.

is seen, for example, in a reduction of target thickness or changes in the target stoichiometry. In the regime of low-energy nuclear astrophysics experiments, solid targets typically have to be replaced after an irradiation corresponding to accumulated 10^0–10^1 (particle) Coulombs of the beam on target. This is an important practical aspect for the use of massive shielding against environmental radiation in low-background measurement. Compared to experiments on the surface, where secondary cosmic radiation on shielding materials results in diminishing returns beyond a certain thickness of shielding, much more massive shielding setups of lead and copper have been used at LUNA 400 (Caciolli et al., 2009), where for experiments with solid targets, easy access to the target had to be secured (Boeltzig et al., 2018). More sophisticated, i.e., larger and multilayered, shielding configurations are foreseen in the future as a consequence of an improved understanding of the relevant backgrounds and allowed by the more spacious target station layout at the new MV facility. Target access requirements will continue to be central in future experiments with these setups that employ solid targets.

The effects of target degradation may be avoided, wherever possible, by choosing targets in the gaseous form: a windowless gas target system offers stability over the long data taking periods, up to several weeks, if needed. Another advantage is chemical purity. Solid targets are rarely made by an element alone: possible changes in the stoichiometry should be continuously monitored during the running time.

The gas target system presently in use at the LUNA-400 accelerator is shown in **Figure 1**. It consists of three differential pumping stages, the target chamber, the gas pipeline, and a recycling system (see **Figure 1**). Three pumping stages produce a strong pressure gradient between the interaction chamber and the beamline. A water-cooled collimator is placed between adjacent pumping stages, provides the correct gas flow, and determines the pressure drop. The gas target system can either recycle the gas or let it flow away.

The gas enters the interaction chamber close to the beam stop and flows into the first pumping stage, where 99.5% of the gas is pumped away through a roots pump. Approximately 0.5% of the gas also goes in the second pumping stage, where it is pumped by three turbomolecular pumps. A small amount of gas flows in the third pumping stage through and is pumped away by a turbomolecular pump. A roots pump collects the gas from the previous pumps and is itself connected to the roughing pump or the recycling pump, depending on the running mode.

The target volume, typically 10–40 cm long, is surrounded by the detectors and is delimited by the chamber walls, the calorimeter, and the target chamber collimator. The latter does not only collimate the beam but also makes the pressure decrease steeply towards the first pumping stage.

The ionization of the target gas and the neutralization of the beam prevent the electrical reading of the beam current and a power compensation calorimeter with a constant temperature gradient is used to monitor the beam intensity (Ferraro et al., 2018a; Ferraro et al., 2018b). For the proper characterization of a windowless gas target, the density and the efficiency of the detectors profile along the beam path must be known. The density profile is usually measured using a mock-up scattering chamber equipped with measurement ports for capacitive pressure gauges and thermoresistors. The efficiency profile is, in turn, measured by moving radioactive sources along the beamline. Another method is the resonance scan technique: the target system is filled with selected gases such as ^{14}N or ^{21}Ne and their narrow, strong resonances are excited with a

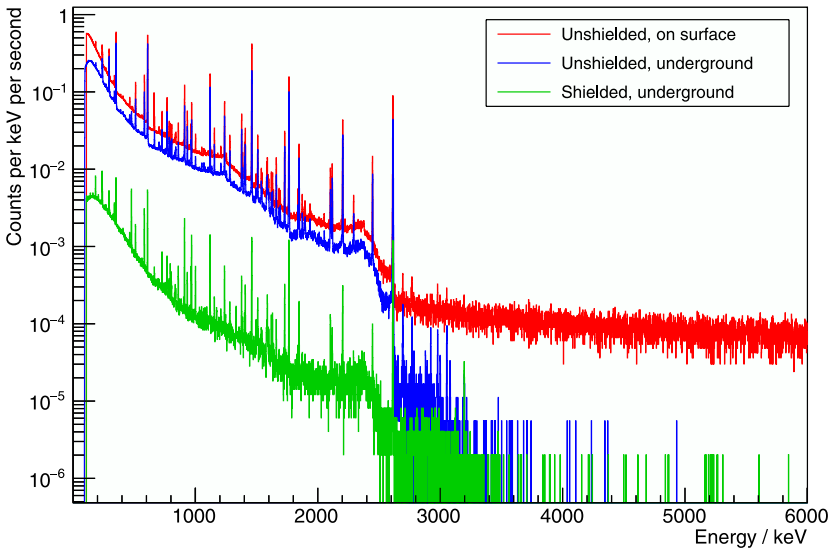

FIGURE 2 | γ-ray background spectra taken with a HPGe detector in the surface laboratory (red line), at Gran Sasso (blue), and at Gran Sasso with 15 cm lead shield (green).

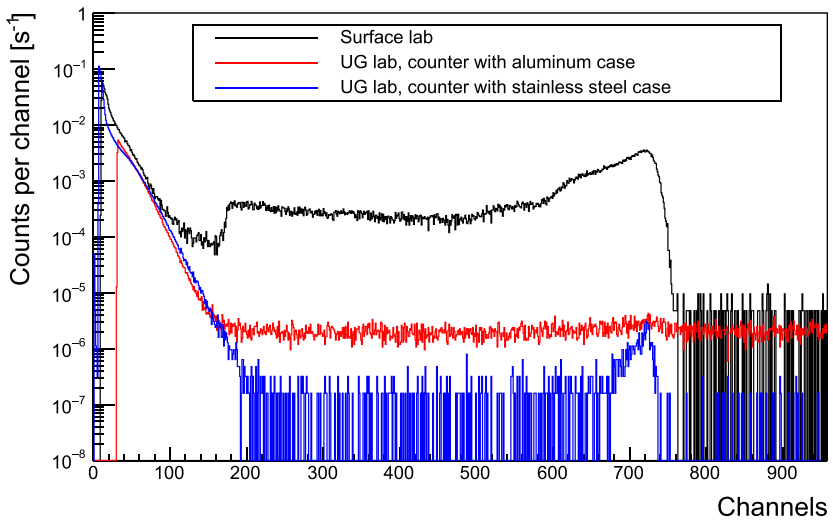

FIGURE 3 | Comparison of neutron background measured by means of ^{3}He counters: the black one is measured in a surface laboratory. Blue and red spectra are measured in the LNGS underground laboratory by means of counters with stainless steel and aluminum cases, respectively.

proton beam of proper energy. The resonance position is then moved along the target by changing the beam energy accordingly. Gas target setups usually ask for heavier detector shielding systems due to the larger dimensions.

The LUNA laboratory is protected by 1,400 m of dolomite rock from cosmic ray–induced effects. This rock overburden completely suppresses the hadronic and the soft electromagnetic component of cosmic rays. Muons are able to penetrate inside the mountain, but their flux is mitigated by about six orders of magnitude when compared with the Earth surface: this makes typically negligible also muon-induced radiations, such as spallation neutrons or cosmogenic-unstable nuclides. Long-lived radioisotopes such as the ones produced by the natural ^{238}U and ^{232}Th decay chains or ^{40}K are present in any laboratory and do not depend on depth but rather on the radiopurity of rocks, buildings, and detector materials. The induced gamma radiations can be mitigated by a suitable passive shielding surrounding the target and the detectors, usually consisting of selected low-background lead and freshly refined electrolytic copper. For the deep underground setting of LUNA, a shielding of 15–25 cm lead with low ^{210}Pb content lined at the inside with 5 cm electrolytic copper has been found to give

excellent background capabilities, as shown in **Figure 2**. Impurities in the detector and target, on the other hand, must be minimized by proper material selection.

From the point of view of neutron background, the underground location allows for a reduction of 3 orders of magnitude with respect to above-ground measurements (**Figure 3**) even without any further shielding. To further increase the sensitivity in view of neutron emitting reactions that are going to be studied with the MV facility, a deep study devoted to selection material was performed to reduce intrinsic background of detectors such as ^{3}He counters. We recall that a typical counter consists of a gas-filled tube with a high voltage applied across the anode and cathode: a neutron passing through the tube will interact with a ^{3}He atom to produce tritium and a proton. These two particles ionize the surrounding gas atoms to create charges, which in turn ionize other gas atoms in an avalanche-like multiplication process.

Indeed, alpha particle decays, coming from impurities of uranium and thorium in the counter cases, represent the main source of intrinsic background. By selecting stainless steel cases instead of standard aluminum ones, a reduction of one order of magnitude was achieved as shown in **Figure 3**: the blue and the red spectra were measured in the Gran Sasso with stainless steel and aluminum counters, respectively. The black spectrum is the background in a surface lab with a stainless steel counter. As a matter of fact, the new MV facility, together with the extremely low gamma and neutron background achieved by the LUNA collaboration, provides a unique sensitivity to assess the key processes of post-main sequence stellar burning.

Neutron Sources for the s-Process

The basic idea of the s-process was born in the 50's, with the famous article by Burbidge et al. (1957). It consists of a series of "slow" neutron captures and β-decays along the neutron-rich side of the valley of stability, close to the stability line. This process is responsible for the production of about half of the elemental abundances between iron and bismuth, as stated in Käppeler et al. (2011), the other part being produced by the rapid neutron-capture process (r-process) and, to a lesser extent, by the proton capture processes.

The s-process takes place in a low neutron flux, where the neutron-capture rate is lower than the β-decay rate of the resulting unstable nuclei. Such conditions are satisfied in the helium-burning shell of low-mass thermally pulsing stars in the AGB (main s-process) or in the helium-burning core of massive stars in the Red Giant Branch (weak s-process). The main s-process is mostly responsible for the production of elements with $90 \leq A \leq 209$ (i.e., from zirconium to bismuth), while the weak s-process contributes to elements in the range $56 \leq A \leq 90$ (i.e., from iron to zirconium).

It is well established that the ^{13}C(α,n)^{16}O reaction (Q_{value} = 2.216 MeV) is the principal neutron source for the main s-process, while the major neutron source of weak s-process is the ^{22}Ne(α,n)^{25}Mg reaction (Q_{value} = −0.478 keV). The cross-section of both these reactions greatly depends on temperature, the existence of excited states close to the reaction threshold, and the initial abundances of the interacting species.

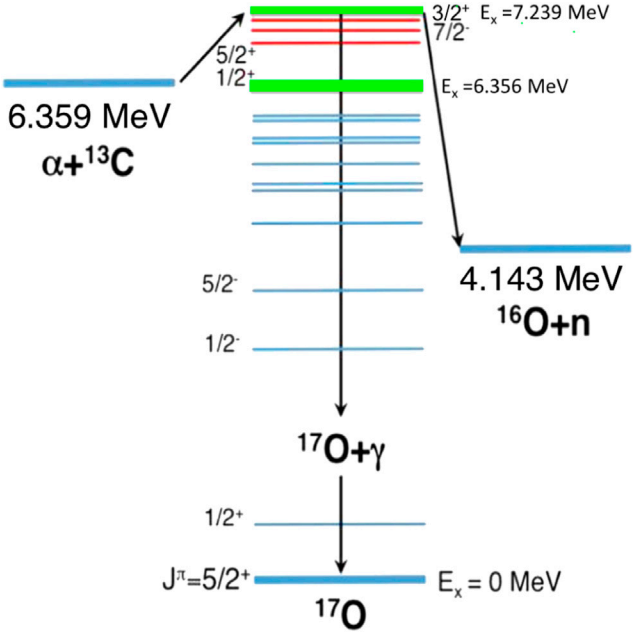

FIGURE 4 | (Colour online) Schematic diagram adapted from Cristallo et al. (2018) of the ^{13}C(α,n)^{16}O nuclear reaction process, together with the competing exit channel ^{17}O+γ. The excited states of interest for AGB nucleosynthesis are highlighted in green.

The Main s-Process and the ^{13}C(α,n)^{16}O Reaction

Käppeler (1999) attributed the formation of the main s-process elements to thermally pulsing stars in the asymptotic giant branch (TP-AGB) with mass $1.5M_{\odot} < M \leq 3M_{\odot}$. More recently, Cristallo et al. (2018) indicated a slightly broader mass interval, between 1.2 and $4M_{\odot}$.

The structure of TP-AGB stars is organized in the following layers: a carbon-oxygen core, a He-burning shell, a He-rich intershell, a H-burning shell, and a H-rich envelope. While the H-burning shell produces helium, the core contracts and heats up the basis of the He-burning shell, whose energy production increases. Eventually, the energy produced by the He-burning shell is not anymore radiated away efficiently and a thermonuclear runaway occurs, known as "helium shell flash" or "thermal pulse." This translates into an expansion of the He-rich intershell and the cooldown of the H-burning shell, which extinguishes. Also, the He-burning shell is affected by the expansion and cools down until extinction. A new contraction takes over and causes the initial reignition of the H-burning shell and of the He-burning shell afterward, until another thermal pulse occurs. A reservoir of ^{13}C, produced via the ^{12}C(p,γ)^{13}N($\beta^{+}\nu$)^{13}C reaction chain, forms the so-called ^{13}C pocket at the interface between the He-rich intershell and the H-rich envelope. As of today, the exact formation mechanism of such a pocket is still debated, as stated by Cristallo et al. (2018). During this phase, which lasts some 10^{4} years, the ^{13}C(α,n)^{16}O reaction takes place and provides neutrons for the main s-process.

In the article by Cristallo et al. (2018), the authors claim that, in the most metal-rich stellar models with an almost solar composition, a small amount of ^{13}C might survive and be engulfed into the convective zone generated by the incoming thermal pulse. This scenario would affect several branching points along the s-process path, and excesses of ^{60}Fe, ^{86}Kr, ^{87}Rb, or ^{96}Zr are expected compared to the radiative (low neutron density) ^{13}C burst. The unburned ^{13}C left at the end of the interpulse and available to produce neutrons in the subsequent pulse depends on the rate of the ^{13}C(α,n)^{16}O reaction.

The relevant astrophysical temperature for this process is ~0.1 GK, corresponding to a Gamow energy window between 140 and 250 keV. Indeed, the energy range of interest could be even larger, as discussed in the research by Kimura and Bonasera (2013), since the S(E) factor is energy-dependent. In **Figure 4**, the level scheme of ^{13}C(α,n)^{16}O nuclear reaction process is shown. The excited states of interest for AGB nucleosynthesis are highlighted in green and red. In particular, green levels are broad states which must be taken into account for any ^{13}C(α,n)^{16}O cross-section evaluation in the astrophysical region of interest. These are the $(1/2)^+$ near-threshold state and the $(3/2)^+$ at E_x = 7239 keV.

It is important to mention that the energy level of the near-threshold state is debated: Ajzenberg-Selove (1986) attributed to this state as subthreshold energy of $E_x = -(3 \pm 8)$ keV, while recently a study by Faestermann et al. (2015) deduced a positive energy value at $E_x = (4.7 \pm 3.0)$ keV.

State-of-the-Art

A conspicuous number of measurements of the ^{13}C(α,n)^{16}O cross-section have been carried out over the past 45 years.

We focus the attention on crucial direct and indirect measurements performed as follows.

The following are some of the direct measurements performed:

- Drotleff et al. (1993) measured the cross-section of the ^{13}C(α,n)^{16}O reaction in the 370–1000 keV energy range with ^{3}He proportional counters embedded in a moderating polyethylene matrix. This is still the dataset with the lowest point ever measured with direct measurement. The low-energy points reveal a S-factor enhancement, possibly due to a $1/2^+$ subthreshold resonance, mentioned by Ajzenberg-Selove (1986).
- Brune et al. (1993) used ^{3}He counters to measure the resonances of the ^{13}C(α,n)^{16}O reaction, at E_α = 656 and 802 keV: the authors concluded that the resonance strengths for these two states are too weak, compared to the nonresonant contribution, to affect the stellar reaction rates;
- Harissopulos et al. (2005) measured the ^{13}C(α,n)^{16}O reaction absolute cross-section in an energy range E = 0.8–8 MeV in steps of 10 keV with a setup similar to Drotleff's one. The main aim of the measurement was the geoneutrino background subtraction required by neutrino experiments such as Borexino and Kamland, as explained in the study by Araki et al. (2005). An overall uncertainty of 4% was achieved.
- Heil et al. (2008) promoted a new study of the ^{13}C(α,n)^{16}O cross-section in the energy range E = 420–900 keV. Heil used a different approach, employing a n-γ converter consisting of a Cd-doped paraffin sphere surrounded with 42 BaF_2 γ detectors. In the central hole, a neutron converter was installed. A detailed uncertainties analysis is described in the article. The authors recognized the main source of systematic error as the change of target stoichiometry caused by the buildup during the beam irradiation. At higher energies, overall uncertainties could be reduced to the level of 5%.
- Recent measurements at high energy are due to Febbraro et al. (2020), covering the same energy range spanned by Harissopulos. They improved the precision and accuracy by means of a setup sensitive to the neutron energies, also measuring the excited state transitions via secondary γ-ray detection. With this setup, they discriminated against neutrons emitted from different energy groups and they could measure the individual partial cross-sections of the ^{13}C(α,n)^{16}O reaction to the ground state and second excited state of the ^{16}O final nucleus.

At low energies, uncertainties of direct measurements are larger than 50%: they are dominated by the low counting statistics caused by unfavorable S/N ratio.

Moreover, going down in energy, direct measurements face limits of the fast dropping of the cross-section due to the Coulomb barrier and the increase of the screening effect.

For this reason, complementary indirect studies have been developed to better constrain the cross-section of this neutron source in the relevant energy region for astrophysics. These measurements were mostly aimed to determine the spectroscopic factor and/or the asymptotic normalization coefficient (ANC) of the 1/2+ level of ^{17}O near threshold, which represents the largest source of uncertainty at low energies. Kubono et al. (2003) evaluated a spectroscopic factor S_α = 0.01, but data were reanalyzed by Keeley et al. (2003), indicating a factor of 40 larger contributions. The ANC method was approached for the first time in the work by Johnson et al. (2006) that used the ^{6}Li(^{13}C, d)^{17}O sub-Coulomb transfer reaction. These results were recently revisited in the article by Avila et al. (2015).

Other indirect measurements were obtained with the Trojan Horse Method (THM): in this approach, projectiles (or targets) are selected and described as clusters of two particles in quasi-free kinematics. One is involved in reaction, while the other constituent cluster, called the spectator nucleus "s," is emitted without interacting with the system. For further information on the method, one could refer to Tumino et al. (2018a) and Tumino et al. (2018b). Using this technique, the ^{13}C(^{6}Li, n ^{16}O)d reaction was studied in quasi-free kinematic conditions (the deuteron inside the ^{6}Li beam is considered as a spectator to the three-body reaction), as described in La Cognata et al. (2013). This work covered an energy range between −0.3 and 1.2 MeV and allowed studing the near-threshold resonance at E_x = 6356 keV. In general, THM results need to be normalized to selected direct data and

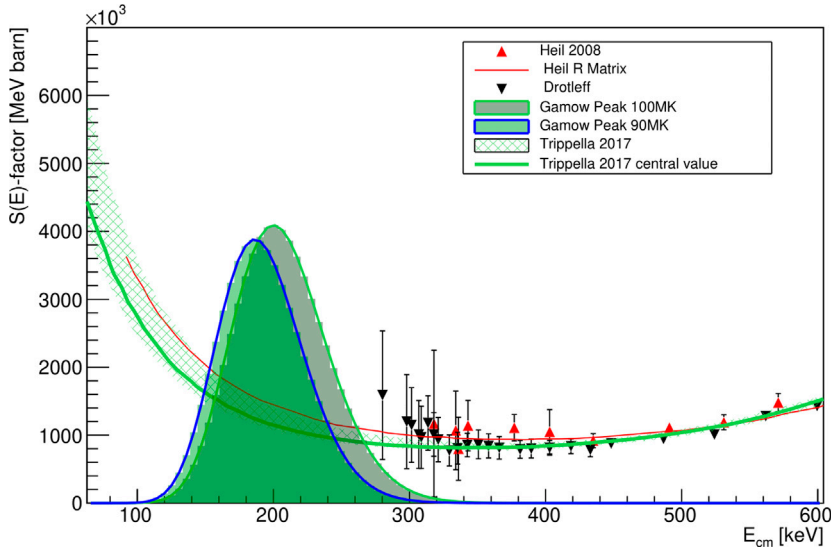

FIGURE 5 | Selection of most recent $^{13}C(\alpha,n)^{16}O$ measurements. Among the direct measurements, the Drotleff and the Heil data are represented, indicated by black triangles and red triangles, respectively. The solid red curve indicates the R matrix extrapolation by Heil. The most recent indirect measurement by THM by Trippella et al. is indicated by the green squared area and the central value is the green curve. In the plot, the Gamow window for two different stellar scenarios is drawn.

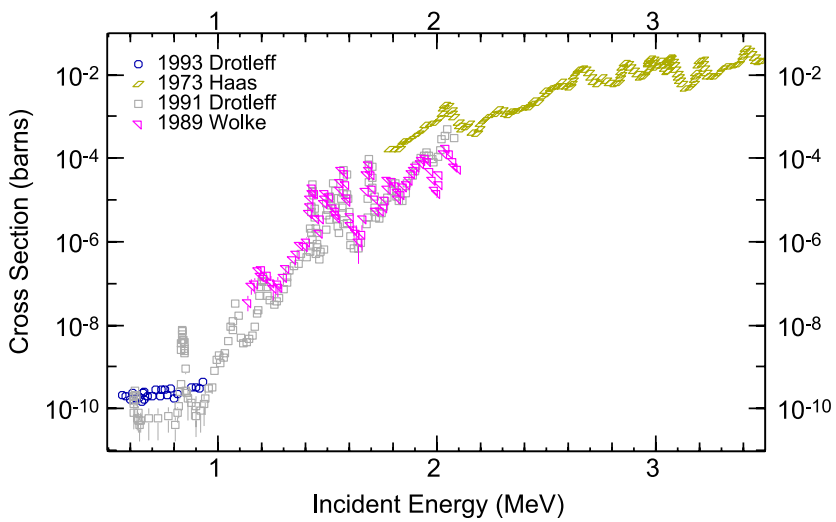

FIGURE 6 | A subset of the previous measurements of the $^{22}Ne(\alpha,n)^{25}Mg$ reaction cross-section. Data retrieved from the EXFOR database version of October 8, 2020. Blue circles are upper limits.

their uncertainty strongly depends on the choice of the reference direct measurements: in the first THM analysis by La Cognata et al. (2013), data were scaled to the astrophysical S-factor recommended by Heil et al. in the energy region between ~0.6 and 1.2 MeV. As a result, a THM S-factor was good in agreement with the direct ones, but with a squared Coulomb-modified ANC (7.7 ± 0.3) fm^{-1}, it was not in agreement with independent assessments of the ANCs, whose weighted average is (3.9 ± 0.5) fm^{-1}. After the new evaluation of the near-threshold resonance energy by Faestermann et al. (2015), setting its center at 4.7 keV above the ^{13}C–α threshold, data by THM were reanalyzed by Trippella and La Cognata (2017), normalizing experimental data with respect to the ANC parameter of the threshold resonance obtained by Avila et al. (2015). Trippella obtained an ANC value of (3.6 ± 0.7) fm^{-1}, in agreement with literature.

Data from the most recent works (direct and indirect methods) are shown in **Figure 5**.

From direct measurements (high uncertainties at low energy and a large scatter in absolute values among datasets) and indirect measurements (e.g., discrepancy in the spectroscopic factor evaluation and uncertain normalization of THM), there is a clear indication that more direct data with about 10% overall uncertainty are mandatory at both low and high energy.

The LUNA Direct Measurement

Taking advantage of the low environmental background of LNGS and the highly intense and stable alpha beam provided by the LUNA 400 accelerator, recently the LUNA collaboration put huge efforts into the measurement of the $^{13}C(\alpha,n)^{16}O$ cross-section at low energy with the goal to reach an overall uncertainty near 10%. A detector based on 18 ^{3}He counters arranged in a polyethylene moderator has been developed in order to maximize its efficiency. ^{13}C targets used during the measurement at LUNA have been produced evaporating 99% ^{13}C isotopically enriched powder on tantalum backing using the evaporator installed at the nuclear institute of research Atomki (Debrecen, Hungary). Hereby, the key points of the LUNA experiment are summarized. As already said before, the installation of the accelerator in the LNGS underground laboratory allows a neutron background reduction of 3 orders of magnitude with respect to above-ground measurements. Moreover, special attention was paid to reduce the α particle intrinsic background from detectors.

A further step for the background reduction was performed, acquiring the raw preamplifiers signals coming from detectors with Caen V1724 digitizers and rejecting alpha signals with a pulse shape discrimination analysis described in the article by Balibrea-Correa et al. (2018). This allowed reaching an overall background in the whole detector of about 1 count/h, 2 orders of magnitude lower than previous experiments performed in surface laboratories as described in the article by Csedreki et al. (2019).

Possible beam-induced background sources were investigated shooting alpha beam on blank tantalum backings. The neutron detection rate was compatible with the background measurement, making negligible the in-beam background.

The degradation monitoring under an intense alpha beam is crucial during the cross-section measurement performed at LUNA. The well-known NRRA (Nuclear Resonant Reaction Analysis) technique is not applicable due to the lack of resonances in the dynamic energy range of the accelerator. For this reason, a new method of analysis was developed.

Data taking at LUNA consisted in long α-beam runs with accumulated charges of ≈1C per run, interspersed by short proton-beam runs with moderator opened and HPGe detector in close geometry, with typical accumulated charges of 0.2 C at most. During the last mentioned proton run, the target degradation can be checked by performing a gamma shape analysis on the direct capture deexcitation to the ground state peak of $^{13}C(p,\gamma)^{14}N$ reaction with the HPGe detector.

Further information and details can be found in the study by Ciani et al. (2020).

Thanks to the unprecedented background reduction for this kind of direct measurement and the novel approach to monitoring target degradation, it was possible to measure the experimental yield of the $^{13}C(\alpha,n)^{16}O$ reaction in an energy range from 400 keV down to 305 keV in laboratory system energy, 40 keV lower than data in the literature: for the first time, LUNA collaboration measured with a direct technique cross-section inside the Gamow window reaching unprecedented overall uncertainty (<20%). Final results and astrophysical implications will be published within the end of 2020.

The LUNA collaboration is planning to extend the measurement of the $^{13}C(\alpha,n)^{16}O$ at higher energies at the new MV facility in the LNGS laboratory. This will give the unique possibility of providing a complete dataset over a wide energy range and avoiding renormalization to other datasets with unknown systematic uncertainties.

The Weak s-Process and the $^{22}Ne(\alpha,n)^{25}Mg$ Reaction

About half of the elements between iron and yttrium ($56 \lesssim A \lesssim 90$) are produced via the weak s-process in massive stars with initial mass $M > 8M_{\odot}$ (Käppeler et al., 2011). In such stars, ^{22}Ne is a byproduct of He-burning starting from preexisting CNO isotopes.

The reaction $^{22}Ne(\alpha,n)^{25}Mg$ has a negative Q-value of −478 keV and requires relatively high temperatures to be ignited. At the base of the convective envelope around the He core of massive stars, the temperature is sufficiently high (>0.25 GK) to make this reaction a relevant source of neutrons for the weak s-process until core He-burning extinguishes (Peters, 1968; Couch et al., 1974; Lamb et al., 1977; Prantzos et al., 1990; Raiteri et al., 1991a). Its effectiveness as a neutron source, though, depends also on the cross-section of the competing reaction, $^{22}Ne(\alpha,\gamma)^{26}Mg$.

When core He-burning runs out, ^{22}Ne is still rather abundant [about 1% in mass as claimed in the article by Pignatari et al. (2010)] and the reaction $^{22}Ne(\alpha,n)^{25}Mg$ is reactivated during shell C burning (Raiteri et al., 1991b) at a temperature of about 1 GK. At this stage, the $^{12}C(^{12}C,\alpha)^{20}Ne$ process yields α particles (Arnett and Truran, 1969) and even larger neutron fluxes are provided as a consequence of the higher temperature.

Besides the broad interest in the main neutron source in the weak s-process, some contributions also to the main s-process are worth mentioning in low-mass ($M < 3M_{\odot}$) AGB stars during thermal pulses (Gallino et al., 1988; Hollowell and Iben, 1988) and in intermediate-mass ($4M_{\odot} < M < 8M_{\odot}$) AGB stars (Bisterzo et al., 2014; Bisterzo et al., 2015), whereas predicted abundances of ^{86}Kr, ^{87}Rb, and ^{96}Zr are at variance with observations (Lugaro et al., 2003; Garcia-Hernandez et al., 2006; Garcia-Hernandez et al., 2007; Garcia-Hernandez et al., 2009; van Raai et al., 2012).

State-of-the-Art

Considering the weak s-process during core He-burning, the low-energy part of the Gamow window of the $^{22}Ne(\alpha,n)^{25}Mg$ reaction extends down to the boundary of the (α,n) threshold, located at $E_{\alpha,lab} = 575$ keV. At such low energies, measurements have so far suffered from low signal and high background, especially because of the small cross-section. For this reason, different groups only succeeded to directly study the resonances down to $E_{\alpha,lab} =$ 830 keV (see **Figure 6**). Other attempts to study the

resonances at lower energies by means of indirect methods often obtained inconsistent results. In the following, we summarize the most relevant direct studies of this reaction.

Back in the 60s, Ashery (1969) discovered that this reaction proceeds through many resonances in the compound nucleus. Other experimental studies conducted by Haas and Bair (1973), Mak et al. (1974), and Wolke et al. (1989) reported about 1 MeV and above.

Harms et al. (1991) investigated the energy range between $E_{\alpha,\mathrm{lab}} = 0.73$ and 2.10 MeV with a windowless, recirculating gas target system and two ^{3}He ionization chambers in close geometry. The resonance at $E_{\alpha,\mathrm{lab}} = 830$ keV was clearly detected, but it was not possible to show the existence of resonances at lower energies. Soon after, Drotleff et al. (1991) Drotleff et al. (1993) explored a lower energy range using the same gas target and an improved 4π detector, including two concentric circles of eight ^{3}He counters in a polyethylene moderator. Despite the improved sensitivity, no new low-energy resonances were observed in this experiment.

Giesen et al. (1993) performed a direct measurement with implanted ^{22}Ne targets to search for low-energy resonances. The background from $^{11}\mathrm{B}(\alpha,\mathrm{n})^{14}\mathrm{N}$, however, limited the sensitivity at lower energies. At the same time, they investigated the excited levels with natural parity in ^{26}Mg thanks to an indirect technique, the α-transfer.

Later, Jaeger et al. (2001) developed a new detector with twelve ^{3}He counters arranged in an optimized geometry. This upgrade allowed achieving a sensitivity of ∼10 pb and constraining the strength of the $E_{\alpha,\mathrm{lab}} = 830$ keV resonance to $\omega\gamma = (118 \pm 11)$ μeV. The upper limit on the tentative resonance at $E_{\alpha,\mathrm{lab}} = 633$ keV was significantly lowered. Based on these results, Jaeger et al. (2001) calculated the reaction rate under the assumption that the strength of the hypothetical resonance at $E_{\alpha,\mathrm{lab}} = 633$ keV was at 10% of its observed upper limit. However, the occurrence of such a resonance was ruled out by Longland et al. (2009), who demonstrated that the corresponding excited state at $E_x = 11,150$ keV in ^{26}Mg has unnatural parity.

At that time, it was clear that only a very low-background setup in an underground laboratory could have made possible a direct investigation of the resonances at lower energies.

The focus then moved to the evaluation of the reaction rate and its implications, mostly using direct cross-section measurements at relatively high energy and indirect data.

Longland et al. (2012) used a sophisticated statistical approach to calculate the ^{22}Ne(α,n)^{25}Mg reaction rate, including a careful treatment of the uncertainties. This led to a reduction of the uncertainties on calculated rates and raised the need for new, more precise and more sensitive measurements.

Bisterzo et al. (2015) estimated the impact of the ^{22}Ne(α,n)^{25}Mg uncertainty on the isotopic abundances close to and within the branching of the s-path for the main s-process. They provided a new evaluation of the reaction rate that was a factor of 2 higher than Longland et al. (2012). Even if this new rate was still able to reproduce the contribution of s-only isotopes from the main s-process within the solar uncertainties, Bisterzo et al. (2015) underlined how a sizeable change could be caused by low-energy resonances.

In the following years, several indirect studies attempted to improve the knowledge of this reaction. A new experimental investigation by Talwar et al. (2016) used α inelastic scattering to identify the important resonances and the α transfer technique to indirectly measure their width. The resulting ^{22}Ne(α,n)^{25}Mg reaction rate was close to the rate in Longland et al. (2012). Soon after, Massimi et al. (2017) studied neutron-capture reactions on ^{25}Mg, observing several excited states of ^{26}Mg and in particular at $E_x = 11.112$ MeV. In the same article, an R-matrix analysis was developed to assign spin and parity values to the excited states in ^{26}Mg without ambiguity and to calculate the upper limits on the reaction rates of the ^{22}Ne(α,n)^{25}Mg and ^{22}Ne(α,γ)^{26}Mg reactions. In the same work, Massimi et al. (2017) studied the impact of these new rates on the evolution of stars with initial mass M between 2 and 25$M_\odot$. It was observed that for a 25$M_\odot$ star, the uncertainty of the ^{22}Ne(α,n)^{25}Mg reaction rate was responsible for large differences in the weak s-process abundances, up to a factor of 50 in the Sr region. Noticeable changes were also found in intermediate-mass AGB models (IMS-AGBs, $3 < M/M_\odot < 7$) with an increase of ∼50% in the abundances of Y and La.

The continued interest in this reaction is demonstrated by two very recent experimental studies by Ota et al. (2020) and Jayatissa et al. (2020) with α transfer reactions: Ota et al. (2020) studied the $^{22}\mathrm{Ne}(^6\mathrm{Li},\mathrm{d})^{26}\mathrm{Mg}$ in inverse kinematics, detecting outgoing deuterons and ^{25,26}Mg in coincidence. In addition, Jayatissa et al. (2020) studied the $^{22}\mathrm{N}(^7\mathrm{Li},\mathrm{t})^{26}\mathrm{Mg}$ reaction.

The new evaluation of the reaction rate, based on spin-parity assignments by Jayatissa et al. (2020) combined with data from Ota et al. (2020), resulted in lower rates than previous evaluations, especially at low temperatures (see **Figure 7**). The lower rate is also the result of excluding an excited state at $E_x = 11.112$ MeV, corresponding to $E_{\alpha,\mathrm{lab}} = 598$ keV, observed by Massimi et al. (2017) and not observed in these studies.

In conclusion, the thermonuclear reaction rate of this reaction is still largely uncertain: several evaluations are present in the literature (see **Figure 7**), based on theoretical considerations, direct and indirect measurements, differing up to a factor of 5 in the temperature range relevant to the s-process in core He burning. The presence of low-energy resonances in the ^{22}Ne(α,n)^{25}Mg reaction below $E_{\alpha,\mathrm{lab}} = 830$ keV is expected, based on known levels in ^{26}Mg, but no such resonances have been directly observed yet. Nevertheless, they might contribute significantly to the reaction rate around 0.2 GK and cause sizeable changes in the prediction of weak s-process abundances.

The direct measurement of the ^{22}Ne(α,n)^{25}Mg reaction cross-section will be carried out at the new MV facility at LNGS (Guglielmetti, 2014; Prati, 2019), using a windowless gas target (see **Figure 1**) of enriched ^{22}Ne. Such an experiment could provide precise and accurate cross-section measurements down to about $E_{\alpha,\mathrm{lab}} \sim 600$ keV. Most of the background is expected to be due to the $^{11}\mathrm{B}(\alpha,\mathrm{n})^{14}\mathrm{N}$ reaction, as already reported by past experiments; therefore, a proper reduction of contaminants poses a crucial challenge, combined with the development of an optimized detector setup.

SHADES (Scintillator-He3 Array for Deep underground Experiments on the S-process) is an ERC starting grant (Grant

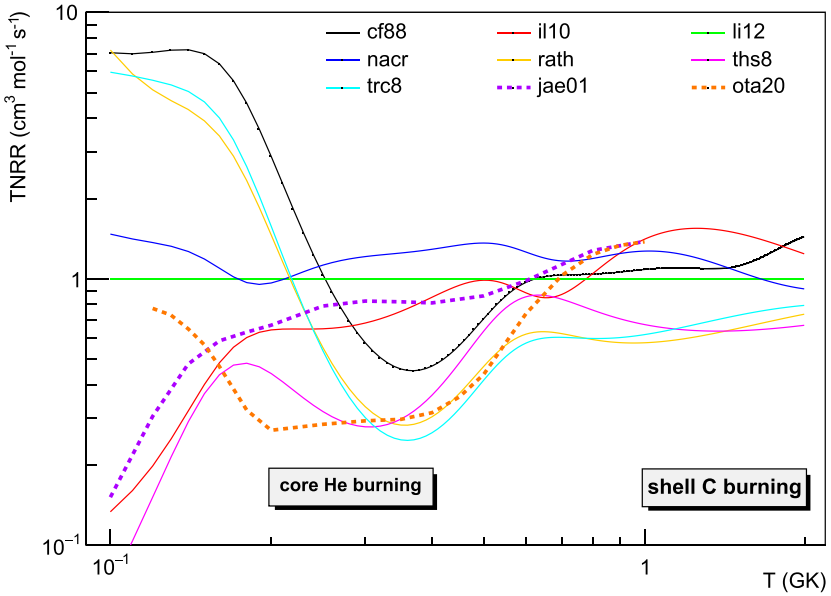

FIGURE 7 | A subset of the ^{22}Ne(α,n)^{25}Mg reaction rate evaluations, relative to Longland et al. (2012). Solid lines refer to the evaluations reported in the JINA REACLIB database as in Cyburt et al. (2010). In particular, cf88 = Caughlan and Fowler (1988); nacr = Angulo et al. (1999); rath = Rauscher and Thielemann (2000); ths8 = Cyburt et al. (2010); il10 = Iliadis et al. (2010); trc8 = REFIT: Cyburt et al. (2010); li12 = Longland et al. (2012). Dashed lines: jae01 = Jaeger et al. (2001); ota20 = Ota et al. (2020).

agreement ID: 852016), recently awarded to realize a new setup for the measurement of the ^{22}Ne(α,n)^{25}Mg reaction at energies of astrophysical interest. SHADES includes the development of a novel neutron detector and a gas target to be used at LUNA. The detector combines an array of ^{3}He counters with their high detection efficiency and liquid scintillators, which act as moderators for the reaction neutrons while at the same time providing information on the neutron energy. The combination of ^{3}He tubes and scintillator, together with recently studied signal processing techniques, as shown in Balibrea-Correa et al. (2018), will be able to limit backgrounds from external and internal sources and a beam-induced background to acceptable levels. The new detector will allow an increase of at least two orders of magnitude in sensitivity, allowing for the first time a measurement of the reaction cross-section in the energy range relevant to the s-process in core He burning.

THE ^{12}C(α,γ)^{16}O REACTION

The reaction ^{12}C(α,γ)^{16}O competes with the so-called triple-α process (^{4}He + ^{4}He $\rightarrow$ ^{8}Be followed by ^{4}He + ^{8}Be $\rightarrow$ ^{12}C) during stellar helium burning (Burbidge et al., 1957). The astrophysical rates of both reactions influence the ratio of ^{12}C/^{16}O produced during the helium-burning phase, which in turn determines the following steps of stellar evolution. Due to the central role of these nuclides, understanding their ratio in helium burning has been identified as a problem of "paramount importance" for nuclear astrophysics, as shown in Fowler (1984). Compared to the triple-α process, the cross-section of ^{12}C(α,γ)^{16}O is significantly less well-known and, in spite of extensive experimental efforts, a better understanding of this reaction remains desirable. A recent comprehensive review on the state of understanding ^{12}C(α,γ)^{16}O can be found in deBoer et al. (2017).

Owing to the sharp drop of the charged particle reaction cross-sections towards the energy regions relevant for astrophysics, direct measurements in the energy region of interest are not available, making extrapolations necessary. Such extrapolations are challenging due to the nuclear structure of the compound nucleus ^{16}O: the cross-section in the energy range of interest is characterized by the presence of broad resonances (including subthreshold states). It is crucial to study the interference between states of the same J^π but also to account for angular effects from the interference of processes with different J^π (as outlined in deBoer et al., 2017). In particular, the E1 and E2 components of capture to the ground state are of comparable strength in the energy range of interest, and the extrapolated cross-section is very sensitive to the interference of these two components.

Different experimental approaches have been taken to directly study the ^{12}C(α,γ)^{16}O reaction: in normal kinematics, a fixed ^{12}C target (solid or gaseous) is bombarded by α particles, detecting γ-rays from the reaction; inverse kinematics employs a ^{12}C beam impinging on a helium target. Inverse kinematics experiments have been performed as measurements of the γ-rays from the reaction or detecting the ^{16}O nuclei in a recoil separator (Kremer et al., 1988; Schürmann et al., 2005; Matei et al., 2006; Schürmann et al., 2011). Studies of the inverse reaction ^{16}O(γ_0, p)^{12}C at high-intensity γ-ray facilities allow us to infer information on the ground state transitions. Other reactions to study the nuclear structure of ^{16}O are used to constrain extrapolations of the reaction ^{12}C(α,γ)^{16}O in frameworks such as R-matrix theory in deBoer et al. (2017).

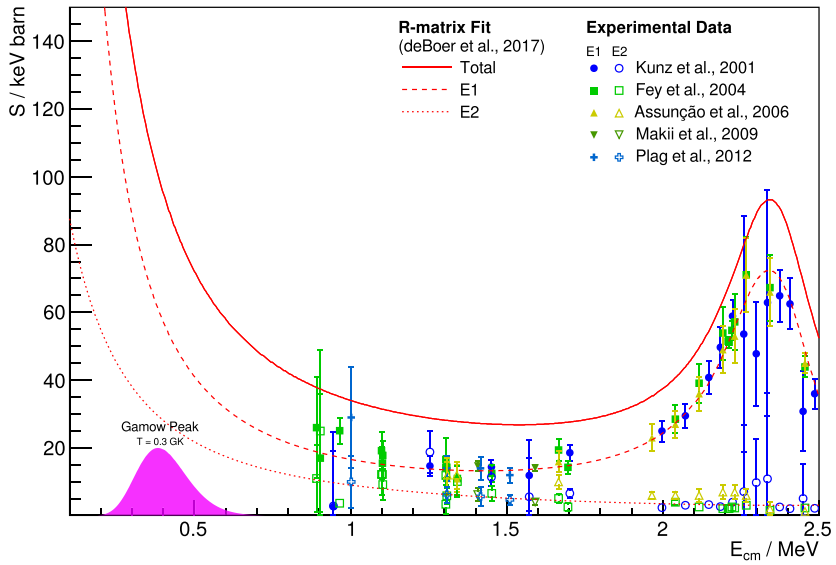

FIGURE 8 | Overview of recent experimental data (Kunz et al., 2001; Fey, 2004; Assunção et al., 2006; Makii et al. 2009; Plag et al., 2012) for the ground state capture in $^{12}C(\alpha,\gamma)^{16}O$, with the results of R-matrix fits from deBoer et al. (2017) for comparison. All data are unscaled. The location of the Gamow window for a stellar temperature of 0.3 GK is shown for reference.

When measuring the γ-rays from reaction, angular distribution measurements at multiple detector angles yield information to disentangle the E1 and E2 components, while a total absorption spectroscopy setup, detecting the total γ-ray energy, yields the total cross-section with a large detection efficiency. **Figure 8** summarizes the current situation of direct measurements, showing recent direct measurements of this reaction at low energies for illustration. These measurements extend down to about 0.9 MeV center of mass energy but are characterized by increasing uncertainties when approaching these low energies. As the cross-section drops rapidly towards these energies, backgrounds—environmental and beam-induced—are increasingly relevant. For example, experiments in normal kinematics are affected by backgrounds from the reaction $^{13}C(\alpha,n)^{16}O$, which has a cross-section that is of the order of 10^6 times that of $^{12}C(\alpha,\gamma)^{16}O$. Neutrons can produce background signals directly in the detector or through secondary radiation in the environment of the detector. This background can be reduced by using ^{12}C targets depleted in ^{13}C or with the help of bunched beams that allow disentangling the prompt γ-ray signal from neutron-induced backgrounds by time of flight.

Additional data at lower energies are desirable to better constrain the energy dependence of the extrapolation, and further experiments will aim to shed light on it in the future. Direct measurements are expected to contribute to this effort by pushing the lower limit for the available cross-section data further below 1 MeV center of mass energy. This includes promising measurements with a recoil mass separator, as in Fujita et al. (2015). On the side of the new underground accelerator facilities, new exciting opportunities for the study of this reaction will become available shortly. Measurements of $^{12}C(\alpha,\gamma)^{16}O$ are among the scientific goals of the new MV facility at LNGS and the Felsenkeller shallow-underground accelerator laboratory for nuclear astrophysics, as in Bemmerer et al. (2018). Both accelerators will provide beams not only of α particles but also of carbon ions, allowing for underground measurements of this reaction in inverse kinematics. The scientific program of JUNA at JPL, as outlined in Liu (2017), includes the study of $^{12}C(\alpha,\gamma)^{16}O$ as well. To take full advantage of the high-intensity α beam and the deep underground location of JUNA, the minimization of beam-induced backgrounds, such as those created on ^{13}C, has been identified as crucial.

THE $^{12}C+^{12}C$ REACTION

At the end of the core helium burning, the central part of the star becomes more massive, contracts, and heats up. The contraction and the possible consequent collapse can be halted by the ignition of carbon burning or by the pressure of degenerate electrons. There are several factors preventing the ignition temperature before carbon burning is reached prior to electron degeneracy. For instance, plasma neutrinos are produced near the center of the star and they cause a decrease in the central temperature while leaving it. In addition, in the case of intermediate-mass stars, the second dredge-up further reduces the temperature of the star core, with the convective envelope penetrating into the H-exhausted shell. Depending on the star mass, it may attain the physical condition for C burning or become a carbon-oxygen white dwarf. The minimum initial mass of a star able to experience a C-burning phase is called M_{up}. The value of M_{up} was proposed for the first time by Becker and Iben (1980), who found $M_{up} = 9M_{\odot}$ for a star with nearly solar composition. However, there are many uncertainties: those affecting the $^{12}C+^{12}C$ and $^{12}C+\alpha$ rates are the most important nuclear ones. As a matter of fact, the value of M_{up} separates the progenitors of

C-O white dwarfs, novae, and type Ia supernovae from those of core-collapse supernovae, neutron stars, and stellar-mass black holes. Finally, if the star mass is slightly higher than M_{up}, an off-center carbon ignition takes place in degenerate conditions and the star may end its life as an O-Ne white dwarf.

Stellar models predict that carbon burning, triggered by the $^{12}C+^{12}C$, occurs for center of mass energies between 0.9 and 3.4 MeV. The reaction can proceed through different channels corresponding to the emission of a photon, a neutron, a proton, one or two α particles, or a ^{8}Be nucleus. Among these channels, the two most relevant are the $^{12}C(^{12}C,p)^{23}Na$ and $^{12}C(^{12}C,\alpha)^{20}Ne$; alpha particles can produce neutrons through $^{13}C(\alpha,n)^{16}O$ and $^{22}Ne(\alpha,n)^{25}Mg$ reactions. These neutrons are fundamental for the synthesis of elements heavier than Fe through the s-process.

The $^{12}C+^{12}C$ reaction rate at the center of mass energies ≈ 1.5 MeV also affects the physical conditions in the SNIA explosion. In particular, carbon burning can be ignited in an explosive condition when the material is accreted on the surface of a white dwarf in a close binary system, as in Bravo et al. (2011). A variation in the rate would modify the extension of the convective core prior to the explosion, the degree of neutronization, and the temperature at the beginning of the thermonuclear runaway. The knowledge of SNIA is fundamental in cosmology since these systems allow the measurements of distances and of the expansion rate of high redshift galaxies Tutusaus et al. (2019).

Unfortunately, the Gamow window of the $^{12}C+^{12}C$ reaction, 0.7–3.4 MeV depending on the astrophysical scenario, is much lower than the height of the Coulomb barrier, 6.7 MeV approximately, making the direct measurement of the cross-section extremely difficult.

State-of-the-Art

The two most relevant channels in the $^{12}C+^{12}C$ reaction are the emission of protons and α particles, with a Q-value of 2.24 MeV and 4.62 MeV, respectively. The proton and alpha channels can be measured by detecting either the charged particles or the gamma decay. In particular, the largest branching is for the deexcitation of the first excited state to the ground state of the ^{23}Na or ^{20}Ne. Above 2 MeV, the first excited state transition to the ground state accounts for approximately 50% of the total cross-section and produces photons of 440 keV and 1634 keV in the case of proton or alpha emission, respectively.

The challenge in obtaining a reliable measurement of the $^{12}C+^{12}C$ cross-section at low energies is related to its exponentially falling behavior, which produces a very low counting rate; in this scenario, any natural or beam-induced background can seriously affect the measurement. The latter is due to impurities in the carbon target, mainly hydrogen and deuterium, because they can form bonds with carbon. The main background related to the gamma measurements comes from the $^{2}H(^{12}C,p_1\gamma)^{13}C$ and $^{1}H(^{12}C,\gamma)^{13}N$ reactions, as detailed in the experimental work by Spillane et al. The Compton background of the primary peaks could completely dominate the carbon fusion γ-ray peaks, as in Spillane et al. (2007). As far as the particle measurements are concerned, it is kinematically impossible to find protons in the carbon fusion region of interest if the particle detectors are placed at backward angles.

The most recent articles focusing on the $^{12}C+^{12}C$ cross-section measurement at low energies are summarized as follows.

Jiang et al. (2018) have recently measured the $^{12}C+^{12}C$ fusion cross-section in the energy range 2.5–5 MeV. The authors studied the two main channels: $^{12}C(^{12}C,p)^{23}Na$ and $^{12}C(^{12}C,\alpha)^{20}Ne$ at Argonne National Laboratory using a Gammasphere array of 100 Compton-suppressed Ge spectrometers in coincidence with silicon detectors. The measurement was pushed down to 2.84 MeV and 2.96 MeV for the p and α channels, respectively; the results are in good agreement with other measurements using γ Spillane et al. (2007) and charged particle detection Zickefoose et al. (2018), but with smaller uncertainties.

Tumino et al. (2018a) and Tumino et al. (2018b) measured the cross-section of the $^{12}C(^{12}C,p)^{23}Na$ and $^{12}C(^{12}C,\alpha)^{20}Ne$ reactions through the indirect THM. A 30 MeV beam was delivered on a natural carbon target; charged particles were detected through ΔE-E position-sensitive silicon detectors. The THM results for α and p channels are in good agreement with direct data except for the 2.14 MeV region, where the claim of a strong resonance by previous works Spillane et al. (2007) is not confirmed. Instead, the indirect data show a resonance at 2.095 MeV, one order of magnitude less intense with respect to the 2.14 MeV resonance found by Spillane in the $^{20}Ne+\alpha$ channel and of similar intensity in the $^{23}Na+p$ one. In addition, several low-energy resonances are evident below 1.5 MeV, never detected before in a direct measurement. The results of the THM raised some criticism, as in Mukhamedzhanov et al. (2019), mainly because of the neglected Coulomb interaction between ^{2}H, the spectator nucleus in the THM, and ^{24}Mg.

$^{12}C(^{12}C,p)^{23}Na$ has also been measured by Zickefoose et al. (2018) in the 2–4 MeV energy range by particle spectroscopy. The beam, provided by the tandem accelerator of the Center for Isotopic Research on the Cultural and Environmental (CIRCE) heritage, was sent onto highly ordered pyrolytic graphite targets; protons were detected through ΔE-E silicon detectors. The total S-factor, including also the contribution of the α channel, has been obtained using the ratio between the p-channel and total S-factor provided by Becker et al. (1981). Due to the poor statistics and beam-induced background problems, this work needs a further experimental effort to improve the knowledge of the total S-factor in the relevant energy range. For this reason, the experimental campaign continued with a new study devoted to the reduction of light species contaminant, especially ^{1}H and ^{2}H in the carbon targets, as in Morales-Gallegos et al. (2018). Measurements were done with natural graphite and highly ordered pyrolytic graphite targets. ^{1}H and ^{2}H content were reduced up to 70–85% by means of diffusion at high temperatures (higher than 1,000°C). A further reduction of a factor of 2.5 was obtained, enclosing the scattering chamber in dry nitrogen to minimize leaks into the rest gas within the chamber. The bulk contamination finally achieved by the authors is 0.3 ppm. Further measurements are planned with the new experimental setup.

An upper limit on the $^{12}C+^{12}C$ S-factor has been recently suggested from the measurement of the $^{12}C+^{13}C$ reaction by

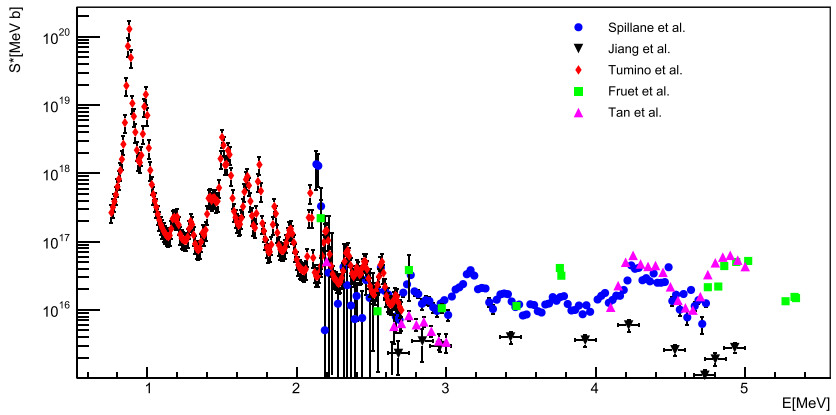

FIGURE 9 | S-factor values obtained by Spillane et al. (2007), Jiang et al. (2018), Tumino et al. (2018a), Tumino et al. (2018b), Fruet et al. (2020), and Tan et al. (2020).

Zhang et al. (2020); in fact, it has been observed that the $^{12}C+^{13}C$ and $^{13}C+^{13}C$ cross-sections at energies below and above the Coulomb barrier are upper bounds of the nonresonant contribution of the $^{12}C+^{12}C$ cross-section. The measurement of the $^{13}C+^{13}C$ reaction was performed by studying the $^{12}C(^{13}C, p)^{24}Na$ channel; ^{24}Na has a half-life of 15.0 h, allowing an activation measurement. The resulting upper limit on the $^{12}C+^{12}C$ S-factor agrees nicely with available direct experimental data down to ≈2.5 MeV, while for lower energies, the THM results are significantly higher compared to the Zhang upper limit. However, this result should be taken with caution, considering that the obtained upper limit is only valid for the nonresonant component of the $^{12}C+^{12}C$ cross-section. Recent theoretical calculations of the $^{12}C+^{12}C$ subbarrier fusion cross-section highlighting the role of resonances can be found in Bonasera and Natowitz (2020).

Another step forward in the knowledge of the $^{12}C+^{12}C$ rate has been recently moved by Fruet et al. (2020). They performed a direct measurement down to ≈2.2 MeV using the particle-gamma coincidence technique. The experiment was performed at the Andromede accelerator facility at IPN Orsay, France, with a ^{12}C beam, maximum beam current of 2 pμA for astrophysically relevant energies, impinging on a natural carbon target. Charged particles were detected through three annular silicon strip detectors covering 30% of the total solid angle. For gamma-ray detection, an array of $LaBr_3(Ce)$ scintillator detectors has been employed. The results are in good agreement with the data reported by Jiang et al. (2018) and Tumino et al. (2018a), Tumino et al. (2018b). However, a more prominent resonance has been observed around 3.8 MeV compared to other measurements (Spillane et al., 2007; Zickefoose et al., 2018).

The most recent measurement of the $^{12}C+^{12}C$ cross-section has been performed by Tan et al. (2020) at the University of Notre Dame. The simultaneous detection of protons and alphas, through a silicon detector array, and γ-rays with a 109% HPGe detector, allowed for particle-γ coincidence technique. The S-factor upper limit at 2.2 MeV for proton (p_1) and alpha (α_1) channels is lower than THM data. We note that the upper limit for the proton channel disagrees significantly with the recent measurement of Fruet et al. (2020). The discrepancy is less evident, but still present, for the alpha channel. In the energy region between 2.5 and 3 MeV, there is some tension between the results of Tan et al. (2020) and previous measurements Jiang et al. (2018) for both proton and alpha channels. The S-factor results at the center of mass energies above 4 MeV agree nicely with other data.

A comparison between the total S-factor values obtained by Spillane et al. (2007), Jiang et al. (2018), Tumino et al. (2018a), Tumino et al. (2018b), Fruet et al. (2020), and Tan et al. (2020) is shown in **Figure 9**. It should be underlined that Tumino et al. (2018a), Tumino et al. (2018b) data are normalized to direct measurements, so a difference in the absolute value of the S-factor can also be attributed to systematic errors affecting direct data. Significant discrepancies between the results of the reported experiments are evident in the whole energy range and, for this reason, a further experimental effort is needed.

The Measurement in an Underground Laboratory

An underground location, such as the one of the LUNA experiment, is the perfect environment to perform the measurement of the $^{12}C+^{12}C$ cross-section detecting γ-rays emitted in the decay of the ^{23}Na and ^{20}Ne excited states. A high-efficiency and ultralow intrinsic background germanium detector (HPGe) is suitable for the measurement in combination with a massive lead shielding to avoid the contribution of the low-energy gamma-rays coming from the decay of the ^{238}U and ^{232}Th chains. In **Figure 10**, the counting rate, expressed in counts per day, is reported as a function of the interaction energy. To calculate the rate, the S-factor provided by Spillane et al. (2007) has been adopted, considering that the decay of the first excited state to the ground state accounts for ≈50% of the total cross-section and produces photons of 440 keV and 1634 keV in the case of proton or alpha emission, respectively. It is evident that if the trend of the S-factor observed by Tumino et al. (2018a), Tumino et al. (2018b) is confirmed, the reaction rates can be higher by 1–3 orders of magnitude. The two horizontal lines represent a typical rate of γ background measured at LNGS with a shielded setup, as in Caciolli et al. (2009) (blue and red line for 440 keV and 1636 keV γ energies, respectively). In particular, for the proton

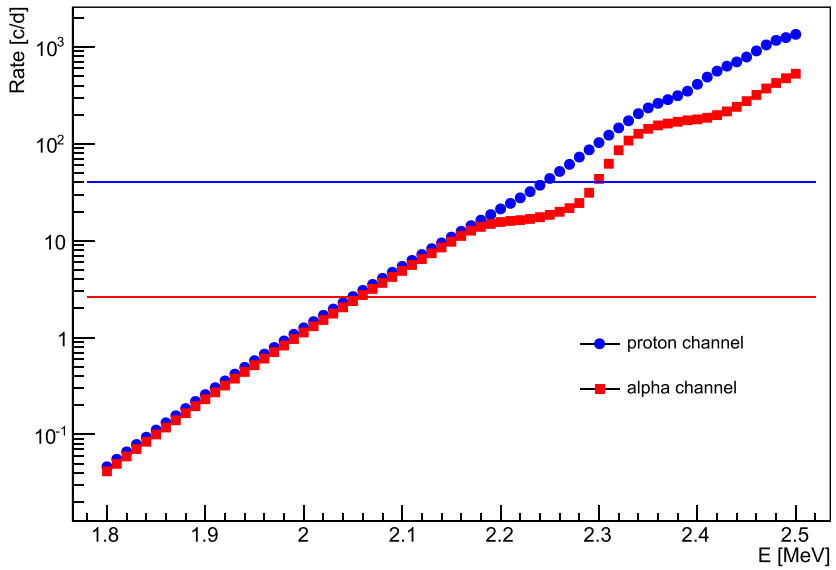

FIGURE 10 | Counting rate, in counts per day, obtained considering data provided by Spillane et al. (2007), a γ detection efficiency of 6% and 2% for 440 keV and 1636 keV γ energies, respectively, and a beam current of 50–150 μA. The two horizontal lines represent a typical rate of γ background measured at LNGS with a shielded setup Caciolli et al. (2009) (blue and red lines for 440 keV and 1636 keV γ energies, respectively).

channel, crucial issues are the choice of the materials to limit the intrinsic contaminants and proper detectors shielding. In addition, constant nitrogen fluxing around the setup could help to further reduce the background, avoiding radon contaminants. The γ-detection efficiency adopted in the calculation is just a standard value; new high-efficiency setups will be developed for future measurements. From a rough estimation considering the data provided by Spillane et al. (2007) and the setup described in **Figure 10**, we can say that the dominant contribution to the background for the proton channel will come from the environmental radioactivity if a 0.3 ppm H contamination level is achieved in the targets (Morales-Gallegos et al., 2018) making the induced background not an issue at least down to ~2 MeV. The limitation in the alpha channel is conversely related to the low rate. To provide the total cross-section, the measurement of the charged particle channels is also needed. In this case, the advantage of the underground location is less evident but still present; in fact, secondary particles produced by the passage of cosmic rays through the detectors could contribute to the background and they are effectively reduced at LNGS (Bruno et al., 2015).

CONCLUSIONS

The enhancement in the sensitivity provided by the strong background reduction in an underground laboratory, together with the best experimental techniques, have made it possible, during twenty-five years of LUNA activity, to take clear steps forward in the knowledge of nuclear processes relevant to astrophysical scenarios. The installation of a new MV accelerator in the Gran Sasso laboratory will allow over a broad time window of at least twenty years extending these studies to key processes of helium, carbon, and neon burning phases. Even if more extensively studied, also other important processes of H burning will be better constrained, thanks to the new facility. An example is the $^{14}N(p,\gamma)^{15}O$ reaction, presently known only at energies well above the Gamow peak. By combining the existing LUNA 400 kV machine with new LUNA-MV facility, it will be possible to cover the necessary energy range with a sufficient overlap and without any hole between 200 keV and 1.5 MeV, allowing the reduction of the systematics in the extrapolations down to the 5% level. The $^{14}N(p,\gamma)^{15}O$ reaction will also be suitable to perform the commissioning and the tuning of the LUNA-MV accelerator.

As already said, the success of the LUNA approach has motivated similar facilities already in operation in the United States or under construction in the Republic of China. This worldwide effort will allow in the next decades taking important steps forward in the field of nuclear astrophysics.

AUTHOR CONTRIBUTIONS

SZ wrote the introduction and the conclusion, GC the section on $^{13}C(\alpha,n)$ reaction, FF the section on $^{22}Ne(\alpha,n)$ reaction, AB the section on $^{12}C(\alpha,\gamma)$, and FC the section on $^{12}C+^{12}C$.

REFERENCES

Ajzenberg-Selove, F. (1986). Energy levels of light nuclei A = 16–17. *Nucl. Phys. A* 460, 1–110. doi:10.1016/0375-9474(86)90038-2

Angulo, C., Arnould, M., Rayet, M., Descouvemont, P., Baye, D., Leclercq-Willain, C., et al. (1999). A compilation of charged-particle induced thermonuclear reaction rates. *Nucl. Phys. A* 656, 3–183. doi:10.1016/S0375-9474(99)00030-5

Araki, T., Enomoto, S., Furuno, K., Gando, Y., Ichimura, K., Ikeda, H., et al. (2005). Experimental investigation of geologically produced antineutrinos with KamLAND. *Nature* 436, 499–503. doi:10.1038/nature03980

Arnett, W. D., and Truran, J. W. (1969). Carbon-burning nucleosynthesis at constant temperature. *Astrophys. J.* 157, 339. doi:10.1086/150072

Ashery, D. (1969). Study of the ^{22}Ne(α, n)^{25}Mg reaction: a possible source of stellar neutrons. *Nucl. Phys. A* 136, 481–495. doi:10.1016/0375-9474(69)90122-5

Assunção, M., Fey, M., Lefebvre-Schuhl, A., Kiener, J., Tatischeff, V., Hammer, J. W., et al. (2006). E1 and E2 S factors of ^{12}C(*α*, γ_0)^{16}O from γ-ray angular distributions with a 4π-detector array. *Phys. Rev. C* 73, 055801. doi:10.1103/PhysRevC.73.055801

Avila, M. L., Rogachev, G. V., Koshchiy, E., Baby, L. T., Belarge, J., Kemper, K. W., et al. (2015). New measurement of the α asymptotic normalization coefficient of the 1/2+ state in ^{17}O at 6.356 MeV that dominates the ^{13}C(α,n)^{16}O reaction rate at temperatures relevant for the *s* process. *Phys. Rev. C* 91, 048801. doi:10.1103/PhysRevC.91.048801

Balibrea-Correa, J., Ciani, G. F., Buompane, R., Cavanna, F., Csedreki, L., Depalo, R., et al. (2018). Improved pulse shape discrimination for high pressure ^{3}He counters. *Nucl. Instrum. Methods Phys. Res. Sect. A* 906, 103–109. doi:10.1016/j.nima.2018.07.086

Becker, H. W., Kettner, K. U., Rolfs, C., and Trautvetter, H. P. (1981). The ^{12}C+^{12}C reaction at subcoulomb energies (ii). *Zeitschrift für Physik A Atoms Nucl.* 303, 305–312. doi:10.1007/BF01421528

Becker, S. A., and Iben, J. I. (1980). The asymptotic giant branch evolution of intermediate-mass stars as a function of mass and composition. II. Through the first major thermal pulse and the consequences of convective dredge-up. *Astrophys. J.* 237, 111–129. doi:10.1086/157850

Bemmerer, D., Cowan, T. E., Grieger, M., Hammer, S., Hensel, T., Junghans, A. R., et al. (2018). Felsenkeller 5 MV underground accelerator: towards the holy Grail of nuclear astrophysics ^{12}C(*α*, γ)^{16}O. *EPJ Web Conf.* 178, 01008. doi:10.1051/epjconf/201817801008

Bethe, A., and Critchfield, C. (1938). The Formation of deuterons by proton combination. *Phys. Rev.* 54, 248. doi:10.1103/PhysRev.54.248

Bisterzo, S., Gallino, R., Käppeler, F., Wiescher, M., Imbriani, G., Straniero, O., et al. (2015). The branchings of the main s-process: their sensitivity to α-induced reactions on ^{13}C and ^{22}Ne and to the uncertainties of the nuclear network. *Mon. Not. R. Astron. Soc.* 449, 506–527. doi:10.1093/mnras/stv271

Bisterzo, S., Travaglio, C., Gallino, R., Wiescher, M., and Käppeler, F. (2014). Galactic chemical evolution and solar s-process abundances: dependence on the ^{13}C-pocket structure. *Astrophys. J.* 787, 10. doi:10.1088/0004-637X/787/1/10

Boeltzig, A., Best, A., Imbriani, G., Junker, M., Aliotta, M., Bemmerer, D., et al. (2018). Improved background suppression for radiative capture reactions at LUNA with HPGe and BGO detectors. *J. Phys. G Nucl. Part. Phys.* 45, 025203. doi:10.1088/1361-6471/aaa163

Bonasera, A., and Natowitz, J. B. (2020). Calculation of the ^{12}C+^{12}C sub-barrier fusion cross section in an imaginary-time-dependent mean field theory. *Phys. Rev. C* 102, 061602. doi:10.1103/PhysRevC.102.061602

Bonetti, R., Broggini, C., Campajola, L., Corvisiero, P., D'Alessandro, A., Dessalvi, M., et al. (1999). First measurement of the ^{3}He(^{3}He, 2p)^{4}He cross-section down to the lower edge of the solar Gamow peak. *Phys. Rev. Lett.* 82, 5205–5208. doi:10.1103/PhysRevLett.82.5205

Bravo, E., Piersanti, L., Domínguez, I., Straniero, O., Isern, J., and Escartin, J. A. (2011). Type Ia supernovae and the ^{12}C+^{12}C reaction rate. *Astron. Astrophys.* 535, A114. doi:10.1051/0004-6361/201117814

Broggini, C., Bemmerer, D., Caciolli, A., and Trezzi, D. (2018). LUNA: Status and prospects. *Prog. Part. Nucl. Phys.* 98, 55–84. doi:10.1016/j.ppnp.2017.09.002

Broggini, C., Straniero, O., Taiuti, M., De Angelis, G., Benzoni, G., Bruno, G., et al. (2019). Experimental nuclear astrophysics in Italy. *Rivista del Nuovo Cimento.* 42, 103–152. doi:10.1393/ncr/i2019-10157-1

Brune, C. R., Licot, I., and Kavanagh, R. W. (1993). Low-energy resonances in ^{13}C(α,n). *Phys. Rev. C* 48, 3119–3121. doi:10.1103/PhysRevC.48.3119

Bruno, C. G., Scott, D. A., Formicola, A., Aliotta, M., Davinson, T., Anders, M., et al. (2015). Resonance strengths in the ^{17,18}O(p, α)^{14,15}N reactions and background suppression underground. *Eur. Phys. J. A* 51, 94. doi:10.1140/epja/i2015-15094-y

Burbidge, E. M., Burbidge, G. R., Fowler, W. A., and Hoyle, F. (1957). Synthesis of the elements in stars. *Rev. Mod. Phys.* 29, 547–650. doi:10.1103/RevModPhys.29.547

Caciolli, A., Agostino, L., Bemmerer, D., Bonetti, R., Broggini, C., Confortola, F., et al. (2009). Ultra-sensitive in-beam γ-ray spectroscopy for nuclear astrophysics at LUNA. *Eur. Phys. J. A* 39, 179–186. doi:10.1140/epja/i2008-10706-3

Casella, C., Costantini, H., Lemut, A., Limata, B., Bonetti, R., Broggini, C., et al. (2002). First measurement of the d(p,γ)^{3}He cross section down to the solar Gamow peak. *Nucl. Phys. A* 706, 203–216. doi:10.1016/S0375-9474(02)00749-2

Caughlan, G. R., and Fowler, W. A. (1988). Thermonuclear reaction rates. *Atomic Data Nucl. Data Tables* 40, 283–334. doi:10.1016/0092-640X(88)90009-5

Cavanna, F., and Prati, P. (2018). Direct measurement of nuclear cross-section of astrophysical interest: results and perspectives. *Int. J. Mod. Phys. A* 33, 1843010–1843346. doi:10.1142/S0217751X18430108

Chen, C., Li, Y. J., Zhang, H., and Li, Z. H. (2020). Preparation of large-area isotopic magnesium targets for the ^{25}Mg(p, γ)^{26}Al experiment at JUNA. *Nucl. Sci. Tech.* 31, 91. doi:10.1007/s41365-020-00800-y

Ciani, G. F., Csedreki, L., Balibrea-Correa, J., Best, A., Aliotta, M., Barile, F., et al. (2020). A new approach to monitor ^{13}C-targets degradation *in situ* for ^{13}C(α,n)^{16}O cross-section measurements at LUNA. *Eur. Phys. J. A* 56, 75. doi:10.1140/epja/s10050-020-00077-0

Couch, R. G., Schmiedekamp, A. B., and Arnett, W. D. (1974). S-PROCESS nucleosynthesis in massive stars: core helium burning. *Astrophys. J.* 190, 95–100. doi:10.1086/152851

Cristallo, S., Cognata, M. L., Massimi, C., Best, A., Palmerini, S., Straniero, O., et al. (2018). The importance of the ^{13}C(α, n)^{16}O reaction in asymptotic giant branch stars. *Astrophys. J* 859, 105. doi:10.3847/1538-4357/aac177

Csedreki, L., Ciani, G. F., Best, A., Balibrea-Correa, J., and Gyürky, G. (2019). "The LUNA neutron detector array for the direct measurement of the ^{13}C(α, n)^{16}O nuclear reaction," in *Nuclei in the Cosmos XV*. Editors A. Formicola, M. Junker, L. Gialanella, and G. Imbriani (Cham: Springer International Publishing)), 331–334.

Cyburt, R. H., Amthor, A. M., Ferguson, R., Meisel, Z., Smith, K., Warren, S., et al. (2010). The JINA Reaclib database: its recent updates and impact on type-I X-ray bursts. *Astrophys. J. Suppl.* 189, 240–252. doi:10.1088/0067-0049/189/1/240

deBoer, R., Görres, J., Wiescher, M., Azuma, R., Best, A., Brune, C., et al. (2017). The ^{12}C(*α*, γ)^{16}O reaction and its implications for stellar helium burning. *Rev. Mod. Phys.* 89, 035007. doi:10.1103/RevModPhys.89.035007

Drotleff, H. W., Denker, A., Hammer, J. W., Knee, H., Küchler, S., Streit, D., et al. (1991). New22Ne(α,n)25Mg-resonances at very low energies relevant for the astrophysical s-process. *Z. Physik A - Hadrons and Nuclei*, 338, 367–368. doi:10.1007/BF01288203

Drotleff, H. W., Denker, A., Knee, H., Soine, M., Wolf, G., Hammer, J. W., et al. (1993). Reaction rates of the s-process neutron sources ^{22}Ne(α, n)^{25}Mg and ^{13}C(α, n)^{16}O. *Astrophys. J.* 414, 735. doi:10.1086/173119

Eddington, A. S. (1920). The internal Constitution of the stars. *Sci. Mon.* 11, 297–303.

Faestermann, T., Mohr, P., Hertenberger, R., and Wirth, H. F. (2015). Broad levels in ^{17}O and their relevance for the astrophysical *s* process. *Phys. Rev. C* 92, 052802. doi:10.1103/PhysRevC.92.052802

Febbraro, M., deBoer, R. J., Pain, S. D., Toomey, R., Becchetti, F. D., Boeltzig, A., et al. (2020). New ^{13}C(α,n)^{16}O cross section with implications for neutrino mixing and geoneutrino measurements. *Phys. Rev. Lett.* 125, 062501. doi:10.1103/PhysRevLett.125.062501

Ferraro, F., Takács, M. P., Piatti, D., Mossa, V., Aliotta, M., Bemmerer, D., et al. (2018a). A high-efficiency gas target setup for underground experiments, and redetermination of the branching ratio of the 189.5 kev ^{22}Ne(p, γ)^{23}Na resonance. *Eur. Phys. J. A* 54, 44. doi:10.1140/epja/i2018-12476-7

Ferraro, F., Takács, M. P., Piatti, D., Mossa, V., Cavanna, F., Aliotta, M., et al. (2018b). Direct capture cross section and the Ep= 71 and 105 keV Resonances

in the 22Ne(p,γ)23Na reaction. *Phys. Rev. Lett.*, 121, 172701. doi:10.1103/PhysRevLett.121.172701

Fey, M. (2004). *Im Brennpunkt der Nuklearen Astrophysik: Die Reaktion $^{12}C(\alpha, \gamma)^{16}O$*. Stuttgart: Ph.D. Universität Stuttgart.

Formicola, A., Imbriani, G., Junker, M., Bemmerer, D., Bonetti, R., Broggini, C., et al. (2003). The LUNA II 400 kV accelerator. *Nucl. Instrum. Methods A* 507, 609–616. doi:10.1016/S0168-9002(03)01435-9

Fowler, W. A. (1984). The quest for the origin of the elements. *Science* 226, 922–935. doi:10.1126/science.226.4677.922

Fruet, G., Courtin, S., Heine, M., Jenkins, D. G., Adsley, P., Brown, A., et al. (2020). Advances in the direct study of carbon burning in massive stars. *Phys. Rev. Lett.* 124, 192701. doi:10.1103/PhysRevLett.124.192701

Fujita, K., Yamaguchi, H., Ban, T., Hamamoto, K., Narikiyo, Y., Tao, N., et al. (2015). Direct measurement of the ^{4}He(^{12}C, ^{16}O)γ total cross section near stellar energies. *EPJ Web Conf.* 93, 03005. doi:10.1051/epjconf/20159303005

Gallino, R., Busso, M., Picchio, G., Raiteri, C. M., and Renzini, A. (1988). On the role of low-mass asymptotic giant branch stars in producing a solar system distribution of s-process isotopes. *Astrophys. J. Lett.* 334, L45. doi:10.1086/185309

Garcia-Hernandez, D. A., Garcia-Lario, P., Plez, B., Manchado, A., D'Antona, F., Lub, J., et al. (2007). Lithium and zirconium abundances in massive galactic O-rich AGB stars. *Astron. Astrophys.* 462, 711–730. doi:10.1051/0004-6361:20065785

Garcia-Hernandez, D. A., Garcia-Lario, P., Plez, B., D'Antona, F., Manchado, A., and Trigo-Rodriguez, J. M. (2006). Rubidium-rich asymptotic giant branch stars. *Science* 314, 1751–1754. doi:10.1126/science.1133706

Garcia-Hernandez, D. A., Manchado, A., Lambert, D. L., Plez, B., Garcia-Lario, P., D'Antona, F., et al. (2009). Rb-rich asymptotic giant branch stars in the magellanic clouds. *Astrophys. J* 705, L31–L35. doi:10.1088/0004-637x/705/1/l31

Giesen, U., Browne, C., Görres, J., Graff, S., Iliadis, C., Trautvetter, H. P., et al. (1993). The astrophysical implications of low-energy resonances in ^{22}Ne+α. *Nucl. Phys.* 561, 95–111. doi:10.1016/0375-9474(93)90167-V

Greife, U., Arpesella, C., Barnes, C., Bartolucci, F., Bellotti, E., Broggini, C., et al. (1994). Laboratory for underground nuclear astrophysics (LUNA). *Nucl. Instrum. Methods Phys. Res. Sect. A* 350, 327–337. doi:10.1016/0168-9002(94)91182-7

Guglielmetti, A. (2014). The LUNA experiment at gran Sasso laboratory. *EPJ Web Conf.* 78, 07001. doi:10.1051/epjconf/20147807001

Haas, F. X., and Bair, J. K. (1973). Total neutron yield from the (α,n) reaction on ^{21,22}Ne. *Phys. Rev. C* 7, 2432–2436. doi:10.1103/PhysRevC.7.2432

Harissopulos, S., Becker, H. W., Hammer, J. W., Lagoyannis, A., Rolfs, C., and Strieder, F. (2005). Cross section of the ^{13}C(α,n)^{16}O reaction: a background for the measurement of geo-neutrinos. *Phys. Rev. C* 72, 062801. doi:10.1103/PhysRevC.72.062801

Harms, V., Kratz, K. L., and Wiescher, M. (1991). Properties of ^{22}Ne(α, n)Mg resonances. *Phys. Rev. C* 43, 2849–2861. doi:10.1103/PhysRevC.43.2849

Heil, M., Detwiler, R., Azuma, R. E., Couture, A., Daly, J., Görres, J., et al. (2008). The ^{13}C(α,n) reaction and its role as a neutron source for the s process. *Phys. Rev. C* 78, 025803. doi:10.1103/PhysRevC.78.025803

Hollowell, D., and Iben, J. (1988). Nucleosynthesis of solar system material in a low-mass, low-metallicity asymptotic giant branch star. *Astrophys. J. Lett.* 333, L25. doi:10.1086/185279

Iliadis, C., Longland, R., Champagne, A., Coc, A., and Fitzgerald, R. (2010). Charged-particle thermonuclear reaction rates: ii. tables and graphs of reaction rates and probability density functions. *Nucl. Phys.* 841, 31–250. doi:10.1016/j.nuclphysa.2010.04.009

Iliadis, C. *Nuclear physics of stars. Physics textbook.* (Weinheim: Wiley-VCH), 2 edn. (2015). OCLC.

Jaeger, M., Kunz, R., Mayer, A., Hammer, J. W., Staudt, G., Kratz, K. L., et al. (2001). ^{22}Ne(α, n)^{25}Mg: the key neutron source in massive stars. *Phys. Rev. Lett.* 87, 202501. doi:10.1103/PhysRevLett.87.202501

Jayatissa, H., Rogachev, G., Goldberg, V., Koshchiy, E., Christian, G., Hooker, J., et al. (2020). Constraining the ^{22}Ne(α, γ)^{26}Mg and ^{22}Ne(α, n)^{25}Mg reaction rates using sub-Coulomb α-transfer reactions. *Phys. Lett. B* 802, 135267. doi:10.1016/j.physletb.2020.135267

Jiang, C. L., Santiago-Gonzalez, D., Almaraz-Calderon, S., Rehm, K. E., Back, B. B., Auranen, K., et al. (2018). Reaction rate for carbon burning in massive stars. *Phys. Rev. C* 97, 012801. doi:10.1103/PhysRevC.97.012801

Johnson, E. D., Rogachev, G. V., Mukhamedzhanov, A. M., Baby, L. T., Brown, S., Cluff, W. T., et al. (2006). Astrophysical reaction rate for the neutron-generator reaction ^{13}C(α,n)^{16}O in asymptotic giant branch stars. *Phys. Rev. Lett.* 97, 192701. doi:10.1103/PhysRevLett.97.192701

Käppeler, F., Gallino, R., Bisterzo, S., and Aoki, W. (2011). The *s* process: nuclear physics, stellar models, and observations. *Rev. Mod. Phys.* 83, 157–193. doi:10.1103/RevModPhys.83.157

Käppeler, F. (1999). The origin of the heavy elements: the s process. *Prog. Part. Nucl. Phys.* 43 (43), 419–483.

Keeley, N., Kemper, K., and Khoa, D. T. (2003). DWBA analysis of the ^{13}C(^{6}Li,d)^{17}O reaction at 10 MeV/nucleon and its astrophysical implications. *Nucl. Phys.* 726, 159–172. doi:10.1016/S0375-9474(03)01622-1

Kimura, S., and Bonasera, A. (2013). Gamow peak approximation near strong resonances. *Phys. Rev. C* 87, 058801. doi:10.1103/PhysRevC.87.058801

Kremer, R. M., Barnes, C. A., Chang, K. H., Evans, H. C., Filippone, B. W., Hahn, K. H., et al. (1988). Coincidence measurement of the $^{12}C(\alpha, \gamma)^{16}O$ cross section at low energies. *Phys. Rev. Lett.* 60, 1475–1478. doi:10.1103/PhysRevLett.60.1475

Kubono, S., Abe, K., Kato, S., Teranishi, T., Kurokawa, M., Liu, X., et al. (2003). Determination of the Subthreshold state contribution in ^{13}C(α,n)^{16}O, the main neutron-source reaction for the s process. *Phys. Rev. Lett.* 90, 062501. doi:10.1103/PhysRevLett.90.062501

Kunz, R., Jaeger, M., Mayer, A., Hammer, J. W., Staudt, G., Harissopulos, S., et al. (2001). $^{12}C(\alpha, \gamma)^{16}O$: the key reaction in stellar nucleosynthesis. *Phys. Rev. Lett.* 86, 3244–3247. doi:10.1103/PhysRevLett.86.3244

La Cognata, M., Spitaleri, C., Trippella, O., Kiss, G. G., Rogachev, G. V., Mukhamedzhanov, A. M., et al. (2013). On the measurement of the ^{13}C(α,n)^{16}O *S*-factor at negative energies and its influence on the s-process. *Astrophys. J* 777, 143. doi:10.1088/0004-637X/777/2/143

Lamb, S. A., Howard, W. M., Truran, J. W., and Iben, J. I. (1977). Neutron-capture nucleosynthesis in the helium-burning cores of massive stars. *Astrophys. J.* 217, 213–221. doi:10.1086/155571

Liu, W., Li, Z., He, J., Tang, X., Lian, G., An, Z., et al. (2016). Progress of Jinping underground laboratory for nuclear astrophysics (JUNA). *Science China physics. Mech. Astron.* 59, 642001. doi:10.1007/s11433-016-5785-9

Liu, W. P. (2017). Underground nuclear astrophysics experiment JUNA in China. *J. Phys. Soc. Japan.* 758, 335c. doi:10.7566/JPSCP.14.011101

Longland, R., Iliadis, C., and Karakas, A. I. (2012). Reaction rates for the s-process neutron source ^{22}Ne+α. *Phys. Rev. C* 85, 065809. doi:10.1103/PhysRevC.85.065809

Longland, R., Iliadis, C., Rusev, G., Tonchev, A. P., deBoer, R. J., Görres, J., et al. (2009). Photoexcitation of astrophysically important states in ^{26}Mg. *Phys. Rev. C* 80, 055803. doi:10.1103/PhysRevC.80.055803

Lugaro, M., Herwig, F., Lattanzio, J. C., Gallino, R., and Straniero, O. (2003). s-process nucleosynthesis in asymptotic giant branch stars: a test for stellar evolution. *Astrophys. J* 586, 1305–1319. doi:10.1086/367887

Mak, H. B., Ashery, D., and Barnes, C. (1974). Cross sections of the ^{21}Ne(α, n)^{24}Mg and ^{22}Ne(α, n)^{25}Mg reactions at low energies of astrophysical interest. *Nucl. Phys.* 226, 493–505. doi:10.1016/0375-9474(74)90496-5

Makii, H., Nagai, Y., Shima, T., Segawa, M., Mishima, K., Ueda, H., et al. (2009). E1 and E2 cross sections of the $^{12}C(\alpha, \gamma_0)^{16}O$ reaction using pulsed α beams. *Phys. Rev. C* 80, 065802. doi:10.1103/PhysRevC.80.065802

Massimi, C., Altstadt, S., Andrzejewski, J., Audouin, L., Barbagallo, M., Bécares, V., et al. (2017). Neutron spectroscopy of ^{26}Mg states: constraining the stellar neutron source ^{22}Ne(α, n)^{25}Mg. *Phys. Lett. B* 768, 1–6. doi:10.1016/j.physletb.2017.02.025

Matei, C., Buchmann, L., Hannes, W. R., Hutcheon, D. A., Ruiz, C., Brune, C. R., et al. (2006). Measurement of the cascade transition via the first excited state of ^{16}O in the $^{12}C(\alpha, \gamma)^{16}O$ reaction, and its S factor in stellar helium burning. *Phys. Rev. Lett.* 97, 242503. doi:10.1103/PhysRevLett.97.242503

Morales-Gallegos, L., Aliotta, M., Bruno, C. G., Buompane, R., Davinson, T., De Cesare, M., et al. (2018). Reduction of deuterium content in carbon targets for ^{12}C+^{12}C reaction studies of astrophysical interest. *Eur. Phys. J. A* 54, 132. doi:10.1140/epja/i2018-12564-8

Mossa, V., Stöckel, K., Cavanna, F., Ferraro, F., Aliotta, M., Barile, F., et al. (2020). Setup commissioning for an improved measurement of the D(p,γ)^{3}He cross section at Big Bang Nucleosynthesis energies. *Eur. Phys. J. A* 56, 144. doi:10.1140/epja/s10050-020-00149-1

Mukhamedzhanov, A. M., Pang, D. Y., and Kadyrov, A. S. (2019). Astrophysical factors of $^{12}C+^{12}C$ fusion extracted using the trojan horse method. *Phys. Rev. C* 99, 064618. doi:10.1103/PhysRevC.99.064618

Ota, S., Christian, G., Lotay, G., Catford, W., Bennett, E., Dede, S., et al. (2020). Decay properties of $^{22}Ne+\alpha$ resonances and their impact on s-process nucleosynthesis. *Phys. Lett. B* 802, 135256. doi:10.1016/j.physletb.2020.135256

Peters, J. G. (1968). Nucleosynthesis by the s-PROCESS in stars of 9 and 15 solar masses. *Astrophys. J.* 154, 225. doi:10.1086/149753

Pignatari, M., Gallino, R., Heil, M., Wiescher, M., Käppeler, F., Herwig, F., et al. (2010). The weak *s*-process in massive stars and its dependence on the neutron capture cross sections. *Astrophys. J* 710, 1557–1577. doi:10.1088/0004-637x/710/2/1557

Plag, R., Reifarth, R., Heil, M., Käppeler, F., Rupp, G., Voss, F., et al. (2012). $^{12}C(\alpha, \gamma)^{16}O$ studied with the Karlsruhe 4π BaF_2 detector. *Phys. Rev. C* 86, 015805. doi:10.1103/PhysRevC.86.015805

Prantzos, N., Hashimoto, M., and Nomoto, K. (1990). The s-process in massive stars: yields as a function of stellar mass and metallicity. *Astron. Astrophys.* 234, 211.

Prati, P. (2019). "Nuclei in the Cosmos XV", in *Nuclear reaction of astrophysical interest with LUNA projects*. Editors A. Formicola, M. Junker, L. Gialanella, and G. Imbriani (Cham: Springer), 247–252.

Raiteri, C. M., Busso, M., Gallino, R., Picchio, G., and Pulone, L. (1991a). S-process nucleosynthesis in massive stars and the weak component. I. Evolution and neutron captures in a 25 M_{sun} star. *Astrophys. J.* 367, 228. doi:10.1086/169622

Raiteri, C. M., Busso, M., Gallino, R., and Picchio, G. (1991b). S-process nucleosynthesis in massive stars and the weak component. II. Carbon burning and galactic Enrichment. *Astrophys. J.* 371, 665. doi:10.1086/169932

Rauscher, T., and Thielemann, F. K. (2000). Astrophysical reaction rates from statistical model calculations. *Atom. Data Nucl. Data Tables* 75, 1–351. doi:10.1006/adnd.2000.0834

Robertson, D., Couder, M., Greife, U., Strieder, F., and Wiescher, M. (2016). Underground nuclear astrophysics studies with CASPAR. *EPJ Web Conf.* 109, 09002. doi:10.1051/epjconf/201610909002

Rolfs, C., and Rodney, W. (1988). *Cauldrons in the Cosmos*. Chicago: The University of Chicago Press.

Schürmann, D., Di Leva, A., Gialanella, L., Kunz, R., Strieder, F., De Cesare, N., et al. (2011). Study of the 6.05 MeV cascade transition in $^{12}C(\alpha, \gamma)^{16}O$. *Phys. Lett. B* 703, 557–561. doi:10.1016/j.physletb.2011.08.061

Schürmann, D., Di Leva, A., Gialanella, L., Rogalla, D., Strieder, F., De Cesare, N., et al. (2005). First direct measurement of the total cross-section of $^{12}C(\alpha, \gamma)^{16}O$. *Eur. Phys. J. A* 26, 301–305. doi:10.1140/epja/i2005-10175-2

Sen, A., Domínguez-Cañizares, G., Podaru, N., Mous, D., Junker, M., and Imbriani, G. (2019). A high intensity, high stability 3.5 MV Singletron^{TM} accelerator. *Nucl. Instrum. Methods Phys. Res. B* 460, 390–395. doi:10.1016/j.nimb.2018.09.016

Spillane, T., Raiola, F., Rolfs, C., Schürmann, D., Strieder, F., Zeng, S., et al. (2007). $^{12}C+^{12}C$ fusion reactions near the Gamow energy. *Phys. Rev. Lett.* 98, 122501. doi:10.1103/PhysRevLett.98.122501

Talwar, R., Adachi, T., Berg, G. P. A., Bin, L., Bisterzo, S., Couder, M., et al. (2016). Probing astrophysically important states in the ^{26}Mg nucleus to study neutron sources for the *s* process. *Phys. Rev. C* 93, 055803. doi:10.1103/PhysRevC.93.055803

Tan, W. P., Boeltzig, A., Dulal, C., deBoer, R. J., Frentz, B., Henderson, S., et al. (2020). New measurement of $^{12}C+^{12}C$ fusion reaction at astrophysical energies. *Phys. Rev. Lett.* 124, 192702. doi:10.1103/PhysRevLett.124.192702

Trippella, O., and Cognata, M. La. (2017). Concurrent application of ANC and THM to assess the $^{13}C(\alpha,n)^{16}O$ absolute cross section at astrophysical energies and possible consequences for neutron production in low-mass AGB stars. *Astrophys. J.* 837, 41. doi:10.3847/1538-4357/aa5eb5

Tumino, A., Spitaleri, C., La Cognata, M., Cherubini, S., Guardo, G. L., Gulino, M., et al. (2018a). An increase in the $^{12}C+^{12}C$ fusion rate from resonances at astrophysical energies. *Nature* 557, 687–690. doi:10.1038/s41586-018-0149-4

Tumino, A., Spitaleri, C., Cherubini, S., D´Agata, G., Luca, G., Gulino, M., et al. (2018b). The trojan horse method in nuclear astrophysics. *EPJ Web Conf.* 184, 01016. doi:10.1051/epjconf/201818401016

Tutusaus, I., Lamine, B., and Blanchard, A. (2019). Model-independent cosmic acceleration and redshift-dependent intrinsic luminosity in type-Ia supernovae. *Astron. Astrophys.* 625, A15. doi:10.1051/0004-6361/201833032

van Raai, M. A., Lugaro, M., Karakas, A. I., García-Hernández, D. A., and Yong, D. (2012). Rubidium, zirconium, and lithium production in intermediate-mass asymptotic giant branch stars. *Astron. Astrophys.* 540, A44. doi:10.1051/0004-6361/201117896

von Weizsäcker, C. F. (1938). Über Elementumwandlungen im Innern der Sterne, ii. *Phys. Z.* 39, 633–646.

Wolfgang Hammer, J., Bulski, G., Grum, W., Kratschmer, W., Postner, H., and Schleussner, G. (1986). Scorpion, the Stuttgart scattering facility for fast polarized neutrons. *Nucl. Instrum. Methods Phys. Res. Sect. A.* 244, 455–476. doi:10.1016/0168-9002(86)91069-7

Wolke, K., Becker, H. W., Rolfs, C., Schröder, U., Trautvetter, H. P., Harms, V., et al. (1989). Helium burning of ^{22}Ne. *Zeitschrift für Physik A Hadrons Nucl.* 334, 491–510. doi:10.1007/BF01294757

Zhang, N., Wang, X., Tudor, D., Bucher, B., Burducea, I., Chen, H., et al. (2020). Constraining the $^{12}C+^{12}C$ astrophysical S-factors with the $^{12}C+^{13}C$ measurements at very low energies. *Phys. Lett. B* 801, 135170. doi:10.1016/j.physletb.2019.135170

Zickefoose, J., Di Leva, A., Strieder, F., Gialanella, L., Imbriani, G., De Cesare, N., et al. (2018). Measurement of the $^{12}C(^{12}C, p)^{23}Na$ cross section near the Gamow energy. *Phys. Rev. C* 97, 065806. doi:10.1103/PhysRevC.97.065806

Conflict of Interest: The authors declare that the research was conducted in the absence of any commercial or financial relationships that could be construed as a potential conflict of interest.

frontiers in Astronomy and Space Sciences

REVIEW
published: 09 March 2021
doi: 10.3389/fspas.2021.616201

Light Elements in the Universe

Sofia Randich and Laura Magrini*

INAF Osservatorio Astrofisico di Arcetri, Firenze, Italy

Due to their production sites, as well as to how they are processed and destroyed in stars, the light elements are excellent tools to investigate a number of crucial issues in modern astrophysics: from stellar structure and non-standard processes at work in stellar interiors to age dating of stars; from pre-main sequence evolution to the star formation histories of young clusters and associations and to multiple populations in globular clusters; from Big Bang nucleosynthesis to the formation and chemical enrichment history of the Milky Way Galaxy and its populations, just to cite some relevant examples. In this paper, we focus on lithium, beryllium, and boron (LiBeB) and on carbon, nitrogen, and oxygen (CNO). LiBeB are rare elements, with negligible abundances with respect to hydrogen; on the contrary, CNO are among the most abundant elements in the Universe, after H and He. Pioneering observations of light-element surface abundances in stars started almost 70 years ago and huge progress has been achieved since then. Indeed, for different reasons, precise measurements of LiBeB and CNO are difficult, even in our Sun; however, the advent of state-of-the-art ground- and space-based instrumentation has allowed the determination of high-quality abundances in stars of different type, belonging to different Galactic populations, from metal-poor halo stars to young stars in the solar vicinity and from massive stars to cool dwarfs and giants. Noticeably, the recent large spectroscopic surveys performed with multifiber spectrographs have yielded detailed and homogeneous information on the abundances of Li and CNO for statistically significant samples of stars; this has allowed us to obtain new results and insights and, at the same time, raise new questions and challenges. A complete understanding of the light-element patterns and evolution in the Universe has not been still achieved. Perspectives for further progress will open up soon thanks to the new generation instrumentation that is under development and will come online in the coming years.

Keywords: stars, galaxy, stellar populations, abundances, nucleosynthesis, spectroscopy, stars abundances

OPEN ACCESS

Edited by:
Livio Lamia,
University of Catania, Italy

Reviewed by:
Sara Palmerini,
University of Perugia, Italy
Aldo Serenelli,
Institute of Space Sciences (ICE), Spain

****Correspondence:***
Sofia Randich
sofia.randich@inaf.it

Specialty section:
This article was submitted to Nuclear Physics, a section of the journal Frontiers in Astronomy and Space Sciences

Received: *11 October 2020*
Accepted: *12 January 2021*
Published: *09 March 2021*

Citation:
Randich S and Magrini L (2021) Light Elements in the Universe. Front. Astron. Space Sci. 8:616201. doi: 10.3389/fspas.2021.616201

1 INTRODUCTION

The most abundant isotope of lithium, ^{7}Li[1], is the heaviest element created during Big Bang nucleosynthesis (BBN) and its primordial abundance can be used to probe the standard model of cosmology (e.g., Wagoner, 1973, Steigman, 2006, and references therein). Also, Li abundance in the interstellar medium (ISM) increases by a factor larger than 10 during the evolution of the Galaxy, as originally pointed out by Rebolo et al. (1988); this suggests one or more sites of fresh Li production.

^{6}Li, ^{9}Be, ^{10}B, and ^{11}B are instead not produced in significant quantities neither during BBN nor in stars. They are created by the interaction of energetic Galactic cosmic rays (GCRs) with the

[1]Unless differently indicated, hereafter we will refer to Li, without indicating the isotope.

interstellar medium (Reeves et al., 1970; Meneguzzi et al., 1971) that can happen in two different channels, namely, a direct process in which protons and α-particles in GCRs collide with CNO nuclei in the ISM or an inverse process where CNO nuclei instead collide with protons and α-particle in the ISM. Observations and in particular the trends between the abundance and metallicity allow discriminating between the two channels. In the first case, Be and B should behave as secondary elements and their abundances in metal-poor stars should show a linear correlation with the metal content ([Fe/H] or [O/H]) and a slope around two; in the second case, Be and B should behave instead as primary elements and the slope should be around one. Given its origin and due to the fact that during the early stages of Galactic evolution (<0.5–1 Gyr) GCRs were generated and transported on a Galactic scale, the Be production site was widespread; to a first approximation, the Be abundance should thus have one value at a given time over the whole Galaxy (Beers et al., 2000; Suzuki and Yoshii, 2001) and it can be used as an ideal cosmic clock to investigate the formation histories of the different Galactic populations (Pasquini et al., 2004; Pasquini et al., 2005; Smiljanic et al., 2009b).

Lithium, beryllium, and boron are also unique because they are fragile elements and they are destroyed in stellar interiors by fusion reactions at progressively higher temperatures of 2.5–3, 3.5, and 5×10^6 K, respectively. It is worth mentioning the contribution of electron capture on ^{7}Be, which is an important channel for ^{7}Be destruction but also produces ^{7}Li according to physical conditions and how they affect the ^{7}Be lifetime (Simonucci et al., 2013). This is relevant also in the context of the Galactic evolution of Li.

Being so fragile, these elements are depleted from stellar atmospheres whenever a mechanism is present that is able to transport material down to the stellar region where the temperature is high enough for Li/Be/B burning to occur. LiBeB are hence excellent tracers of stellar physics and, in particular, of mixing processes, both the standard ones (i.e., convection) and the non standard ones, in stars in different evolutionary phases, from the pre- to the post-main sequence (MS) phases (e.g., Pinsonneault, 1997; Eggleton et al., 2006; Randich, 2006; Busso et al., 2007; Denissenkov et al., 2009; Lattanzio et al., 2015; Charbonnel et al., 2020; and references therein). Also, given the different destruction temperatures, simultaneous measurements of the abundances of the three elements allow us to reconstruct a "tomography" of stellar interiors and to understand how deep the mixing has extended.

After the MS, during the first dredge-up (FDU) event, due to dilution, surface Li abundances are expected to decrease by a factor from 30 to 60, depending on the initial stellar mass and metallicity (Iben, 1967) and Li abundances of stars on the red giant branch should be A(Li) < 1.5 dex[2] (e.g., Brown et al., 1989; Mallik et al., 2003; Gonzalez et al., 2009). Classical models do not predict any further decreasing trend of Li abundance in the subsequent evolutionary phases; on the contrary, the abundance of Li is observed to decrease again after the luminosity bump on the red giant branch (RGB; e.g., Charbonnel et al., 1998; Gratton et al., 2000; Lind et al., 2009b). The further decrease in Li has been ascribed to several non standard processes, including the presence of thermohaline (double diffusive) instability (e.g., Eggleton et al., 2006, Eggleton et al., 2008; Charbonnel and Zahn, 2007; Sengupta and Garaud, 2018), thermohaline and gravitational mixing (e.g., Stancliffe and Glebbeek, 2008; Angelou et al., 2011; Henkel et al., 2018), magnetic buoyancy in a dynamo process (e.g., Busso et al., 2007; Cristallo et al., 2008; Nordhaus et al., 2008; Denissenkov et al., 2009; Cristallo and Vescovi, 2020), and rotation (e.g., Denissenkov and Tout, 2000; Denissenkov and VandenBerg, 2003; Denissenkov and Herwig, 2004).

In addition to several processes that destroy it, lithium can be created via the so-called Cameron-Fowler mechanism (Cameron and Fowler, 1971), in both low-mass and more massive stars which may represent sources of Li enrichment in the Galaxy (see, e.g., Sackmann and Boothroyd, 1999; Charbonnel and Balachandran, 2000; Negueruela et al., 2020).

Finally, it is now well known and expected based on theoretical arguments that Li depletion in stars depends on both age and mass; in particular, Li is since long considered as an excellent and independent age tracer for both young low-mass stars and older solar-type stars, although, as we will discuss in the following, the Li-age relationship is complex and depends on other parameters. Thanks to this, lithium has been extensively used to identify and characterize young stellar populations, to study ages and age dispersion (hence star formation histories) in star-forming regions (e.g., Tagliaferri et al., 1994; Palla et al., 2005; Sacco et al., 2007; Jeffries et al., 2017; and references therein), to derive cluster ages through the lithium depletion boundary method (LDB, Stauffer, 2000) and to age date stars hosting exoplanets.

Carbon, nitrogen, and oxygen are among the most abundant elements in the Universe (Asplund et al., 2009). They are crucial for several astrophysical fields, including, e.g., the formation of planetary systems and astrobiology (e.g., Lodders and Fegley, 2002; Suárez-Andrés et al., 2016), stellar structure and evolution (e.g., Salaris and Cassisi, 2005; Busso et al., 2007; Charbonnel and Zahn, 2007; Lattanzio et al., 2015; Lagarde et al., 2019), stellar nucleosynthesis (e.g., van den Hoek and Groenewegen, 1997; Meynet and Maeder, 2002), and Galactic chemical evolution (e.g., Chiappini et al., 2003; Vincenzo et al., 2016). However, their origins are still debated and the role in their production in stars with different masses, metallicities, and rotational velocities is still not definitively settled. In addition, they have shown a great potential to investigate stellar evolution, since they can probe the internal structure through the mixing processes in the giant phase, in which the material processed in the interior to the stellar photospheres is dredged up, modifying C and N abundances. Last by not least, C and N abundances in evolved stars are now commonly used to estimate the ages of stars, in a complementary way to other methods, such as isochrone fitting, asteroseismology, or gyrochronology (see, e.g., Salaris et al., 2015; Martig et al., 2016; Masseron et al., 2017; Casali et al., 2019; Hasselquist et al., 2019).

For the reasons briefly summarized above, in spite of the observational difficulties, LiBeB and CNO are among the most

[2]A(Li) = log N(Li)/N(H)+12

studied elements of the periodic table. Huge progress has been achieved in the last few years and it is indeed impossible to summarize in this review the state of the art in all fields. We have selected a number of key topics, while we remind to the recent literature for several issues that we will not cover. The latter include the multiple populations of globular clusters (e.g., Gratton et al., 2004, Gratton et al., 2012; Renzini 2008; D'Orazi et al., 2015; Milone et al., 2017; D'Antona et al., 2019; Milone et al., 2020a, Milone et al., 2020b); the abundances of C, N, and O from emission-line spectra of H II regions and planetary nebulae (e.g., Toribio San Cipriano et al., 2016; Toribio San Cipriano et al., 2017; Esteban et al., 2018, Esteban et al., 2019, Esteban et al., 2020; Stanghellini and Haywood, 2018); post-main sequence Li evolution (e.g., Charbonnel et al., 2020; Deepak and Reddy, 2020; Kumar and Reddy, 2020; and references therein), Li-rich giant stars and their nature (e.g., Casey et al., 2016, Casey et al., 2019; Gao et al., 2019; Gonçalves et al., 2020; Jorissen et al., 2020; Martell et al., 2020; Sanna et al., 2020; Wheeler et al., 2020; Yan et al., 2020); boron abundances in massive stars (e.g., Proffitt et al., 2016, and references therein); light elements in the context of exoplanet hosting stars (e.g., Delgado Mena et al., 2012; Delgado Mena et al., 2014); the lithium depletion boundary (see, e.g., Stauffer, 2000; Lodieu, 2020; Martín et al., 2020; an references therein); ^{6}Li/^{7}Li isotopic ratio and its implications for Li nucleosynthesis (e.g., González Hernández et al., 2019, and references therein).

2 OBSERVATIONAL CHALLENGES

Due to the low abundances of LiBeB in stellar atmospheres, they are primarily observed in their respective resonance lines. Furthermore, due to its low ionization potential (5.39 eV), a large fraction of Li in stars is ionized. Since the resonance line of Li II is located in the extreme UV and is not observable, one should rely on the resonance line of neutral Li, a doublet at 670.774 and 670.789 nm. The strength of the doublet depends strongly on the star temperature and, of course, abundance. The Li feature is strong in cool stars with high Li content, while it may be extremely weak in warm stars that have suffered large amounts of depletion; to give an idea, the Li line equivalent width may reach 1 Å or so in cool pre-main sequence (PMS) stars and be as weak as just 2 mÅ in our Sun. Also, the Li doublet is separated by 0.4 Å only from a Fe I line, and it is blended with it when the spectral resolution is not high enough or the star is a rapid rotator. Hence, precise measurements of the equivalent width may need high-spectral resolution and high signal-to-noise ratio (S/N), to resolve and measure such tiny lines. We mention in passing that a subordinated Li I line exists at 610.3 nm which is detectable and measurable for high Li abundances only (Gratton and D'Antona, 1989).

Beryllium and boron observations are considerably more difficult, since their resonance lines are located at 313.042 and 313.106 nm, close to the atmospheric cut-off (Be II), and at 249.68 and 249.77 nm, observable only from space (B I). For this reason, Li, with its main resonant doublet falling in the optical, is the most studied among the three elements, while fewer observations have been obtained for Be and B.

The lines described above are used to measure LiBeB abundances in cool stars, both unevolved and evolved ones. In particular, we mention that Li is fully ionized in stars warmer than about 8500 K; hence the Li I lines can be observed and measured only in stars later than the A2–A3 spectral type (e.g., Takeda et al., 2012, and references therein). With a few exceptions, Be II are normally used for stars later than the F spectral type; due to the severe blending and to the fact that the blending lines may become dominant, Be measurements are difficult (if not impossible) in stars cooler than about 4700 K (Smiljanic et al., 2011; Takeda and Tajitsu, 2014). Of the three light elements, B is the only one that can be observed in hot stars. For these stars, other transitions have indeed been employed in the literature; in particular, the 136.2 nm B II and 206.6 nm B III line have allowed the determination of B in B- and A-type stars (see, e.g., Cunha, 2010; Kaufer, 2010).

As for the analysis and abundance determination, issues are present for all the three elements. Li can be determined by using equivalent widths or spectral synthesis; as mentioned, the Li line may be blended with the close-by Fe line, whose contribution hence should be taken into account. In very cool stars (below ~4000 K), the spectral region becomes full of molecular bands and appropriate analysis should be performed, considering pseudoequivalent widths and corresponding curves of growth (e.g., Palla et al., 2007). Also, correct determination of Li abundances would need nonlocal thermodynamical equilibrium (non-LTE) and 3D effects to be taken into account, as these are important in certain regions of the parameter space (see, e.g., Lind et al., 2009a; Harutyunyan et al., 2018; and references therein).

Both Be II and B I features are in even more crowded spectral regions than Li; deriving the abundances requires the use of spectrum synthesis methods, good knowledge of the atomic and molecular line lists, and correct treatment of the UV opacity; these represent key factors even when determining the Be abundance of the Sun (e.g., Balachandran and Bell, 1998). Like lithium, boron is affected by NLTE effects (Kiselman and Carlsson, 1996) which may significantly impact the inferred abundances and results, while NLTE effects are not important (or cancel each other) for Be (Garcia Lopez et al., 1995). We refer to Garcia Lopez et al. (1995), Primas et al. (1997), Boesgaard et al. (2005), and Takeda et al. (2011) for a more detailed discussion of Be and B abundance determination.

C abundances are determined using lines of different origin, namely, permitted lines of C I, forbidden lines [C I], and molecular lines of C_2, CH, and CO. Although there are many [C I] lines in the solar spectrum, the ideal lines for abundance measurements should be weak and unblended, with accurate atomic data and transition probabilities, possibly formed in LTE. There are several lines with such characteristics, including lines in the optical range at 477.5, 505.2, and 538.0 nm and several lines in the near-infrared. Among the forbidden lines, the [C I] 872.7 nm line has been successfully used to measure C abundance since it is weak and it forms in LTE conditions. The C_2 Swan bands offer numerous weak lines, which are useful for the computation of C abundance. The CH radical contributes to the spectrum through three electronic transitions, which produce three bands in the

blue and violet spectral ranges (at ~420 nm, at ~390 nm, and at ~314 nm). The commonly used lines in the optical range are the CH G-bandhead at 431 nm and the C_2 bandhead at 563.5 nm. Finally, the CO lines provide the combined abundance of carbon and oxygen, and they can be used to measure C once the oxygen abundance is measured, e.g., from its [O I] lines, or vice versa.

Most N I lines are blended with weak CN lines, whose contribution can be estimated from other stronger CN lines in the spectra. In giant stars, several CN lines, weak and unblended, allow us to extract the N abundance, given an independent determination of the C abundance, e.g., from atomic lines or from C_2 molecular bands. The CN lines provide the best way to obtain the N abundance, since the N I lines are too weak and located in the ultraviolet regions. The strongest CN lines are located in the near-UV (388.3 nm). In addition, the NH lines, whose strongest NH bandhead is located in the near-UV, would allow us to obtain a direct measurement of nitrogen (Pasquini et al., 2008), but they produce discrepant values with respect to N from CN (see, e.g., Spite et al., 2005).

The [O I] lines at 557.7 nm (blended with a C_2 doublet and thus less useful to compute O abundance), 630.0, and 636.3 nm are crucial to determine stellar oxygen abundances. Recently, also oxygen recombination lines have been used to measure its abundances, such as O I triplet at 777.1 nm, strongly affected by NLTE (Caffau et al., 2008), and the weak line at 615.8 nm (e.g., Bertran de Lis et al., 2015). Also, the OH lines in the near-UV, at ~330 nm, and in the near-infrared H band and the CO lines, more widely distributed in the spectral range, can be used. The latter, as already said, needs a previous measurement of C abundance to be used to infer O abundance.

The use of molecular bands to measure CNO abundances has been experimented also with *ad hoc* photometric filters to measure CH, NH, CN, and OH. Such observations have been used to reveal multiple stellar populations in globular clusters (Piotto et al., 2015) and they are at the basis of the chromosome map (see Milone et al., 2017). In addition, a molecular band of CH and CN in the optical and near-infrared ranges allows us to derive the isotopic composition, in particular, $^{12}C/^{13}C$ (see, e.g., Smith et al., 2002; Tautvaišienė et al., 2015; Drazdauskas et al., 2016). C, N, and O measurements from molecular bands are usually more viable in the spectra of giants, both because their surface abundance is enriched in C and N and because their lower temperature makes the molecular bands dominant. Recent updates in the use of molecular bands are summarized in Barbuy et al. (2018).

3 HISTORICAL OVERVIEW

3.1 Lithium

The first measurement of Li in the Sun was obtained by Greenstein and Richardson (1951) who already discovered back at that time that our star has a factor of ~100 lower abundance than what measured in the Earth and meteorites (which are representatives of the material from which the Sun has formed), implying depletion from the stellar surface. To our knowledge, the first quantitative measurement of Li in relatively large samples of stars started in the early sixties by Bonsack and collaborators (Bonsack, 1959; Bonsack and Greenstein, 1960); they found that young T Tauri stars are characterized by very high lithium abundances and that *it seems, then, that basically the stars cooler than the Sun destroy lithium and that the efficiency of destruction is highly variable but increases with decreasing temperature.* Since then, some 2000 papers have appeared in the literature reporting observations of Li in all types of stars and environments (from young T Tauri stars to evolved giants; from field stars to open and globular cluster members; from the thin disc of our Galaxy to its halo) and allowing a broad number of issues to be addressed and solved, as well as opening numerous new questions, some of which remain unanswered. The interest in lithium observations has indeed not decreased during the years and the major current spectroscopic surveys are yielding new results, as we will discuss in the following sections. We list below, necessarily in a schematic way and with a personal perspective, the main findings and open questions arisen since the early studies.

3.1.1 Li Depletion in Stars, Stellar Physics, and Mixing Mechanisms

According to the standard theory of stellar evolution, which does not consider the effects of processes such as rotation, magnetic fields, chromospheric activity and starspots, diffusion, mass loss, and mass accretion, surface Li depletion starts during the PMS phases when stars are fully convective or the surface convection zone (SCZ) is very extended. The amount of depletion during the PMS should depend on mass, age, and metallicity, as well as on a number of critical parameters in standard models, like, e.g., convection efficiency (see, e.g., Pinsonneault, 1997; Jeffries, 2006). Stars more massive than the Sun are predicted to deplete little (if any) lithium during the PMS, since the radiative core develops (much) earlier than Li burning is complete and the temperature at the base of the convective envelope becomes too low (see Figure 1 in Jeffries, 2006). No further Li depletion is expected during the MS phases for these objects. Stars with masses similar to the Sun are instead expected to deplete Li in the PMS phases, but depletion should stop around 15 Myr, when about only 40% of the initial Li content is retained. Lower-mass stars remain in the PMS phase longer and reach a higher temperature (and density) at the base of their deeper SCZ, so they are predicted to deplete larger amounts of Li in the PMS phases. Finally, fully convective stars (masses below 0.4 $M_\odot$) start depleting Li very early during the PMS evolution and, depending on their mass, deplete it very quickly (the lower the mass is, the slower Li depletion occurs). The SCZs of solar-type stars become shallower during the MS, so no further Li destruction is expected to occur, while later-type stars, whose SCZs remain deep with hot enough bases, continue depleting lithium also on the MS. As mentioned, the standard theory also predicts that Li depletion should depend on metallicity, since at fixed mass, more metal-rich stars have deeper SCZs, due to the increased opacity (e.g., Deliyannis et al., 1990).

These predictions of standard models are supported by observations in very general and statistical terms: young, PMS stars are significantly more Li rich than older stars of a similar

type; within the same cluster, Li abundance declines with decreasing effective temperature (i.e., mass); metal-poor old halo stars have very likely undergone much less Li depletion (if any) than their metal-rich counterparts. However, thanks to the overwhelming amount of Li measurements that have been obtained during the last decades, it is now well established that Li is not only a function of age, mass, and metallicity and its behavior is considerably more complex than initially thought.

First, observations of open clusters with ages around 30–40 Myr, whose solar mass stars have just arrived on the Zero Age Main Sequence (ZAMS), indicate that these stars still maintain their initial Li content, suggesting that the Sun and similar stars have depleted all their lithium during the MS life, rather than during the PMS (e.g., Randich et al., 2001; Jeffries et al., 2009). Second, a comparison of star clusters of different ages indeed shows that solar-type stars deplete Li during the MS, at variance with standard model predictions, but confirming the original finding of Zappala (1972). Third, and equally unexpectedly, substantial Li depletion has been observed in warm MS stars with very thin convective envelopes; more specifically, stars in a narrow temperature range around 6500 K show an abrupt decline in Li with respect to both warmer and cooler counterparts (the so-called Li dip, see, e.g., Boesgaard and Tripicco, 1986; Balachandran, 1990). Fourth, otherwise similar stars with the same temperature in the same cluster may show a large dispersion in Li abundances (a factor of 10 or more); this has been seen both among cool members of young and very young clusters, like the 100 Myr old Pleiades (e.g., Soderblom et al., 1993; Randich et al., 2001), and among solar-type stars in much older clusters (Pasquini et al., 1997; Pace et al., 2012). The Li scatter among young cluster members seems to be linked to the stellar rotation, since rapid rotators generally show higher lithium abundances than stars with lower rotational velocities. Finally, the metallicity dependence is not yet observationally well established and contrasting results have been proposed.

All these observational pieces of evidence indicate that Li depletion is driven by other processes, besides convection, and that non standard physics cannot be neglected in stellar models, since it very likely results in enhanced or inhibited Li depletion, depending on the stellar mass and evolutionary stage. In fact, in parallel with the increasing volume of available Li abundances, a broad variety of models of different complexity and including one or more non standard processes have been proposed. These include mass accretion in the PMS phases, enhanced radii due to magnetic fields and/or starspots, mass loss, atomic diffusion, internal gravity waves, rotation, and angular momentum transport induced mixing, star-planet interaction, and, possibly, a combination of them (see, e.g., Swenson and Faulkner, 1992; Charbonnel and Talon, 2008; Charbonnel and Lagarde, 2010; Baraffe and Chabrier, 2010; Somers and Pinsonneault, 2014; Somers, 2016; Amard et al., 2019; Deal et al., 2020; Dumont et al., 2020; and references therein). As a matter of fact, as of today, a consensus on the main mechanisms driving or inhibiting Li depletion on the PMS and MS phases has not yet been reached.

Since, for a fixed mass, Li depletion increases with time in both the PMS and MS phases, Li is in principle an excellent age indicator (see Soderblom et al., 2014); indeed, timescales for the depletion can be derived and Li measurements have been used to age date stars and to identify age dispersions within young clusters (e.g., Sestito and Randich, 2005; Palla et al., 2005, to cite a few early studies). However, given the uncertainties mentioned above, the observed scatter in Li for stars of the same age, and the effect of non standard mixing processes, the use of Li to derive precise individual stellar ages is not straightforward.

3.1.2 Primordial Lithium

As mentioned, ^{7}Li is the heaviest element produced in significant amounts during BBN. ^{7}Li production is a sensitive function of the baryon-to-photon ratio, it can be estimated in the framework of standard BBN (SBBN), and it can be compared with Li measurements in old stars that have formed during the very early phases of the Galaxy evolution. In a seminal paper, Spite and Spite (1982) found a remarkably constant (irrespective of the temperature and metallicity) Li abundance—the then so-called Spite *plateau*—in a small sample of warm halo stars. Under the assumption that these stars had not suffered any depletion and that no Galactic enrichment had yet taken place, they interpreted the *plateau* value, A(Li) = 2.05 ± 0.15, as the primordial Li abundance. Also, given the factor of ~10 difference between that value and Li abundance measured in young T Tauri stars, they suggested that one or more sources had contributed to the enrichment of Li during the Galaxy lifetime. Indeed, a great fraction of subsequent observational and theoretical studies were stimulated by Figures 5 and 6 in Spite and Spite (1982). The existence of a *plateau* was confirmed by several following studies (e.g., Pinsonneault et al., 1992, Pinsonneault et al., 1999; Ryan et al., 1999; Meléndez and Ramírez, 2004; Bonifacio et al., 2007, to cite a few) based on a much larger number of stars and more accurate, modern analysis. While the reported *plateau* value is not identical in the different studies, the highest estimate is not larger than A(Li) = 2.4, with a more typical value around A(Li) = 2.2 (e.g., Spite et al., 2012). During the years, there have also been claims that stars belonging to the *plateau* were actually characterized by both a dispersion and trends with effective temperature and [Fe/H]. In particular, at very low metallicities ([Fe/H] < −2.7), abundances show a large scatter that gets larger towards decreasing metallicity (the meltdown, Sbordone et al., 2010). While the reasons for this "meltdown" were not understood, it suggested that some Spite *plateau* stars may have depleted their initial lithium. The true challenge, however, occurred with the measurement of the cosmic microwave background (CMB) provided by WMAP and Planck satellites, according to which the expected primordial abundance is A(Li) = 2.7, a factor of about three to four higher than the abundances of the Spite *plateau* (see, e.g., Cyburt et al., 2016; Mathews et al., 2020; and references therein). In other words, the stellar Li measurements are inconsistent with the CMB (and deuterium observations), and the discrepancy is larger than 5σ. This is referred to as the cosmological Li problem. The obvious question is whether the disagreement is due to uncertainties in stellar physics, or rather due to new, non standard physics that modifies SBBN. On the cosmological side, different explanations have been proposed (see, e.g.,

Mathews et al., 2020); at the same time, numerous studies have instead invoked non standard mixing mechanisms that would cause Li depletion in halo stars (e.g., Tognelli et al., 2020, and references therein).

3.1.3 Galactic Evolution of Lithium

As noted above, a Galactic source is required to account for the increase from the initial value, being the Spite *plateau* or the SBBN value, to that measured in young, metal-rich populations and in the material from which the Sun formed. An established channel is the spallation of atoms in the interstellar medium by energetic cosmic rays (like for ^{6}Li, Be, and B); however, spallation processes integrated along the Galactic life can account for only about 10% of the required amount of ^{7}Li. Based on theoretical investigations, many additional possible contributors to the Li enrichment have been suggested, such as Asymptotic Giant Branch (AGB) stars, red giants, supernovae, novae, and, recently, active stars (e.g., Cameron and Fowler, 1971; D'Antona and Matteucci, 1991; Travaglio et al., 2001; Romano et al., 2001; Cescutti and Molaro, 2019; Kelly et al., 2020). So far no firm conclusions have been reached on the site(s) of Li production and this is called the Galactic Li problem. Since different sources have different evolutionary time scales, like for the other elements, the empirical determination of the distribution of Li vs. metallicity and rate of Li increase provides a tool to assess the relative contributions of the sites of enrichment. We note that, since Li is destroyed in stars, at each metallicity, a large dispersion in abundance is seen; it is hence common to assume that the upper envelope of the distribution of Li abundances as a function of [Fe/H], which should be representative of the pristine Li in the ISM, traces the abundance evolution.

In order to put tight constraints on models and sources of Li production, statistically robust and homogeneous data sets are needed, well covering a large metallicity range and different populations. Up to a few years ago, not many observational studies were available, mostly based on small or inhomogeneous samples of few hundreds of stars (Lambert and Reddy, 2004; Ramírez et al., 2012; Delgado Mena et al., 2015). As we will discuss in **Section 4.4.1**, things changed with the advent of large spectroscopic programs.

We conclude this section by noting that the three topics discussed above are tightly linked; a complete understanding of mixing mechanisms and Li depletion in stars of different mass and metallicity would allow a final answer to be put on the cosmological Li problem (at least from the stellar side) and, at the same time, the secure determination of the initial value of Li in the early Galaxy, which is critical in models of Galactic evolution.

3.2 Beryllium and Boron

Due to the observational difficulties, much fewer studies have been performed on beryllium and even less for boron. Nevertheless, those studies have allowed important insights to be obtained in the different areas.

3.2.1 Stellar Physics

Simultaneous measurements of Li, Be, and B allow tighter constraints to be put on the mixing processes at work in stars, since different non standard processes predict different trends of Be vs. Li depletion (e.g., Deliyannis, 2000). Beryllium observations in the Sun were first performed by Greenstein and Tandberg Hanssen (1954), who found that, at variance with lithium, Be was undepleted in our star. Since then, not only were many additional measurements of beryllium in the Sun performed, but also a number of studies aimed to simultaneously measure lithium, beryllium, and, at times, boron in MS stars in the Milky Way (MW) field and star clusters. Crucially, state-of-the-art high-resolution spectrographs with high near-UV efficiency, like UVES on the ESO VLT and HIRES on Keck, have allowed measurements of Be both in bright stars in close-by clusters and also in fainter members of more distant, old clusters, pioneered by Randich et al. (2002).

We refer to Boesgaard and Tripicco (1986), Boesgaard (2005), and Randich (2010) for detailed reviews of the results of observations of Be to trace stellar mixing in solar-type and warmer stars, while we just summarize here the main findings and issues. Specifically, several studies have clearly indicated that stars warmer than about 6000 K, included those in the Li dip, have depleted some amount of Be, a Be dip is seen, as well as a Be vs. Li correlation; this supports rotation induced mixing as the main driver of Li and Be depletion. On the contrary, cooler, solar-type stars in clusters, like the Sun, do not show, within the errors (admittedly not negligible), any evidence of substantial Be depletion, nor any Be vs. Li correlations. As noted by Randich (2010), stars that cover two orders of magnitude in Li abundances and have different ages and metallicities do share a similar Be content (see Figure 3 in that paper). These results suggest a shallower mixing in solar-type stars; i.e., the mixing is deep enough to cause Li but not Be depletion to occur. As for solar analogs in the field, the results generally agree with those for the clusters (e.g., Takeda and Tajitsu, 2009); note however that Takeda et al. (2011), based on a larger sample, detected a very small fraction of stars that had significantly depleted Be. They also claimed that, although the solar twins in their sample roughly share similar Be abundances, there may be a tendency of higher Be for more rapid rotators, while the Sun itself may have depleted some Be. To conclude, stars warmer than about 6000 K deplete some Be and show a Be vs. Li correlation, while cooler stars are normally undepleted.

Boron provides a further probe of mixing since it survives to greater depths than Li and Be. However, as already mentioned, boron observations are extremely challenging, hence limited to relatively small samples of bright stars. In the context of the use of B as a mixing tracer, studies have been performed mainly by Ann Boesgaard and collaborators using STIS and GHRS on board the *Hubble Space Telescope*; see also Primas et al. (1999). Only bright, stars warmer than the Sun in the field were observed. Stars that were depleted in Be were found to be also B deficient and a correlation between B and Be was evidenced (see, e.g., Boesgaard et al., 2005; Boesgaard, 2005; and references therein), although the slope of the correlations is smaller than that of Be vs. Li.

3.2.2 Galactic Evolution of Be and B

As mentioned in **Section 1**, both Be and B are produced by cosmic ray spallation. Investigating their evolution in the Galaxy thus allows constraints to be put on the production mechanism as

well as on Galactic evolution in general and the intensity spectrum of cosmic rays as a function of time.

The study on the Galactic evolution of Be started about 40 years ago (Molaro and Beckman, 1984), although measurements of Be in stars were obtained before that (as discussed above). However only in the early 90s, large enough samples of stars (including metal-poor ones) were observed, allowing the evolution with metallicity to be traced. Specifically, Boesgaard and King (1993) found a quadratic dependence (a linear correlation with a slope around 2) of Be abundances vs. [Fe/H] for low-metallicity halo stars, apparently confirming the CR direct spallation process as the main production channel; on the contrary, the study by Gilmore et al. (1992) revealed a different trend, a linear correlation with a slope around 1 between A (Be) and [Fe/H]. Thanks to the advent of high-resolution spectrographs on large telescopes, this early result was confirmed by later studies, based on much larger samples of stars extending to lower metallicities and providing strong support to the inverse spallation or "supernova" scenario (see, e.g., Primas, 2010; Boesgaard et al., 2011; Smiljanic, 2014; Prantzos, 2012; and references therein), although the exact slope may change based on the analyzed samples (see, e.g., Smiljanic et al., 2009b). Also, some authors claimed that the slope with metallicity may be higher when looking at the trend of Be vs. oxygen rather than iron, while Boesgaard et al. (2011) even suggested the possible presence of two slopes for different metallicity regimes. Furthermore, a dispersion around the main relationship was seen for metallicities [Fe/H] above ~−1.5, where the halo-to-disc transition occurs (Primas, 2010).

Although based on much fewer data, a similar linear dependence of boron on metallicity (slope ~1) as for beryllium was also found based on the first B observations in metal-poor stars by Duncan et al. (1992). This was confirmed by later studies (see, e.g., Garcia Lopez et al., 1998, and references therein); interestingly, the possibility of two slopes also for this element was proposed by Boesgaard et al. (2004). Finally, the constant B/Be ratio measured for metal-poor stars clearly supported the idea that both elements were created by the same channel (see discussion in Garcia Lopez et al., 1998).

3.2.3 Beryllium as a Cosmochronometer

The idea that beryllium could be used as a cosmochronometer or a cosmic clock was successfully tested by Pasquini et al. (2004) who performed the first measurement of Be in turn-off (TO) stars in a globular cluster. Indeed, Be abundances suggested that the cluster NGC 6397 formed 0.2–0.3 Gyr after the onset of star formation in the Galaxy, in excellent agreement with the cluster age obtained through MS fitting. The result and the hypothesis that Be can be used as a clock for the early formation of the Galaxy were further tested confirmed by Pasquini et al. (2007). Based on these positive tests, a number of studies successfully exploited Be as a cosmochronometer, or the equivalent of a timescale, to study the star formation history in the halo and thick disc of our Galaxy (Pasquini et al., 2005; Smiljanic et al., 2009b), and stellar populations in general. These studies supported the idea that Be can indeed be used to separate different populations within the same Galactic component, which would also explain the observed scatter in Be.

3.3 CNO

The modern approach to the study of CNO abundances started with Suess and Urey (1956), whose tables of abundances provided fundamental constraints to theories of nucleosynthesis in stars. Cameron (1968), in his pioneering work, measured the abundances of several elements in the solar photosphere, including C, N, and O (see also Cameron, 1973). Lambert (1968) and Lambert (1978) gave a summary of all accessible atomic and molecular signatures of carbon, nitrogen, and oxygen, identifying the best ones to measure abundances. The historical paper of Lambert (1978) gave an overview of the observational methods and challenges for the CNO elemental abundances.

Significant progress has been achieved since the first determination by Lambert (1978), including detailed physics, as NLTE and 3D modeling (Asplund et al., 2004; Asplund, 2005; Caffau et al., 2008; Asplund et al., 2009). However, while the literature determinations of C and N solar abundances are more stable, the solar oxygen abundance is still under debate. Since its first determination by Lambert (1978), who gave abundances 12 + log (O/H) = 8.92, it has been revised several times, producing progressively lower values. Asplund et al. (2009) recommended a solar oxygen abundance 12 + log(O/H) = 8.69 ± 0.05, but the redetermination of Caffau et al. (2008) with 3D solar model atmospheres yielded again a higher solar abundance 12 + log (O/H) = 8.76 ± 0.07.

The interest in C, N, and O abundances has increased with time, thanks to the multiple applications of their study in astrophysics. There are indeed several open issues and questions still debated, which we briefly address in the following.

3.3.1 The Role of C and N Photospheric Abundances to Constraint Stellar Physics, Mixing Mechanisms, and Stellar Age Dating

While stellar physics and evolution are well known and constrained, there are still aspects, as the occurrence of non standard mixing processes after the bump luminosity on the red giant branch, which produce changes in the abundances of light elements (see, e.g., Eggleton et al., 2006; Denissenkov et al., 2009; Busso et al., 2007; Busso et al., 2010; Lattanzio et al., 2015; Lagarde et al., 2019; and references therein) and that still need to be fully understood. A statistically significant sample of stars, as the ones collected by the spectroscopic surveys, e.g., Gaia-ESO, APOGEE, GALAH, and LAMOST (see the next section), spanning broad intervals in stellar properties, as mass and metallicity, is indeed necessary to progress in this field and to distinguish among the different transport mechanisms, as, e.g., cool bottom processing (e.g., Boothroyd et al., 1995), deep diffusive mixing (e.g., Denissenkov et al., 1998), rotation (e.g., Charbonnel, 1995; Denissenkov and Herwig, 2004), thermohaline instability (e.g., Eggleton et al., 2006; Charbonnel and Zahn, 2007; Charbonnel and Lagarde, 2010), and magnetic fields (e.g., Busso et al., 2007, Busso et al., 2010; Palmerini and Maiorca, 2010; Cristallo and Vescovi, 2020).

Understanding the surface abundances of C and N in giant stars has also important implications to our ability to use the [C/N] ratio to trace stellar ages (see, e.g., Masseron and Gilmore, 2015; Martig et al., 2016; Ness et al., 2016; Lagarde et al., 2019; Casali et al., 2019; Hasselquist et al., 2019).

3.3.2 The Multiple Nucleosynthesis Sites of the CNO Elements and the Role of Stellar Rotation

Although the main sites of production of CNO are known (massive stars for O and a combination of massive and low- and intermediate-mass stars (LIMS) for C and N) (see **Section 4.3** for details and references and Kobayashi et al. (2020) for a recent review), there are still open issues about the relative importance of the two major sites of production and their contribution to the global evolution of carbon and nitrogen (see, e.g., Gustafsson et al., 1999; Henry et al., 2000; Matteucci and Chiappini, 2003; Bensby and Feltzing, 2006; Mattsson, 2010), including the role of massive low-metallicity stars (e.g., Vincenzo et al., 2016). In addition, stellar rotation and mass loss play an important role in setting the final yields of massive stars, in particular for oxygen, carbon, and nitrogen, with notable implications and effects in modeling the chemical evolution of galaxies (see Meynet et al., 2018, for a review).

The evolution of nitrogen, and in particular of the N/O abundance ratio, has been studied in our Galaxy with observations of samples of stars and H II regions (e.g., Christlieb et al., 2004; Israelian et al., 2004; Carigi et al., 2005; Esteban et al., 2005; Spite et al., 2005; Lyubimkov et al., 2013; Esteban and García-Rojas, 2018; Lyubimkov et al., 2019) to put constraints on both Galactic evolution and nucleosynthesis processes. Chiappini et al. (2005) interpreted the origin and evolution of nitrogen in our Galaxy comparing the observed abundances in the Milky Way Galaxy with their two-infall model (originally developed in Chiappini et al., 1997), similarly to Gavilán et al. (2006), who introduced a primary component in the production of N from intermediate-mass stars to explain to observed abundances. They attributed the dispersion of N/O at a given metallicity to the variation of the star formation rates (SFRs) across the Galactic disc, as confirmed by the work of Mollá et al. (2006). Subsequent works (Chiappini et al., 2006; Kobayashi and Nakasato, 2011) showed that yields that take into account rotation are necessary to explain the N/O vs. O/H relation in our Galaxy. More recently, Vincenzo and Kobayashi (2018b) reproduced the observed trends with inhomogeneous enrichment from AGB stars. Despite the numerous works dedicated to these elements, their origin is still debated and not fully clarified (see also Kobayashi et al., 2020). Large spectroscopic surveys, combined with state-of-the-art chemical evolution models and stellar yields, allow us to take a step forward in understanding the origin of these elements (see, e.g., Magrini et al., 2018; Hayes et al., 2018; Romano et al., 2019; Griffith et al., 2019; Franchini et al., 2020).

4 THE LIGHT ELEMENTS IN THE ERA OF SPECTROSCOPIC SURVEYS

In the last decade, a variety of large spectroscopic surveys or big observational programs have been started/completed and they are allowing us to get new valuable insights on stellar physics and Galactic archaeology in general. Those surveys collect spectra characterized by different resolving powers and covering different spectral intervals, reach different limiting magnitudes, and focus on a variety of populations. Some of them are public (i.e., the products are periodically released to the community), while others are not. The main characteristics of the surveys of interest here are summarized in **Table 1**. We briefly discuss below a few important aspects.

Most of these recent large spectroscopic surveys, such as GALAH (Bland-Hawthorn et al., 2018), Gaia-ESO (Gilmore et al., 2012; Randich et al., 2013, hereafter GES), and LAMOST (Xiang et al., 2017), are designed to work in the optical spectral range, which is rich in abundance diagnostics, including the Li doublet, atomic and molecular lines of oxygen, carbon, and nitrogen.

The spectroscopic surveys APOGEE and APOGEE-2 (Majewski et al., 2017; Zasowski et al., 2017) collected spectra of the Milky Way stellar populations in the near-infrared. They have measured molecular transitions to derive oxygen, carbon, and nitrogen abundances (García Pérez et al., 2016), now available also in their public release DR16. New techniques working on low-resolution spectra, for instance, the LAMOST spectra at R = 1800, have also been developed to measure elemental abundances, including oxygen (Ting et al., 2017), even when no oxygen lines are present (Ting et al., 2018). These new methods are based on a data-driven approach, in which a sample of higher-resolution spectra, for which stellar parameters and abundances have been determined, is used to create *labels* that can be transferred to lower-resolution spectra, allowing us to determine not only parameters and abundances but also ages and masses, even from blended features using the whole information contained in the spectrum.

Three of the above-quoted surveys, LAMOST, GALAH, and GES, include the Li I line in the covered spectral range and crucially yield lithium abundances for large, statistically significant samples of stars belonging to different stellar populations, including star clusters. We mention in particular that the Gaia-ESO Survey has targeted more than 60 open clusters; they well cover the age-metallicity-distance parameter space and include stars of different spectral types, hence providing the largest, homogeneous available data set for lithium in star clusters. We stress here that, as the following discussion will also highlight, open star clusters represent fundamental tools to address many of the topics presented in this review, since they provide homogeneous samples of stars covering different masses and evolutionary stages, spanning large age intervals, and being located in a different part of the Galaxy.

In the following, we will present some of the main results, from published papers. We stress however that full exploitation of those data sets has still to be completed; thus, we will also anticipate a few preliminary figures based on the latest internal release of GES, iDR6, in order to show its potential. We also note that smaller, but important, spectroscopic programs have been recently performed; findings from these projects will also be discussed, when relevant.

We finally mention that invaluable contributions have come from the exquisite astrometry of the *Gaia* space mission and its

TABLE 1 | Characteristics of the main large spectroscopic surveys.

Survey	Spectral coverage	R	Covered populations	N_{stars}	Lim mag	Li	CNO
GALAH	470–790 nm[a]	28,000	Discs (clusters)	10^6	12 < V < 14	✓	✓
APOGEE	1.51–1.70 μm	22,500	Discs/halo (clusters)	10^5	7 < H < 13.8		✓
APOGEE-2	1.51–1.70 μm	22,500	Discs/halo (clusters)	10^5	7 < H < 13.8		✓
GES-Giraffe[b]	647–679 nm	17,000	Clusters	10^5	V < 19	✓	
GES-UVES	480–680 nm	47,000	Discs/bulge/clusters	10^4	V < 16	✓	✓
LAMOST	370–910 nm	1,800	Discs/anticenter/spheroid	2.5×10^6	R < 19	✓	✓

[a]*Spectral range divided into four windows.*
[b]*HR15N setup is used for the observations of open clusters with F-G-K-M stars; the other GES-Giraffe setups are used for field stars or for hot stars in star clusters.*

DR2 and recent EDR3 data releases (Gaia Collaboration et al., 2016; Gaia Collaboration et al., 2018; Gaia Collaboration et al., 2020), allowing the determination of a number of crucial parameters for the study of the light elements, as well as from new measurements of rotational periods for large numbers of clusters from the ground with a variety of projects, and from space with the CoRoT, Kepler/K2, and TESS missions.

4.1 Stellar Physics and Mixing

4.1.1 Pre-main Sequence Evolution

The new spectroscopic surveys and, in particular, the Gaia-ESO Survey have observed statistically significant samples of members of many young clusters and star-forming regions, well covering, for the first time, the age range between a few Myr and 100 Myr; this allows us to obtain further insights on the PMS evolution of lithium, while opening new challenges. We refer to Bouvier et al. (2016), Jeffries et al. (2017), Franciosini et al. (2020), and Bouvier (2020) for detailed discussions and presentations of the results, while we summarize below the main findings.

Bouvier et al. (2016) investigated the lithium-rotation connection, which had been shown to hold for the older Pleiades and other clusters (see **Section 3.1.1**), at very young ages. They found that a dispersion in Li and a relationship between Li and rotation is already present among low-mass members (0.5–1.2 $M_\odot$) of the NGC 2264 cluster (~5 Myr), with faster rotators being more Li rich, by about 0.2 dex, than slowly rotating stars. The difference in lithium between slow and fast rotators is much smaller than what is seen in the older Pleiades, but it suggests that non standard physics is already active during the PMS of low-mass stars. Several possible explanations were proposed by Bouvier et al. (2016), among which planet ingestion, the effect of the accretion history, early angular momentum evolution, or magnetic fields and activity that would result in enhanced radii and reduced Li burning, as originally proposed by Somers and Pinsonneault (2014) and Somers and Pinsonneault (2015) (see also Somers et al., 2020, for a very recent update). More specifically, rotation and magnetism have since long been identified as non standard processes that may also affect the structure of young stars and hence Li depletion (Spruit and Weiss 1986; Martin and Claret, 1996; Ventura et al., 1998; Mendes et al., 1999; D'Antona et al., 2000; Feiden and Chaboyer, 2013; Spada et al., 2018) and the new data sets indeed confirm that this is the case and in principle allow constraints to be put on the models.

Recent additional observational pieces of evidence of the action of non standard physics and the effect of magnetic fields in young stars were provided by Messina et al. (2016) and Jeffries et al. (2017). The second paper pointed out in particular that standard PMS evolutionary models do not reproduce simultaneously the color-magnitude diagram (CMD) and the lithium depletion pattern of the young Gamma Velorum cluster: specifically, while the CMD could be well fitted with an age of ~7.5 Myr, the strong Li depletion observed among M-type stars would imply a significantly larger age. Jeffries et al. (2017) were able to reconcile both the Li pattern and the CMD at a common age of ~18–21 Myr, by assuming that the radius of low-mass stars is inflated by ~10%; following a semianalytical approach, they modified stellar models accordingly, considering (almost) fully convective stars with a simple polytropic structure. This resulted in significant older ages than in the standard scenario and in a significant shift of the center of the lithium depleted region towards lower effective temperatures.

Independent evidence of inflated radii has been also found in older clusters like the Pleiades (e.g., Jackson et al., 2016, Jackson et al., 2018; Somers and Stassun, 2017). The quoted authors suggested that radius inflation is likely linked to the magnetic activity and/or starspots and is responsible for the observed dispersion in Li abundances. Note that, as well known, the level of activity is linked to rotation; hence, this would explain the Li-rotation connection. Indeed, Somers and Stassun (2017) demonstrated a triple correlation between rotation rate, radius inflation, and enhanced lithium abundance. The issue is further explored by Franciosini et al. (2020), who extends the analysis to four open clusters with ages between ~20 and 100 Myr observed within GES (Gamma Vel, NGC 2547, NGC 2451 B, and NGC 2516) and investigate the effect of magnetic activity and starspots on PMS evolution models of lithium depletion as a function of age.

4.1.2 The MS Phases

A great contribution to the investigation of the evolution of lithium during the MS phases of stars more massive than the Sun has been provided by the WIYN Open Cluster Survey (WOCS, Mathieu, 2000). This program has started about 20 years ago and the results for a number of open clusters have been published during the years, following the evolution of Li from the MS to the tip of the red giant branch. The observed clusters cover a large range in metallicity but are mostly older

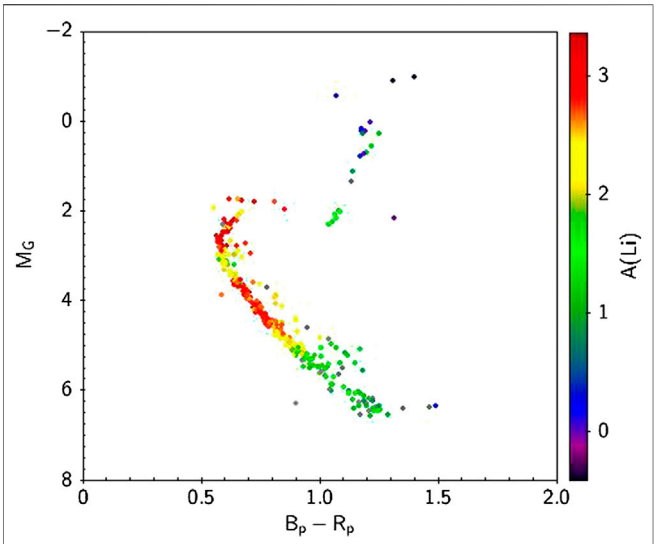

FIGURE 1 | Absolute *Gaia* G magnitude vs. B_p-R_p color for the cluster NGC 2420 (age ~1.7 Gyr) color-coded by Li abundance. Cluster parameters (distance and reddening in particular) were retrieved from Cantat-Gaudin et al. (2020).

than 1 Gyr. The main recent results on Li evolution during the MS have been summarized by Twarog et al. (2020) (see also Deliyannis et al., 2019; Anthony-Twarog et al., 2018a, Anthony-Twarog et al., 2018b). Specifically, the existence of the Li dip has been confirmed in many clusters; additionally, the new data suggested that the blue-, warm-, or high-mass side of the Li dip is very sharp (they defined it as the "cliff") and its position (magnitude or temperature) does not appear to change with the cluster age; the mass at which the cliff is seen is determined by the cluster metallicity, with higher masses for more metal-rich clusters. Stars warmer than the dip presumably retain their initial Li content; on the contrary, stars on the red side of the dip seem to sit on a plateau, with no trend of A(Li) with increasing magnitude (decreasing mass). Rotation and rotational evolution (spindown) appear as the critical factors for the appearance of the Li dip and its boundaries.

As for cooler, lower-mass stars, in intermediate-age clusters, recent WOCS observations of M35 have shown that this cluster behaves similarly to the younger Pleiades, since a dispersion in Li is seen among cool stars, as well as a relationship with rotation and radii (Anthony-Twarog et al., 2018a; Jeffries et al., 2020); this, on the one hand, provides some support for models with inflated radii and lower Li depletion in the faster rotators (more active stars), as discussed above. At the same time, the authors claim that rotational mixing cannot be excluded: given the saturation of magnetic activity, stars would have similar levels of activity, and Li depletion during the PMS may be inhibited for all of them, while additional mixing would subsequently deplete more Li in slow rotators that undergo angular momentum loss (Jeffries et al., 2020). To summarize, the issue is not settled. While new data have confirmed the dispersion among low-mass stars in clusters and have shown that this dispersion sets in early during the PMS, the final reason for it has not yet been definitively confirmed.

As mentioned, GES and in particular its Li data set for open clusters sampling a broad age and metallicity range (from a few Myr to several Gyr, from −0.5 to +0.3 dex in [Fe/H]) offer a great opportunity to further investigate the evolution of Li in MS stars or different temperature. **Figure 1** is a nice illustration of the evolution of lithium in a cluster color-magnitude diagram (CMD). Specifically, the figure shows the *Gaia* B_p-R_p vs. G diagram for NGC 2420 (age around 1.7 Gyr, slightly subsolar metallicity), highlighting the changes in Li abundances for stars of different masses along the MS and after it. The dip is clearly visible for stars just below the TO, as well as the decrease of Li along the MS and post-MS evolution.

In **Figures 2–4**, we instead plot Li abundance as a function of absolute G magnitude or effective temperature (T_{eff}) for clusters with different ages and/or metallicities. The figures highlight a number of interesting points. First, the dip is clearly visible in all clusters; noticeably, it is already present in the 400 Myr old NGC 3532, hence one of the youngest clusters where the dip is detected. Some scatter is present (possibly due to cluster membership to be refined), but its position, shape, and lowest lithium value in both the A(Li) vs. T_{eff} and A(Li) vs. G diagrams do not greatly depend on metallicity, confirming that the dip occurs at higher masses for more metal-rich clusters (this is just because at a fixed temperature, the mass is higher for more metal-rich stars). On the contrary, the direct comparison of the shape of the dip for NGC 2420 and NGC 3532 (similar metallicities; different ages) may suggest that the dip is shallower at younger ages and its high-mass (blue) side occurs at slightly fainter magnitudes. We also note that presumably

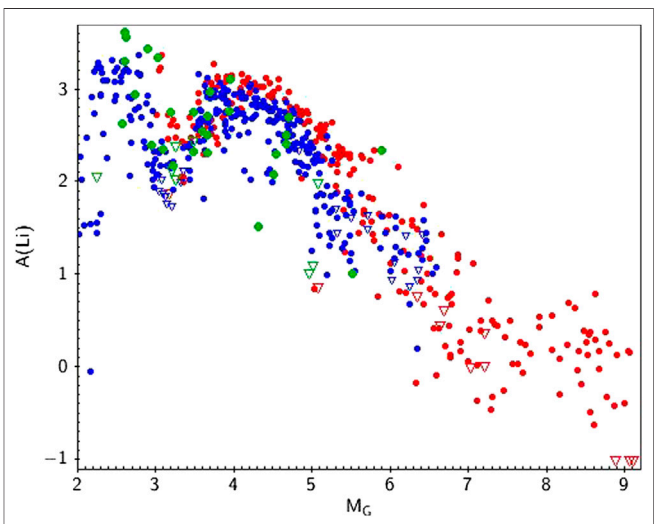

FIGURE 2 | Lithium abundance vs. absolute G magnitude for NGC 3532 (red symbols; age ~400 Myr, [Fe/H] = 0 ± 0.04), NGC 2420 (blue symbols; age ~1.7 Gyr, [Fe/H] = −0.16 ± 0.07), and Ruprecht 134 (green symbols; age~1.7 Gyr, [Fe/H] +0.27 ± 0.04). Filled symbols and open triangles denote Li detections and upper limits, respectively. Typical errors in A (Li) are 0.1 dex. Cluster parameters (distance and reddening in particular) were retrieved from (Cantat-Gaudin et al., 2020), while the average metallicities were derived from GES iDR6 data.

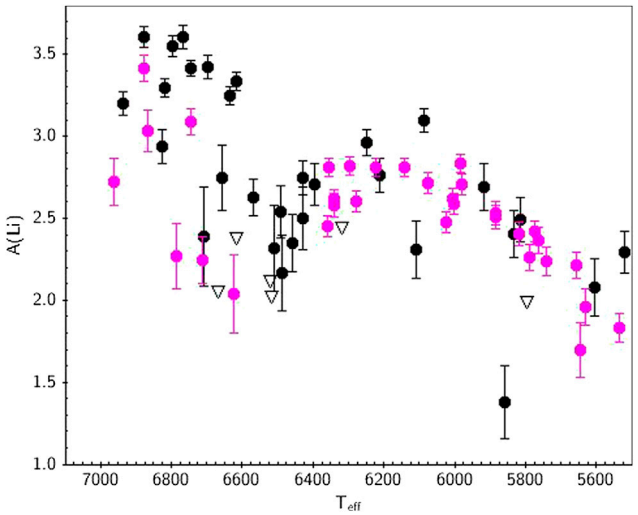

FIGURE 3 | Lithium abundance vs. effective temperature for NGC 2355 (pink symbols; age 1 Gyr, [Fe/H] = −0.10 ± 0.03) and Ruprecht 134 (black symbols). Symbol as in the previous figure. Typical errors in effective temperature are of the order of 60–80 K. Cluster parameters (distance and reddening in particular) were retrieved from (Cantat-Gaudin et al., 2020), while average metallicities were derived from GES data.

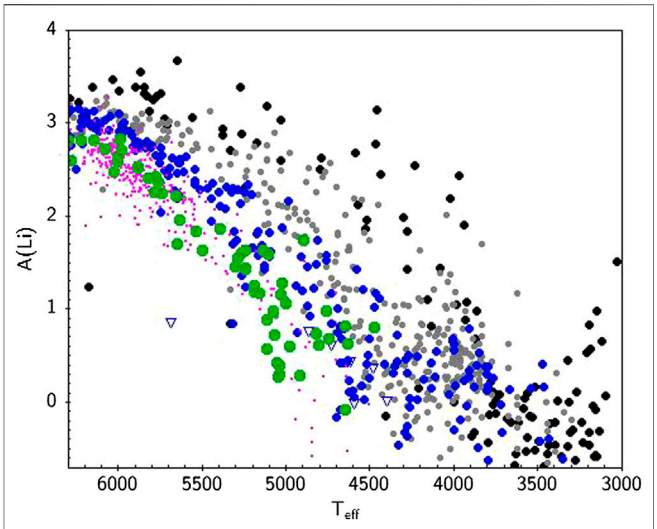

FIGURE 4 | Lithium abundance vs. effective temperature for a set of clusters with similar metallicity (around or slightly below solar) and different ages, from very young to extremely old. Namely, IC 2602 and NGC 2547 (black symbols, age ~30–50 Myr), NGC 2516 (grey symbols, age ~100 Myr), NGC 3532 (blue symbols, age 400 Myr), NGC 2355 (green symbols, age ~1 Gyr), and Berkeley 39 (pink symbols, age ~6 Gyr). Errors in Li and temperature are as in previous figures. Cluster parameters (distance and reddening in particular) were retrieved from (Cantat-Gaudin et al., 2020).

undepleted stars on the blue/bright side of the dip seem are slightly more Li rich in the most metal-rich cluster (Ruprecht 134), which has implications for the investigation of the Galactic evolution of lithium (see **Section 4.4.1**).

As for stars cooler than the dip, **Figure 4** represents to our knowledge the first homogeneous comparison of the Li vs. temperature distribution from the ZAMS phases up to several Gyrs. The final GES data set includes many more clusters, covering well the age-metallicity parameter space; the figure is therefore anticipation of the excellent potential of this survey to investigate in detail the Li-age evolution, as a function of metallicity and stellar mass (see also **Section 4.2** below). The figure confirms that, for all effective temperatures (or masses), Li depletion is at work on the MS. If we focus on solar-type and warmer stars, for which no depletion on the MS is expected from standard models, the figure indicates a continuous depletion, up to about 1 Gyr, when no more depletion occurs, as the distributions of NGC 2355 (age ~1 Gyr) and Be 39 (age ~6 Gyr) clearly show. Furthermore, all clusters show moderate, if any, dispersion; most importantly, a very minor fraction of cluster members with temperatures similar to the Sun is as Li depleted as it, suggesting that our star has likely had a peculiar Li evolution history. The spread in Li seen among solar-type stars in M67 (discussed earlier in this paper) also seems to be an exception. For lower-mass/cooler stars, the diagram shows the well-known trend of decreasing A(Li) towards lower temperature; depletion increases with age and it becomes faster for lower masses; the scatter within the same cluster appears larger with respect to warmer stars.

GES also provides projected rotational velocities (vsin*i*), which allow further investigation of the Li-rotation relationship. In **Figure 5**, we plot Li abundances vs. the absolute G magnitudes, color-coded by rotational velocity for three clusters with different ages, but similar metallicities. The figure clearly highlights the evolution of the Li dip with time (we note that it is present already at ~100 Myr), the fact that stars in the dip typically have faster rotational velocities than stars outside the dip (in particular, those on the red side of it), and, on average, the Li-rotation connection among low-mass stars (at least in NGC 2516).

As mentioned, the above plots and analysis are preliminary ones, mainly aimed to show the state of the art of Li observations in clusters. A full analysis of the complete data set—we recall that this will also be available to the community through the ESO archive—will provide a detailed view of the Li-age-mass-metallicity-rotation relationships, which will hopefully enable tighter constraints to be put on the models.

4.1.3 Beryllium and Boron

Beryllium and boron observations carried out prior to 2010–2015 already exploited available state-of-the-art instrumentation at its best. As a consequence, much fewer studies have been performed in the last five years or so and relatively little progress has been achieved. Among the few recent studies, Desidera et al. (2016) characterized the four Be depleted solar-type stars previously reported by Takeda et al. (2011), finding that all of them are binaries and proposing that the ultra-beryllium depletion may be due to the presence of a brown dwarf companion. Hence, Be depletion seems to be related to very peculiar circumstances, rather than being the normality.

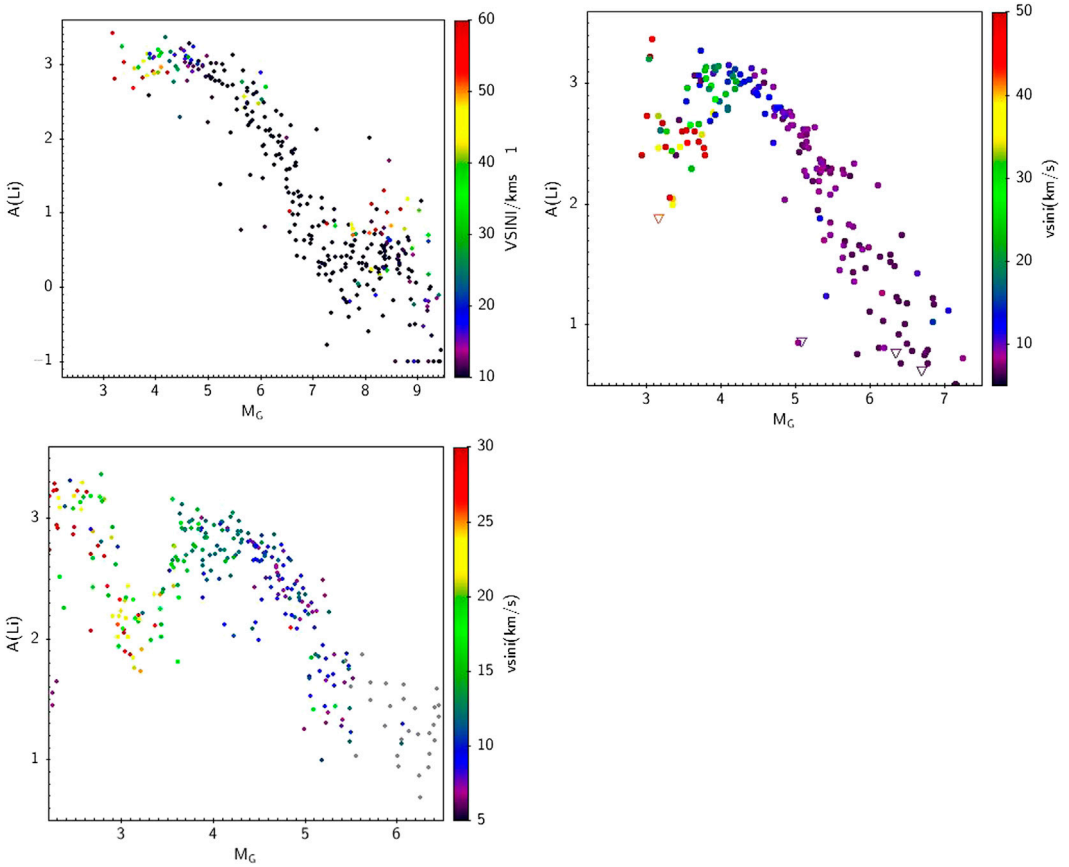

FIGURE 5 | Lithium abundance vs. absolute G magnitude, color-coded by projected rotational velocities (from GES). Upper, middle, lower panels: NGC 2516, NGC 3532, NGC 2420. Errors in A (Li) are as from previous figures.

As for warmer stars, Boesgaard et al. (2016) determined Li, Be, and B for 79 Hyades dwarfs in the Li dip, confirming both Li and Be dip, as well as detecting a small drop in B abundance across the dip. The B vs. Be correlation is in good agreement with models including rotational mixing. Finally, Boesgaard et al. (2020) very recently determined both Li and Be abundances along the subgiant branch of M67; these stars have evolved from MS stars in the region of the Li and Be dip. They found both a marked decline in Li and a corresponding decrease in Be abundances. They showed that the Be vs. Li pattern could also in this case be well fitted by the models including mixing due to rotation (plus post-MS dilution).

To summarize, a Be vs. Li correlation is now confirmed among F-type stars, probing that, for those stars, the mixing extends down to the Be burning region; the mixing mechanism seems to be shallower and more complex for solar twins, but relatively few data are available, in particular when compared to the wealth of Li measurements from the spectroscopic surveys that we have discussed above.

4.1.4 Mixing and Extramixing in Giant Stars

The CNO cycle is at the basis of the production of C, N, and O in stellar interiors. It consists of a set of nuclear reactions, whose final product is the conversion of H in He, and in which C, N, and O atoms play as catalysts (see, e.g., Salaris and Cassisi, 2005). The total amount of C, N, and O is globally unchanged during the CNO cycle. However, the relative abundances of the three elements might evolve with time, driven by the rate of the slowest reaction, which is the one involving a proton capture on ^{14}N. Thus, at equilibrium conditions, in the stellar core, the abundance of N increases, despite decreasing ^{12}C abundance and of decreasing in the ^{12}C/^{13}C isotopic ratio. Also, oxygen abundances can be modified, being transformed into N at higher temperatures than C. However, it happens at deeper layers in the stars, which are not reached during the first dredge-up, and consequently, the surface abundance of ^{16}O is almost unchanged.

At the end of the MS, the amount of CNO-processed material in the core is directly related to the initial stellar mass. More massive stars, reaching higher temperature, would have a larger fraction of the core in which the ^{12}C can reach burning temperature and thus can be converted in ^{14}N, with a consequent overabundance in N. After the main sequence, in the ascending phase to the giant branch, during the core contraction, the convective envelope reaches zone in which elements modified by the CNO cycle are present (Iben, 1991),

in the so-called first dredge-up (FDU) episode. The FDU is a mixing episode that modifies the surface abundances, since the photospheric abundances are mixed with material enriched in nitrogen and depleted in carbon.

Carbon and nitrogen abundances on the surfaces of evolved stars indeed allow probing their interiors. Their [C/N] ratio, which depends on the mass of the star, can be exploited to derive ages for field red giants (see, e.g., Martig et al., 2016; Ness et al., 2016; Masseron et al., 2017; Casali et al., 2019; and next section) but also to amplitude of the mixing process and the existence of non-canonical processes, called "extramixing," which might be driven by different phenomena, such as rotation, magnetic buoyancy, thermohaline, or gravitational mixing (e.g., Denissenkov et al., 2009; Eggleton et al., 2006; Charbonnel and Lagarde, 2010; Busso et al., 2010; Lattanzio et al., 2015; Cristallo and Vescovi, 2020, among many) and which largely modify also the Li abundance (see **Section 3.3.1**). After the FDU, an extramixing episode occurs at the bump luminosity on the RGB, modifying the photospheric abundances of some elements, including Li, C, and N (e.g., Gilroy, 1989; Gilroy and Brown, 1991; Gratton et al., 2000; Mikolaitis et al., 2012; Smiljanic et al., 2009a; Tautvaišiene et al., 2000; Tautvaišienė et al., 2010, Tautvaišienė et al., 2013, Tautvaišienė et al., 2015, Tautvaišienė et al., 2016). The subsequent dredge-up episodes, namely, the second and third dredge-up (SDU and TDU, respectively), happen in the early-AGB phase, in which the products of the hydrogen burning are brought to the surface at the beginning of the AGB phase (SDU) (see, e.g., Iben and Renzini, 1983; Frost et al., 1998). The AGB phase is characterized by a thermally unstable He-burning shell, with thermal pulses in which the material manufactured in the He-burning shell is convectively mixed and transported close to the base of the H-burning shell. The products of the two shells can be involved in further nucleosynthesis. In addition, after the extinction of the He-burning thermal pulse, the outer convective zone deeply penetrates into the hydrogen and helium burning shells where, eventually, it can transport carbon to the surface (TDU). The TDU might happen several times, possibly producing a C-enhanced star. In what follows, we focus on the comparison between models and observations of RGB stars that have only passed through the FDU.

Using GES data, Lagarde et al. (2019) investigated the effects of thermohaline mixing on C and N observed abundances by performing a comparison with simulations of the observed fields using a model of stellar population synthesis. The C and N abundances in a sample of open and globular clusters, spanning a wide range of ages and metallicities, show the impact of thermohaline mixing at low metallicity. The incidence of thermohaline mixing is indeed able to explain the [C/N] value observed in the lower-mass and older giant stars, as shown their **Figure 6**.

Additional important information on the nature of the mixing processes in evolved stars is related to the carbon isotopic ratio, $^{12}C/^{13}C$. It indeed abruptly decreases when the thermohaline mixing develops during the RGB phase (see, e.g., Charbonnel and Lagarde, 2010). There are several works that investigated the behavior of the C isotopic ratio in star clusters (e.g., Mikolaitis et al., 2012; Drazdauskas et al., 2016; Tautvaišienė et al., 2016), exploiting the advantage of groups of stars that have the same age, metallicity, and origin, from which distance and age and, consequently, their mass and evolutionary status can be precisely determined. The value of $^{12}C/^{13}C$ provides further constraints on the mixing models; in particular, the low values of the carbon isotopic ratio in red clump stars cannot be reproduced without models including extramixing process (see Figure 11 in Lagarde et al., 2019). We recall that thermohaline mixing and all other non standard processes are not derived from first principle physics and they are subject to uncertain parametrization. In this framework, the observations play a crucial role in calibrating and improving their understanding.

4.2 Light Elements as Independent Tools to Derive Stellar Ages

The measurements of stellar ages are very challenging, since they cannot be directly obtained from observations (see, e.g., Soderblom et al., 2014; Randich et al., 2018; and references therein). They are usually estimated through the so-called isochrone fitting, i.e., a comparison between observed quantities (magnitudes and colors) or derived quantities (as, e.g., surface gravities, and effective temperatures) and the outcomes of stellar evolution models. The method is more effective for stars belonging to clusters (see, e.g., Randich et al., 2018), for which we can observe several coeval member stars in different evolutionary stages, while it produces large uncertainties for isolated stars, especially if they are located in regions of the plane for which isochrones of different ages are almost overlapping. Other well-established methods are related to asteroseismology, which provide powerful means to probe stellar interiors (see, e.g., Ulrich, 1986; Lebreton and Montalbán, 2009; Soderblom, 2010; Davies and Miglio, 2016; Bellinger, 2019). The oscillation frequencies measured by asteroseismology are indeed closely related to stellar interior properties and tightly linked with the mass and evolutionary state. Comparing the oscillation spectrum with predictions of stellar models, the age and mass of a star can be determined (Lebreton and Montalbán, 2009). However, ages from oscillation spectra are limited by the number of stars observed by dedicated space telescopes (CoRoT, Kepler, PLATO, and TESS). Alternative methods based on the chemical content of stars have been developed in recent years. We discuss here the use of Li and Be abundances and [C/N] ratios to estimate stellar ages.

4.2.1 Lithium and Beryllium

As anticipated in **Sections 1** and **3**, Li can in principle be used as an age tracer for both PMS and MS stars. The new spectroscopic programs and Li measurements in several young clusters and associations have provided the possibility to identify members of those clusters based on their high lithium abundance, to measure their age, and to infer the age dispersions (e.g., Murphy and Lawson, 2015; Bravi et al., 2018; Prisinzano et al., 2019; Žerjal et al., 2019, to cite a few). However, as discussed above, PMS depletion is significantly more complex than what standard models predict. The evidence for additional depletion or inhibited depletion for stars of the same age, the effects of non

standard processes and other parameters, and the intrinsic difficulty in getting correct Li measurements in PMS stars due to rotation and accretion, eventually are all significant aspects that should be better understood and calibrated and that prevent a precise, quantitative use of Li as an age tracer (e.g., Jeffries, 2017, and references therein).

Similarly, even for stars of similar mass, MS Li depletion is not a simple, continuous function of stellar age only; quantitative use of Li to infer individual stellar ages must hence be done with caution. Inferring ages for field stars similar to the Sun appears particularly important, since it would allow us to age date exoplanet host stars. In this context, a number of recent studies indicate that the so-called solar twins in the MW field deplete lithium by large amounts during their MS life and continue depleting it after the age of 1 Gyr or so (e.g., Meléndez et al., 2014; Carlos et al., 2016; Carlos et al., 2019). Also, in this case, the large number of open clusters observed by GES provides further insights. **Figure 4**, as we have already discussed, suggests that Li depletion in solar-type stars does stop for most of the stars before 1 Gyr, with only a few old cluster members being as depleted as the Sun. In **Figure 6**, we plot the average Li abundance for a number of clusters as a function of age, compared, on a homogeneous basis, to GES field stars. Stars similar to the Sun have been selected following the criteria indicated by Bensby and Lind (2018). The figure clearly indicates that Li depletion among cluster stars increases with increasing age; however, at variance with recent literature results for field stars, but confirming based on more solid statistics the early findings of Sestito and Randich (2005) depletion appears to stop after 1 Gyr. GES MW field stars are all old and, instead, characterized by different amounts of depletion, some of them (actually a minority) being as Li rich as the cluster stars and others being as depleted as the Sun, or even more. While the difference between clusters and field stars is striking and must be further investigated, we conclude that Li is an excellent age indicator for solar twins up to ages around 0.8–1 Gyr; instead, it cannot be easily used as an age tracer for older stars.

We close this section by noting that, after the papers cited in the previous sections aimed to use beryllium as a cosmochronometer, no further studies were performed, due to the limit of current instrumentation to reach fainter targets.

4.2.2 Using [C/N] Ratio to Infer Ages of Giant Stars

Several recent works (Masseron and Gilmore, 2015; Salaris et al., 2015; Martig et al., 2016; Ness et al., 2016; Ho et al., 2017; Ho et al., 2017; Lagarde et al., 2017; Feuillet et al., 2018; Casali et al., 2019; Hasselquist et al., 2019) have proposed using the [C/N] abundance ratio measured in the photospheres of evolved stars as an age indicator. In giant stars, the quantity and abundance of the CNO-processed material in the core are proportional to the initial mass. More massive stars, reaching higher temperatures, can convert a larger amount of ^{12}C into ^{14}N. During the episodes of convective mixing, the so-called dredge-ups, the convection reaches its maximum penetration and the processed material is brought to the stellar surface, modifying the surface abundances. The method used to derive stellar ages considers RGB stars that have undergone only the FDU. In RGB stars, the photospheres of

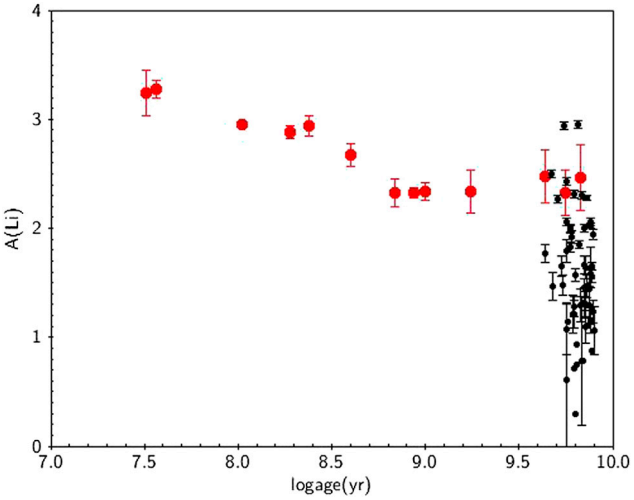

FIGURE 6 | Average Li abundances as a function of age for solar-type members of a fraction of GES clusters. Thin disc dwarfs in the same temperature range are also shown (black symbols). Solar-type stars are defined as in Bensby and Lind (2018). Error bars for the clusters represent the standard deviation around the average value.

massive stars are thus more enriched in N with respect to less massive stars. Since during the RGB phase (short with respect to the MS lifetime), the mass is related to the age, the [C/N] ratio can be used to estimate stellar ages. This is also proven by theoretical stellar models that predict a [C/N] dependence on the mass of the star (hence its age) and, as a second-order effect, on the chemical composition (e.g., Lagarde et al., 2012; Salaris et al., 2015; Lagarde et al., 2017).

Starting from the work of Masseron and Gilmore (2015), several attempts have been done to provide empirical calibrations of the relationships between stellar ages and the [C/N] abundance ratios. A key point to provide reliable empirical relationships is to have samples of stars with an independent and accurate age determination. A possible source of ages comes from asteroseismic samples of field stars observed by the Kepler and CoRoT satellites (e.g., Anders et al., 2017, for the CoroGEE sample of giant stars). Another possibility is to use the ages of stars clusters, which offer the unique opportunity of well-determined ages through isochrone fitting of many members observed across the cluster sequence (see Casali et al., 2019). In addition, star clusters cover large ranges of ages, distances, and metallicities, and they have been extensively observed by two of the major large spectroscopic surveys, GES and APOGEE. Starting from the ages determined with isochrone fitting for the open clusters observed by Gaia-ESO DR5 and by APOGEE DR14, Casali et al. (2019) calibrated a relationship between cluster age and the [C/N] ratio in their evolved stars, accurately selecting them among post-FDU stars and studying the occurrence of noncanonical mixing. In **Figure 7**, we extend the sample of Casali et al. (2019) including more clusters from the last GES data release. In the figure, we plot [C/N] vs. log(Age (yr)) in star clusters from Casali et al. (2019), which includes both GES DR5 and APOGEE DR14 and in new

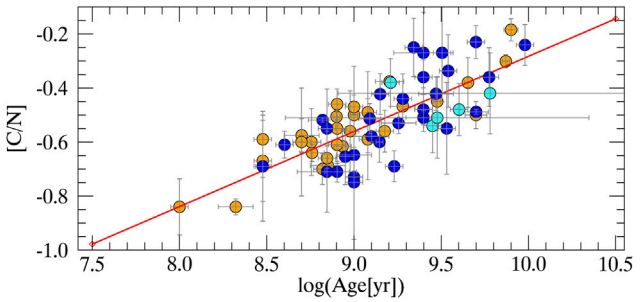

FIGURE 7 | [C/N] vs. log(Age (yr)) in star clusters from Casali et al. (2019), which includes both Gaia-ESO DR5 and APOGEE DR14, and new clusters from Gaia-ESO DR6. The symbols are color-coded by metallicity: [Fe/H] ≤ −0.25 dex (cyan circles), −0.25 < [Fe/H] ≤ 0 (blue circles), and [Fe/H] > 0 (orange circles). The red line is the linear fit to the data.

clusters from GES DR6. The symbols are color-coded by metallicity, indicating a mild dependence on [Fe/H].

As in Figure 8 of Casali et al. (2019), there is a clear relation between the [C/N] abundance ratio and the age of the stars, expressed in logarithmic form. This relationship can be used to infer the ages of giant stars for which we know the evolutionary status and we can measure C and N abundances. The typical uncertainties are in log (age) of ~0.15–0.20 dex. Although ages from [C/N] can be used only with a statistical meaning, they are excellent alternatives to ages from isochrones. They revealed to be useful to trace the differences in ages between the thin and thick disc populations, as shown, for instance, in Figure 13 of Martig et al. (2016) and in Figure 13 of Casali et al. (2019). The latter is reproduced here in **Figure 8**, where [α/Fe] is plotted as a function of [Fe/H] for field stars in the APOGEE DR14 and Gaia-ESO DR5 samples are shown. At a given [Fe/H], stars belonging to the thick disk have higher [α/Fe], and they are older than thin disc stars as confirmed from the age measured with the [C/N] ratio.

Using the results of the APOGEE survey, Hasselquist et al. (2019) exploited the [C/N] abundance ratio as an age indicator, studying the age-metallicity-abundance trends across the MW disk. Dividing their star sample in age bins, they were able to measure the radial metallicity gradient for the youngest stars (age < 2.5 Gyr) finding a slope equal to −0.060 dex kpc^{-1} in the radial range from 6 to 12 kpc, which is in agreement with other tracers, as H II regions, open clusters, Cepheids, and the CoRoGEE sample (see Anders et al., 2017, and references therein). On the other hand, they found that older stars have a flatter gradient (−0.016 dex kpc^{-1}), as predicted by simulations which include stellar migration.

4.3 Nucleosynthesis

4.3.1 Primordial Nucleosynthesis: The Cosmological Li Problem

The new observations and data collected by the recent spectroscopic observations have shed new light on the cosmological lithium problem but have not solved it. Specifically, Guiglion et al. (2016) in the context of the AMBRE project (Worley et al., 2012; de Laverny et al., 2013) measured Li in a sample of 44 metal-poor stars; they found that these stars share a rather constant lithium abundance (A(Li) = 2.08) with a typical dispersion of 0.22 dex and confirmed that the mean lithium abundance of metal-poor stars in the Galaxy is lower by 0.4–0.5 dex than the SBBN value. For the most metal-poor stars in their sample, they found further evidence for the meltdown.

Very recently, Gao et al. (2020) reported Li abundances for a very large sample (>10^5) F-G-K dwarf and subgiant stars observed in the context of GALAH, K2-HERMES, and TESS-HERMES. They divided the sample into "warm" (warmer than the Li dip, see **Section 4.1.2**) and cool stars. The metal-poor ([Fe/H] < −1) cool group very well resembles the Spite plateau, with "low" Li abundances (average around A(Li) = 2.35–2.4); the warm group contains only more metal-rich stars (−1<[Fe/H] <−0.5), which also show a plateau, but with a higher average abundance (A(Li) = 2.69 ± 0.06), roughly consistent with SBBN predictions. The authors of the paper hence claim that these stars have preserved their initial, primordial Li and that both Li depletion and Galactic enrichment have not been significant at these metallicities, thus apparently solving the inconsistency.

The Gaia-ESO Survey has mainly focused on observations of stars in the Galactic discs, with fewer targets in the halo. Also, most of the Milky Way fields have been observed with instrument settings that do not cover the Li line. Nevertheless, GES does eventually include a few halo stars with Li measurements and thus offers an opportunity to further investigate the primordial Li issue, although with a relatively small sample.

In **Figure 9**, we plot Li abundances as a function of metallicity for warm dwarf/TO MW stars (T_{eff} > 6000 K; log > 3.8). The figure shows the usual dispersion for metallicities above [Fe/H] ~−0.8, due to variable amounts of depletion. Stars with upper limits are typically cooler than stars with Li detections and, as expected, most Li-rich stars in the "metal-rich" regime are very warm and warmer than the dip. On the other hand, with exception of one Li-depleted target, metal-poor stars clearly identify the plateau; GES data do not evidence a cool and a

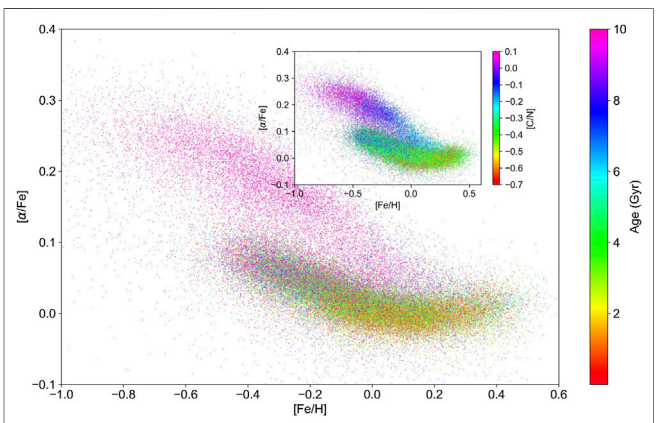

FIGURE 8 | [α/Fe] as a function of [Fe/H] for MW field stars in the APOGEE DR14 and Gaia-ESO DR5 samples. The stars are color-coded by ages computed with the relation between ages and [C/N] in Casali et al. (2019). Inner panel: the same plot but color-coded by [C/N].

warm (with higher Li) plateau, but, noticeably, one of the plateau stars is relatively warm (warmer than the dip) and shares the same Li abundance as the other stars. We mention in passing that, by considering the nine stars lying on the metal-poor Li plateau, we obtain an average value A(Li) = 2.24 ± 0.12, perfectly consistent with previous values in the literature and still a factor of ~4 below the cosmological abundance.

4.3.2 The Origin of C, N, and O and the Role of Rotation

Carbon, nitrogen, and oxygen are among the most abundant elements in the Universe. Their abundance ratios give important insights into both stellar physics and Galactic chemical evolution. Their origin, together with other elements, has been extensively discussed in recent reviews and books (see, e.g., Rauscher and Patkós, 2011; Matteucci, 2012; Nomoto et al., 2013; Kobayashi et al., 2020). An effective illustration of the differences in the production sites and time scales of the CNO elements and Fe is in Figure 1 of the review by Maiolino and Mannucci (2019). On one hand, oxygen, like most of the α elements, is produced by massive stars ($M > 8\ M_{\odot}$), which terminate their lives as core-collapse SNe, with short time scales for its release in the interstellar medium. On the other hand, a lower fraction of carbon and nitrogen is produced by massive stars. Most of their production is due to intermediate-mass stars ($2\ M_{\odot} < M < 8\ M_{\odot}$), with longer time scales and thus contributing to the ISM enrichment at later times. In this general overview, there are still several open issues concerning the nucleosynthesis of the CNO elements. As said above, carbon is produced by both massive and LIMS stars. However, the relative importance of the two major sites of production and their contribution to the global evolution of carbon over time is still unclear. For instance, some works (e.g., Gustafsson et al., 1999; Henry et al., 2000) are in favor of a dominant contribution from metal-rich massive stars, while others (e.g., Matteucci and Chiappini, 2003; Bensby and Feltzing, 2006; Mattsson, 2010) find more evidence for the production of C in LIMS during the latest stages of their evolution.

Nitrogen is mostly produced by LIMS, in which it can have both a primary and secondary origin (e.g., van den Hoek and Groenewegen, 1997; Henry et al., 2000; Meynet and Maeder, 2002). The former is produced during the thermal pulses, when some helium products might be transported into the hydrogen burning shell to produce primary nitrogen (Meynet and Maeder, 2002); the latter is the product of the CNO cycle, in which N is formed at expenses of the C and O already present in the star, and thus it increases with metallicity (e.g., Vincenzo et al., 2016). However, to explain the observed plateau in N/O at low metallicity, a production of N in short-living rapidly rotating massive stars is necessary (e.g., Henry et al., 2000; Roy et al., 2020).

Oxygen is almost entirely produced by massive stars and ejected into the interstellar medium via the explosion of core-collapse (type II) SNe. However, convection, rotation, and mass loss play a major role largely affecting the resulting yields (for a review, see Meynet et al., 2018). For instance, the rotation might increase the total metallic yields and in particular the yields of carbon and oxygen by a factor of 1.5–2.5 and of nitrogen over 2-order of magnitude (cf. Hirschi et al., 2004; Chieffi and Limongi, 2013; Limongi and Chieffi, 2018; Meynet et al., 2018).

The effects of rotation on the final yields are even larger at low metallicity and thus particularly important for the nucleosynthesis of the first generations of massive stars in the Universe (see Limongi and Chieffi, 2018, for a recent set of yields with stellar rotation). Rotation appears to drive the internal mixing and trigger several instabilities like shear instabilities or meridional currents. These instabilities are even more efficient at low metallicity, where stars are more compact and the gradients of the angular velocity are, in general, steeper (see Maeder and Meynet, 2001). The changes in the yields affect the results on the global chemical evolution in the Galaxy. Adopting yields from rotating models and making some assumption on the distribution of rotational velocities in massive stars, chemical evolution models for the halo of our Galaxy are able to explain better the observed trends of N/O and C/O (see, e.g., Chiappini et al., 2003; Chiappini et al., 2005; Prantzos, 2019). In particular, the recent work of Prantzos (2019) probed, for the first time, the effect of rotation in the production of N by using a metallicity-dependent distribution of the rotational velocities, rather than a single velocity, and thus reconciling the results of the model with the observations (see their Figure 14.3).

The advent of large spectroscopic surveys made it possible the investigation, based on sizeable statistical samples, of the behavior of carbon in different populations of our Galaxy, and its origin, for which the relative importance of massive and LIMS is still a matter of debate (e.g., Gustafsson et al., 1999; Henry et al., 2000; Chiappini et al., 2003; Matteucci and Chiappini, 2003; Bensby and Feltzing, 2006; Gavilán et al., 2006; Mattsson, 2010; Amarsi et al., 2019; Romano et al., 2019). Recently, the determination of carbon abundance from stellar spectra has been extended to nearby galaxies (see Conroy et al., 2014).

Recent constraints of the origin of C from chemical evolution are presented Franchini et al. (2020), who, thanks to a sample of F-G-K stars from the GES DR5, complemented with *Gaia* DR2 astrometry investigated the behaviors of [C/H], [C/Fe], and [C/Mg] vs. [Fe/H], [Mg/H], and age. The detected trends pose important constraints to the origin of C, suggesting that it is primarily produced in massive stars. In addition, the increase of [C/Mg] for young thin-disk stars might indicate a contribution from low-mass stars, polluting the ISM at later epochs, or increased production from massive stars at high metallicity, due to the enhanced mass loss (see, e.g., Magrini et al., 2017; Prantzos et al., 2020; Chieffi and Limongi, 2020). The GALAH survey is providing detailed abundances for a large sample of stars (70,000 stars in their DR2, see Buder et al., 2018). Griffith et al. (2019) presented C abundances from about 12,000 stars in GALAH DR2, separating the two disc components in the plane [C/Mg] vs. [Mg/H] and suggested that about 75% of solar C comes from core-collapse supernovae, while the remaining fraction is due to other sources with a delayed release of C. Romano et al. (2020) compared the data from both GALAH and GES with the results of Galactic chemical evolution models, concluding that more than 60% of the solar C abundance comes from massive stars. Their results are more generally extended, as they claim that the majority of C in the Universe

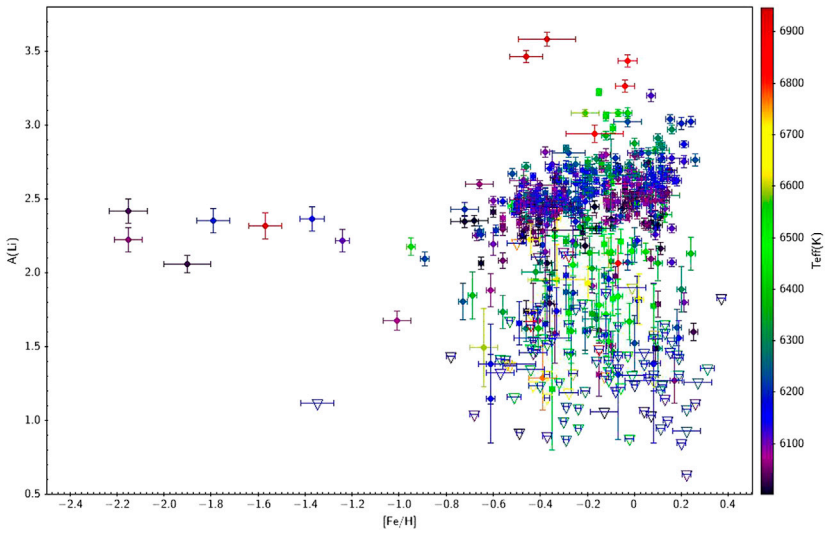

FIGURE 9 | Li abundances as a function of [Fe/H] for GES MW field stars. Only TO stars are shown. The stars are color-coded by effective temperature. Errors in A(Li) are as in previous figures, while typical errors in [Fe/H] are of the order of 0.05–0.1 dex.

comes from massive (fast) rotators, with a non-negligible contribution from intermediate-mass stars.

The data from GES are also contributing to our understanding of the evolution of oxygen. Franchini et al. (2021) analyzed the oxygen abundances of a stellar sample representative of the thin and thick discs, aiming at investigating possible differences in their oxygen content and at understanding the origin of the Galactic oxygen enrichment. They found a systematic difference between the [O/Fe] content in the thin and thick disc populations at a given [Fe/H], with the thick disc being more enhanced in [O/Fe] and [O/H] with respect to thin disc stars, and a monotonic decrease of [O/Fe] with increasing metallicity, even at very high metallicity. Their result suggests that the oxygen enrichment is mostly due to massive stars, through core-collapse supernovae, with no evidence of contributions from SNIa or AGB stars. In addition, they found that oxygen and magnesium do not follow the same evolution (see also Magrini et al., 2017), since they do not evolve in lockstep and thus they might have a different origin. Interestingly, they found that the abundance ratio [Mg/O] correlates with stellar ages, and thus it might be used as a good indicator of ages.

Finally, new NLTE abundances for carbon and oxygen have been provided for the GALAH survey (Amarsi et al., 2020). For C and O, the NLTE corrections have minor effects with respect to the LTE abundances. The observed trend in the GALAH survey of [C/Fe] vs. [Fe/H] indicates a decrease that reflects the different timescales for the production of iron (from SNIa) and of carbon (from AGB and massive stars). For O, there is a step linear decrease in [O/Fe] that reflects the two main mechanisms of production of these elements: SNIa for iron and massive stars from oxygen. The results from GALAH are in general good agreement with previous high-spectral resolution observations (Bensby et al., 2014; Amarsi et al., 2019), but they are not completely consistent with the results of the APOGEE survey (Hayes et al., 2018) that indicates a plateau in the [O/Fe] and even a slight increase in [C/Fe] at super solar metallicities. This can be due to the determination of C and O abundances in APOGEE from molecular lines, which can be affected by important systematics (see also Weinberg et al., 2019, for oxygen).

4.4 Galactic Evolution

4.4.1 Lithium, Be, and B

As mentioned in the introduction, many sources of Li production have been proposed to contribute to the Li enrichment in the Galaxy and to explain the increase from the Big Bang value to the meteoritic value, among which are asymptotic AGB stars ejecta, red giants, supernovae, cosmic ray spallation, and novae. While it is not yet clear which of them provides the dominant contribution, a few recent observational highlights have provided new constraints. In particular, the lines ^{7}Li or ^{7}Be (which then decay into ^{7}Li) have been detected in novae at the early stages, showing that these systems may represent an important source of Li enrichment (Izzo et al., 2015; Tajitsu et al., 2015; Izzo et al., 2019; Molaro et al., 2020b). Also, the spectroscopic surveys have resulted in the detection and better characterization of large samples of Li-rich and super-Li-rich giants and highlighted their importance as Li producers (see, e.g., Martell et al., 2020; de la Reza, 2020; Deepak and Reddy, 2020; Kumar et al., 2020; and references therein).

At the same time, thanks to the numerous spectroscopic observations, the empirical evolution of Li with metallicity has been much better constrained, also separating the distribution in the different Galactic components. As far as the thin disc is concerned, many recent studies based on field star samples in the solar vicinity have suggested that the upper envelope of the Li vs. [Fe/H] distribution, which should be representative of the original interstellar medium abundance, declines at supersolar metallicities (Delgado Mena et al., 2015; Guiglion et al., 2016;

Bensby and Lind, 2018; Fu et al., 2018; Stonkutė et al., 2020). On the theoretical side, it is difficult to explain and model this result (Grisoni et al., 2019), but it has been speculated that it may be due to reduced production in the metal-rich regime (Prantzos et al., 2017; Fu et al., 2018; Grisoni et al., 2019), for example, because of lower AGB yields and/or a lower occurrence of nova or binary systems at high metallicity. However, different studies (Cummings et al., 2012; Bensby and Lind 2018; Guiglion et al., 2019), instead, suggested that those findings might be affected by selection biases; in particular, metal-rich field stars in the solar vicinity would be old stars migrated from the inner parts of the disc, depleting lithium as they traveled and got older. In other words, Li in those stars may not be representative of the original ISM value.

Those latter suggestions were tested in a very recent paper by Randich et al. (2020). They proposed the idea that Li measurements in metal-rich, young populations, that have presumably not depleted any Li and hence retain their original Li content, would allow tracing the evolution of Li in the ISM at high metallicity; to this aim, they exploited GES observations of open clusters and, specifically, of cluster members with supposedly pristine unprocessed Li, representative of the ISM value (very young PMS stars or stars on the warm side of the dip). Their results are reported in **Figure 10**; specifically, they very clearly demonstrated that previous claims of a Li decline at supersolar metallicities were due to selection biases in the used samples and that Li abundance in the ISM instead does not decrease at high metallicity but may actually increase. The data presented by Randich et al. (2020) also suggested—for the first time—the presence of a mild trend of A(Li) with Galactocentric distance, or a shallow gradient, to be confirmed with the analysis of the full data set.

Interestingly, in the last few years, Li observations in the Galactic thick disc and even Bulge have been reported (Delgado Mena et al., 2015; Bensby and Lind 2018; Fu et al., 2018; Bensby et al., 2020; Stonkutė et al., 2020). The different studies on the thick disc are not in agreement: indeed, some studies claim that Li rises with metallicity; others find that the distribution is flat or even decreases. Bensby and Lind (2018) convincingly showed that these discrepancies are very likely due to how the thick disc samples were selected; in particular, using chemical abundance criteria to define the thin and thick disc samples may lead to contamination of thin-disk stars into the thick disk samples. They hence concluded that there is a steady decrease of Li with metallicity in the thick disc, in turn implying that it has not undergone significant Li production during the first few billion years in the history of the Galactic disc. This suggests that the sources of Li production have longer evolutionary timescales.

Gravitational microlensing events offer an excellent opportunity to obtain spectra of unevolved stars in the Galactic Bulge. The analysis of 91 such targets (dwarfs and subgiants) by Bensby et al. (2020) has shown that old (age > 8 Gyr) Bulge stars with subsolar metallicities behave similarly to the thick disc and do not show any sign of Li production.

As for beryllium and boron, little progress has been made in the last few years. We just cite Molaro et al. (2020a) who collected lithium and beryllium measurements from the literature to investigate their trends in the Gaia-Enceladus Galaxy (Helmi et al., 2018). They found that the Be behavior for low-metallicity stars is similar to the Galactic one, while at somewhat higher metallicity ([Fe/H] > −1), the slope is shallower and the relationship is characterized by a smaller dispersion. On the one hand, this confirms that the scatter seen among MW stars is likely due to the fact that different components had been considered, which are mixed up in the Galactic halo; on the other hand, this may mean a reduced production of Be (or enhanced production of Fe) in Gaia-Enceladus (see discussion in Molaro et al., 2020a). In any case, this pilot result clearly highlights the usefulness of Be, along with *Gaia* data, to investigate in detail the formation of the Galactic halo and discs.

4.4.2 The Galactic Evolution of CNO

The abundance ratio trends of C, N, and O over Fe and over H vs. metallicity have profound implications for our understanding of the evolutionary status of the Galactic systems in which these elements are observed, since these elements are produced on different time scales and by stars with different masses (e.g., Chiappini et al., 2003, Chiappini et al., 2005; Cescutti et al., 2009; Vincenzo and Kobayashi, 2018a; Limongi and Chieffi, 2018; Prantzos, 2019). Galactic evolution of C, N, and O can be studied by determining their abundances in main-sequence F-G-K stars, spanning large ranges of ages and metallicities. Their atmospheres still essentially preserve the initial chemical composition of their parent molecular cloud, and thus, combining stars of different ages, they can trace the Galactic chemical evolution of these elements. For oxygen, we can also use abundances in evolved giant stars, since the surface abundance of this element is only slightly modified by stellar evolution, and photospheric abundances of evolved stars maintain the original oxygen abundance. Other good traces of the spatial distribution of CNO abundances are Cepheid stars, with their well-constrained distances (see, e.g., Lemasle et al., 2013; Genovali et al., 2015; Maciel and Andrievsky, 2019).

An alternative way to stellar spectroscopy is to measure the chemical composition of H II regions and planetary nebulae from their optical and ultraviolet emission-line spectra, both collisional excited lines, for oxygen and nitrogen, and recombination lines, for carbon and oxygen (e.g., Deharveng et al., 2000; Esteban et al., 2017, Esteban et al., 2018, Esteban et al., 2019; Stanghellini and Haywood, 2018; Arellano-Córdova et al., 2020; Esteban et al., 2020; Stanghellini et al., 2020). Abundances of H II regions and planetary nebulae are excellent probes of the radial abundance gradient of the Milky Way (e.g., Esteban et al., 2017, Esteban et al., 2018; Arellano-Córdova et al., 2020; Stanghellini et al., 2020). For a discussion on the methods and on the challenging issues on nebular abundances, we refer to Kewley et al. (2019) and García-Rojas (2020). In addition, the recent review of Maiolino and Mannucci (2019) summarizes the use of N/O and C/O abundance ratios as tracers of the evolution of the Milky Way and of nearby galaxies.

In this review, we focus on the recent results based on stellar spectroscopy in our Galaxy, for which we present some recent works making use of N/O and C/O abundance ratios to infer insights on the formation of our Galaxy. The wide range of ages spanned by stars in the Milky Way field populations and in

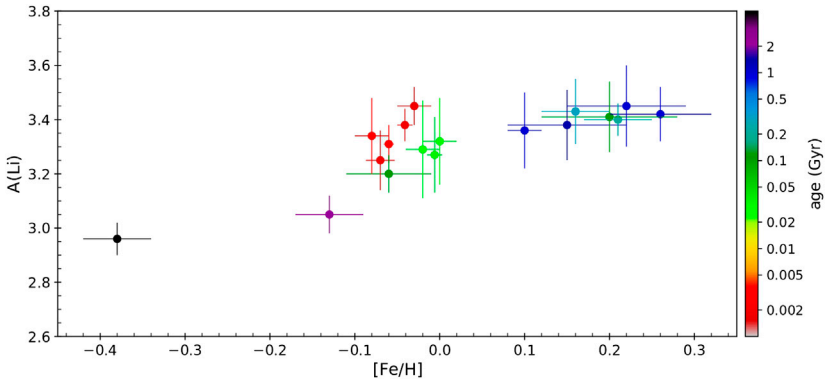

FIGURE 10 | Average maximum Li abundance for the open clusters considered in the sample of Randich et al. (2020) as a function of the cluster metallicity. Clusters are color-coded by age [figure reproduced from Randich et al. (2020)].

clusters allows us, indeed, to trace the chemical evolution of these elements.

In this framework, the abundance ratio N/O is a useful tool to study the interplay between Galactic processes (e.g., star formation efficiency, infall timescale, and outflow loading factor), thanks to the different origins and time scales of N and O (e.g., Vincenzo et al., 2016; Vincenzo and Kobayashi, 2018a; Magrini et al., 2018). In particular, the production of N in LIMS stars makes N/O a sort of clock to measure the time interval from the most recent star formation burst (e.g., Henry et al., 2000; Mollá et al., 2006). In addition, the evolution of the N/O ratio in galaxies, from low to high metallicity, is essential to understand its mechanisms of production and to validate some methods of measurement of O/H, which implicitly depend on the N/O ratio (cf. Berg et al., 2019; Roy et al., 2020). In a recent work, Magrini et al. (2018) discussed the abundances of N and O in open clusters and in field stars belonging in different portions of the thin and thick discs, showing a wide range of N/O, with values typical of the secondary production of N. This behavior is comparable to the one of H II regions located at different Galactocentric distances in external massive galaxies (see, e.g., Bresolin et al., 2004). There is also a general agreement with the global behavior of N/O vs. metallicity shown by a large sample of galaxies in the Local Universe (Belfiore et al., 2017). It is shown in **Figure 11**, where in the inner panel, we plot log (N/O) vs. [O/H] as a function of both stellar mass and radius in the sample of resolved galaxies (Belfiore et al., 2017), and in the main panel, we show log (N/O) vs. [Fe/H] in the Milky Way samples of field stars and open clusters of Magrini et al. (2018). Comparing the observed N/O vs. [Fe/H] in both cluster and field stars, with a grid of chemical evolution models, based on the models of Vincenzo et al. (2016), has provided further constraints to the inside-out formation of the Galactic disc, confirming a radial variation of the star formation and of the infall and outflow rates.

Also, the C/O ratio can be used to investigate the scenarios of the formation of our Galaxy. Recently, Amarsi et al. (2019) performed new calculations of C and O abundances in a sample of Galactic stars, considering NLTE and 3D effects, which improved the quality of the abundances and reduced the scatter. They found higher values of [C/O] at a given [O/H] in thin-disk stars with respect to the thick disc ones. The observed separation in the composition of the thin disc and of the thick disc is likely due to two main infall episodes, which happened in the Milky Way (Chiappini et al., 1997). In addition, thanks to their high-quality abundances, they detect an underdensity in the [C/O] vs. [O/H] plane, which might correspond to the onset of the second infall episode (see, e.g., Romano et al., 2019).

5 NEW PERSPECTIVES

Most of the forthcoming surveys and multiobject spectrographs, like 4MOST (de Jong et al., 2012), MOONS (Cirasuolo et al., 2011; Cirasuolo and Consortium 2020; Gonzalez et al., 2020), and WEAVE (Dalton et al., 2012), will focus on the optical and near-infrared range. MOONS will allow the measurement of chemical abundances, including CNO elements (Cirasuolo et al., 2014), in its high-resolution mode, observing two spectral regions at R~20,000 (within the J- and H-bands). The 4MOST instrument will carry out several surveys focusing on stellar objects, aiming at performing Galactic archaeology of different components of the Milky Way and the Magellanic Clouds (see, e.g., Feltzing et al., 2018). The high-resolution mode R~20,000 enables accurate abundance measurements of about 15 elements. In the spectral ranges of 4MOST, the G-band of CH (429–432 nm) will be included from which it is possible to derive the abundance of carbon, the CN band at 414–422 nm for the N abundance, and the atomic line [OI] at 630 nm for oxygen. The Li doublet at 670.8 nm will also crucially be covered. Similar bands and atomic lines will be observed in the high-resolution mode of WEAVE (R~20,000), with two spectral windows in blue/green and in red (blue 404–465 nm or green 473–545 nm arms and red arm 595–68 nm).

Complementary to this, new planned instruments will enrich our knowledge of the light-element abundances in different ways. For example, MAVIS, an adaptive-optics assisted imager and spectrographer designed for VLT (McDermid 2019), will have a high-resolution mode both in blue and in red (R~10,000–12,000), enabling the measurement

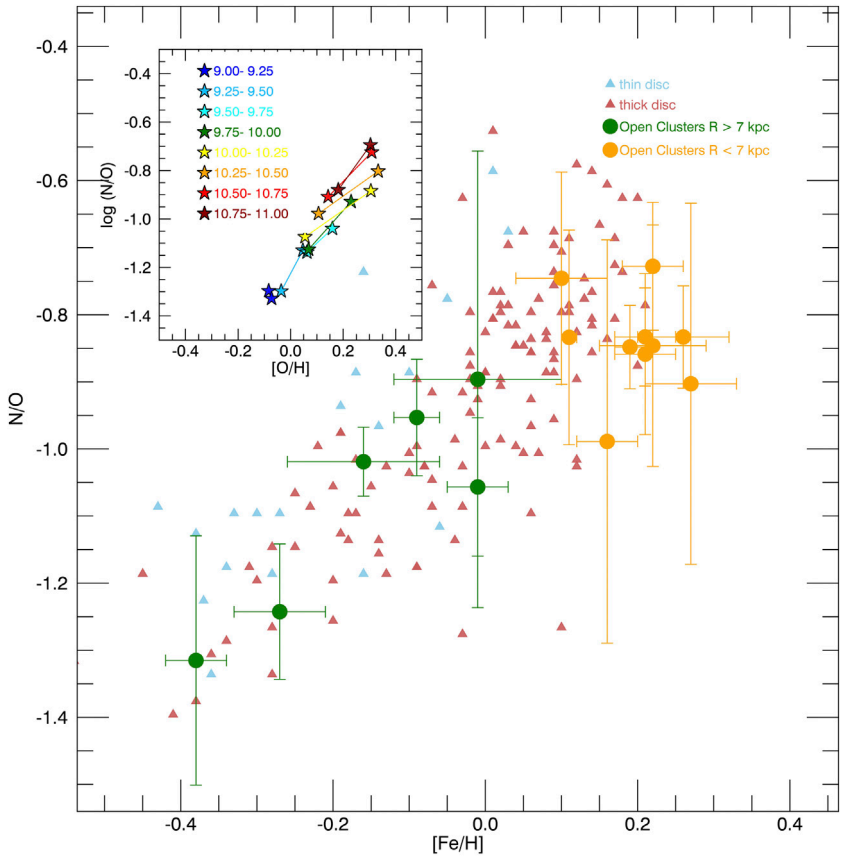

FIGURE 11 | log (N/O) vs. [Fe/H] in the Milky Way samples of field stars (blue and pink triangles and thin and thick discs, respectively) and of open clusters (in green clusters with $R_{GC} \geq 7$ kpc and in orange clusters with $R_{GC} \leq 7$ kpc) of Magrini et al. (2018). Inner panel: log (N/O) vs. [O/H] as a function of both stellar mass and radius in the sample of resolved galaxies of Belfiore et al. (2017). For each mass bin (see the legend for the range in the logarithm of the stellar mass of each bin), the uppermost star represents the innermost radial bin while the lower star represents the outermost radial bin.

of C and N from molecular bands and possibly Li in resolved stellar populations beyond the Milky Way.

Crucially, near-UV spectroscopy on the VLT will also be possible in the next few years with CUBES (Barbuy et al., 2014; Smiljanic, 2020). This will be a high-throughput, medium resolution (R ~ 20,000) spectrograph, operating between 300 and 400 nm. Phase A of the instrument started in Summer 2020. The instrument will allow us to observe significantly fainter objects than previously possible in the near-UV, opening up a new parameter space and allowing Be measurements in a variety of populations, including open and globular clusters. At the same time, CUBES measurements of CNO abundances from CN, NH, and OH bands will be possible for the same objects, offering excellent opportunities to further investigate the evolution of those elements (and in particular Be vs. O) based on homogeneous abundance determinations.

Finally, we mention that a concept study for a very high-resolution multiobject spectrograph to be put on the ESO VLT has been started. Such an instrument may indeed allow measurements of key isotopes in cluster and MW field stars.

AUTHOR CONTRIBUTIONS

SR is responsible for the sections and discussion dedicated to Li, Be, and B, while LM focused on the review of C, N, and O. Both authors equally participated in the elaboration of the manuscript.

FUNDING

LM and SR acknowledge the funding from MIUR Premiale 2016: Mitic. LM acknowledges the funding from the INAF PRIN-SKA 2017.

ACKNOWLEDGMENTS

The data used in the review have been obtained from the GES Survey Data Archive and prepared and hosted by the Wide Field Astronomy Unit, Institute for Astronomy, University of Edinburgh, which is funded by the UK Science and Technology Facilities Council (STFC).

REFERENCES

Amard, L., Palacios, A., Charbonnel, C., Gallet, F., Georgy, C., Lagarde, N., et al. (2019). First grids of low-mass stellar models and isochrones with self-consistent treatment of rotation. From 0.2 to 1.5 $M_{\odot}$ at seven metallicities from PMS to TAMS. *Astron. Astrophys.* 631, A77. doi:10.1051/0004-6361/201935160

Amarsi, A. M., Lind, K., Osorio, Y., Nordlander, T., Bergemann, M., Reggiani, H., et al. (2020). *The GALAH Survey: non-LTE departure coefficients for large spectroscopic surveys*.arXiv e-prints.

Amarsi, A. M., Nissen, P. E., and Skúladóttir, Á. (2019). Carbon, oxygen, and iron abundances in disk and halo stars. Implications of 3D non-LTE spectral line formation. *Astron. Astrophys.* 630, A104. doi:10.1051/0004-6361/201936265

Anders, F., Chiappini, C., Rodrigues, T. S., Miglio, A., Montalbán, J., Mosser, B., et al. (2017). Galactic archaeology with asteroseismology and spectroscopy: red giants observed by CoRoT and APOGEE. *Astron. Astrophys.* 597, A30. doi:10.1051/0004-6361/201527204

Angelou, G. C., Church, R. P., Stancliffe, R. J., Lattanzio, J. C., and Smith, G. H. (2011). Thermohaline mixing and its role in the evolution of carbon and nitrogen abundances in globular cluster red giants: the test case of Messier 3. *Astrophys. J.* 728, 79. doi:10.1088/0004-637X/728/2/79

Anthony-Twarog, B. J., Deliyannis, C. P., Harmer, D., Lee-Brown, D. B., Steinhauer, A., Sun, Q., et al. (2018a). Li in open clusters: cool dwarfs in the young, subsolar-metallicity cluster M35 (NGC 2168). *Astron. J.* 156, 37. doi:10.3847/1538-3881/aacb1f

Anthony-Twarog, B. J., Lee-Brown, D. B., Deliyannis, C. P., and Twarog, B. A. (2018b). WIYN open cluster study. LXXVI. Li evolution among stars of low/intermediate mass: the metal-deficient open cluster NGC 2506. *Astron. J.* 155, 138. doi:10.3847/1538-3881/aaad66

Arellano-Córdova, K. Z., Esteban, C., García-Rojas, J., and Méndez-Delgado, J. E. (2020). The Galactic radial abundance gradients of C, N, O, Ne, S, Cl, and Ar from deep spectra of H II regions. *Mon. Not. R. Astron. Soc.* 496, 1051–1076. doi:10.1093/mnras/staa1523

Asplund, M. (2005). New light on stellar abundance analyses: departures from LTE and homogeneity. *Annu. Rev. Astron. Astrophys.* 43, 481–530. doi:10.1146/annurev.astro.42.053102.134001

Asplund, M., Grevesse, N., Sauval, A. J., Allende Prieto, C., and Kiselman, D. (2004). Line formation in solar granulation. IV. [O I], O I and OH lines and the photospheric O abundance. *Astron. Astrophys.* 417, 751–768. doi:10.1051/0004-6361:20034328

Asplund, M., Grevesse, N., Sauval, A. J., and Scott, P. (2009). The chemical composition of the sun. *Annu. Rev. Astron. Astrophys.* 47, 481–522. doi:10.1146/annurev.astro.46.060407.145222

Balachandran, S. C., and Bell, R. A. (1998). Shallow mixing in the solar photosphere inferred from revised beryllium abundances. *Nature* 392, 791–793. doi:10.1038/33879

Balachandran, S. (1990). Lithium depletion and rotation in main-sequence stars. *Astrophys. J.* 354, 310–332. doi:10.1086/168691

Baraffe, I., and Chabrier, G. (2010). Effect of episodic accretion on the structure and the lithium depletion of low-mass stars and planet-hosting stars. *Astron. Astrophys.* 521, A44. doi:10.1051/0004-6361/201014979

Barbuy, B., Bawden Macanhan, V., Bristow, P., Castilho, B., Dekker, H., Delabre, B., et al. (2014). CUBES: cassegrain U-band Brazil-ESO spectrograph. *Astrophys. Sp. Sci.* 354, 191–204. doi:10.1007/s10509-014-2039-z

Barbuy, B., Trevisan, J., and de Almeida, A. (2018). Calculation of molecular line intensity in stellar atmospheres. *Publ. Astron. Soc. Austr.* 35, 46. doi:10.1017/pasa.2018.33

Beers, T. C., Suzuki, T. K., and Yoshii, Y. (2000). "The light elements Be and B as stellar chronometers in the early galaxy," in *The light elements and their evolution of IAU Symposium*. Editors L. da Silva, R. de Medeiros, and M. Spite, vol. 198, 425.

Belfiore, F., Maiolino, R., Tremonti, C., Sánchez, S. F., Bundy, K., Bershady, M., et al. (2017). SDSS IV MaNGA - metallicity and nitrogen abundance gradients in local galaxies. *Mon. Not. R. Astron. Soc.* 469, 151–170. doi:10.1093/mnras/stx789

Bellinger, E. P. (2019). A seismic scaling relation for stellar age. *Mon. Not. R. Astron. Soc.* 486, 4612–4621. doi:10.1093/mnras/stz714

Bensby, T., Feltzing, S., and Oey, M. S. (2014). Exploring the Milky Way stellar disk. A detailed elemental abundance study of 714 F and G dwarf stars in the solar neighbourhood. *Astron. Astrophys.* 562, A71. doi:10.1051/0004-6361/201322631

Bensby, T., and Feltzing, S. (2006). The origin and chemical evolution of carbon in the Galactic thin and thick discs. *Mon. Not. R. Astron. Soc.* 367, 1181–1193. doi:10.1111/j.1365-2966.2006.10037.x

Bensby, T., Feltzing, S., Yee, J. C., Johnson, J. A., Gould, A., Asplund, M., et al. (2020). Chemical evolution of the Galactic bulge as traced by microlensed dwarf and subgiant stars. VII. Lithium. *Astron. Astrophys.* 634, A130. doi:10.1051/0004-6361/201937401

Bensby, T., and Lind, K. (2018). Exploring the production and depletion of lithium in the Milky Way stellar disk. *Astron. Astrophys.* 615, A151. doi:10.1051/0004-6361/201833118

Berg, D. A., Erb, D. K., Henry, R. B. C., Skillman, E. D., and McQuinn, K. B. W. (2019). The chemical evolution of carbon, nitrogen, and oxygen in metal-poor dwarf galaxies. *Astrophys. J.* 874, 93. doi:10.3847/1538-4357/ab020a

Bertran de Lis, S., Delgado Mena, E., Adibekyan, V. Z., Santos, N. C., and Sousa, S. G. (2015). Oxygen abundances in G- and F-type stars from HARPS. Comparison of [OI] 6300 Å and OI 6158 Å. *Astron. Astrophys.* 576, A89. doi:10.1051/0004-6361/201424633

Bland-Hawthorn, J., Sharma, S., Tepper-Garcia, T., Binney, J., Freeman, K., Hayden, M., et al. (2018). *The GALAH survey and Gaia DR2: dissecting the stellar disc's phase space by age, action, chemistry and location*. ArXiv e-prints

Boesgaard, A. M., Deliyannis, C. P., and Steinhauer, A. (2005). Boron depletion in F and G dwarf stars and the beryllium-boron correlation. *Astrophys. J.* 621, 991–998. doi:10.1086/427687

Boesgaard, A. M., and King, J. R. (1993). Galactic evolution of beryllium. *Astron. J.* 106, 2309. doi:10.1086/116803

Boesgaard, A. M. (2005). "Light elements in main sequence stars: Li, Be, B, C, O," in Cosmic abundances as records of stellar evolution and nucleosynthesis of astronomical Society of the Pacific Conference Series. Editors I. Barnes, G. Thomas, and F. N. Bash, 33639.

Boesgaard, A. M., Lum, M. G., and Deliyannis, C. P. (2020). Correlated depletion and dilution of lithium and beryllium revealed by subgiants in M67. *Astrophys. J.* 888, 28. doi:10.3847/1538-4357/ab4fdb

Boesgaard, A. M., Lum, M. G., Deliyannis, C. P., King, J. R., Pinsonneault, M. H., and Somers, G. (2016). Boron abundances across the "Li-Be dip" in the Hyades cluster. *Astrophys. J.* 830, 49. doi:10.3847/0004-637X/830/1/49

Boesgaard, A. M., McGrath, E. J., Lambert, D. L., and Cunha, K. (2004). Boron benchmarks for the galactic disk. *Astrophys. J.* 606, 306–318. doi:10.1086/382672

Boesgaard, A. M., Rich, J. A., Levesque, E. M., and Bowler, B. P. (2011). Beryllium and alpha-element abundances in a large sample of metal-poor stars. *Astrophys. J.* 743, 140. doi:10.1088/0004-637X/743/2/140

Boesgaard, A. M., and Tripicco, M. J. (1986). Lithium in the Hyades cluster. *Astrophys. J.* 302, L49. doi:10.1086/184635

Bonifacio, P., Molaro, P., Sivarani, T., Cayrel, R., Spite, M., Spite, F., et al. (2007). First stars VII - lithium in extremely metal poor dwarfs. *Astron. Astrophys.* 462, 851–864. doi:10.1051/0004-6361:20064834

Bonsack, W. K., and Greenstein, J. L. (1960). The abundance of lithium in T Tauri stars and related objects. *Astrophys. J.* 131, 83. doi:10.1086/146810

Bonsack, W. K. (1959). The abundance of lithium and convective mixing in stars of type. *Astrophys. J.* 130, 843. doi:10.1086/146777

Boothroyd, A. I., Sackmann, I. J., and Wasserburg, G. J. (1995). Hot bottom burning in asymptotic giant branch stars and its effect on oxygen isotopic abundances. *Astrophys. J.* 442, L21. doi:10.1086/187806

Bouvier, J., Lanzafame, A. C., Venuti, L., Klutsch, A., Jeffries, R., Frasca, A., et al. (2016). The Gaia-ESO Survey: a lithium-rotation connection at 5 Myr?. *Astron. Astrophys.* 590, A78. doi:10.1051/0004-6361/201628336

Bouvier, J. (2020). The lithium-rotation connection in young stars. *Mem. Soc. Astron. Italiana.* 91, 39.

Bravi, L., Zari, E., Sacco, G. G., Randich, S., Jeffries, R. D., Jackson, R. J., et al. (2018). The Gaia-ESO Survey: a kinematical and dynamical study of four young open clusters. *Astron. Astrophys.* 615, A37. doi:10.1051/0004-6361/201832645

Bresolin, F., Garnett, D. R., Kennicutt, J., and Robert, C. (2004). Abundances of metal-rich H II regions in M51. *Astrophys. J.* 615, 228–241. doi:10.1086/424377

Brown, J. A., Sneden, C., Lambert, D. L., Dutchover, J., and Edward (1989). A search for lithium-rich giant stars. *Astrophys. J.* 71, 293. doi:10.1086/191375

Buder, S., Asplund, M., Duong, L., Kos, J., Lind, K., Ness, M. K., et al. (2018). The GALAH Survey: second data release. *Mon. Not. R. Astron. Soc.* 478, 4513–4552. doi:10.1093/mnras/sty1281

Busso, M., Palmerini, S., Maiorca, E., Cristallo, S., Straniero, O., Abia, C., et al. (2010). On the need for deep-mixing in asymptotic giant branch stars of low mass. *Astrophys. J.* 717, L47–L51. doi:10.1088/2041-8205/717/1/L47

Busso, M., Wasserburg, G. J., Nollett, K. M., and Calandra, A. (2007). Can extra mixing in RGB and AGB stars Be attributed to magnetic mechanisms?. *Astrophys. J.* 671, 802–810. doi:10.1086/522616

Caffau, E., Ludwig, H. G., Steffen, M., Ayres, T. R., Bonifacio, P., Cayrel, R., et al. (2008). The photospheric solar oxygen project. I. Abundance analysis of atomic lines and influence of atmospheric models. *Astron. Astrophys.* 488, 1031–1046. doi:10.1051/0004-6361:200809885

Cameron, A. G. W. (1968). "A new table of abundances of the elements in the solar system", in *Origin and distribution of the elements*, 125–143.

Cameron, A. G. W. (1973). Abundances of the elements in the solar system. *Space Sci. Rev.* 15, 121–146. doi:10.1007/BF00172440

Cameron, A. G. W., and Fowler, W. A. (1971). Lithium and the s-PROCESS in red-giant stars. *Astrophys. J.* 164, 111. doi:10.1086/150821

Cantat-Gaudin, T., Anders, F., Castro-Ginard, A., Jordi, C., Romero-Gómez, M., Soubiran, C., et al. (2020). Painting a portrait of the Galactic disc with its stellar clusters. *Astron. Astrophys.* 640, A1. doi:10.1051/0004-6361/202038192

Carigi, L., Peimbert, M., Esteban, C., and García-Rojas, J. (2005). Carbon, nitrogen, and oxygen galactic gradients: a solution to the carbon enrichment problem. *Astrophys. J.* 623, 213–224. doi:10.1086/428491

Carlos, M., Meléndez, J., Spina, L., dos Santos, L. A., Bedell, M., Ramirez, I., et al. (2019). The Li-age correlation: the Sun is unusually Li deficient for its age. *Mon. Not. R. Astron. Soc.* 485, 4052–4059. doi:10.1093/mnras/stz681

Carlos, M., Nissen, P. E., and Meléndez, J. (2016). Correlation between lithium abundances and ages of solar twin stars. *Astron. Astrophys.* 587, A100. doi:10.1051/0004-6361/201527478

Casali, G., Magrini, L., Tognelli, E., Jackson, R., Jeffries, R. D., Lagarde, N., et al. (2019). The Gaia-ESO survey: calibrating a relationship between age and the [C/N] abundance ratio with open clusters. *Astron. Astrophys.* 629, A62. doi:10.1051/0004-6361/201935282

Casey, A. R., Ho, A. Y. Q., Ness, M., Hogg, D. W., Rix, H.-W., Angelou, G. C., et al. (2019). Tidal interactions between binary stars can drive lithium production in low-mass red giants. *Astrophys. J.* 880, 125. doi:10.3847/1538-4357/ab27bf

Casey, A. R., Ruchti, G., Masseron, T., Randich, S., Gilmore, G., Lind, K., et al. (2016). The Gaia-ESO Survey: revisiting the Li-rich giant problem. *Mon. Not. R. Astron. Soc.* 461, 3336–3352. doi:10.1093/mnras/stw1512

Cescutti, G., Matteucci, F., McWilliam, A., and Chiappini, C. (2009). The evolution of carbon and oxygen in the bulge and disk of the Milky Way. *Astron. Astrophys.* 505, 605–612. doi:10.1051/0004-6361/200912759

Cescutti, G., and Molaro, P. (2019). ^{7}Li evolution in the thin and thick discs of the milky way. *Mon. Not. R. Astron. Soc.* 482, 4372.

Charbonnel, C. (1995). A consistent explanation for 12C/13C, 7Li and 3He anomalies in red giant stars. *Astrophys. J.* 453, L41. doi:10.1086/309744

Charbonnel, C., and Balachandran, S. C. (2000). The Nature of the lithium rich giants. Mixing episodes on the RGB and early-AGB. *Astron. Astrophys.* 359, 563–572.

Charbonnel, C., Brown, J. A., and Wallerstein, G. (1998). Mixing processes during the evolution of red giants with moderate metal deficiencies: the role of molecular-weight barriers. *Astron. Astrophys.* 332, 204–214.

Charbonnel, C., Lagarde, N., Jasniewicz, G., North, P. L., Shetrone, M., Krugler Hollek, J., et al. (2020). Lithium in red giant stars: constraining non-standard mixing with large surveys in the Gaia era. *Astron. Astrophys.* 633, A34. doi:10.1051/0004-6361/201936360

Charbonnel, C., and Lagarde, N. (2010). Thermohaline instability and rotation-induced mixing. I. Low- and intermediate-mass solar metallicity stars up to the end of the AGB. *Astron. Astrophys.* 522, A10. doi:10.1051/0004-6361/201014432

Charbonnel, C., and Talon, S. (2008). "Deep inside low-mass stars," in The art of modeling stars in the 21st Century of IAU Symposium. Editors L. Deng and K. L. Chan, 252, 163–174. doi:10.1017/S1743921308022710

Charbonnel, C., and Zahn, J. P. (2007). Thermohaline mixing: a physical mechanism governing the photospheric composition of low-mass giants. *Astron. Astrophys.* 467, L15–L18. doi:10.1051/0004-6361:20077274

Chiappini, C., Hirschi, R., Matteucci, F., Meynet, G., Ekstroem, S., and Maeder, A. (2006). "The impact of stellar rotation on the CNO abundance patterns in the Milky Way at low metallicities". in International Symposium on Nuclear Astrophysics - Nuclei in the Cosmos.

Chiappini, C., Matteucci, F., and Ballero, S. K. (2005). The origin of nitrogen. Implications of recent measurements of N/O in Galactic metal-poor halo stars. *Astron. Astrophys.* 437, 429–436. doi:10.1051/0004-6361:20042292

Chiappini, C., Matteucci, F., and Gratton, R. (1997). The chemical evolution of the galaxy: the two-infall model. *Astrophys. J.* 477, 765–780. doi:10.1086/303726

Chiappini, C., Romano, D., and Matteucci, F. (2003). Oxygen, carbon and nitrogen evolution in galaxies. *Mon. Not. R. Astron. Soc.* 339, 63–81. doi:10.1046/j.1365-8711.2003.06154.x

Chieffi, A., and Limongi, M. (2013). Pre-supernova evolution of rotating solar metallicity stars in the mass range 13–120$m_{\odot}$ and their explosive yields. *Astrophys. J.* 764, 21. doi:10.1088/0004-637X/764/1/21

Chieffi, A., and Limongi, M. (2020). The pre-supernova core mass-radius relation of massive stars: understanding its formation and evolution. *Astrophys. J.* 890, 43. doi:10.3847/1538-4357/ab6739

Christlieb, N., Gustafsson, B., Korn, A. J., Barklem, P. S., Beers, T. C., Bessell, M. S., et al. (2004). HE 0107-5240, a chemically ancient star. I. A detailed abundance analysis. *Astrophys. J.* 603, 708–728. doi:10.1086/381237

Cirasuolo, M., Afonso, J., Bender, R., Bonifacio, P., Evans, C., Kaper, L., et al. (2011). MOONS: the multi-object optical and near-infrared spectrograph. *The Messenger* 145, 11–13.

Cirasuolo, M., Afonso, J., Carollo, M., Flores, H., Maiolino, R., Oliva, E., et al. (2014). "MOONS: the multi-object optical and near-infrared spectrograph for the VLT" in Proc. SPIE, of Society of Photo-Optical Instrumentation Engineers (SPIE) Conference Series, 9147, 91470N. doi:10.1117/12.2056012

Cirasuolo, M., and consortium, t. M. (2020). *MOONS: the new multi-object spectrograph for the VLT*.arXiv e-printsarXiv:2009.00628

Conroy, C., Graves, G. J., and van Dokkum, P. G. (2014). Early-type galaxy archeology: ages, abundance ratios, and effective temperatures from full-spectrum fitting. *Astrophys. J.* 780, 33. doi:10.1088/0004-637X/780/1/33

Cristallo, S., Straniero, O., Gallino, R., Lederer, M. T., Piersanti, L., and Domínguez, I. (2008). "Progresses in AGB modelling," in Evolution and nucleosynthesis in AGB stars of American Institute of Physics Conference Series. Editors R. Guandalini, S. Palmerini, and M. Busso, 1001, 3–10. doi:10.1063/1.2916987

Cristallo, S., and Vescovi, D. (2020). Lithium evolution in RGB and AGB stars. *Mem. Soc. Astron. Italiana.* 91, 67.

Cummings, J. D., Deliyannis, C. P., Anthony-Twarog, B., Twarog, B., and Maderak, R. M. (2012). Lithium abundances of the super-metal-rich open cluster NGC 6253. *Astron. J.* 144, 137. doi:10.1088/0004-6256/144/5/137

Cunha, K. (2010). "Boron abundances in the Galactic disk," in *Light elements in the Universe*. Editors C. Charbonnel, M. Tosi, F. Primas, and C. Chiappini, 268, 243–248. doi:10.1017/S1743921310004199

Cyburt, R. H., Fields, B. D., Olive, K. A., and Yeh, T.-H. (2016). Big bang nucleosynthesis: present status. *Rev. Mod. Phys.* 88, 015004. doi:10.1103/RevModPhys.88.015004

Dalton, G., Trager, S. C., Abrams, D. C., Carter, D., Bonifacio, P., Aguerri, J. A. L., et al. (2012). "WEAVE: the next generation wide-field spectroscopy facility for the William Herschel Telescope", in Proc. SPIE of Society of Photo-Optical Instrumentation Engineers (SPIE) Conference Series, 8446, 84460P. doi:10.1117/12.925950

Davies, G. R., and Miglio, A. (2016). Asteroseismology of red giants: from analysing light curves to estimating ages. *Astron. Nachr.* 337, 774. doi:10.1002/asna.201612371

de Jong, R. S., Bellido-Tirado, O., Chiappini, C., Depagne, É., Haynes, R., Johl, D., et al. (2012). "4MOST: 4-metre multi-object spectroscopic telescope", in Proc. SPIE of Society of Photo-Optical Instrumentation Engineers (SPIE) Conference Series. 8446, 84460T. doi:10.1117/12.926239

de la Reza, R. (2020). On the super lithium rich giant star phenomena. *Mem. Soc. Astron. Italiana* 91, 63.

de Laverny, P., Recio-Blanco, A., Worley, C. C., De Pascale, M., Hill, V., and Bijaoui, A. (2013). The AMBRE project: stellar parameterisation of ESO archived spectra. *The Messenger* 153, 18–21.

Deal, M., Goupil, M. J., Marques, J. P., Reese, D. R., and Lebreton, Y. (2020). Chemical mixing in low mass stars. I. Rotation against atomic diffusion including radiative acceleration. *Astron. Astrophys.* 633, A23. doi:10.1051/0004-6361/201936666

Deepakand Reddy, B. E. (2020). Lithium in the Galaxy: current status and contribution from the low-mass giants?. *Mem. Soc. Astron. Italiana* 91, 134–137.

Deharveng, L., Peña, M., Caplan, J., and Costero, R. (2000). Oxygen and helium abundances in Galactic Hii regions - II. Abundance gradients. *Mon. Not. R. Astron. Soc.* 311, 329–345. doi:10.1046/j.1365-8711.2000.03030.x

Delgado Mena, E., Bertrán de Lis, S., Adibekyan, V. Z., Sousa, S. G., Figueira, P., Mortier, A., et al. (2015). Li abundances in F stars: planets, rotation, and Galactic evolution. *Astron. Astrophys.* 576, A69. doi:10.1051/0004-6361/201425433

Delgado Mena, E., Israelian, G., González Hernández, J. I., Santos, N. C., and Rebolo, R. (2012). Be abundances in cool main-sequence stars with exoplanets. *Astrophys. J.* 746, 47. doi:10.1088/0004-637X/746/1/47

Delgado Mena, E., Israelian, G., González Hernández, J. I., Sousa, S. G., Mortier, A., Santos, N. C., et al. (2014). Li depletion in solar analogues with exoplanets. Extending the sample. *Astron. Astrophys.* 562, A92. doi:10.1051/0004-6361/201321493

Deliyannis, C. P., Anthony-Twarog, B. J., Lee-Brown, D. B., and Twarog, B. A. (2019). Li evolution and the open cluster NGC 6819: a correlation between Li depletion and spindown in dwarfs more massive than the F-dwarf Li-dip. *Astron. J.* 158, 163. doi:10.3847/1538-3881/ab3fad

Deliyannis, C. P., Demarque, P., and Kawaler, S. D. (1990). Lithium in halo stars from standard stellar evolution. *Astrophys. J.* 73, 21. doi:10.1086/191439

Deliyannis, C. P. (2000). "Lithium and Beryllium as diagnostics of stellar interior physical processes," in Stellar clusters and associations: convection, rotation, and dynamos of Astronomical Society of the Pacific Conference Series. Editors R. Pallavicini, G. Micela, and S. Sciortino, 198, 235.

Denissenkov, P. A., Da Costa, G. S., Norris, J. E., and Weiss, A. (1998). The puzzling MgAl anticorrelation in globular-cluster red giants: primordial plus deep mixing scenario?. *Astron. Astrophys.* 333, 926–941.

Denissenkov, P. A., and Herwig, F. (2004). Enhanced extra mixing in low-mass red giants: lithium production and thermal stability. *Astrophys. J.* 612, 1081–1091. doi:10.1086/422575

Denissenkov, P. A., Pinsonneault, M., and MacGregor, K. B. (2009). Magneto-thermohaline mixing in red giants. *Astrophys. J.* 696, 1823–1833. doi:10.1088/0004-637X/696/2/1823

Denissenkov, P. A., and Tout, C. A. (2000). On a physical mechanism for extra mixing in globular cluster red giants. *Mon. Not. R. Astron. Soc.* 316, 395–406. doi:10.1046/j.1365-8711.2000.03498.x

Denissenkov, P. A., and VandenBerg, D. A. (2003). Canonical extra mixing in low-mass red giants. *Astrophys. J.* 593, 509–523. doi:10.1086/376410

Desidera, S., D'Orazi, V., and Lugaro, M. (2016). Is beryllium ultra-depletion in solar-type stars linked to the presence of a white dwarf companion?. *Astron. Astrophys.* 587, A46. doi:10.1051/0004-6361/201527410

Drazdauskas, A., Tautvaišienė, G., Randich, S., Bragaglia, A., Mikolaitis, Š., and Janulis, R. (2016). The extent of mixing in stellar interiors: the open clusters Collinder 261 and Melotte 66. *Astron. Astrophys.* 589, A50. doi:10.1051/0004-6361/201628138

Dumont, T., Palacios, A., Charbonnel, C., Richard, O., Amard, L., Augustson, K., et al. (2020). *Lithium depletion and angular momentum transport in solar-type stars*.arXiv e-printsarXiv:2012.03647

Duncan, D. K., Lambert, D. L., and Lemke, M. (1992). The abundance of boron in three halo stars. *Astrophys. J.* 401, 584. doi:10.1086/172088

D'Antona, F., and Matteucci, F. (1991). Galactic evolution of lithium. *Astron. Astrophys.* 248, 62.

D'Antona, F., Ventura, P., Fabiola Marino, A., Milone, A. P., Tailo, M., Di Criscienzo, M., et al. (2019). The lithium test for multiple populations in globular clusters: lithium in NGC 2808. *Astrophys. J.* 871, L19. doi:10.3847/2041-8213/aafbec

D'Antona, F., Ventura, P., and Mazzitelli, I. (2000). First results on pre-main-sequence evolution, including a magnetic field. *Astrophys. J.* 543, L77–L80. doi:10.1086/318172

D'Orazi, V., Gratton, R. G., Angelou, G. C., Bragaglia, A., Carretta, E., Lattanzio, J. C., et al. (2015). Lithium abundances in globular cluster giants: NGC 1904, NGC 2808, and NGC 362. *Mon. Not. R. Astron. Soc.* 449, 4038–4047. doi:10.1093/mnras/stv612

Eggleton, P. P., Dearborn, D. S. P., and Lattanzio, J. C. (2008). Compulsory deep mixing of ^{3}He and CNO isotopes in the envelopes of low-mass red giants. *Astrophys. J.* 677, 581–592. doi:10.1086/529024

Eggleton, P. P., Dearborn, D. S. P., and Lattanzio, J. C. (2006). Deep mixing of ^{3}He: reconciling big bang and stellar nucleosynthesis. *Science* 314, 1580. doi:10.1126/science.1133065

Esteban, C., Bresolin, F., García-Rojas, J., and Toribio San Cipriano, L. (2020). Carbon, nitrogen, and oxygen abundance gradients in M101 and M31. *Mon. Not. R. Astron. Soc.* 491, 2137–2155. doi:10.1093/mnras/stz3134

Esteban, C., Fang, X., García-Rojas, J., and Toribio San Cipriano, L. (2017). The radial abundance gradient of oxygen towards the Galactic anti-centre. *Mon. Not. R. Astron. Soc.* 471, 987–1004. doi:10.1093/mnras/stx1624

Esteban, C., García-Rojas, J., Arellano-Córdova, K. Z., and Méndez-Delgado, J. E. (2019). *Galactic abundance gradients from deep spectra of HII regions*.arXiv e-printsarXiv:1905.10129

Esteban, C., García-Rojas, J., Peimbert, M., Peimbert, A., Ruiz, M. T., Rodríguez, M., et al. (2005). Carbon and oxygen galactic gradients: observational values from H II region recombination lines. *Astrophys. J.* 618, L95–L98. doi:10.1086/426889

Esteban, C., and García-Rojas, J. (2018). Revisiting the radial abundance gradients of nitrogen and oxygen of the Milky Way. *Mon. Not. R. Astron. Soc.* 478, 2315–2336. doi:10.1093/mnras/sty1168

Esteban, C., Toribio San Cipriano, L., and García-Rojas, J. (2018). "The abundance discrepancy in HII regions," in *Chemical abundances in gaseous nebulae*. Editors G. Hägele, M. Cardaci, and E. Pérez-Montero, 23.

Feiden, G. A., and Chaboyer, B. (2013). "Magnetic field induced radius inflation of low-mass stars," in *EAS Publications Series*. Editors K. Pavlovski, A. Tkachenko, and G. Torres (EAS Publications Series), 64, 127–130. doi:10.1051/eas/1364017

Feltzing, S., Bensby, T., Bergemann, M., Chiappini, C., Christlieb, N., Cioni, M. R., et al. (2018). "Galactic archeology with 4MOST," in *Rediscovering our galaxy*. Editors C. Chiappini, I. Minchev, E. Starkenburg, and M. Valentini, 334, 225–232. doi:10.1017/S1743921317008730

Feuillet, D. K., Bovy, J., Holtzman, J., Weinberg, D. H., García-Hernández, D., Hearty, F. R., et al. (2018). Age-resolved chemistry of red giants in the solar neighbourhood. *Mon. Not. R. Astron. Soc.* 477, 2326–2348. doi:10.1093/mnras/sty779

Franchini, M., Morossi, C., Di Marcantonio, P., Chavez, M., Adibekyan, V., Bensby, T., et al. (2021). The Gaia-ESO survey: oxygen abundance in the galactic thin and thick disks. *Astron. J.* 161, 9. doi:10.3847/1538-3881/abc69b

Franchini, M., Morossi, C., Di Marcantonio, P., Chavez, M., Adibekyan, V. Z., Bayo, A., et al. (2020). The Gaia-ESO survey: carbon abundance in the galactic thin and thick disks. *Astrophys. J.* 888, 55. doi:10.3847/1538-4357/ab5dc4

Franciosini, E., Tognelli, E., Degl'Innocenti, S., Prada Moroni, P. G., and Randich, S. (2020). Lithium evolution in young open clusters from the Gaia-ESO Survey. *Mem. Soc. Astron. Italiana* 91, 80.

Frost, C. A., Lattanzio, J. C., and Wood, P. R. (1998). Degenerate thermal pulses in asymptotic giant branch stars. *Astrophys. J.* 500, 355–359. doi:10.1086/305730

Fu, X., Romano, D., Bragaglia, A., Mucciarelli, A., Lind, K., Delgado Mena, E., et al. (2018). The Gaia-ESO Survey: lithium enrichment histories of the Galactic thick and thin disc. *Astron. Astrophys.* 610, A38. doi:10.1051/0004-6361/201731677

Gaia CollaborationPrusti, T., de Bruijne, J. H. J., Brown, A. G. A., Vallenari, A., et al. (2016). The Gaia mission. *Astron. Astrophys.* 595, A1. doi:10.1051/0004-6361/201629272

Gaia CollaborationBrown, A. G. A., Vallenari, A., Prusti, T., de Bruijne, et al. (2018). Gaia Data Release 2. Summary of the contents and survey properties. *Astron. Astrophys.* 616, A1. doi:10.1051/0004-6361/201833051

Gaia CollaborationBrown, A. G. A., Vallenari, A., Prusti, T., de Bruijne, J. H. J., Babusiaux, C., et al. (2020). *Gaia early data release 3: summary of the contents and survey properties*.arXiv e-printsarXiv:2012.01533

Gao, Q., Shi, J.-R., Yan, H.-L., Yan, T.-S., Xiang, M.-S., Zhou, Y.-T., et al. (2019). Lithium-rich giants in LAMOST survey. I. The catalog. *Astrophys. J.* 245, 33. doi:10.3847/1538-4365/ab505c

Gao, X., Lind, K., Amarsi, A. M., Buder, S., Bland-Hawthorn, J., Campbell, S. W., et al. (2020). The GALAH survey: a new constraint on cosmological lithium and

Galactic lithium evolution from warm dwarf stars. *Mon. Not. R. Astron. Soc.* 497, L30–L34. doi:10.1093/mnrasl/slaa109

Garcia Lopez, R. J., Lambert, D. L., Edvardsson, B., Gustafsson, B., Kiselman, D., and Rebolo, R. (1998). Boron in very metal poor stars. *Astrophys. J.* 500, 241. doi:10.1086/305722

Garcia Lopez, R. J., Severino, G., and Gomez, M. T. (1995). Galactic evolution of beryllium. I. NLTE effects and accuracy of beryllium abundances in metal-poor stars. *Astron. Astrophys.* 297, 787.

García Pérez, A. E., Allende Prieto, C., Holtzman, J. A., Shetrone, M., Mészáros, S., Bizyaev, D., et al. (2016). ASPCAP: the APOGEE stellar parameter and chemical abundances Pipeline. *Astron. J.* 151, 144. doi:10.3847/0004-6256/151/6/144

García-Rojas, J. (2020). *Physical conditions and chemical abundances in photoionized nebulae from optical spectra*.arXiv e-printsarXiv:2001.03388

Gavilán, M., Mollá, M., and Buell, J. F. (2006). Low and intermediate mass star yields. II. The evolution of nitrogen abundances. *Astron. Astrophys.* 450, 509–521. doi:10.1051/0004-6361:20053590

Genovali, K., Lemasle, B., da Silva, R., Bono, G., Fabrizio, M., Bergemann, M., et al. (2015). On the α-element gradients of the Galactic thin disk using Cepheids. *Astron. Astrophys.* 580, A17. doi:10.1051/0004-6361/201525894

Gilmore, G., Gustafsson, B., Edvardsson, B., and Nissen, P. E. (1992). Is beryllium in metal-poor stars of galactic or cosmological origin?. *Nature* 357, 379–384. doi:10.1038/357379a0

Gilmore, G., Randich, S., Asplund, M., Binney, J., Bonifacio, P., Drew, J., et al. (2012). The Gaia-ESO public spectroscopic survey. *The Messenger.* 147, 25–31.

Gilroy, K. K., and Brown, J. A. (1991). Carbon isotope ratios along the giant branch of M67. *Astrophys. J.* 371, 578. doi:10.1086/169922

Gilroy, K. K. (1989). Carbon isotope ratios and lithium abundances in open cluster giants. *Astrophys. J.* 347, 835. doi:10.1086/168173

González Hernández, J. I., Bonifacio, P., Caffau, E., Ludwig, H. G., Steffen, M., Monaco, L., et al. (2019). The ^{6}Li/^{7}Li isotopic ratio in the metal-poor binary CS22876-032. *Astron. Astrophys.* 628, A111. doi:10.1051/0004-6361/201936011

Gonzalez, O. A., Mucciarelli, A., Origlia, L., Schultheis, M., Caffau, E., Di Matteo, P., et al. (2020). *MOONS surveys of the Milky way and its satellites*.arXiv e-printsarXiv:2009.00635

Gonzalez, O. A., Zoccali, M., Monaco, L., Hill, V., Cassisi, S., Minniti, D., et al. (2009). Li-rich red giant branch stars in the Galactic bulge. *Astron. Astrophys.* 508, 289–295. doi:10.1051/0004-6361/200912469

Gonçalves, B. F. O., da Costa, J. S., de Almeida, L., Castro, M., and do Nascimento, J. (2020). Li-rich giant stars under scrutiny: binarity, magnetic activity and the evolutionary status after Gaia DR2. *Mon. Not. R. Astron. Soc.* 498, 2295–2308. doi:10.1093/mnras/staa2408

Gratton, R. G., Carretta, E., and Bragaglia, A. (2012). Multiple populations in globular clusters. Lessons learned from the Milky Way globular clusters. *Astron. Astrophys. Rev.* 20, 50. doi:10.1007/s00159-012-0050-3

Gratton, R. G., and D'Antona, F. (1989). HD 39853 : a high velocity K5 III star with an exceptionally large Li content. *Astron. Astrophys.* 215, 66–78.

Gratton, R. G., Sneden, C., Carretta, E., and Bragaglia, A. (2000). Mixing along the red giant branch in metal-poor field stars. *Astron. Astrophys.* 354, 169–187.

Gratton, R., Sneden, C., and Carretta, E. (2004). Abundance variations within globular clusters. *Annu. Rev. Astron. Astrophys.* 42, 385–440. doi:10.1146/annurev.astro.42.053102.133945

Greenstein, J. L., and Richardson, R. S. (1951). Lithium and the internal circulation of the sun. *Astrophys. J.* 113, 536. doi:10.1086/145424

Greenstein, J. L., and Tandberg Hanssen, E. (1954). The abundance of beryllium in the sun. *Astrophys. J.* 119, 113. doi:10.1086/145800

Griffith, E., Johnson, J. A., and Weinberg, D. H. (2019). Abundance ratios in GALAH DR2 and their implications for nucleosynthesis. *Astrophys. J.* 886, 84. doi:10.3847/1538-4357/ab4b5d

Grisoni, V., Matteucci, F., Romano, D., and Fu, X. (2019). Evolution of lithium in the Milky Way halo, discs, and bulge. *Mon. Not. R. Astron. Soc.* 489, 3539–3546. doi:10.1093/mnras/stz2428

Guiglion, G., Chiappini, C., Romano, D., Matteucci, F., Anders, F., Steinmetz, M., et al. (2019). Explaining the decrease in ISM lithium at super-solar metallicities in the solar vicinity. *Astron. Astrophys.* 623, A99. doi:10.1051/0004-6361/201834203

Guiglion, G., de Laverny, P., Recio-Blanco, A., Worley, C. C., De Pascale, M., Masseron, T., et al. (2016). The AMBRE project: constraining the lithium evolution in the Milky Way. *Astron. Astrophys.* 595, A18. doi:10.1051/0004-6361/201628919

Gustafsson, B., Karlsson, T., Olsson, E., Edvardsson, B., and Ryde, N. (1999). The origin of carbon, investigated by spectral analysis of solar-type stars in the Galactic Disk. *Astron. Astrophys.* 342, 426–439.

Harutyunyan, G., Steffen, M., Mott, A., Caffau, E., Israelian, G., González Hernández, J. I., et al. (2018). 3D non-LTE corrections for Li abundance and ^{6}Li/^{7}Li isotopic ratio in solar-type stars. I. Application to HD 207129 and HD 95456. *Astron. Astrophys.* 618, A16.

Hasselquist, S., Holtzman, J. A., Shetrone, M., Tayar, J., Weinberg, D. H., Feuillet, D., et al. (2019). APOGEE [C/N] abundances across the galaxy: migration and infall from red giant ages. *Astrophys. J.* 871, 181. doi:10.3847/1538-4357/aaf859

Hayes, C. R., Majewski, S. R., Shetrone, M., Fernández-Alvar, E., Allende Prieto, C., Schuster, W. J., et al. (2018). Disentangling the galactic halo with APOGEE. I. Chemical and kinematical investigation of distinct metal-poor populations. *Astrophys. J.* 852, 49. doi:10.3847/1538-4357/aa9cec

Helmi, A., Babusiaux, C., Koppelman, H. H., Massari, D., Veljanoski, J., and Brown, A. G. A. (2018). The merger that led to the formation of the Milky Way's inner stellar halo and thick disk. *Nature.* 563, 85–88. doi:10.1038/s41586-018-0625-x

Henkel, K., Karakas, A. I., Casey, A. R., Church, R. P., and Lattanzio, J. C. (2018). Thermohaline mixing in extremely metal-poor stars. *Astrophys. J.* 863, L5. doi:10.3847/2041-8213/aad552

Henry, R. B. C., Edmunds, M. G., and Köppen, J. (2000). On the cosmic origins of carbon and nitrogen. *Astrophys. J.* 541, 660–674. doi:10.1086/309471

Hirschi, R., Meynet, G., and Maeder, A. (2004). Stellar evolution with rotation. XII. Presupernova models. *Astron. Astrophys.* 425, 649–670. doi:10.1051/0004-6361:20041095

Ho, A. Y. Q., Rix, H.-W., Ness, M. K., Hogg, D. W., Liu, C., and Ting, Y.-S. (2017). Masses and ages for 230,000 LAMOST giants, via their carbon and nitrogen abundances. *Astrophys. J.* 841, 40. doi:10.3847/1538-4357/aa6db3

Iben, I., Jr. (1991). "Asymptotic giant branch stars: thermal pulses, carbon production, and dredge up; neutron sources and S-process nucleosynthesis," in *Evolution of stars: the photospheric abundance connection of IAU Symposium*. Editors G. Michaud and A. V. Tutukov, 145, 257.

Iben, I., Jr., and Icko (1967). Stellar evolution.VI. Evolution from the main sequence to the red-giant branch for stars of mass 1 M_{sun}, 1.25 M_{sun}, and 1.5 M_{sun}. *Astrophys. J.* 147, 624. doi:10.1086/149040

Iben, I., Jr., and Renzini, A. (1983). Asymptotic giant branch evolution and beyond. *Annu. Rev. Astron. Astrophys.* 21, 271–342. doi:10.1146/annurev.aa.21.090183.001415

Israelian, G., Ecuvillon, A., Rebolo, R., García-López, R., Bonifacio, P., and Molaro, P. (2004). Galactic evolution of nitrogen. *Astron. Astrophys.* 421, 649–658. doi:10.1051/0004-6361:20047132

Izzo, L., Della Valle, M., Mason, E., Matteucci, F., Romano, D., Pasquini, L., et al. (2015). Early optical spectra of nova V1369 cen show the presence of lithium. *Astrophys. J.* 808, L14. doi:10.1088/2041-8205/808/1/L14

Izzo, L., Molaro, P., Della Valle, M., and Bonifacio, P. (2019). "Classical novae as lithium factories in the Galaxy", in *AAS/High energy astrophysics division*.

Jackson, R. J., Deliyannis, C. P., and Jeffries, R. D. (2018). The inflated radii of M dwarfs in the Pleiades. *Mon. Not. R. Astron. Soc.* 476, 3245–3262. doi:10.1093/mnras/sty374

Jackson, R. J., Jeffries, R. D., Randich, S., Bragaglia, A., Carraro, G., Costado, M. T., et al. (2016). The Gaia-ESO Survey: stellar radii in the young open clusters NGC 2264, NGC 2547, and NGC 2516. *Astron. Astrophys.* 586, A52. doi:10.1051/0004-6361/201527507

Jeffries, R. D. (2017). Ages and age spreads in young stellar clusters. *Mem. Soc. Astron. Italiana* 88, 637.

Jeffries, R. D., Jackson, R. J., Deliyannis, C. P., and Sun, Q. (2020). Lithium in the young suns of Messier 35. *Mem. Soc. Astron. Italiana* 91, 88.

Jeffries, R. D., Jackson, R. J., Franciosini, E., Randich, S., Barrado, D., Frasca, A., et al. (2017). The Gaia-ESO Survey: lithium depletion in the Gamma Velorum cluster and inflated radii in low-mass pre-main-sequence stars. *Mon. Not. R. Astron. Soc.* 464, 1456–1465. doi:10.1093/mnras/stw2458

Jeffries, R. D., Jackson, R. J., James, D. J., and Cargile, P. A. (2009). Low-mass members of the young cluster IC 4665 and pre-main-sequence lithium depletion. *Mon. Not. R. Astron. Soc.* 400, 317–329. doi:10.1111/j.1365-2966.2009.15453.x

Jeffries, R. D. (2006). *Pre-main-sequence lithium depletion*. 163, 61. doi:10.1007/978-3-540-34136-9_61

Jorissen, A., Van Winckel, H., Siess, L., Escorza, A., Pourbaix, D., and Van Eck, S. (2020). Li-rich K giants, dust excess, and binarity. *Astron. Astrophys.* 639, A7. doi:10.1051/0004-6361/202037585

Kaufer, A. (2010). "Observations of light elements in massive stars," in *Light elements in the Universe*. Editors C. Charbonnel, M. Tosi, and F. Primas, 268, 317–324. doi:10.1017/S1743921310004291

Kelly, D. E., Christian, D. J., Mathioudakis, M., and Jevremović, D. (2020). Can active late-type stars contribute to the Galactic lithium abundance?. *Res. Astron. Astrophys.* 20, 104. doi:10.1088/1674-4527/20/7/104

Kewley, L. J., Nicholls, D. C., and Sutherland, R. S. (2019). Understanding galaxy evolution through emission lines. *Annu. Rev. Astron. Astrophys.* 57, 511–570. doi:10.1146/annurev-astro-081817-051832

Kiselman, D., and Carlsson, M. (1996). The NLTE formation of neutral-boron lines in cool stars. *Astron. Astrophys.* 311, 680–689.

Kobayashi, C., Karakas, A. I., and Lugaro, M. (2020). The origin of elements from carbon to uranium. *Astrophys. J.* 900, 179. doi:10.3847/1538-4357/abae65

Kobayashi, C., and Nakasato, N. (2011). Chemodynamical simulations of the milky way galaxy. *Astrophys. J.* 729, 16. doi:10.1088/0004-637X/729/1/16

Kumar, Y. B., Reddy, B. E., Campbell, S. W., Maben, S., Zhao, G., and Ting, Y.-S. (2020). Discovery of ubiquitous lithium production in low-mass stars. *Nature Astron.* 4, 1059–1063. doi:10.1038/s41550-020-1139-7

Kumar, Y. B., and Reddy, B. E. (2020). Evolution of lithium in low-mass giants: an observational perspective. *J. Astrophys. Astron.* 41, 49. doi:10.1007/s12036-020-09660-9

Lagarde, N., Decressin, T., Charbonnel, C., Eggenberger, P., Ekström, S., and Palacios, A. (2012). Thermohaline instability and rotation-induced mixing. III. Grid of stellar models and asymptotic asteroseismic quantities from the pre-main sequence up to the AGB for low- and intermediate-mass stars of various metallicities. *Astron. Astrophys.* 543, A108. doi:10.1051/0004-6361/201118331

Lagarde, N., Reylé, C., Robin, A. C., Tautvaišienė, G., Drazdauskas, A., Mikolaitis, Š., et al. (2019). The Gaia-ESO Survey: impact of extra mixing on C and N abundances of giant stars. *Astron. Astrophys.* 621, A24. doi:10.1051/0004-6361/201732433

Lagarde, N., Robin, A. C., Reylé, C., and Nasello, G. (2017). Population synthesis to constrain Galactic and stellar physics. I. Determining age and mass of thin-disc red-giant stars. *Astron. Astrophys.* 601, A27. doi:10.1051/0004-6361/201630253

Lambert, D. L., and Reddy, B. E. (2004). Lithium abundances of the local thin disc stars. *Mon. Not. R. Astron. Soc.* 349, 757–767. doi:10.1111/j.1365-2966.2004.07557.x

Lambert, D. L. (1978). The abundances of the elements in the solar photosphere - VIII. Revised abundances of carbon, nitrogen and oxygen. *Mon. Not. R. Astron. Soc.* 182, 249–272. doi:10.1093/mnras/182.2.249

Lambert, D. L. (1968). The abundances of the elements in the solar photosphere-I, Carbon, nitrogen and oxygen. *Mon. Not. R. Astron. Soc.* 138, 143. doi:10.1093/mnras/138.2.143

Lattanzio, J. C., Siess, L., Church, R. P., Angelou, G., Stancliffe, R. J., Doherty, C. L., et al. (2015). On the numerical treatment and dependence of thermohaline mixing in red giants. *Mon. Not. R. Astron. Soc.* 446, 2673–2688. doi:10.1093/mnras/stu2238

Lebreton, Y., and Montalbán, J. (2009). "Stellar ages from asteroseismology," in The ages of stars of IAU Symposium. Editors E. E. Mamajek, D. R. Soderblom, and R. F. G. Wyse, 258, 419–430. doi:10.1017/S1743921309032074

Lemasle, B., François, P., Genovali, K., Kovtyukh, V. V., Bono, G., Inno, L., et al. (2013). Galactic abundance gradients from Cepheids. α and heavy elements in the outer disk. *Astron. Astrophys.* 558, A31. doi:10.1051/0004-6361/201322115

Limongi, M., and Chieffi, A. (2018). Presupernova evolution and explosive nucleosynthesis of rotating massive stars in the metallicity range -3 ≤ [Fe/H] ≤ 0. *Astrophys. J.* 237, 13. doi:10.3847/1538-4365/aacb24

Lind, K., Asplund, M., and Barklem, P. S. (2009a). Departures from LTE for neutral Li in late-type stars. *Astron. Astrophys.* 503, 541–544. doi:10.1051/0004-6361/200912221

Lind, K., Primas, F., Charbonnel, C., Grundahl, F., and Asplund, M. (2009b). Signatures of intrinsic Li depletion and Li-Na anti-correlation in the metal-poor globular cluster NGC 6397. *Astron. Astrophys.* 503, 545–557. doi:10.1051/0004-6361/200912524

Lodders, K., and Fegley, B. (2002). Atmospheric chemistry in giant planets, Brown dwarfs, and low-mass dwarf stars. I. Carbon, nitrogen, and oxygen. *Icarus.* 155, 393–424. doi:10.1006/icar.2001.6740

Lodieu, N. (2020). The age of the Hyades from the lithium depletion boundary. *Mem. Soc. Astron. Italiana* 91, 84.

Lyubimkov, L. S., Korotin, S. A., and Lambert, D. L. (2019). Oxygen abundance and the N/C versus N/O relation for AFG supergiants and bright giants. *Mon. Not. R. Astron. Soc.* 489, 1533–1542. doi:10.1093/mnras/stz2285

Lyubimkov, L. S., Lambert, D. L., Poklad, D. B., Rachkovskaya, T. M., and Rostopchin, S. I. (2013). Carbon, nitrogen and oxygen abundances in atmospheres of the 5-11$M_{\odot}$ B-type main-sequence stars. *Mon. Not. R. Astron. Soc.* 428, 3497–3508. doi:10.1093/mnras/sts287

Maciel, W. J., and Andrievsky, S. (2019). *Galactic radial abundance gradients: cepheids and photoionized nebulae*.arXiv e-printsarXiv:1906.01686

Maeder, A., and Meynet, G. (2001). Stellar evolution with rotation. VII. . Low metallicity models and the blue to red supergiant ratio in the SMC. *Astron. Astrophys.* 373, 555–571. doi:10.1051/0004-6361:20010596

Magrini, L., Randich, S., Kordopatis, G., Prantzos, N., Romano, D., Chieffi, A., et al. (2017). The Gaia-ESO Survey: radial distribution of abundances in the Galactic disc from open clusters and young-field stars. *Astron. Astrophys.* 603, A2. doi:10.1051/0004-6361/201630294

Magrini, L., Vincenzo, F., Randich, S., Pancino, E., Casali, G., Tautvaišienė, G., et al. (2018). The Gaia-ESO survey: the N/O abundance ratio in the milky way. *Astron. Astrophys.* 618, A102. doi:10.1051/0004-6361/201833224

Maiolino, R., and Mannucci, F. (2019). De re metallica: the cosmic chemical evolution of galaxies. *Astron. Astrophys. Rev.* 27, 3. doi:10.1007/s00159-018-0112-2

Majewski, S. R., Schiavon, R. P., Frinchaboy, P. M., Allende Prieto, C., Barkhouser, R., Bizyaev, D., et al. (2017). The Apache point observatory galactic evolution experiment (APOGEE). *Astron. J.* 154, 94. doi:10.3847/1538-3881/aa784d

Mallik, S. V., Parthasarathy, M., and Pati, A. K. (2003). Lithium and rotation in F and G dwarfs and subgiants. *Astron. Astrophys.* 409, 251–261. doi:10.1051/0004-6361:20031084

Martell, S., Simpson, J., Balasubramaniam, A., Buder, S., Sharma, S., Hon, M., et al. (2020). *The GALAH survey: lithium-rich giant stars require multiple formation channels*.arXiv e-printsarXiv:2006.02106

Martig, M., Fouesneau, M., Rix, H.-W., Ness, M., Mészáros, S., García-Hernández, D. A., et al. (2016). Red giant masses and ages derived from carbon and nitrogen abundances. *Mon. Not. R. Astron. Soc.* 456, 3655–3670. doi:10.1093/mnras/stv2830

Martin, E. L., and Claret, A. (1996). Stellar models with rotation: an exploratory application to pre-main sequence Lithium Depletion. *Astron. Astrophys.* 306, 408.

Martín, E. L., Lodieu, N., and Béjar, V. J. S. (2020). Search for the sub-stellar lithium depletion boundary in the open star cluster Coma Berenices. *Astron. Astrophys.* 640, A9. doi:10.1051/0004-6361/202037907

Masseron, T., and Gilmore, G. (2015). Carbon, nitrogen and α-element abundances determine the formation sequence of the Galactic thick and thin discs. *Mon. Not. R. Astron. Soc.* 453, 1855–1866. doi:10.1093/mnras/stv1731

Masseron, T., Lagarde, N., Miglio, A., Elsworth, Y., and Gilmore, G. (2017). Nitrogen depletion in field red giants: mixing during the He flash?. *Mon. Not. R. Astron. Soc.* 464, 3021–3028. doi:10.1093/mnras/stw2632

Mathews, G. J., Kedia, A., Sasankan, N., Kusakabe, M., Luo, Y., Kajino, T., et al. (2020). Cosmological solutions of the lithium problem. *Mem. Soc. Astron. Italiana* 91, 29.

Mathieu, R. D. (2000). "The WIYN open cluster study," in Stellar clusters and associations: convection, rotation, and dynamos of Astronomical Society of the Pacific Conference Series. Editors R. Pallavicini, G. Micela, and S. Sciortino, 198, 517.

Matteucci, F. (2012). *Chemical evolution of galaxies*. doi:10.1007/978-3-642-22491-1

Matteucci, F., and Chiappini, C. (2003). *Chemical evolution of galaxies: the origin of C, N, O*, in Astronomical Society of the Pacific Conference Series, 304–384.

Mattsson, L. (2010). The origin of carbon: low-mass stars and an evolving, initially top-heavy IMF?. *Astron. Astrophys.* 515, A68. doi:10.1051/0004-6361/200913315

McDermid, R. (2019). "MAVIS: sharper than JWST", in *The very large telescope in 2030*, 22. doi:10.5281/zenodo.3356256

Meléndez, J., and Ramírez, I. (2004). Reappraising the spite lithium plateau: extremely thin and marginally consistent with WMAP data. *Astrophys. J.* 615, L33–L36. doi:10.1086/425962

Meléndez, J., Schirbel, L., Monroe, T. R., Yong, D., Ramírez, I., and Asplund, M. (2014). HIP 114328: a new refractory-poor and Li-poor solar twin. *Astron. Astrophys.* 567, L3. doi:10.1051/0004-6361/201424172

Mendes, L. T. S., D'Antona, F., and Mazzitelli, I. (1999). Theoretical models of low-mass, pre-main sequence rotating stars. I. The effects on lithium depletion. *Astron. Astrophys.* 341, 174–180.

Meneguzzi, M., Audouze, J., and Reeves, H. (1971). "the formation of Li Be B by galactic cosmic rays in space, and its relation with stellar observations", in 12th international cosmic ray conference (ICRC12) International Cosmic Ray Conference, 7, 2576.

Messina, S., Lanzafame, A. C., Feiden, G. A., Millward, M., Desidera, S., Buccino, A., et al. (2016). The rotation-lithium depletion correlation in the β Pictoris association and the LDB age determination. *Astron. Astrophys.* 596, A29. doi:10.1051/0004-6361/201628524

Meynet, G., Choplin, A., Ekström, S., and Georgy, C. (2018). "Massive stars: stellar models and stellar yields, impact on galactic archaeology," in Rediscovering our galaxy of IAU symposium. Editors C. Chiappini, I. Minchev, E. Starkenburg, and M. Valentini, 334, 170–177. doi:10.1017/S1743921317010808

Meynet, G., and Maeder, A. (2002). The origin of primary nitrogen in galaxies. *Astron. Astrophys.* 381, L25–L28. doi:10.1051/0004-6361:20011554

Mikolaitis, Š., Tautvaišienė, G., Gratton, R., Bragaglia, A., and Carretta, E. (2012). C, N, O abundances and carbon isotope ratios in evolved stars of the open clusters Collinder 261 and NGC 6253. *Astron. Astrophys.* 541, A137. doi:10.1051/0004-6361/201218831

Milone, A. P., Marino, A. F., Da Costa, G. S., Lagioia, E. P., D'Antona, F., Goudfrooij, P., et al. (2020a). Multiple populations in globular clusters and their parent galaxies. *Mon. Not. R. Astron. Soc.* 491, 515–531. doi:10.1093/mnras/stz2999

Milone, A. P., Marino, A. F., Renzini, A., Li, C., Jang, S., Lagioia, E. P., et al. (2020b). A chromosome map to unveil stellar populations with different magnesium abundances. The case of ω Centauri. *Mon. Not. R. Astron. Soc.* 497, 3846–3859. doi:10.1093/mnras/staa2119

Milone, A. P., Piotto, G., Renzini, A., Marino, A. F., Bedin, L. R., Vesperini, E., et al. (2017). The Hubble space telescope UV legacy survey of galactic globular clusters - IX. The atlas of multiple stellar populations. *Mon. Not. R. Astron. Soc.* 464, 3636–3656. doi:10.1093/mnras/stw2531

Molaro, P., and Beckman, J. (1984). An upper limit to the abundance of 9Be in the population II star HD 76932 from a high resolution spectrum with the IUE. *Astron. Astrophys.* 139, 394–400.

Molaro, P., Cescutti, G., and Fu, X. (2020a). Lithium and beryllium in the Gaia-Enceladus galaxy. *Mon. Not. R. Astron. Soc.* 496, 2902–2909. doi:10.1093/mnras/staa1653

Molaro, P., Izzo, L., Bonifacio, P., Hernanz, M., Selvelli, P., and della Valle, M. (2020b). Search for ^{7}Be in the outbursts of four recent novae. *Mon. Not. R. Astron. Soc.* 492, 4975–4985. doi:10.1093/mnras/stz3587

Mollá, M., Vílchez, J. M., Gavilán, M., and Díaz, A. I. (2006). The nitrogen-to-oxygen evolution in galaxies: the role of the star formation rate. *Mon. Not. R. Astron. Soc.* 372, 1069–1080. doi:10.1111/j.1365-2966.2006.10892.x

Murphy, S. J., and Lawson, W. A. (2015). New low-mass members of the Octans stellar association and an updated 30–40 Myr lithium age. *Mon. Not. R. Astron. Soc.* 447, 1267–1281. doi:10.1093/mnras/stu2450

Negueruela, I., Alonso-Santiago, J., Tabernero, H. M., Marco, A., Castro, N., and Dorda, R. (2020). Detection of lithium in massive stars. *Mem. Soc. Astron. Italiana.* 91, 114.

Ness, M., Hogg, D. W., Rix, H.-W., Martig, M., Pinsonneault, M. H., and Ho, A. Y. Q. (2016). Spectroscopic determination of masses (and implied ages) for red giants. *Astrophys. J.* 823, 114. doi:10.3847/0004-637X/823/2/114

Nomoto, K., Kobayashi, C., and Tominaga, N. (2013). Nucleosynthesis in stars and the chemical enrichment of galaxies. *Annu. Rev. Astron. Astrophys.* 51, 457–509. doi:10.1146/annurev-astro-082812-140956

Nordhaus, J., Busso, M., Wasserburg, G. J., Blackman, E. G., and Palmerini, S. (2008). Magnetic mixing in red giant and asymptotic giant branch stars. *Astrophys. J.* 684, L29. doi:10.1086/591963

Pace, G., Castro, M., Meléndez, J., Théado, S., and do Nascimento, J. (2012). Lithium in M 67: from the main sequence to the red giant branch. *Astron. Astrophys.* 541, A150. doi:10.1051/0004-6361/201117704

Palla, F., Randich, S., Flaccomio, E., and Pallavicini, R. (2005). Age spreads in star-forming regions: the lithium test in the orion nebula cluster. *Astrophys. J.* 626, L49–L52. doi:10.1086/431668

Palla, F., Randich, S., Pavlenko, Y. V., Flaccomio, E., and Pallavicini, R. (2007). Old stars in young clusters: lithium-depleted low-mass stars of the orion nebula cluster. *Astrophys. J.* 659, L41–L44. doi:10.1086/516733

Palmerini, S., and Maiorca, E. (2010). Extra-mixing in red giant stars: challenges for nuclear physics. *J. Phys. Conf. Ser.* 202, 012030. doi:10.1088/1742-6596/202/1/012030

Pasquini, L., Bonifacio, P., Randich, S., Galli, D., and Gratton, R. G. (2004). Beryllium in turnoff stars of NGC 6397: early Galaxy spallation, cosmochronology and cluster formation. *Astron. Astrophys.* 426, 651–657. doi:10.1051/0004-6361:20041254

Pasquini, L., Bonifacio, P., Randich, S., Galli, D., Gratton, R. G., and Wolff, B. (2007). Beryllium abundance in turn-off stars of NGC 6752. *Astron. Astrophys.* 464, 601–607. doi:10.1051/0004-6361:20066260

Pasquini, L., Ecuvillon, A., Bonifacio, P., and Wolff, B. (2008). Nitrogen abundance in turn-off stars of NGC 6397 and NGC 6752. *Astron. Astrophys.* 489, 315–320. doi:10.1051/0004-6361:200809963

Pasquini, L., Galli, D., Gratton, R. G., Bonifacio, P., Randich, S., and Valle, G. (2005). Early star formation in the Galaxy from beryllium and oxygen abundances. *Astron. Astrophys.* 436, L57–L60. doi:10.1051/0004-6361:200500124

Pasquini, L., Randich, S., and Pallavicini, R. (1997). Lithium in M 67: evidence for spread in a solar age cluster. *Astron. Astrophys.* 325, 535–541.

Pinsonneault, M. H., Deliyannis, C. P., and Demarque, P. (1992). Evolutionary models of halo stars with rotation. II. Effects of metallicity on lithium depletion, and possible implications for the primordial lithium abundance. *Astrophys. J.* 78, 179. doi:10.1086/191624

Pinsonneault, M. H., Walker, T. P., Steigman, G., and Narayanan, V. K. (1999). Halo star lithium depletion. *Astrophys. J.* 527, 180–198. doi:10.1086/308048

Pinsonneault, M. (1997). Mixing in stars. *Annu. Rev. Astron. Astrophys.* 35, 557–605. doi:10.1146/annurev.astro.35.1.557

Piotto, G., Milone, A. P., Bedin, L. R., Anderson, J., King, I. R., Marino, A. F., et al. (2015). The Hubble space telescope UV legacy survey of galactic globular clusters. I. Overview of the project and detection of multiple stellar populations. *Astron. J.* 149, 91. doi:10.1088/0004-6256/149/3/91

Prantzos, N., Abia, C., Cristallo, S., Limongi, M., and Chieffi, A. (2020). Chemical evolution with rotating massive star yields II. A new assessment of the solar s- and r-process components. *Mon. Not. R. Astron. Soc.* 491, 1832–1850. doi:10.1093/mnras/stz3154

Prantzos, N., de Laverny, P., Guiglion, G., Recio-Blanco, A., and Worley, C. C. (2017). The AMBRE project: a study of Li evolution in the Galactic thin and thick discs. *Astron. Astrophys.* 606, A132. doi:10.1051/0004-6361/201731188

Prantzos, N. (2019). "Galactic chemical evolution with rotating massive star yields," in *Nuclei in the Cosmos XV*, 219, 83–89. doi:10.1007/978-3-030-13876-9_14

Prantzos, N. (2012). Production and evolution of Li, Be, and B isotopes in the Galaxy. *Astron. Astrophys.* 542, A67. doi:10.1051/0004-6361/201219043

Primas, F. (2010). "Beryllium and boron in metal-poor stars," in Light elements in the Universe of IAU Symposium. Editors C. Charbonnel, M. Tosi, F. Primas, and C. Chiappini, 268, 221–230. doi:10.1017/S1743921310004163

Primas, F., Duncan, D. K., Peterson, R. C., and Thorburn, J. A. (1999). A new set of HST boron observations. I. Testing light elements stellar depletion. *Astron. Astrophys.* 343, 545–557.

Primas, F., Duncan, D. K., Pinsonneault, M. H., Deliyannis, C. P., and Thorburn, J. A. (1997). Hubble space telescope beryllium abundances in the α centauri system. *Astrophys. J.* 480, 784–793. doi:10.1086/304004

Prisinzano, L., Damiani, F., Kalari, V., Jeffries, R., Bonito, R., Micela, G., et al. (2019). The Gaia-ESO Survey: age spread in the star forming region NGC 6530 from the HR diagram and gravity indicators. *Astron. Astrophys.* 623, A159. doi:10.1051/0004-6361/201834870

Proffitt, C. R., Lennon, D. J., Langer, N., and Brott, I. (2016). Stellar boron abundances near the main-sequence turnoff of the open cluster NGC 3293 and implications for the efficiency of rotationally driven mixing in stellar envelopes. *Astrophys. J.* 824, 3. doi:10.3847/0004-637X/824/1/3

Ramírez, I., Fish, J. R., Lambert, D. L., and Allende Prieto, C. (2012). Lithium abundances in nearby FGK dwarf and subgiant stars: internal destruction,

galactic chemical evolution, and exoplanets. *Astrophys. J.* 756, 46. doi:10.1088/0004-637X/756/1/46

Randich, S., Gilmore, G., and Consortium, Gaia-E. S. O. (2013). The Gaia-ESO large public spectroscopic survey. *The Messenger.* 154, 47–49.

Randich, S. (2010). "Lithium and beryllium in Population I dwarf stars," in Light elements in the Universe of IAU Symposium. Editors C. Charbonnel, M. Tosi, F. Primas, and C. Chiappini, 268, 275–283. doi:10.1017/S1743921310004242

Randich, S. (2006). *Mixing on the main sequence: lithium and beryllium in old open clusters*. 173, 63. doi:10.1007/978-3-540-34136-9_63

Randich, S., Pallavicini, R., Meola, G., Stauffer, J. R., and Balachandran, S. C. (2001). Membership, lithium, and metallicity in the young open clusters: enlarging the sample. *Astron. Astrophys.* 372, 862–878. doi:10.1051/0004-6361:20010339

Randich, S., Pasquini, L., Franciosini, E., Magrini, L., Jackson, R. J., Jeffries, R. D., et al. (2020). The Gaia-ESO Survey: galactic evolution of lithium at high metallicity. *Astron. Astrophys.* 640, L1. doi:10.1051/0004-6361/202038688

Randich, S., Primas, F., Pasquini, L., and Pallavicini, R. (2002). UVES Be observations of early-G dwarfs in old clusters. *Astron. Astrophys.* 387, 222–232. doi:10.1051/0004-6361:20020355

Randich, S., Tognelli, E., Jackson, R., Jeffries, R. D., Degl'Innocenti, S., Pancino, E., et al. (2018). The Gaia-ESO Survey: open clusters in Gaia-DR1. A way forward to stellar age calibration. *Astron. Astrophys.* 612, A99. doi:10.1051/0004-6361/201731738

Rauscher, T., and Patkós, A. (2011). *Origin of the chemical elements*, 611. doi:10.1007/978-1-4419-0720-2_12

Rebolo, R., Molaro, P., and Beckman, J. E. (1988). Lithium abundances in metal-deficient dwarfs. *Astron. Astrophys.* 192, 192–205.

Reeves, H., Fowler, W. A., and Hoyle, F. (1970). Galactic cosmic ray origin of Li, Be and B in stars. *Nature* 226, 727–729. doi:10.1038/226727a0

Renzini, A. (2008). Origin of multiple stellar populations in globular clusters and their helium enrichment. *Mon. Not. R. Astron. Soc.* 391, 354–362. doi:10.1111/j.1365-2966.2008.13892.x

Romano, D., Franchini, M., Grisoni, V., Spitoni, E., Matteucci, F., and Morossi, C. (2020). *On the variation of carbon abundance in galaxies and its implications*.arXiv e-printsarXiv:2005.05717

Romano, D., Matteucci, F., Ventura, P., and D'Antona, F. (2001). The stellar origin of ^{7}Li. Do AGB stars contribute a substantial fraction of the local Galactic lithium abundance?. *Astron. Astrophys.* 374, 646.

Romano, D., Matteucci, F., Zhang, Z.-Y., Ivison, R. J., and Ventura, P. (2019). The evolution of CNO isotopes: the impact of massive stellar rotators. *Mon. Not. R. Astron. Soc.* 490, 2838–2854. doi:10.1093/mnras/stz2741

Roy, A., Dopita, M. A., Krumholz, M. R., Kewley, L. J., Sutherland, R. S., and Heger, A. (2020). *On the origin of nitrogen at low metallicity*.arXiv e-printsarXiv:2005.03038

Ryan, S. G., Norris, J. E., and Beers, T. C. (1999). The spite lithium plateau: ultrathin but Postprimordial. *Astrophys. J.* 523, 654–677. doi:10.1086/307769

Sacco, G. G., Randich, S., Franciosini, E., Pallavicini, R., and Palla, F. (2007). Lithium-depleted stars in the young σ Orionis cluster. *Astron. Astrophys.* 462, L23–L26. doi:10.1051/0004-6361:20066434

Sackmann, I. J., and Boothroyd, A. I. (1999). Creation of ^{7}Li and destruction of ^{3}He, ^{9}Be, ^{10}B, and ^{11}B in low-mass red giants, due to deep circulation. *Astrophys. J.* 510, 217–231. doi:10.1086/306545

Salaris, M., and Cassisi, S. (2005). *Evolution of stars and stellar populations*.

Salaris, M., Pietrinferni, A., Piersimoni, A. M., and Cassisi, S. (2015). Post first dredge-up [C/N] ratio as age indicator. Theoretical calibration. *Astron. Astrophys.* 583, A87. doi:10.1051/0004-6361/201526951

Sanna, N., Franciosini, E., Pancino, E., Mucciarelli, A., Tsantaki, M., Charbonnel, C., et al. (2020). The Gaia-ESO Survey: an extremely Li-rich giant in globular cluster NGC 1261. *Astron. Astrophys.* 639, L2. doi:10.1051/0004-6361/202038435

Sbordone, L., Bonifacio, P., Caffau, E., Ludwig, H. G., Behara, N. T., González Hernández, J. I., et al. (2010). The metal-poor end of the Spite plateau. I. Stellar parameters, metallicities, and lithium abundances. *Astron. Astrophys.* 522, A26. doi:10.1051/0004-6361/200913282

Sengupta, S., and Garaud, P. (2018). The effect of rotation on fingering convection in stellar interiors. *Astrophys. J.* 862, 136. doi:10.3847/1538-4357/aacbc8

Sestito, P., and Randich, S. (2005). Time scales of Li evolution: a homogeneous analysis of open clusters from ZAMS to late-MS. *Astron. Astrophys.* 442, 615–627. doi:10.1051/0004-6361:20053482

Simonucci, S., Taioli, S., Palmerini, S., and Busso, M. (2013). Theoretical estimates of stellar e-captures. I. The half-life of ^{7}Be in evolved stars. *Astrophys. J.* 764, 118. doi:10.1088/0004-637X/764/2/118

Smiljanic, R. (2020). *Near-UV spectroscopy with the VLT*. arXiv e-printsarXiv:2006.04385

Smiljanic, R. (2014). Stellar abundances of beryllium and CUBES. *Ap&SS.* 354, 55–64. doi:10.1007/s10509-014-1916-9

Smiljanic, R., Gauderon, R., North, P., Barbuy, B., Charbonnel, C., and Mowlavi, N. (2009a). CNONa and ^{12}C/^{13}C in giant stars of 10 open clusters. *Astron. Astrophys.* 502, 267–282. doi:10.1051/0004-6361/200811113

Smiljanic, R., Pasquini, L., Bonifacio, P., Galli, D., Gratton, R. G., Randich, S., et al. (2009b). Beryllium abundances and star formation in the halo and in the thick disk. *Astron. Astrophys.* 499, 103–119. doi:10.1051/0004-6361/200810592

Smiljanic, R., Randich, S., and Pasquini, L. (2011). Mixing at young ages: beryllium abundances in cool main-sequence stars of the open clusters IC 2391 and IC 2602. *Astron. Astrophys.* 535, A75. doi:10.1051/0004-6361/201117157

Smith, V. V., Terndrup, D. M., and Suntzeff, N. B. (2002). Carbon isotopic abundances in the red giants of ω centauri (NGC 5139). *Astrophys. J.* 579, 832–840. doi:10.1086/342921

Soderblom, D. R., Hillenbrand, L. A., Jeffries, R. D., Mamajek, E. E., and Naylor, T. (2014). "Ages of young stars," in *Protostars and planets VI*. Editors H. Beuther, R. S. Klessen, C. P. Dullemond, and T. Henning, 219. doi:10.2458/azu_uapress_9780816531240-ch010

Soderblom, D. R., Jones, B. F., Balachand ran, S., Stauffer, J. R., Duncan, D. K., Fedele, S. B., et al. (1993). The evolution of the lithium abundances of solar-type stars. III. The Pleiades. *Astron. J.* 106, 1059. doi:10.1086/116704

Soderblom, D. R. (2010). The ages of stars. *Annu. Rev. Astron. Astrophys.* 48, 581–629. doi:10.1146/annurev-astro-081309-130806

Somers, G. (2016). *Exploring non-standard stellar physics with lithium depletion*. Ph.D. thesis, The Ohio State University.

Somers, G., Cao, L., and Pinsonneault, M. H. (2020). The spots models: a grid of theoretical stellar evolution tracks and isochrones for testing the effects of starspots on structure and colors. *Astrophys. J.* 891, 29. doi:10.3847/1538-4357/ab722e

Somers, G., and Pinsonneault, M. H. (2014). A tale of two anomalies: depletion, dispersion, and the connection between the stellar lithium spread and inflated radii on the pre-main sequence. *Astrophys. J.* 790, 72. doi:10.1088/0004-637X/790/1/72

Somers, G., and Pinsonneault, M. H. (2015). Rotation, inflation, and lithium in the Pleiades. *Mon. Not. R. Astron. Soc.* 449, 4131–4146. doi:10.1093/mnras/stv630

Somers, G., and Stassun, K. G. (2017). A measurement of radius inflation in the Pleiades and its relation to rotation and lithium depletion. *Astron. J.* 153, 101. doi:10.3847/1538-3881/153/3/101

Spada, F., Arlt, R., Küker, M., and Sofia, S. (2018). Solar radius and luminosity variations induced by the internal dynamo magnetic fields. *Astron. Nachr.* 339, 545–558. doi:10.1002/asna.201813521

Spite, F., and Spite, M. (1982). Abundance of lithium in unevolved stars and old disk stars: interpretation and consequences. *Astron. Astrophys.* 115, 357.

Spite, M., Cayrel, R., Plez, B., Hill, V., Spite, F., Depagne, E., et al. (2005). First stars VI - abundances of C, N, O, Li, and mixing in extremely metal-poor giants. Galactic evolution of the light elements. *Astron. Astrophys.* 430, 655–668. doi:10.1051/0004-6361:20041274

Spite, M., Spite, F., and Bonifacio, P. (2012). The cosmic lithium problem . an observer's perspective. *Memorie della Societa Astronomica Italiana Supplementi.* 22, 9.

Spruit, H. C., and Weiss, A. (1986). "Colors and luminosities of stars with spots". in *Max Planck Institut fur Astrophysik Report*, 225.

Stancliffe, R. J., and Glebbeek, E. (2008). Thermohaline mixing and gravitational settling in carbon-enhanced metal-poor stars. *Mon. Not. R. Astron. Soc.* 389, 1828–1838. doi:10.1111/j.1365-2966.2008.13700.x

Stanghellini, L., Bucciarelli, B., Lattanzi, M. G., and Morbidelli, R. (2020). The population of galactic planetary nebulae: a study of distance scales and central stars based on the second Gaia release. *Astrophys. J.* 889, 21. doi:10.3847/1538-4357/ab59e4

Stanghellini, L., and Haywood, M. (2018). Galactic planetary nebulae as probes of radial metallicity gradients and other abundance patterns. *Astrophys. J.* 862, 45. doi:10.3847/1538-4357/aacaf8

Stauffer, J. (2000). "Age-dating open clusters with the lithium depletion boundary test," in Stellar clusters and associations: convection, rotation, and dynamos, of Astronomical Society of the Pacific Conference Series. Editors R. Pallavicini, G. Micela, and S. Sciortino, 198, 255.

Steigman, G. (2006). Primordial nucleosynthesis: successes and challenges. *Int. J. Mod. Phys. E.* 15, 1–35. doi:10.1142/S0218301306004028

Stonkutė, E., Chorniy, Y., Tautvaišienė, G., Drazdauskas, A., Minkevičiūtė, R., Mikolaitis, Š., et al. (2020). High-resolution spectroscopic study of dwarf stars in the northern sky: lithium, carbon, and oxygen abundances. *Astron. J.* 159, 90. doi:10.3847/1538-3881/ab6a19

Suárez-Andrés, L., Israelian, G., González Hernández, J. I., Adibekyan, V. Z., Delgado Mena, E., Santos, N. C., et al. (2016). CNO behaviour in planet-harbouring stars. I. Nitrogen abundances in stars with planets. *Astron. Astrophys.* 591, A69. doi:10.1051/0004-6361/201628455

Suess, H. E., and Urey, H. C. (1956). Abundances of the elements. *Rev. Mod. Phys.* 28, 53–74. doi:10.1103/RevModPhys.28.53

Suzuki, T. K., and Yoshii, Y. (2001). A new model for the evolution of light elements in an inhomogeneous galactic halo. *Astrophys. J.* 549, 303–319. doi:10.1086/319049

Swenson, F. J., and Faulkner, J. (1992). Lithium dilution through main-sequence mass loss. *Astrophys. J.* 395, 654. doi:10.1086/171686

Tagliaferri, G., Cutispoto, G., Pallavicini, R., Rand ich, S., and Pasquini, L. (1994). Photometric and spectroscopic studies of cool stars discovered in EXOSAT X-ray images II. Lithium abundances. *Astron. Astrophys.* 285, 272–284.

Tajitsu, A., Sadakane, K., Naito, H., Arai, A., and Aoki, W. (2015). Explosive lithium production in the classical nova V339 Del (Nova Delphini 2013). *Nature* 518, 381–384. doi:10.1038/nature14161

Takeda, Y., Kang, D.-I., Han, I., Lee, B.-C., Kim, K.-M., Kawanomoto, S., et al. (2012). Lithium, sodium, and Potassium abundances in sharp-lined A-type stars. *Publ. Astron. Soc. Jpn.* 64, 38. doi:10.1093/pasj/64.2.38

Takeda, Y., and Tajitsu, A. (2009). High-dispersion spectroscopic study of solar twins: HIP 56948, HIP 79672, and HIP 100963. *Publ. Astron. Soc. Jpn.* 61, 471. doi:10.1093/pasj/61.3.471

Takeda, Y., Tajitsu, A., Honda, S., Kawanomoto, S., Ando, H., and Sakurai, T. (2011). Beryllium abundances of solar-analog stars. *Publ. Astron. Soc. Jpn.* 63, 697. doi:10.1093/pasj/63.3.697

Takeda, Y., and Tajitsu, A. (2014). Spectroscopic study on the beryllium abundances of red giant stars*. *Publ. Astron. Soc. Jpn.* 66, 91. doi:10.1093/pasj/psu066

Tautvaišiene, G., Edvardsson, B., Tuominen, I., and Ilyin, I. (2000). Chemical composition of evolved stars in the open cluster M 67. *Astron. Astrophys.* 360, 499–508.

Tautvaišienė, G., Barisevičius, G., Chorniy, Y., Ilyin, I., and Puzeras, E. (2013). Red clump stars of the Milky Way - laboratories of extra-mixing. *Mon. Not. R. Astron. Soc.* 430, 621–627. doi:10.1093/mnras/sts663

Tautvaišienė, G., Drazdauskas, A., Bragaglia, A., Randich, S., and Ženovienė, R. (2016). CNO abundances and carbon isotope ratios in evolved stars of the open clusters NGC 2324, NGC 2477, and NGC 3960. *Astron. Astrophys.* 595, A16. doi:10.1051/0004-6361/201629273

Tautvaišienė, G., Drazdauskas, A., Mikolaitis, Š., Barisevičius, G., Puzeras, E., Stonkutė, E., et al. (2015). The Gaia-ESO Survey: CNO abundances in the open clusters Trumpler 20, NGC 4815, and NGC 6705. *Astron. Astrophys.* 573, A55. doi:10.1051/0004-6361/201424989

Tautvaišienė, G., Edvardsson, B., Puzeras, E., Barisevičius, G., and Ilyin, I. (2010). C, N and O abundances in red clump stars of the Milky Way. *Mon. Not. R. Astron. Soc.* 409, 1213–1219. doi:10.1111/j.1365-2966.2010.17381.x

Ting, Y.-S., Conroy, C., Rix, H.-W., and Asplund, M. (2018). Measuring oxygen abundances from stellar spectra without oxygen lines. *Astrophys. J.* 860, 159. doi:10.3847/1538-4357/aac6c9

Ting, Y.-S., Rix, H.-W., Conroy, C., Ho, A. Y. Q., and Lin, J. (2017). Measuring 14 elemental abundances with R = 1800 LAMOST spectra. *Astrophys. J.* 849, L9. doi:10.3847/2041-8213/aa921c

Tognelli, E., Prada Moroni, P. G., Degl'Innocenti, S., Salaris, M., and Cassisi, S. (2020). Protostellar accretion in low mass metal poor stars and the cosmological lithium problem. *Astron. Astrophys.* 638, A81. doi:10.1051/0004-6361/201936723

Toribio San Cipriano, L., Domínguez-Guzmán, G., Esteban, C., García-Rojas, J., Mesa-Delgado, A., Bresolin, F., et al. (2017). Carbon and oxygen in H II regions of the Magellanic Clouds: abundance discrepancy and chemical evolution. *Mon. Not. R. Astron. Soc.* 467, 3759–3774. doi:10.1093/mnras/stx328

Toribio San Cipriano, L., García-Rojas, J., Esteban, C., Bresolin, F., and Peimbert, M. (2016). Carbon and oxygen abundance gradients in NGC 300 and M33 from optical recombination lines. *Mon. Not. R. Astron. Soc.* 458, 1866–1890. doi:10.1093/mnras/stw397

Travaglio, C., Randich, S., Galli, D., Lattanzio, J., Elliott, L. M., Forestini, M., et al. (2001). Galactic chemical evolution of lithium: interplay between stellar sources. *Astrophys. J.* 559, 909.

Twarog, B. A., Anthony-Twarog, B. J., Deliyannis, C. P., and Steinhauer, A. (2020). *Intermediate-to-Low mass stars in open clusters and the evolution of Li*.arXiv e-printsarXiv:2006.11157

Ulrich, R. K. (1986). Determination of stellar ages from asteroseismology. *Astrophys. J.* 306, L37. doi:10.1086/184700

van den Hoek, L. B., and Groenewegen, M. A. T. (1997). New theoretical yields of intermediate mass stars. *Agents Actions Suppl.* 123, 305–328. doi:10.1051/aas:1997162

Ventura, P., Zeppieri, A., Mazzitelli, I., and D'Antona, F. (1998). Pre-main sequence Lithium burning: the quest for a new structural parameter. *Astron. Astrophys.* 331, 1011–1021.

Vincenzo, F., and Kobayashi, C. (2018a). Evolution of N/O ratios in galaxies from cosmological hydrodynamical simulations. *Mon. Not. R. Astron. Soc.* 478, 155–166. doi:10.1093/mnras/sty1047

Vincenzo, F., and Kobayashi, C. (2018b). Extragalactic archaeology with the C, N, and O chemical abundances. *Astron. Astrophys.* 610, L16. doi:10.1051/0004-6361/201732395

Vincenzo, F., Matteucci, F., Belfiore, F., and Maiolino, R. (2016). Modern yields per stellar generation: the effect of the IMF. *Mon. Not. R. Astron. Soc.* 455, 4183–4190. doi:10.1093/mnras/stv2598

Wagoner, R. V. (1973). Big-Bang nucleosynthesis revisited. *Astrophys. J.* 179, 343–360. doi:10.1086/151873

Weinberg, D. H., Holtzman, J. A., Hasselquist, S., Bird, J. C., Johnson, J. A., Shetrone, M., et al. (2019). Chemical cartography with APOGEE: multi-element abundance ratios. *Astrophys. J.* 874, 102. doi:10.3847/1538-4357/ab07c7

Wheeler, A., Ness, M., and Hogg, D. W. (2020). *An unsupervised method for identifying-enriched stars directly from spectra: Li in LAMOST*.arXiv e-printsarXiv:2009.03920

Worley, C. C., de Laverny, P., Recio-Blanco, A., Hill, V., Bijaoui, A., and Ordenovic, C. (2012). The AMBRE Project: stellar parameterisation of the ESO:FEROS archived spectra. *Astron. Astrophys.* 542, A48. doi:10.1051/0004-6361/201218829

Xiang, M. S., Liu, X. W., Yuan, H. B., Huo, Z. Y., Huang, Y., Wang, C., et al. (2017). LAMOST Spectroscopic Survey of the Galactic Anticentre (LSS-GAC): the second release of value-added catalogues. *Mon. Not. R. Astron. Soc.* 467, 1890–1914. doi:10.1093/mnras/stx129

Yan, H.-L., Zhou, Y.-T., Zhang, X., Li, Y., Gao, Q., Shi, J.-R., et al. (2020). Most lithium-rich low-mass evolved stars revealed as red clump stars by asteroseismology and spectroscopy. *Nature Astron.* doi:10.1038/s41550-020-01217-8

Zappala, R. R. (1972). Lithium abundances of stars in open clusters. *Astrophys. J.* 172, 57. doi:10.1086/151328

Zasowski, G., Cohen, R. E., Chojnowski, S. D., Santana, F., Oelkers, R. J., Andrews, B., et al. (2017). Target selection for the SDSS-IV APOGEE-2 survey. *Astron. J.* 154, 198. doi:10.3847/1538-3881/aa8df9

Žerjal, M., Ireland, M. J., Nordlander, T., Lin, J., Buder, S., Casagrande, L., et al. (2019). The GALAH Survey: lithium-strong KM dwarfs. *Mon. Not. R. Astron. Soc.* 484, 4591–4600. doi:10.1093/mnras/stz296

Conflict of Interest: The authors declare that the research was conducted in the absence of any commercial or financial relationships that could be construed as a potential conflict of interest.

frontiers in Physics

REVIEW
published: 30 March 2021
doi: 10.3389/fphy.2020.602920

Transfer Reactions As a Tool in Nuclear Astrophysics

Faïrouz Hammache and Nicolas de Séréville**

IJCLab, Université Paris-Saclay, CNRS/IN2P3, Orsay, France

Nuclear reaction rates are one of the most important ingredients in describing how stars evolve. The study of the nuclear reactions involved in different astrophysical sites is thus mandatory to address most questions in nuclear astrophysics. Direct measurements of the cross-sections at stellar energies are very challenging–if at all possible. This is essentially due to the very low cross-sections of the reactions of interest (especially when it involves charged particles), and/or to the radioactive nature of many key nuclei. In order to overcome these difficulties, various indirect methods such as the transfer reaction method at energies above or near the Coulomb barrier are used to measure the spectroscopic properties of the involved compound nucleus that are needed to calculate cross-sections or reaction rates of astrophysical interest. In this review, the basic features of the transfer reaction method and the theoretical concept behind are first discussed, then the method is illustrated with recent performed experimental studies of key reactions in nuclear astrophysics.

Keywords: transfer reactions, angular distributions, distorted wave born approximation, spectroscopic factors, nuclear astrophysics

OPEN ACCESS

Edited by:
Rosario Gianluca Pizzone, Laboratori Nazionali del Sud (INFN), Italy

Reviewed by:
Giovanni Luca Guardo, Laboratori Nazionali del Sud (INFN), Italy
Antonio Caciolli, University of Padua, Italy
Antonio M. Moro, Sevilla University, Spain
Stefan Typel, Technische Universität Darmstadt, Germany

****Correspondence:***
Faïrouz Hammache
fairouz.hammache@ijclab.in2p3.fr
Nicolas de Séréville
nicolas.de-sereville@ijclab.in2p3.fr

Specialty section:
This article was submitted to Nuclear Physics, a section of the journal Frontiers in Physics

Received: *04 September 2020*
Accepted: *01 December 2020*
Published: *30 March 2021*

Citation:
Hammache F and de Séréville N (2021) Transfer Reactions As a Tool in Nuclear Astrophysics. Front. Phys. 8:602920. doi: 10.3389/fphy.2020.602920

1 INTRODUCTION

Our understanding of stellar evolution in the Universe has been largely improved thanks to the interaction between three fields: observation, stellar modeling and nuclear physics. All these fields are in constant development: new telescopes and satellites open more and more windows on the cosmos, stellar modeling relies on ever-increasing computing and nuclear physics takes advantage of new facilities (radioactive beams, high-intensity beams, underground laboratories) and sophisticated detection systems.

Nuclear reaction rates are one of the most important ingredients in describing how stars evolve. The study of the nuclear reactions involved in different astrophysical sites is thus essential to address most questions in nuclear astrophysics.

Experimental techniques for determining cross sections fall into two main categories: direct measurements, in which the reaction of interest is reproduced, even though the energy range may be different from that of the stellar site and indirect measurements, in which a different reaction is coupled with theoretical modeling to obtain the cross-section of interest or to access the spectroscopic properties (excitation energies, spins and parities, decay widths, . . .) of the nuclei involved.

Direct measurements at stellar energies are very challenging - if at all possible. This is mainly due to the very small cross-sections (sub nanobarns) of the reactions of interest (in particular when charged particles are involved), and/or to the radioactive nature of many key nuclei.

Although direct measurements of the charged-particle cross-sections are possible at the energies of interest in some cases, they are often carried out at higher energies and then extrapolated down

to the energies of astrophysical interest using $\mathcal{R}$-matrix calculations for example [1]. However, these extrapolations can easily lead to erroneous results; for example if they do not take into account the contribution of possible unobserved resonances at very low energies, or if they neglect the contribution of sub-threshold resonances. The effect of these resonances may change the extrapolated cross-section at astrophysical energies by a tremendous factor (sometimes orders of magnitude).

The other issue concerning direct measurements is due to the radioactive nature of the nuclei involved in the reactions occurring in explosive sites (classic novae, supernovae, X-ray bursts, ...) or in the radiative captures (n,γ) in the *r*-process [2–4] and sometimes in the *s*-process [5]. Here, the cross sections at stellar energies are often substantial but their study requires either the production of radioactive beams (which intensity is often weak, rarely exceeding 10^5 or 10^6 pps) or, for nuclei with relatively long half life, the production of radioactive targets with a sufficiently large areal density, which is often very difficult. Therefore, direct measurements of such reactions are very challenging, and in the case of *r*-process reactions, they are impossible.

To overcome these problems (sub–threshold resonances, radioactive nuclei, ...) indirect techniques such as transfer reaction method [6], Coulomb dissociation method [7–9], Asymptotic Normalization Coefficient (ANC) method [10–12], surrogate reactions [13] and Trojan Horse Method (THM) [14–16] are good alternatives. In these various methods, the experiments are usually carried out at higher energies than the Coulomb barrier which implies higher cross-sections than in direct measurements. Moreover these methods allow also the use of stable beams to study reactions involving radioactive nuclei not far from the valley of stability. However these methods lead to results which depend on the choice of the model and its parameters in addition to the experimental errors. This is why, to reduce the overall uncertainty on the cross sections of the reactions, it is important to combine various experimental approaches.

We would like to emphasize that ANC and Trojan Horse methods as well as surrogate method are also based on transfer reactions. However, the THM and ANC method require particular kinematics conditions. For instance the transfer reactions used in ANC method need to be performed at energies where the reaction process is very peripheral in order to deduce an ANC value weakly sensitive on the potential parameters. Concerning the Trojan Horse Method, it consists in obtaining information on the two-body reaction of astrophysical interest at low relative energies by studying a three body reaction at energies above the Coulomb barrier. The basic idea of this method relies on the assumption that the three body reaction can occur via a quasi free reaction mechanism that is dominant at particular energies and angles. For the surrogate method, the transfer reaction is used to populate the resonant states of interest and then measure their decay probability to deduce the cross section of the reaction of interest from the product of the measured quantity and the calculated compound nucleus formation cross-section. All these particular transfer reactions will not be discussed in this manuscript except the ANC method which will be described a little bit more in **section 3.2.4**.

In this review we focus on the transfer reaction method where a composite nucleus is produced in a two body reaction by transferring one or several nucleons from a projectile to a target nucleus. Transfer reactions are a unique tool to access key spectroscopic information concerning the structure of the composite nucleus. In particular the spectroscopic factor (C^2S), which is related to the overlap between the wave function of the composite nucleus configuration with the one of the target nucleus, is a prime objective of such studies.

In the next section we will present the type of reactions (resonant and direct capture) which can be studied with transfer reactions. In **Section 3**, the description of the method and basic theoretical concepts behind such reactions are recalled. In **Section 4**, the experimental needs and challenges for transfer reaction studies are presented. Some examples of recently performed experimental studies using stable and radioactive beams together with a variety of detection systems are presented in **Section 5**. We then conclude with some perspectives in a last section.

2 NUCLEAR REACTIONS OF ASTROPHYSICAL INTEREST

Thermonuclear reaction rates are key physical inputs to computational stellar models, and they are defined per particle pair (in $cm^3\ s^{-1}$) as [17]:

$$\langle \sigma v \rangle = \sqrt{\frac{8}{\pi\mu}}\ \frac{1}{(kT)^{\frac{3}{2}}} \int_0^\infty \sigma(E) E e^{-E/kT} dE, \tag{1}$$

where μ is the reduced mass of the interacting nuclei, k is the Boltzmann constant, T is the temperature at which the reaction rate is evaluated, and $\sigma(E)$ is the energy-dependent cross-section of the reaction. In order to evaluate the cross-section of nuclear reactions of astrophysical interest two processes should be considered: the resonant capture and the direct capture. Both processes are represented schematically in **Figure 1** (left and middle panel, respectively) for a radiative capture reaction $A(x,\gamma)C$, and illustrated with the case of the ^{17}O(p,γ)^{18}F reaction [18] (right panel). In case of the resonant capture process (left panel) the relative energy in the center of mass between the projectile x and the target A must be close to the resonant energy E_r; the astrophysical S-factor[1] exhibits a strong energy dependence as it can be seen from the $E_r^{c.m.}$ = 557 and 677 keV resonances in the ^{17}O(p,γ)^{18}F reaction. On the contrary the direct capture process may occur at any center of mass energy (middle panel), and the energy dependence of the S-factor is very smooth (see horizontal dashed lines in right panel). Both the direct and resonant capture will now

[1] $S(E) = \sigma(E) \times E \times e^{2\pi\eta}$, where η is the Sommerfeld parameter.

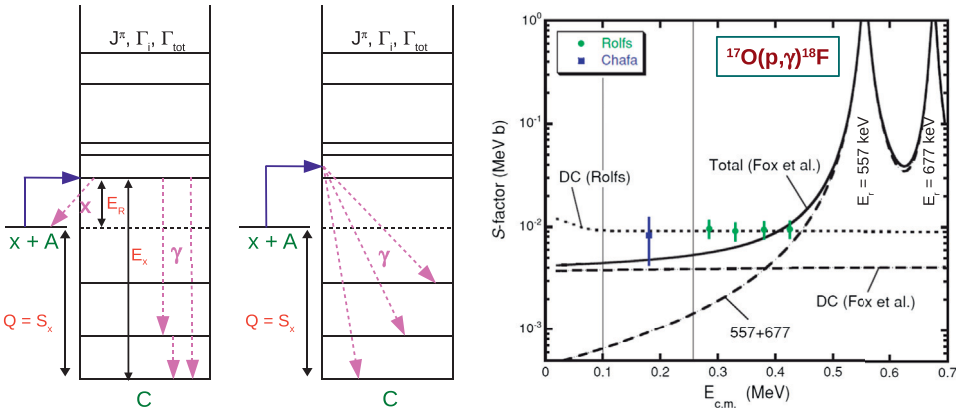

FIGURE 1 | (Color online) Schematic view of a resonant (**left panel**) and direct (**middle panel**) capture process for a radiative capture reaction. The contribution of these two processes is shown in the case of the ^{17}O(p,γ)^{18}F reaction (**right panel**) where the energy dependence of the astrophysical *S*-factor is presented (adapted from ref. 18).

be presented in more details emphasizing the link with transfer reactions.

2.1 Resonant Capture

In a resonant capture reaction $x + A \rightarrow C^* \rightarrow y + B$ the two participants of the entrance channel form an excited state of the compound nucleus C which further decays into the $y + B$ exit channel. The y participant can be any kind of neutral or charged particle or an electromagnetic radiation; in the latter case the reaction is called a radiative capture and B is the ground state of the compound nucleus. As represented in **Figure 1** (left panel) the resonant capture only occurs at relative energies in the center of mass very close to the resonance energy defined as $E_r = E_x - Q$, where E_x is the energy of the excited state in the compound nucleus, and Q is the Q-value of the radiative capture reaction. The cross-section of a resonance is conveniently described by the one-level Breit–Wigner formula [17]:

$$\sigma(E) = \frac{\lambda^2}{4\pi} \frac{2J_{C^*} + 1}{(2J_A + 1)(2J_x + 1)} \frac{\Gamma_x \Gamma_y}{(E - E_r)^2 + \Gamma^2/4}, \quad (2)$$

where λ is the de Broglie wavelength, J_A, J_x, and J_{C^*} are the spin of the entrance channel participants and of the excited state in the compound nucleus, respectively. The partial widths Γ_x and Γ_y represent the probability of formation and decay of the compound nucleus in its excited state E_x, respectively. The total width of the excited state is given by $\Gamma = \Gamma_x + \Gamma_y + \ldots$ Because of the time reverse invariance of the electromagnetic and nuclear processes, the probability of formation of a given state in the compound nucleus or its decay, from or to the $x + A$ channel, is characterized by the same particle width Γ_x.

Transfer reactions are powerful tools to derive several quantities needed to calculate the cross-section given by **Equation 2**. They can be used to determine the transferred orbital angular momentum ℓ, which 1) allows the determination of the parity of the compound nucleus state, and 2) may help to constrain its spin. Transfer reactions are also used to determine the excitation energies (and therefore resonance energies for unbound states), and the partial widths of the compound nucleus states [19]. The partial width associated to the formation of the compound nucleus in a given excitation energy (C^*) is given by the product of the spectroscopic factor and the single-particle width:

$$\Gamma_x = C^2 S_x \times \Gamma_x^{s.p.}. \quad (3)$$

The single-particle width is the decay probability of the compound nucleus state (C^*) when it is considered as a pure $x + A$ (particle-core) configuration. However, nuclear states are in most of the cases an admixture of configurations, and the spectroscopic factor C^2S_x is related to the overlap probability between the antisymmetrized wave function of the $x + A$ channel and the compound nucleus state C^*. The spectroscopic factor is one of the quantities derived from the analysis of transfer reactions.

2.2 Direct Capture

The direct capture is an electromagnetic process which can not be neglected at low energies, and which may even be dominant for radiative captures where the level density is low [20] and the compound states lie at higher energies than the energies of interest [21].

For $A(x,\gamma)C$ capture reactions where the direct capture component is dominant, the capture occurs on bound states of the final nucleus in a one step process (see **Figure 1**, middle panel). The direct capture is possible at all bombarding energies and the cross-section varies smoothly with the energy. The total cross-section of the direct capture process is given by the following expression [22]:

$$\sigma_{total}^{DC}(E) = \sum_i C_i^2 S_i \sigma_i^{DC}(E), \quad (4)$$

where E is the energy of the incident projectile and the sum runs over all available final bound states i of the residual nucleus, $C_i^2 S_i$

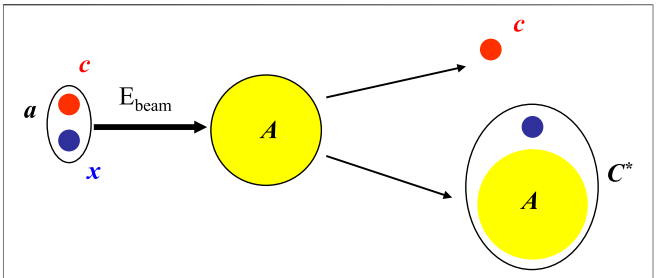

FIGURE 2 | Sketch of a transfer reaction where the particle *x* is transferred from the projectile *a* to the target nucleus *A* forming the final state C^*.

is the spectroscopic factor of the final state *i* (see **Section 3.1**), and σ_i^{DC} is the calculated DC cross-section using the following equation [23]:

$$\sigma_i^{DC} \propto \frac{1}{2I_A+1}\frac{1}{2S_x+1}\int d\Omega \sum_{M_A M_x M_C \sigma} \left|T_{M_A M_x M_C,\sigma}\right|^2, \quad (5)$$

where I_A, I_C, and S_x (M_A, M_x and M_C) are the spins (magnetic quantum numbers) of the target nucleus *A*, residual nucleus *C* and projectile *x* respectively and σ the polarization of the electromagnetic radiation, it can be ± 1.

In case of a dipole transition, $T = T^{E1}$. This transition depends on the overlap integrals of the radial parts of the bound-state wave function in the exit channel $u_{l_b I_C}(r)$, the scattering wave function $\chi_{l_x j_x}$ in the entrance channel and the transition operator O^{E1} [24].

$$I^{E1}_{l_b I_C; l_x j_x} \propto \int dr\, u_{l_b I_C}(r) O^{E1}(r) \chi_{l_x j_x}(r)\,, \quad (6)$$

where l_b is the orbital angular momentum of the two $A + x$ clusters in the nucleus *C*. The complete DC formalism can be found in ref. 24 and the computer code TEDCA [25] can be used to calculate its cross-section.

3 TRANSFER REACTION METHOD

Transfer reactions in which one nucleon or a cluster of nucleons are exchanged between the target and the projectile are often used in nuclear structure studies to determine the energy position and the orbital occupation of the excited states of many nuclei. Likewise it is widely used in nuclear astrophysics to determine the partial decay widths of nuclear states involved in resonant reactions, and to evaluate the direct capture cross-section.

3.1 General Concepts

Let's consider the simple case of a radiative capture $A(x,\gamma)C$. Whether the reaction proceeds through a resonant or direct capture, the spectroscopic factor C^2S_x of the unbound or bound states, respectively, in the compound nucleus *C* is needed to evaluate the cross-section (see **Section 2**). It is then relevant to populate the excited states of the compound nucleus *C* by transferring the particle *x*, which can be a single nucleon or a cluster of nucleons, to the target nucleus *A* (see **Figure 2**). The transfer reaction will then be $A(a,c)C$, where *a* is a composite system made of *x* and *c*. The valence states of the final nucleus *C* will be populated, and the reaction mechanism will be considered as a one step direct reaction if the reaction occurs without perturbation of the target (core) nucleus *A* or the projectile *a* [6].

Once the particle *x* is transferred to the target *A*, the projectile component *c* will continue its movement and should be detected. By measuring its emission angle and energy, the energy of the populated states in nucleus *C* can be obtained using two-body kinematic properties if the masses of the interacting nuclei are known. A precise measurement of the energies of the excited states of interest is very important to calculate accurately the resonance energies involved in the evaluation of the thermonuclear reaction rates.

From a comparison of the shape of the measured angular distributions to those predicted by theory, it is possible to deduce the transferred angular momentum ℓ which indicates, for single-nucleon transfer, into which orbital the nucleon has been transferred. Indeed, the shape of measured differential cross-sections exhibits features that are sensitive to the transferred orbital momentum ℓ and the knowledge of the latter may constrain the spin of the populated states. Note that the spin of the populated states can be obtained from polarization measurements [26]. The magnitude of the differential cross-sections is sensitive to the spectroscopic strengths of the populated states and their analysis using an adequate formalism allows the extraction of the spectroscopic factor C^2S_x.

When the direct transfer mechanism is dominant the measured transfer angular distributions are often analyzed using the Distorted Wave Born Approximation (DWBA) formalism (see **Section 3.2.1**). However other reaction mechanisms such as the compound nucleus mechanism, the multi-step transfer reaction mechanism, the projectile breakup and the transfer to continuum [6] can occur. The contribution of these mechanisms can be evaluated by using Hauser Feshbach calculations [27], coupled reaction channel calculations (CRC), adiabatic distorted wave approximation (ADWA) (see **Section 3.2.5**) and continuum discretized coupled channel (CDCC) calculations [28], respectively.

The angular distributions of direct reactions display a characteristic shape which often shows a forward protuberant peak and smaller peaks at larger center-of-mass angles (see **Figure 5** in **Section 5.2**). This is in contrast to the compound nucleus mechanism where the angular distribution shows an almost flat and symmetric shape with respect to 90° in the center-of-mass. Hence to be more sensitive to the direct reaction mechanism, transfer measurements need to be performed at relatively small detection angles (typically $\theta_{c.m} \leqslant 50°$).

3.2 Elements of Theory

3.2.1 Distorted Wave Born Approximation

The most commonly used theoretical model to describe direct transfer reaction cross-sections is the Distorted Wave Born Approximation (DWBA) which relies on the following assumptions:

- the entrance and exit channels processes are dominated by the elastic scattering
- the transfer process is weak enough to be treated as a first order perturbation
- the nucleon(s) transfer occurs directly between the two active channels $a + A$ and $c + C$
- the transferred nucleon(s) is directly deposited on the final state with no rearrangement of the core configuration

The transfer reaction cross-section is proportional to the square of the transition amplitude which in case of the DWBA model, and in the *post* representation[2], is given by ref. 30:

$$T_{i\to f}^{DWBA} = J\iint \chi_f^{(-)}\left(\overrightarrow{k}_f, \overrightarrow{r}_f\right)^* \langle c, C|V_{cC} - U_{cC}|a, A\rangle \chi_i^{(+)}\left(\overrightarrow{k}_i, \overrightarrow{r}_i\right) d\overrightarrow{r}_i d\overrightarrow{r}_f \,, \tag{7}$$

where χ_i and χ_f are the distorted wave functions describing the elastic scattering process in the entrance and exit channel, respectively; $\overrightarrow{k}$ and $\overrightarrow{r}$ being the wave number and the relative coordinates for the considered channel, and J is the Jacobian for the transformation to these coordinates. The term $V_{cC} - U_{cC}$ describes the non-elastic scattering processes, V_{cC} being the sum of all interaction between c and C while U_{cC} being the optical potential describing the $c + C$ elastic scattering. For transfer reactions where the transferred nucleon(s) are small compared to the target, the term $V_{cC} - U_{cC}$ is often approximated by the potential V_{cx}[3], and the quantity $\langle c, C|V_{cx}|a, A\rangle$ is then the form factor of the reaction. Since the V_{cx} potential only acts on the projectile the form factor can be factorized as $\langle c, C|V_{cx}|a, A\rangle = \langle C|A\rangle\langle c|V_{cx}|a\rangle$. The form factor contains all the information concerning the angular momentum selection rules and the nuclear structure. It embeds the overlap function describing the transferred nucleon or group of nucleons in the projectile a and in the final bound state C. In the latter case the radial part of the overlap function $I_{xA}^{C}(r)$ is usually approximated by a model wave-function of the bound state C as follows [11]:

$$I_{xA}^{C}(r) \approx S_{xA}^{1/2}\,\varphi_{xA}(r), \tag{8}$$

where $\varphi_{xA}(r)$ is the radial part of the bound state wave-function describing the relative $x + A$ motion, and S_{xA} is the spectroscopic factor of the $x + A$ configuration. The wave function $\varphi_{xA}(r)$ does not contain the intrinsic wave functions of x and A. The full relation between the form factor $\langle C|A\rangle$ and the radial overlap can be found in ref. 31 (see **Equations 3**, **4**).

The spectroscopic factor S_{xA} expresses the overlap probability between the $x + A$ wave-function and the final bound-state configuration C. It can be extracted from the ratio of the measured differential cross-section to the one calculated by the DWBA for the relevant single-particle or cluster transfer:

$$\left(\frac{d\sigma}{d\Omega}\right)_{exp} = S_{xA}S_{xc}\left(\frac{d\sigma}{d\Omega}\right)_{DWBA}. \tag{9}$$

The product of the spectroscopic factors corresponding to the configuration of the $x + A$ bound state (S_{xA}) and of the projectile (S_{xc}) is involved in the previous expression. Hence, by knowing one of the spectroscopic factors it is possible to extract the other one. Therefore the light projectile in transfer reaction is usually chosen to have a strong cluster configuration, e.g., $S_{xc} \approx 1$, as in the case of the (d, p) reaction for example.

3.2.2 Finite-Range and Zero-Range Calculations

The calculation of the DWBA transfer reaction cross-section involves the evaluation of the transition amplitude (see **Equation 7**) which is of the form of a six-dimensional integral over the two relative coordinate variables $\overrightarrow{r}_i$ and $\overrightarrow{r}_f$. In a finite-range DWBA calculation (FR-DWBA) the integral appearing in the transition amplitude is undertaken exactly over the two radial coordinates. While computational resources nowadays allow finite-range calculations to be performed rather easily, this was not always the case and the evaluation of the six-dimensional integral required some approximations. The most common is the zero-range approximation (ZR-DWBA) which relies on the assumption that the form factor has a small range, either because it is proportional to a short range interaction, or because the internal wave-function of the projectile has a small range. The physical meaning of such approximation is that the light particle in the exit channel is emitted at the same point at which the light particle in the entrance channel is absorbed. Under this assumption the DWBA transition amplitude reduces to a three-dimensional integral which is much more tractable from a numerical point of view, and only the form factor describing the interaction of the transferred particle with the core in the final nucleus has to be considered. The integrand of the transition amplitude is proportional to the product of the projectile internal wave-function and the interaction potential between its c and x components, i.e. $D(\overrightarrow{r}_{cx}) = V_{cx}\phi_{cx}$, and in the zero-range approximation one has:

$$D\left(\overrightarrow{r}_{cx}\right) = D_0\delta\left(\overrightarrow{r}_c - \overrightarrow{r}_x\right), \tag{10}$$

where D_0 can be calculated exactly for light systems [6, 30].

The zero-range (ZR) approximation is usually a good assumption when calculating the cross-section of a direct transfer reaction induced by light projectile. In the case of the typical (d, p) stripping reaction this is partially justified by the small size of the deuteron in comparison to the size of the other interacting nuclei, and by the s-wave nature of its dominant configuration. However, the zero range assumption is no longer valid if the projectile is not in an s-wave internal state, or has a very large size. For these cases, finite range DWBA calculations are mandatory in order to provide reliable theoretical cross-

[2]The transition amplitudes can be given in either a *post* or *prior* form depending on whether it is based on the interactions in the exit or entrance channel, respectively. DWBA calculations with either form are equivalent [6, 29].

[3]The V_{cC} potential can be separated in two parts: $V_{cC} = V_{cx} + V_{cA}$, which leads to $V_{cC} - U_{cC} = V_{cx} + (V_{cA} - U_{cC})$. The no-remnant approximation is often used to neglect the $(V_{cA} - U_{cC})$ term.

sections. The (^{7}Li,t) α-particle transfer reaction provides a good example where the $\alpha + t$ system is in a relative p-state, thus making the ZR assumption very poor and sometimes wrong.

3.2.3 Reduced and Partial Decay Widths

Once the spectroscopic factor S_x[4] of the state of interest is extracted, its reduced decay width γ_x^2 can be determined using the following formulas [32]:

$$\gamma_x^2 = S_x \times \gamma_{x,s.p.}^2, \tag{11}$$

where $\gamma_{x,s.p.}^2$ is the single-particle reduced width defined as:

$$\gamma_{x,s.p.}^2 = \frac{\hbar^2 R}{2\mu}\left|\varphi(R)\right|^2, \tag{12}$$

where μ is the reduced mass of the $A + x$ channel, and $\varphi(R)$ is the radial part of the wave function describing the relative motion of the $A + x$ system forming the bound state of C calculated at a channel radius R. The radial part of the wave function is normalized such as $\int_0^\infty r^2\varphi(r)dr = 1$, and the radius R is chosen where $\varphi(r)$ reaches its asymptotic behavior.

In case of unbound states the partial decay width Γ_x is related to the reduced decay width by ref. 33:

$$\Gamma_x = 2\,P_l(R,E)\,\gamma_x^2, \tag{13}$$

where $P_l(R,E)$ is the Coulomb and centrifugal barriers penetrability for relative angular momentum l. The penetrability factor is calculated at the energy of the resonant state for the same radius R as the one used to determine the reduced decay width.

A common procedure to determine the partial decay width for an unbound state is to use the weakly-bound approximation. In this approach the radial form factor is calculated for a very weakly bound state (typical binding energies between 5 and 50 keV) and is further used to calculate the reduced decay width using **Equation 11**. The partial width is then obtained with **Equation 13** evaluated at the energy of the resonance. It has been shown that for proton or neutron resonances having single-particle widths small compared to their resonance energy, the weakly-bound approximation gives spectroscopic information within 15% with results obtained using an unbound form factor [34].

3.2.4 Asymptotic Normalization Coefficients

As mentioned in the introduction, the ANC method is a particular case of transfer reactions. It relies on the peripheral nature of the reaction process that makes the calculations free from the geometrical parameters (radius, diffuseness) of the binding potential of the nucleus of interest and less sensitive to the entrance and exit channel potentials. The ANC method was extensively used for direct proton-capture reactions of astrophysical interest where the binding energy of the captured charged particle is low [35] and also for reactions where the capture occurs through loosely sub-threshold resonance states [36, 37]. These very peripheral transfer reactions performed at sub-Coulomb energies are good tools to determine asymptotic normalization coefficients (ANCs) which are weakly sensitive to the calculations and which may be linked to the partial width of a resonance [11]. Nevertheless, ANC's can also be determined from transfer reactions performed at energies above the Coulomb barrier.

The asymptotic normalization coefficient C describes the amplitude of the tail of the radial overlap function at radii beyond the nuclear interaction radius and in case of a bound state it can be related to the spectroscopic factor using the following expression [11]:

$$C^2 = S_x \frac{R^2\varphi^2(R)}{W^2_{-\eta_{xA},l+1/2}(2k_{xA}R)}, \tag{14}$$

where $W_{-\eta_{xA},l+1/2}(2k_{xA}R)$ is the Whittaker function describing the asymptotic behavior of the bound state wave function, characterized by η_{xA} the Sommerfield parameter of the $x + A$ bound state, l the relative orbital momentum and k_{xA} the wave number of the $x + A$ bound state.

3.2.5 Adiabatic Distorted Wave Approximation

When one of the participants of the transfer reaction is a loosely bound system, the DWBA may not be suited to analyze the data since the breakup of this system becomes an important additional reaction channel to consider. This is the case when deuterons are involved in the transfer reaction since they can break up easily into their constituents due to their small binding energy ($BE = 2.224$ MeV). The Adiabatic Distorted Wave Approximation (ADWA) was developed to take into account the breakup channel, and it was first introduced in the case of the (d,p) stripping reaction [38]. In this approximation, the effective potential including the deuteron breakup is calculated by taking into account the proton and the neutron interactions with the target nucleus, as well as a corrective term describing the proton-neutron interaction [39]. Various studies have shown that using the ADWA results in a substantial improvement of the description of (d,p) angular distributions for deuteron energies larger than 20 MeV [40]. A comparison of DWBA and ADWA calculations is given in **Section 5.4** for the ^{60}Fe(d,p)^{61}Fe reaction.

An interesting feature of the ADWA method is that its implementation is very similar to the DWBA calculations, thus any pre-existing inputs for the DWBA calculations can be easily adapted to perform ADWA calculations. The only difference is in the optical model potential parameters (see **Section 3.3.1**) describing the interaction of the deuteron with the target. While in the DWBA this potential is adjusted to reproduce the elastic scattering differential cross-section, it is no longer the case for the ADWA since it includes the treatment of the deuteron breakup. Therefore the optical potential used in ADWA will not be adapted to provide a good description of the deuteron elastic scattering, but it will give instead a better description of the transfer differential cross-section.

[4]In the followng we define $S_x \equiv S_{xA}$ in order to simplify the notations.

3.3 Ingredients for a Distorted Wave Born Approximation Calculation

To calculate the transfer DWBA differential cross sections, a number of computer codes are available such as FRESCO [41], DWUCK [42], TWOFNR [43] and PTOLEMY [44], to cite a few of them. They all require the same ingredients which are the distorted waves in the entrance and exit channel, and the two overlap functions which describe the relative motion of the transferred nucleon in the projectile and in the final state (see **Sec. 3.2.1**). These ingredients are calculated using optical model and interaction potentials whose parameters are the main inputs for any DWBA code.

3.3.1 Distorted Waves

The distorted waves are the solution of the Schrödinger equation for elastic scattering by an appropriate optical-model potential. This potential has usually a central (both real and imaginary parts), a spin-orbit and a Coulomb component; and its most common shape is a Woods-Saxon well. The best way to determine the potential parameters is to analyze the differential cross-section of the elastic scattering in the entrance and exit reaction channel at the same energy as the reaction under study. When elastic measurements are not available, one should use potential parameters deduced from measurements performed in the mass region close to the nuclei of interest at close incident energies. Another alternative is to use global potential parametrisations obtained by fitting a large number of elastic scattering data. The radius, diffuseness and depth of the different components of the potential usually have an energy and Z, A dependence allowing to derive a potential parameter set adapted to the reaction under study. The most commonly used global parametrisations for protons, neutrons and deuterons are those of Perey and Perey [45], Daehnick et al. [46] and Koning et al. [47].

3.3.2 The $\langle C|A\rangle$ Overlap Function

The radial part of the overlap function is usually approximated by the radial part of the wave-function describing the relative motion of the transferred nucleon x to the core A to form the bound state C (see **Equation 8**). It is obtained by solving the Schrödinger equation for an interaction potential usually having a Woods-Saxon form. In this procedure the depth of the real part of the volume component of the potential is adjusted to reproduce the binding energy of the bound state.

The shape of the bound state wave-function is dictated by the orbitals to which the nucleon or group of nucleons are transferred. In the case of a single nucleon transfer reaction, the nucleon is transferred to an orbital characterized by the usual quantum numbers (n, l), where the principal quantum number n gives the number of nodes of the wave-function, and the transferred orbital angular momentum l is obtained from selection rules and parity conservation. The case of multi nucleon transfer is more delicate since the transferred nucleons may be dropped on different orbitals. In this case the number of nodes N of the radial wave-function is obtained using the Talmi-Moshinsky relation [48]:

$$(2N + L) + (2n + l) = \sum_i (2n_i + l_i) \tag{15}$$

where (n, l) are the intrinsic quantum numbers of the transferred cluster, and (n_i, l_i) characterize the orbitals to which the individual nucleons forming the cluster are transferred. Here, N, n and n_i counts the number of nodes excluding that at zero radius. The transferred angular momentum L is obtained as for the single-nucleon transfer case from selection rules and parity conservation. Note that the previous relation is strictly valid for harmonic oscillator functions and hence is only approximate for a general case. A detailed example is presented in **Section 5.3** for the ^{13}C(^{7}Li,t)^{17}O α-particle transfer reaction.

The radial form factor strongly depends on the radius and the diffuseness of the potential. Different realistic (r, a) sets can be used and the selected ones are those giving the best description of the measured angular distributions.

3.3.3 The $\langle c|a\rangle$ Overlap Function

The way the projectile is treated depends on the type of DWBA calculation. If the zero-range approximation is used, then it is enough to know the value of D_0^2 (see **Section 3.2.2**), and numerical values for typical transfer reactions can be found in the literature [6]. In case a finite-range DWBA calculation is considered, the same exact procedure as for the final bound state can be used to determine the radial part of the wave-function describing the relative motion of the transferred nucleon x in the projectile a. In case of light-ions overlaps like $\langle d|n + p\rangle$ there are better choices such as the the Reid soft-core potential [49] which gives realistic wave-functions. Note also that recent advances now provide one-nucleon spectroscopic overlaps, spectroscopic factors and ANCs in light nuclei ($A \leq 7$) based on the realistic two- and three-nucleon interactions using, for example, the Green's function Monte Carlo (GFMC) method [50].

3.4 Uncertainties on Spectroscopic Factors, ANCs and Reduced Widths

The uncertainty associated to the extracted spectroscopic factors depends on the accuracy of the measured differential cross-sections, and mainly on the uncertainties related to the different parameters used in the DWBA calculation. This includes the optical potential parameters used to describe the wave functions of the relative motion in the entrance and exit channels, and the geometry parameters of the potential well describing the interaction of the transferred particle with the core in the final nucleus. In case of a one-nucleon transfer reaction these uncertainties give rise to a typical uncertainty on the spectroscopic factor of about 25–35% [51], which is increased to 30%–40% in case of an α-particle transfer reaction [52, 53]. However, the DWBA model remains very useful and even essential for reactions that cannot be studied directly and whose uncertainty on cross sections is more than a factor two.

Concerning the reduced widths and ANCs deduced from transfer reactions (see **Equations 11**, **12** and **Equation 14**, respectively), their uncertainties depend, not only on the

spectroscopic factors uncertainty but also on the potential parameters used to calculate the radial wave function of the relative motion between the transferred nucleon(s) and the core nucleus. Since the spectroscopic factor determination also depends on the aforementioned potential parameters its uncertainty is then correlated to the determination of the radial wave-function. It is then mandatory that the same optical potential parameters must be used in deriving the spectroscopic factor and the radial wave function to determine the reduced width and the ANC. Their associated relative uncertainties may therefore be different from the one of the spectroscopic factors.

We would like to point out that the spectroscopic factors defined here are experimental quantities subject to the uncertainties mentioned above. In theory, they can be defined properly but there is a long discussion in recent years whether they can be considered as a well-defined observable [54]. A direct use of proper many-body wave functions for the structure of the nuclei in the calculation of the matrix elements would remove the problem of defining spectroscopic factors and allow better testing of nuclear structure. However, these many-body calculations are up to now possible only for light nuclei [55–58], and not for most of the nuclei involved in the various nucleosynthesis processes studied in nuclear astrophysics.

4 EXPERIMENTAL NEEDS AND CHALLENGES FOR TRANSFER REACTION STUDIES

We have seen so far that the analysis of experimental angular distributions obtained from two-body transfer reactions is a unique tool to access key spectroscopic information (energy of excited states, spectroscopic factors and transferred angular momentum) concerning the composite nucleus produced by transferring one or several nucleons from a projectile to a target. A sketch of such transfer reaction is given in **Figure 2** and in the vast majority of experimental approaches the goal is to measure the energy and angle of the emitted light particle *c*. It is then possible to determine the excitation energy of the composite nucleus by using the two-body kinematic properties of the reaction. In addition, the number of light particles detected at different angles is the main ingredient used to extract the angular distribution.

While one is usually interested in a specific transfer reaction channel characterized by the light particle *c*, many other processes ((in)elastic scattering, fusion-evaporation, etc . . .) produce many other kinds of particles which need to be disentangled from *c*. It is therefore a requirement for the experimental detection system to have a good particle identification capability. Moreover it is important that the resolution in the center of mass be the best as possible in order to separate the different excited states of the composite nucleus. Another need for the detection system is to cover the forward angles in the center of mass where the direct mechanism is dominant, thus allowing a good description of the angular distribution by the DWBA method.

While the center of mass frame is best suited for describing the reaction mechanism, the experimental study occurs in the laboratory frame. There are two experimental possibilities to perform a given two-body reaction study: either the projectile is lighter than the target (direct kinematics), or the projectile is heavier than the target (inverse kinematics). Choosing one or the other option will have profound consequences on the nature of the experimental system. To illustrate this point the kinematic lines (E_{lab} vs θ_{lab}) of the tritons coming out from the ^{15}O(^{7}Li,t)^{19}Ne α-particle transfer reaction are presented in **Figure 3** in the case of direct (left panel) and indirect (right panel) kinematics[5]. The population of the ground-state and the excited state at 4.033 MeV in ^{15}O are represented. Square markers are spaced by 10° in the center of mass and the filled square corresponds to 0°.

The first striking difference is that the forward angles in the center of mass correspond to forward/backward angles in the laboratory frame in case of direct/inverse kinematics[6]. In addition the tritons have a rather large energy (about 30 MeV) in case of direct kinematics, while the energy is much smaller (about 3 MeV) in case of inverse kinematics. These two observations will dictate very different experimental setups, and the specifics concerning direct and inverse kinematics studies are now detailed.

4.1 Direct Kinematics Studies

Historically transfer reactions were performed using stable beams in direct kinematics. The first detection systems were based on collimated silicon detectors mounted in a $\Delta E - E$ fashion allowing Particle IDentification (PID) based on the energy loss and residual energy deposited in each detector. In such experimental studies several of these telescopes were positioned at different detection angles around the target. Small angles in the laboratory frame were preferred since in direct kinematics forward center of mass angles correspond to forward laboratory angles. One of the limiting aspect of this approach is the intrinsic energy resolution of the silicon detectors which is typically $\approx 15 - 20$ keV. This can be easily superseded by the use of magnetic spectrographs of high resolving power $E/\Delta E = 3000 - 5000$ such as the Enge Split-Pole [59] or Q3D [60] design (see examples in **Sections 5.3, 5.2**, respectively). The detection system at the focal plane of the spectrometers usually comprises one (or two) position sensitive detectors recording the magnetic rigidity of the light particles entering the acceptance; a gas detector measuring the energy loss of the particles; and a plastic scintillator where the residual energy of the particle is deposited.

The differential cross section corresponding to a populated state in the residual nucleus is calculated from the light particle

[5]Strictly speaking one should not consider the case of direct kinematics for the present reaction since a target containing ^{15}O nuclei is impossible to produce due to its short half-life of 122.24 s.

[6]This is usually the case for stripping reactions. In the case of pick-up transfer reactions (e.g., (p,d) (d,^{3}He)...), the forward angles in the center of mass correspond to forward angles in the laboratory frame also in inverse kinematics.

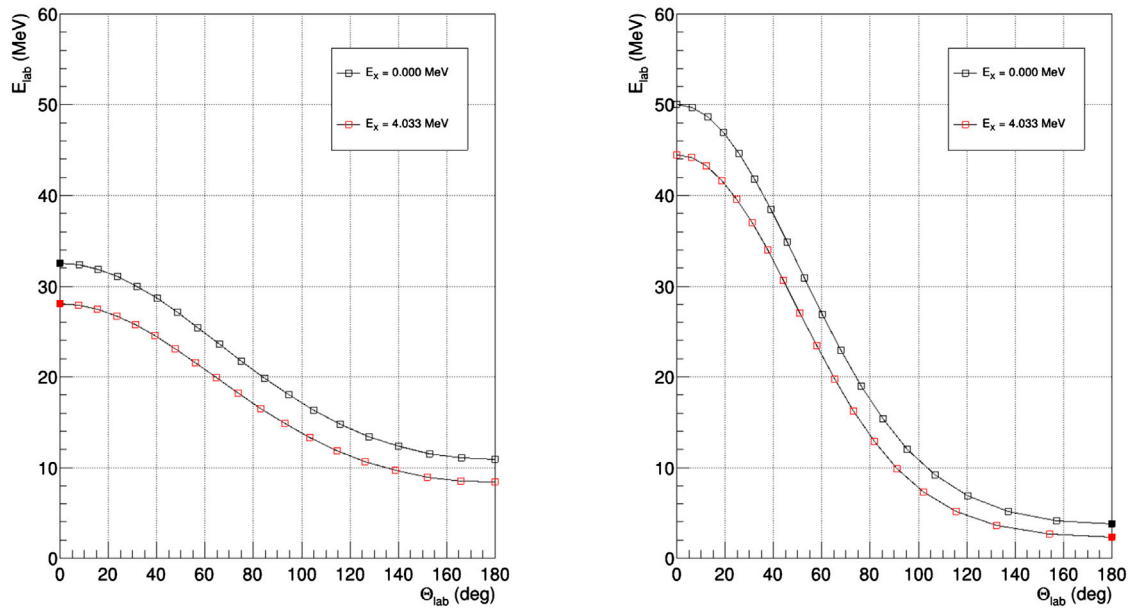

FIGURE 3 | (Color online) Kinematic calculations for the $^{15}O(^{7}Li,t)^{19}Ne$ reaction showing the triton energy as a function of the laboratory angle in case of direct (left panel) and indirect (right panel) kinematics. Both calculations are performed for the same center of mass energy.

yield determined at each detection angle $N_c(\theta_{lab})$ using the following formula:

$$\left(\frac{d\sigma}{d\Omega}\right)_{c.m.}(\theta_{c.m.}) = \frac{N_c(\theta_{lab})}{Q(\theta_{lab})N_{target}\Delta\Omega_{lab}}J(\theta_{lab}) \qquad (16)$$

where $Q(\theta_{lab})$ is the accumulated charge at each angle, N_{target} is the number of target atoms per unit area, $\Delta\Omega_{lab}$ is the solid angle, and $J(\theta_{lab})$ is the Jacobian for the laboratory to center-of-mass transformation of the $A(a,c)C$ reaction at each detection angle.

Transfer reaction studies with stable beams in direct kinematics are rather straightforward. While the spectrometer requires a dedicated hall the complexity of the detection system is usually low with a limited number of electronic channels. The main delicate point in such approach comes from the targets. First because they must be very thin (between tens and hundreds of μg cm^{-2}) in order to limit their contribution to the overall energy resolution budget. They are then extremely delicate to produce and fragile to manipulate. Their purity is another point which deserves a special care because reactions on any other nuclei present in the target may produce unwanted contamination peaks hindering the states of interest. It is then of uttermost importance to have isotopically enriched material when needed, to limit the backing material thickness when the target cannot be self-supported, and to choose carefully the compound form. Concerning the last point and as an example of a transfer reaction on fluorine nuclei, lithium or calcium fluoride targets will not produce the same background, and one or the other compound may be best suited depending on the reaction studied.

4.2 Inverse Kinematics Studies

The advent of radioactive ion beams (RIBs) allows to perform transfer reaction studies involving nuclei far from the valley of stability (see example in **Section 5.4**). Beam intensities are much smaller than for stable beams and should be preferably at least 10^5 pps in order to perform a transfer reaction study. The beam properties are one of the crucial aspects in such studies, and depending on how the RIB is produced it may be contaminated with other species and have a large emittance. Therefore, detectors tracking the beam position, such as CATS [61], PPACs [62] to cite a few of them, are usually used to reconstruct the position of the incident ions at the target location event by event. Identification of the incident beam with respect to other species is also undertaken with standard time of flight and energy loss techniques. In contrast to the direct kinematics case the solid state targets are much more simpler and easier to handle with CH_2, CD_2, and LiF being mainly used. On the other hand, gas targets can be very complex and usually relies on supersonic gas jet [63] or cryogenics [64] technology.

The fact that RIB intensities are much smaller than in the case of stable beams experiment has a profound impact on the design of the detection setup. Let us illustrate this point with the case of

the $^{15}O(^{7}Li,t)^{19}Ne$ reaction. For a stable beam study of this reaction in direct kinematics we could consider the following typical parameters: a $^{7}Li^{3+}$ beam intensity of about 100 pnA, a target thickness of about 100 μg/cm^2, and a spectrometer solid angle $\Delta\Omega \approx 5$ msr. In an inverse kinematics study of this reaction [65] the ^{15}O beam intensities are about 10^7 pps which is six orders of magnitude lower than for the stable beam experiment. The ways of compensating this dramatic loss is to increase the triton detection efficiency and the target thickness. Concerning the charged particle detection system, it is usually based on large acceptance silicon systems where the angular information needed to reconstruct the excitation energy mostly comes from a very high segmentation of the silicon array. Among the many existing arrays, and to only cite a few of them, TIARA [66] uses single-sided silicon stripped detectors, MUST2 [67] and SHARC [68] are based on double-silicon stripped detectors, and ORRUBA [69] relies on resistive silicon detectors. If we consider a close to 2π sr coverage for these detectors, this is about three orders of magnitude more than a typical spectrometer acceptance in direct kinematics. The last parameter than can be tuned to compensate the lower RIB intensities is the target thickness which is typically in the mg/cm^2 range, one order of magnitude higher than for direct kinematics studies. The target thickness must be carefully chosen and results from a trade-off between excitation energy resolution and counting rate. In order to mitigate this trade-off it is more and more usual to add in the detection setup a high performance (efficiency and resolution) γ-ray spectrometer. In that case the reconstructed excitation energy of the residual nucleus based on the charged particle alone does not provide the resolution to separate all populated states, however the coincidence with γ-rays provides a clean measurement and allows to isolate the contribution of a single state to the excitation energy spectrum. The major silicon arrays cited previously have been coupled to efficient γ-ray spectrometers such as EXOGAM [70], AGATA [71], TIGRESS [72] and GRETINA [73], with the following combinations: TIARA-EXOGAM, MUST2-EXOGAM, MUGAST-AGATA, SHARC-TIGRESS and ORRUBA-GRETINA.

Transfer reaction studies with radioactive ion beams are very challenging and require complex experimental setups. Tremendous progresses over the past 20 years have been made concerning the development of both highly efficient and granular charged particles and γ-rays spectrometer. Despite of these achievements RIB transfer experiments typically last between one and two weeks with a limited level of accumulated statistics. However this is a unique way to explore regions of the nuclear charts where some of the most extreme astrophysical processes occur.

5 EXAMPLES OF EXPERIMENTAL TRANSFER REACTION STUDIES

After some general considerations on the type of transfer reactions useful in nuclear astrophysics, three examples will be presented. The first two examples concern the study of the resonant part of the $^{30}Si(p,\gamma)^{31}P$ and $^{13}N(\alpha,p)^{16}O$ reactions studied by means of the one proton (^{3}He,d) reaction, and the α-particle (^{7}Li,t) transfer reaction on the mirror reaction, respectively. The last example concerns the study of the direct capture component of the $^{60}Fe(n,\gamma)^{61}Fe$ reaction through the one neutron (d,p) transfer reaction.

5.1 Transfer Reactions in Nuclear Astrophysics

Several transfer reactions can be used to extract spectroscopic factor for the same states of astrophysical interest. The one-proton (^{3}He,d), (^{4}He,t) and (d,n) transfer reactions can be used to extract the proton spectroscopic factor of states involved in proton captures reactions. Similarly the one-neutron (α,^{3}He) and (d,p) transfer reactions can be used to study the resonant and direct components of neutron capture cross-sections. The choice between these transfer reactions is driven by considerations on a good linear and angular momentum matching [30]. The transferred linear momentum depends strongly on the beam energy and on the Q-value of the transfer reaction. Since in nuclear astrophysics small transferred angular momenta are relevant in most of the cases because of the low associated centrifugal barrier, transfer reactions having a smaller Q-value are generally mostly used. As such, the (d,p) and (^{3}He,d) transfer reaction are a very common choice for one-neutron and one-proton transfer reactions, respectively.

In the case of one-proton transfer reactions both the (^{3}He,d) reaction [74, 75] and the (d,n) reaction [76] have been used extensively, though the neutron detection may bring some experimental complexity. For the one-neutron transfer case the (d,p) reaction has been mostly used [77–79]. Note that the different momentum matching of two reactions transferring the same nucleon can provide useful hints on the nature of the populated states. In that case the same state is populated in a different way according to the reaction, and a distinction between low and high spins may be established (see ref. 80 for a comparison of the (^{3}He,d) and (^{4}He,t) reactions).

The (p,d) and (p,t) pickup reactions are very valuable tools to study proton-rich nuclei of astrophysical interest such as in classical novae and type I X-ray bursts. The Q-values of both reactions are strongly negative, and in case of the (p,t) reaction proton beam energies larger than 30 MeV are often needed favoring the use of cyclotron instead of electrostatic accelerators. The (p,d) direct reaction mechanism can be well described by the DWBA formalism and it is then possible to extract useful spectroscopic information from the analysis of the angular distributions [81]. This is more complicated in the case of (p,t) reactions since the two neutrons can be transferred as a pair in a single step or in the possible two steps (p,d) (d,t) path which requires to know the spectroscopic factor and energy of the intermediate states. This makes the analysis of the angular distribution more delicate [82] and not as reliable as a single particle transfer reaction. Despite these complications the (p,t) reaction is widely used because of its selectivity which mainly populates natural spin and parity states (if a single step is assumed) of even-even nuclei.

Alpha-particle transfer reactions are very useful to study the spectroscopy of nuclei involved in α-induced reactions such as

(α,γ), (α,n) and (α,p) reactions in helium rich environments. The most generally used transfer reactions are the (^{6}Li,d) and (^{7}Li,t) reactions. At the time of early studies the (^{6}Li,d) reaction was used extensively because the $L = 0$ relative motion of the α-particle and deuteron in ^{6}Li allowed for a Zero-Range DWBA treatment. This approximation is not correct in the case of the (^{7}Li,t) reaction for which the α-particle and triton are in a $L = 1$ relative motion. Multi-step effects may be important in α-particle transfer reactions [83], however a comparison of the two transfer reactions off ^{12}C has shown that these effects are reduced when using a ^{7}Li beam [32, 84]. In addition the transfer cross-sections to low spin states are enhanced in case of the (^{7}Li,t) transfer reaction due probably to the non-zero α-particle angular momentum in ^{7}Li [85], and the angular distributions show much stronger direct features by exhibiting more forward pronounced maxima [86]. However the angular distributions have less oscillatory structures than those from (^{6}Li,d) due to the fact that the α+t cluster in ^{7}Li exists in a relative *p*-state which implies two transferred ℓ values that superimpose to form a state of a given spin and parity in the final nucleus [86]. According to [86], in comparison to (^{6}Li,d) (^{7}Li,t) transfer reaction seems to populate more selectively states with α structure.

5.2 Case of the ^{30}Si(p,γ)^{31}P Reaction

Globular clusters are vital testing grounds for models of stellar evolution and the early stages of the formation of galaxies. Abundance anomalies such as the enhancement of potassium and depletion of magnesium have been reported in the globular cluster NGC 2419 [87]. They can be explained in terms of an earlier generation of stars polluting the presently observed stars, however, the nature and properties of the polluting sites is not clear (see refs. 88 and 89 for a review). It has been shown that the potential range of temperatures and densities of the polluting sites depends on the strength of a number of critical reaction rates including $^{30}\mathrm{Si}\,(p,\gamma)^{31}\mathrm{P}$ [90].

Several resonances are known in the Gamow window $E_r^{\mathrm{c.m.}} = 100 - 500$ keV associated to the temperature range of interest between 100 and 250 MK. Their fractional contribution to the $^{30}\mathrm{Si}\,(p,\gamma)^{31}\mathrm{P}$ reaction rate have been calculated and several resonances have been identified as dominating the reaction rate [90]. While the strength of the highest resonances having $E_r^{c.m.} > 400$ keV can be accessed by direct measurement this is not the case for lower energy resonances because of the much smaller barrier penetrability. Since the partial proton width of the corresponding ^{31}P state is expected to be much smaller than the radiative partial width, the resonance strength is then proportional to the particle width. As described in **Section 2.1** the proton partial width is related to the proton spectroscopic factor which can be in turn determined from a one-proton transfer reaction. The shape of the angular distribution will give some precious insights on the angular momentum of the transferred proton ℓ which will allow to constrain the unknown spin-parity of the resonances to $J = \ell \pm 1/2$.

The importance of low-lying resonances above the p + ^{30}Si threshold $S_p = 7297$ keV has been investigated using the one-proton ^{30}Si(^{3}He,d)^{31}P transfer reaction. The experiment was performed with a $^3\mathrm{He}^{2+}$ beam of about 200 enA accelerated to 25 MeV by the TANDEM accelerator of the Maier-Leibniz-Laboratory at Munich. The beam impinged a thin target (20 μg/cm^2) of enriched silicon oxyde located at the object focal point of the Q3D magnetic spectrometer [60]. The deuterons were momentum analyzed and detected by the focal plane system allowing their clear identification from other light particles, and the measurement of their magnetic rigidity. A typical deuteron magnetic rigidity spectrum at a spectrometer angle $\theta = 16^\circ$ is displayed in **Figure 4**. Since the Q3D magnetic spectrometer has been tuned to cancel the kinematic broadening of the ^{30}Si(^{3}He,d)^{31}P reaction, narrow peaks are associated to ^{31}P states (red components) while the broad structures (unlabeled blue components) correspond to reactions on other target elements such as ^{12}C and ^{16}O. The extremely good energy resolution of about 6–7 keV (FWHM) in the center-of-mass allows a clear separation of the two components of the 7,719 and 7,737-keV doublet relevant in the present study.

The differential cross-sections corresponding to populated ^{31}P states were calculated from the deuteron yield determined at each spectrometer angle, and examples are shown in **Figure 5** for states populated by different transferred angular momentum [91]. In all cases the rapidly varying cross-section on a limited forward center-of-mass angular range is indicative of states which are populated through a direct mechanism. The differential cross-sections also have a very characteristic shape which depends on the transferred angular momentum, e.g., the position of the first minimum of the cross-section increases with the magnitude of the transferred angular momentum. Finite-range DWBA calculations performed with the FRESCO code [41] are represented in blue for a selection of bound and unbound states, and a very good agreement is obtained with the experimental data. For unbound states the weakly bound approximation is assumed, and a bound form factor corresponding to a state bound by 10 keV is considered.

While the optical potential parameters for the entrance channel come from an experimental study of the same transfer reaction at the same bombarding energy [92], the parameters for the exit channel come from set F of Daehnick et al. global deuteron potentials [46]. The proton form factor was obtained by adjusting the depth of a standard Woods-Saxon well in order to reproduce the experimental proton separation energy of each ^{31}P state. The geometry of the well had a radius and diffuseness of $r_0 = 1.25$ fm and $a_0 = 0.65$ fm, respectively.

The finite-range calculations have been performed using the $\langle ^3\mathrm{He}|\mathrm{d}\rangle$ overlap obtained by the Green's function Monte Carlo method using the Argonne v_{18} two-nucleon and Illinois-7 three-nucleon interactions [50]. The shape of the angular distribution is very similar to the case of a zero-range DWBA calculation (red curve) and the forward angles are similarly well described. A difference of 20% is observed between the spectroscopic factors extracted with both calculations. A zero-range DWBA calculation has also been performed using non-local and finite-range corrections (see refs. 92 and 93 for the parameters) for comparison, and a spectroscopic factor lower by 30% with respect to a zero-range calculation is obtained in agreement with previous work [92, 93]. Note that with modern

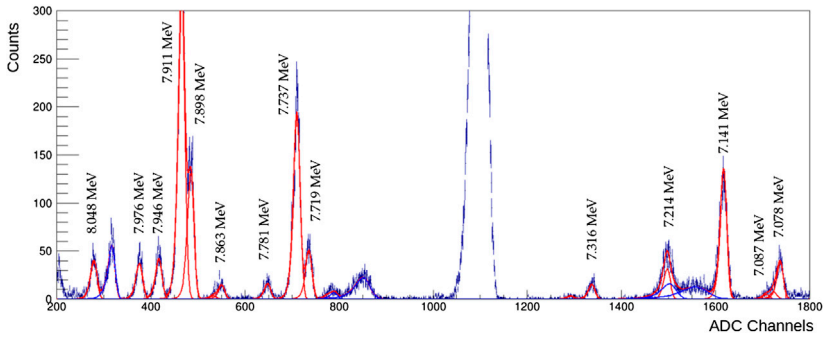

FIGURE 4 | (Color online) Deuteron magnetic rigidity spectrum at a spectrometer angle of 16°. Excitation energies in ^{31}P between 7.0 and 8.1 MeV are covered. The best fit of the spectrum is shown together with individual contributions for ^{31}P states (red) and contamination peaks (blue).

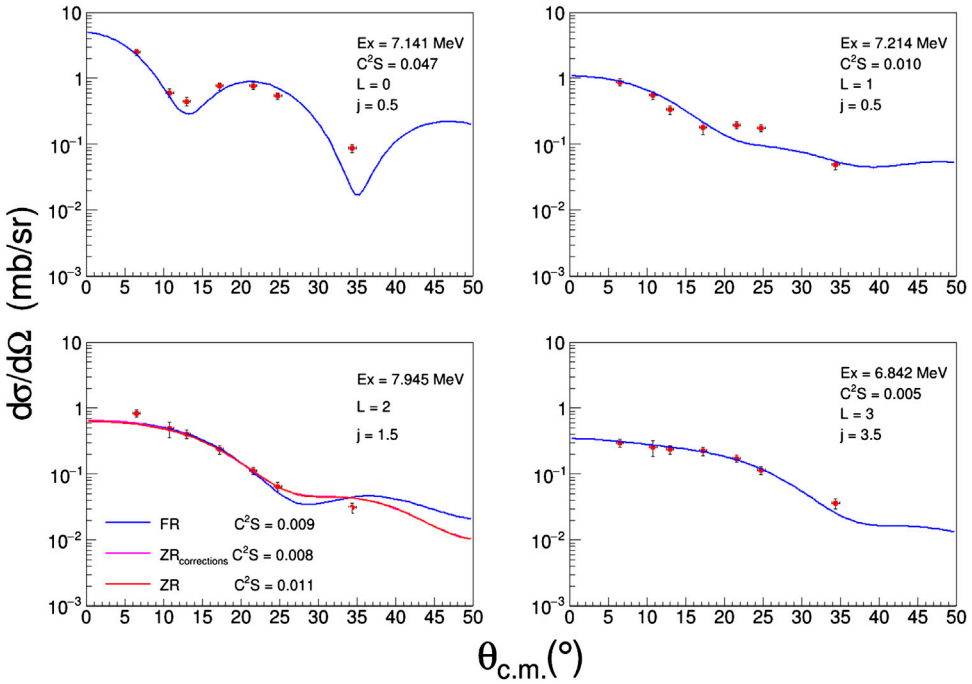

FIGURE 5 | (Color online) Selection of experimental differential cross-sections of ^{31}P states populated with the ^{30}Si(^{3}He,d)^{31}P transfer reaction. Each panel correspond to a different transferred relative angular momentum, and the blue solid lines represent finite-range DWBA calculations normalized to the data. Zero-range calculations are also reported in case of the 7.945 MeV state (see text for details).

computational resources finite-range DWBA calculations should always be preferred.

The proton spectroscopic factors obtained from the finite-range DWBA analysis have been used to derive the proton partial widths using **Equation 13**. The weakly-bound approximation was assumed and the validity of this assumption was explored by performing zero-range DWBA calculations to unbound states with the DWUCK4 code [42] which relies on the Vincent and Fortune complex integration procedure of the radial integrals [94]. In addition, DWUCK4 calculates the proton partial widths and a maximum difference of 15% was observed with the weakly-bound approximation. This is related to the fact that the proton wave functions, even for unbound levels, are well described in the weakly-bound approximation because the high Coulomb barrier leads to a strong suppression of the wave function at large radii.

5.3 Case of the ^{13}N(α,p)^{16}O Reaction

It has been recently suggested that hydrogen ingestion into the helium shell of massive stars could lead to high ^{13}C and ^{15}N excesses when the shock of a core-collapse supernova (CCSN) passes through its helium shell [95]. This prediction questions the origin of extremely high ^{13}C and ^{15}N abundances observed in rare

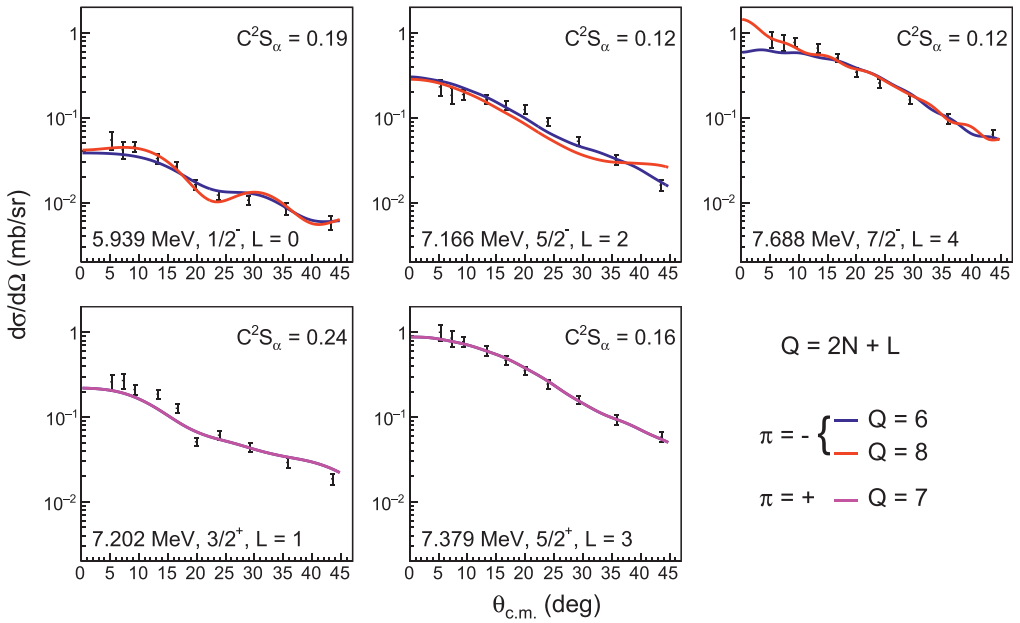

FIGURE 6 | (Color online) Selection of experimental differential cross-sections of ^{17}O states populated with the ^{13}C(^{7}Li,t)^{17}O transfer reaction. Negative- and positive-parity states are in the upper and lower row, respectively. Solid lines represent finite-range DWBA calculations normalized to the data for different values for the number of quanta *Q* in the relative α+^{13}C motion (see text for more details).

presolar SiC grains which is usually attributed to classical novae [96]. In this context the ^{13}N(α,p)^{16}O reaction plays an important role since it is in competition with ^{13}N β^+-decay to ^{13}C.

The evaluation of the ^{13}N(α,p)^{16}O reaction rate in the temperature range of interest between 0.4 and 1 GK requires a detailed knowledge of the structure of the compound nucleus ^{17}F within around 2.5 MeV above the ^{13}N+α threshold. Spins and parities are known in most cases and the energy and total widths of the states are known experimentally [97]. Given that the ^{13}N+α threshold S_α = 5818.7 (4) keV is much higher than the ^{16}O + p threshold S_p = 600.27 (25) keV, the states in the region of interest decay mainly by proton emission, so that $\Gamma_p \approx \Gamma_{tot}$. Their contribution to the reaction rate is therefore directly proportional to their unknown alpha-particle widths, which can be calculated from the spectroscopic factors obtained in an adequate α-particle transfer reaction.

The ^{13}N(^{7}Li,t)^{17}F transfer reaction would be the most evident reaction to perform. However, while not impossible, such an experimental study in inverse kinematics would require the use of an intense radioactive ^{13}N beam ($> 10^7$ pps) with a complex setup including an identification station at 0°, a large coverage charged particle array for the triton detection and an efficient γ-ray array needed to cope with the relatively high ^{17}F level density. Such setups have recently been used for the study of the ^{7}Li(^{15}O,tγ)^{19}Ne reaction at GANIL [65] and the ^{7}Li(^{17}O,tγ)^{21}Ne reaction at TRIUMF [98]. Given that, the α-particle widths of the ^{17}F states were deduced from the properties of ^{17}O analog states when such a correspondence is established [99]. The ^{13}C(^{7}Li,t)^{17}O reaction measurement [52] using a stable beam in direct kinematics was performed at the Tandem-ALTO facility in Orsay, France. A 34-MeV ^{7}Li^{3+} beam of about 100 enA impinged an enriched ^{13}C target of 80 μg/cm^2, and the tritons were momentum analyzed and focused on the focal-plane detection system of an Enge Split-Pole spectrometer [59]. The energy resolution of about 50 keV (FWHM) allowed to separate all the states of interest (see **Figure 2** in ref. 99) and to extract their angular distributions.

Examples of differential cross-sections for positive and negative parity ^{17}O states populated with different transferred angular momentum *L* are shown in **Figure 6**, together with finite-range DWBA calculations performed with the FRESCO code. An excellent agreement is observed between the theory and the experiment which supports a single step direct mechanism for the population of ^{17}O states using the ^{13}C(^{7}Li,t)^{17}O reaction. However unlike the single nucleon transfer reactions the angular distributions obtained from (^{7}Li,t) reactions are usually less pronounced with much less marked angular minima and maxima. Also, the shape of the angular distributions is not so sensitive to the transferred angular momentum *L* as can be observed in **Figure 6** which makes its determination more delicate.

Details about the ingredients needed for the FR-DWBA calculations, such as the optical potential parameters, the overlap between the α+t and ^{7}Li systems, and the geometry of the Woods-Saxon potential used to compute the wave-function describing the α+^{13}C relative motion, can be found in ref. 99. An important ingredient is the number of nodes *N* (defined here as excluding the origin) of the radial part of the α+^{13}C wave-function. Even though there is a limited sensitivity of the angular distributions to the number of nodes *N*, its determination should be whenever possible guided by microscopic considerations such as a cluster description of the

TABLE 1 | Alpha-particle spectroscopic factors and widths for negative-parity ^{17}O states obtained when considering a number of quanta in the relative α+^{13}C motion $Q = 6$ and $Q = 8$. Comparison with alpha widths from the literature is provided.

NNDC [97]			Q = 6			Q = 8		
E_x (keV)	J^π	Γ_α (keV)	N, L	C^2S_α	Γ_α (keV)	N, L	C^2S_α	Γ_α (keV)
5939 (4)	1/2$^-$		3, 0	0.19		4, 0	0.12	
7166 (8)	5/2$^-$	3.3×10^{-3}	2, 2	0.12	3.4×10^{-3}	3, 2	0.074	3.7×10^{-3}
7688 (9)	7/2$^-$	1.0×10^{-2}	1, 4	0.12	3.3×10^{-3}	2, 4	0.055	3.5×10^{-3}

states or from the insight of shell-model calculations. The link between these two views is not straightforward but there have been recent efforts to perform FR-DWBA calculations of the ^{12}C(^{7}Li,t)^{16}O reaction with the (N, L) parameters for the various components of the α+^{12}C wave functions obtained from shell model calculations [100]. In case of ^{17}O while lower states are well described by a single neutron above a close ^{16}O core, high energy states have been theoretically predicted [101], and observed for some of them [102], to be dominated by a mixture of 2p-1h/4p-3h and 3p-2h/5p-4h configurations[7] for negative- and positive-parity ^{17}O states, respectively. In the following discussion we make use of the number of quanta $Q = 2N + L$ for the relative α+^{13}C motion.

In the case of positive-parity states in ^{17}O, the 5p-4h configuration is not expected to be populated in direct α-particle transfer since the shell model overlap between a 5p-4h configuration in ^{17}O and the ^{13}C in its ground state and an α-particle would be zero. Since the experimental angular distributions are well described by a one step direct reaction mechanism this would mean that the reaction mechanism is sensitive to the 3p-2h configuration, either because the states have a dominant 3p-2h configuration, or, if they have a dominant 5p-4h configuration, because the (^{7}Li,t) mechanism is sensitive to the small admixture of 3p-2h configuration. When the two neutrons and protons of the transferred α-particle are positioned on the orbitals respecting a 3p-2h configuration one obtains $Q = 7$ for the number of quanta in the relative α+^{13}C motion from which can be derived the number of nodes N of the radial part of the wave function using the Talmi-Moshinsky relation [48] (see **Section 3.3.2**).

In a similar way for negative-parity states in ^{17}O, the 2p-1h and 4p-3h configurations can be associated to the number of quanta $Q = 6$ and $Q = 8$, respectively. Both cases are displayed in **Figure 6** and the two calculations show very similar behaviors except for angles larger than 35°. This emphasizes that the shape of the angular distributions in DWBA are not particularly sensitive to the number of nodes N. In the present case, without a better knowledge of the ^{17}O states structure, a choice has therefore to be made for Q and hence N. The value of the number of nodes has a strong impact on the alpha spectroscopic factors which can vary by a factor of almost two as reported in **Table 1** for a few states. However this has a much limited impact on the determination of the alpha width which only varies by less than ten percent in the present case. This is explained by the fact that when computing the reduced α-particle width (see **Equation. 11**), there is a compensation effect between the spectroscopic factor and the radial part of the α+^{13}C wave function whose shape depends strongly on its number of nodes. Similar effects were also observed in the study of the ^{15}N(^{7}Li,t)^{19}F reaction [103].

The ^{13}N(α,p)^{16}O reaction rate was calculated based on the previous spectroscopic information, and it was found to be within a factor of two of the previous evaluation done by Caughlan and Fowler [104]. A detailed Monte-Carlo study was then used to propagate the nuclear uncertainties to the reaction rate, and a factor of uncertainty of two to three was obtained. This translates into an overall uncertainty in the ^{13}C production of a factor of 50 when using the lower and upper reaction rates [99].

5.4 Case of the ^{60}Fe(n,γ)^{61}Fe Reaction

^{60}Fe(n,γ)^{61}Fe plays an important role in the abundance of ^{60}Fe which characteristic gamma-ray lines at 1173.23 and 1332.44 keV coming from the decay-chain of ^{60}Fe-^{60}Co-^{60}Ni have been observed by the spacecrafts missions RHESSI in 2004 [105] and INTEGRAL in 2007 [106]. The observation of these gamma-ray lines indicates that the nucleosynthesis of ^{60}Fe is still active in the Galaxy since its lifetime 2.6 million years is much smaller than the galactic time evolution which is around 10 billion years. An excess of ^{60}Fe has also been observed in deep ocean crusts and sediments as well as in lunar soils [107–109] and in galactic cosmic rays (CRIS/ACE) [110]. All these observations have underlined the need for accurate nuclear information concerning the stellar nucleosynthesis and destruction of this nucleus. ^{60}Fe is mainly produced in massive stars through the weak *s*-process component and it is released in the interstellar medium by the subsequent core-collapse supernovae explosion [111]. Thus, all ^{60}Fe observations give the opportunity to test stellar models that describe the evolution of massive stars. However, the important uncertainties surrounding the cross-section of the destruction reaction ^{60}Fe(n,γ)^{61}Fe imply large uncertainties on the predictions of ^{60}Fe abundance by stellar models.

The direct measurement of the cross-section of this reaction is very challenging due to the radioactive nature of ^{60}Fe. An alternative method would be to determine the cross-section through the activation method, which was performed by Uberseder et al. [112] or by the (d,p) transfer reaction to determine the excitation energies, orbital angular momenta and neutron spectroscopic factors of ^{61}Fe states that are important for the calculation of the direct component (**Section 2.2**) of the (n,γ) reaction cross-section in the region of astrophysical interest ($E_{c.m} \simeq 30$ *keV*). This method was chosen by Giron et al. [113] to study the strength of the contribution of the direct component to the ^{60}Fe(n,γ)^{61}Fe reaction.

[7]where the *x*p-*y*h notation has the usual meaning of *x* particles in the *sd*-shell and *y* holes in the 1*p* orbitals.

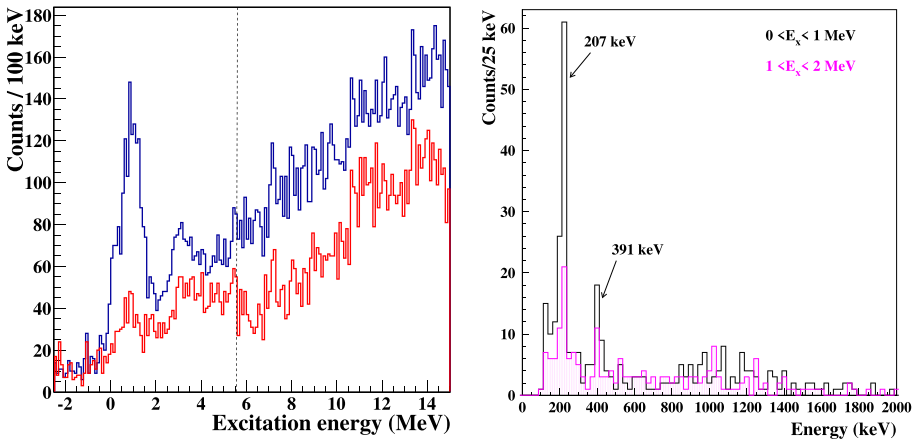

FIGURE 7 | (Color online) Left: Measured ^{61}Fe excitation energy spectrum in coincidences with gammas (red curve) and without coincidences (blue curve). The vertical dashed line corresponds to the neutron threshold. Right: Energy spectrum of the γ-rays in coincidences with protons detected in MUST2 or S1 detectors: Black, for an excitation energy gate between 0 to 1 MeV; pink, for a gate between 1 to 2 MeV.

Since ^{60}Fe is radioactive, it is very difficult to produce an ^{60}Fe target with enough areal density to perform the (d,p) reaction measurement with a deuteron beam. Consequently, the ^{60}Fe(d,p)^{61}Fe measurement was performed in inverse kinematics [113], using the 27 A.MeV ^{60}Fe secondary beam produced by fragmentation at LISE spectrometer line of GANIL and a deuterated polypropylene CD_2 target of 2.6 mg/cm^2 to induce the reaction.

The ^{60}Fe beam intensity produced was of about 10^5 pps which is the usual beam intensities one can get with radioactive beams not far from the valley of stability. As discussed in **Section 4** these low intensities required the use of large area and highly segmented silicon strip detector arrays placed at backward angles in the laboratory; four MUST2 telescopes [67] and an S1 annular DSSSD from Micron Semiconductor Ltd., in order to increase the angular coverage of the protons detection (from 2° to 23° in center of mass) and hence the statistics. The ^{60}Fe beam being produced by fragmentation has a large emittance. Therefore, to determine precisely the location of the proton emission point on the target and its emission angle, two multi-wire proportional chambers (MWPC) called CATS were used to track the beam. To disentangle the different populated states in ^{61}Fe that can not be discriminated with particle detection, four Germanium clovers (EXOGAM) [70] were used to detect the emitted γ-rays from the decay of the populated states in ^{61}Fe. As for the residual fragments, they were identified in mass and charge using their energy loss in the ionization chamber and the time of flight between the plastic scintillator at the end of the line and one of the CATS detectors.

The reconstructed ^{61}Fe energy spectrum using MUST2 energy and angle measurements is displayed in **Figure 7** (left panel), with and without γ coincidences.

Two peaks are observed below the neutron threshold S_n = 5.58 MeV. The first peak is around 1 MeV and the other at 3 MeV. The width of these peaks is 1.5 and 2 MeV respectively which is much larger than the expected excitation energy resolution, namely 800 keV. This is an indication that several levels are present in the peaks observed. The importance of detecting the γ-rays is obvious in this case.

One can also observe a drop of about a factor three in the counts of the main peak around 1 MeV when comparing the excitation energy spectrum with and without γ-ray coincidence while it is between 1.6 to a factor 2 everywhere else. This is a strong indication of the population of the isomeric state at 861 keV whose γ-rays can not be detected because they are emitted when ^{61}Fe ions are stopped in the plastic which is at a far distance from the EXOGAM detectors. Indeed the lifetime of the isomeric state (τ = 239 ns) is much longer than the time of flight of ^{61}Fe ions ($\simeq$ 13 ns) between the CD_2 target and the plastic.

From the observation of the gamma-ray spectra corresponding to two energy gates in the first peak, from 0 to 1 MeV and from 1 to 2 MeV in **Figure 7** (right panel) and from the comparison of the excitation energy spectrum with and without γ-ray coincidence in **Figure 7** (left panel), three states were clearly identified: the known 207 keV, the 391 keV and the isomeric state at 861 keV.

To extract the proton angular distributions of the identified states, a deconvolution of the first peak observed in ^{61}Fe excitation energy spectrum around 1 MeV was performed considering the ground state (gs), the three well identified populated states at 207 keV ($J^\pi = 5/2^-$), 391 ($J^\pi = 1/2^-$) and 861 keV ($J^\pi = 9/2^+$) and also a higher level centered at 1600 keV representing a mixture of the non-identified higher states between 1.2 and 2 MeV [113].

An example of the extracted proton angular distributions is displayed in **Figure 8** for the 861 keV state. The blue and the green curves are zero-range (ZR) and finite-range (FR) Adiabatic distorded wave approximation (ADWA) calculations, respectively (see **Section 3.1.4**). The magenta curve does not take into account the deuteron breakup, and is a zero range calculation using Daehnick et al. global parametrization [46] for the optical potential describing the entrance channel. All calculations were performed with the FRESCO code. Given the large statistical uncertainties all three calculations give a similar reduced chi-square. However, the incident beam energy of 27 A.MeV would correspond to an

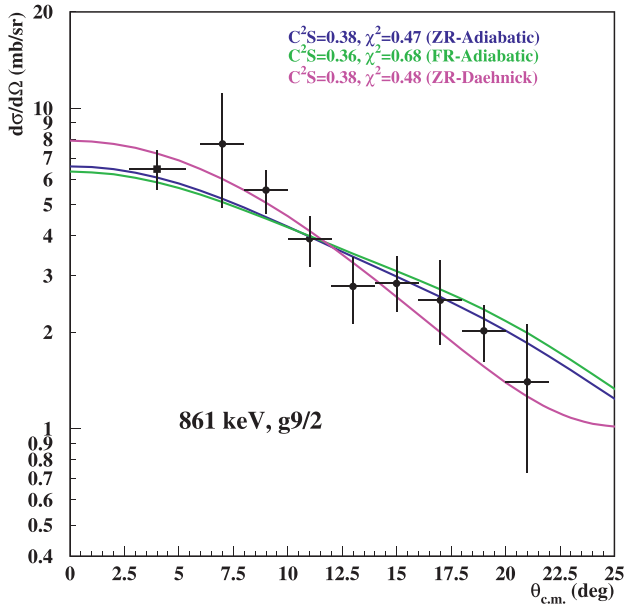

FIGURE 8 | (Color online) Experimental differential cross-sections for the 861 keV excited state, together with the different calculations normalized to the data. See text for details.

TABLE 2 | Comparison of the spectroscopic factors obtained in this work and those prediced in LNPS shell-model calculations.

States	C2S	C2S
keV	This work	Shell-model
g.s	0.15±0.06	0.07
270	0.34±0.10	0.42
391	0.58±0.20	0.71
861	0.38±0.07	0.52

incident deuteron energy of 54 MeV, and deuteron breakup should then be considered, therefore favoring the ADWA calculations. The main effect of taking into account the deuteron breakup is a noticeable difference in the shape of the differential cross-section with respect to the DWBA calculation, e.g., different position of the first angular minimum. Note as well that, in the present case, the ZR- and FR-ADWA calculations give similar results both in terms of the shape of the differential cross-section, and of the spectroscopic factors which differs by only 5%.

A comparison between the C^2S obtained in this work [113] with those predicted by shell-model calculations within a *fpgd* valence space using the LNPS[8], effective interaction [114] shows a very good agreement within the experimental error bars between the experimental results and the calculations (see **Table 2**). This confirms further the reliability of the LNPS shell-model calculations in the mass region around N = 34.

The direct component of $^{60}Fe(n,\gamma)^{61}Fe$ was calculated using the experimental C^2S for the first four excited states of ^{61}Fe and its value was found to be 0.2 mb at 25 keV. This represents 2% of the total cross-section measured in ref. 112.

6 SUMMARY AND PERSPECTIVES

In this review, we have focused in the transfer reaction method which has been widely used to derive very useful spectroscopic information (spectroscopic factors, partial widths, orbital momenta and resonance energies) needed to evaluate resonant and non-resonant reaction rates of astrophysical interest. The theoretical description of the method has been recalled and a review of its use in some recent experimental studies using stable and radioactive beams with different detection systems has been given.

The current development of exotic radioactive ion beams in many facilities around the world opens new opportunities for the study of astrophysical processes involving nuclei far from the valley of stability, such as the *r*- and *rp*-processes for examples. While transfer reactions in inverse kinematics have been performed with radioactive species since many years, their limited production rates always pushed forward the development of efficient detection systems. The implementation of such systems now relies on coupling in a compact way state of the art charged particles and γ-ray arrays; the design being always driven by a compromise between γ-ray detection efficiency and excitation energy resolution obtained from the charged-particles array. Recent examples are the MUGAST silicon array [115] coupled to the AGATA γ-ray spectrometer [71] at GANIL, and annular silicon detector coupled with the TIGRESS γ-ray array [72] at TRIUMF, to cite a few of them. Owing to the inverse kinematics of such measurements, the fusion and evaporation between the beam and the target usually induces a large background which must be coped with. Several experimental efforts have been focused on the development of dedicated targets limiting such induced background and energy straggling such as the JENSA windowless supersonic jet gas target [63].

On the theoretical side, many progresses have been made to describe one-nucleon overlap functions as well as to understand the three-body dynamics related to the deuteron breakup degrees of freedom, including the nonlocality effects [116] (and references therein). Prediction of nuclear properties based on a realistic description of the strong interaction is at the heart of the ab initio effort in low-energy nuclear theory. Ab initio calculations have long been limited to light nuclei [117], but with the ever-increasing computing power and its associated decreasing cost, ab initio calculations for many more nuclei are now in development [118]. These approaches are now used not only for predictions of binding energies but also to calculate one nucleon overlap functions [119, 120] and nucleon optical potentials [121, 122]. Developments of optical potentials calculations using microscopic models have also been recently undertaken [123] and the most recent WLH[9] microscopic global optical potential could be very useful for the

[8]Lenzi, Nowack, Poves and Sieja

[9]Whitehead, Li and Holt

future transfer reaction experiments involving proton and neutron-rich isotopes [124]. However, as Timofeyuk and Johnson pointed out so well *"providing an input from ab-initio approaches to a transfer reaction amplitude based on an oversimplified distorted-wave approximation does not make the reaction description truly microscopic. To date only four truly ab-initio calculations of one-nucleon transfer have been published"* [116], involving light nuclei not heavier than ^{8}Li [55–58].

Despite their use since more than 50 years, transfer reactions remain a powerful method in nuclear astrophysics which is still promised to have a bright future in the forthcoming decades to provide a better insight on the reactions that govern the Cosmos.

AUTHOR CONTRIBUTIONS

All authors have made a substantial, direct, and intellectual contribution to the work and approved it for publication.

ACKNOWLEDGMENTS

NdS thanks Anne Meyer for providing angular distributions and α-particle partial widths in case of $Q = 8$ for the ^{13}C(^{7}Li,t)^{17}O study. NdS also thanks Sarah Harrouz for making available material concerning her ^{30}Si(^{3}He,d)^{31}P analysis prior to publication. FH and NdS thank D. Beaumel for a careful reading of the manuscript and stimulating discussions.

REFERENCES

1. Lane AM, Thomas RG. R-matrix theory of nuclear reactions. *Rev. Mod. Phys* (1958) 30:257–353. doi:10.1103/RevModPhys.30.257
2. Thielemann FK, Arcones A, Käppeli R, Liebendörfer M, Rauscher T, Winteler C, et al. What are the astrophysical sites for the r-process and the production of heavy elements?. *Prog. Part Nucl Phys* (2011) 66:346–53. doi:10.1016/j.ppnp.2011.01.032
3. Arnould M, Goriely S, Takahashi K. The r-process of stellar nucleosynthesis: astrophysics and nuclear physics achievements and mysteries. *Phys. Rep* (2007) 450:97–213. doi:10.1016/j.physrep.2007.06.002
4. Mumpower M, Surman R, Aprahamian A. Variances in r-process predictions from uncertain nuclear rates. *J. Phys. Conf. Ser* (2015) 599:012031. doi:10.1088/1742-6596/599/1/012031
5. Käppeler F, Gallino R, Bisterzo S, Aoki W. The s process: nuclear physics, stellar models, and observations. *Rev. Mod. Phys* (2011) 83:157–94. doi:10.1103/RevModPhys.83.157
6. Satchler R. *Direct nuclear reactions*. 68 ed. Oxford: Clarendon Press, international series of monographs on physics (1983).
7. Bertulani CA, Baur G.Relativistic Coulomb collisions and the virtual radiation spectrum. *Nucl. Phys* (1985) 442:739–752. doi:10.1016/S0375-9474(85)80039-7
8. Baur G, Bertulani CA, Rebel H. Coulomb dissociation as a source of information on radiative capture processes of astrophysical interest. *Nucl. Phys* (1986) 458:188–204. doi:10.1016/0375-9474(86)90290-3
9. Baur G, Rebel H. Coulomb dissociation studies as a tool of nuclear astrophysics. *J. Phys. G Nucl. Phys* (1994) 20:1–33. doi:10.1088/0954-3899/20/1/005
10. Mukhamedzhanov AM, Timofeyuk NK. Astrophysical S-factor for the reaction Be+p→B+γ. *Sov. J. Exp. Theor. Phys. Lett* (1990) 51:282–284.
11. Mukhamedzhanov AM, Tribble RE. Connection between asymptotic normalization coefficients, subthreshold bound states, and resonances. *Phys. Rev. C* (1999) 59:3418–3424. doi:10.1103/PhysRevC.59.3418
12. Mukhamedzhanov AM, Gagliardi CA, Tribble RE. Asymptotic normalization coefficients, spectroscopic factors, and direct radiative capture rates. *Phys. Rev. C* (2001) 63:024612. doi:10.1103/PhysRevC.63.024612
13. Ratkiewicz A, Cizewski JA, Escher JE, Potel G, Burke JT, Casperson RJ, et al. Towards neutron capture on exotic nuclei: Demonstrating *(d,p γ)* as a surrogate reaction for *(n,γ)*. *Phys. Rev. C* (2019) 122:052502. doi:10.1103/PhysRevLett.122.052502
14. Baur G. Breakup reactions as an indirect method to investigate low-energy charged-particle reactions relevant for nuclear astrophysics. *Phys. Lett. B* (1986) 178:135–138. doi:10.1016/0370-2693(86)91483-8
15. Typel S, Baur G. Theory of the Trojan-Horse method. *Ann. Phys* (2003) 305:228–265. doi:10.1016/S0003-4916(03)00060-5
16. Spitaleri C, Mukhamedzhanov AM, Blokhintsev LD, La Cognata M, Pizzone RG, Tumino A. The Trojan Horse method in nuclear astrophysics. *Phys. Atom. Nucl* (2011) 74:1725–1739. doi:10.1134/S1063778811110184
17. Iliadis C. *Nuclear Physics of Stars*. (Wiley-VCH Verlag GmbH Co. KGaA,Boschstr. 12, 69469 Weinheim, Germany) (2007). doi:10.1002/9783527618750
18. Newton JR, Iliadis C, Champagne AE, Cesaratto JM, Daigle S, Longland R. Measurement of O(p,γ) F between the narrow resonances at E=193 and 519 keV. *Phys. Rev. C* (2010) 81:045801. doi:10.1103/PhysRevC.81.045801
19. Bardayan DW. Transfer reactions in nuclear astrophysics. *J. Phys. G Nucl. Phys* (2016) 43:043001. doi:10.1088/0954-3899/43/4/043001
20. Mohr P. Low-energy He(α,α)He elastic scattering and the He(α,γ)Be reaction. *Phys. Rev. C* (2009) 79:065804. doi:10.1103/PhysRevC.79.065804
21. Hammache F, Heil M, Typel S, Galaviz D, Sümmerer K, Coc A, et al. High-energy breakup of Li as a tool to study the big bang nucleosynthesis reaction H(α,γ)Li. *Phys. Rev. C* (2010) 82:065803. doi:10.1103/PhysRevC.82.065803
22. Goriely S. Direct neutron captures and the r-process nucleosynthesis. *Astron. Astrophys* (1997) 325:414–424.
23. Krausmann E, Balogh W, Oberhummer H, Rauscher T, Kratz K, Ziegert W. Direct neutron capture for magic-shell nuclei. *Phys. Rev. C Nucl. Phys* (1996) 53:469–474. doi:10.1103/PhysRevC.53.469
24. Kim BT, Izumoto T, Nagatani K. Radiative capture reaction He(α,γ)Be at low energies. *Phys. Rev. C* (1981) 23:33–41. doi:10.1103/PhysRevC.23.33
25. Krauss H. *Computer code TEDCA* TU Wien (unpublished) (1992).
26. Knutson LD, Haeberli W. Polarization effects in transfer reactions. *Prog. Part Nucl. Phys* (1980) 3:127–61. doi:10.1016/0146-6410(80)90031-9
27. Hauser W, Feshbach H. The inelastic scattering of neutrons. *Phys. Rev* (1952) 87:366–73. doi:10.1103/PhysRev.87.366
28. Nunes F. Continuum-discretised coupled channels methods. *Scholarpedia* (2011) 6:10497. doi:10.4249/scholarpedia.10497
29. Thompson IJ, Nunes FM. *Nuclear reactions for astrophysics*: Principles, Calculation and Applications of Low-Energy Reactions (Cambridge University Press) (2009). doi:10.1017/CBO9781139152150
30. Austern N. *Direct nuclear reaction theories*. New York: John Wiley & Sons (1970).
31. Macfarlane MH, Schiffer JP. Transfer reactions. *Pure Appl. Phys* (1974) 40:169–194. doi:10.1016/B978-0-12-165202-9.50011-7
32. Becchetti FD, Flynn ER, Hanson DL, Sunier JW. C(Li, t)O and stellar helium fusion. *Nucl. Phys* (1978) 305:293–312. doi:10.1016/0375-9474(78)90179-3
33. Rolfs CE, Rodney WS. Book-review–cauldrons in the cosmos–nuclear astrophysics. *S&T* (1989) 77:42
34. Ray L, Coker WR, Udagawa T. Exact finite-range DWBA treatment of heavy-ion-induced reactions to unbound residual states. *Phys. Lett. B* (1975) 56:318–20. doi:10.1016/0370-2693(75)90308-1
35. Tribble RE. Indirect techniques in nuclear astrophysics: the ANC method. *Nucl. Instrum. Methods Phys. Res. B* (2005) 241:204–208. doi:10.1016/j.nimb.2005.07.026
36. Brune CR, Geist WH, Kavanagh RW, Veal K. Sub-Coulomb α transfers on C and the C(α,γ)O S factor. *Phys. Rev. C* (1999) 83:4025–4028. doi:10.1103/PhysRevLett.83.4025

37. Avila ML, Rogachev GV, Koshchiy E, Baby LT, Belarge J, Kemper KW, et al. New measurement of the α asymptotic normalization coefficient of the 1/2 state in O at 6.356 MeV that dominates the C(α,n)O reaction rate at temperatures relevant for the ṡ-process. *Phys. Rev. C* (2015) 91:048801. doi:10.1103/PhysRevC.91.048801
38. Johnson RC, Soper PJ. Contribution of deuteron breakup channels to deuteron stripping and elastic scattering. *Phys. Rev. C* (1970) 1:976–989. doi:10.1103/PhysRevC.1.976
39. Wales GL, Johnson RC. Deuteron break-up effects in *(p,d)* reactions at 65 MeV. *Nucl. Phys* (1976) 274:168–176. doi:10.1016/0375-9474(76)90234-7
40. King GB, Lovell AE, Nunes FM. Uncertainty quantification due to optical potentials in models for *(d,p)* reactions. *Phys. Rev. C* (2018) 98:044623. doi:10.1103/PhysRevC.98.044623
41. Thompson IJ. Coupled reaction channels calculations in nuclear physics. *Comput. Phys. Rep* (1988) 7:167.
42. Kunz P (1996). Available from: https://oecd-nea.org/tools/abstract/detail/nesc9872.
43. Igarashi M. Twofnr finite-range dwba code. *Tech. rep.* (1977).
44. Macfarlane MH, Pieper SC. A program for heavy-ion direct-reaction calculations. *Tech. Rep. ANL-76-11, Rev.* 1, (1970). p. 76–111. Argonne National Laboratory.
45. Perey CM, Perey FG. Compilation of phenomenological optical-model parameters 1954-1975. *Atomic Data Nucl. Data Tables* (1976) 17:1. doi:10.1016/0092-640X(76)90007-3
46. Daehnick WW, Childs JD, Vrcelj Z. Global optical model potential for elastic deuteron scattering from 12 to 90 MeV. *Phys. Rev. C* (1980) 21:2253–2274. doi:10.1103/PhysRevC.21.2253
47. Koning AJ, Delaroche JP. Local and global nucleon optical models from 1 keV to 200 MeV. *Nucl. Phys* (2003) 713:231–310. doi:10.1016/S0375-9474(02)01321-0
48. Moshinsky M. Transformation brackets for harmonic oscillator functions. *Nucl. Phys* (1959) 13:104–16. doi:10.1016/0029-5582(59)90143-9
49. Reid RV. Local phenomenological nucleon-nucleon potentials. *Ann Phys* (1968) 50:411–448. doi:10.1016/0003-4916(68)90126-7
50. Brida I, Pieper SC, Wiringa RB. Quantum Monte Carlo calculations of spectroscopic overlaps in A7 nuclei. *Phys. Rev. C* (2011) 84:024319. doi:10.1103/PhysRevC.84.024319
51. Flavigny F, Keeley N, Gillibert A, Obertelli A. Single-particle strength from nucleon transfer in oxygen isotopes: sensitivity to model parameters. *Phys. Rev. C* (2018) 97:034601. doi:10.1103/PhysRevC.97.034601
52. Pellegriti MG, Hammache F, Roussel P, Audouin L, Beaumel D, Descouvemont P, et al. Indirect study of the C(α,n)O reaction via the C(Li,t)O transfer reaction. *Phys. Rev. C* (2008) C77:042801. doi:10.1103/PhysRevC.77.042801
53. Oulebsir N, Hammache F, Roussel P, Pellegriti MG, Audouin L, Beaumel D, et al. Indirect study of the C(α,γ)O reaction via the C(Li,t)O transfer reaction. *Phys. Rev. C* (2012) 85:035804. doi:10.1103/PhysRevC.85.035804
54. Duguet T, Hergert H, Holt JD, Somà V. Nonobservable nature of the nuclear shell structure: meaning, illustrations, and consequences. *Phys. Rev. C* (2015) 92:034313. doi:10.1103/PhysRevC.92.034313
55. Arai K, Aoyama S, Suzuki Y, Descouvemont P, Baye D. Tensor force manifestations in ab initio study of the 2H(d,γ)4He, 2H(d,p)3H, and 2H(d,n)3He reactions. *Phys. Rev. Lett* (2011) 107:132502. doi:10.1103/PhysRevLett.107.132502
56. Navrátil P, Quaglioni S. Ab initio many-body calculations of the (3)H(d,n)(4)He and (3)He(d,p)(4)He fusion reactions. *Phys. Rev. Lett* (2012) 108:042503. doi:10.1103/PhysRevLett.108.042503
57. Deltuva A, Fonseca AC. Calculation of multichannel reactions in the four-nucleon system above breakup threshold. *Phys. Rev. Lett* (2014) 113:102502. doi:10.1103/PhysRevLett.113.102502
58. Raimondi F, Hupin G, Navrátil P, Quaglioni S. Deuteron-induced nucleon transfer reactions within an ab initio framework: first application to Ƥ-shell nuclei. *Phys. Rev. C* (2016) 93:054606. doi:10.1103/PhysRevC.93.054606
59. Spencer JE, Enge HA. Split-pole magnetic spectrograph for precision nuclear spectroscopy. *Nucl. Instrum. Methods* (1967) 49:181
60. Löffler M, Scheerer HJ, Vonach H. The ion optical properties of the Munich Q3D-spectrograph investigated by means of a special experimental ray tracing method. *Nucl. Instrum. Methods* (1973) 111:1–12. doi:10.1016/0029-554X(73)90090-6
61. Ottini-Hustache S, Mazur C, Auger F, Musumarra A, Alamanos N, Cahan B, et al. CATS, a low pressure multiwire proportionnal chamber for secondary beam tracking at GANIL. *Nucl. Instrum. Methods Phys. Res* (1999) 431:476–484. doi:10.1016/S0168-9002(99)00380-0
62. Kumagai H, Ohnishi T, Fukuda N, Takeda H, Kameda D, Inabe N, et al. Development of parallel plate Avalanche counter (PPAC) for BigRIPS fragment separator. *Nucl. Instrum. Methods Phys. Res. B* (2013) 317:717–727. doi:10.1016/j.nimb.2013.08.050
63. Schmidt K, Chipps KA, Ahn S, Bardayan DW, Browne J, Greife U, et al. Status of the JENSA gas-jet target for experiments with rare isotope beams. *Nucl. Instrum. Methods Phys. Res* (2018) 911:1–9. doi:10.1016/j.nima.2018.09.052
64. Ryuto H, Kunibu M, Minemura T, Motobayashi T, Sagara K, Shimoura S, et al. Liquid hydrogen and helium targets for radioisotope beams at RIKEN. *Nucl. Instrum. Methods Phys. Res* (2005) 555:1–5. doi:10.1016/j.nima.2005.08.102
65. Sanchez Rojo J, Diget CA, de Séréville N, et al. (2019). In preparation.
66. Labiche M, Catford WN, Lemmon RC, Timis CN, Chapman R, Orr NA, et al. TIARA: a large solid angle silicon array for direct reaction studies with radioactive beams. *Nucl. Instrum. Methods Phys. Res* (2010) 614:439–448. doi:10.1016/j.nima.2010.01.009
67. Pollacco E, Beaumel D, Roussel-Chomaz P, Atkin E, Baron P, Baronick JP, et al. MUST2: a new generation array for direct reaction studies. *Eur. Phys. J. A Suppl* (2005) 25:287–288. doi:10.1140/epjad/i2005-06-162-5
68. Diget CA, Fox SP, Smith A, Williams S, Porter-Peden M, Achouri L, et al. SHARC: silicon highly-segmented array for reactions and coulex used in conjunction with the TIGRESS γ-ray spectrometer. *J. Instrum* (2011) 6:P02005. doi:10.1088/1748-0221/6/02/P02005
69. Bardayan DW, Ahn S, Blackmon JC, Burkhart AJ, Chae KY, Cizewski JA, et al. Construction and commissioning of the SuperORRUBA detector. *Nucl. Instrum. Methods Phys. Res* (2013) 711:160–165. doi:10.1016/j.nima.2013.01.035
70. Simpson J, Azaiez F, De France G, Fouan G, Gerl J, Julin R, et al. The EXOGAM array: a radioactive beam gamma-ray spectrometer. *Acta Phys. Hungarica New Ser. Heavy ion* (2000) 11:159–88.
71. Akkoyun S, Algora A, Alikhani B, Ameil F, de Angelis G, Arnold L, et al. AGATA—advanced GAmma tracking array. *Nucl. Instrum. Methods Phys. Res* (2012) 668:26–58. doi:10.1016/j.nima.2011.11.081
72. Hackman G, Svensson CE. The TRIUMF-ISAC gamma-ray escape suppressed specrometer, TIGRESS. *Hyperfine Interact* (2014) 225:241–251. doi:10.1007/s10751-013-0905-7
73. Paschalis S, Lee IY, Macchiavelli AO, Campbell CM, Cromaz M, Gros S, et al. The performance of the gamma-ray energy tracking in-beam nuclear array GRETINA. *Nucl. Instrum. Methods Phys. Res* (2013) 709:44–55. doi:10.1016/j.nima.2013.01.009
74. Parikh A, Wimmer K, Faestermann T, Hertenberger R, José J, Wirth HF, et al. Isotopic S/S ratio as a diagnostic of presolar grains from novae. *Phys. Lett. B* (2014) 737:314–319. doi:10.1016/j.physletb.2014.08.071
75. Gillespie SA, Parikh A, Barton CJ, Faestermann T, José J, Hertenberger R, et al. First measurement of the S(p ,γ)Cl reaction rate through indirect methods for presolar nova grains. *Phys. Rev. C* (2017) 96:025801. doi:10.1103/PhysRevC.96.025801
76. Adekola AS, Bardayan DW, Blackmon JC, Brune CR, Chae KY, Domizioli C, et al. First proton-transfer study of F+p resonances relevant for novae. *Phys. Rev. C* (2011) 83:052801. doi:10.1103/PhysRevC.83.052801
77. de Séréville N, Coc A, Angulo C, Assunção M, Beaumel D, Berthoumieux E, et al. Indirect study of Ne states near the F+p threshold. *Nucl. Phys* (2007) 791:251–266. doi:10.1016/j.nuclphysa.2007.02.003
78. Kozub RL, Arbanas G, Adekola AS, Bardayan DW, Blackmon JC, Chae KY, et al. Neutron single particle structure in 131Sn and direct neutron capture cross sections. *Phys. Rev. Lett* (2012) 109:172501. doi:10.1103/PhysRevLett.109.172501
79. SwanChipps S, Hammache F, de Séréville N, Roussel P, Burgunder J, Moukaddam M, et al. Spectroscopy of Fe via the neutron transfer reaction H(Fe,p) Fe. *Phys. Rev. C* (2017) 95:035806. doi:10.1103/PhysRevC.95.035806
80. Wang TF, Champagne AE, Hadden JD, Magnus PV, Smith MS, Howard AJ, et al. Proton threshold states in Si and the destruction of Al at low stellar

temperatures. *Nucl. Phys* (1989) 499:546–564. doi:10.1016/0375-9474(89)90545-9
81. Bardayan DW, Chipps KA, Ahn S, Blackmon JC, deBoer RJ, Greife U, et al. The first science result with the JENSA gas-jet target: confirmation and study of a strong subthreshold F(p,α)O resonance. *Phys. Lett. B* (2015) 751:311–315. doi:10.1016/j.physletb.2015.10.073
82. Bardayan DW, Howard JA, Blackmon JC, Brune CR, Chae KY, Hix WR, et al. Astrophysically important Si states studied with the Si(p,t)Si reaction. II. Spin of the 5.914-MeV Si level and galactic Al production. *Phys. Rev. C* (2006) 74:045804. doi:10.1103/PhysRevC.74.045804
83. Keeley N, Drummer TL, Bartosz EE, Brune CR, Cathers PD, Fauerbach M, et al. Multistep processes in the C(Li,d) stripping reaction. *Phys. Rev. C* (2003) 67:044604. doi:10.1103/PhysRevC.67.044604
84. Kemper KW, Ophel TR. The non-statistical population of the 11.10 MeV (4) state in O by C(Li,d). *Aust. J. Phys* (1980) 33:197. doi:10.1071/PH800197a
85. Bethge K, Pullen DJ, Middleton R. Level Structure of O and the C(Li,d) and C(Li, t) reactions. *Phys. Rev. C* (1970) 2:395–401. doi:10.1103/PhysRevC.2.395
86. Bethge K. Alpha-particle transfer reactions. *Annu. Rev. Nucl. Part Sci* (1970) 20:255–288. doi:10.1146/annurev.ns.20.120170.001351
87. Cohen JG, Kirby EN. The bizarre chemical inventory of NGC 2419, an extreme outer Halo globular cluster. *APJ (Acta Pathol Jpn)* (2012) 760:86. doi:10.1088/0004-637X/760/1/86
88. Charbonnel C. Multiple stellar populations and their evolution in globular clusters: a nucleosynthesis perspective. *EAS Publ. Ser* (2016) 80-81:177–226. doi:10.1051/eas/1680006
89. Bastian N, Lardo C. Multiple stellar populations in globular clusters. *Annu. Rev. Astron. Astrophys* (2018) 56:83–136. doi:10.1146/annurev-astro-081817-051839
90. Dermigny JR, Iliadis C. Sensitivity to thermonuclear reaction rates in modeling the abundance anomalies of NGC 2419. *APJ (Acta Pathol Jpn)* (2017) 848:14. doi:10.3847/1538-4357/aa8ad0
91. Harrouz DS, de Séréville N, et al. (2020). In preparation.
92. Vernotte J, Khendriche A, Berrier-Ronsin G, Grafeuille S, Kalifa J, Rotbard G, et al. 30Si(3He,d)31P reaction at 25 MeV. *Phys. Rev. C Nucl. Phys* (1990) 41:1956–1974. doi:10.1103/PhysRevC.41.1956
93. WildenthalTamisier RH. Normalization of and Finite-Range Effects in (He,d) and (t, d) reactions. *Phys. Rev* (1966) 149:791–797. doi:10.1103/PhysRev.149.791
94. Vincent CM, Fortune HT. New method for distorted-wave analysis of stripping to unbound states. *Phys. Rev. C* (1970) 2:782–792. doi:10.1103/PhysRevC.2.782
95. Pignatari M, Zinner E, Hoppe P, Jordan CJ, Gibson BK, Trappitsch R, et al. Carbon-rich presolar grains from massive stars: subsolar C/C and N/N ratios and the mystery of N. *APJ (Acta Pathol Jpn)* (2015) 808:L43. doi:10.1088/2041-8205/808/2/L43
96. Amari S, Gao X, Nittler LR, Zinner E, José J, Hernanz M, et al. Presolar grains from novae. *APJ (Acta Pathol Jpn)* (2001) 551:1065–1072. doi:10.1086/320235
97. Tilley DR, Weller HR, Cheves CM. Energy levels of light nuclei A = 16-17. *Nucl. Phys* (1993) 564:1–183. doi:10.1016/0375-9474(93)90073-7
98. Williams M, Laird AM, Diget CA, Davids B, et al. (2019). In preparation.
99. Meyer A, de Séréville N, Laird AM, Hammache F, Longland R, Lawson T, et al. Evaluation of the N(α ,p)O thermonuclear reaction rate and its impact on the isotopic composition of supernova grains. *Phys. Rev. C* (2020) 102:035803. doi:10.1103/PhysRevC.102.035803
100. Weintraub WD, Keeley N, Kemper KW, Kravvaris K, Maréchal F, Robson D, et al. Analyzing powers and the role of multistep processes in the C(Li,t)O reaction. *Phys. Rev. C* (2019) 100:024604. doi:10.1103/PhysRevC.100.024604
101. Brown GE, Green AM. Even parity states of O and O. *Nucl. Phys. A* (1966) 75:401–417. doi:10.1016/0029-5582(66)90771-1
102. Cunsolo A, Foti A, Immè G, Pappalardo G, Raciti G, Saunier N. C(Li, t) O reaction at E(Li)=34 MeV. *Phys. Rev. C* (1981) 24:2127–2135. doi:10.1103/PhysRevC.24.2127
103. de Oliveira F, Coc A, Aguer P, Angulo C, Bogaert G, Kiener J, et al. Determination of α-widths in F relevant to fluorine nucleosynthesis. *Nucl. Phys* (1996) 597:231–252. doi:10.1016/0375-9474(95)00455-6
104. Caughlan GR, Fowler WA. Thermonuclear reaction rates V. *Atomic Data Nucl. Data Tables* (1988) 40:283–334. doi:10.1016/0375-9474(78)90179-3
105. Smith DM. RHESSI results on γ-ray lines from diffuse radioactivity. *New Rev* (2004) 48:87–91. doi:10.1016/j.newar.2003.11.011
106. Wang W, Harris MJ, Diehl R, Halloin H, Cordier B, Strong AW, et al. SPI observations of the diffuse Fe emission in the galaxy. *Astron. Astrophys* (2007) 469:1005–1012. doi:10.1051/0004-6361:20066982
107. Knie K, Korschinek G, Faestermann T, Dorfi EA, Rugel G, Wallner A. 60Fe anomaly in a deep-sea manganese crust and implications for a nearby supernova source. *Phys. Rev. Lett* (2004) 93:171103. doi:10.1103/PhysRevLett.93.171103
108. Wallner A, Feige J, Kinoshita N, Paul M, Fifield LK, Golser R, et al. Recent near-Earth supernovae probed by global deposition of interstellar radioactive (60)Fe. *Nature* (2016) 532:69–72. doi:10.1038/nature17196
109. Fimiani L, Cook DL, Faestermann T, Gómez-Guzmán JM, Hain K, Herzog G, et al. Interstellar <mml:mmultiscripts>Fe 60 </mml:mmultiscripts> on the surface of the moon. *Phys. Rev. C* (2016) 116:151104. doi:10.1103/PhysRevLett.116.151104
110. WinklerHonda WR, Israel MH, Christian ER, Cummings AC, de Nolfo GA, Lave KA, et al. Observation of the ^{60}Fe nucleosynthesis-clock isotope in galactic cosmic rays. *Science* (2016) 352:677–80. doi:10.1126/science.aad6004
111. WiedenbeckLeske M, Chieffi A. Nucleosynthesis of Fe in massive stars. *New Rev* (2006) 50:474–476. doi:10.1016/j.newar.2006.06.005
112. Uberseder E, Reifarth R, Schumann D, Dillmann I, Pardo CD, Görres J, et al. Measurement of the 60Fe(n, gamma)61Fe cross section at stellar temperatures. *Phys. Rev. Lett* (2009) 102:151101. doi:10.1103/PhysRevLett.102.151101
113. WiescherHeil S, Hammache F, de Séréville N, Roussel P, Burgunder J, Moukaddam M, et al. Spectroscopy of Fe via the neutron transfer reaction H(Fe,p) Fe. *Phys. Rev. C* (2017b) 95:035806. doi:10.1103/PhysRevC.95.035806
114. Lenzi SM, Nowacki F, Poves A, Sieja K. Island of inversion around Cr64. *Phys. Rev. Lett* (2010) 82:054301. doi:10.1103/PhysRevC.82.054301
115. Assié M, et al. (2020) In preparation. Available from: http://grit.in2p3.fr.
116. Timofeyuk NK, Johnson RC. Theory of deuteron stripping and pick-up reactions for nuclear structure studies. *Prog. Part Nucl. Phys* (2020) 111:103738. doi:10.1016/j.ppnp.2019.103738
117. Navrátil P, Quaglioni S, Hupin G, Romero-Redondo C, Calci A. Unified ab initio approaches to nuclear structure and reactions. *Physica Scripta* 91 (2016) 053002. doi:10.1088/0031-8949/91/5/053002
118. Cipollone A, Barbieri C, Navrátil P. Chiral three-nucleon forces and the evolution of correlations along the oxygen isotopic chain. *Phys. Rev. C* (2015) 92:014306. doi:10.1103/PhysRevC.92.014306
119. Navrátil P. Cluster form factor calculation in the ab initio no-core shell model. *Phys. Rev. C* (2004) 70:054324. doi:10.1103/PhysRevC.70.054324
120. Flavigny F, Gillibert A, Nalpas L, Obertelli A, Keeley N, Barbieri C, et al. Limited asymmetry dependence of correlations from single nucleon transfer. *Phys. Rev. Lett* (2013) 110:122503. doi:10.1103/PhysRevLett.110.122503
121. UtsunoBeaumel J, Danielewicz P, Hagen G, Nunes FM, Papenbrock T. Optical potential from first principles. *Phys. Rev. C* (2017) 95:024315. doi:10.1103/PhysRevC.95.024315
122. Rotureau J, Danielewicz P, Hagen G, Jansen GR, Nunes FM. Microscopic optical potentials for calcium isotopes. *Phys. Rev. C* (2018) 98:044625. doi:10.1103/PhysRevC.98.044625
123. Dickhoff WH, Charity RJ. Recent developments for the optical model of nuclei. *Prog. Part Nucl. Phys* (2019) 105:252–299. doi:10.1016/j.ppnp.2018.11.002
124. Whitehead TR, Lim Y, Holt JW. Microscopic global optical potential for rare isotope reactions (2020). arXiv e-printsarXiv:200908436

Conflict of Interest: The authors declare that the research was conducted in the absence of any commercial or financial relationships that could be construed as a potential conflict of interest.

frontiers in Astronomy and Space Sciences

REVIEW
published: 21 April 2021
doi: 10.3389/fspas.2021.617765

Massive Star Modeling and Nucleosynthesis

*Sylvia Ekström**

Department of Astronomy, Geneva University, Versoix, Switzerland

After a brief introduction to stellar modeling, the main lines of massive star evolution are reviewed, with a focus on the nuclear reactions from which the star gets the needed energy to counterbalance its gravity. The different burning phases are described, as well as the structural impact they have on the star. Some general effects on stellar evolution of uncertainties in the reaction rates are presented, with more precise examples taken from the uncertainties of the $^{12}C(\alpha,\gamma)^{16}O$ reaction and the sensitivity of the *s*-process on many rates. The changes in the evolution of massive stars brought by low or zero metallicity are reviewed. The impact of convection, rotation, mass loss, and binarity on massive star evolution is reviewed, with a focus on the effect they have on the global nucleosynthetic products of the stars.

Keywords: stars: evolution, stars: massive, nucleosynthesis, reaction rates, numerical models, stars: modeling

OPEN ACCESS

Edited by:
Rosario Gianluca Pizzone, Laboratori Nazionali del Sud (INFN), Italy

Reviewed by:
Marco Pignatari, University of Hull, United Kingdom
Scilla Degl'Innocenti, University of Pisa, Italy

***Correspondence:**
Sylvia Ekström
sylvia.ekstrom@unige.ch

Specialty section:
This article was submitted to Nuclear Physics, a section of the journal Frontiers in Astronomy and Space Sciences

Received: *15 October 2020*
Accepted: *22 March 2021*
Published: *21 April 2021*

Citation:
Ekström S (2021) Massive Star Modeling and Nucleosynthesis. Front. Astron. Space Sci. 8:617765. doi: 10.3389/fspas.2021.617765

1. INTRODUCTION TO STELLAR MODELING

Massive stars are key drivers of the evolution of the Universe, through the chemical and kinetic imprint they impose on their surrounding. Their intense luminosity makes them dominant contributors to the spectra of galaxies, and tracers of star formation in the early Universe. However, as they are much rarer than low- or intermediate-mass stars, it has for a long time been impossible to have statistically significant observations of massive stars, and our understanding relied mainly on stellar models. Since a couple of decades, large surveys (either dedicated to massive stars or wide enough to include a significant number of them) are starting to fill this gap and provide observational constraints that highlight the strengths and weaknesses of our massive stars models. In parallel, the improvement of computational facilities makes it possible to study some physical processes (like convection) from first principles in hydrodynamical simulations. While a full evolution of the entire star for its complete lifetime is not possible in 3D, the hydrodynamical simulations can provide precious recipes for 1D secular evolution modeling. This review intends to summarize the safe grounds and challenges of massive star evolution modeling and nucleosynthesis, with a focus on the role played by the reaction rates of importance in the modeling.

The evolution of stars is a long and desperate struggle against gravity. Thanks to their gaseous nature, they resist most of their lifetime by adjusting on a thermal structure that provides the pressure needed to exactly counterbalance the gravitational pull, and settle on what is called hydrostatic equilibrium, where the pressure gradient exactly compensate for the gravity:

$$\frac{dP}{dr} = -g\rho \tag{1}$$

with P the pressure (gas and radiation), r the internal radius, $g = -\frac{GM_r}{r^2}$ the local gravity at radius r with internal mass M_r, and ρ the density.

This equation is the first of the four equations of the internal structure of stars, developed by Sir Eddington in his series of papers about the constitution of stars (Eddington, 1916, 1917, 1918). To fully describe a stellar structure, we need three other equations: the mass continuity

$$\frac{\mathrm{d}M}{\mathrm{d}r} = 4\pi r^2 \rho, \tag{2}$$

the conservation of energy

$$\frac{\mathrm{d}L}{\mathrm{d}r} = 4\pi r^2 \rho \left(\epsilon + \epsilon_{\mathrm{grav}}\right), \tag{3}$$

with L the local luminosity, ϵ the energy generated inside the star through nuclear burning, and ϵ_{grav} the gravitational energy, and finally an expression for the radiative transfer

$$\frac{\mathrm{d}T}{\mathrm{d}r} = -\frac{3\kappa\rho}{acT^3}\frac{L_r}{4\pi r^2} \tag{4}$$

with T the temperature, κ the opacity of the gas, and a and c the constants of radiation and light speed respectively. In this equation, we need to define the opacity of the stellar matter κ. This is usually done through data tables provided by large opacity projects such as OPAL[1] or the OP[2] projects.

To close this set of equations, we need an equation of state (EOS) linking P, T, and ρ in an expression like

$$\Delta \ln \rho = \alpha \Delta \ln P - \delta \Delta \ln T - \varphi \Delta \ln \mu. \tag{5}$$

where the dependence of ρ on the gradient of chemical composition $\Delta \ln \mu$ has been added. If we combine Equations (1) and (2), we obtain that $\Delta \ln P = \frac{4}{3}\Delta \ln \rho$, and with Equation (5) we have:

$$\Delta \ln T = \left(\frac{4\alpha - 3}{3\delta}\right) \Delta \ln \rho. \tag{6}$$

In this general expression for the hydrostatic equilibrium, all the subtleties of the physics are hidden in the values for α, δ, and φ. For example, in the case of a perfect gas ($P = \frac{\rho}{\mu m_{\mathrm{H}}} kT$, with k the Boltzmann's constant and m_{H} the hydrogen mass), we have $\alpha = \delta = \varphi = 1$. Neglecting the gradient of composition, Equation 6 becomes $\Delta \ln T = \frac{1}{3}\Delta \ln \rho$, which gives the 1/3 slope of the evolution of stars in a diagram of T as a function of ρ (**Figure 1**). In this region of the diagram, if there is an increase in energy, which drives an increase in temperature, the pressure will react to it and restore the equilibrium. In contrast, for a degenerate non-relativistic gas we have $\alpha = 3/5$ and $\delta = 0$. The annihilation of δ has for consequence that the evolution of T is no longer linked to that of P or ρ. Instead of having a stable nuclear reactor (for which any increase in T is compensated by a readjustment of P that restores the equilibrium), the star enters an unstable regime where nuclear deflagration is possible. Of course, stars are not just composed of gas, and the radiation contributes to the total pressure: $P_{\mathrm{tot}} = \frac{\rho}{\mu m_{\mathrm{H}}} kT + \frac{1}{3}aT^4$. The more massive the star, the stronger the radiation component becomes.

[1]https://opalopacity.llnl.gov
[2]http://opacities.osc.edu

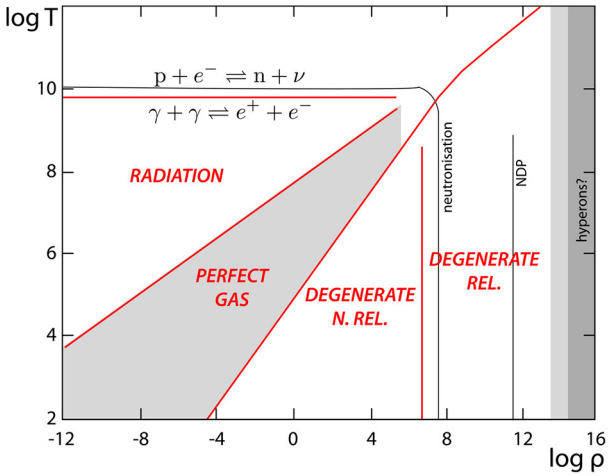

FIGURE 1 | T vs. ρ diagram showing the different regimes of the state of matter.

While most of the time we observe only the surface of stars, their fate depends almost uniquely on what happens deep in their cores. We saw that the center of a star evolves more or less on a slope of 1/3 in the T vs. ρ diagram. But sooner or later, it will hit the limit between perfect gas and degenerate gas, which has a slope 2/3. The phase at which this limit is attained defines the *type* of a star. *Low-mass stars* become degenerate at the end of core H burning; *intermediate-mass stars* reach it after core He burning; *massive stars* are able to go through all fusion phases before entering too much into the degenerate zone. The exact masses at which the transitions occur depend on the input physics of the models, but roughly, below 2 $M_{\odot}$ we have low-mass stars, between 2 and 10 $M_{\odot}$ we have intermediate-mass stars, and above 10 $M_{\odot}$ we have massive stars (Siess, 2008; Jones et al., 2013).

To solve the equation of the conservation of energy, Equation (3), we need to determine the energy generated inside the star (ϵ). The nuclear reaction rates providing this energy are usually included in stellar evolution codes either through analytical expressions based on T and ρ, or through tables of the rates as a function of the temperature. In many cases, several determinations of a given reaction rates have been performed, and sometime large uncertainties remain. The consequences of these uncertainties will be presented in section 3.

2. MASSIVE STARS EVOLUTION AND NUCLEOSYNTHESIS

2.1. Main Sequence

Like all types of stars, massive stars start their nuclear journey with H fusion. Like intermediate-mass stars, they do so dominantly through the CNO cycle, which has a much steeper dependence on temperature than the *pp*-chains:

$$\epsilon_{pp}(T) = \epsilon_{pp}(T_0)\left(\frac{T}{T_0}\right)^4$$

$$\epsilon_{\mathrm{CNO}}(T) = \epsilon_{\mathrm{CNO}}(T_0)\left(\frac{T}{T_0}\right)^{17}$$

The CNO cycle dominates upon *pp*-chains when $T \gtrsim 20$ MK. The transition from a *pp*-chain dominated H burning to a CNO-cycle dominated H burning marks the limit between the typical low-mass stars structure (with a radiative core and a convective envelope) and the intermediate-mass and massive stars structure (having a convective core and a radiative envelope).

Details of the nuclear reactions occurring inside the stars can be found in Iliadis (2007), we will just summarize the main ones here. The principle of the CNO cycle is to produce He from H using C, N, and O as catalysts, through a cycle of reactions (CNO1):

$$^{12}\mathrm{C}(p,\gamma)^{13}\mathrm{N}(\beta^+\nu)^{13}\mathrm{C}(p,\gamma)^{14}\mathrm{N}(p,\gamma)^{15}\mathrm{O}(\beta^+\nu)^{15}\mathrm{N}(p,\alpha)^{12}\mathrm{C}.$$

At the end of this chain, the ^{12}C atom used at the beginning of the chain is released along with the α particle, which is why we called it a catalyst. While α-decay is the dominant channel for the proton capture by ^{15}N, the γ-decay channel can occur and leads to a secondary cycle (CNO2):

$$^{14}\mathrm{N}(p,\gamma)^{15}\mathrm{O}(\beta^+\nu)^{15}\mathrm{N}(p,\gamma)^{16}\mathrm{O}(p,\gamma)^{17}\mathrm{F}(\beta^+\nu)^{17}\mathrm{O}(p,\alpha)^{14}\mathrm{N}.$$

The same branching between (p,α) and (p,γ) channels occurs for the proton capture on ^{17}O, leading to a tertiary cycle (CNO3):

$$^{17}\mathrm{O}(p,\gamma)^{18}\mathrm{F}(\beta^+\nu)^{18}\mathrm{O}(p,\alpha)^{15}\mathrm{N}.$$

Generally, the (p,α) channel is a thousand times more probable than the (p,γ) one, favoring CNO1 over CNO2, and CNO2 over CNO3. The slowest reaction of the complete CNO cycle is $^{14}\mathrm{N}(p,\gamma)^{15}\mathrm{O}$ (with a timescale of around 10^8 yrs), which results in an accumulation of ^{14}N in zones where H-burning has left its imprint. Note however that the sum C+N+O remains mostly unchanged in those layers during H burning.

When the temperature is high enough, the H burning into He can occur through two other cycles: the Ne-Na and Mg-Al cycles. Though the reaction rates for these cycles are subject to large uncertainties, they are supposed to play a role in the anti-correlation between O and Na observed in multiple populations of globular clusters (Gratton et al., 2004, and references therein). Also the synthesis of ^{26}Al in H-burning with $T > 35-40$ MK makes it a tracer of the formation of massive stars in the Galaxy (Prantzos and Diehl, 1996).

When H becomes depleted in the core, the burning starts moving outwards, to the border of the contracting core. This translates at the surface by a hook in the Hertzsprung-Russell (HR) diagram, the star moving toward a higher effective temperature (see the red dot on the black track of **Figure 4**). When H is completely depleted, the core stops producing any energy, and the star is sustained only by the H-burning shell.

Below the shell, the core contracts rapidly, while the envelope expands. The reason for this "mirror" behavior across the shell is debated since the 70s (see the Appendix of Sugimoto and Fujimoto, 2000, for a historical review of the proposed mechanisms). A simple and somehow intuitive explanation can be found in Padmanabhan (2001). At this moment of the evolution, the typical timescale becomes of the order of or shorter than the Kelvin-Helmholtz timescale $\left(\tau_{\mathrm{KH}} = \frac{GM^2}{RL}\right)$. In that case, both the conservation of energy ($\Omega + U =$ constant) and the virial theorem ($\Omega + 2U = 0$) must hold, with Ω and U the potential and internal energy respectively. The only way of achieving this is to conserve both Ω and U separately. If we have most of the mass in the core compared to that in the envelope, $M_{\mathrm{c}} \gg M_{\mathrm{env}}$, we can express the potential energy as:

$$|\Omega| \approx \frac{GM_{\mathrm{c}}^2}{R_{\mathrm{c}}} + \frac{GM_{\mathrm{c}}M_{\mathrm{env}}}{R_\star} \approx \text{constant}$$

with R_{c} and $R_\star$ the radius of the core and the star respectively. Since the location of the shell is more or less constant, we can consider M_{c} and M_{env} to be constant, and hence we have:

$$-\frac{GM_{\mathrm{c}}^2}{R_{\mathrm{c}}^2}\frac{dR_{\mathrm{c}}}{dt} - \frac{GM_{\mathrm{c}}M_{\mathrm{env}}}{R_\star^2}\frac{dR_\star}{dt} = 0$$

$$\longrightarrow \frac{dR_\star}{dR_{\mathrm{c}}} \approx -\left(\frac{M_{\mathrm{c}}}{M_{\mathrm{env}}}\right)\left(\frac{R_\star}{R_{\mathrm{c}}}\right)^2$$

which means that the core contraction implies the envelope's expansion. Note that a more detailed description of this mirror behavior invokes the thermal equilibrium inside the H-burning shell (Sugimoto and Fujimoto, 2000), and the evolution of the entropy in the envelope (Hekker et al., 2020).

Eventually, the star evolves rapidly to low T_{eff}, crossing the HR diagram and becoming a red supergiant (RSG). Its luminosity increases while its core contracts until it reaches the temperature of He fusion.

2.2. Helium Burning

Helium is fused through a three-particles reaction, the so-called 3α reaction. It is actually a two-steps reaction, with first the formation of unstable ^{8}Be by the fusion of two α particles. The lifetime of ^{8}Be is 6.7×10^{-17} s. In a second step, ^{12}C is produced through the reaction $^8\mathrm{Be}(\alpha,\gamma)$. The probability that the unstable ^{8}Be captures another α before its own α-disintegration is increased by a resonance level in the ^{12}C atom. The resonant level has been predicted by Hoyle (1954) on considerations based on the observed abundances of ^{12}C. The 3α reaction is extremely sensitive in temperature:

$$\epsilon_{3\alpha}(T) = \epsilon_{3\alpha}(T_0)\left(\frac{T}{T_0}\right)^{41}$$

During He burning, carbon is built up, but when the temperature is hot enough, the reaction $^{12}\mathrm{C}(\alpha,\gamma)^{16}\mathrm{O}$ consumes part of the carbon. The more massive the star, the more efficiently C is converted into O, so the ratio C/O left at the end of He burning decreases for more massive stars. This ratio, together with the mass of the CO core left after central He burning, plays a key role in the compactness of the stellar core, and hence in its ability to explode or not (Chieffi and Limongi, 2020). Though

$^{12}C(\alpha,\gamma)^{16}O$ is one of the key reactions in stellar evolution, its rate is still uncertain and subject to numerous studies in the literature (see section 3).

Two other reactions contribute to the destruction of He nuclei, $^{16}O(\alpha,\gamma)^{20}Ne$ and $^{20}Ne(\alpha,\gamma)^{24}Mg$. Below $T = 0.3$ GK, however, these reactions are only negligible compared to 3α and $^{12}C(\alpha,\gamma)^{16}O$. Stellar He burning is thus the main astrophysical site for the synthesis of oxygen in the Universe. **Figure 2** (*top left*) shows the abundances profiles at the end of central He burning.

Helium burning is also an important site for nucleosynthesis beyond the iron peak and the slow neutron-capture process (*s*-process). Indeed, when the nitrogen produced by the CNO cycle diffuses into a He-burning zone, it will be rapidly converted into ^{22}Ne through the chain of reactions $^{14}N(\alpha,\gamma)^{18}F(\beta^+\nu)^{18}O(\alpha,\gamma)^{22}Ne$. This ^{22}Ne can then react further with an α through $^{22}Ne(\alpha,n)^{25}Mg$, producing a neutron. Though it is in some way self-poisoning, since the ^{25}Mg is a neutron eater through the reaction $^{25}Mg(n,\gamma)^{26}Mg$, the $^{22}Ne(\alpha,n)^{25}Mg$ reaction is a neutron source for the so-called "weak *s*-process," building up nuclei up to strontium (Raiteri et al., 1991a,b; Kaeppeler et al., 1994; Käppeler et al., 2011; Frischknecht et al., 2016). It is considered that massive stars undergoing this *s*-process during He burning are the main producers of ^{36}S, ^{37}Cl, ^{40}Ar, and ^{40}K in the Universe (Woosley et al., 2002). The $^{22}Ne(\alpha,n)^{25}Mg$ reaction enters in direct competition with the $^{22}Ne(\alpha,\gamma)^{26}Mg$. The preferred channel for ^{22}Ne destruction depend strongly on the ratio of these two reactions, and hence the strength of *s*-process elements creation (Pignatari et al., 2010), but large uncertainties remain for these two reactions (see section 3).

2.3. Advanced Phases

At the end of He burning, the star is sustained by two burning shells (H and He) while its core contracts until it reaches a temperature that is high enough for the fusion of carbon.

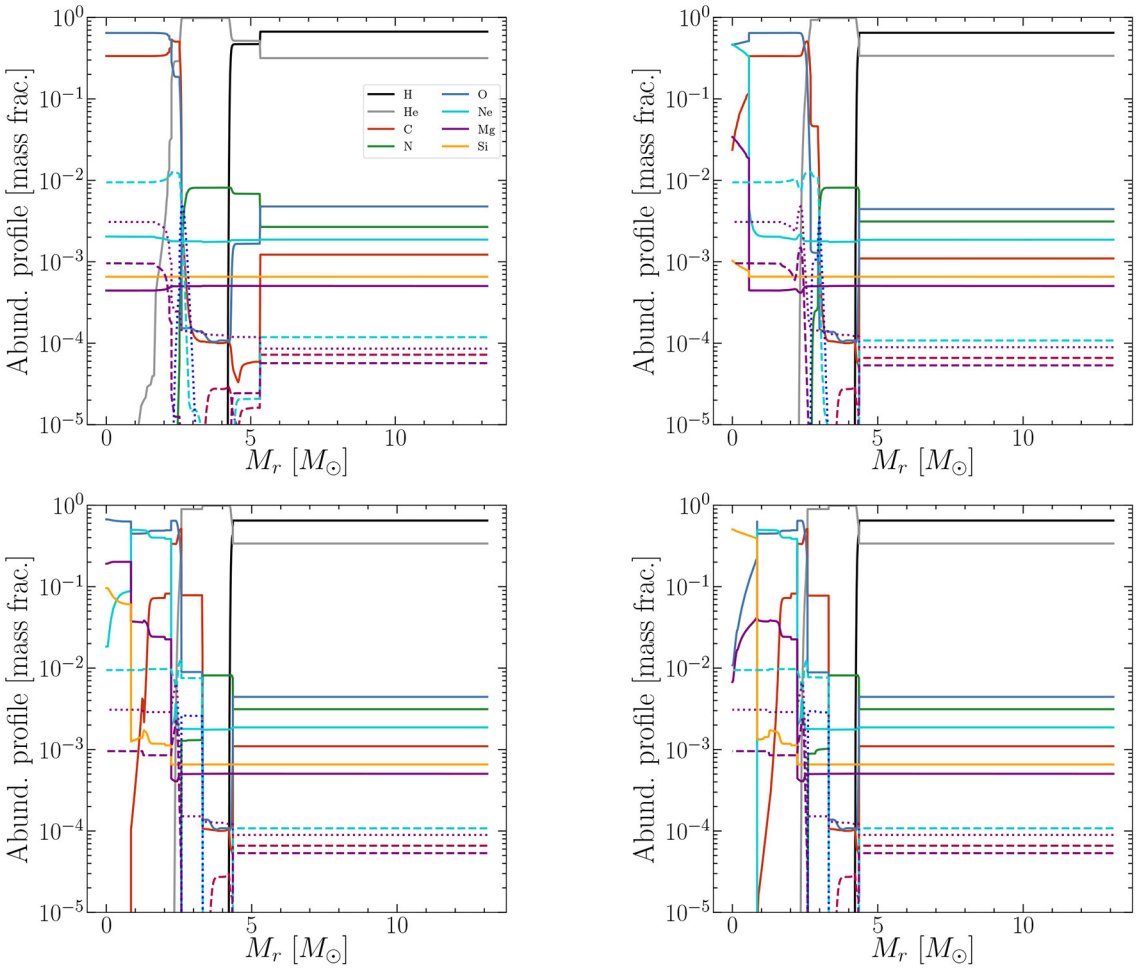

FIGURE 2 | Abundances profiles at the end of He burning (*top left*), C burning (*top right*), Ne burning (*bottom left*), and O burning (*bottom right*). The precise temporal locations are marked by gray arrows in **Figure 3**. The species shown are indicated with their colors in the legend on the top left panel. Solid lines are used for the main isotopes (^{1}H, ^{4}He, ^{12}C, ^{14}N, ^{16}O, ^{20}Ne, ^{24}Mg, and ^{28}Si). For some species, other isotopes are shown with the corresponding colors but dashed (^{13}C, ^{15}N, ^{17}O, ^{22}Ne, and ^{25}Mg) or dotted lines (^{18}O and ^{26}Mg).

2.3.1. Carbon Burning

The fusion of two ^{12}C nuclei forms a ^{24}Mg atom that is highly excited. The excess energy ($\sim$ 14 MeV) is more easily removed by the ejection of a light massive particle (p, n, α) than a photon. So the main channels for carbon fusion are ^{12}C(^{12}C,α)^{20}Ne, ^{12}C(^{12}C,p)^{23}Na, ^{12}C(^{12}C,n)^{23}Mg, with a global sensitivity in temperature that is relatively moderate:

$$\epsilon_{\mathrm{C}}(T) = \epsilon_{\mathrm{C}}(T_0)\left(\frac{T}{T_0}\right)^{28}$$

The α and p channels have almost the same probability to occur. Secondary reactions like ^{23}Na(p,α)^{20}Ne and ^{16}O(α,γ)^{20}Ne also take place, however the oxygen destruction is weak. At the end of central C burning, the core is mainly composed of ^{16}O, ^{20}Ne, and ^{23}Na.

After C exhaustion in the core, the C burning proceeds in a succession of convective shells appearing and disappearing. If the CO core mass left after central He burning is smaller than $3\,M_{\odot}$, the star has to wait for the disappearance of the second C convective shell before its core becomes massive enough to start central Ne burning (see **Figure 3**), while if M_{CO} is larger, Ne burning can occur rapidly after C exhaustion (Chieffi and Limongi, 2020). The transition mass lies somewhere between 15 and 20 $M_{\odot}$, the precise value depending strongly on the physics of the models.

The less massive of massive stars ($M < 30\,M_{\odot}$) have a quite efficient s-process in the C-burning shells, creating nuclei with $A = 60 - 90$ (Käppeler et al., 2011). Above $M = 30\,M_{\odot}$, most of the ^{22}Ne is consumed at the end of He burning, but below that mass, a significant amount of ^{22}Ne may survive (see however Talwar et al., 2016). The reaction ^{22}Ne(α, n)^{25}Mg can be reactivated during shell C burning thanks to α particles released via ^{12}C(^{12}C,α)^{20}Ne. During shell C burning, the temperature is a factor of 3-4 higher than during core He burning, the density is higher by a factor of 100, and the cross section of the ^{22}Ne(α, n)^{25}Mg reaction is much higher. Though the neutron exposure is short, the high neutron density (a factor of 1000 higher than during He burning) helps building neutron-rich isotopes (The et al., 2007). In contrast with core C burning, the s-process elements produced in the C-burning shell are easily ejected during the supernova, and are not destroyed by photo-disintegration reactions during core O and Si burning. They will be affected by the explosive event at the end of the stellar evolution but not dramatically destroyed (Rauscher et al., 2002).

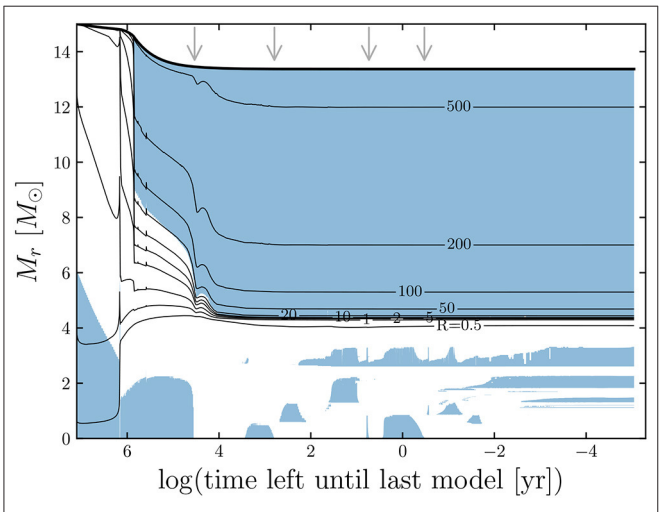

FIGURE 3 | Kippenhahn diagram of a 15 $M_{\odot}$ model at solar metallicity, computed until the end of central O burning. The blue shaded regions are convective. Iso-radii are over-plotted (in solar radius units). The gray arrows mark the temporal location of the abundances profiles of **Figure 2**.

2.3.2. Beyond Carbon

Though oxygen is next in line in terms of atomic mass, its greater stability imposes extremely high temperatures ($T >$ 1 GK) to be able to burn, a temperature regime higher than the one in which photo-disintegration reactions can take place and halt the core contraction. The neon atoms present in the core can thus be photo-disintegrated through ^{20}Ne(γ,α)^{16}O. Neon can also react with an α particle and build magnesium through the reaction ^{20}Ne(α,γ)^{24}Mg. Some silicon is further produced by ^{24}Mg(α,γ)^{28}Si. Neon burning is extremely sensitive in temperature:

$$\epsilon_{\mathrm{Ne}}(T) = \epsilon_{\mathrm{Ne}}(T_0)\left(\frac{T}{T_0}\right)^{49}$$

At the end of Ne burning, the core (composed mainly of ^{16}O, ^{24}Mg, and ^{28}Si) contracts again, reaching 2 GK and is at last able to burn oxygen. As in the case of C burning and the resulting ^{24}Mg atom, the sulfur atom created through ^{16}O(^{16}O,γ)^{32}S is highly excited, with many overlapping compounds levels. The excess energy ($\sim$ 16.5 MeV) is most efficiently removed by the emission of a light massive particle. The channels for oxygen fusion are mainly p-, α-, and n-emitting reactions: ^{16}O(^{16}O,p)^{31}P, ^{16}O(^{16}O,α)^{28}Si, and ^{16}O(^{16}O,n)^{31}S, but two-particles emissions are also quite probable: ^{16}O(^{16}O,2p)^{30}Si and ^{16}O(^{16}O,2α)^{24}Mg. The temperature sensitivity of O burning is less acute than that of Ne burning:

$$\epsilon_{\mathrm{O}}(T) = \epsilon_{\mathrm{O}}(T_0)\left(\frac{T}{T_0}\right)^{34}$$

The cross-section determination at the energy of the Gamow peak at a typical $T = 2.2$ GK is subject to large variations according to different authors and analysis techniques. The branching ratio between the different O-burning channels is still widely unknown. Both uncertainties result in the rates for O burning being know only up to a factor of 3.

The ^{31}P produced can further interact with a proton with two possible disintegration channels: ^{31}P(p,γ)^{32}S or ^{31}P(p,α)^{28}Si. The ^{32}S can further be transformed into ^{36}Ar through ^{32}S(α,p)^{35}Cl(p,γ)^{36}Ar.

At the end of O burning, the core of the star mainly consists in ^{28}Si and ^{32}S. Silicon has a too large Coulomb barrier to be able to fuse with itself, so at that stage of the evolution, the star gets its energy mainly from photo-disintegration reactions, followed by

captures of the light particles released. Ascending and descending chains of reactions take place, reaching an equilibrium flow in some sub-domains of nuclei, as for instance the domain $A = 25 - 40$ or $A = 46 - 64$. Though the two domains are linked with much less active reaction rates, slowly the nuclei of the iron peak ($A > 40$) are accumulating, while the abundance of the lighter nuclei decreases. Around the iron peak, electron captures start taking place [^{53}Mn(e^-,ν)^{53}Cr, ^{54}Fe(e^-,ν)^{54}Mn, ^{55}Fe(e^-,ν)^{55}Mn, ^{55}Co(e^-,ν)^{55}Fe, ^{56}Co(e^-,ν)^{56}Fe], adding a significant contribution from the weak interactions to thermal neutrino emission (see section 2.3.3).

The sensitivity in temperature of the network of reactions involved in silicon burning is high:

$$\epsilon_{\mathrm{Si}}(T) = \epsilon_{\mathrm{Si}}(T_0)\left(\frac{T}{T_0}\right)^{47}$$

An interesting feature for stellar evolution modeling is that since equilibrium flows are rapidly attained, the precise rates of the nuclear reactions do not really matter. We only need to compute their equilibrium ratios, that depends mainly on atomic masses and binding energies.

At the end of Si burning, the whole network of nuclei reaches equilibrium, from proton to iron-peak elements. This is known as the *nuclear statistical equilibrium*. Only the weak interactions cannot get to equilibrium, because the neutrinos are escaping the star, preventing the reverse reaction to occur. During the bulk of Si burning, these weak interactions induce a neutron excess $\eta = \sum_i \frac{N_n,i - N_p,i}{A_i} X_i > 0$[3]. The neutron excess influences the relative abundances of isotopes. A large neutron excess favors neutron-rich isotopes, playing a role as important as the binding energies themselves: for a given η, the nuclides having an individual neutron excess $(N - Z)/A \simeq \eta$ will be the most abundant.

2.3.3. General Remarks

Shell burning episodes usually occur in conditions that are hotter and denser than the conditions prevailing in the core of the corresponding burning. This makes the nucleosynthetic results of shell burning slightly different from core burning.

From the end of central He burning onwards, there is a disconnect between the core and the envelope, because the timescales of evolution start to have orders of magnitude of difference. This disconnect implies that the surface of the star cannot translate the internal evolution anymore, and doesn't evolve (in an HR diagram, for example). While the envelope is still living on the Kelvin-Helmholtz timescale:

$$\tau_{\mathrm{KH}} = \frac{GM^2}{RL_\gamma} \quad (7)$$

(with obvious meanings for the variables G, M, and R, and L_γ the photon luminosity of the star), the core lives on the nuclear timescale, contraction plus burning time:

$$\tau_{\mathrm{contr}} + \tau_{12} = \frac{\frac{1}{2}\Delta\Omega + E_{12}M_{\mathrm{core}}}{L_\nu}$$

[3] $\eta = 0$ if the matter is made of species with $A = 2Z$.

(with $\Delta\Omega$ the potential energy released by contraction, E_{12} the energy production by C burning, M_{core} the mass of the core where the burning takes place, and L_ν the neutrino luminosity).

Both expressions involve the luminosity of the star, but in the nuclear timescale of advanced phases, it is the neutrino luminosity that plays the major role, being orders of magnitudes higher than the photon luminosity. The neutrino loss is not related to the nuclear reactions, which globally do not involve neutrinos. Actually, when the temperature reaches 10^9 K, neutrinos can be produced by three different mechanisms (Beaudet et al., 1967): electron-positron pair annihilation ($e^-e^+ \rightarrow \nu\bar{\nu}$), photo-production ($\gamma e^\pm \rightarrow \nu\bar{\nu}e^\pm$), or plasmon decay (plasmon $\rightarrow \nu\bar{\nu}$). Once created, neutrinos escape freely from the star, taking away a large part of the energy produced by the nuclear burning (Woosley and Janka, 2005). This high energy loss accelerates the pace of the evolution, as can be seen from **Table 1**, which presents the lifetimes in the different burning phases of a 25 $M_\odot$ stellar model (Hirschi et al., 2004). In contrast, the modeling itself takes longer and longer, so while we started on the main sequence with a computation that was a factor of 50 billions times more rapid than the true evolution, we finish the modeling of a star 10 times slower than nature.

2.4. Explosion

Once it is composed of iron-peak elements, the core cannot extract energy from nuclear reactions and hence collapses. Depending on its mass, it will form a neutron star or a black hole (Woosley et al., 2002).

The mechanism leading from collapse to explosion is very complex and a full description is out of the scope of this review. The reader is referred to the reviews by Janka (2012) or Müller et al. (2016) for a detailed description. I will just summarize here the general picture drawn by supernova simulations.

The core collapses in the free-fall timescale, reaching quickly supra-nuclear densities, which makes it rebounce, creating a shock. The shock moves slightly outwards, but stalls, being insufficient to reverse the velocity field of the in-falling matter, and becoming an accretion shock. The neutronization of the core generates a strong neutrino flux that is trapped by the density of the in-falling matter around the shock (*neutrino-sphere*). The neutrinos energy heats this region, creating a negative entropy gradient which drives convection in the standing shock region, transferring heat to the stellar matter. Early 1D supernova

TABLE 1 | Lifetimes in the different nuclear burning phases for non-rotating and rotating stellar models of 25 $M_\odot$ (from Hirschi et al., 2004 A&A, 425, 649, reproduced with permission ©ESO).

Nuclear lifetime	$V_{\mathrm{ini}} = 0$	$V_{\mathrm{ini}} = 300$ km s^{-1}
τ_{H}	6.55 Myr	7.97 Myr
τ_{He}	685 000 yr	620 000 yr
τ_{C}	317 yr	173 yr
τ_{Ne}	321 d	161 d
τ_{O}	116 d	89 d
τ_{Si}	1 d	18 h

simulations have identified a critical neutrino luminosity that is needed to be able to power an explosion (Burrows and Goshy, 1993; Müller and Janka, 1995). Multi-D simulations show that a breaking of spherical symmetry brought by convective movements can reduce the critical neutrino luminosity. A large-scale hydrodynamical instability, the so-called *standing accretion shock instability* (SASI, see Foglizzo, 2002; Scheck et al., 2004; Buras et al., 2006; Burrows et al., 2006) induces advective acoustic cycles and increases the non-sphericity even more. When rotation is taken into account, the centrifugal force helps the breaking of spherical symmetry (Nakamura et al., 2014), but the neutron star that is formed has a larger radius and is cooler, so the neutrino luminosity is lower (Marek and Janka, 2009; Summa et al., 2018), which could prevent a successful explosion. When the rotation is fast, it presents an angle-dependent neutrino emission, and sustains violent SASI spiraling that increase the volume where heat can be transferred from the neutrino to the matter, particularly in the equatorial plane (Nakamura et al., 2014; Summa et al., 2018). When magnetic fields are added to the simulations, the magnetic pressure creates a polar expansion and stimulates also spiral SASI movements, favoring the explosion (Kuroda et al., 2020).

Note that the perfect supernova simulation, including all needed ingredients with an exquisite treatment in full 3D with a perfect resolution of all time- and space-scales at play is yet to come. It is a very active field of research that benefits highly from any improvement in computational power and/or numerical solver. Also, improvements in the progenitor stellar models with which the supernova simulations are fed, especially in what concerns convection (see section 5.1), might give fundamental ingredients to the simulations (Müller et al., 2016). From an observational point of view, it is not clear whether a star that is still very massive at the end of its evolution is able to explode as a supernova or will just collapse directly into a black hole. The lack of identified massive progenitors for SN type Ibc, and the maximal mass of type II events progenitors (Maund and Smartt, 2005; Maund et al., 2005; Crockett et al., 2008; Smartt et al., 2009) suggests that above $M_{\rm ini} \simeq 25 - 30\,M_{\odot}$, the collapse cannot be reversed and a black hole is formed without any SN (Allan et al., 2020) or with a failed SN. The debate is still not settled to date (see for example Smartt et al., 2009; Yoon et al., 2012; Kochanek, 2014; Suzuki and Maeda, 2018; Farrell et al., 2020).

In special mass domains, there are two other mechanisms that have been identified as the cause of the supernova explosion. In the low-mass end of massive stars ($M <= 10\,M_{\odot}$), carbon ignites in degenerate conditions, by an off-center flame that reaches progressively the center (Nomoto, 1984; García-Berro et al., 1997; Siess, 2007). At the end of carbon burning, the core is a degenerate mixture of O, Ne, and some Mg, supported by the pressure of electron degeneracy. Electron-captures on ^{24}Mg followed by that on ^{20}Ne (Eldridge and Tout, 2004; Jones et al., 2013) removes a source of pressure, driving an electron-capture core-collapse supernova (EC-SN). The occurrence of an EC-SN depends on several stellar parameters: the mass of the ONe core at the end of C burning, the growth rate of the core, but also the mass-loss rate, since an efficient mass loss can halt the growth of the core (Poelarends et al., 2008).

At the other end of the mass domain lies the region of pair-instability supernovae (PISN). When the central temperature is of the order of 1-2 GK, the photons energy is of the same order of magnitude as the rest mass energy of an electron-positron pair. We saw in section 1 that massive stars are dominated by radiation pressure. If the conditions for pair creation are met (for CO core masses $M_{\rm CO}$ between 30 and 135 $M_{\odot}$ Woosley et al., 2002), photons are removed from the pressure support of the star, destabilizing the hydrostatic equilibrium by lowering the adiabatic index $\left.\frac{\partial \ln P}{\partial \ln \rho}\right|_{\rm ad}$ below 4/3 (Barkat et al., 1967; Rakavy and Shaviv, 1967). If a sufficiently large part of the star lies in this region, the core collapses, triggering violent oxygen burning that disrupts the star entirely, leaving no remnant at all (Ober et al., 1983; El Eid and Langer, 1986; Woosley et al., 2002). For $M_{\rm CO}$ between 30 and 60 $M_{\odot}$, a more regular supernova can be triggered by pulsational pair-instability (PPISN, Chatzopoulos and Wheeler, 2012; Chen et al., 2014; Woosley, 2017; Leung et al., 2019; Marchant et al., 2019). For CO cores larger than 140 $M_{\odot}$, the oxygen burning is not powerful enough to reverse the collapse, and a black hole (BH) is formed (Woosley et al., 2002). The PISN or PPISN are supposed to occur more frequently at low metallicity because the low radiative mass loss allows the star to have a larger core (see section 4). In a time when the observation of gravitational waves starts giving access to the mass of BH formed in the early Universe (Abbott et al., 2016a,b, 2017), the existence of PISN predicts a gap in the possible mass of observed BH (Heger et al., 2003; Belczynski et al., 2016; Woosley, 2019) that can now be confronted to observations. Recently, the detection of GW190521 implying the merger of two BHs, one of which having a mass inside the mass gap predicted (85 $M_{\odot}$, Abbott et al., 2020), has stirred the pot of stellar modeling and presented a real challenge to theory. One of the proposed explanations is of direct interest in this review since it highlights the role the ^{12}C$(\alpha,\gamma)^{16}$O reaction rate plays in shaping the fate of massive stars (Costa et al., 2020, see also section 3).

But let us go back to the more standard supernovae and turn to the explosive yields. Once exploded, depending on the envelope composition, the supernova will be characterized as type II (H and He rich), type Ib (H deficient), or type Ic (H and He deficient). During the explosion, the shock wave passes through the star, and the high temperature of the shock triggers nuclear burning. The type of burning and nucleosynthetic result depends almost uniquely on the temperature reached in a specific layer, whatever the initial composition. The iron-peak elements and silicon expelled during a core-collapse supernova come from the silicon and oxygen shells reprocessed by the explosive front with temperatures of the order of 4-5 GK, not from the core itself that ends up locked inside the remnant. To date, most of the explosive yields are determined from 1D stellar supernova progenitors in which either a piston is applied, or a thermal bomb. The mass cut (above which matter is expelled in the explosion) does not come naturally from such simulations and has to be fixed arbitrarily. Often the amount of nickel ejected is used to set the mass cut (Limongi and Chieffi, 2003; Umeda and Nomoto, 2008). The nucleosynthesis is then computed by simulating the passage of the shock wave: the maximum temperature and density

are often determined within the radiation-dominated shock approximation (Weaver and Woosley, 1980; Arnett, 1996; Chieffi and Limongi, 2002; Woosley et al., 2002). In this framework, the shock temperature is a function of the energy released and the radius of the layer: $T_{\rm shock} = \left(\frac{4}{3\pi a}\right)^{1/4} E_{\rm expl}^{1/4}\, r^{-3/4}$, and the density during the shock is obtained by multiplying the pre-shock density by a factor of between 4 (mild shock) and 7 (strong shock). The density and temperature evolve then in the hydrodynamical timescale of an adiabatic expansion at the escape velocity $V_{\rm esc} = \sqrt{\frac{2GM}{r}}$: $\rho(t) = \rho_{\rm shock}\, e^{t/\tau_{\rm HD}}$ with $\tau_{\rm HD} = \left(\frac{1}{\rho}\frac{\partial\rho}{\partial t}\right)^{-1} = \frac{R}{3V_{\rm esc}} = \frac{446}{\sqrt{\rho}}$, and $T \propto \rho^{\gamma-1}$, with γ the adiabatic index. An example of pre-SN vs. post-SN yields is presented in Rauscher et al. (2002, Figure 7). Iron-peak elements are massively produced during the explosion, while the light elements up to Al and the *s*-process elements are not drastically modified by the explosion (except for a few isotopes).

While piston- or bomb-triggered explosions give a fairly appropriate result for the nucleosynthesis of the intermediate or outer layers of the stars, the very innermost layers' nucleosynthesis is sensitive to the electron fraction $Y_e = \langle Z/A \rangle$, which depends strongly on the neutrino or antineutrino captures by protons and neutrons (Curtis et al., 2019). A careful treatment of neutrino transport is needed, and the effects of asymmetries could be significant on the nucleosynthetic budget (Pruet et al., 2005). Given the complexity of multi-D core-collapse simulations, and the necessity to wait for the delayed explosion to deploy, only a few attempts to derived nucleosynthetic yields from multi-D simulations of iron-core collapse supernovae have been performed. The simulations themselves are conducted with a limited chemical network (mainly H and the α elements, plus a tracer of the neutron-rich species, see Wongwathanarat et al., 2015), so a detailed nucleosynthesis needs to be post-processed (Pruet et al., 2005; Harris et al., 2017; Yoshida et al., 2017; Eichler et al., 2018; Wanajo et al., 2018).

3. EFFECTS OF NUCLEAR RATES UNCERTAINTIES

Most nuclear reaction rates are determined in laboratory experiments, with conditions that are very far from stellar conditions. Different methods are then applied to extrapolate those rates down to the much lower energies of stellar burnings, but in many of them, large uncertainties remain. A very difficult problem the extrapolations meet is the possibility to miss a low-energy resonance that would significantly change the reaction rates. Many reaction rates still suffer from a lack of robust determination, but it would be beyond the scope of this paper to review them all. I will just present here some general trends and the examples of the $^{12}C(\alpha,\gamma)^{16}O$ reaction, and the reactions affecting the *s*-process.

Depending whether the uncertainty touches a reaction that is a main energy producer for the star, or only a marginal reaction, the effects of varying the rates have very different outcomes. Of course, the first effect we expect concerns simply the nucleosynthetic products: a stronger (weaker) rate will produce more (less) child nuclides, and reduce more (less) efficiently the abundance of the parent nuclides. Varying reaction rates that do not count strongly in the energy budget of the star usually results in just this nucleosynthetic outcome. In that case, differences in physical assumptions in the models (rotation, overshoot value) have a much stronger effect than a change in the rate itself (see for instance Siess et al., 2004, about the $^{13}C(\alpha,n)^{16}O$ reaction).

However, if the reaction is a dominant energy source for the star, the outcome is much more complicated than the naive picture of "*increased rates = increased production of child nuclides*." Stars are self-gravitating systems that adapt their structure to get the energy needed to sustain their gravity. A stronger (weaker) rate can make the burning to take place in lower (higher) T and ρ conditions, modifying strongly the stellar structure. In some cases, the global nucleosynthetic budget will not be that much affected because the structural compensations will be sufficient to keep a similar nucleosynthetic outcome, but in other cases, the structural changes will lead to modifications of the full evolutionary path, with strong consequences on the nucleosynthetic result at large.

The $^{12}C(\alpha,\gamma)^{16}O$ reaction is a good example of a reaction that is of paramount importance for massive stars, by playing a role on the C/O ratio at the end of He burning. Though it is a key reaction for massive star evolution, shaping the future path to the supernova, it is still not determined robustly, and the successive attempts (Caughlan et al., 1985; Caughlan and Fowler, 1988; Angulo et al., 1999; Kunz et al., 2002; Katsuma, 2008; deBoer et al., 2017; Holt et al., 2019) show very different behaviors as a function of the temperature (see Figure 1 from El Eid et al., 2009). As in increasingly massive stars, a stronger rate leaves the core deprived in C, inducing a shorter C-burning timescale (Tur et al., 2007). Since C burning is the longer of the advanced burning phases, it is the one that allows the largest energy loss through neutrinos escape. A shorter C-burning phase helps the star to keep a higher entropy, to have a larger migration of the C-burning shell, and hence to end up with a larger O and Si core, affecting its explodability. In that line, let us mention that variations in the $^{12}C(\alpha,\gamma)^{16}O$ reaction can affect the possibility of a low-metallicity star to end up as pair-instability supernova or not and modify the limiting masses for PISN (Takahashi, 2018; Costa et al., 2020; Farmer et al., 2020).

A good example of an energetically marginal reaction network which suffers from many uncertainties is the *s*-process. These uncertainties are either direct (concerning the neutron-producing reaction) or indirect (concerning reactions not directly linked to the *s*-process but that set the stage for it in the structure of the star). The main neutron producer for the weak *s*-process, the $^{22}Ne(\alpha,n)^{25}Mg$ reaction is still uncertain to about a factor of 2. More complicated for stellar evolution, the competing reaction $^{22}Ne(\alpha,\gamma)^{26}Mg$ is also very uncertain, particularly concerning the strength of low-energy resonances (Kaeppeler et al., 1994; Rauscher et al., 2002; Karakas et al., 2006; Talwar et al., 2016). These uncertainties affect the relative efficiency of these two competing α captures on neon, in particular at temperatures typical of He burning. As mentioned above, some reactions affecting the structure of the star can also modify the result of

the *s*-process. The uncertainties flawing the determination of the $^{12}C(\alpha,\gamma)^{16}O$ reaction play a role in the nucleosynthetic results of the weak *s*-process (Tur et al., 2007, 2009; deBoer et al., 2017) since the $^{22}Ne(\alpha,n)^{25}Mg$ reaction becomes more efficient at the end of He burning, when the $^{12}C(\alpha,\gamma)^{16}O$ reaction starts competing on the α capture (Pignatari et al., 2010). The 3α rates are better constrained, but even a variation at the level of 10% (Austin, 2005) plays a significant role since this rate is directly confronted to the $^{12}C(\alpha,\gamma)^{16}O$ rate in determining the conditions for C burning, affecting the *s*-process products (Tur et al., 2007, 2010). Variations in the $^{12}C(\alpha,\gamma)^{16}O$ rates have an impact on the shell C-burning *s*-process production as well (El Eid et al., 2004; The et al., 2007; deBoer et al., 2017), because the C/O ratio at the end of He burning determines the future structure of the shell C burning (number and thickness of the shells). During carbon burning, the carbon fusion reaction is also the subject of debate because low-energy resonances are complicated to determine (Gasques et al., 2007; Tumino et al., 2018; Fruet et al., 2020; Tan et al., 2020). Again, by changing the condition of T and ρ at which carbon burning occurs, a variation in the carbon fusion rate modifies the width of the core and subsequent shells and affects the *s*-process yields (Gasques et al., 2007; Bennett et al., 2012).

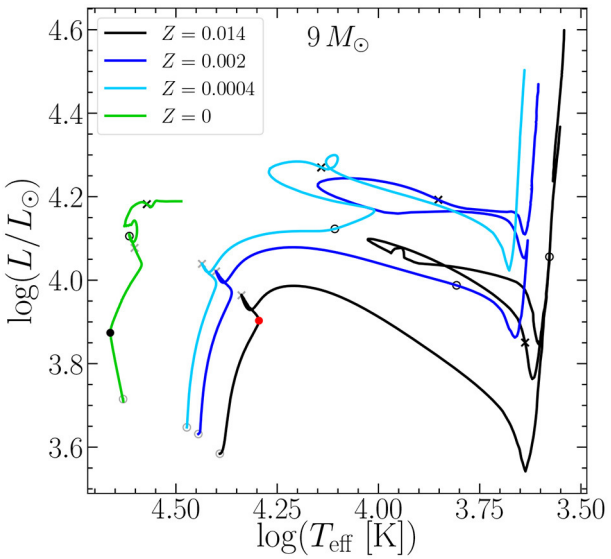

FIGURE 4 | HR diagram for $9\,M_\odot$ models at different metallicities: $Z = 0.014$ (Ekström et al., 2012), $Z = 0.002$ (Georgy et al., 2013a), $Z = 0.0004$ (Groh et al., 2019), and $Z = 0$ (Murphy et al., 2021). The beginning and end of fusion phases are marked with a circle and a cross respectively (gray: H burning; black: He burning). The red dot on the black track marks the hook described in section 2.1. The filled black dot on the green track marks the point where the CNO cycle is ignited in the $Z = 0$ model as described in section 4.

4. EFFECT OF METALLICITY

Except for the extreme case of $Z = 0$, lowering the metallicity does not modify the burning phases and the reactions themselves, but it changes the conditions in which they take place. When there is less C available, the CNO cycle is weaker and the star has to contract further in order to get enough energy to counterbalance its gravity. This effect, along with the fact that the star has a more transparent envelope, makes low-Z stars hotter and more compact.

A variation in metallicity changes slightly the conditions in which hydrogen burns, but mostly it changes the maximal amount of helium at the end of H burning. This has an impact on the He core size (Woosley and Weaver, 1995). However, after that, the nucleosynthesis of heavy elements depends almost exclusively on the mass of the core (whatever the initial mass), and not on metallicity itself.

When no metals at all are present, the star cannot halt its initial contraction until the core is marginally hot enough to fuse He. The carbon produced through 3α is immediately used to start the CNO cycle. The limit in metallicity for this behavior is around $Z = 10^{-8}$. **Figure 4** shows the HR diagram for $9\,M_\odot$ models at decreasing metallicity. We see clearly in the track of the $Z = 0$ model (green line) that the evolution on the main sequence starts while the star is still contracting (blueward evolution). When the CNO cycle is ignited, the contraction is halted and the evolution proceeds redwards as normal (a filled black dot marks this turn on the track). The time needed to produce enough carbon is longer for less massive stars, and gets ever shorter for more massive stars. Between 20 and 25 $M_\odot$, the CNO cycle starts directly on the ZAMS (Siess et al., 2002; Ekström et al., 2008; Murphy et al., 2021) and no main sequence "knee" is visible anymore. At the end of H burning, the zero-metallicity stars (or zero-like) have a hot enough core to enter into He burning very smoothly, without the usual strong contraction. As a result, He is burnt in a very blue location of the HR diagram. Another consequence is that the H-burning shell is not hotter than the MS core, in contrast with what we saw previously, so the shell is powered only by the *pp*-chains reactions.

An important feature found in low-metallicity stars is the interactions between H- and He-burning zones (shell or core Woosley and Weaver, 1995; Hirschi, 2007; Ekström et al., 2008; Heger and Woosley, 2010; Ritter et al., 2018b). We will see in section 5.1 that connections between burning shells is a common feature during the advanced phases, but a low metallicity favors the connection between H and He shells in earlier phases of the evolution. The carbon brought from the He-burning region into the H-burning shell boosts the CNO cycle in the shell, producing a significant amount of nitrogen (called *primary* because it is directly produced from newly synthesized carbon, Truran and Cameron, 1971; Edmunds and Pagel, 1978). In non-rotating models, this feature is found in a restricted mass domain, between 25 and 35 $M_\odot$ (Chieffi and Limongi, 2004; Heger and Woosley, 2010; Limongi and Chieffi, 2012), but in more recent models, Clarkson and Herwig (2021) find it to happen in a much larger mass domain ($15 - 140\,M_\odot$) and for all sorts of convection treatments. Rotating models have also been found to show these burning zones interactions in the full range of masses through rotational mixing (Hirschi, 2007; Ekström et al., 2008; Frischknecht et al., 2012, 2016; Choplin et al., 2017b).

Choplin et al. (2017a) have evoked a late mixing of this type to reproduce the puzzling $^{12}C/^{13}C$ and C/N in some carbon-enriched extremely metal-poor stars. The chemical connection between the two burning zones allows some nitrogen to diffuse back into the He-burning region, building Ne and producing neutrons that can be used for *s*-process (Pignatari et al., 2008; Frischknecht et al., 2016), as we saw in section 2.2. Another important impact a shell CNO-boost can have when it occurs during core He burning is the reduction of the size of the CO core.

By drastically reducing the radiative mass loss (see section 5.3), a low or zero metallicity helps the stars keep most of their mass until the end of the evolution. This influences the type of explosive event that will end the star's evolution. Low-metallicity stars can have very high mass at the time of explosion, but they also have very large CO cores. In this case, they are good candidates for pair-instability supernovae (Woosley et al., 2002), as we saw in section 2.4.

5. IMPORTANT PROCESSES IN MASSIVE STAR EVOLUTION

Some processes play an important role in stellar evolution and have to be considered when modeling stars. They can have repercussions on the nucleosynthetic budget of the star.

5.1. Convection

A very basic ingredient of stellar evolution is the treatment of convection. Being a multi-dimensional (multi-D) process because of its turbulent nature, it is impossible to model it from first principles in one-dimensional (1D) evolution codes.

The implementation of convection in stellar codes follows two steps. The first one is to identify the convective or radiative nature of the layer. There are two different criteria assessing the stability to convection: the Schwarzschild or the Ledoux criteria. The *Schwarzschild criterion* (Schwarzschild, 1958) states that a stellar layer is unstable to convection if the radiative thermal gradient is larger than the adiabatic thermal gradient:

$$\frac{3}{16\pi acG}\frac{\kappa LP}{MT^4} = \nabla_{\rm rad} > \nabla_{\rm ad} = \frac{P\delta}{C_P\rho T}$$

with $a = \frac{4\sigma}{c}$ the radiation constant (where σ is the Stefan-Boltzmann constant), κ the opacity, $\delta = -\frac{{\rm d}\ln\rho}{{\rm d}\ln T}$ (see Equation 5), C_P the specific heat at constant pressure, and obvious meanings for c, G, L, M, P, T, and ρ. The *Ledoux criterion* (Ledoux, 1947) adds a dependence on the gradient of chemical composition: $\nabla_{\rm rad} > \nabla_{\rm ad} + \frac{\varphi}{\delta}\nabla_\mu$ (with φ and δ as in Equation (5). Care must be taken in the way this is done because the definition of the border as the place where $\nabla_{\rm ad} = \nabla_{\rm rad}$ is valid only from within the convective zone (Gabriel et al., 2014). During the main sequence, both definitions lead to similar convective core size in massive stars, but after the main sequence, using one or the other leads to important changes in the way the star crosses the HR diagram, in the surface chemical enrichment amplitude (Georgy et al., 2014), and in the final He core mass (Hirschi et al., 2004).

The second step concerns the definition of the temperature stratification and the chemical mixing in convective zones. In the deep interior of stars, convection can be considered adiabatic, and the mixing is usually considered instantaneous, except during the very late stages of evolution when the nuclear timescale becomes shorter than the convective timescale. At the surface, however, these considerations are no more valid, and the most used framework is the mixing length theory (MLT Vitense, 1953; Böhm-Vitense, 1958). Note that more sophisticated and non-local theories have been proposed (Shaviv and Salpeter, 1973; Roxburgh, 1978; Kuhfuss, 1986; Langer, 1986; Canuto, 1992, 2011a,b,c,d,e; Xiong et al., 1997; Deng et al., 2006; Gabriel and Belkacem, 2018), but none of them are used routinely in stellar evolution codes. The MLT considers that the convective cell travels a fixed distance before being dissipated. This distance, the mixing length, is taken as a multiple of the pressure height scale: $\ell = \alpha_{\rm MLT}H_P$, with $H_P = -\frac{dr}{dP}P$, and $\alpha_{\rm MLT}$ a free parameter needing to be calibrated. The calibration is usually done on the Sun, and the value inferred is then used in all stellar models, although there is no reason for it to be a constant and indeed some works show a dependence on the stellar parameters or the metallicity (Magic et al., 2015; Song et al., 2020). Varying the value for $\alpha_{\rm MLT}$ has also been shown to impact the light curve and spectral evolution of type II supernova (SN) models (Dessart et al., 2013).

A confrontation of the characteristics of models computed with this definition for the convective boundary with observations shows that it leads to too small cores (see for example Maeder and Mermilliod, 1981; Aerts et al., 2003; Aerts, 2008; Moravveji et al., 2015; Claret and Torres, 2016; Deheuvels et al., 2016), which gave rise to the notion of *overshoot*: the convective movement does not stop where the acceleration stops, and the convective cell overshoots into the radiative layer where it is braked and stopped after a certain distance. Stellar models include overshoot in different ways, the most commonly used being either penetrative or diffusive overshoot. In the penetrative scheme, the border of the convective region is displaced by a distance that is a fraction of the pressure scale height $d_{\rm ov} = \alpha_{\rm ov}H_P$ (Shaviv and Salpeter, 1973; Maeder, 1975). In the diffusive scheme, an extra mixing is applied at the border of the convective zone with an exponentially-decaying diffusive coefficient $D_{\rm ov} = D_0 \exp\left(2\frac{r-r0}{f_{\rm ov}H_P}\right)$ with r_0 the location of the boundary, and D_0 a reference diffusion coefficient, often taken as $D_{\rm MLT}$ (Herwig et al., 1997, based on hydro simulations by Freytag et al. 1996). In any case, the overshoot implementation includes at least one free parameter ($\alpha_{\rm ov}$ or $f_{\rm ov}$ in the two examples above) that needs to be calibrated. The two more used methods are either the width of the main sequence in an HR diagram (Herwig, 2000; Bressan et al., 2012; Ekström et al., 2012; Choi et al., 2016), or the velocity drop at the end of the main sequence (Brott et al., 2011a). More recently, it has been proposed to calibrate the overshoot on binary stars systems (Tkachenko et al., 2020). Some studies indicate that there could be a dependence of the overshoot with the mass of the star (see for example Castro et al., 2014; Claret and Torres, 2016), and so using a fixed value would lead either to overestimate the overshoot in the lower

mass domain, or to underestimate it in the higher mass domain. In any case, a calibration is only valid for the models on which it was determined, since the differences in the input physics of the different stellar evolution codes have repercussions on the determination of the border of the convective zones. Note that since the work of Denissenkov et al. (2013), the term *convective boundary mixing* (CBM) is starting to take over the old term of overshoot, since it covers all sorts of hydrodynamical instabilities resulting in mixing.

Multi-D hydro simulations are essential in this field to improve the way convection is implemented in 1D stellar evolution codes. In the last 15 years or so, there has been a number of simulations exploring different convection regimes: cool stars envelopes (Freytag and Höfner, 2008; Chiavassa et al., 2009; Magic et al., 2013; Viallet et al., 2013), He-burning shells (Herwig et al., 2006; Woodward et al., 2015), or advanced-phases burning shells like C-burning shell (Cristini et al., 2017), O-burning shell (Meakin and Arnett, 2007; Müller et al., 2016; Jones et al., 2017), or Si-burning shell (Couch et al., 2015), and very recently, ZAMS convective cores (Higl et al., 2021). These simulations show that indeed, there is a mixing at the boundary of the convective zone, mainly due to plumes, gravity waves, or the turn-over of the convective eddies (Herwig et al., 2006; Meakin and Arnett, 2007; Jones et al., 2017; Arnett et al., 2019; Edelmann et al., 2019). Jones et al. (2017) calibrated the $f_{\rm ov}$, or $f_{\rm CBM}$ parameter of the exponentially-decaying diffusive coefficient implementation of CBM on an O-burning shell, finding a value of $f_{\rm CBM} = 0.03$. Higl et al. (2021) find that the value for $f_{\rm CBM}$ should increase with mass, well in line with the results of Claret and Torres (2016). Many simulations show that the bottom CBM occurs in a narrower region than the top CBM. The challenge is now to translate the multi-D results into relations between quantities that are followed in 1D models. A 3-to-1D procedure is proposed by Arnett et al. (2015), who apply a Reynolds-average Navier-Stokes treatment (Meakin and Arnett, 2007; Viallet et al., 2013) to the simulation results. In the advanced-phases shell simulations, the border of the convective zones has been shown to evolve in space and time following a turbulent entrainment that can be parametrized by the bulk Richardson number Ri_B (Meakin and Arnett, 2007; Garcia and Mellado, 2014; Müller et al., 2016; Cristini et al., 2017, 2019): $V_{\rm ent}/V_{\rm conv} = A\,\mathrm{Ri}_B^{-n}$, where $V_{\rm ent}$ is the entrainment velocity, $V_{\rm conv}$ is the convection velocity, and A and n are parameters expressing the efficiency of the entrainment. The bulk Richardson number expresses the ratio between the stabilization potential of the boundary and the turbulent kinetic energy: $\mathrm{Ri}_B = \frac{\Delta B \ell}{V_{\rm conv}^2}$ with ℓ the length scale for the turbulent motion, and $\Delta B = \int_{r_1}^{r_2} N^2\, dr$ the buoyancy jump across the boundary expressed in term of the buoyancy frequency (or Brunt-Väisälä frequency) $N^2 = \frac{g}{H_P}\left[\delta\left(\nabla_{\rm ad} - \nabla\right) + \varphi\nabla_\mu\right]$. A first implementation in a 1D stellar evolution code has been performed by Staritsin (2013), which computed models of 16 and a 24 $M_\odot$. The efficiency parameters were taken to be $n = 1$, in agreement with the 3D results, and $A \simeq 4 \cdot 10^{-4}$ calibrated on asteroseismic results (Briquet et al., 2011). They find that the extent of the mixed region above the convection-unstable one is decreasing with time, reducing the amount of newly synthesized He with respect to the classical overshoot implementation. This reduction of the core size in turn reduces the luminosity increase of the model during the main sequence. Recently, Scott et al. (2021) presented a grid of models, with mass ranging between 1.5 and 60 $M_\odot$, computed with the entrainment law and compared them to similar models computed with a penetrative overshoot. They find that the entrainment CBM scheme leads to a natural increase of the mixed region with mass, improving agreement with the observational constraints derived by Castro et al. (2014). In contrast with Staritsin (2013), they obtain an entrained mass that increases with time. This difference is due to the difference in the implementation: Staritsin (2013) scales the instantaneous entrained distance with the Richardson number ($d_{\rm ent} = V_{\rm ent}\Delta t$), while Scott et al. (2021), following Cristini et al. (2019), scale the mass entrainment rate ($\dot{M}_{\rm ent}$) with $\mathrm{Ri}_{\rm B}$, building a cumulative entrainment. Note that while the cumulative implementation reproduces the trend seen in the hydro simulation, it is not clear how the secular evolution differs from the evolution on a dynamical timescale probed by 3D modeling. Moreover, Higl et al. (2021) tried to calibrate A and n in 2D modeling of ZAMS convective cores of intermediate-mass models, but failed in finding a satisfactory solution through the whole mass range (1.3 to 3.5 $M_\odot$), an indication that more stellar parameters might be necessary to adjust the entrainment law. They suggest that it could scale not only with Ri_B but also with the Peclet number.

Viallet et al. (2015) suggest that different convection regimes (and hence different overshoot schemes) should be used depending on the conditions in which the convection takes place and the importance of radiation. Where the radiation plays an important role, it reduces the efficiency of convection. They recommend to use the diffusive scheme on convective envelopes, while in the deep interior, penetrative overshoot seems more adequate in the phases when the star is cooled by photons, and entrainment should be used in advanced phases when the cooling is due to neutrinos.

The hydro simulations have also revealed the excitation of internal gravity waves (IGW) by the convective eddies and plumes penetration in the radiative zone above. Rogers et al. (2013) and more recently Edelmann et al. (2019) have computed in 2D and 3D respectively the IGW spectrum and amplitude expected in a star with a convective core and a radiative envelope. Space asteroseismology has detected a low-frequency stochastic variability in O- and B-type stars (Blomme et al., 2011; Buysschaert et al., 2015; Aerts et al., 2018; Bowman et al., 2019a,b). This signal has been attributed to IGW generated by the convective core (Bowman et al., 2019b), or sub-surface convective zones (Blomme et al., 2011; Lecoanet et al., 2019). If the ability of IGW to transport angular momentum inside radiative envelopes is confirmed, it would make them good candidates to explain strong angular momentum transport in some observed intermediate-mass or massive stars (Aerts et al., 2017, 2019), or even the strange case of the counter-rotating envelope observed for the late B-type star KIC 10526294 (Triana et al., 2015).

An important feature seen in the advanced phases of both 1D and multi-D models is the merger of the O-burning shell with

the Ne shell above, or even the C-burning shell (Rauscher et al., 2002; Woosley et al., 2002; Tur et al., 2007; Andrassy et al., 2020; Yadav et al., 2020). According to Collins et al. (2018), it happens commonly in SN progenitors models between 16 and 26 $M_\odot$, very shortly prior to the collapse. Of course, the amplitude of this phenomenon is strongly related to the CBM efficiency (Davis et al., 2019) and to the spatial resolution (Farmer et al., 2016), but the fact that it also appears in 3D modeling tells us that it is a process we have to account for. Ritter et al. (2018a) show that it is responsible for overproductions of P, Cl, K, and Sc that could reconcile the nucleosynthetic predictions with the observations of odd-Z elements in the Galaxy. Similarly, the merger of the Si-burning shell up to the C-burning shell drives an overproduction of Cr (Côté et al., 2020). By changing the compactness, shell mergers can also impact the explodability of the models (Davis et al., 2019), and build asymmetries that can help revive the shock and increase the amplitude of the SASI instability (Andrassy et al., 2020; Yadav et al., 2020).

5.2. Rotation

A spinning star is affected by rotation in two different ways. First, the centrifugal force helps it counterbalance its own gravity. This has an effect on the hydrostatic equilibrium the star is settling on, making it behave like a slightly lower-mass non-rotating star. In an HR diagram, this translates into a slight shift toward lower $T_{\rm eff}$ and L at the very beginning of the evolution. The centrifugal force increases also the mass loss experienced by the star, the gravitational pull being slightly lower. The star shape is not spherical anymore but oblate, with an equatorial radius larger than the polar one. In the framework of the Roche model, where the gravitational potential is approximated by $\frac{GM_r}{r}$ (with M_r the mass coordinate at the internal radius r), we can express the oblateness as a function of the ratio of the centrifugal force to the gravity at the equator: $\frac{R_{\rm eq}}{R_{\rm pol}} = 1 + \frac{1}{2}\frac{a_{\rm cen}}{g_{\rm eq}} = 1 + \frac{1}{2}\frac{\Omega^2 R_{\rm eq}^3}{GM}$. When the star is rotating at the critical limit, we have $a_{\rm cen} = g_{\rm eq}$, and hence the maximal oblateness corresponds to $R_{\rm eq} = \frac{3}{2}R_{\rm pol}$. In this case, the outer layers of the star are no longer bound to it and can be lost through a mechanical mass loss (Georgy et al., 2013b).

The second effect is actually the more important for the whole evolution of the star: internal mixing. Rotation induces several instabilities, the first one being the meridional circulation (Eddington, 1925; Vogt, 1925; Sweet, 1950; Zahn, 1992; Maeder and Zahn, 1998). The oblateness of the star prevents it to be both in hydrostatic and thermal equilibrium at the same time. This impossibility drives a large scale circulation inside the star, which transports angular momentum and chemicals by an advecto-diffusive mixing (Zahn, 1992; Maeder and Zahn, 1998). Moreover, if the star does not rotate like a rigid body, the differential rotation induces a shear mixing that diffuses both angular momentum and chemicals through the star. The transport of angular momentum can thus be written as:

$$\rho\frac{\partial}{\partial t}\left(r^2\bar{\Omega}\right)_{M_r} = \frac{1}{5r^2}\frac{\partial}{\partial r}\left(\rho r^4\bar{\Omega}U(r)\right) + \frac{1}{r^2}\frac{\partial}{\partial r}\left(\rho D_\Omega\, r^4\frac{\partial\bar{\Omega}}{\partial r}\right) \quad (8)$$

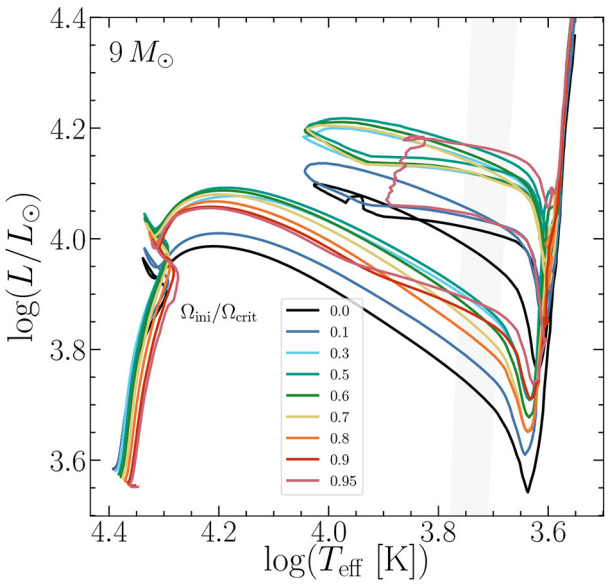

FIGURE 5 | Hertzsprung-Russell diagram for 9 $M_\odot$ models with increasing rotation (models from Georgy et al., 2013b).

with $\bar{\Omega}$ the mean angular velocity at radius r, $U(r)$ the radial component of the meridional circulation, and D_Ω the diffusion coefficient corresponding to the various diffusive processes transporting Ω, like shear mixing or convection.

In the case of chemicals, it has been shown by Chaboyer and Zahn (1992) that despite the advective nature of meridional flows, the net effect on the chemical mixing can be satisfactorily approximated by a diffusive-only process. The changes in chemical composition in a layer of the stellar interior can be expressed as:

$$\rho\frac{{\rm d}X_i}{{\rm d}t} = \frac{1}{r^2}\frac{\partial}{\partial r}\left(\rho r^2 D\frac{\partial X_i}{\partial r}\right) + \left(\frac{{\rm d}X_i}{{\rm d}t}\right)_{\rm nucl}$$

with ρ the density in the layer, X_i the mass fraction abundance of species i in the layer, r the internal radius at that layer, D the diffusion coefficient taking into account all the diffusive processes included ($D = D_{\rm conv} + D_{\rm shear} + D_{\rm eff,U}$, where "conv" is for convection, and "eff,U" is for the meridional circulation effective diffusive process), and $\left(\frac{{\rm d}X_i}{{\rm d}t}\right)_{\rm nucl}$ expresses the change in composition due to the nuclear reactions in the layer.

Figure 5 shows evolutionary tracks in the HRD for the 9 $M_\odot$ models of Georgy et al. (2013b) at solar metallicity. For increasing initial rotation $\Omega_{\rm ini}/\Omega_{\rm crit}$[4], the tracks start on lower $T_{\rm eff}$ and L, the gravitation of the star being partially lifted by the centrifugal force. Over the course of the main sequence, the mixing effects start dominating over the hydrostatic one, so the convective H-burning core recedes more slowly and hence the tracks are getting more luminous (without a net change in $T_{\rm eff}$). For really rapid

[4] $\Omega_{\rm crit}$ is the critical angular momentum at which the centrifugal force counterbalances gravity.

rotation ($\Omega_{ini}/\Omega_{crit} \geq 0.6$), the hydrostatic effects start playing again an important role and though the cores are still larger, L decreases slightly. The luminosity difference between rotating and non-rotating models remains throughout the whole further evolution. Roughly summarized, the rotating star begins its life behaving like a lower-mass star because of the hydrostatic effect of rotation, and ends its life behaving like a higher-mass star because of the rotational mixing.

Concerning the stellar nucleosynthesis, the increase of the core makes the central burnings to occur in a hotter and slightly less dense environment. Central H burning is longer because the core is being replenished with fresh H by mixing (see **Table 1**). In contrast, central He burning is generally shorter, mostly because of the higher luminosity induced by the larger core. Many features of the behavior of massive stars in advanced phases depend on the mass of the CO core left by He burning, as for example the ability to ignite carbon or not, off-center or at the center, convectively or radiatively. Rotation lowers the different limiting masses for these features. The mass of the core also defines almost uniquely the final luminosity of the star just before the supernova explosion (Farrell et al., 2020). The link between the core mass and the initial mass can differ strongly whether rotation is taken into account or not, and of course depending on the treatment of convection or the inclusion of overshooting (see section 5.1), so it is not straightforward to link the luminosity of a SN progenitor to its initial mass. Another important quantity for the advanced-phases behavior is the C/O ratio at the end of He burning (Chieffi and Limongi, 2020). By increasing the central temperature, rotation helps the star build more oxygen at the expense of carbon, so the C/O ratio is lower in rotating models.

Rotational mixing also chemically connects different regions inside the star. This can have profound effects on the nucleosynthesis. Rotating stars are good producers of primary nitrogen, because ^{12}C and ^{16}O produced in the core are diffused upwards into the H-burning shell, and then immediately processed into ^{14}N through the CNO cycle. This ^{14}N can diffuse back into the He-burning core and be further transformed into ^{22}Ne by two successive α captures (Meynet and Maeder, 2002a,b; Hirschi, 2007). As seen above, the reaction ^{22}Ne(α,n)^{25}Mg is a neutron producer that plays an important role in the *s*-process nucleosynthesis, and rotation is able to increase the *s*-process elements production as well as to shift the peak to heavier elements (Pignatari et al., 2008; Chiappini et al., 2011; Frischknecht et al., 2016).

More generally, by modifying the chemical structure of the star, rotation modifies the path it will follow, for example in an HR diagram. Generally, rotation favors a redward evolution (Meynet and Maeder, 2002a), but rapid rotation can mix so strongly the star that it follows a quasi chemically-homogeneous blueward evolution (CHE, see Maeder, 1987; Langer, 1992). This is more easily the case at low metallicity (Szécsi et al., 2015; Choi et al., 2016) since the compactness of the star makes the mixing time shorter ($\tau_{mix} \simeq \frac{R^2}{D}$, with D the mixing coefficient, see Maeder and Meynet, 2001).

The implementation of the effects of rotation in 1D stellar evolution codes suffers from a native problem: the non-1D nature of rotation by definition. Stellar codes implement those effects in very different ways, and unsurprisingly, their results are widely different. Even when the same code uses different implementation of the same advecto-diffusive scheme for the transport of angular momentum, the results show large variations (Meynet et al., 2013). When different codes are compared, the picture becomes even more blurred because not only the rotation implementation is different, but some basic scheme of resolution and the treatment of convection also are different. Martins and Palacios (2013) have performed a comparison of stellar tracks coming from published grids (Bertelli et al., 2008; Brott et al., 2011a; Ekström et al., 2012; Chieffi and Limongi, 2013, without any attempt to benchmark the physical ingredients and parametrization) and added models computed with two other codes, STAREVOL (Siess et al., 1997; Decressin et al., 2009) and MESA (Paxton et al., 2011, 2013). Without rotation, large differences appear, the main culprit being the treatment of convection, as shown also in Jones et al. (2015). The divergence occurs principally after the main sequence. When rotation is switched on, the divergence in the HR diagram between codes is larger on the main sequence, and starts sooner, but is slightly reduced in the post main sequence, probably thanks to mixing effects that reduce the dispersion in luminosity (see Figure 7 in Martins and Palacios, 2013).

The physics of rotation has been partially tested in multi-D hydro simulations. Simulations focussing on the shear mixing (Prat and Lignières, 2013, 2014; Prat et al., 2016) have shown a good agreement with the 1D prescription of Zahn (1992). Edelmann et al. (2017) have shown that 2D models are unstable to the dynamical shear (triggered in the zones where the gradient of Ω is very steep) in the locations predicted by 1D models. In this work, the profile of Ω is affected during about 150 min in both 2D and 1D models. In the 2D model, the instability stops in the previously unstable layer, while in the 1D model the shear mixing is still active, but with such a low diffusion coefficient that it would not be seen in the 2D model due to the hydro timescale. The instability in both models propagates to neighboring layers (much quicker in the 1D than in the 2D model), until the stability is restored. Since the hydro simulation does not include any evolution process impacting the structure (contraction/expansion or energy production/loss), the Ω profile cannot evolve further. The resulting mixing on the chemicals is much stronger in the 2D model, but occurs on a much shorter timescale than the usual evolutionary timescale of 1D models. The net effect, if confirmed by 3D models, could point to the need to apply a lower diffusion coefficient, or a stronger one but on a larger region of the model. The diffusive effect of erasing the Ω gradient is expected to reinforce the advective part of the meridional circulation, that will tend to build it again. Unfortunately, the spatial and temporal resolutions needed to model the meridional circulation are still out of reach of hydro simulations, so only the diffusive part of the net transport of angular momentum can be explored with this tool.

The best observational constraints we can hope for come from surface enrichments, and from asteroseismology. However, they are not at the same level of accuracy concerning the process under scrutiny. Surface enrichments probe the mixing of chemicals, which might be the result of different processes

(rotation, but also convection, IGW, magnetic fields, binary tides,...) while asteroseismology probes precisely the transport of angular momentum inside the star. On the nucleosynthesis side, the CNO cycle is expected to shift the chemical balance of the elements toward nitrogen, depleting carbon and oxygen. The nucleosynthetic behavior is clearly framed theoretically in a diagram of N/C vs. N/O with the two following assumptions (Maeder et al., 2014; Martins et al., 2015a):

1. in the lower mass domain, we can consider that only the first CN cycle is really active, so the oxygen content remains the same and only carbon is transformed into nitrogen. In that case, we have that dC = -dN (in numbers), so $\mathrm{d}\left(\frac{\mathrm{N}}{\mathrm{C}}\right) = \frac{\mathrm{dN}}{\mathrm{C}}\left(1+\frac{\mathrm{N}}{\mathrm{C}}\right)$, while $\mathrm{d}\left(\frac{\mathrm{N}}{\mathrm{O}}\right) = \frac{\mathrm{dN}}{\mathrm{O}}$. In the N/C vs. N/O diagram, this case draws a curve $\frac{\mathrm{d\,log(N/C)}}{\mathrm{d\,log(N/O)}} = 1+\frac{\mathrm{N}}{\mathrm{C}}$;
2. in the higher mass domain, carbon is immediately put to equilibrium by the CN cycle and stays constant, so we have that $\mathrm{d}\left(\frac{\mathrm{N}}{\mathrm{C}}\right) = \frac{\mathrm{dN}}{\mathrm{C}}$, while oxygen is converted into nitrogen and dO = -dN, so $\mathrm{d}\left(\frac{\mathrm{N}}{\mathrm{O}}\right) = \frac{\mathrm{dN}}{\mathrm{O}}\left(1+\frac{\mathrm{N}}{\mathrm{O}}\right)$. In the N/C vs. N/O diagram, this case draws a curve $\frac{\mathrm{d\,log(N/C)}}{\mathrm{d\,log(N/O)}} = \frac{1}{(1+\mathrm{N/O})}$.

This N/C vs. N/O diagram constitutes a kind of sanity check for the abundances observed at the surface of stars, that should lie somewhere between the two limiting lines described above, whatever the source or the physics of surface enrichment (mixing, mass loss, internal gravity waves, ...). If there is a source of mixing, like rotation, or if mass loss removes a large enough part of the envelope of the star, one expects the nucleosynthetic products to be brought up to the surface of stars and they will populate different parts of this diagram, but always between the two limiting lines. Nitrogen enrichments are thus used as tracers of mixing.

When rotational mixing is to be tested, a plot of N enrichment vs. surface velocity (the so-called *Hunter diagram*, after Hunter et al., 2009), or variations of it (Maeder et al., 2009; Brott et al., 2011b; Aerts et al., 2014; Martins et al., 2017) are considered. In the work of Brott et al. (2011b), 60% of the observed stars are located in parts of this diagram where evolutionary models predict they would. The 40% that are off can be regrouped in two categories: the slow rotators showing strong enrichments, and the unenriched rapid rotators. This result has led to a strong challenge of rotational mixing. The problem with this approach (that we could summarize as "*rapid rotators should be enriched, slow rotators should not*") is that the surface enrichment of a star is not simply a function of its rotational velocity. It has been shown to be a complex function of mass, age, rotation rate, metallicity, and multiplicity (Maeder et al., 2009). When a heterogeneous sample of stars are confronted to models in such a diagram, it is difficult to draw firm conclusions about whether rotational mixing is effective or not. Moreover, depending on the angular momentum transport efficiency (mild core-envelope coupling leading to differential rotation, or strong coupling leading to solid-body rotation), the same data can give different answers. Martins et al. (2015a) show that in a given sample of 74 observed O-type stars, 80–90% are consistent with the predictions of the two different mild-coupling sets of models (Ekström et al., 2012; Chieffi and Limongi, 2013), while the strong-coupling set of models (Brott et al., 2011a) can only account for 50% of the sample. The differences are linked to both the enrichment process and the surface velocity evolution. The strong-coupling models experience a strong and rapid N enrichment which then remains constant, and the surface velocity is maintained almost constant through the main sequence because of the solid-body rotation. The mild-coupling models have a more progressive enrichment, and the surface velocity changes through the main sequence under the influence of structural modifications (radius inflation) and angular momentum budget (transport from the contracting core, removal by stellar winds). In such models, the strongest enrichments can be associated with only moderate or even slow rotation velocities (Martins et al., 2017), matching the observations. In the work of Aerts et al. (2014) on 68 massive stars, a strong correlation of N enrichment with T_{eff}, and also with the acoustic mode frequency is found, but no clear correlation with the rotational frequency: they find a slightly higher than average enrichment for the most rapid rotators, and a larger and larger dispersion for decreasing rotational frequencies. Actually this behavior is qualitatively compatible with what is expected by mild-coupling models from such an heterogeneous sample, ranging from 5 to 40 $M_{\odot}$ in very different evolutionary status. The large dispersion of the N enrichment of the slower rotators may arise from a group formed from truly slower rotators (with moderate or no enrichment) mixed with previously rapid rotators that are highly enriched but braked. However, this work points to the need to explore the effects of IGW in the transport of angular momentum and species in massive stellar models and to study their interaction with rotation. The very detailed work by Markova et al. (2018) on 53 Galactic O stars points to the fact that the efficiency of rotational mixing might need to be revised downwards for the mild-coupling models (in line with the 2D result of Edelmann et al., 2017), or upwards for the strong-coupling models. This last trend is echoed in the work by Dufton et al. (2018) on 54 B-type stars in the LMC with low projected rotational velocities. While 75–80% of the observed stars follow the models predictions, the fraction of N-enriched apparently slow rotators is too high to be explained by rapidly-rotating stars being seen pole-on. This fraction is however compatible with the fraction of stars found to have a significant enough surface magnetic field to be detected by the MiMes survey (7% of B-type stars, see Wade et al., 2014). Magnetic fields leading to simultaneously the braking-down of the star's rotational velocity and a strong N enrichment (Meynet et al., 2011) is hence proposed by the authors as a possible solution for these stars, along with stellar mergers (see section 5.4). Binaries interactions can only partly explain the result for the very strong N enrichment of ON stars (Martins et al., 2015b), so these peculiar stars still present a puzzle for stellar models.

The treatment of rotation leading to a mild coupling, that seems to be the best fit for the bulk of the surface enrichments of main-sequence massive stars, implies a differential rotation inside the models. Asteroseismology is able to probe stellar interiors and give informations on the rotational profile inside the stars. Unfortunately, to date, only a handful of β Cephei

stars (main sequence stars with masses between 7 and 20 $M_{\odot}$) have been analyzed by asteroseismic techniques allowing to probe their internal rotation profile. On the seven stars observed, only three have yielded a clear detection of the core-to-envelope rotation ratio: ν Eri (Pamyatnykh et al., 2004; Dziembowski and Pamyatnykh, 2008), V836 Cen (also known as HD 129929, Aerts et al., 2003; Dupret et al., 2004), and 12 Lac (Dziembowski and Pamyatnykh, 2008). The first two are compatible with differential rotation (with $\Omega_{\rm core}/\Omega_{\rm env} > 1$.) For 12 Lac the answer depends on the model used to fit the asteroseismic data, one model being compatible with a flat profile ($\Omega_{\rm core}/\Omega_{\rm env} = 1$) and the other with a differential rotation ($\Omega_{\rm core}/\Omega_{\rm env} \sim 5$). For one other star, V2052 Oph (Briquet et al., 2012), the presence of a magnetic field have lead to the conclusion that the star should have a flat profile. The fifth one for which an analysis of the rotation profile has been intended, θ Oph (Briquet et al., 2007; Walczak et al., 2019) is a member of a triple system, with an SPB tertiary (Slowly Pulsating B-type star) contributing significantly to the light of the primary. Both analyses are compatible with rigid rotation in the envelope. While the overall picture of these analyses would advocate a 50%-50% fraction of differentially and rigidly rotating β Cephei stars, this sample is way too small to give us firm answers about the rotation profiles in massive stars, and only when statistically-significant large asteroseismic surveys will have yielded their results will we be able to assess whether the same problem of angular momentum occurs in massive stars as in low-mass stars. We might not have to wait too long: Labadie-Bartz et al. (2020) have identify 86 new β Cephei stars and 97 candidates from the KELT project (Kilodegree Extremely Little Telescope exoplanet survey) that will be included in the target list of TESS (Transiting Exoplanet Survey Satellite).

Low-mass stars modeling have undergone a revolution when asteroseismic results have started to reveal the stellar interiors that where impossible to probe before. An important result brought by the unprecedented precision and wealth of data yielded by the satellites CoRoT and Kepler is the need for an additional transport mechanism inside the radiative zone of low-mass stars in order to explain the rotation profile of red giants and sub-giants (Beck et al., 2012; Eggenberger et al., 2012; Deheuvels et al., 2014). The asteroseismic analyses show that there is a stronger coupling between the contracting core and the expanding envelope after the main sequence. This additional transport could also extract some angular momentum from the core and reconcile the predictions of the models with the measurements of the core rotation of white dwarfs (Suijs et al., 2008; Fuller et al., 2019). The physical mechanism is not yet understood, but some characterization of its behavior with evolutionary status or mass have been performed (Cantiello et al., 2014; Spada et al., 2016; Eggenberger et al., 2017, 2019a). The proposed solution of a modified Tayler-Spruit magnetic dynamo (Fuller et al., 2019) has been shown to be unable to reproduce the observations of both red giants and sub-giants (Eggenberger et al., 2019b; den Hartogh et al., 2020). Explorations of the role of IGW (see section 5.1) in the angular momentum transport in red giants and sub-giants have shown that they are not efficient enough to solve the problem, though they could play a role (Fuller et al., 2014; Pinçon et al., 2017).

Would the same additional mechanism be needed in massive stars? It has been shown that the cores of supernova progenitors were rotating too fast to explain the spin rate of young neutron stars (Suijs et al., 2008), suggesting the need for a stronger core-envelope coupling during the nuclear lifetime of the stars. This conclusion rests on the assumption that there is conservation of angular momentum between the collapsing star and the resulting neutron star after the explosion. However, as we saw in section 2.4, the explosion mechanism involves large-scale convective instabilities, and it has been shown that SASI sloshing or spiral movements can redistribute the angular momentum of the progenitor and alter the amount that is enclosed in the neutron star (Blondin and Mezzacappa, 2007; Wongwathanarat et al., 2010, 2013; Kazeroni et al., 2017). In section 5.1, we saw that convective penetration generates IGW in the radiative zone above. These IGW have been shown to be able to modify significantly the spin of the pre-SN core during the very late stages of nuclear burning (Fuller et al., 2015). These late-time alterations suggest that the spin rates of young pulsars might not be good constraints on the angular momentum transport during the evolution of massive stars. In any case, solid-body rotation is disfavored by surface enrichment observations of main sequence stars so far, so if confirmed by large-scale asteroseismic campaigns, the strong coupling mechanism should be effective only in the advanced phases of the evolution.

5.3. Mass Loss

Massive stars experience mass loss throughout their life, either as a thin and fast main-sequence wind, a thick and slow RSG wind, or a thick and very fast WR wind uncovering the stellar core. Luminous blue variables (LBVs) shed mass in episodic dramatic bursts, sometimes close to disruption. The fate of massive stars depends strongly on the mass loss they experience (Vanbeveren et al., 1998a,b; Meynet et al., 2015), and so does the type of supernova they will make (Georgy, 2012).

Mass loss is not explicitly modeled in 1D stellar evolution codes. Modelers rely on prescriptions to implement this very important process. Some prescriptions are empirical or semi-empirical, others are theoretical. The most common description of stellar mass loss is the radiatively-driven wind theory (Lucy and Solomon, 1970), with the CAK formalism from Castor et al. (1975). However, this driving seems to fail to describe the winds of advanced phases stars like RSG or WR. RSG winds show variations of more than 2 orders of magnitude for a given luminosity (van Loon et al., 2005; Mauron and Josselin, 2011). This scatter could come from the analysis being performed on field stars of mixed ages and masses: the relation between mass loss and luminosity seems much more straightforward when stars in clusters are observed (Beasor and Davies, 2016, 2018). Very recently, Kee et al. (2021) have proposed a relation between RSG mass loss and strong atmospheric turbulence. Beside a more or less steady wind, RSGs seem to undergo episodic mass-loss events, linked in one way or the other to dust production (van Loon et al., 2005), like we recently witnessed in the case of Betelgeuse (Levesque and Massey, 2020). Our difficulty as modelers is that we cannot include these particular events in the stellar modeling, hence we need to use averaged rates accounting

for the total mass-loss budget of a star, steady and episodic flows altogether. WR winds also deviate from the pure CAK theory as they show a strong dependence on the Eddington factor $\Gamma_{\rm Edd} = \frac{\kappa L}{4\pi cGM}$, which seems to play a major role as the driver of the WR mass loss (Vink, 2006; Gräfener et al., 2011; Vink et al., 2011; Bestenlehner et al., 2014).

For a given location in the HR diagram, some overlapping prescriptions give very different results. Generally, observations give different mass-loss rates depending on the diagnostic line used. This has been pointing toward a problem of clumping in the wind (Najarro et al., 2011; Šurlan et al., 2013; Rauw et al., 2015). While accounting for clumping tends to reduce the mass loss inferred, the inclusion of light leakage (porosity) compensates in some cases this reduction (Oskinova et al., 2007; Sundqvist et al., 2014).

Beside the problem of clumping and porosity, low-luminosity late O-type dwarf stars present what has been called the "*weak-wind problem*": below a luminosity of $\log(L/L_\odot) \simeq 5.2$, their observed mass-loss rates are orders of magnitude lower than predicted by theoretical mass-loss prescriptions (Martins et al., 2005; Marcolino et al., 2009; Najarro et al., 2011; Oskinova et al., 2011; Muijres et al., 2012). Recently, de Almeida et al. (2019) have shown that late O giants (luminosity class III) show the same trend as the dwarf (luminosity class V). The reason for this downshift in mass-loss rates below a given luminosity is still debated. Oskinova (2016) propose that most of the late O stars winds are in the hot gas phase, and hence accessible only through X-rays diagnostics. More recently Vilhu and Kallman (2019) have proposed that the weak-wind problem could be linked to a velocity porosity (*vorocity*, Owocki, 2014) in the wind stratification.

Although mass loss concerns the surface of a star, it can have some deep repercussions and actually modify the nucleosynthetic yields. If the mass loss during the main sequence is high, it has time to modify the structure of the star and its core mass, changing the conditions for nucleosynthesis in the subsequent advanced phases. If the mass loss in the advanced phases is high, it can remove parts of the star that will no longer be available for nucleosynthesis (hydrostatic shell burning or explosive nucleosynthesis) and hence change the yields. In the extreme case of WR stars, the He-burning phase ends with a star that is reduced to its naked core. The core cannot increase anymore since the H-burning shell was stripped off, and it can only decrease even more since mass loss can still remove some mass during the latest phases.

The radiative mass loss is dependent on the metallicity of the star ($\dot{M} \propto Z^{0.85}$), since metals offer the largest number of electron transitions. Note that the Z exponent is not firmly determined yet (Mokiem et al., 2007). Low-metallicity stars retain more mass and angular momentum than their high-Z counterparts. They are more prone to reach the critical velocity and lose mass mechanically in a decretion disk (Owocki, 2004; Krtička et al., 2011; Georgy et al., 2013b; Granada et al., 2013). This mechanism is thought to be the driver of the Be phenomenon: B-type stars presenting H_α emission lines that are supposed to come from a disk around the (more or less) rapidly rotating star (Secchi, 1866; Struve, 1931; Dachs et al., 1986). Rapidly-rotating low-metallicity massive stars are also supposed to be the progenitors of long soft GRBs (Yoon et al., 2006).

5.4. Binarity

Binarity is a game-changer for stellar evolution. It populates region of the HR diagram that single star populations cannot reach, and strongly changes the expected spectral outputs (Eldridge and Stanway, 2020). Most massive stars are born in multiple systems (Sana et al., 2008, 2009; Moe and Di Stefano, 2017). While single stars grids of models have to deal with a parameter space essentially of three parameters (mass, chemical composition, and rotation rate), binaries open a huge combination of mass ratios and separations. The distribution of orbital periods favors close binary systems and a uniform distribution of mass ratios (Sana et al., 2012; Moe and Di Stefano, 2017), which means that interactions between the components are very common. Analyses of spectral populations of external galaxies need to take the effect of binarity into account (Eldridge et al., 2008; Eldridge and Stanway, 2009, 2020).

Concerning the effects binarity has on stellar evolution, I refer the reader to the review by Langer (2012) for a detailed description. I will only summarize them here. The most basic modifications brought by binarity are linked to rotation and mass loss.

5.4.1. Rotation

A star in a binary system will tend to synchronize its spin to the orbital period, and this process will trigger tidal mixing (Zahn, 1977, 2008), dissipating the excess kinetic energy. The torque exerted at the surface is larger for large angular velocity differences ($\Omega - \omega$, with Ω the star's angular velocity and ω the orbital angular velocity), and for small separations a. According to Zahn (1977, 2008), the time needed to achieve synchronization is:

$$\frac{1}{t_{\rm sync}} = -\frac{d}{dt}\left|\frac{2\,(\Omega-\omega)}{\omega}\right|^{-5/3} = 5\cdot 2^{5/3}\left(\frac{GM}{R^3}\right)^{1/2}\frac{MR^2}{I}\,q^2\,(1+q)^{5/6}\,E_2\left(\frac{R}{a}\right)^{17/2}$$

where $q = \frac{m}{M}$ is the ratio of the companion mass over the star's mass, I the inertia, and E_2 a parameter describing the coupling between the tidal potential and the gravity mode dissipating it in the radiative envelope of massive stars. We see that there is a strong dependence on the ratio between the star's radius and the semi-major axis $\frac{R}{a}$. It is expected that the binary components will synchronize before the orbit achieves circularization, so the time for circularization can be expressed supposing $\Omega = \omega$, as:

$$\frac{1}{t_{\rm circ}} = \frac{d\ln e}{dt} = \frac{21}{2}\left(\frac{GM}{R^3}\right)^{1/2} q\,(1+q)^{11/6}\,E_2\left(\frac{R}{a}\right)^{21/2}$$

with e the eccentricity.

The internal tides increase the rotational mixing experienced by the star, magnifying the effects described in section 5.2. The strong mixing can in some cases keep the star extremely compact through quasi CHE, preventing the filling of its Roche lobe and the mass transfer that it would trigger (Song et al., 2016).

5.4.2. Mass Transfer

Binary components can either shed or receive mass through the filling of the Roche lobe, which radius can be approximated as $R_L = a \frac{0.49\, q^{2/3}}{0.6\, q^{2/3} + \ln(1+q^{1/3})}$ (Eggleton, 1983). Their are three different cases of mass transfer episodes:

- **case A** when the mass transfer occurs while the primary is still on the main sequence. This requires very close binaries at birth;
- **case B** when the mass transfer occurs after the primary has left the main sequence;
- **case C** when it occurs after central He burning.

The component that is the donor experiences a strong mass and angular-momentum loss, while the receiver gains both mass and angular momentum, but the efficiency of the transfer on the gainer is usually limited either by the thermal response to the accretion ($\dot{M}_g \leq M_g/\tau_{KH}$, with τ_{KH} as Equation 7, see Eldridge et al., 2008), or by the maximal amount of angular momentum the star can absorb before reaching the critical limit (Langer, 2012). It is not clear how the non-accreted mass is removed, maybe in the form of a circum-binary disk that will be later erased by radiation (Vanbeveren et al., 1998b; Langer, 2012). In case the angular-momentum criterion is used to modulate the accretion on the receiver, the efficiency of the accretion changes with time, early accretion episodes (case A) being more efficient than later ones. If the mass donor has experienced rotational mixing or evolutionary dredge-ups, the matter that is accreted by the mass gainer has a more heavy molecular weight than its own envelope. Some thermohaline mixing is then expected (Cox and Giuli, 1968; Kippenhahn et al., 1980; Bitzaraki et al., 2003).

Since the more massive stars evolve quicker than the less massive ones, it is usually the more massive (primary) component that starts shedding mass on the secondary, sometimes losing enough mass to invert the mass ratio, like in Algol-type systems. The evolution of the orbit of the binary depends critically on the mass ratio between the mass donor star and the mass gainer $q = M_d/M_g$ (Siess et al., 2013):

$$\frac{\dot{a}}{a} = 2\frac{\dot{J}_{orb}}{J_{orb}} - 2\left(\frac{\dot{M}_d}{M_d} + \frac{\dot{M}_g}{M_g}\right) + \frac{\dot{M}_d + \dot{M}_g}{M_d + M_g} + \frac{2e\dot{e}}{1-e^2} \quad (9)$$

In the simple case of conservative mass transfer, we have $\dot{J}_{orb} = 0$, $\dot{M}_g = -\dot{M}_d$, and if we suppose the orbit to be circularized, we can rewrite Equation (9) as:

$$\frac{\dot{a}}{a} = 2\,(q-1)\,\frac{\dot{M}_d}{M_d}$$

As long as the mass donor remains the more massive component ($q > 1$), the orbital separation tends to shrink ($\dot{a}/a < 0$ because the donor loses mass and hence $\dot{M}_d < 0$). When the mass ratio gets inverted and the mass gainer becomes more massive than the donor ($q < 1$), the separation increases ($\dot{a}/a > 0$), a minimum separation being reached when $M_g = M_d$.

It is usually considered that donors with a radiative envelope (as it is the case in case A mass transfer for massive stars) experience stable mass transfer because the radiative envelope settles on a smaller radius after the mass transfer. In contrast, convective envelopes tend to readjust to the same radius after the initial mass transfer, or even to expand, while the Roche lobe radius has decreased, so the mass transfer evolves into an unstable kind of runaway (Paczyński and Sienkiewicz, 1972). Note however that it has been shown that this is a too simplified picture, and that the adjustment of the envelope depends strongly on the donor's radius and the mass ratio (Podsiadlowski et al., 2002; Woods and Ivanova, 2011; Passy et al., 2012b; Pavlovskii et al., 2017). If an unstable mass transfer occurs, it is supposed to end in what is called a common-envelope (CE) phase. When this happens, the two components are dragged into a spiraling-in process, in which orbital energy is released (Livio, 1989). This energy might be sufficient to unbind the envelope, leaving a very tight system where the donor has become a naked core. It is not clear at all how the CE phase should be treated in binary models. Multi-D numerical simulations seem to indicate that it is difficult to really unbind the whole envelope (Ricker and Taam, 2008, 2012; Passy et al., 2012a; Ohlmann et al., 2016). In case the released orbital energy is not sufficient, the outcome is the merger of the two components, forming a rejuvenated rapidly-rotating single star (Schneider et al., 2019, 2020).

Mass transfer can alter the size of the core of the donor if it happens before the end of core He burning. Since the core mass defines the nucleosynthesis conditions of the advanced phases, it can have repercussions on the stellar yields. However, it has been shown that this effect is moderate when models of galactic chemical evolution include binaries (De Donder and Vanbeveren, 2002).

6. DISCUSSION AND PERSPECTIVES

Stellar models are advanced numerical experiments, needing to describe a very complex physical object. They will be as good as the physics processes they include, and the way those processes are implemented. We saw that the most important processes for massive stars evolution are highly multi-dimensional, and are a challenge to implement in 1D stellar evolution codes. They come with all sorts of free parameters that need to be calibrated. One never knows whether the calibration will hold when they explore different mass or metallicity domains than the ones the calibration was performed on. These calibrations make the models to be only descriptive, their predictive nature is extremely uncertain.

Could we imagine that the twenty-first century stellar models would be fully 3D models, computed from birth to collapse with the high resolution needed to capture in a consistent way the complexity of turbulence and transport processes? Large state-of-the-art hydro simulations have 1536^3 cells, and the computation of just 1000 seconds of carbon shell burning requires 10 million CPU-hours. The computation of a full star during its whole life on 1000 billions CPUs would last for 10 Gyr! So we are bound to 1D stellar models, and we need to take them into the 21st century.

The way to go comes from combining large-scale surveys (for statistical relevance), asteroseismic observations (for constraints

on the internal conditions), and multi-D simulations (for constraints on the physical processes from first principles). With these strong observational constraints, and with recipes developed from hydro simulations, we can hope to improve the modeling of stars and lead them to a point where they can become predictive one day.

Hydro simulations have started to yield valuable recipes for convection, but they are still lacking for early phases like H or He burning. The long timescales involved and the necessity to include radiative transport are still a difficult hurdle to overcome. The 3D simulations have shown that convective penetration generates IGW that are able to transport both angular momentum and chemicals. Their implementation in massive stars modeling still needs to be attempted. Also the physics of rotation is still elapsing a complete ab initio 3D modeling. A few simulations of the complex but crucial phase of common envelope in binaries have been performed. More are needed before we will be able to derive prescriptions that can be used in 1D models or in population synthesis.

Dedicated simulations of the winds of hot stars are now coming with results that are much more in agreement with the observations (Sundqvist et al., 2019; Björklund et al., 2020). They need to be implemented in stellar evolution codes so that we can assess the changes they bring to the outcomes of stellar modeling.

On the observation side, constraints can be difficult to interpret, because of the high fraction of massive stars that are in binary systems and that have their evolution modified by binary interactions (Sana et al., 2012; de Mink et al., 2014). It has been proposed that the best single stars could be binaries with orbital separations wide enough for the components not to have been interacting strongly (de Mink et al., 2011). However, the high rate of hierarchical multiplicity in massive stars (Duchêne and Kraus, 2013; Moe and Di Stefano, 2017) does complicate the picture, since a wide binary could be composed of one or two close binary systems. Hierarchical multiplicity has been shown to affect strongly the evolution (Toonen et al., 2016).

On the asteroseismology side, the satellites CoRoT and Kepler have shown that extremely valuable informations can be retrieved with this technique. TESS has started harvesting very promising results, and PLATO will have extended observation durations. Unfortunately, both missions have large pixel sizes that are not suitable for crowded regions. There is a need for missions dedicated to high-resolution asteroseismic campaigns, like the HAYDN project (Miglio et al., 2019).

AUTHOR CONTRIBUTIONS

The author confirms being the sole contributor of this work and has approved it for publication.

ACKNOWLEDGMENTS

The author thanks Raphael Hirschi, Cyril Georgy, Patrick Eggenberger, and Georges Meynet for fruitful discussions. She is grateful to the referees who helped improving significantly this review. She acknowledges the STAREX grant from the ERC Horizon 2020 research and innovation programme (grant agreement No. 833925), and the COST Action ChETEC (CA 16117) supported by COST (European Cooperation in Science and Technology).

REFERENCES

Abbott, B. P., Abbott, R., Abbott, T. D., Abernathy, M. R., Acernese, F., Ackley, K., et al. (2016a). GW151226: observation of gravitational waves from a 22-solar-mass binary black hole coalescence. *Phys. Rev. Lett.* 116:241103. doi: 10.1103/PhysRevLett.116.241103

Abbott, B. P., Abbott, R., Abbott, T. D., Abernathy, M. R., Acernese, F., Ackley, K., et al. (2016b). Observation of gravitational waves from a binary black hole merger. *Phys. Rev. Lett.* 116:061102. doi: 10.1103/PhysRevLett.116.061102

Abbott, B. P., Abbott, R., Abbott, T. D., Acernese, F., Ackley, K., Adams, C., et al. (2017). GW170104: observation of a 50-solar-mass binary black hole coalescence at redshift 0.2. *Phys. Rev. Lett.* 118:221101. doi: 10.1103/PhysRevLett.118.221101

Abbott, R., Abbott, T. D., Abraham, S., Acernese, F., Ackley, K., Adams, C., et al. (2020). Properties and astrophysical implications of the 150 $M_{\odot}$ binary black hole merger GW190521. *Astrophys. J. Lett.* 900:L13. doi: 10.3847/2041-8213/aba493

Aerts, C. (2008). "Core overshoot and nonrigid internal rotation of massive stars: current status from asteroseismology," in *IAU Symposium*, Vol. 250, eds F. Bresolin, P. A. Crowther, and J. Puls, 237.

Aerts, C., Bowman, D. M., Símon-Díaz, S., Buysschaert, B., Johnston, C., Moravveji, E., et al. (2018). K2 photometry and HERMES spectroscopy of the blue supergiant ρ Leo: rotational wind modulation and low-frequency waves. *Mon. Not. R. Astron. Soc.* 476:1234. doi: 10.1093/mnras/sty308

Aerts, C., Mathis, S., and Rogers, T. M. (2019). Angular momentum transport in stellar interiors. *Annu. Rev. Astron. Astrophys.* 57:35. doi: 10.1146/annurev-astro-091918-104359

Aerts, C., Molenberghs, G., Kenward, M. G., and Neiner, C. (2014). The surface nitrogen abundance of a massive star in relation to its oscillations, rotation, and magnetic field. *Astrophys. J.* 781:88. doi: 10.1088/0004-637X/781/2/88

Aerts, C., Thoul, A., Daszyńska, J., Scuflaire, R., Waelkens, C., Dupret, M. A., et al. (2003). Asteroseismology of HD 129929: core overshooting and nonrigid rotation. *Science* 300:1926. doi: 10.1126/science.1084993

Aerts, C., Van Reeth, T., and Tkachenko, A. (2017). The interior angular momentum of core hydrogen burning stars from gravity-mode oscillations. *Astrophys. J. Lett.* 847:L7. doi: 10.3847/2041-8213/aa8a62

Allan, A. P., Groh, J. H., Mehner, A., Smith, N., Boian, I., Farrell, E. J., et al. (2020). The possible disappearance of a massive star in the low-metallicity galaxy PHL 293B. *Mon. Not. R. Astron. Soc.* 496:1902. doi: 10.1093/mnras/staa1629

Andrassy, R., Herwig, F., Woodward, P., and Ritter, C. (2020). 3D hydrodynamic simulations of C ingestion into a convective O shell. *Mon. Not. R. Astron. Soc.* 491:972. doi: 10.1093/mnras/stz2952

Angulo, C., Arnould, M., Rayet, M., Descouvemont, P., Baye, D., Leclercq-Willain, C., et al. (1999). A compilation of charged-particle induced thermonuclear reaction rates. *Nucl. Phys. A* 656:3.

Arnett, D. (1996). *Supernovae and Nucleosynthesis: An Investigation of the History of Matter from the Big Bang to the Present*. Princeton University Press.

Arnett, W. D., Meakin, C., Hirschi, R., Cristini, A., Georgy, C., Campbell, S., et al. (2019). 3D Simulations and MLT. I. Renzini's Critique. *Astrophys. J.* 882:18. doi: 10.3847/1538-4357/ab21d9

Arnett, W. D., Meakin, C., Viallet, M., Campbell, S. W., Lattanzio, J. C., and Mocák, M. (2015). Beyond mixing-length theory: a step toward 321D. *Astrophys. J.* 809:30. doi: 10.1088/0004-637X/809/1/30

Austin, S. M. (2005). Making carbon in stars. *Nucl. Phys. A* 758:375. doi: 10.1016/j.nuclphysa.2005.05.178

Barkat, Z., Rakavy, G., and Sack, N. (1967). Dynamics of supernova explosion resulting from pair formation. *Phys. Rev. Lett.* 18:379. doi: 10.1103/PhysRevLett.18.379

Beasor, E. R., and Davies, B. (2016). The evolution of red supergiants to supernova in NGC 2100. *Mon. Not. R. Astron. Soc.* 463:1269. doi: 10.1093/mnras/stw2054

Beasor, E. R., and Davies, B. (2018). The evolution of red supergiant mass-loss rates. *Mon. Not. R. Astron. Soc.* 475:55. doi: 10.1093/mnras/stx3174

Beaudet, G., Petrosian, V., and Salpeter, E. E. (1967). Energy losses due to neutrino processes. *Astrophys. J.* 150:979.

Beck, P. G., Montalban, J., Kallinger, T., De Ridder, J., Aerts, C., García, R. A., et al. (2012). Fast core rotation in red-giant stars as revealed by gravity-dominated mixed modes. *Nature* 481, 55–57. doi: 10.1038/nature10612

Belczynski, K., Heger, A., Gladysz, W., Ruiter, A. J., Woosley, S., Wiktorowicz, G., et al. (2016). The effect of pair-instability mass loss on black-hole mergers. *Astron. Astrophys.* 594:A97. doi: 10.1051/0004-6361/201628980

Bennett, M. E., Hirschi, R., Pignatari, M., Diehl, S., Fryer, C., Herwig, F., et al. (2012). The effect of ^{12}C +^{12}C rate uncertainties on the evolution and nucleosynthesis of massive stars. *Mon. Not. R. Astron. Soc.* 420:3047. doi: 10.1111/j.1365-2966.2012.20193.x

Bertelli, G., Girardi, L., Marigo, P., and Nasi, E. (2008). Scaled solar tracks and isochrones in a large region of the Z-Y plane. I. From the ZAMS to the TP-AGB end for 0.15-2.5 $M_{\odot}$ stars. *Astron. Astrophys.* 484:815. doi: 10.1051/0004-6361:20079165

Bestenlehner, J. M., Gräfener, G., Vink, J. S., Najarro, F., de Koter, A., Sana, H., et al. (2014). The VLT-FLAMES Tarantula Survey. XVII. Physical and wind properties of massive stars at the top of the main sequence. *Astron. Astrophys.* 570:A38. doi: 10.1051/0004-6361/201423643

Bitzaraki, O. M., Tout, C. A., and Rovithis-Livaniou, H. (2003). Thermohaline-mixing – binary evolution. *New Astron.* 8:23. doi: 10.1016/S1384-1076(02)00199-9

Björklund, R., Sundqvist, J. O., Puls, J., and Najarro, F. (2020). New predictions for radiation-driven, steady-state mass-loss and wind-momentum from hot, massive stars II. A grid of O-type stars in the Galaxy and the Magellanic Clouds. *arXiv preprints* arXiv:2008.06066. doi: 10.1051/0004-6361/202038384

Blomme, R., Mahy, L., Catala, C., Cuypers, J., Gosset, E., Godart, M., et al. (2011). Variability in the CoRoT photometry of three hot O-type stars. HD 46223, HD 46150, and HD 46966. *Astron. Astrophys.* 533:A4. doi: 10.1051/0004-6361/201116949

Blondin, J. M., and Mezzacappa, A. (2007). Pulsar spins from an instability in the accretion shock of supernovae. *Nature* 445:58. doi: 10.1038/nature05428

Böhm-Vitense, E. (1958). Über die Wasserstoffkonvektionszone in Sternen verschiedener Effektivtemperaturen und Leuchtkräfte. Mit 5 Textabbildungen. *ZA* 46:108.

Bowman, D. M., Aerts, C., Johnston, C., Pedersen, M. G., Rogers, T. M., Edelmann, P. V. F., et al. (2019a). Photometric detection of internal gravity waves in upper main-sequence stars. I. Methodology and application to CoRoT targets. *Astron. Astrophys.* 621:A135. doi: 10.1051/0004-6361/201833662

Bowman, D. M., Burssens, S., Pedersen, M. G., Johnston, C., Aerts, C., Buysschaert, B., Michielsen, M., et al. (2019b). Low-frequency gravity waves in blue supergiants revealed by high-precision space photometry. *Nat. Astron.* 3:760. doi: 10.1038/s41550-019-0768-1

Bressan, A., Marigo, P., Girardi, L., Salasnich, B., Dal Cero, C., Rubele, S., et al. (2012). PARSEC: stellar tracks and isochrones with the PAdova and TRieste Stellar Evolution Code. *Mon. Not. R. Astron. Soc.* 427:127. doi: 10.1111/j.1365-2966.2012.21948.x

Briquet, M., Aerts, C., Baglin, A., Nieva, M. F., Degroote, P., Przybilla, N., et al. (2011). An asteroseismic study of the O9V star HD 46202 from CoRoT space-based photometry. *Astron. Astrophys.* 527:A112. doi: 10.1051/0004-6361/201015690

Briquet, M., Morel, T., Thoul, A., Scuflaire, R., Miglio, A., Montalbán, J., et al. (2007). An asteroseismic study of the β Cephei star θ Ophiuchi: constraints on global stellar parameters and core overshooting. *Mon. Not. R. Astron. Soc.* 381:1482. doi: 10.1111/j.1365-2966.2007.12142.x

Briquet, M., Neiner, C., Aerts, C., Morel, T., Mathis, S., Reese, D. R., et al. (2012). Multisite spectroscopic seismic study of the β Cep star V2052 Ophiuchi: inhibition of mixing by its magnetic field. *Mon. Not. R. Astron. Soc.* 427:483. doi: 10.1111/j.1365-2966.2012.21933.x

Brott, I., de Mink, S. E., Cantiello, M., Langer, N., de Koter, A., Evans, C. J., et al. (2011a). Rotating massive main-sequence stars. I. Grids of evolutionary models and isochrones. *Astron. Astrophys.* 530:A115. doi: 10.1051/0004-6361/201016113

Brott, I., Evans, C. J., Hunter, I., de Koter, A., Langer, N., Dufton, P. L., et al. (2011b). Rotating massive main-sequence stars. II. Simulating a population of LMC early B-type stars as a test of rotational mixing. *Astron. Astrophys.* 530:A116. doi: 10.1051/0004-6361/201016114

Buras, R., Rampp, M., Janka, H. T., and Kifonidis, K. (2006). Two-dimensional hydrodynamic core-collapse supernova simulations with spectral neutrino transport. I. Numerical method and results for a 15 M⊙ star. *Astron. Astrophys.* 447:1049. doi: 10.1051/0004-6361:20053783

Burrows, A., and Goshy, J. (1993). A theory of supernova explosions. *Astrophys. J. Lett.* 416:L75.

Burrows, A., Livne, E., Dessart, L., Ott, C. D., and Murphy, J. (2006). A new mechanism for core-collapse supernova explosions. *Astrophys. J.* 640:878. doi: 10.1086/500174

Buysschaert, B., Aerts, C., Bloemen, S., Debosscher, J., Neiner, C., Briquet, M., et al. (2015). Kepler's first view of O-star variability: K2 data of five O stars in Campaign 0 as a proof of concept for O-star asteroseismology. *Mon. Not. R. Astron. Soc.* 453:89. doi: 10.1093/mnras/stv1572

Cantiello, M., Mankovich, C., Bildsten, L., Christensen-Dalsgaard, J., and Paxton, B. (2014). Angular momentum transport within evolved low-mass stars. *Astrophys. J.* 788:93. doi: 10.1088/0004-637X/788/1/93

Canuto, V. M. (1992). Turbulent convection with overshooting: reynolds stress approach. *Astrophys. J.* 392:218.

Canuto, V. M. (2011a). Stellar mixing. I. Formalism. *Astron. Astrophys.* 528:A76. doi: 10.1051/0004-6361/201014447

Canuto, V. M. (2011b). Stellar mixing. II. Double diffusion processes. *Astron. Astrophys.* 528:A77. doi: 10.1051/0004-6361/201014448

Canuto, V. M. (2011c). Stellar mixing. III. The case of a passive tracer. *Astron. Astrophys.* 528:A78. doi: 10.1051/0004-6361/201015372

Canuto, V. M. (2011d). Stellar Mixing. IV. The angular momentum problem. *Astron. Astrophys.* 528:A79. doi: 10.1051/0004-6361/201014449

Canuto, V. M. (2011e). Stellar mixing. V. Overshooting. *Astron. Astrophys.* 528:A80. doi: 10.1051/0004-6361/201014450

Castor, J. I., Abbott, D. C., and Klein, R. I. (1975). Radiation-driven winds in of stars. *Astrophys. J.* 195:157.

Castro, N., Fossati, L., Langer, N., Simón-Díaz, S., Schneider, F. R. N., and Izzard, R. G. (2014). The spectroscopic Hertzsprung-Russell diagram of Galactic massive stars. *Astron. Astrophys.* 570:L13. doi: 10.1051/0004-6361/201425028

Caughlan, G. R., and Fowler, W. A. (1988). Thermonuclear reaction rates V. *Atom. Data Nucl. Data Tables* 40:283.

Caughlan, G. R., Fowler, W. A., Harris, M. J., and Zimmerman, B. A. (1985). Tables of thermonuclear reaction rates for low-mass nuclei (1 &le Z <= 14). *Atom. Data Nucl. Data Tables* 32:197.

Chaboyer, B., and Zahn, J.-P. (1992). Effect of horizontal turbulent diffusion on transport by meridional circulation. *Astron. Astrophys.* 253:173.

Chatzopoulos, E., and Wheeler, J. C. (2012). Effects of rotation on the minimum mass of primordial progenitors of pair-instability supernovae. *Astrophys. J.* 748:42. doi: 10.1088/0004-637X/748/1/42

Chen, K.-J., Woosley, S., Heger, A., Almgren, A., and Whalen, D. J. (2014). Two-dimensional simulations of pulsational pair-instability supernovae. *Astrophys. J.* 792:28. doi: 10.1088/0004-637X/792/1/28

Chiappini, C., Frischknecht, U., Meynet, G., Hirschi, R., Barbuy, B., Pignatari, M., et al. (2011). Imprints of fast-rotating massive stars in the Galactic Bulge. *Nature* 472:454. doi: 10.1038/nature10000

Chiavassa, A., Plez, B., Josselin, E., and Freytag, B. (2009). Radiative hydrodynamics simulations of red supergiant stars. I. interpretation of interferometric observations. *Astron. Astrophys.* 506:1351. doi: 10.1051/0004-6361/200911780

Chieffi, A., and Limongi, M. (2002). The explosive yields produced by the first generation of core collapse supernovae and the chemical composition of extremely metal poor stars. *Astrophys. J.* 577:281. doi: 10.1086/342170

Chieffi, A., and Limongi, M. (2004). Explosive yields of massive stars from $Z = 0$ to $Z = Z_{\odot}$. *Astrophys. J.* 608:405. doi: 10.1086/392523

Chieffi, A., and Limongi, M. (2013). Pre-supernova evolution of rotating solar metallicity stars in the mass range 13-120 M $_{\odot}$ and their explosive yields. *Astrophys. J.* 764:21. doi: 10.1088/0004-637X/764/1/21

Chieffi, A., and Limongi, M. (2020). The presupernova core mass - radius relation of massive stars: understanding its formation and evolution. *Astrophys. J.* 890:43. doi: 10.3847/1538-4357/ab6739

Choi, J., Dotter, A., Conroy, C., Cantiello, M., Paxton, B., and Johnson, B. D. (2016). Mesa isochrones and stellar tracks (MIST). I. Solar-scaled models. *Astrophys. J.* 823:102. doi: 10.3847/0004-637X/823/2/102

Choplin, A., Ekström, S., Meynet, G., Maeder, A., Georgy, C., and Hirschi, R. (2017a). Pre-supernova mixing in CEMP-no source stars. *Astron. Astrophys.* 605:A63. doi: 10.1051/0004-6361/201630182

Choplin, A., Hirschi, R., Meynet, G., and Ekström, S. (2017b). Are some CEMP-s stars the daughters of spinstars? *Astron. Astrophys.* 607:L3. doi: 10.1051/0004-6361/201731948

Claret, A., and Torres, G. (2016). The dependence of convective core overshooting on stellar mass. *Astron. Astrophys.* 592:A15. doi: 10.1051/0004-6361/201628779

Clarkson, O., and Herwig, F. (2021). Convective H-He interactions in massive population III stellar evolution models. *Mon. Not. R. Astron. Soc.* 500:2685. doi: 10.1093/mnras/staa3328

Collins, C., Müller, B., and Heger, A. (2018). Properties of convective oxygen and silicon burning shells in supernova progenitors. *Mon. Not. R. Astron. Soc.* 473:1695. doi: 10.1093/mnras/stx2470

Costa, G., Bressan, A., Mapelli, M., Marigo, P., Iorio, G., and Spera, M. (2020). Formation of GW190521 from stellar evolution: the impact of the hydrogen-rich envelope, dredge-up and $^{12}C(\alpha, \gamma)^{16}O$ rate on the pair-instability black hole mass gap. *arXiv preprints* arXiv:2010.02242. doi: 10.1093/mnras/staa3916

Côté, B., Jones, S., Herwig, F., and Pignatari, M. (2020). Chromium nucleosynthesis and silicon-carbon shell mergers in massive stars. *Astrophys. J.* 892:57. doi: 10.3847/1538-4357/ab77ac

Couch, S. M., Chatzopoulos, E., Arnett, W. D., and Timmes, F. X. (2015). The three-dimensional evolution to core collapse of a massive star. *Astrophys. J. Lett.* 808:L21. doi: 10.1088/2041-8205/808/1/L21

Cox, J. P., and Giuli, R. T. (1968). *Principles of stellar structure*. New York, NY: Gordon & Breach.

Cristini, A., Hirschi, R., Meakin, C., Arnett, D., Georgy, C., and Walkington, I. (2019). Dependence of convective boundary mixing on boundary properties and turbulence strength. *Mon. Not. R. Astron. Soc.* 484:4645. doi: 10.1093/mnras/stz312

Cristini, A., Meakin, C., Hirschi, R., Arnett, D., Georgy, C., Viallet, M., et al. (2017). 3D hydrodynamic simulations of carbon burning in massive stars. *Mon. Not. R. Astron. Soc.* 471, 279–300. doi: 10.1093/mnras/stx1535

Crockett, R. M., Eldridge, J. J., Smartt, S. J., Pastorello, A., Gal-Yam, A., Fox, D. B., et al. (2008). The type IIb SN 2008ax: the nature of the progenitor. *Mon. Not. R. Astron. Soc.* 391:L5. doi: 10.1111/j.1745-3933.2008.00540.x

Curtis, S., Ebinger, K., Fröhlich, C., Hempel, M., Perego, A., Liebendörfer, M., et al. (2019). PUSHing core-collapse supernovae to explosions in spherical symmetry. III. Nucleosynthesis yields. *Astrophys. J.* 870:2. doi: 10.3847/1538-4357/aae7d2

Dachs, J., Hanuschik, R., Kaiser, D., and Rohe, D. (1986). Geometry of rotating envelopes around Be stars derived from comparative analysis of H-alpha emission line profiles. *Astron. Astrophys.* 159:276.

Davis, A., Jones, S., and Herwig, F. (2019). Convective boundary mixing in a post-He core burning massive star model. *Mon. Not. R. Astron. Soc.* 484:3921. doi: 10.1093/mnras/sty3415

de Almeida, E. S. G., Marcolino, W. L. F., Bouret, J. C., and Pereira, C. B. (2019). Probing the weak wind phenomenon in Galactic O-type giants. *Astron. Astrophys.* 628:A36. doi: 10.1051/0004-6361/201834266

De Donder, E., and Vanbeveren, D. (2002). The chemical evolution of the solar neighbourhood: the effect of binaries. *New Astron.* 7:55. doi: 10.1016/S1384-1076(01)00090-2

de Mink, S. E., Langer, N., and Izzard, R. G. (2011). Binaries are the best single stars. *Bull. Soc. R. Sci. Liege* 80:543.

de Mink, S. E., Sana, H., Langer, N., Izzard, R. G., and Schneider, F. R. N. (2014). The incidence of stellar mergers and mass gainers among massive stars. *Astrophys. J.* 782:7. doi: 10.1088/0004-637X/782/1/7

deBoer, R. J., Görres, J., Wiescher, M., Azuma, R. E., Best, A., Brune, C. R., et al. (2017). The $^{12}C(\alpha, \gamma)^{16}O$ reaction and its implications for stellar helium burning. *Rev. Mod. Phys.* 89:035007. doi: 10.1103/RevModPhys.89.035007

Decressin, T., Mathis, S., Palacios, A., Siess, L., Talon, S., Charbonnel, C., et al. (2009). Diagnoses to unravel secular hydrodynamical processes in rotating main sequence stars. *Astron. Astrophys.* 495:271. doi: 10.1051/0004-6361:200810665

Deheuvels, S., Brandão, I., Silva Aguirre, V., Ballot, J., Michel, E., Cunha, M. S., et al. (2016). Measuring the extent of convective cores in low-mass stars using Kepler data: toward a calibration of core overshooting. *Astron. Astrophys.* 589:A93. doi: 10.1051/0004-6361/201527967

Deheuvels, S., Doğan, G., Goupil, M. J., Appourchaux, T., Benomar, O., Bruntt, H., et al. (2014). Seismic constraints on the radial dependence of the internal rotation profiles of six Kepler subgiants and young red giants. *Astron. Astrophys.* 564:A27. doi: 10.1051/0004-6361/201322779

den Hartogh, J. W., Eggenberger, P., and Deheuvels, S. (2020). Asteroseismology of evolved stars to constrain the internal transport of angular momentum. III. Using the rotation rates of intermediate-mass stars to test the Fuller-formalism. *Astron. Astrophys.* 634:L16. doi: 10.1051/0004-6361/202037568

Deng, L., Xiong, D. R., and Chan, K. L. (2006). An anisotropic nonlocal convection theory. *Astrophys. J.*, 643:426. doi: 10.1086/502707

Denissenkov, P. A., Herwig, F., Bildsten, L., and Paxton, B. (2013). MESA models of classical nova outbursts: the multicycle evolution and effects of convective boundary mixing. *Astrophys. J.* 762:8. doi: 10.1088/0004-637X/762/1/8

Dessart, L., Hillier, D. J., Waldman, R., and Livne, E. (2013). Type II-Plateau supernova radiation: dependences on progenitor and explosion properties. *Mon. Not. R. Astron. Soc.* 433:1745. doi: 10.1093/mnras/stt861

Duchêne, G., and Kraus, A. (2013). Stellar multiplicity. *Annu. Rev. Astron. Astrophys.* 51, 269–310. doi: 10.1146/annurev-astro-081710-102602

Dufton, P. L., Thompson, A., Crowther, P. A., Evans, C. J., Schneider, F. R. N., de Koter, A., et al. (2018). The VLT-FLAMES Tarantula Survey. XXVIII. Nitrogen abundances for apparently single dwarf and giant B-type stars with small projected rotational velocities. *Astron. Astrophys.* 615:A101. doi: 10.1051/0004-6361/201732440

Dupret, M.-A., Thoul, A., Scuflaire, R., Daszyńska-Daszkiewicz, J., Aerts, C., Bourge, P.-O., et al. (2004). Asteroseismology of the β Cep star HD 129929. II. Seismic constraints on core overshooting, internal rotation and stellar parameters. *Astron. Astrophys.* 415:251. doi: 10.1051/0004-6361:20034143

Dziembowski, W. A., and Pamyatnykh, A. A. (2008). The two hybrid B-type pulsators: ν Eridani and 12 Lacertae. *Mon. Not. R. Astron. Soc.* 385:2061. doi: 10.1111/j.1365-2966.2008.12964.x

Eddington, A. S. (1916). On the radiative equilibrium of the stars. *Mon. Not. R. Astron. Soc.* 77:16.

Eddington, A. S. (1917). On the radiative equilibrium of the stars. *Mon. Not. R. Astron. Soc.* 77:596.

Eddington, A. S. (1918). On the conditions in the interior of a star. *Astrophys. J.* 48:205.

Eddington, A. S. (1925). Circulating currents in rotating stars. *Observatory* 48:73.

Edelmann, P. V. F., Ratnasingam, R. P., Pedersen, M. G., Bowman, D. M., Prat, V., and Rogers, T. M. (2019). Three-dimensional Simulations of Massive Stars. I. Wave Generation and Propagation. *Astrophys. J.* 876:4. doi: 10.3847/1538-4357/ab12df

Edelmann, P. V. F., Röpke, F. K., Hirschi, R., Georgy, C., and Jones, S. (2017). Testing a one-dimensional prescription of dynamical shear mixing with a two-dimensional hydrodynamic simulation. *Astron. Astrophys.* 604:A25. doi: 10.1051/0004-6361/201629873

Edmunds, M. G., and Pagel, B. E. J. (1978). Nitrogen synthesis and the "age" of galaxies. *Mon. Not. R. Astron. Soc.* 185, 77–80.

Eggenberger, P., Deheuvels, S., Miglio, A., Ekström, S., Georgy, C., Meynet, G., et al. (2019a). Asteroseismology of evolved stars to constrain the internal transport of angular momentum. I. Efficiency of transport during the subgiant phase. *Astron. Astrophys.* 621:A66. doi: 10.1051/0004-6361/201833447

Eggenberger, P., den Hartogh, J. W., Buldgen, G., Meynet, G., Salmon, S. J. A. J., and Deheuvels, S. (2019b). Asteroseismology of evolved stars to constrain the internal transport of angular momentum. II. Test of a revised prescription for transport by the Tayler instability. *Astron. Astrophys.* 631:L6. doi: 10.1051/0004-6361/201936348

Eggenberger, P., Lagarde, N., Miglio, A., Montalbán, J., Ekström, S., Georgy, C., et al. (2017). Constraining the efficiency of angular momentum transport with

asteroseismology of red giants: the effect of stellar mass. *Astron. Astrophys.* 599:A18. doi: 10.1051/0004-6361/201629459

Eggenberger, P., Montalbán, J., and Miglio, A. (2012). Angular momentum transport in stellar interiors constrained by rotational splittings of mixed modes in red giants. *Astron. Astrophys.* 544:L4. doi: 10.1051/0004-6361/201219729

Eggleton, P. P. (1983). Approximations to the radii of Roche lobes. *Astrophys. J.* 268:368.

Eichler, M., Nakamura, K., Takiwaki, T., Kuroda, T., Kotake, K., Hempel, M., et al. (2018). Nucleosynthesis in 2D core-collapse supernovae of 11.2 and 17.0 $M_{\odot}$ progenitors: implications for Mo and Ru production. *J. Phys. G Nucl. Phys.* 45:014001. doi: 10.1088/1361-6471/aa8891

Ekström, S., Georgy, C., Eggenberger, P., Meynet, G., Mowlavi, N., Wyttenbach, A., et al. (2012). Grids of stellar models with rotation. I. Models from 0.8 to 120 $M_{\odot}$ at solar metallicity (Z = 0.014). *Astron. Astrophys.* 537:A146. doi: 10.1051/0004-6361/201117751

Ekström, S., Meynet, G., Chiappini, C., Hirschi, R., and Maeder, A. (2008). Effects of rotation on the evolution of primordial stars. *Astron. Astrophys.* 489:685. doi: 10.1051/0004-6361:200809633

El Eid, M. F., and Langer, N. (1986). The evolution of very luminous stars. II. Pair creation supernova in massive Wolf-Rayet stars. *Astron. Astrophys.* 167:274.

El Eid, M. F., Meyer, B. S., and The, L. S. (2004). Evolution of massive stars up to the end of central oxygen burning. *Astrophys. J.* 611:452. doi: 10.1086/422162

El Eid, M. F., The, L. S., and Meyer, B. S. (2009). Massive stars: input physics and stellar models. *Space Sci. Rev.* 147, 1–29. doi: 10.1007/s11214-009-9517-6

Eldridge, J. J., Izzard, R. G., and Tout, C. A. (2008). The effect of massive binaries on stellar populations and supernova progenitors. *Mon. Not. R. Astron. Soc.* 384:1109. doi: 10.1111/j.1365-2966.2007.12738.x

Eldridge, J. J., and Stanway, E. R. (2009). Spectral population synthesis including massive binaries. *Mon. Not. R. Astron. Soc.* 400:1019. doi: 10.1111/j.1365-2966.2009.15514.x

Eldridge, J. J., and Stanway, E. R. (2020). Population and spectral synthesis: it doesn't work without binaries. *arXiv preprints* arXiv:2005.11883.

Eldridge, J. J., and Tout, C. A. (2004). The progenitors of core-collapse supernovae. *Mon. Not. R. Astron. Soc.* 353:87. doi: 10.1111/j.1365-2966.2004.08041.x

Farmer, R., Fields, C. E., Petermann, I., Dessart, L., Cantiello, M., Paxton, B., et al. (2016). On variations of pre-supernova model properties. *Astrophys. J. Suppl.* 227:22. doi: 10.3847/1538-4365/227/2/22

Farmer, R., Renzo, M., de Mink, S., Fishbach, M., and Justham, S. (2020). Constraints from gravitational wave detections of binary black hole mergers on the $^{12}C(\alpha,\gamma)^{16}O$ rate. *arXiv preprints* arXiv:2006.06678. doi: 10.3847/2041-8213/abbadd

Farrell, E. J., Groh, J. H., Meynet, G., and Eldridge, J. J. (2020). The uncertain masses of progenitors of core-collapse supernovae and direct-collapse black holes. *Mon. Not. R. Astron. Soc.* 494:L53. doi: 10.1093/mnrasl/slaa035

Foglizzo, T. (2002). Non-radial instabilities of isothermal Bondi accretion with a shock: vortical-acoustic cycle vs. post-shock acceleration. *Astron. Astrophys.* 392:353. doi: 10.1051/0004-6361:20020912

Freytag, B., and Höfner, S. (2008). Three-dimensional simulations of the atmosphere of an AGB star. *Astron. Astrophys.* 483:571. doi: 10.1051/0004-6361:20078096

Freytag, B., Ludwig, H. G., and Steffen, M. (1996). Hydrodynamical models of stellar convection. The role of overshoot in DA white dwarfs, A-type stars, and the Sun. *Astron. Astrophys.* 313:497.

Frischknecht, U., Hirschi, R., Pignatari, M., Maeder, A., Meynet, G., Chiappini, C., et al. (2016). s-process production in rotating massive stars at solar and low metallicities. *Mon. Not. R. Astron. Soc.* 456:1803. doi: 10.1093/mnras/stv2723

Frischknecht, U., Hirschi, R., and Thielemann, F.-K. (2012). Non-standard s-process in low metallicity massive rotating stars. *Astron. Astrophys.* 538:L2. doi: 10.1051/0004-6361/201117794

Fruet, G., Courtin, S., Heine, M., Jenkins, D. G., Adsley, P., Brown, A., et al. (2020). Advances in the direct study of carbon burning in massive stars. *Phys. Rev. Lett.* 124:192701. doi: 10.1103/PhysRevLett.124.192701

Fuller, J., Cantiello, M., Lecoanet, D., and Quataert, E. (2015). The spin rate of pre-collapse stellar cores: wave-driven angular momentum transport in massive stars. *Astrophys. J.* 810:101. doi: 10.1088/0004-637X/810/2/101

Fuller, J., Lecoanet, D., Cantiello, M., and Brown, B. (2014). Angular momentum transport via internal gravity waves in evolving stars. *Astrophys. J.* 796:17. doi: 10.1088/0004-637X/796/1/17

Fuller, J., Piro, A. L., and Jermyn, A. S. (2019). Slowing the spins of stellar cores. *Mon. Not. R. Astron. Soc.* 485:3661. doi: 10.1093/mnras/stz514

Gabriel, M., and Belkacem, K. (2018). A non-local mixing-length theory able to compute core overshooting. *Astron. Astrophys.* 612:A21. doi: 10.1051/0004-6361/201731835

Gabriel, M., Noels, A., Montalbán, J., and Miglio, A. (2014). Proper use of Schwarzschild Ledoux criteria in stellar evolution computations. *Astron. Astrophys.* 569:A63. doi: 10.1051/0004-6361/201423442

Garcia, J. R., and Mellado, J. P. (2014). The two-Layer structure of the entrainment zone in the convective boundary layer. *J. Atmos. Sci.* 71:1935. doi: 10.1175/JAS-D-13-0148.1

García-Berro, E., Ritossa, C., and Iben, Icko, J. (1997). On the evolution of stars that form electron-degenerate cores processed by carbon burning. III. The inward propagation of a carbon-burning flame and other properties of a 9 $M_{\odot}$ model star. *Astrophys. J.* 485:765.

Gasques, L. R., Brown, E. F., Chieffi, A., Jiang, C. L., Limongi, M., Rolfs, C., et al. (2007). Implications of low-energy fusion hindrance on stellar burning and nucleosynthesis. *Phys. Rev. C* 76:035802. doi: 10.1103/PhysRevC.76.035802

Georgy, C. (2012). Yellow supergiants as supernova progenitors: an indication of strong mass loss for red supergiants? *Astron. Astrophys.* 538:L8. doi: 10.1051/0004-6361/201118372

Georgy, C., Ekström, S., Eggenberger, P., Meynet, G., Haemmerlé, L., Maeder, A., et al. (2013a). Grids of stellar models with rotation. III. Models from 0.8 to 120 $M_{\odot}$ at a metallicity Z = 0.002. *Astron. Astrophys.* 558:A103. doi: 10.1051/0004-6361/201322178

Georgy, C., Ekström, S., Granada, A., Meynet, G., Mowlavi, N., Eggenberger, P., et al. (2013b). Populations of rotating stars. I. Models from 1.7 to 15 $M_{\odot}$ at $Z = 0.014$, 0.006, and 0.002 with $\Omega/\Omega_{\rm crit}$ between 0 and 1. *Astron. Astrophys.* 553:A24. doi: 10.1051/0004-6361/201220558

Georgy, C., Saio, H., and Meynet, G. (2014). The puzzle of the CNO abundances of α Cygni variables resolved by the Ledoux criterion. *Mon. Not. R. Astron. Soc.* 439:L6. doi: 10.1093/mnrasl/slt165

Gräfener, G., Vink, J. S., de Koter, A., and Langer, N. (2011). The Eddington factor as the key to understand the winds of the most massive stars. Evidence for a Γ-dependence of Wolf-Rayet type mass loss. *Astron. Astrophys.* 535:A56. doi: 10.1051/0004-6361/201116701

Granada, A., Ekström, S., Georgy, C., Krtička, J., Owocki, S., Meynet, G., et al. (2013). Populations of rotating stars. II. Rapid rotators and their link to Be-type stars. *Astron. Astrophys.* 553:A25. doi: 10.1051/0004-6361/201220559

Gratton, R., Sneden, C., and Carretta, E. (2004). Abundance variations within globular clusters. *Annu. Rev. Astron. Astrophys.* 42:385. doi: 10.1146/annurev.astro.42.053102.133945

Groh, J. H., Ekström, S., Georgy, C., Meynet, G., Choplin, A., Eggenberger, P., et al. (2019). Grids of stellar models with rotation. IV. Models from 1.7 to 120 $M_{\odot}$ at a metallicity Z = 0.0004. *Astron. Astrophys.* 627:A24. doi: 10.1051/0004-6361/201833720

Harris, J. A., Hix, W. R., Chertkow, M. A., Lee, C. T., Lentz, E. J., and Messer, O. E. B. (2017). Implications for post-processing nucleosynthesis of core-collapse supernova models with Lagrangian particles. *Astrophys. J.* 843:2. doi: 10.3847/1538-4357/aa76de

Heger, A., Fryer, C. L., Woosley, S. E., Langer, N., and Hartmann, D. H. (2003). How massive single stars end their life. *Astrophys. J.* 591:288. doi: 10.1086/375341

Heger, A., and Woosley, S. E. (2010). Nucleosynthesis and evolution of massive metal-free stars. *Astrophys. J.* 724, 341–373. doi: 10.1088/0004-637X/724/1/341

Hekker, S., Angelou, G. C., Elsworth, Y., and Basu, S. (2020). Mirror principle and the red-giant bump: the battle of entropy in low-mass stars. *Mon. Not. R. Astron. Soc.* 492:5940. doi: 10.1093/mnras/staa176

Herwig, F. (2000). The evolution of AGB stars with convective overshoot. *Astron. Astrophys.* 360:952.

Herwig, F., Bloecker, T., Schoenberner, D., and El Eid, M. (1997). Stellar evolution of low and intermediate-mass stars. IV. Hydrodynamically-based overshoot and nucleosynthesis in AGB stars. *Astron. Astrophys.* 324:L81.

Herwig, F., Freytag, B., Hueckstaedt, R. M., and Timmes, F. X. (2006). Hydrodynamic simulations of He shell flash convection. *Astrophys. J.* 642, 1057–1074. doi: 10.1086/501119

Higl, J., Müller, E., and Weiss, A. (2021). Calibrating core overshooting parameters with two-dimensional hydrodynamical simulations. *Astron. Astrophys.* 646:A133. doi: 10.1051/0004-6361/202039532

Hirschi, R. (2007). Very low-metallicity massive stars: pre-SN evolution models and primary nitrogen production. *Astron. Astrophys.* 461:571. doi: 10.1051/0004-6361:20065356

Hirschi, R., Meynet, G., and Maeder, A. (2004). Stellar evolution with rotation. XII. Pre-supernova models. *Astron. Astrophys.* 425:649. doi: 10.1051/0004-6361:20041095

Holt, R. J., Filippone, B. W., and Pieper, S. C. (2019). Impact of $^{16}O(\gamma, \alpha)^{12}C$ measurements on the $^{12}C(\alpha, \gamma)^{16}O$ astrophysical reaction rate. *Phys. Rev. C* 99(5):055802. doi: 10.1103/PhysRevC.99.055802

Hoyle, F. (1954). On nuclear reactions occuring in very hot STARS.I. The synthesis of elements from carbon to nickel. *Astrophys. J. Suppl.* 1:121.

Hunter, I., Brott, I., Langer, N., Lennon, D. J., Dufton, P. L., Howarth, I. D., et al. (2009). The VLT-FLAMES survey of massive stars: constraints on stellar evolution from the chemical compositions of rapidly rotating Galactic and Magellanic Cloud B-type stars. *Astron. Astrophys.* 496:841. doi: 10.1051/0004-6361/200809925

Iliadis, C. (2007). *Nuclear Physics of Stars*. Wiley-VCH.

Janka, H.-T. (2012). Explosion mechanisms of core-collapse supernovae. *Annu. Rev. Nucl. Part. Sci.* 62:407. doi: 10.1146/annurev-nucl-102711-094901

Jones, S., Andrassy, R., Sandalski, S., Davis, A., Woodward, P., and Herwig, F. (2017). Idealized hydrodynamic simulations of turbulent oxygen-burning shell convection in 4π geometry. *Mon. Not. R. Astron. Soc.* 465, 2991–3010. doi: 10.1093/mnras/stw2783

Jones, S., Hirschi, R., Nomoto, K., Fischer, T., Timmes, F. X., Herwig, F., et al. (2013). Advanced burning stages and fate of 8-10 $M_{\odot}$ stars. *Astrophys. J.* 772:150. doi: 10.1088/0004-637X/772/2/150

Jones, S., Hirschi, R., Pignatari, M., Heger, A., Georgy, C., Nishimura, N., et al. (2015). Code dependencies of pre-supernova evolution and nucleosynthesis in massive stars: evolution to the end of core helium burning. *Mon. Not. R. Astron. Soc.* 447, 3115–3129. doi: 10.1093/mnras/stu2657

Kaeppeler, F., Wiescher, M., Giesen, U., Goerres, J., Baraffe, I., El Eid, M., et al. (1994). Reaction rates for 18O(alpha, gamma) 22Ne, 22Ne(alpha, gamma) 26Mg, and 22Ne(alpha, n) 25Mg in stellar helium burning and s-Process nucleosynthesis in massive stars. *Astrophys. J.* 437:396.

Käppeler, F., Gallino, R., Bisterzo, S., and Aoki, W. (2011). The s process: nuclear physics, stellar models, and observations. *Rev. Mod. Phys.* 83, 157–194. doi: 10.1103/RevModPhys.83.157

Karakas, A. I., Lugaro, M. A., Wiescher, M., Görres, J., and Ugalde, C. (2006). The uncertainties in the $^{22}Ne+\alpha$-capture reaction rates and the production of the heavy magnesium isotopes in asymptotic giant branch stars of intermediate mass. *Astrophys. J.* 643:471. doi: 10.1086/502793

Katsuma, M. (2008). Low-energy cross sections in the $^{12}C(\alpha,\gamma)^{16}O$ reaction. *Phys. Rev. C* 78:034606. doi: 10.1103/PhysRevC.78.034606

Kazeroni, R., Guilet, J., and Foglizzo, T. (2017). Are pulsars spun up or down by SASI spiral modes? *Mon. Not. R. Astron. Soc.* 471, 914–925. doi: 10.1093/mnras/stx1566

Kee, N. D., Sundqvist, J. O., Decin, L., de Koter, A., and Sana, H. (2021). Analytic, dust-independent mass-loss rates for red supergiant winds initiated by turbulent pressure.*Astron. Astrophys.* 646:A180. doi: 10.1051/0004-6361/202039224

Kippenhahn, R., Ruschenplatt, G., and Thomas, H. C. (1980). The time scale of thermohaline mixing in stars. *Astron. Astrophys.* 91:175.

Kochanek, C. S. (2014). Failed supernovae explain the compact remnant mass function. *Astrophys. J.* 785:28. doi: 10.1088/0004-637X/785/1/28

Krtička, J., Owocki, S. P., and Meynet, G. (2011). Mass and angular momentum loss via decretion disks. *Astron. Astrophys.* 527:A84. doi: 10.1051/0004-6361/201015951

Kuhfuss, R. (1986). A model for time-dependent turbulent convection. *Astron. Astrophys.* 160, 116–120.

Kunz, R., Fey, M., Jaeger, M., Mayer, A., Hammer, J. W., Staudt, G., et al. (2002). Astrophysical reaction rate of $^{12}C(\alpha, \gamma)^{16}O$. *Astrophys. J.* 567:643. doi: 10.1086/338384

Kuroda, T., Arcones, A., Takiwaki, T., and Kotake, K. (2020). Magnetorotational explosion of a massive star supported by neutrino heating in general relativistic three-dimensional simulations. *Astrophys. J.* 896:102. doi: 10.3847/1538-4357/ab9308

Labadie-Bartz, J., Handler, G., Pepper, J., Balona, L., Cat, P. D., Stevens, D. J., et al. (2020). New beta cephei stars from the KELT project. *Astron. J.* 160:32. doi: 10.3847/1538-3881/ab952c

Langer, N. (1986). Non-local treatment of convection and overshooting from stellar convective cores. *Astron. Astrophys.* 164:45.

Langer, N. (1992). Helium enrichment in massive early type stars. *Astron. Astrophys.* 265, L17–L20.

Langer, N. (2012). Presupernova evolution of massive single and binary stars. *Annu. Rev. Astron. Astrophys.* 50:107. doi: 10.1146/annurev-astro-081811-125534

Lecoanet, D., Cantiello, M., Quataert, E., Couston, L.-A., Burns, K. J., Pope, B. J. S., et al. (2019). Low-frequency variability in massive stars: core generation or surface phenomenon? *Astrophys. J. Lett.* 886:L15. doi: 10.3847/2041-8213/ab5446

Ledoux, P. (1947). Stellar models with convection and with discontinuity of the mean molecular weight. *Astrophys. J.* 105:305. doi: 10.1086/144905

Leung, S.-C., Nomoto, K., and Blinnikov, S. (2019). Pulsational pair-instability Supernovae. I. Pre-collapse evolution and pulsational mass ejection. *Astrophys. J.* 887:72. doi: 10.3847/1538-4357/ab4fe5

Levesque, E. M., and Massey, P. (2020). Betelgeuse just is not that cool: effective temperature alone cannot explain the recent dimming of betelgeuse. *Astrophys. J. Lett.* 891:L37. doi: 10.3847/2041-8213/ab7935

Limongi, M., and Chieffi, A. (2003). Evolution, explosion, and nucleosynthesis of core-collapse supernovae. *Astrophys. J.* 592:404. doi: 10.1086/375703

Limongi, M., and Chieffi, A. (2012). Presupernova evolution and explosive nucleosynthesis of zero metal massive stars. *Astrophys. J. Suppl.* 199:38. doi: 10.1088/0067-0049/199/2/38

Livio, M. (1989). Common envelope evolution of binary stars. *Space Sci. Rev.* 50:299.

Lucy, L. B., and Solomon, P. M. (1970). Mass loss by hot stars. *Astrophys. J.* 159:879.

Maeder, A. (1975). Stellar evolution III: the overshooting from convective cores. *Astron. Astrophys.* 40:303.

Maeder, A. (1987). Evidences for a bifurcation in massive star evolution. The ON-blue stragglers. *Astron. Astrophys.* 178:159.

Maeder, A. and Mermilliod, J. C. (1981). The extent of mixing in stellar interiors: evolutionary models and tests based on the HR diagrams of 34 open clusters. *Astron. Astrophys.*, 93:136.

Maeder, A., and Meynet, G. (2001). Stellar evolution with rotation. VII. Low metallicity models and the blue to red supergiant ratio in the SMC. *Astron. Astrophys.* 373:555. doi: 10.1051/0004-6361:20010596

Maeder, A., Meynet, G., Ekström, S., and Georgy, C. (2009). Modeling massive stars with rotation: the case of Nitrogen enrichments. *Coast* 158:72. doi: 10.1553/cia158

Maeder, A., Przybilla, N., Nieva, M.-F., Georgy, C., Meynet, G., Ekström, S., et al. (2014). Evolution of surface CNO abundances in massive stars. *Astron. Astrophys.* 565:A39. doi: 10.1051/0004-6361/201220602

Maeder, A., and Zahn, J.-P. (1998). Stellar evolution with rotation. III. Meridional circulation with MU -gradients and non-stationarity. *Astron. Astrophys.* 334:1000.

Magic, Z., Collet, R., Asplund, M., Trampedach, R., Hayek, W., Chiavassa, A., et al. (2013). The Stagger-grid: a grid of 3D stellar atmosphere models. I. Methods and general properties. *Astron. Astrophys.* 557:A26. doi: 10.1051/0004-6361/201321274

Magic, Z., Weiss, A., and Asplund, M. (2015). The Stagger-grid: a grid of 3D stellar atmosphere models. III. The relation to mixing length convection theory. *Astron. Astrophys.* 573:A89. doi: 10.1051/0004-6361/201423760

Marchant, P., Renzo, M., Farmer, R., Pappas, K. M. W., Taam, R. E., de Mink, S. E., et al. (2019). Pulsational pair-instability supernovae in very Close binaries. *Astrophys. J.* 882:36. doi: 10.3847/1538-4357/ab3426

Marcolino, W. L. F., Bouret, J. C., Martins, F., Hillier, D. J., Lanz, T., and Escolano, C. (2009). Analysis of Galactic late-type O dwarfs: more constraints on the weak wind problem. *Astron. Astrophys.* 498:837. doi: 10.1051/0004-6361/200811289

Marek, A., and Janka, H.-T. (2009). Delayed neutrino-driven supernova explosions aided by the standing accretion-shock instability. *Astrophys. J.* 694:664. doi: 10.1088/0004-637X/694/1/664

Markova, N., Puls, J., and Langer, N. (2018). Spectroscopic and physical parameters of Galactic O-type stars. III. Mass discrepancy and rotational mixing. *Astron. Astrophys.* 613:A12. doi: 10.1051/0004-6361/201731361

Martins, F., Hervé, A., Bouret, J. C., Marcolino, W., Wade, G. A., Neiner, C., et al. (2015a). The MiMeS survey of magnetism in massive stars: CNO surface abundances of Galactic O stars. *Astron. Astrophys.* 575:A34. doi: 10.1051/0004-6361/201425173

Martins, F., and Palacios, A. (2013). A comparison of evolutionary tracks for single Galactic massive stars. *Astron. Astrophys.* 560:A16. doi: 10.1051/0004-6361/201322480

Martins, F., Schaerer, D., Hillier, D. J., Meynadier, F., Heydari-Malayeri, M., and Walborn, N. R. (2005). On stars with weak winds: the Galactic case. *Astron. Astrophys.* 441:735. doi: 10.1051/0004-6361:20052927

Martins, F., Simón-Díaz, S., Barbá, R. H., Gamen, R. C., and Ekström, S. (2017). A study of the effect of rotational mixing on massive stars evolution: surface abundances of Galactic O7-8 giant stars. *Astron. Astrophys.* 599:A30. doi: 10.1051/0004-6361/201629548

Martins, F., Simón-Díaz, S., Palacios, A., Howarth, I., Georgy, C., Walborn, N. R., et al. (2015b). Surface abundances of ON stars. *Astron. Astrophys.* 578:A109. doi: 10.1051/0004-6361/201526130

Maund, J. R., and Smartt, S. J. (2005). Hubble Space Telescope imaging of the progenitor sites of six nearby core-collapse supernovae. *Mon. Not. R. Astron. Soc.* 360:288. doi: 10.1111/j.1365-2966.2005.09034.x

Maund, J. R., Smartt, S. J., and Schweizer, F. (2005). Luminosity and mass limits for the progenitor of the type Ic supernova 2004gt in NGC 4038. *Astrophys. J. Lett.* 630:L33. doi: 10.1086/491620

Mauron, N., and Josselin, E. (2011). The mass-loss rates of red supergiants and the de Jager prescription. *Astron. Astrophys.* 526:A156. doi: 10.1051/0004-6361/201013993

Meakin, C. A., and Arnett, D. (2007). Turbulent convection in stellar interiors. I. Hydrodynamic simulation. *Astrophys. J.* 667:448. doi: 10.1086/520318

Meynet, G., Chomienne, V., Ekström, S., Georgy, C., Granada, A., Groh, J., et al. (2015). Impact of mass-loss on the evolution and pre-supernova properties of red supergiants. *Astron. Astrophys.* 575:A60. doi: 10.1051/0004-6361/201424671

Meynet, G., Eggenberger, P., and Maeder, A. (2011). Massive star models with magnetic braking. *Astron. Astrophys.* 525:L11. doi: 10.1051/0004-6361/201016017

Meynet, G., Ekström, S., Maeder, A., Eggenberger, P., Saio, H., Chomienne, V., et al. (2013). "Models of rotating massive stars: impacts of various prescriptions," in *Studying Stellar Rotation and Convection*, volume 865 of *Lecture Notes in Physics*, eds M. Goupil, K. Belkacem, C. Neiner, F. Lignières, and J. J. Green (Berlin; Heidelberg), 3.

Meynet, G., and Maeder, A. (2002a). Stellar evolution with rotation. VIII. Models at $Z = 10^{-5}$ and CNO yields for early galactic evolution. *Astron. Astrophys.* 390:561. doi: 10.1051/0004-6361:20020755

Meynet, G., and Maeder, A. (2002b). The origin of primary nitrogen in galaxies. *Astron. Astrophys.* 381:L25. doi: 10.1051/0004-6361:20011554

Miglio, A., Girardi, L., Grundahl, F., Mosser, B., Bastian, N., Bragaglia, A., et al. (2019). HAYDN – High-precision AsteroseismologY of DeNse stellar fields (ESA Voyage 2050 White Paper). *arXiv preprints* arXiv:1908.05129.

Moe, M., and Di Stefano, R. (2017). Mind your Ps and Qs: the interrelation between period (P) and mass-ratio (Q) distributions of binary stars. *Astrophys. J. Suppl. Ser.* 230:15. doi: 10.3847/1538-4365/aa6fb6

Mokiem, M. R., de Koter, A., Vink, J. S., Puls, J., Evans, C. J., Smartt, S. J., et al. (2007). The empirical metallicity dependence of the mass-loss rate of O- and early B-type stars. *Astron. Astrophys.* 473:603. doi: 10.1051/0004-6361:20077545

Moravveji, E., Aerts, C., Pápics, P. I., Triana, S. A., and Vandoren, B. (2015). Tight asteroseismic constraints on core overshooting and diffusive mixing in the slowly rotating pulsating B8.3V star KIC 10526294. *Astron. Astrophys.* 580:A27. doi: 10.1051/0004-6361/201425290

Muijres, L. E., Vink, J. S., de Koter, A., Müller, P. E., and Langer, N. (2012). Predictions for mass-loss rates and terminal wind velocities of massive O-type stars. *Astron. Astrophys.* 537:A37. doi: 10.1051/0004-6361/201015818

Müller, B., Viallet, M., Heger, A., and Janka, H.-T. (2016). The last minutes of oxygen shell burning in a massive star. *Astrophys. J.* 833:124. doi: 10.3847/1538-4357/833/1/124

Müller, E., and Janka, H. T. (1995). "Convection in type-II supernovae:the first second," in *Seventeeth Texas Symposium on Relativistic Astrophysics and Cosmology*, Vol. 759, eds H. Böhringer, G. E. Morfill, and J. E. Trümper, 368.

Murphy, L. J., Groh, J. H., Ekström, S., Meynet, G., Pezzotti, C., Georgy, C., et al. (2021). Grids of stellar models with rotation - V. Models from 1.7 to 120 $M_{\odot}$ at zero metallicity. *Mon. Not. R. Astron. Soc.* 501:2745. doi: 10.1093/mnras/staa3803

Najarro, F., Hanson, M. M., and Puls, J. (2011). L-band spectroscopy of Galactic OB-stars. *Astron. Astrophys.* 535:A32. doi: 10.1051/0004-6361/201016003

Nakamura, K., Kuroda, T., Takiwaki, T., and Kotake, K. (2014). Impacts of rotation on three-dimensional hydrodynamics of core-collapse supernovae. *Astrophys. J.* 793:45. doi: 10.1088/0004-637X/793/1/45

Nomoto, K. (1984). "Type-II supernovae from 8-10 solar mass progenitors," in *Stellar Nucleosynthesis. Proceedings of the 3rd. Workshop of the Advanced School of Astronomy of the Ettore Majorana Centre for Scientific Culture*, eds C. Chiosi and A. Renzini (Dordrecht), 239.

Ober, W. W., El Eid, M. F., and Fricke, K. J. (1983). Evolution of massive pregalactic stars - Part Two - nucleosynthesis in pair creation supernovae and pregalactic enrichment. *Astron. Astrophys.* 119:61.

Ohlmann, S. T., Röpke, F. K., Pakmor, R., and Springel, V. (2016). Hydrodynamic moving-mesh simulations of the common envelope phase in binary stellar systems. *Astrophys. J. Lett.* 816:L9. doi: 10.3847/2041-8205/816/1/L9

Oskinova, L. M. (2016). X-ray diagnostics of massive star winds. *Adv. Space Res.* 58:739. doi: 10.1016/j.asr.2016.06.030

Oskinova, L. M., Hamann, W. R., and Feldmeier, A. (2007). Neglecting the porosity of hot-star winds can lead to underestimating mass-loss rates. *Astron. Astrophys.* 476:1331. doi: 10.1051/0004-6361:20066377

Oskinova, L. M., Todt, H., Ignace, R., Brown, J. C., Cassinelli, J. P., and Hamann, W. R. (2011). Early magnetic B-type stars: X-ray emission and wind properties. *Mon. Not. R. Astron. Soc.* 416:1456. doi: 10.1111/j.1365-2966.2011.19143.x

Owocki, S. (2014). Theory of winds from hot, luminous massive stars. *arXiv preprints* arXiv:1409.2084.

Owocki, S. P. (2004). "Rotation and mass ejection: the launching of Be-star disks (invited review)," in *Stellar Rotation*, volume 215 of *IAU Symposium*, eds A. Maeder and P. Eenens (San Francisco, CA), 515.

Paczyński, B., and Sienkiewicz, R. (1972). Evolution of close binaries VIII. Mass exchange on the dynamical time scale. *Acta Astron.* 22:73.

Padmanabhan, T. (2001). *Theoretical Astrophysics, Volume 2: Stars and Stellar Systems*. Cambridge University Press.

Pamyatnykh, A. A., Handler, G., and Dziembowski, W. A. (2004). Asteroseismology of the β Cephei star ν Eridani: interpretation and applications of the oscillation spectrum. *Mon. Not. R. Astron. Soc.* 350:1022. doi: 10.1111/j.1365-2966.2004.07721.x

Passy, J.-C., De Marco, O., Fryer, C. L., Herwig, F., Diehl, S., Oishi, J. S., et al. (2012a). Simulating the common envelope phase of a red giant using smoothed-particle hydrodynamics and uniform-grid codes. *Astrophys. J.* 744:52. doi: 10.1088/0004-637X/744/1/52

Passy, J.-C., Herwig, F., and Paxton, B. (2012b). The response of giant stars to dynamical-timescale mass loss. *Astrophys. J.* 760:90. doi: 10.1088/0004-637X/760/1/90

Pavlovskii, K., Ivanova, N., Belczynski, K., and Van, K. X. (2017). Stability of mass transfer from massive giants: double black hole binary formation and ultraluminous X-ray sources. *Mon. Not. R. Astron. Soc.* 465:2092. doi: 10.1093/mnras/stw2786

Paxton, B., Bildsten, L., Dotter, A., Herwig, F., Lesaffre, P., and Timmes, F. (2011). Modules for experiments in stellar astrophysics (MESA). *Astrophys. J. Suppl.* 192:3. doi: 10.1088/0067-0049/192/1/3

Paxton, B., Cantiello, M., Arras, P., Bildsten, L., Brown, E. F., Dotter, A., et al. (2013). Modules for experiments in stellar astrophysics (MESA): planets, oscillations, rotation, and massive stars. *Astrophys. J. Suppl.* 208:4. doi: 10.1088/0067-0049/208/1/4

Pignatari, M., Gallino, R., Heil, M., Wiescher, M., Käppeler, F., Herwig, F., et al. (2010). The Weak s-process in massive stars and its dependence on the neutron capture cross sections. *Astrophys. J.* 710:1557. doi: 10.1088/0004-637X/710/2/1557

Pignatari, M., Gallino, R., Meynet, G., Hirschi, R., Herwig, F., and Wiescher, M. (2008). The s-process in massive stars at low metallicity: the effect of primary ^{14}N from fast rotating stars. *Astrophys. J. Lett.* 687:L95. doi: 10.1086/593350

Pinçon, C., Belkacem, K., Goupil, M. J., and Marques, J. P. (2017). Can plume-induced internal gravity waves regulate the core rotation of subgiant stars? *Astron. Astrophys.* 605:A31. doi: 10.1051/0004-6361/201730998

Podsiadlowski, P., Rappaport, S., and Pfahl, E. D. (2002). Evolutionary sequences for low- and intermediate-mass X-ray binaries. *Astrophys. J.* 565:1107. doi: 10.1086/324686

Poelarends, A. J. T., Herwig, F., Langer, N., and Heger, A. (2008). The supernova channel of super-AGB stars. *Astrophys. J.* 675:614. doi: 10.1086/520872

Prantzos, N. and Diehl, R. (1996). Radioactive 26Al in the galaxy: observations versus theory. *Phys. Rep.* 267:1.

Prat, V., Guilet, J., Viallet, M., and Müller, E. (2016). Shear mixing in stellar radiative zones. II. Robustness of numerical simulations. *Astron. Astrophys.* 592:A59. doi: 10.1051/0004-6361/201527946

Prat, V., and Lignières, F. (2013). Turbulent transport in radiative zones of stars. *Astron. Astrophys.* 551:L3. doi: 10.1051/0004-6361/201220577

Prat, V., and Lignières, F. (2014). Shear mixing in stellar radiative zones. I. Effect of thermal diffusion and chemical stratification. *Astron. Astrophys.* 566:A110. doi: 10.1051/0004-6361/201423655

Pruet, J., Woosley, S. E., Buras, R., Janka, H. T., and Hoffman, R. D. (2005). Nucleosynthesis in the hot convective bubble in core-collapse supernovae. *Astrophys. J.* 623, 325–336. doi: 10.1086/428281

Raiteri, C. M., Busso, M., Gallino, R., and Picchio, G. (1991a). S-process nucleosynthesis in massive stars and the weak component. II. Carbon burning and galactic enrichment. *Astrophys. J.* 371:665.

Raiteri, C. M., Busso, M., Gallino, R., Picchio, G., and Pulone, L. (1991b). S-Process nucleosynthesis in massive stars and the weak component. I. Evolution and neutron captures in a 25 M_{sun} star. *Astrophys. J.* 367:228.

Rakavy, G., and Shaviv, G. (1967). Instabilities in highly evolved stellar models. *Astrophys. J.* 148:803.

Rauscher, T., Heger, A., Hoffman, R. D., and Woosley, S. E. (2002). Nucleosynthesis in massive stars with improved nuclear and stellar physics. *Astrophys. J.* 576:323. doi: 10.1086/341728

Rauw, G., Hervé, A., Nazé, Y., González-Pérez, J. N., Hempelmann, A., Mittag, M., et al. (2015). Simultaneous X-ray and optical spectroscopy of the Oef supergiant λ Cephei. *Astron. Astrophys.* 580:A59. doi: 10.1051/0004-6361/201526057

Ricker, P. M., and Taam, R. E. (2008). The interaction of stellar objects within a common envelope. *Astrophys. J. Lett.* 672:L41. doi: 10.1086/526343

Ricker, P. M., and Taam, R. E. (2012). An AMR study of the common-envelope phase of binary evolution. *Astrophys. J.* 746:74. doi: 10.1088/0004-637X/746/1/74

Ritter, C., Andrassy, R., Côté, B., Herwig, F., Woodward, P. R., Pignatari, M., et al. (2018a). Convective-reactive nucleosynthesis of K, Sc, Cl and p-process isotopes in O-C shell mergers. *Mon. Not. R. Astron. Soc.* 474:L1. doi: 10.1093/mnrasl/slx126

Ritter, C., Herwig, F., Jones, S., Pignatari, M., Fryer, C., and Hirschi, R. (2018b). NuGrid stellar data set - II. Stellar yields from H to Bi for stellar models with M_{ZAMS} = 1-25 $M_{\odot}$ and Z = 0.0001-0.02. *Mon. Not. R. Astron. Soc.* 480:538. doi: 10.1093/mnras/sty1729

Rogers, T. M., Lin, D. N. C., McElwaine, J. N., and Lau, H. H. B. (2013). Internal gravity waves in massive stars: angular momentum transport. *Astrophys. J.* 772:21. doi: 10.1088/0004-637X/772/1/21

Roxburgh, I. W. (1978). Convection and stellar structure. *Astron. Astrophys.* 65:281.

Sana, H., de Mink, S. E., de Koter, A., Langer, N., Evans, C. J., Gieles, M., et al. (2012). Binary interaction dominates the evolution of massive stars. *Science*, 337:444. doi: 10.1126/science.1223344

Sana, H., Gosset, E., and Evans, C. J. (2009). The massive star binary fraction in young open clusters - II. NGC6611 (Eagle Nebula). *Mon. Not. R. Astron. Soc.* 400:1479. doi: 10.1111/j.1365-2966.2009.15545.x

Sana, H., Gosset, E., Nazé, Y., Rauw, G., and Linder, N. (2008). The massive star binary fraction in young open clusters - I. NGC 6231 revisited. *Mon. Not. R. Astron. Soc.* 386:447. doi: 10.1111/j.1365-2966.2008.13037.x

Scheck, L., Plewa, T., Janka, H. T., Kifonidis, K., and Müller, E. (2004). Pulsar recoil by large-scale anisotropies in supernova explosions. *Phys. Rev. Lett.* 92:011103. doi: 10.1103/PhysRevLett.92.011103

Schneider, F. R. N., Ohlmann, S. T., Podsiadlowski, P., Röpke, F. K., Balbus, S. A., Pakmor, R., et al. (2019). Stellar mergers as the origin of magnetic massive stars. *Nature* 574, 211. doi: 10.1038/s41586-019-1621-5

Schneider, F. R. N., Ohlmann, S. T., Podsiadlowski, P., Röpke, F. K., Balbus, S. A., and Pakmor, R. (2020). Long-term evolution of a magnetic massive merger product. *Mon. Not. R. Astron. Soc.* 495, 2796–2812. doi: 10.1093/mnras/staa1326

Schwarzschild, M. (1958). *Structure and Evolution of the Stars*. Princeton University Press.

Scott, L. J. A., Hirschi, R., Georgy, C., Arnett, W. D., Meakin, C., Kaiser, E. A., et al. (2021). Convective core entrainment in 1D main sequence stellar models. *Mon. Not. R. Astron. Soc.* arXiv:2103.06196. doi: 10.1093/mnras/stab752

Secchi, A. (1866). Schreiben des Herrn Prof. Secchi, Directors der Sternwarte des Collegio Romano, an den Herausgeber. *Astron. Nachrichten* 68:63.

Shaviv, G., and Salpeter, E. E. (1973). Convective overshooting in stellar interior models. *Astrophys. J.* 184, 191–200.

Siess, L. (2007). Evolution of massive AGB stars. II. model properties at non-solar metallicity and the fate of Super-AGB stars. *Astron. Astrophys.* 476:893. doi: 10.1051/0004-6361:20078132

Siess, L. (2008). "Structural and chemical evolution of low- and intermediate-mass stars„" in *Stellar Nucleosynthesis 50 Years After B^2FH*, Vol. 32 of *EAS Publications Series*, eds C. Charbonnel and J.-P. Zahn, 131.

Siess, L., Forestini, M., and Dougados, C. (1997). Synthetic Hertzsprung-Russell diagrams of open clusters. *Astron. Astrophys.* 324:556.

Siess, L., Goriely, S., and Langer, N. (2004). Nucleosynthesis of s-elements in rotating AGB stars. *Astron. Astrophys.* 415:1089. doi: 10.1051/0004-6361:20034281

Siess, L., Izzard, R. G., Davis, P. J., and Deschamps, R. (2013). BINSTAR: a new binary stellar evolution code. Tidal interactions. *Astron. Astrophys.* 550:A100. doi: 10.1051/0004-6361/201220327

Siess, L., Livio, M., and Lattanzio, J. (2002). Structure, evolution, and nucleosynthesis of primordial stars. *Astrophys. J.* 570:329. doi: 10.1086/339733

Smartt, S. J., Eldridge, J. J., Crockett, R. M., and Maund, J. R. (2009). The death of massive stars - I. Observational constraints on the progenitors of Type II-P supernovae. *Mon. Not. R. Astron. Soc.* 395:1409. doi: 10.1111/j.1365-2966.2009.14506.x

Song, H. F., Meynet, G., Maeder, A., Ekström, S., and Eggenberger, P. (2016). Massive star evolution in close binaries. Conditions for homogeneous chemical evolution. *Astron. Astrophys.* 585:A120. doi: 10.1051/0004-6361/201526074

Song, N., Alexeeva, S., Sitnova, T., Wang, L., Grupp, F., and Zhao, G. (2020). Impact of the convective mixing-length parameter α on stellar metallicity. *Astron. Astrophys.* 635:A176. doi: 10.1051/0004-6361/201937110

Spada, F., Gellert, M., Arlt, R., and Deheuvels, S. (2016). Angular momentum transport efficiency in post-main sequence low-mass stars. *Astron. Astrophys.* 589:A23. doi: 10.1051/0004-6361/201527591

Staritsin, E. I. (2013). Turbulent entrainment at the boundaries of the convective cores of main-sequence stars. *Astron. Rep.* 57, 380–390. doi: 10.1134/S1063772913050089

Struve, O. (1931). On the origin of bright lines in spectra of stars of class B. *Astrophys. J.* 73:94.

Sugimoto, D., and Fujimoto, M. Y. (2000). Why stars become red giants. *Astrophys. J.* 538:837. doi: 10.1086/309150

Suijs, M. P. L., Langer, N., Poelarends, A.-J., Yoon, S.-C., Heger, A., and Herwig, F. (2008). White dwarf spins from low-mass stellar evolution models. *Astron. Astrophys.* 481:L87. doi: 10.1051/0004-6361:200809411

Summa, A., Janka, H.-T., Melson, T., and Marek, A. (2018). Rotation-supported neutrino-driven supernova explosions in three dimensions and the critical luminosity condition. *Astrophys. J.* 852:28. doi: 10.3847/1538-4357/aa9ce8

Sundqvist, J. O., Björklund, R., Puls, J., and Najarro, F. (2019). New predictions for radiation-driven, steady-state mass-loss and wind-momentum from hot,

massive stars. I. Method and first results. *Astron. Astrophys.* 632:A126. doi: 10.1051/0004-6361/201936580

Sundqvist, J. O., Puls, J., and Owocki, S. P. (2014). Mass loss from inhomogeneous hot star winds. III. An effective-opacity formalism for line radiative transfer in accelerating, clumped two-component media, and first results on theory and diagnostics. *Astron. Astrophys.* 568:A59. doi: 10.1051/0004-6361/201423570

Šurlan, B., Hamann, W. R., Aret, A., Kubát, J., Oskinova, L. M., and Torres, A. F. (2013). Macroclumping as solution of the discrepancy between Hα and P v mass loss diagnostics for O-type stars. *Astron. Astrophys.* 559:A130. doi: 10.1051/0004-6361/201322390

Suzuki, A., and Maeda, K. (2018). Constraining the final fates of massive stars by oxygen and iron enrichment history in the galaxy. *Astrophys. J.* 852:101. doi: 10.3847/1538-4357/aaa024

Sweet, P. A. (1950). The importance of rotation in stellar evolution. *Mon. Not. R. Astron. Soc.* 110:548.

Szécsi, D., Langer, N., Yoon, S.-C., Sanyal, D., de Mink, S., Evans, C. J., et al. (2015). Low-metallicity massive single stars with rotation. Evolutionary models applicable to I Zwicky 18. *Astron. Astrophys.* 581:A15. doi: 10.1051/0004-6361/201526617

Takahashi, K. (2018). The low detection rate of pair-instability supernovae and the effect of the core carbon fraction. *Astrophys. J.* 863:153. doi: 10.3847/1538-4357/aad2d2

Talwar, R., Adachi, T., Berg, G. P. A., Bin, L., Bisterzo, S., Couder, M., et al. (2016). Probing astrophysically important states in the ^{26}Mg nucleus to study neutron sources for the s process. *Phys. Rev. C* 93:055803. doi: 10.1103/PhysRevC.93.055803

Tan, W. P., Boeltzig, A., Dulal, C., deBoer, R. J., Frentz, B., Henderson, S., et al. (2020). New measurement of C 12 +C 12 fusion reaction at astrophysical energies. *Phys. Rev. Lett.* 124:192702. doi: 10.1103/PhysRevLett.124.192702

The, L.-S., El Eid, M. F., and Meyer, B. S. (2007). s-Process nucleosynthesis in advanced burning phases of massive stars. *Astrophys. J.* 655:1058. doi: 10.1086/509753

Tkachenko, A., Pavlovski, K., Johnston, C., Pedersen, M. G., Michielsen, M., Bowman, D. M., et al. (2020). The mass discrepancy in intermediate- and high-mass eclipsing binaries: The need for higher convective core masses. *Astron. Astrophys.* 637:A60. doi: 10.1051/0004-6361/202037452

Toonen, S., Hamers, A., and Portegies Zwart, S. (2016). The evolution of hierarchical triple star-systems. *Comput. Astrophys. Cosmol.* 3:6. doi: 10.1186/s40668-016-0019-0

Triana, S. A., Moravveji, E., Pápics, P. I., Aerts, C., Kawaler, S. D., and Christensen-Dalsgaard, J. (2015). The internal rotation profile of the B-type star KIC 10526294 from frequency inversion of its dipole gravity modes. *Astrophys. J.* 810:16. doi: 10.1088/0004-637X/810/1/16

Truran, J. W., and Cameron, A. G. W. (1971). Evolutionary models of nucleosynthesis in the galaxy. *Astrophys. Space Sci.* 14:179. doi: 10.1007/BF00649203

Tumino, A., Spitaleri, C., La Cognata, M., Cherubini, S., Guardo, G. L., Gulino, M., et al. (2018). An increase in the ^{12}C + ^{12}C fusion rate from resonances at astrophysical energies. *Nature* 557:687. doi: 10.1038/s41586-018-0149-4

Tur, C., Heger, A., and Austin, S. M. (2007). On the sensitivity of massive star nucleosynthesis and evolution to solar abundances and to uncertainties in helium-burning reaction rates. *Astrophys. J.* 671:821. doi: 10.1086/523095

Tur, C., Heger, A., and Austin, S. M. (2009). Dependence of s-process nucleosynthesis in massive stars on triple-alpha and 12C(alpha,gamma)16O reaction rate uncertainties. *Astrophys. J.* 702:1068. doi: 10.1088/0004-637X/702/2/1068

Tur, C., Heger, A., and Austin, S. M. (2010). Production of 26Al, 44Ti, and 60Fe in core-collapse supernovae: sensitivity to the rates of the triple alpha and 12C(alpha,gamma)16O reactions. *Astrophys. J.* 718:357. doi: 10.1088/0004-637X/718/1/357

Umeda, H., and Nomoto, K. (2008). How much 56Ni can be produced in core-collapse supernovae? Evolution and explosions of 30-100 Msol stars. *Astrophys. J.* 673:1014. doi: 10.1086/524767

van Loon, J. T., Cioni, M.-R. L., Zijlstra, A. A., and Loup, C. (2005). An empirical formula for the mass-loss rates of dust-enshrouded red supergiants and oxygen-rich Asymptotic Giant Branch stars. *Astron. Astrophys.* 438:273. doi: 10.1051/0004-6361:20042555

Vanbeveren, D., De Donder, E., Van Bever, J., Van Rensbergen, W., and De Loore, C. (1998a). The WR and O-type star population predicted by massive star evolutionary synthesis. *New Astron.* 3:443. doi: 10.1016/S1384-1076(98)00020-7

Vanbeveren, D., De Loore, C., and Van Rensbergen, W. (1998b). Massive stars. *Astron. Astrophys. Rev.* 9:63.

Viallet, M., Meakin, C., Arnett, D., and Mocák, M. (2013). Turbulent convection in stellar interiors. III. Mean-field analysis and stratification effects. *Astrophys. J.* 769:1. doi: 10.1088/0004-637X/769/1/1

Viallet, M., Meakin, C., Prat, V., and Arnett, D. (2015). Toward a consistent use of overshooting parametrizations in 1D stellar evolution codes. *Astron. Astrophys.* 580:A61. doi: 10.1051/0004-6361/201526294

Vilhu, O., and Kallman, T. R. (2019). Models for weak wind and momentum problems in the winds of hot stars. *arXiv preprints* arXiv:1906.05581.

Vink, J. S. (2006). "Massive star feedback – from the first stars to the present," in *Stellar Evolution at Low Metallicity: Mass Loss, Explosions, Cosmology*, volume 353 of *Astronomical Society of the Pacific Conference Series*, eds H. J. G. L. M. Lamers, N. Langer, T. Nugis, and K. Annuk, 113.

Vink, J. S., Muijres, L. E., Anthonisse, B., de Koter, A., Gräfener, G., and Langer, N. (2011). Wind modelling of very massive stars up to 300 solar masses. *Astron. Astrophys.* 531:A132. doi: 10.1051/0004-6361/201116614

Vitense, E. (1953). Die Wasserstoffkonvektionszone der Sonne. Mit 11 Textabbildungen. *ZA* 32:135.

Vogt, H. (1925). Zum Strahlungsgleichgewicht der Sterne. *Astron. Nachrichten* 223:229.

Wade, G. A., Grunhut, J., Alecian, E., Neiner, C., Aurière, M., Bohlender, D. A., et al. (2014). "The magnetic characteristics of Galactic OB stars from the MiMeS survey of magnetism in massive stars," in *IAU Symposium*, Vol. 302, 265.

Walczak, P., Daszyńska-Daszkiewicz, J., Pigulski, A., Pamyatnykh, A., Moffat, A. F. J., Handler, G., et al. (2019). Seismic modelling of early B-type pulsators observed by BRITE - I. θ Ophiuchi. *Mon. Not. R. Astron. Soc.* 485:3544. doi: 10.1093/mnras/stz639

Wanajo, S., Müller, B., Janka, H.-T., and Heger, A. (2018). Nucleosynthesis in the innermost ejecta of neutrino-driven supernova explosions in two dimensions. *Astrophys. J.* 852:40. doi: 10.3847/1538-4357/aa9d97

Weaver, T. A., and Woosley, S. E. (1980). "Evolution and explosion of massive stars," in *Ninth Texas Symposium on Relativistic Astrophysics*, Vol. 336, 335.

Wongwathanarat, A., Janka, H.-T., and Müller, E. (2010). Hydrodynamical neutron star kicks in three dimensions. *Astrophys. J. Lett.* 725:L106. doi: 10.1088/2041-8205/725/1/L106

Wongwathanarat, A., Janka, H. T., and Müller, E. (2013). Three-dimensional neutrino-driven supernovae: neutron star kicks, spins, and asymmetric ejection of nucleosynthesis products. *Astron. Astrophys.* 552:A126. doi: 10.1051/0004-6361/201220636

Wongwathanarat, A., Müller, E., and Janka, H. T. (2015). Three-dimensional simulations of core-collapse supernovae: from shock revival to shock breakout. *Astron. Astrophys.* 577:A48. doi: 10.1051/0004-6361/201425025

Woods, T. E., and Ivanova, N. (2011). Can we trust models for adiabatic mass loss? *Astrophys. J. Lett.* 739:L48. doi: 10.1088/2041-8205/739/2/L48

Woodward, P. R., Herwig, F., and Lin, P.-H. (2015). Hydrodynamic simulations of H entrainment at the top of He-shell flash convection. *Astrophys. J.* 798:49. doi: 10.1088/0004-637X/798/1/49

Woosley, S., and Janka, T. (2005). The physics of core-collapse supernovae. *Nat. Phys.* 1, 147–154. doi: 10.1038/nphys172

Woosley, S. E. (2017). Pulsational pair-instability supernovae. *Astrophys. J.* 836:244. doi: 10.3847/1538-4357/836/2/244

Woosley, S. E. (2019). The evolution of massive helium stars, including mass loss. *Astrophys. J.* 878:49. doi: 10.3847/1538-4357/ab1b41

Woosley, S. E., Heger, A., and Weaver, T. A. (2002). The evolution and explosion of massive stars. *Rev. Mod. Phys.* 74:1015. doi: 10.1103/RevModPhys.74.1015

Woosley, S. E., and Weaver, T. A. (1995). The evolution and explosion of massive stars. II. Explosive hydrodynamics and nucleosynthesis. *Astrophys. J. Suppl.* 101:181.

Xiong, D. R., Cheng, Q. L., and Deng, L. (1997). Nonlocal time-dependent convection theory. *Astrophys. J. Suppl.* 108:529.

Yadav, N., Müller, B., Janka, H. T., Melson, T., and Heger, A. (2020). Large-scale mixing in a violent oxygen-neon shell merger prior to a core-collapse supernova. *Astrophys. J.* 890:94. doi: 10.3847/1538-4357/ab66bb

Yoon, S., Langer, N., and Norman, C. (2006). Single star progenitors of long gamma-ray bursts. I. Model grids and redshift dependent GRB rate. *Astron. Astrophys.* 460:199. doi: 10.1051/0004-6361:20065912

Yoon, S.-C., Gräfener, G., Vink, J. S., Kozyreva, A., and Izzard, R. G. (2012). On the nature and detectability of Type Ib/c supernova progenitors. *Astron. Astrophys.* 544:L11. doi: 10.1051/0004-6361/201219790

Yoshida, T., Suwa, Y., Umeda, H., Shibata, M., and Takahashi, K. (2017). Explosive nucleosynthesis of ultra-stripped Type Ic supernovae: application to light trans-iron elements. *Mon. Not. R. Astron. Soc.* 471:4275. doi: 10.1093/mnras/stx1738

Zahn, J.-P. (1977). Tidal friction in close binary stars. *Astron. Astrophys.* 57:383–394.

Zahn, J.-P. (1992). Circulation and turbulence in rotating stars. *Astron. Astrophys.* 265:115.

Zahn, J.-P. (2008). "Tidal dissipation in binary systems," in *EAS Publications Series*, Vol. 29, eds M.-J. Goupil and J.-P. Zahn, 67–90.

Conflict of Interest: The author declares that the research was conducted in the absence of any commercial or financial relationships that could be construed as a potential conflict of interest.

frontiers in Astronomy and Space Sciences

REVIEW
published: 13 May 2021
doi: 10.3389/fspas.2021.604872

Theoretical Predictions of Surface Light Element Abundances in Protostellar and Pre-Main Sequence Phase

E. Tognelli[1,2], S. Degl'Innocenti[1,3], P. G. Prada Moroni[1,3], L. Lamia[4,5,6], R. G. Pizzone[5], A. Tumino[5,7], C. Spitaleri[4,5] and A. Chiavassa[8]*

[1]Universitá di Pisa, Dipartimento di Fisica "Enrico Fermi", Pisa, Italy, [2]INAF, Osservatorio Astronomico d'Abruzzo, Teramo, Italy, [3]INFN, Sezione di Pisa, Pisa, Italy, [4]Dipartimento di Fisica e Astronomia, Università di Catania, Catania, Italy, [5]INFN - Laboratori Nazionali del Sud, Catania, Italy, [6]CSFNSM-Centro Siciliano di Fisica Nucleare e Struttura della Materia, Catania, Italy, [7]Dipartimento di Ingegneria e Architettura, Universitá di Enna, Enna, Italy, [8]Université Côte d'Azur, Observatoire de la Côte d'Azur, CNRS, Nice, France

OPEN ACCESS

Edited by:
Paul Denis Stevenson, University of Surrey, United Kingdom

Reviewed by:
Maria Lugaro, Hungarian Academy of Sciences (MTA), Hungary
Oscar Straniero, Astronomical Observatory of Abruzzo (INAF), Italy

***Correspondence:**
E. Tognelli
emanuele.tognelli@for.unipi.it

Specialty section:
This article was submitted to Nuclear Physics, a section of the journal Frontiers in Astronomy and Space Sciences

Received: *10 September 2020*
Accepted: *02 February 2021*
Published: *13 May 2021*

Citation:
Tognelli E, Degl'Innocenti S, Prada Moroni PG, Lamia L, Pizzone RG, Tumino A, Spitaleri C and Chiavassa A (2021) Theoretical Predictions of Surface Light Element Abundances in Protostellar and Pre-Main Sequence Phase. Front. Astron. Space Sci. 8:604872. doi: 10.3389/fspas.2021.604872

Theoretical prediction of surface stellar abundances of light elements–lithium, beryllium, and boron–represents one of the most interesting open problems in astrophysics. As well known, several measurements of ^{7}Li abundances in stellar atmospheres point out a disagreement between predictions and observations in different stellar evolutionary phases, rising doubts about the capability of present stellar models to precisely reproduce stellar envelope characteristics. The problem takes different aspects in the various evolutionary phases; the present analysis is restricted to protostellar and pre-Main Sequence phases. Light elements are burned at relatively low temperatures (T from ≈ 2 to ≈ 5 million degrees) and thus in the early evolutionary stages of a star they are gradually destroyed at different depths of stellar interior mainly by (p, α) burning reactions, in dependence on the stellar mass. Their surface abundances are strongly influenced by the nuclear cross sections, as well as by the extension toward the stellar interior of the convective envelope and by the temperature at its bottom, which depend on the characteristics of the star (mass and chemical composition) as well as on the energy transport in the convective stellar envelope. In recent years, a great effort has been made to improve the precision of light element burning cross sections. However, theoretical predictions surface light element abundance are challenging because they are also influenced by the uncertainties in the input physics adopted in the calculations as well as the efficiency of several standard and non-standard physical processes active in young stars (i.e. diffusion, radiative levitation, magnetic fields, rotation). Moreover, it is still not completely clear how much the previous protostellar evolution affects the pre-Main Sequence characteristics and thus the light element depletion. This paper presents the state-of-the-art of theoretical predictions for protostars and pre-Main Sequence stars and their light element surface abundances, discussing the role of (p, α) nuclear reaction rates and other input physics on the stellar evolution and on the temporal evolution of the predicted surface abundances.

Keywords: Nuclear reactions, nucleosynthesis, abundances, stars:evolution, stars:pre-main sequence

1 INTRODUCTION

Light elements – lithium, beryllium and boron (hereafter Li, Be and B) – are burned at relatively low temperatures (T from ≈ 2 to ≈ 5 million degrees) easy to reach in stellar interiors at the bottom of the convective envelope, even during the early pre-Main Sequence (pre-MS) evolution. Therefore, surface light elements are depleted if the mixing processes become efficient enough to bring them down to the destruction region. This property makes such elements very good tracers of the mixing efficiency in stellar envelopes whose theoretical treatment is still a difficult task in stellar physics. Due to the different burning temperatures, the comparison between theory and observation for Li, Be and B, if possible, would be very useful to constrain theoretical models and in particular the extension of the convective envelope. The most of the observations concern the abundance of ^{7}Li because, in most stars, surface ^{6}Li is completely destroyed during the pre-MS phase and Be and B isotopic measurements are very problematic (e.g., Cunha, 2010; Kaufer, 2010; Delgado Mena et al., 2012).

A huge amount of data for surface ^{7}Li abundances are available both for disk, thick disk and halo field stars and for open clusters; however, the well known discrepancy between predictions and observations of this quantity in clusters or in the Sun (the so-called "lithium-problem") is still an open question (see e.g., Charbonnel et al., 2000; Jeffries, 2000; Piau and Turck-Chièze, 2002; Xiong and Deng, 2002; Sestito et al., 2003; Jeffries, 2006; Talon, 2008).

The theoretical prediction of surface light element abundances is complex because they are sensitive to both the input physics (i.e., equation of state, reaction rates, opacity, etc…) and chemical element abundances (i.e., initial abundance of deuterium, helium, metals, etc…) adopted in stellar models, together with the assumed efficiency of microscopic diffusion and radiative acceleration (see e.g., Piau and Turck-Chièze, 2002; Richard et al., 2002; Burke et al., 2004; Richard et al., 2005; Tognelli et al., 2012; Tognelli et al., 2015). The situation is even more complicated because surface light element abundances seem to be affected by additional "non standard" physical processes, not routinely included in stellar evolutionary codes, as the possible presence of relevant magnetic fields and mass accretion processes in some young pre-MS stars (see e.g., Baraffe and Chabrier, 2010; MacDonald and Mullan, 2012; Feiden and Chaboyer, 2013; Somers and Pinsonneault, 2014; Somers and Pinsonneault, 2015). Moreover, rotation-induced mixing, turbulent mixing, gravity waves and mass loss processes could play a role, though mainly for Main Sequence and more evolved stars (see e.g., Montalbán and Schatzman, 2000; Talon and Charbonnel, 2010; Pace et al., 2012; Charbonnel et al., 2013 and references therein).

The pre-MS is the first stellar phase where the star evolves as a fully formed object. To reach this evolutionary stage, the future star has to accrete mass, until its final value, in the previous "protostellar phase." The details of this phase, when matter of the protostellar cloud is still falling on the surface of the protostar, are complex and uncertain. The full understanding of how the protostellar accreting phase affects the predictions for pre-MS characteristics (and thus light element abundances) is still an open problem. The inclusion of the protostellar accretion phase in evolutionary codes produces stars in the early pre-MS phase different from what expected in standard non accreting models, in which stars essentially contract along the Hayashi track. This eventually results in differences between standard and accreting models still visible during the whole pre-MS or the MS phase, with effects on both the structure and chemical composition of the stellar models (Baraffe et al., 2009; Baraffe and Chabrier, 2010; Tognelli et al., 2013; Kunitomo et al., 2018; Tognelli et al., 2020).

Light element burning cross sections are fundamental ingredients in the predictions of the time behavior of light element stellar surface abundances. In recent years new values for (p,α) reaction rates have been proposed, mainly estimated using the Trojan Horse Method, greatly improving the precision of these quantities.

The present review summarizes the state-of-the-art of theoretical predictions for protostars and pre-MS stars and their light element surface abundances, in the light of recent improvements in the adopted input physics, updated reaction rates and description of the formation and evolution of pre-MS stars.

The paper is structured as it follows. In **Section 2** we qualitatively show the location of observed young pre-MS stars in the HR diagram and we compared it to the predictions of standard non accreting models. In **Section 3** we give a brief overview of the main characteristics and evolutionary stages of a pre-MS model without protostellar accretion. In **Section 4** we introduce the protostellar accretion phase, discussing the differences between spherical and disc accretion, along with the main parameters the determine the structure of an accreting protostar. In **Section 5** we analyze the burning of light elements (Li, Be and B) in pre-MS stars and the predicted surface abundances during the pre-MS for stellar models of different masses without or with protostellar accretion phase. In **Section 6** we review the impact of updated cross sections for the burning of light elements and their impact in the predictions of surface abundances in pre-MS stellar models. In **Section 7** we summarize the main aspects highlighted in the review.

2 OBSERVATIONAL DATA OF PRE-MAIN SEQUENCE STARS AS TEST OF THEORETICAL MODELS

This review is focused on theoretical predictions for protostellar/pre-MS models, which can be validated only through comparison with observational data. Given the difficulty in directly observing the stellar formation and the protostellar phase, only an investigation of the characteristics of very young pre-MS stars, close to the end of the protostellar phase, can indirectly give information on the previous accretion period. The availability of observations for very young pre-MS stars is thus fundamental. A great number of data is available for young pre-MS stars (ages ~ 1 Myr) with solar or slightly

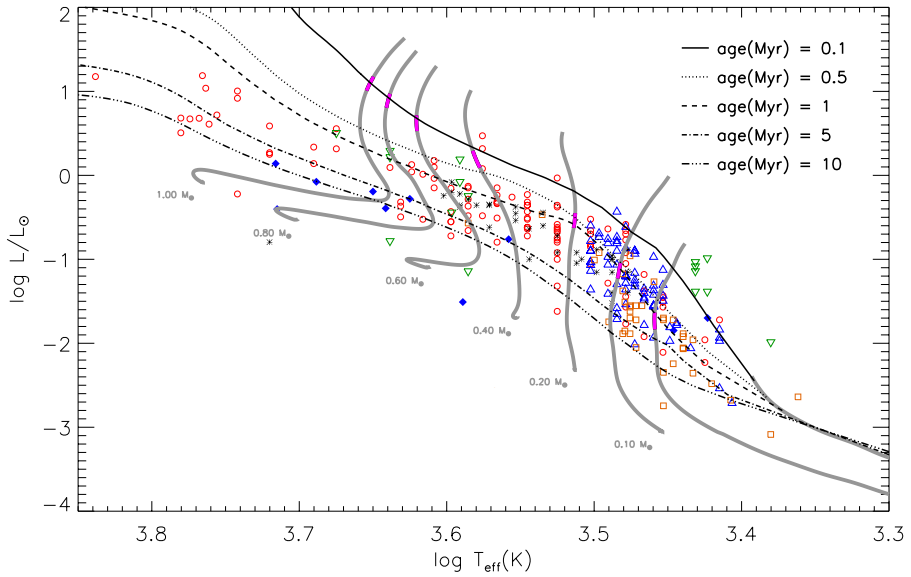

FIGURE 1 | HR diagram for young pre-MS stars extracted from the literature, compared with a set of standard evolutionary models and isochrones from the PISA database (Tognelli et al., 2011; Tognelli et al., 2018).

sub-solar metallicity; among these objects, some of them show a still detectable accretion disc, or protoplanetary disc, and very low accretion rates (see e.g. Hartmann and Kenyon, 1996; Muzerolle et al., 2000; Calvet et al., 2005; Muzerolle et al., 2005a; Muzerolle et al., 2005b; Bae et al., 2013; Ingleby et al., 2014). Such residual accretion discs show clear footprints of a previous accretion phase.

As an example, **Figure 1** shows a sample of young pre-MS stars compared to standard isochrones from 0.1 to 10 Myr and evolutionary tracks for masses in the range [0.01, 1.0] $M_{\odot}$ (Tognelli et al., 2011). Such observed stars are fully formed, in the sense that the measured accretion rates are extremely small, thus, they have already reached their final mass. Thus they can be considered stars evolving as constant mass structures. This figure is intended to qualitatively show the position of observed young stars in a HR diagram; they are located in a region which theoretically corresponds to pre-MS models undergoing to a gravitational contraction (we will discuss this evolutionary stage in more details in **Section 3**). Standard stellar models generally agree with data for young stars in the colour-magnitude (CM) or in the HR diagram (see e.g., Tognelli, 2013; Randich et al., 2018), as qualitatively shown in figure. We remark that stellar models should be able to populate such region of the HR diagram where young stars are observed. Thus, the simple comparison with observations of young associations/clusters (especially in the GAIA era) in the HR/CM diagram can put strong constraints on stellar evolution theoretical predictions (see e.g., Babusiaux et al., 2018; Randich et al., 2018; Bossini et al., 2019). This is a fundamental point especially when accretion phases are taken into account (see **Section 4**), helping in constraining free parameters adopted in model computations.

Other constraints are provided from pre-MS stars in double-lined eclipsing binary (EB) systems, whose masses and radii can be determined with high precision. In recent years, an increasing number of EB systems have been studied in detail, giving the possibility to check pre-MS model predictions against data (see e.g., Mathieu et al., 2007; Gennaro et al., 2012).

Further constraints come from the measurements in low-mass stars of the surface abundance of lithium-7, which, being an element whose destruction rate is extremely sensitive to the temperature, can be used to test the temporal evolution of the pre-MS stellar structures (Charbonnel et al., 2000; Piau and Turck-Chièze, 2002; Randich, 2010; Tognelli et al., 2012). These issues will be discussed in the present rewiew.

3 GENERAL CHARACTERISTICS OF STANDARD PRE-MAIN SEQUENCE EVOLUTION

The pre-MS evolution starts at the end of the accretion phase and ends with the Zero Age Main Sequence, or simply ZAMS, position[1]. The star is totally formed, and the mass can be considered constant at least for the whole pre-MS and Main Sequence (MS) evolution. The first consistent description of the pre-MS evolution was given by Hayashi (1961) and Hayashi and Nakano (1963); the basic idea is that a pre-MS star starts from a cold, expanse and luminous model. Due to the low temperatures,

[1]The ZAMS corresponds to the phase when central hydrogen begins to be burned into helium with secondary burning elements at equilibrium and nuclear energy production fully supporting the star.

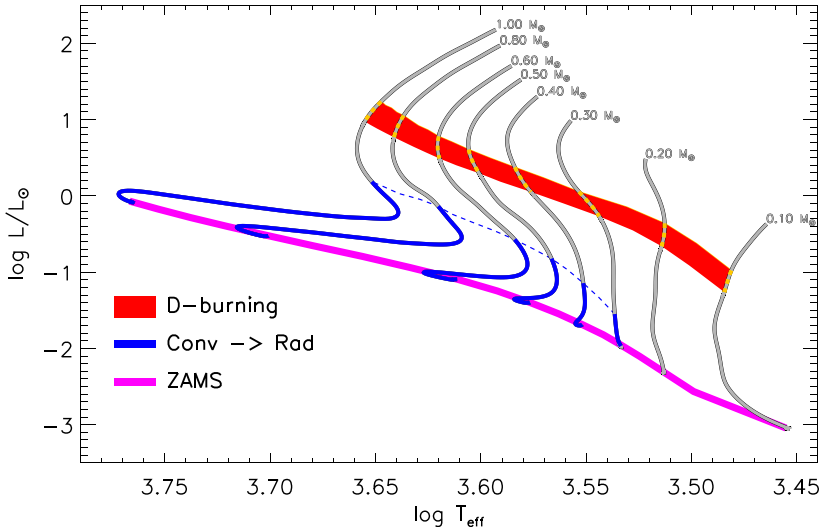

FIGURE 2 | HR diagram for low-mass stars with indicated the main evolutionary stages during the pre-MS evolution: Hayashi track (fully convective star, gray line), partially convective star (blue line), locus of the Zero Age Main Sequence (ZAMS, magenta line). The locus corresponding to the deuterium burning is indicated by the red stripe.

the opacity of the stellar matter is large and thus the radiative temperature gradient in the whole structure is larger than the adiabatic one. This leads to convective motions extended within the entire stellar structure; thus the star is fully mixed and chemically homogeneous. **Figure 2** shows an example of the evolution of pre-MS solar metallicity low mass stars in the mass range [0.1, 1.0] $M_{\odot}$ computed using the PISA stellar evolutionary code (Degl'Innocenti et al., 2008; Dell'Omodarme et al., 2012), with the adopted input physics/parameters described in Tognelli et al. (2018) and Tognelli et al. (2020); the same figure also shows a qualitative representation of some of the main evolutionary stages characteristics of such mass range.

Due to their low temperatures, during these first stages of the standard pre-MS evolution, stars cannot produce the nuclear energy required to balance the surface energy losses by radiation and their evolution essentially consists in a gravitational contraction. The evolution time scale is thus given by the thermal (Kelvin-Helmholtz) time scale, which is the time of energy transport throughout the star. It is common to define the Kelvin-Helmholtz time scale as the ratio between the total gravitational energy of the star and its luminosity L:

$$\tau_{KH} = \frac{\beta}{2}\frac{GM^2}{RL}. \quad (1)$$

The factor β takes into account the density profile inside the star. For an (unrealistic) model of homogeneous and spherical star with a constant density, $\beta = 5/3$. The gravitational contraction leads to an internal temperature increase. We recall that for non-degenerate structures[2] the central temperature, T_c, depends on the stellar mass M, the radius R and the chemical composition (mean molecular weight μ) in the following way:

$$T_c \propto \frac{\mu M}{R}. \quad (2)$$

From the relation above a contraction naturally leads to a rise in T_c. Using this result, the Stephan-Boltzmann law ($L \propto R^2 T_{\rm eff}^4$) and the virial theorem, it can be shown that the luminosity of the star decreases following a simple power law, $L \propto t^{-2/3}$.

The gravitational contraction is the only energy source until the central temperature reaches about 10^6 K, when the deuterium burning reaction $D(p,\gamma)^3He$ (D-burning) becomes efficient. Such a reaction generates the energy required to maintain the star stable on nuclear time scales, longer than the thermal one. This is guaranteed also by the steep dependence on the temperature of the energy generation rate, ϵ_{pD}, ($\epsilon_{pD} \propto T_c^{12}$); such a dependence limits the T_c increase, halting the gravitational contraction (because of the $T_c \propto 1/R$ relation).

The ignition of the D-burning, due to the produced energy flux, maintains the star fully convective and deuterium is burnt in the whole star. The D-burning phase is shown in **Figure 2** as a the red stripe, which indicates the part of the Hayashi track where D-burning provides more than 10% of the total stellar luminosity, for stars with different masses.

The nuclear time scale of D-burning depends on the characteristics of the star, mainly on the mass. The luminosity of a star at the beginning D-burning phase increases with the stellar mass; this means that increasing the stellar mass the D-burning increases its efficiency to balance the higher energy losses at the stellar surface. Thus the rate of deuterium destruction increases with mass. The typical nuclear D-burning time scale for masses in the range 0.1 – 1 $M_{\odot}$ varies between about 0.1–2 Myr, depending on the mass; as an example the D-burning phase lasts

[2]When talking about *degeneration* we refer to electron quantum degeneracy.

about $1–2 \times 10^6$ yr for 0.1 $M_\odot$ and about 10^5 yr for a 1 $M_\odot$ (see e.g., Chabrier and Baraffe, 1997; D'Antona and Mazzitelli, 1997; Tognelli et al., 2011).

The duration of the D-burning phase in pre-MS depends not only on the stellar mass but it is also proportional to the original stellar deuterium mass fraction abundance. Observations suggest that for disc stars a value of $X_D \approx 2 \times 10^{-5}$ should be adopted (see e.g., the review by Sembach, 2010); such a value is smaller than that predicted by the BBN ($X_D \approx 4 \times 10^{-5}$, see e.g., Steigman et al., 2007; Pettini et al., 2008; Pitrou et al., 2018; Mossa et al., 2020), as expected – e.g., by galactic evolution models – because deuterium is destroyed in stars.

Once deuterium has been completely exhausted in the whole star a pure gravitational contraction phase starts again. As for the previous evolution the stellar luminosity is well approximated by the power law $L \propto t^{-2/3}$. This second gravitational contraction increases the temperature and density in the inner region of the star. Depending on the total mass, such a temperature increase could lead to a drop in the radiative opacity κ_R. For stars with $M \gtrsim 0.3\,M_\odot$, the internal opacity drop reduces the radiative gradient leading to the formation of a central radiative stable zone. As a consequence of this fact, the star leaves the Hayashi track in the HR diagram, shifting toward larger temperatures as the radiative core grows in mass, until the star efficiently ignites the central hydrogen burning (reaching the ZAMS). This part of the stellar evolution is traditionally called the *Henyey track* and corresponds to the blue part of the evolutionary track in **Figure 2**. For $M < 0.3\,M_\odot$, the temperature increase is not enough to produce such an opacity drop and the star continues its contraction along the Hayashi line. In this mass range, if the total mass is larger than approximately 0.08 $M_\odot$, the contraction continues until the central temperature is large enough to ignite central hydrogen burning, which becomes the main energy source of the star (see e.g., Iben, 2013). On the other hand, if $M < 0.08\,M_\odot$, during the contraction the star become so dense that the pressure is dominated by the degenerate electron contribution; in such a configuration the pressure is only very slightly dependent on the temperature. Then the contraction slows down and the star (called brown dwarf) evolves along a cooling sequence which, in the HR diagram, follows a precise mass-radius relation.

This general picture describes the evolution of a pre-MS star in the standard case; theoretical calculations are started when the star is a fully formed object, chemically homogeneous at high luminosity (large radius) on the Hayashi line. However, it is well known that stars undergo a formation phase, the *protostellar phase*, during which the mass is accreted from the protostellar cloud and/or from a disk to reach the final stellar mass. The inclusion of such a phase could, at least in principle, modify the standard theoretical picture.

4 PROTOSTELLAR ACCRETION PHASE

The stellar formation process starts with the collapse and the fragmentation of a molecular cloud that contracts forming denser cores which eventually become protostars and then stars. During this process, the protostellar mass progressively increases as the matter in the cloud falls onto the central dense object. The cloud collapse is a complex hydrodynamic problem, in which one has also to take into account cooling processes by molecules and dust. At a given time during the collapse a stable hydrostatic core forms, on which mass continues to fall, so that the accretion treatment does not require anymore hydrodinamical models (e.g., Stahler et al., 1980a; Stahler et al., 1980b; Stahler et al., 1981; Hartmann et al., 1997; Baraffe et al., 2012).

Protostellar accretion has been analyzed in the literature starting from the pioneering works by Stahler et al. (1980a), Stahler (1988), Palla and Stahler (1991), Palla and Stahler (1992), Palla and Stahler (1993), Hartmann et al. (1997), and Siess and Livio (1997), to more recent works by Baraffe et al. (2009), Hosokawa and Omukai (2009a), Baraffe and Chabrier (2010), Tognelli (2013), Kunitomo et al. (2017) and Tognelli et al. (2020). Depending on the characteristics of the accretion assumed in the computations (chemical composition, magnetic fields, rotation, geometry. . .) the collapse of the cloud and the stellar formation can produce different evolution whose footprints are still visible in pre-MS stars.

4.1 Cloud Collapse and Protostellar Accretion

The main phases of the protostellar evolution are briefly described below (for more details see Larson, 1969; Larson, 1972; Larson, 2003).

- *Isothermal collapse:* The protostellar cloud, during its first collapse (until the central density is lower than about 10^{-13} g·cm^{-3}) does not warm, because its density is too low to trap the energy produced by the contraction. When the density further increases above this limit the radiation can be partially trapped.
- *Formation of the first Larson core:* the energy trapped inside the denser regions of the cloud prevent a further collapse of this region. A first temporarily hydrostatic core forms (with a mass of about 0.01 $M_\odot$ and a radius of several AU) out of which the matter is still falling on the core. A transition region (shock front) develops close to the core surface where the matter settles and passes from supersonic to subsonic.
- *Second collapse:* the hydrostatic core contracts as long as it radiates energy from its surface. So, although its mass is increasing due to mass accretion, its radius shrinks. The contraction of the core leads to a temperature rise, until the temperature of molecular hydrogen dissociation ($T \sim 2000$ K) is reached. Then contraction energy does not warm anymore the core but it's used to dissociate H_2, forcing the core to break the condition of hydrostatic equilibrium. At this stage, the core density and pressure increase.
- *Formation of the second Larson core:* when H_2 is fully dissociated a further increase of density and pressure, due to contraction, while mass is still falling radially on the core, leads to a second, hydrostatic equilibrium for the central core with a mass of the order of $\sim 0.001\,M_\odot$ (=1 M_J, Jupiter mass) and a radius of about 1 $R_\odot$. From this moment on the

central objects maintains its hydrostatic configuration while its mass increases.

The protostellar evolutionary phases listed above are quite general (for solar metallicity stars) and almost independent of the computation details. Larson (1969) remarked that at some stages of the cloud evolution a hydrostatic central object (second Larson core) forms that can be considered the first protostellar core. The characteristics of this core (i.e., mass, radius, density and central temperature) appear to be barely sensitive to the adopted cloud initial conditions or to the adopted input physics (see e.g., Masunaga and Inutsuka, 2000; Machida et al., 2008; Tomida et al., 2013; Vaytet et al., 2013). Reasonable intervals for the mass, radius and temperature of the stable hydrostatic core are: mass range of 1–20 M_J, radius values of $0.5 - 10\,R_\odot$ and central temperature of $2–6 \times 10^4$ K.

In the HR diagram of **Figure 3** the sequence that identifies the end of the protostellar accretion (when the star becomes visible) is compared to standard isochrones. Interestingly, the end of the protostellar evolution is very close to the position of the 1 Myr standard isochrone. Larson (1969) and Larson (1972) adopting selected accretion parameters, followed the subsequent evolution until the Hayashi track, finding that low mass stars ($M < 1\,M_\odot$) attain, after the protostellar accretion, characteristics similar to that of standard evolution along the Hayashi track. In contrast, as the mass increases ($M > 2\,M_\odot$), models skip the Hayashi line, ending the protostellar phase closer and closer to the MS position, where they join the "standard" track.

It is worth to remark that theoretical models for the protostellar evolution cannot be easily checked with observations, as these accreting phases occur when the star is still embedded inside the cloud and thus the central core is largely masked by the matter around it.

4.2 Protostellar Accretion in Hydrostatic Stellar Evolution Codes

As already discussed, hydrodynamic evolution of accreting stars is still a challenging task from the computational point of view. However, concerning the central protostar, it's not needed to employ a hydrodynamic code, as the protostar itself is in hydrostatic equilibrium after the formation of the second Larson core. In this approximation, the central object can be described using a mono dimensional hydrostatic stellar evolutionary code (see e.g. Stahler et al., 1980a; Stahler et al., 1980b; Siess and Livio, 1997).

On the other hand, hydrodynamic models are needed to predict the structure of the envelope surrounding the protostar, which does not satisfy the hydrostatic conditions but it's essential to determine the characteristics of the accretion flow. More precisely, the envelope gives information about the accretion rate, the percentage of the energy of the falling matter transferred to the star and the accretion geometry. Information about these quantities are needed inputs for hydrostatic protostellar models. Due to the still present uncertainty on hydrodynamic calculations, all the previous accretion parameters are affected by not negligible theoretical indeterminacy, as briefly summarized below.

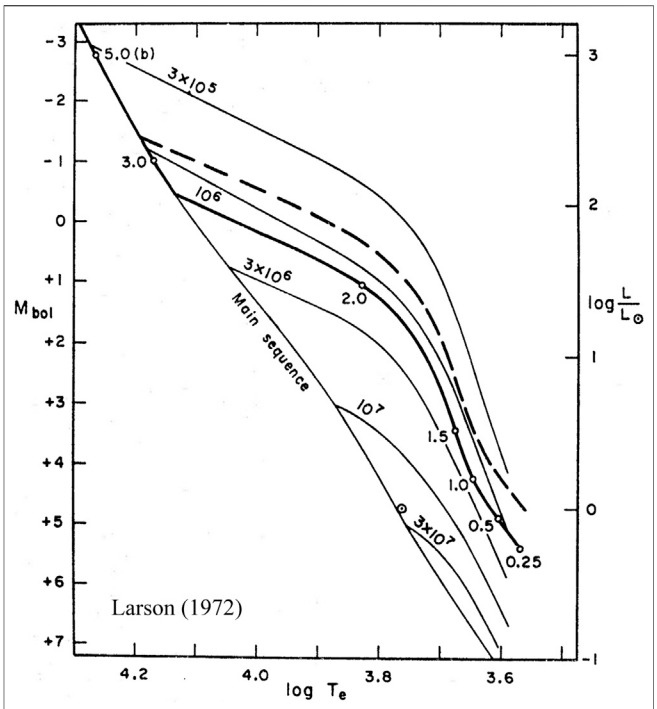

FIGURE 3 | Comparison between standard isochrones (thin solid lines) and the loci of the end of protostellar accreting sequence for two different initial temperatures of the cloud (10 K thick solid and 20 K thick dashed line). Circles mark the position of 0.25, 0.5, 1, 1.5, 2, 3, and 5 $M_\odot$ models. Figure adapted from Larson (1972).

- *Accretion rate.* The accretion rate ($\dot{m}$) defines the rate at which the star changes its mass; $\dot{m}$ can vary by orders of magnitude during the accretion phase, passing from $\dot{m} < 10^{-6} - 10^{-7}\,M_\odot$/yr (quiescent accretion) to rapid and intense episodes of mass accretion (bursts) with $\dot{m} \sim 10^{-4} - 10^{-3}\,M_\odot$/yr, e.g., as observed in FU Ori stars (Hartmann and Kenyon, 1996; Audard et al., 2014; Hartmann et al., 2016).
- *Energy transferred by the accreted matter.* The matter falling to the star before reaching the stellar surface has a kinetic energy that can be estimated approximating the matter velocity to the free fall one. However, when it settles on the stellar surface, the kinetic energy has become equal to zero, so the kinetic energy has been converted into another energy form. It can be thermal energy carried inside the star (the accreted matter is hot), or the energy can be partially or totally radiated (photons) before the matter reaches the stellar surface (at the shock front). The fraction of the kinetic energy transferred to the protostar depends on the characteristics of the accretion flow (i.e., density, accretion geometry, accretion rate, see e.g., Baraffe et al., 2012).

The difficulty in treating simultaneously the protostar and the envelope evolution requires some simplifications, which mainly concern the geometry of the accreting protostar-envelope system:

- *Spherical accretion* (see e.g., Stahler et al., 1980a; Stahler, 1988; Palla and Stahler, 1991; Palla and Stahler, 1992; Palla

and Stahler, 1993; Hosokawa and Omukai, 2009a). The star is supposed to be deeply embedded into the parental cloud and the matter falls on it almost radially. The whole stellar surface is subjected to the accretion and the energy radiated by the star can be reabsorbed by the envelope. The whole protostellar accretion occurs as a radial infall from a cloud that has mass enough to generate the star, at a fixed value of the accretion rate.

- *Disc accretion* (Hartmann et al., 1997; Siess and Livio, 1997; Baraffe et al., 2009; Baraffe and Chabrier, 2010; Tognelli, 2013; Kunitomo et al., 2017). The matter falls from a boundary layer of a circumstellar disc and reaches the star via accretion streams. Most of the stellar surface is not subjected by the accretion and the star is free to radiate its energy, most of which is lost in space. The disc is assumed to be totally decoupled from the central star and it is not treated in the stellar evolution codes. The parameters that define the accretion (accretion rate, disk lifetime, accretion energy) are considered as external free parameters which can be obtained from detailed accretion disc evolution calculations (e.g., Vorobyov and Basu, 2010; Baraffe et al., 2012).

The spherical accretion scenario is likely to describe the first stages of the formation of the protostar when it is still embedded within the cloud that retains an approximate spherical geometry. However, observations suggest that at some stage of protostellar evolution, the cloud collapses to a disc – because of angular momentum conservation – and that it is during the disc accretion that the star gains most of its final mass (see e.g., Natta et al., 2000; Meyer et al., 2007; Watson et al., 2007; Machida et al., 2010 and references therein). So, both scenarios are interesting and describe a part of the protostellar accretion.

The most important difference between spherical and disc accretion, which deeply affects the protostellar evolution, is the amount of energy retained by the accreted matter. Indeed, while in the spherical accretion it's possible to estimate the amount of energy retained by the accreted matter, in disc accretion this quantity is defined by a free parameter ($\alpha_{\rm acc}$). The impact of $\alpha_{\rm acc}$ on the evolution is discussed in the next sections.

4.3 Spherical and Disc Protostellar Accretion

The spherical accretion scenario applies to a star that is deeply embedded in a gas cloud. In this case, the evolution of the star and of the envelope have to be treated simultaneously. This allows (at least in principle) to have a consistent evaluation of the accretion rate and the amount of thermal energy that the accretion flows bring inside the star. Qualitatively, the energy emitted from the stellar surface is not free to escape into space since it has to interact with the matter around the star. Thus such an energy is partially reabsorbed by the matter in the envelope, and it eventually reaches the star. The effect of this process is that the star has a kind of external energy source that warms up the stellar surface. The injection of thermal energy from the accreted mass forces the star to expand or at least to compensate for the radius decrease caused by injection of mass.

The impact of spherical accretion on the formation of pre-MS stars has been largely analyzed in the pioneering works by Larson (Larson, 1969; Larson, 1972; Stahler et al., 1980a; Stahler, 1988; Palla and Stahler, 1991; Palla and Stahler, 1992; Palla and Stahler, 1993), and more recently also by Hosokawa and collaborators (Hosokawa and Omukai, 2009a; Hosokawa and Omukai, 2009b; Hosokawa et al., 2010; Hosokawa et al., 2011). One of the main results of such a spherical accretion scenario is that stars during the accretion phase remain bright and with large radii. Using a mild and constant accretion rate of $10^{-5}\,M_{\odot}$/yr, it is possible to obtain fully accreted stars in a region of the HR diagram that corresponds to the upper envelope of the locus where young pre-MS stars are observed (see **Figure 4**). This sequence was called "*birthline,*" that is the locus of stars with different masses where the accretion ends and the stars become optically visible (Palla and Stahler, 1993).

More recent sets of birthlines can be found in Hosokawa and Omukai (2009a): such accretion models was computed for different values of the accretion rate (from 10^{-6} to $10^{-3}\,M_{\odot}$/yr), adopting a spherical protostellar accretion code (similar to that used by Stahler and Palla). They showed that increasing $\dot{m}$, the birthline moves toward larger luminosities and radii, thus still in full agreement with the observations. Moreover, since spherical accretion models produce low-mass stars (on the birthline) in a region that corresponds to the top of the Hayashi track of standard stellar models (see **Figure 4**), the differences between standard and spherical accreting models in pre-MS low-mass stars are negligible. This validates the results of standard evolutionary tracks/isochrones (at least for ages higher than 1 Myr).

However, it's commonly accepted that stars do not accrete mass spherically during their entire protostellar phase; on the contrary they gain most of their mass from an accretion disc. This motivates the detailed study of protostellar accretion from a disk geometry. Differently from the spherical accretion, in the disc geometry the accretion streams cover only a very limited part of the stellar surface (few percent, see e.g., Hartmann et al., 1997) and almost the whole star is free to radiate its energy into space. Another difference is that all the accretion parameters (i.e., accretion rate, fraction of energy inside the accreted matter, etc..) are treated as external parameters in disc accretion models.

In the disc accretion geometry, it's possible to follow also an analytic approach to analyze the main characteristics of the accreting star. Following the formalism presented in Hartmann et al. (1997), it's possible to write a simple equation for the temporal evolution of the accreting star radius:

$$\frac{\dot{R}}{R} = \frac{7}{3}\frac{R}{GM^2}\left[\beta_D - L_{\rm ph} + \left(\alpha_{\rm acc} - \frac{1}{7}\right)\frac{GM^2}{R}\frac{\dot{m}}{M}\right] \qquad (3)$$

where M and R are the stellar mass and radius, β_D expresses the luminosity due to the deuterium burning (D-burning), $L_{\rm ph}$ is the luminosity of the stellar surface, $\dot{m}$ is the mass accretion rate and $\alpha_{\rm acc}$ represents the fraction of the accretion energy deposed into the star (thermal energy of the accreted matter).

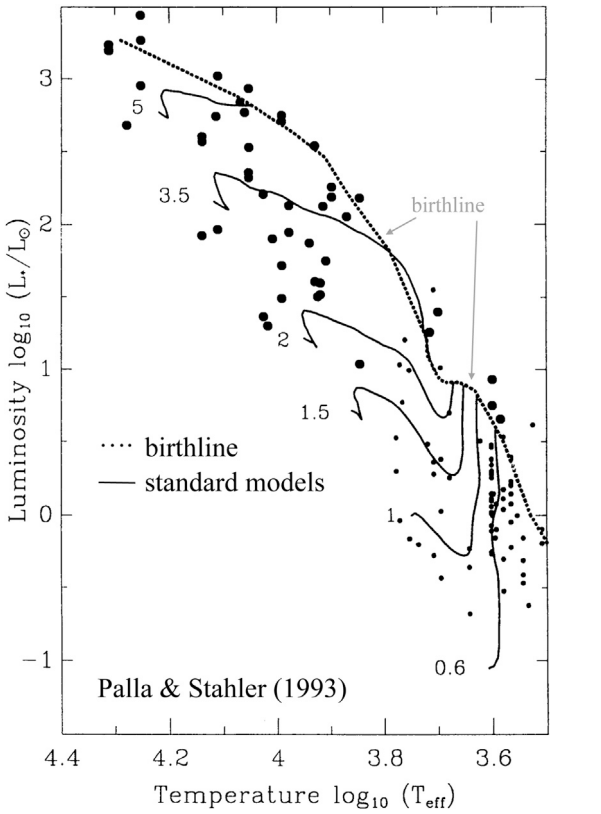

FIGURE 4 | Comparison between standard tracks (solid lines) and the birthline (dotted line). Dots represent T Tauri and Herbig Ae/Be stars. Figure adapted from Palla and Stahler (1993).

Equation 3 contains three terms: the first and second are the normal terms that define the evolution of the star with a surface radiative loss (L_{ph}) with the inclusion of D-burning energy production β_D, while the last term represents the accretion effect, which is proportional to $\dot{m}$. This term accounts for the fraction of the thermal energy of the accreted matter retained by the star, α_{acc}. Such a parameter has to be specified as an external free parameter, ranging from 0 (no energy acquired by the star) to about 1 (or 1/2 in case of thin disc, see e.g., Siess and Livio, 1997). From the same equation, it's also evident that $\alpha_{acc} = 1/7 \equiv \alpha_{acc,cr}$ defines a critical value; for $\alpha_{acc} < \alpha_{acc,cr}$ the third term is negative, and it contributes to the contraction of the star. For $\alpha_{acc} > \alpha_{acc,cr}$ the same term produces a radius expansion. It is common to refer to the case $\alpha_{acc} \sim 0$ (or $\alpha_{acc} \ll \alpha_{acc,cr}$) as *cold disc accretion* and $\alpha_{acc} > \alpha_{acc,cr}$ as *hot disc accretion*.

Looking at **Eq. 3** it is clear that a radius expansion requires a positive value of the right side of the equation, which can be obtained or via an efficient deuterium burning (large β_D) or via an efficient accretion energy transport into the protostar ($\alpha_{acc} > \alpha_{acc,cr}$). These two cases are discussed separately in the next two sections.

4.4 D-Burning During Protostellar Accretion

To check if the D-burning alone can produce a protostar with a large radius, in agreement with observations, we assume $\alpha_{acc} = 0$. From **eq. 3**, to produce a radius increase, D-burning has to supply the star with enough energy to counterbalance the radiative losses at the stellar surface plus the gravitational energy decrease caused by the mass ingestion. If this condition is not satisfied, the protostar contracts and the resulting model at the end of the protostellar phase has a radius much smaller than that observed in young disk stars and expected in spherical accretion cases. The dependency of the radius on original deuterium abundance X_D has been investigated in Tognelli (2013) and more recently in Kunitomo et al. (2017). In Kunitomo et al. (2017) the authors assumed for the second Larson core mass the value M_{seed} = 0.01 $M_\odot$ (=10 M_J). **Figure 5** shows a comparison between birthlines obtained assuming different values of X_D, for a cold accretion scenario with M_{seed} = 10 M_J. When no deuterium is taken into account in the stellar matter, the star inevitably contracts: in this model, the star ignites the hydrogen burning close to the end of the protostellar accretion, thus totally skipping the pre-MS evolution. The situation changes increasing the deuterium mass fraction abundance in the star. To partially reproduce the standard pre-MS evolution, a deuterium content of $X_D \approx 4 \times 10^{-5}$ (i.e., 40 ppm) is required. If a more reliable deuterium content is adopted, $X_D \approx 2 \times 10^{-5}$, the models with protostellar accretion converges to standard models only in the Henyey track; in this case, the evolution along the Hayashi track is missed contrarily to what observed in young clusters. We want to comment about the fact that the uncertainty on galactic deuterium mass fraction abundance is not larger than 10 ppm (see e.g., **Figure 2** and Table 1 in Sembach, 2010), thus an initial deuterium content of $X_D \approx 40$ ppm is an over estimation for disk stars. This fact seems to indicate that deuterium alone is not capable of maintaining the star bright enough to reconcile protostellar cold accretion models and the results obtained in a standard non accreting scenario.

4.5 Accretion Energy

There is another natural way to obtain a radius expansion in protostars, which is assuming that the ingested matter retains part of its internal energy; this means to assume a value of $\alpha_{acc} > \alpha_{acc,cr}$. In Hartmann et al. (1997) it was shown that non-cold accretion models ($\alpha_{acc} > \alpha_{acc,cr}$) can attain a radius expansion large enough to reproduce observed stars; in this case the disc accretion mimics spherical-accretion birthline obtained by Stahler (1988). More recently, Kunitomo et al. (2017) analyzed in more details the impact of α_{acc} on the formation of a 1 $M_\odot$ model, finding that the inclusion of a certain fraction of the total accretion energy [i.e., $\alpha_{acc} \in (0, 1)$] in the star is capable of maintaining the structure at large radii. **Figure 6** shows the birthline computed in Tognelli (2013) – by means of the PISA stellar evolutionary code – for solar metallicity stars using three values of α_{acc} = 0 (cold case), 0.5 and 1 (hot case), for a seed mass value of 5 M_J. From **Figure 6**, it is evident that adopting a value of $\alpha_{acc} \geq 0.5$ models on the birthline are bright and intersect the standard evolutionary tracks in the standard Hayashi track, for all

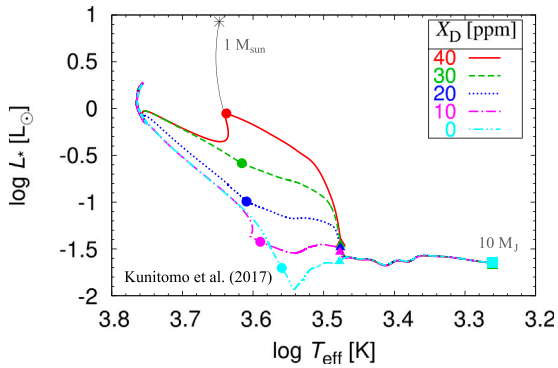

FIGURE 5 | Effect of different deuterium original abundances (see labels), X_D, on the protostellar evolution of 1 $M_\odot$ model. The protostellar accretion starts with a seed mass of 10 M_J, with a constant accretion rate of 10^{-5} $M_\odot \cdot yr^{-1}$. Filled circles indicate the end of the protostellar accretion phase and triangles the beginning of D-burning. Figure adapted from Kunitomo et al. (2017).

the selected mass range [0.1, 2.0] $M_\odot$. Recently, Tognelli et al. (2020) have obtained similar results for metal poor models: they showed that even in the low metallicity case, the inclusion of accretion energy produces expanse objects that intersect the Hayashi track of standard non accreting models at the end of the protostellar accretion stage.

4.6 Connecting the Standard pre-MS and the Protostellar Accretion Phase

From the previous discussion, it emerges that, depending on the characteristics of the protostellar accretion, the protostar could end its first evolution with a structure similar or in some cases profoundly different from that obtained in a normal gravitational contraction along the Hayashi track. The largest discrepancy with standard pre-MS evolution occurs in the case of cold accretion starting from a seed of the order of few Jupiter masses, as in that case the classical Hayashi track is almost completely skipped (see e.g., Baraffe et al., 2009; Tognelli et al., 2020).

Figure 7 shows the evolution in the HR diagram of cold accretion models starting from different M_{seed} and ending with different final masses, as discussed in details in Baraffe et al. (2009). It is difficult to reproduce the Hayashi track of pre-MS stars starting from M_{seed} of few Jupiter masses (i.e., cases A, B, D). Moreover, the position of the 1 Myr model (filled square) in accretion models is relatively far from the standard 1 Myr isochrone; in most of the cases, the position of pre-MS models with the inclusion of cold protostellar accretion at 1 Myr is very close to the standard non accreting 10 Myr isochrone, witnessing the strong impact of cold accretion on pre-MS evolution.

As discussed, it is likely that stars first accrete in a spherical hot scenario and then, at a given stage, switch to a disk-like accretion. In this case the transition from hot to cold accretion occurs for some value of the protostellar mass (possibly dependent on the amount of mass available in the cloud/disk). This mixed scenario has been investigated by Hosokawa et al. (2011) to show that the protostar remains bright enough to end the protostellar phase close to a Hayashi track. Top panel of **Figure 8** shows the models by Hosokawa et al. (2011). The purely hot accretion scenario (purple solid line), which corresponds to a hot birthline obtained assuming a spherical accretion, attains large luminosities and radii well above the standard 1 Myr isochrone. Figure shows also the results of models where the accretion switches from hot to cold at a given value of the stellar mass, namely 0.03 $M_\odot$ (magenta dashed line), 0.1 $M_\odot$ (magenta solid line) and at 0.3 $M_\odot$ (magenta dotted line). It is interesting to notice that in all cases, the birthline is still quite luminous, being very close to the 1 Myr isochrone. Similar results have been obtained for metal poor models by Tognelli et al. (2020) (bottom panel of **Figure 8**).

Baraffe et al. (2009) and Baraffe et al. (2012) investigated also the possibility to produce bright objects using an episodic accretion. The basic idea behind the models is that during intense bursts mass accretion phases the protostar can accrete matter in the hot-accretion configuration [$\alpha_{acc} > \alpha_{acc,cr}$, see the Appendix in Baraffe et al. (2012)], to switch back to cold accretion at the end of each burst. The authors showed that in this case it's still possible to produce models that end their protostellar accretion close to the standard position of the Hayashi track, to reproduce data (see also Tognelli et al., 2020 for metal poor protostars).

What emerges from the previous analysis is that, if one assumes masses and radii typical of the second Larson core, cold models cannot produce the observed bright stars in young clusters, but it is required the presence of hot accretion phases. Thus, the results seem quite comfortable: in most hot disk or spherical geometry, the protostellar accretion leads to pre-MS models with characteristics similar to those predicted in standard pre-MS evolution. More importantly, the position in the HR diagram of such models is in agreement with observational data. On the contrary, for the accretion parameters leading to a final mass model different to that of the standard one, as in the cold accretion scenario, the position in the HR diagram is in disagreement with disk star observations, rising doubts about the validity of such models.

5 LIGHT ELEMENTS SURFACE ABUNDANCES AND NUCLEAR BURNING DURING THE PRE-MS PHASE

Lithium, together with beryllium and boron, belong to the class of light elements burnt in pre-MS, because of their relatively low nuclear destruction temperature (between 2–5 million degree). The threshold values for the burning temperature depend mainly on the considered element, on the stellar mass (density and evolutionary stage) and slightly on the chemical composition of the star (in particular on helium and metals abundances). For pre-MS solar metallicity stars in the mass interval [0.08, 1.0] $M_\odot$, the ranges of burning temperatures for the different elements approximately are: 2.4–3.5 × 10^6 K [$T(^{6,7}Li)$], 3.5–4.0 × 10^6 K [$T(^9Be)$] and 4.2–5.0 × 10^6 K [$T(^{10,11}B)$]. In the literature the temperatures given for the burning are sometimes slightly different form the values reported here; the reason is that

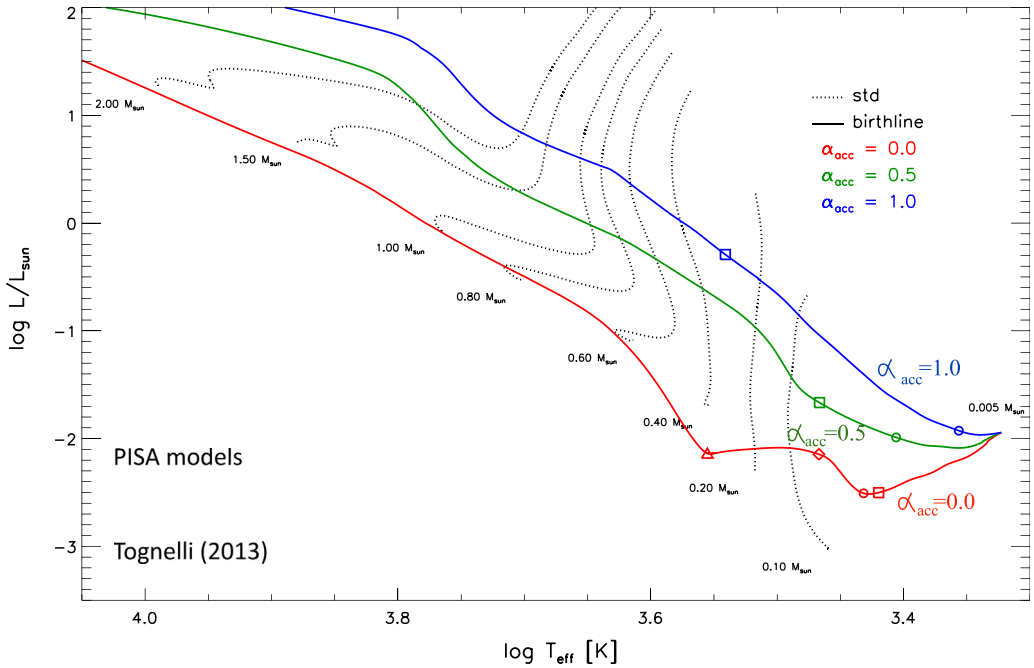

FIGURE 6 | Effect of α_{acc} on the protostellar evolution for three values of, 0 (cold accretion), 0.5 and 1 (hot accretion). Dotted lines are standard pre-MS tracks. Figure adapted from Tognelli (2013).

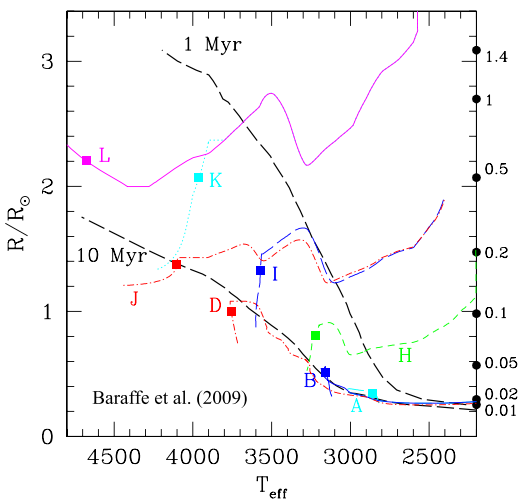

FIGURE 7 | Evolution in the HR diagram of protostellar models with different values of M_{seed}, compared with the standard 1 and 10 Myr isochrones (black long dashed lines). The different letters indicate models with different seeds and final masses (M_{fin}), in particular (A) M_{seed} = 1 M_J, M_{fin} = 0.05 $M_\odot$ (B) M_{seed} = 1 M_J, M_{fin} = 0.1 $M_\odot$ (D) M_{seed}= 1 M_J, M_{fin} = 0.5 $M_\odot$ (H) M_{seed} = 10 M_J, M_{fin} = 0.21 $M_\odot$ (I) M_{seed} = 50 M_J, M_{fin} = 0.55 $M_\odot$ (J) M_{fin} = 1.05 $M_\odot$ (K) M_{seed} = 100 M_J, M_{fin} = 1.1 $M_\odot$ (L) M_{seed} = 100 M_J, M_{fin} = 1.85 $M_\odot$. Filled squares represent the position of the 1 Myr model. Figure adapted from Baraffe et al. (2009).

usually authors do not take into account that stars with different masses ignites these elements at slightly different temperatures because the nuclear burning rates also depends (even if at a lower level) on the density in the region where the burning occurs. Moreover, such temperatures can be different for MS or pre-MS stars with the same mass because of the different time scales in which light elements are destroyed. In MS stars the evolutionary time scale is much longer than that in pre-MS (for the same mass and chemical composition) consequently a smaller burning rate due to a smaller threshold temperature at the bottom of the convective envelope, is compensated by the longer time during which that element is destroyed. As a result the burning of light elements in MS can efficiently occur even at thresholds temperature smaller than those required in pre-MS. Due to the differences in their burning temperatures in pre-MS, Li, Be and B are gradually destroyed at different depths inside the stellar interior and at different ages, in dependence on the stellar mass. As an example, **Figure 9** shows the portion along the evolutionary track where surface Li, Be and B are burnt at the bottom of the convective envelope in a set of solar chemical composition stars in the mass range [0.08, 1.0] $M_\odot$. It is interesting to notice that while Li is burnt (at the bottom of the convective envelope) in the whole selected mass range, surface ^{9}Be burning occurs only for masses between about 0.08 and 0.5 $M_\odot$, while B is burnt in an even smaller mass range (about 0.1–0.3 $M_\odot$).

The abundance of light elements at the stellar surface are strongly influenced by the nuclear burning as well as by the inwards extension of the convective envelope and by the temperature at its bottom. Consequently, the comparison between theory and observation for Li, Be and B surface abundances are useful to constrain theoretical models and in particular the convective envelope depth.

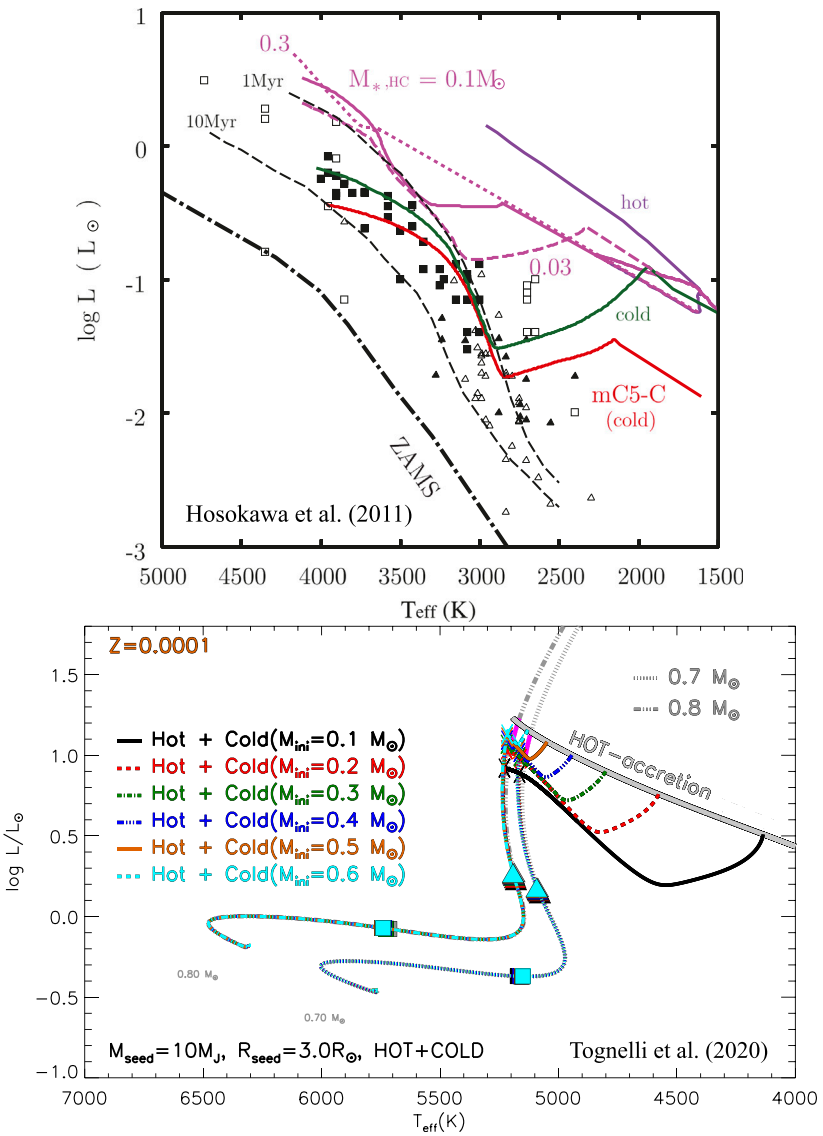

FIGURE 8 | Evolution in the HR diagram of purely and partially hot models computed with an accretion rate $\dot{m}$ = 10^{-5} $M_\odot$/yr. Top panel: comparison between purely hot (solid purple line), purely cold (green and red solid lines) and hot + cold birthlines (magenta lines). The two purely cold cases differ for the seed radius, 3.7 $R_\odot$ (green line) and 1.5 $R_\odot$ (red line, mC5-C). The accretion switches from hot to cold at a given value of the mass, which is 0.03 $M_\odot$ (magenta dashed line), 0.1 $M_\odot$ (magenta solid line), and 0.3 $M_\odot$ (magenta dotted line). Black lines are isochrones of 1 and 10 Myr (dashed lines) and the ZAMS (dot-dashed line) for standard non accreting models. Squares, triangles and circles represent observations of some young pre-MS stars. Figure adapted from Hosokawa et al. (2011). Bottom panel: models at low metallicity (Z = 0.0001) for a total final mass of 0.7 and 0.8 $M_\odot$. The accretion switches from hot to cold at a mass value 0.1, 0.2, 0.3, 0.4, 0.5, and 0.6 $M_\odot$ as indicated in the labels. The thick gray line represents the hot birhtline (α_{acc} = 1). Figure adapted from Tognelli et al. (2020).

From the observational point of view, most of the data for light elements concern the abundance of ^{7}Li whose line (at 670.779 nm) can be safely resolved even in cold stars, as witnessed by the huge amount of data for stars in clusters or isolated stars at different metallicities (see e.g., Sestito and Randich, 2005; Delgado Mena et al., 2014; Delgado Mena et al., 2015; Aguilera-Gómez et al., 2018 and references therein).

^{6}Li burns at a lower temperature with respect to ^{7}Li, consequently it's almost completely destroyed when ^{7}Li burning becomes efficient. Thus a potential detection of observable amounts of ^{6}Li in stellar atmospheres would constrain the destruction of the less fragile ^{7}Li (Copi et al., 1997). Since the depth of the convective zone increases with metallicity, ^{6}Li is almost completely depleted in high metallicity disk stars, as in the Sun (see e.g., Asplund et al., 2009) and it is below the detection level also for most thick disk and halo stars (see e.g., Spite and Spite, 2010). The possible abundance of ^{6}Li below the limit of detection also for halo stars could be explained by the fact that the amount of ^{6}Li formed by the standard Big Bang and by the cosmic rays is supposed to be very low. Moreover, a very small ^{6}Li abundance in these stars would be very difficult to detect, in particular because the lines

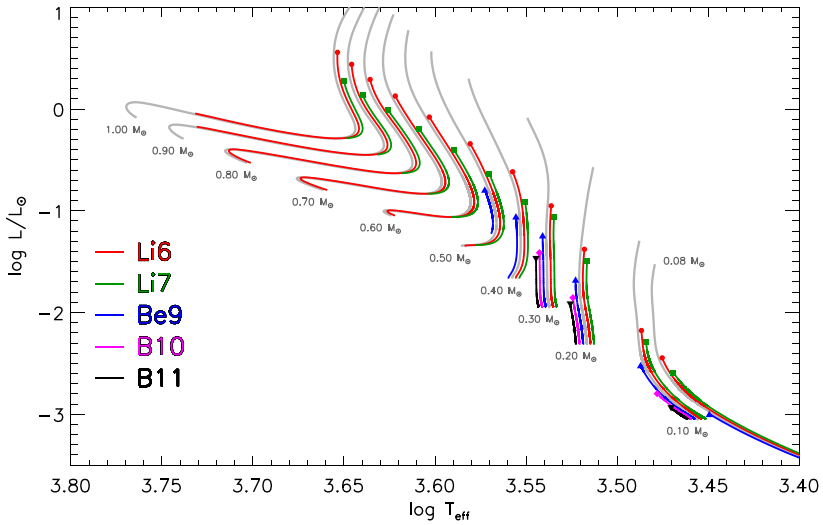

FIGURE 9 | Evolutionary tracks for solar metallicity in the HR diagram with indicated the regions where surface light element abundances decrease due to burning (where the temperature at the bottom of the convective envelope is higher than the burning temperature of Li, Be and B). The stellar models have been computed using the PISA evolutionary code with the same input parameters described in Lamia et al. (2015).

(doublets) of ^{6}Li and ^{7}Li are overlapping (see also discussion in **Sec. 5.5**).

Beryllium and boron measurements are more problematic than ^{7}Li observations. ^{9}Be abundance is measured using near-UV lines, only in stars with $T_{\rm eff} \gtrsim 5000$ K, which corresponds in pre-MS to a mass range where Be is expected to be preserved and not destroyed (see e.g., Garcia Lopez et al., 1995; Santos et al., 2004; Randich et al., 2007; Smiljanic et al., 2010; Delgado Mena et al., 2012; Lamia et al., 2015).

The abundance of the boron isotopes is even more difficult to measure than Be because the boron lines fall mainly in the UV part of the spectra where the Earth atmosphere is not transparent. In addition, for disk metallicity stars, B lines suffer strong blending problems (see, e.g., Cunha, 2010). Similarly to Be, B abundance are available in a mass range where B is expected to be not burnt in standard models. Despite the observational difficulties Be and B surface abundances data are available for some stars even at low metallicities (see e.g., Boesgaard and Novicki, 2005; Lodders et al., 2009; Tan et al., 2009; Primas, 2010; Boesgaard et al., 2011). In the observed stars, the ratio ^{11}B/^{10}B seems to be of the order of four, in agreement with solar values and meteorite results, even if it is very difficult to spectroscopically discriminate among the boron isotopes (see, e.g., Proffitt and Quigley, 1999; Prantzos, 2012). Be and B surface abundances have been also measured in the Sun where, as expected, they are not burned (see e.g., Asplund et al., 2005; Asplund et al., 2009; Lodders et al., 2009; Lodders, 2010).

The temperatures for light elements burning can be reached in stellar interiors during the pre-MS evolution of stars with masses larger than about 0.05–0.1 $M_{\odot}$ (depending on the requested burning threshold temperature). We recall that at the beginning of the pre-MS evolutions stars are, independently of their mass, fully convective. Thus, if a nuclear burning occurs at this evolutionary stage, the burning affects the chemical abundance in the whole star, from the center to the surface. However, as the star contracts and warms up, the opacity decreases at the stellar center and stars with $M \gtrsim 0.3\,M_{\odot}$ develop a radiative core. From this moment on the chemical evolution of the surface is (during the pre-MS) decoupled from that of the center if the bottom of the convective envelope does not reach a region deep and hot enough to process –via nuclear burning– the surface matter. Thus, for partially convective pre-MS stars, a condition to have a partial surface depletion of a specific element is that the bottom of the convective envelope reaches a temperature high enough to make nuclear burning efficient and then recedes toward the external parts of the star at lower temperatures.

Figure 10 shows the temporal evolution of the temperature at the bottom of the convective envelope, $T_{\rm bce}$, for stars with different masses between 0.08 and 1.0 $M_{\odot}$ at solar metallicity, with indicated the approximate values for the Li, Be and B burning temperatures. In fully convective stars $T_{\rm bce}$ coincides with the central temperature, T_c. When stars are fully convective $T_{\rm bce}$ progressively increases until the star reaches the ZAMS, while in stars that develop a radiative core $T_{\rm bce}$ stops increasing when the radiative core forms and $T_{\rm bce}$ slowly decreases as the radiative core grows in mass. This has a direct impact on the interval of time during which the surface light elements depletion occurs. Considering e.g., ^{7}Li abundance in fully convective stars (i.e. $M \leq 0.3\,M_{\odot}$), $T_{\rm bce}$ overcomes $T(^{7}{\rm Li})$ at young ages (i.e., about 50 Myr for 0.1 $M_{\odot}$ and 5 Myr for 0.3 $M_{\odot}$); then surface Li burning continues during the whole pre-MS and MS phase. Since $T_{\rm bce}$ continuously increases, the burning efficiency increases too. On the other hand, in partially convective stars $T_{\rm bce}$ reaches a maximum and then decreases as the star evolves toward the ZAMS. For $M \gtrsim 0.5\,M_{\odot}$, $T_{\rm bce}$ decreases below $T(^{7}{\rm Li})$ at some point during the pre-MS, thus halting the lithium burning at the

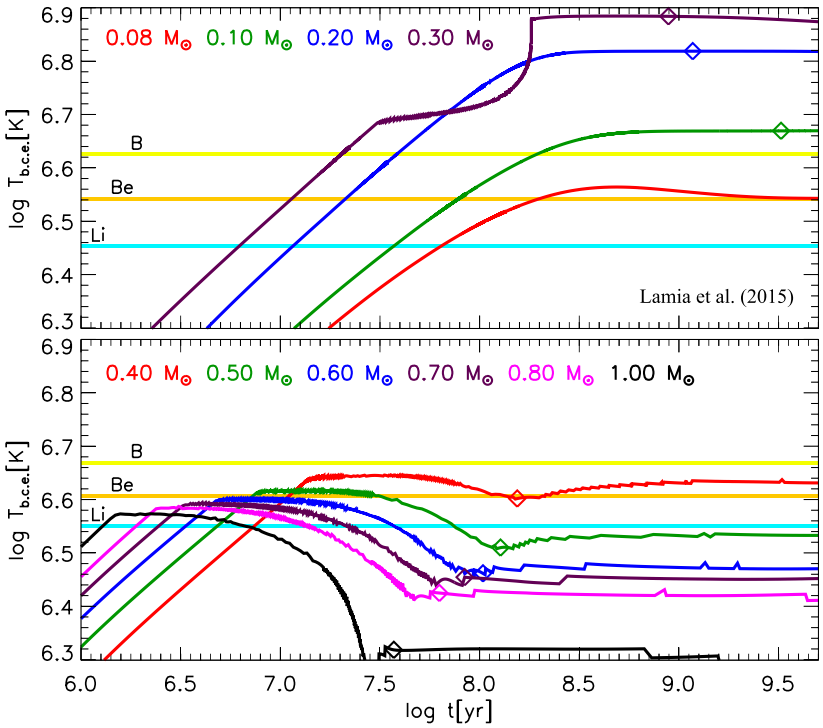

FIGURE 10 | Temporal evolution of the temperature at the bottom of the convective envelope for masses in the range [0.08,1.0] $M_{\odot}$. The threshold temperature required to ignite Li, Be and B burning are indicated as colored horizontal lines. The ZAMS position is marked by a diamond. The not regular behavior of the 0.3 $M_{\odot}$ model at $\log t\,(yr) \sim 7.5 - 8.3$ is caused by the formation of a transient convective core before the ZAMS [figure adapted from Lamia et al. (2015)].

bottom of the convective envelope. From this moment on, surface lithium abundance remains constant during the pre-MS phase. **Figure 10** also shows that increasing the mass of the star the time interval during which surface lithium is destroyed is shorter and the maximum value of $T_{\rm bce}$ reduces too; this is due to the fact that increasing the mass the convective envelope becomes thinner. This indicates that, increasing the mass, surface lithium is destroyed progressively less efficiently.

The situation is similar for the other light elements; clearly one has to take into account the different burning temperatures, so that the mass range in which Be and B are destroyed at the base of the convective envelope is different from that in which lithium is burned. As an example, for solar composition models, Be can be burnt at the bottom of the convective envelope in the mass interval $0.08 \lesssim M/M_{\odot} \lesssim 0.5$. On the other hand B in destroyed only in the mass range $0.1 \lesssim M/M_{\odot} \lesssim 0.3$.

Figure 11 gives an example of the ^{7}Li surface abundance time behavior predicted for stars in the mass range [0.08, 1.0] $M_{\odot}$; it's important to notice that ligh element surface abundances depend not only on the capability of $T_{\rm bce}$ to overcome the threshold temperature for the considered element, but also on the duration of the burning and on the difference between the threshold and $T_{\rm bce}$. In particular, this last quantity is very important because the burning rate of light elements is proportional to T^{a} with $a \approx 20$ for lithium, $a \approx 23$ for beryllium and $a \approx 25$ for boron.

Referring to **Figure 11**, in fully convective stars, i.e., $M \lesssim 0.3\,M_{\odot}$, at a fixed age, the surface lithium depletion progressively increases increasing the stellar mass. For partially convective models, this behavior breaks up and, at a fixed age, the lithium depletion decreases as the mass increases. This is clearly visible in the figure comparing e.g., the predicted lithium abundance at about $\log t\,(yr) = 7.5$ for 0.7, 0.8, 0.9, and 1.0 $M_{\odot}$ models. The amount of residual surface lithium increases with the mass, as the consequence of the decrease of $T_{\rm bce}$ (in time) when the radiative core forms and grows.

Figures 10, **11** refer to a standard evolution, where the star is fully formed at the top of the Hayashi track. The situation can be different if protostellar accretion is taken into account, in particular in those cases where the star at the end of the protostellar phase is compact and faint, which corresponds essentially to the case of cold accretion models. This could affect light element burning in two different ways: 1) in principle for some possible values of the accretion parameters it could be possible the burning of light elements (most likely lithium) during the protostellar phase 2) accretion can change the pre-MS stellar characteristics with respect to those already predicted by the standard scenario so that the light element burning efficiency is changed too. We will discuss the effect of the protostellar accretion on the surface chemical composition in **Section 5.2**.

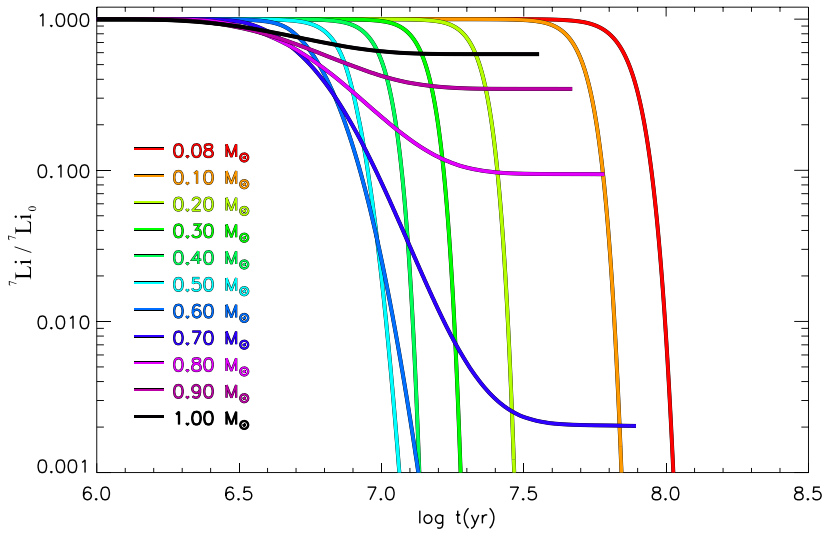

FIGURE 11 | Temporal evolution of surface lithium abundance (normalized to the initial one) during the pre-MS for stars in the mass range [0.08, 1.0] $M_\odot$ and solar chemical composition. Stellar models have been computed using the same input parameters described in Lamia et al. (2015).

5.1 Surface Lithium Abundance in Open Clusters

Many questions are still open about the large discrepancies between the predicted and observed surface lithium abundance in young clusters, where standard models tend to underestimate the surface abundance at a given age (see e.g., D'Antona et al., 2000; D'Antona and Montalbán, 2003; Jeffries, 2006; Tognelli et al., 2012 and references therein). Moreover the presence of a large scatter in the observed Li abundance among stars with similar $T_{\rm eff}$ in young clusters poses questions about the possible mechanisms producing different amounts of lithium depletion in stars with the same mass, age and chemical composition (Jeffries, 2000; King et al., 2000; Clarke et al., 2004; Xiong and Deng, 2006; King et al., 2010).

It is worth noticing that, qualitatively, standard models (without accretion) are capable to produce a pattern of lithium vs. mass (or $T_{\rm eff}$) similar to that observed in young clusters. This pattern can be divided into three regions, and, referring to **Figure 12**, it can be summarized as it follows:

- Starting from a certain value of the effective temperature (that depends on the cluster age) the surface lithium content, at a given cluster age, increases with the $T_{\rm eff}$ (or the stellar mass), until it reaches a plateau corresponding to stars that do not deplete Li (hot stars). Regions (3)–(4) in **Figure 12** correspond to partially convective models of increasing mass. As previously discussed, the more massive is the star, the thinner is the convective envelope and, in turn, the less efficient is the surface Li depletion. The plateau corresponds to stars with a convective envelope so thin that $T_{\rm bce} < T(^7{\rm Li})$.
- For lower masses (and thus $T_{\rm eff}$), e.g., in regions (1)–(2), stars are fully convective and lithium is burned in the whole star. At a fixed age the lithium burning efficiency increases with the stellar mass and lithium surface abundance rapidly changes varying the stellar mass.
- In region (1), reducing the mass (or $T_{\rm eff}$), one approaches the minimum mass that reaches the Li burning temperature in fully convective stars. Below this minimum mass the surface lithium abundance is constant and equal to the original value.

5.2 Lithium Abundance Evolution During Protostellar Accretion

As discussed in the previous section, the inclusion of the protostellar accretion phase could (in dependence of the adopted accretion parameters) drastically alter the evolution of a pre-MS star. In this section we briefly review the main effects of the protostellar accretion phase on the surface lithium abundance during the protostellar and pre-MS evolution as a function of the different possible accretion parameters.

This problem was first analyzed by Baraffe and Chabrier (2010), who showed that the inclusion of protostellar accretion in solar metallicity stars with different input parameters can lead to a variety of cases for which the resulting lithium abundance (in pre-MS or in MS) is different from what expected in standard pre-MS evolution (see also Baraffe et al., 2012; Tognelli, 2013; Kunitomo et al., 2018). We recall that accretion models depend on many parameters, but the main quantities that strongly affect the pre-MS evolution are the seed mass and the accretion energy deposed into the star. The general picture that emerges is that in cold accretion models lithium is efficiently destroyed during the protostellar accretion or at the very beginning of the pre-MS phase. Thus these stars should show a very low surface lithium content.

A detailed analysis of the effect of the protostellar accretion on surface lithium abundance for different subsolar metallicities ($Z = 0.005$, $Z = 0.001$, and $Z = 0.0001$) was discussed in

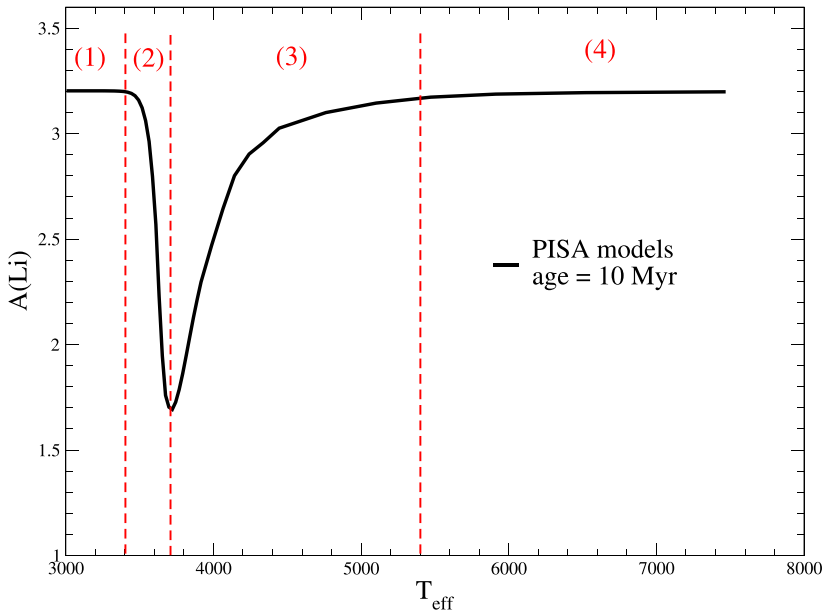

FIGURE 12 | Theoretical surface lithium abundance predicted for solar metallicity stars at 10 Myr, as obtained in standard evolutionary models using the PISA evolutionary code.

Tognelli et al. (2020). We also performed some tests to verify that what obtained for sub-solar metallicity is still valid at solar metallicities.

The results by Tognelli et al. (2020), similarly to what already obtained by Baraffe and Chabrier (2010), show that two scenarios can be found:

- *Pure cold accretion case*. The accretion leads to stellar structures at the end of the protostellar phase different with respect to standard non accreting models, affecting also the lithium burning efficiency. If the seed mass is of the order of few Jupiter masses, the models result to be so compact and hot that start to efficiently deplete lithium before the end of the accretion phase. The level of depletion is mainly determined by the seed mass and it's only slightly affected by the other accretion parameters (accretion rates, initial radius). After the protostellar phase, for masses larger than about 0.1–0.2 $M_\odot$, lithium is completely destroyed in an extremely hot and fully convective pre-MS structure. This prediction is in complete disagreement with observations available for young clusters, where $M \approx 0.8$–$1\ M_\odot$ stars show no relevant lithium depletion (see **Section 5.4** for more details). Moreover, such accreting models are in disagreement with the observed position of very young disk pre-MS stars in the HR diagram. The disagreement between data and accretion models is partially mitigated if a larger seed mass is adopted (of the order of 10 M_J). In this case it is possible to reduce the level of lithium depletion in very low mass stars (i.e., $M \lesssim 0.3\ M_\odot$), but not for stars close to 1 $M_\odot$ where lithium is totally depleted in pre-MS.
- *Hot accretion case*. In **Section 4.6** we showed that if stars accrete part of their mass during an hot accretion phase (during which the protostar is maintained at large radius by the accretion energy), the star at the end of the accretion phase is more similar to a standard evolutionary models. In this case, protostars are relatively cold and they do not deplete an appreciable amount of Li. Then, when the star enters the pre-MS the residual lithium is essentially equal to the original one, as predicted by models without accretion and from this moment on the lithium evolution proceeds as in standard stellar evolutionary models.

These two scenarios embrace many other possible solutions, obtained by modify/tuning the accretion parameters and the accretion history to produce, at least in principle, intermediate scenarios. However, a fine tuning of the accretion parameters that depends also on the stellar mass is unlikely and could produce artificial results (Tognelli et al., 2020). The two extreme scenarios highlight an important point. The expected Li abundance is strictly connected to the protostellar evolution. Stars that due to the inclusion of the protostellar accretion skip the Hayashi track (i.e., pure cold accretion) undergo to an efficient lithium burning during the protostellar phase, in disagreement with standard predictions. This kind of models are excluded, at least for disk metallicities, by observational data.

The possible effects of accretion on stellar characteristics and Li temporal evolution could also be linked to the question of the luminosity spread observed in star forming regions. The problem consists in the fact that stars with the same $T_{\rm eff}$ and the same chemical composition show different luminosities (see e.g., Hillenbrand, 2009; Jeffries, 2009; Da Rio et al., 2010a; Da Rio et al., 2010b). A possible dependence on the protostellar accretion of such a luminosity spread was analyzed by Baraffe et al. (2009); the adoption of a different accretion history during the

protostellar phase can strongly affect the luminosity and $T_{\rm eff}$ of a star at the end of the protostellar phase, as already discussed in previous sections. If this is the case, faint stars, which experienced cold accretion, should show a clear lower lithium content than bright ones. In other words, such a luminosity spread should directly reflect in a surface lithium content spread. This point deserves to be further investigated to clearly confirm or exclude the presence of a correlation between lithium content and luminosity in star forming regions.

5.3 Lithium in Old Metal Poor Stars

An interesting aspect to be discussed about lithium evolution is the cosmological lithium problem. Halo stars show a lithium plateau for $T_{\rm eff} > 5900$ K and [Fe/H] < -1.5, the so called Spite plateau (Spite and Spite, 1982a; Spite & Spite, 1982b), with a constant logarithmic lithium abundance[3] A(Li)-2.4 (Charbonnel and Primas, 2005; Asplund et al., 2006; Meléndez et al., 2010; Sbordone et al., 2010), and references therein. From the theoretical point of view, stars with such temperatures and metallicities are expected to preserve their initial lithium content, moreover galactic enrichment due to cosmic rays and spallation processes should be totally negligible at such low metallicities. Thus the Spite plateau is expected to represent the primordial lithium content produced during the big bang nucleosynthesis (BBN).

However, BBN predicts a primordial lithium content of A(Li)-2.75, (see e.g., Cyburt et al., 2016; Pitrou et al., 2018). This estimate depends on the density of baryons, which is related to the fluctuations of the cosmic microwave background measured with WMAP and Planck satellites. The BBN predictions for the primordial lithium abundance are thus 0.3–0.6 dex larger than the Spite plateau value. This discrepancy constitutes the so called "cosmological lithium problem." Several attempts to introduce new physics (exotic particles) or to review the reaction rates during the BBN have been performed, but without any firm conclusion (see e.g., Fields, 2011; Pizzone et al., 2014; Goudelis et al., 2016; Coc and Vangioni, 2017; Damone et al., 2018; Lamia et al., 2019).

Similarly, on the stellar evolution side, the problem has been analyzed to find a possible mechanism to deplete the same lithium amount for the stars with different masses and metallicities which populate the Spite plateau. Diffusion has been investigated as a possible solution, as it slowly brings surface lithium below the convective region (Richard et al., 2005). This process acts on timescales typical of the MS evolution, but its efficiency depends on the stellar mass and thus in the mass range corresponding to the Spite Plateau the effect of diffusion increases with $T_{\rm eff}$. Thus no Spite plateau would be possible without tuning the diffusion efficiency. Also turbulent mixing could produce an effect similar to that of pure diffusion, on similar time scales, but also in this case an ad hoc tuning is required (see e.g., Richard et al., 2005; Spite et al., 2012 and references therein). Also mass loss coupled to diffusion and turbulent mixing can be tuned to produce a constant lithium depletion along the Spite plateau (Swenson, 1995; Vauclair and Charbonnel, 1995), but, again, there is the need for a fine tuning of the parameters.

Another possibility is that lithium depletion occurs during the pre-MS. In this case, Fu et al. (2015) suggested that a certain level of undershooting[4] at the bottom of the convective envelope of pre-MS stars could increase the depletion of surface lithium. In addition, a residual matter accretion, regulated by the stellar luminosity, could provide gas with pristine chemical composition (and thus lithium to the star), obtaining in pre-MS the depletion level required to produce the Spite plateau. However, in such models, MS diffusion must be inhibited to avoid a $T_{\rm eff}$ (or mass) dependent depletion on MS time scales.

Recently Tognelli et al. (2020) analyzed the possibility to produce a constant lithium depletion in pre-MS taking into account in the models the protostellar evolution with different accretion parameters. As discussed in Sec. s 4.6 and 5.2, depending on the scenario adopted during the protostellar evolution, stars at the beginning of the pre-MS can be profoundly different from the ones evolved starting from the Hayashi track. The reason is that the protostellar phase can deeply affect the thermal structure of a star. As a result, it's possible to induce a lithium depletion in pre-MS or even during the protostellar phase, but it requires the adoption of a fine tuning of the parameters that govern the stellar mass acretion (see e.g., Fu et al., 2015; Tognelli et al., 2020). Moreover, as already discussed, the models that show a significant Li depletion, follow a pre-MS evolution in the HR diagram that is different to that observed for high metallicity pre-MS stars. The lack of Galactic very young and metal poor stellar systems, in which one could observe pre-MS stars with Spite plateau metallicities, avoid the possibility to restrict the range of valid accretion parameters and reach firm conclusions.

To conclude, the proposed mechanisms could in principle alleviate the cosmological lithium problem, but the weakness of all these suggested solutions is that a fine tuning of the parameters is still required to produce a constant lithium depletion reproducing the Spite plateau.

5.4 Uncertainties on Predicted Surface Lithium Abundance

The predicted depletion of surface lithium abundance (and, in general, of the light element surface abundances) is affected by the uncertainties on the input physics adopted in stellar models and on the assumed chemical composition, that influence the extension of convective envelope and temperature structure of the star. In particular, also the uncertainty on the nuclear burning cross sections plays a role in the light element abundance predictions. In the literature there are several attempts to estimate the impact of the uncertainties on the parameters/input physics adopted in stellar models on the predictions of lithium abundance in low and very-low mass stars (see e.g., Piau

[3] $A(Li)$ indicates an observational notation for abundances, where $A(\mathrm{Li}) = \log N_{\rm Li}/N_{\rm H} + 12$, with N being the number of particles of a given specie.

[4] The term "undershooting" indicates a sink of the external convection toward the stellar interior larger than the one predicted in classical models i.e., by the Schwarzschild criterion.

and Turck-Chièze, 2002; Burke et al., 2004; Tognelli et al., 2012; Tognelli et al., 2015). The quantities that mainly affects lithium, as analyzed in the quoted papers, are the following (see e.g., Chapter 3 in Tognelli, 2013):

- *Radiative opacity and equation of state*. The extension of the convective envelope is determined by the Schwarzschild criterion which simply states that a region is convective if the radiative temperature gradient $[\nabla_{rad} \equiv (d \log T / d \log P)_{rad}]$ is larger than the adiabatic one. The radiative gradient is proportional to the Rosseland mean radiative opacity κ_R, thus change in κ_R directly affects the position of the convective unstable boundary. Generally an uncertainty on κ_R of about $\pm 5\%$ is assumed in the computations (Badnell et al., 2005; Blancard et al., 2012; Mondet et al., 2015). Similarly an uncertainty on the adiabatic gradient, ∇_{ad}, thus in the equation of state, modifies the position of the bottom of the convective envelope. An increase in κ_R or a decrease of ∇_{ad} lead to an extension of the convective envelope that can reach deeper and hotter layers, increasing the efficiency of surface lithium burning (see e.g., Tognelli, 2013). The variation of surface lithium abundance, due to the change in the equation of state or radiative opacity, strongly depends on the selected mass range and age. However, in those models that efficiently deplete lithium (e.g., for 0.7 and 0.8 $M_\odot$) a variation in lithium abundance of approximately 0.1–0.2 dex (due to equation of state uncertainty) and 0.4–0.5 dex (due to opacity error) can be obtained. In the worst cases (i.e., $M \sim 0.6\,M_\odot$) a variation of 5% of the radiative opacity can lead to a difference of ~0.8 dex in the predicted lithium content. The effect on surface lithium of the equation of state or radiative opacity reduces as the mass increases.
- *Outer boundary conditions*. The outer boundary conditions are the pressure P_{atm} and temperature T_{atm} at the bottom of the atmosphere. These quantity deeply affect the temperature profile in the convective envelope thus modifying also its depth. The uncertainty on (P_{atm}, T_{atm}) it is not provided by stellar atmospheric calculations, but one can test the effect on the stellar characteristics of the adoption of different atmospheric models available in the literature (see e.g., Tognelli et al., 2011). As said above, the effect on lithium depends on the mass/age of the models; a typical variation of 0.3–0.5 dex is expected, which reduces as the mass increases..
- *Mixing length parameter*. The convection efficiency in super-adiabatic regimes in 1D stellar evolution codes commonly relies on mixing-length theory (MLT) (Böhm-Vitense, 1958). In this formalism, the scale on which the heat is efficiently transported by convection is defined as $\ell = \alpha_{\rm ML} \times H_p$, where H_p is the local pressure scale height and $\alpha_{\rm ML}$ is the mixing length parameter, a free parameter to be calibrated. The extension of the convective envelope and thus the temperature at its bottom and the surface lithium abundance are strongly affected by the adopted $\alpha_{\rm ML}$. The adoption of different values of this quantity within plausible ranges can produce a variation of surface lithium abundance as large as one order of magnitude in those stars where the external envelope is largely super adiabatic and where lithium is efficiently destroyed at the bottom of the convective envelope (i.e., for masses in the range [0.5, 1.0] $M_\odot$ (see e.g., Piau and Turck-Chièze, 2002; Tognelli et al., 2012).
- *Nuclear cross section*. The error on the cross section for the ^{7}Li(p, α)^{4}He reaction directly affects the rate at which lithium is destroyed and thus its temporal evolution. Since the energy released by such reactions is inconsequential for the stellar structure, the only effect is on the surface lithium content at a fixed age. In **Section 6** we will discuss this point in more detail.
- *Chemical composition*. The initial abundance of helium (Y) and metals (Z) in the star is not known, but it can be estimated from the observed [Fe/H], assuming for metal rich stars the same relative abundance of metals of the Sun, while for metal poor galactic stars a suitable alpha-enhancement must be introduced[5]. The conversion of [Fe/H] into Y and Z depends on the assumed values of: 1) the primordial helium mass fraction produced in the BBN (Y_p), 2) the metal-to-helium enrichment ratio ($\Delta Y/\Delta Z$), 3) the metal-to-hydrogen ratio in the Sun $[(Z/X)_\odot]$, 4) and the [α/Fe] (alpha-enhancement) for metal poor stars (Gennaro et al., 2012; Tognelli et al., 2012; Tognelli et al., 2015). The observational error on [Fe/H] has thus to be combined with the uncertainties of such quantities, to estimate the final global uncertainty on the initial helium and metal mass fraction to be used in the computation of stellar models (see e.g., Gennaro et al., 2012; Tognelli et al., 2012; Tognelli et al., 2015); for solar chemical composition, the uncertainty on Y and Z are estimated to be of the order of 4–5% for Y and about 20% for Z (Tognelli et al., 2015). The variations of Y and Z have a strong impact on the lithium burning because they change both the extension of the convective envelope and the temperature inside a star (see e.g., Piau and Turck-Chièze, 2002; Tognelli, 2013; Tognelli et al., 2015); the uncertainty on the chemical composition can produce a variation of the surface lithium abundance up to one order of magnitude, especially in stars with $M \lesssim 0.7\,M_\odot$. The effect reduces at larger masses.

Tognelli (2013) quantitatively evaluated the impact on the predicted surface lithium abundance of the uncertainties in the input physics and in the initial chemical composition discussed above, calculating upper and lower limits of surface ^{7}Li in stellar models. **Figure 13** shows the estimated upper/lower limits (plotted as error bars) of surface lithium abundance and effective temperature, due to the contribution of the input physics uncertainties (top panel) and chemical composition indeterminacy (bottom panel). Stars with different masses at different ages typical of young clusters are shown (for more details on the procedure adopted to obtain these limits see Tognelli et al., 2012; Tognelli, 2013). The errors on the present input physics and the typical uncertainties on the adopted chemical composition have a drastic impact on the predicted

[5]With *alpha enhancement* one indicates an enhancement of the relative abundance of α elements (C, O, Ne, Mg, Si, S, Ar and Ca) with respect to the solar composition. It is generally expressed as: $[\alpha/Fe] = \log(N_\alpha/N_{Fe})_{\rm star} - \log(N_\alpha/N_{Fe})_\odot$.

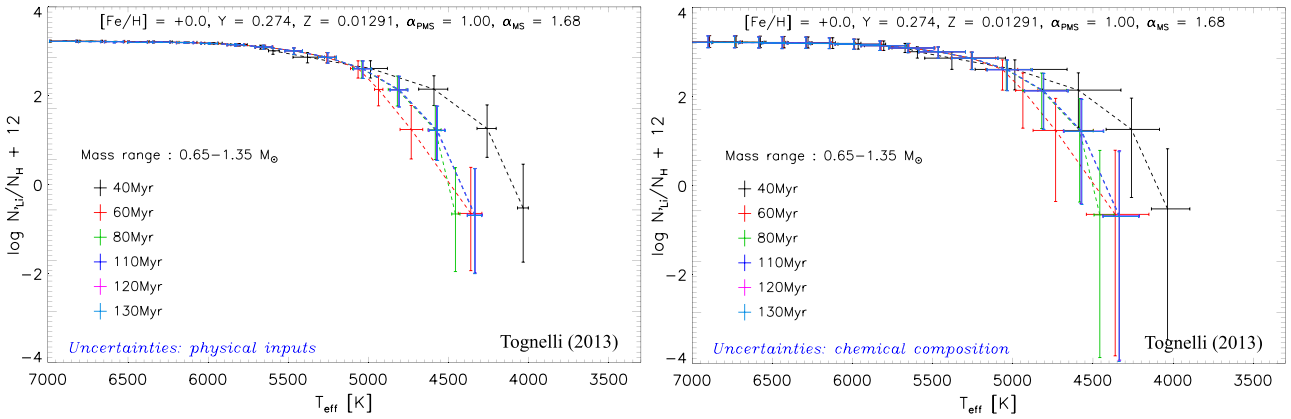

FIGURE 13 | Uncertainties on surface lithium abundance and effective temperature due to the errors on adopted input physics (left panel) and chemical composition (right panel). Figure adapted from Tognelli (2013).

surface lithium abundance, which can vary by more than one order of magnitude, especially for stars with $T_{\rm eff} \lesssim 4700$ K.

In standard models, the only possibility to deplete surface lithium in pre-MS is via convective mixing. If the bottom of the convective envelope reaches a region hot enough to burn lithium, then the surface lithium decreases in time. The level of depletion depends on a key parameter in convective stars, which is the efficiency of convective energy transport. A more efficient convective transport produces hotter stars that consequently experience a more efficient lithium burning. The opposite occurs if the convection efficiency reduces.

A precise physical treatment of external convection would require three-dimensional hydrodynamic models which have been improved in recent years, but only for limited regions of the star corresponding mainly to the atmospheric regions (see e.g., Nordlund et al., 2009; Collet et al., 2011; Freytag et al., 2012; Magic et al., 2013; Trampedach et al., 2013; Trampedach et al., 2014; Trampedach et al., 2015; Pratt et al., 2016, and references therein). These codes are state-of-the-art (magneto) hydrodynamic code that solves the time-dependent hydrodynamic equations for mass, momentum, and energy conservation, coupled with the 3D radiative transfer equation, in order to correctly account for the interaction between the radiation field and the plasma. However, hydrodynamic calculations still cannot cover the wide range of physics quantities needed to model the Galactic stellar populations. Moreover, their results cannot be easily adopted in stellar evolutionary codes, although attempts to implement approximations directly based on 3D simulations in 1D stellar models exist in the literature (e.g., Lydon et al., 1992; Ludwig et al., 1999; Arnett et al., 2015; Arnett et al., 2018). The commonly adopted procedure to treat the convection efficiency in super-adiabatic regimes in 1D stellar evolution codes relies on mixing-length theory (MLT) (Böhm-Vitense, 1958), where convection efficiency depends on the free parameter $\alpha_{\rm ML}$. A variation of such a parameter can produce a large effect on the surface lithium abundance at a given age in stars with a super-adiabatic envelope. This effect is particularly important in stars with masses larger than about 0.5–0.6 $M_\odot$. It has been shown in the literature that models with a reduced convection efficiency ($\alpha_{\rm ML} < \alpha_{\rm ML\odot}$, solar calibrated value) attains a better agreement with data for both young clusters and binary stars (Piau and Turck-Chièze, 2002; D'Antona and Montalbán, 2003; Tognelli et al., 2012).

Figure 14 shows the results obtained by Tognelli et al. (2012) where the observed surface lithium abundance in five young open clusters (IC2602, α Per, Blanco1, Pleiades and NGC2516) has been compared to theoretical predictions obtained adopting two different values for the mixing length parameter during the Pre-MS phase: one calibrated on MS stars to reproduce their colors and the other corresponding to a much less efficient convective energy transport. The best value to be used in pre-MS has been estimated in order to reproduce the A(Li) vs. $T_{\rm eff}$ pattern. The availability of young clusters to perform such an analysis (ages below 100–150 Myr) is mandatory to avoid possible effects due to MS non-standard mixing processes which act on timescales of the order of ~ Gyr. Referring to **Figure 14**, it is evident that in all cases, the adoption of a constant value of $\alpha_{\rm ML}$ (calibrated on MS stars) produces a lithium depletion much larger than observed. On the other hand it is possible to tune $\alpha_{\rm ML}$ during the pre-MS to reproduce the observed lithium pattern and the most important result is that the derived $\alpha_{\rm ML}$ in pre-MS is independent of the cluster age and on the stellar mass. The authors derived a value of $\alpha_{\rm ML,PMS} = 1$. We mention that the reduction of the efficiency of superadiabatic convection in stellar envelope has been put forward as a plausible mechanism to explain the discrepancies in the radius observed and predicted in pre-MS binary systems. A value of $\alpha_{\rm ML} \sim 1$ has been suggested to explain the radius in young binary systems (see e.g., Gennaro et al., 2012).

As said, $\alpha_{\rm ML}$ is a free parameter which reflects the present not precise knowledge of external convection efficiency, thus one should find a physical reason for its variation during the evolution of a given star. A reduced convection efficiency could be motivated by the attempt in 1D evolutionary codes to mimic the main effects of some non-standard mechanisms active in young stars, such as the presence of a not negligible magnetic field (especially in the convective region, see e.g., Ventura et al., 1998).

To this regard (Feiden and Chaboyer, 2013) found that the inclusion of a magnetic field in partially convective stars produces a radius expansion caused by the inhibition of convection efficiency in the convective envelope (see also Feiden and Chaboyer, 2012). **Figure 15** shows the results of their work on evolutionary models computed with and without the inclusion of a magnetic field. The models are compared to the characteristics of YY Gem binary system (both stars have masses of about 0.6 $M_{\odot}$ Torres and Ribas, 2002). Such a system exhibit evidences of a relatively strong magnetic field (surface spots, X-ray, gyrosynchrotron radio emissions, flaring events). Standard models underestimate the radius of the components by about 8%, a difference that can be erased if a magnetic field of 4–5 KG is included in the computations. The stronger is the magnetic field the larger the radius of the star at the same age (left panel). In the radius vs. $T_{\rm eff}$ plane, the inclusion of a magnetic field produces a cooler and brighter star (see right panel of **Figure 15**). Feiden and Chaboyer (2013) also showed that it is possible to reproduce the main effects of a magnetic field in 1D non-magnetic stellar models by using a properly tuned value of the mixing length parameter. To do this an $\alpha_{\rm ML}$ value lower than the solar calibrated one (i.e., close to unity) should be adopted.

The presence of a magnetic field makes the star cooler and modifies the temperature stratification inside the star: this has a direct impact on surface lithium burning efficiency (Feiden, 2016). **Supplementary Figure S1** shows the comparison between the expected surface lithium abundance as a function of $T_{\rm eff}$ in standard non magnetic models of 5 and 10 Myr compared to a model of 10 Myr in which a magnetic field is included [the magnetic field strength $B_{\rm eq}$ shown in figure varies with the mass but in the mass range 0.1–1 $M_{\odot}$ it is of the order of 2–2.6 KG]. The inclusion of the magnetic field has a strong impact on the resulting lithium abundance, drastically reducing the level of depletion and thus pointing in the direction to improve the agreement between data and model predictions for pre-MS stars.

Another aspect related to the presence of magnetic field in the star is the possibility to include in stellar models a surface spots coverage fraction (see e.g., Jackson and Jeffries, 2014; Somers and Pinsonneault, 2015). The effect of the spots is to reduce the outgoing flux at the stellar surface producing a radius inflation and a decrease of the stellar effective temperature. Such an effect goes in the same direction of an artificially decreased convection efficiency and, as expected, leads to a cooler envelope and to a less efficient lithium burning. **Supplementary Figure S2** shows an application of stellar models with surface spots to the surface lithium abundance observed in the Pleiades cluster (see Somers and Pinsonneault, 2015). Standard models predict a level of pre-MS lithium depletion larger than that observed. The agreement can be restored assuming that a certain fraction of the stellar surface is covered by spots; increasing the coverage fraction, the models are cooler and thus the surface lithium depletion is reduced. It's important to notice that the presence of magnetic fields of different strength or a different spot coverage fraction in stars with similar mass can introduce a star-to-star scatter in the surface lithium abundance. This could partially answer another important open question about young clusters, i.e., which is the cause of a spread in the lithium abundance, measured in stars with similar effective temperature. The extent of such spread is much larger than the quoted uncertainties, so it represents a real spread (see e.g., Xiong and Deng, 2006). The inclusion of a different surface spots coverage or different magnetic fields strength could produce stars with similar effective temperatures (but different total masses) thus leading to an apparent dispersion in the lithium abundance.

Additional mechanisms that can alter the level of lithium burning in stars have been analyzed in the literature. An induced extra mixing due to the presence of rotation, gravity waves, diffusion, or mass loss has been put forward to reproduce the surface lithium abundance pattern typical of older stars (ages $\gtrsim$500 Myr). However, such mechanisms are not relevant for the evolution of young pre-MS stars and thus we will not discuss them in this context (see e.g., Landin et al., 2006; Eggenberger et al., 2012; Charbonnel et al., 2013).

5.5 Uncertainties on Atmospheric Models for Surface Lithium Abundance Determination

The determination of surface element abundances involves the interpretation of the observed absorption lines through atmospheric models as accurate as possible. However modeling stellar atmospheres is a difficult task and the uncertainties on the measurements of surface element abundance clearly affects the comparison between theory and observations. Here we limit to briefly discuss the main difficulties in modeling realistic stellar atmospheres, the interested reader can find more details in other reviews (see e.g., Jofré et al., 2019).

The photosphere of low mass stars is covered with a complex and stochastic pattern – associated with convective heat transport – of downflowing cooler plasma and bright areas where hot plasma rises, the so called granulation (Nordlund et al., 2009). As already discussed, convection is a difficult process to understand, because it is non-local and three-dimensional, involving non-linear interactions over many disparate length scales. In recent years it has become possible to use numerical three-dimensional (3D) radiative hydrodynamical (RHD) codes to study stellar convection in atmosphere such as STAGGER CODE (Nordlund et al., 2009; Collet et al., 2011) and CO5BOLD (Freytag et al., 2012). Nowadays, the use of large grids of simulations covering a substantial range of values of effective temperature and surface gravity for stars in different regions of the HR diagram (Ludwig et al., 2009; Magic et al., 2013; Trampedach et al., 2013) have proven that the convection-related surface structures have different size, depth, and temporal variations, depending on the stellar type (Beeck et al., 2013; Tremblay et al., 2013; Magic and Asplund, 2014). Moreover, the related activity (in addition to other phenomena such as magnetic spots, rotation, dust, etc.) has an impact in stellar parameter determination (Bigot et al., 2011; Chiavassa et al., 2012; Creevey et al., 2012), radial velocity (Allende Prieto et al., 2013; Chiavassa et al., 2018), chemical abundances estimates (Asplund et al., 2009; Caffau et al., 2011), and photometric colors (Bonifacio et al., 2018; Chiavassa et al., 2018).

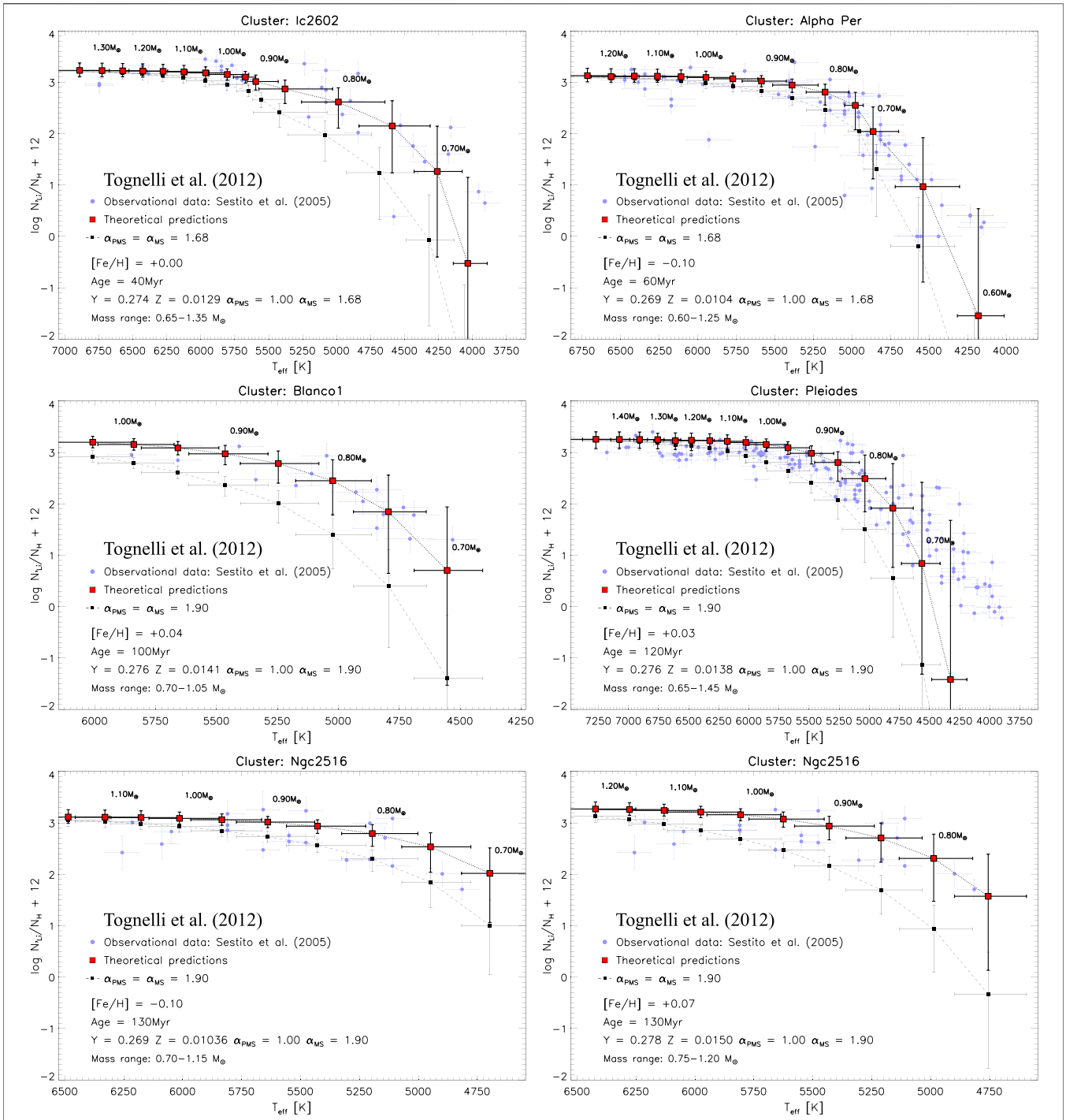

FIGURE 14 | Comparison between data and theoretical model predictions for surface lithium in young clusters. Models with the same mixing length parameter in pre-MS and MS phases, calibrated with MS stars, are shown as dashed lines while models with calibrated convection efficiency in MS and artificially reduced mixing length parameter (α_{ML} = 1) in pre-MS are shown as continuous lines. In the case of NGC2516, the models were computed using two different values of [Fe/H], [Fe/H] = -0.10 (bottom left panel) and [Fe/H] = +0.07 (bottom right panel), as reported in the literature. Figure adapted from Tognelli et al. (2012).

Chemical abundance ratios inferred from spectra of cool stars is based on the understanding of limitations and uncertainties of spectroscopic analyses. In this context, radiation transfer in the atmospheres of late-type stars generally takes place under non-local thermodynamic equilibrium (NLTE) conditions, rather than the idealized LTE (Asplund, 2005). The full 3D NLTE treatment would require to compute NLTE radiative transfer inside radiative hydrodynamical simulations and coupling it to

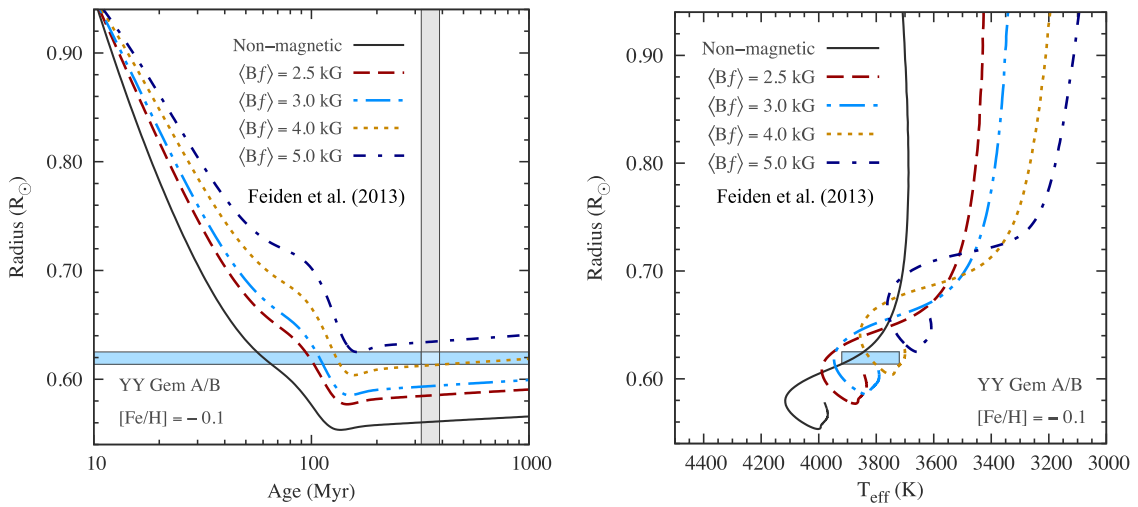

FIGURE 15 | Effect of magnetic fields (for the labeled surface magnetic field strength <B *f*>) on the radius evolution of a partially convective pre-MS star (M = 0.599 $M_{\odot}$). The radius is compared to that of the observed YY Gem binary system (horizontal and vertical stripes). Left panel: radius vs. age. Right panel: stellar radius vs. T_{eff} for magnetic and non magnetic models. Figure adapted from Feiden and Chaboyer (2013).

the equations of gas movements. In these simulations the computational cost is dominated by the radiative transfer calculations which can be greatly reduced by adopting an approximated solution based on the opacity binning or multi-group method (Nordlund, 1982). However, introducing NLTE calculations at this stage would largely increase the computation time making very complicated to obtain a relaxed simulation. This is why 3D NLTE radiative transfer calculations are only affordable in a post-processing manner, i.e., each 3D RHD simulation is computed in LTE and then the so called <3D> models are computed averaging multiple snapshots of 3D RHD simulations over regions of equal optical depth and over the time series (e.g., Asplund et al., 2004; Caffau et al., 2009; Magic et al., 2013; Lind et al., 2017; Nordlander et al., 2017; Amarsi et al., 2018). This approach offers a middle-ground between full 3D NLTE and 1D NLTE, by accounting for NLTE in model atoms of arbitrary size, and through the use of time-independent 1D structures derived from the full 3D hydrodynamic simulations (Bergemann et al., 2017). Using this method, Wang et al. (2021) derived a new 3D NLTE solar abundance of A(Li) = 0.96 ± 0.05, which is 0.09 dex lower than the commonly used value and provided a grids of synthetic spectra and abundance corrections publicly available. Eventually, it has also become possible to undertake large samples of observations from disk and halo stars with this 3D NLTE analysis (Amarsi et al., 2019; Bergemann et al., 2019). Unluckily at present 3D atmospheric calculations are not still available for Pre-Main Sequence atmospheres.

The measurement of surface lithium abundances constitutes an important example of efforts undertaken in this field. In Sec. 5 we mentioned that the stellar surface abundance of ^{6}Li is expected to be negligible, moreover its identification is very difficult. The presence of ^{6}Li in metal-poor halo stars can only be derived from the asymmetry in the red wing of the ^{7}Li doublet line at 670.8 nm. Several authors attempted to detect ^{6}Li using 1D hydrostatic models and assuming LTE for a number of metal-poor stars with [Fe/H], lower than −2 dex (Cayrel et al., 1999; Asplund et al., 2006). Cayrel et al. (2007) pointed out that the intrinsic line asymmetry – due to the stellar surface convection – in the ^{7}Li doublet would be almost indistinguishable from the asymmetry produced by a weak ^{6}Li blend on a (presumed) symmetric ^{7}Li profile.

The total line strength of the Li resonance line determines the ^{7}Li-abundance and the shape of the line profile determines the isotopic ratio due to the shift between ^{6}Li and ^{7}Li isotopic components. Thus it's critical to resolve the strongly differential NLTE effects on the granules and inter-granular regions (**Supplementary Figure S3**), because they have a preferential influence over the blue- and red-shifted part of the line profile, respectively (Lind et al., 2013). To investigate this aspect, Steffen et al. (2012) and Lind et al. (2013) used a 3D NLTE treatment with 3D RHD simulation snapshots carried out with CO5BOLD and STAGGER CODE, respectively. They re-analyzed the Li feature in some metal-poor stars and were not able to confirm the previous claimed detection of ^{6}Li. However, they pointed out that a full understanding of 3D NLTE line formation is necessary to make correct measurements of ^{6}Li, even though from their studies they could give only upper limits for the isotopic ratio ^{6}Li/^{7}Li. In particular, the 3D NLTE approach is important to characterize the calibration lines, to decrease the observational error. Eventually, a very recent publication by González Hernández et al. (2019), confirms the non detection of ^{6}Li for a very metal poor binary star [(Fe/H) ∼−3.7 dex], finding an upper limit for the isotopic ratio of ^{6}Li/^{7}Li < 10%.

6 EFFECTS OF LIGHT ELEMENT BURNING CROSS SECTIONS ON PRE-MAIN SEQUENCE CHARACTERISTICS AND ON LIGHT ELEMENT SURFACE ABUNDANCES

The predicted temporal evolution of light elements is affected by the stellar evolutionary stage and by the model structure, which depends on the input physics adopted in the computations. One of the key ingredients is the adopted light element burning cross section, as derived from measurements of indirect/direct processes. Thus it's worth discussing how the recent determination of such cross sections at energies relevant for stellar evolution have changed the prediction of surface light element abundances in low mass stars.

For stellar calculation the reaction rate of a two body process can be written in the following way (see e.g., Rolfs and Rodney, 1988),

$$N_A\langle\sigma v\rangle_b = \sqrt{\frac{8}{\pi\mu}}\,\frac{N_A}{(K_BT)^{\frac{3}{2}}}\int_0^{+\infty}\sigma(E)_b E e^{-\frac{E}{K_BT}}dE\ \left(\mathrm{cm^3 mol^{-1} s^{-1}}\right) \tag{4}$$

where $\sigma(E)$ is the cross section of the process, the subscript b means that the reaction rate is for two bare nuclei (i.e., without any electron screening effect), T is the temperature in Kelvin (K). In stellar evolution calculations, the energy at which the process occurs are generally so small that it is convenient to write the cross section in terms of another quantity called the astrophysical factor $S(E)$ defined as it follows,

$$S(E)_b = E\sigma(E)_b e^{2\pi\eta(E)} \tag{5}$$

with $\eta(E)$ the Sommerfeld parameter related to the tunnel effect of two interacting charged particles, that can be written as:

$$2\pi\eta(E) = \frac{Z_1Z_2e^2}{2\varepsilon_0\hbar}\sqrt{\frac{\mu}{2E_{\mathrm{cm}}}} = 31.3998Z_1Z_2\sqrt{\frac{A_\mu}{E_{\mathrm{cm}}\,(\mathrm{KeV})}} \tag{6}$$

where $\mu = m_1m_2/(m_1+m_2)$ is the reduced mass and A_μ is the same quantity but expressed in atomic mass units (amu), $E_{\mathrm{cm}}\,(\mathrm{KeV})$ is the energy in the center of mass expressed in KeV. Using this quantity, **Eq. 4** assumes the following form,

$$N_A\langle\sigma v\rangle_b = \sqrt{\frac{8}{\pi\mu}}\,\frac{N_A}{K_BT^{\frac{3}{2}}}\int_0^{+\infty}S(E)_b e^{-2\pi\eta(E)-\frac{E}{K_BT}}dE\ \left(\mathrm{cm^3 mol^{-1} s^{-1}}\right) \tag{7}$$

For many application in stellar astrophysics, it is possible to expand the astrophysical factor around a specific value of the energy, thus obtaining,

$$S(E) \approx S(E_0)\left[1 + \frac{S'(E_0)}{S(E_0)}(E-E_0) + \frac{1}{2}\frac{S''(E_0)}{S(E_0)}(E-E_0)^2 + \dots\right] \tag{8}$$

The quantity E_0 is also known as the Gamow peak energy, and it corresponds to the energy where the exponential quantity inside the integral in **Eq. 7** has its maximum value. E_0 is defined in the following way (Rolfs and Rodney, 1988),

$$E_0 = 1.22\left(A_\mu Z_1^2 Z_2^2 T_6^2\right)^{\frac{1}{3}}\ (\mathrm{KeV}) \tag{9}$$

with T_6 the temperature expressed in million kelvin.

The expansion of $S(E)$ given above depends on the temperature at which the considered reaction occurs (thorough E_0), which in turn depends on the stellar mass. However, at low energy typical of reactions in stars, $S(E)$ varies slowly with the energy, thus it is convenient to expand $S(E)$ around $E \approx 0$: in this case the reaction rate can be evaluated knowing $S(0)$ and its derivatives [usually it is enough to have $S'(0)$ and $S''(0)$].

Light element (p,α) reaction rates have been recently revised through the indirect Trojan Horse Method (THM, see e.g., Baur, 1986; Spitaleri et al., 2003; Spitaleri et al., 2016; Spitaleri et al., 2019 and references therein), which is particularly useful to measure cross sections at astrophysical energies by-passing extrapolation procedure, often affected by systematic uncertainties due, for instance, to electron screening effects. THM allows to measure the astrophysically relevant cross sections in correspondence, or very close, to the Gamow peak without experiencing the lowering of the signal-to-noize ratio due to the presence of the Coulomb barrier between the interacting charged particles. Moreover in the last years THM was successfully applied to reactions induced by unstable beams Pizzone et al. (2016) and Lamia et al. (2019) as well as neutron induced reactions which may play a role also in the context of light element nucleosynthesis and BBN. In particular the ^{3}He(n,p)^{3}H was studied at the astrophysically relevant energies (see Pizzone et al., 2020 and references therein). THM was also applied to reactions between heavier systems, which are relevant in the late stellar evolutionary stages (Tumino et al., 2018). We will discuss the effects of these improvements and of the present errors on nuclear cross sections on the light elements surface abundance calculations in pre-Main Sequence stars.

6.1 Effects of Deuterium Burning Cross Sections on pre-MS Evolution

As discussed in Sec. s 3, 4.3 and 4.4, deuterium burning plays a crucial role in the first stages of pre-MS or protostellar evolution. The value of the cross section of the p(D,γ)^{3}He process in stellar conditions has been reported by several authors (see Adelberger et al., 2011 for a review) both from measurements and theoretical calculations along with its uncertainty. Adelberger et al. (2011) redetermined the best value for the astrophysical factor $S(E)$ for such a reaction at zero energy [$S(0)$] and the uncertainty on it, concluding that the current uncertainty on $S(0)$ for such burning reaction is $\approx 7\%$. Recently, Mossa et al. (2020) redetermined the D+p cross sections at energies typical of the BBN (between 32–263 KeV) – thus larger than those used in stellar calculations – estimating an uncertainty of about 3%.

We tested the impact on pre-MS evolution of the D+p cross section variation, using the uncertainty given by Adelberger et al. (2011) at stellar energies, which is ± 7%. Such a variation of the deuterium burning reaction rate produces a negligible effect on the stellar structure evolution. The negligible effect is related to the large dependency on the temperature of the p(D,γ)^{3}He burning channel (about T^{12}); if $S(0)$ is artificially varied (e.g., reduced) by 7% (independently of the temperature), to obtain the same energy production rate, which sustains the star, an increase of the burning temperature is required. However, given the high temperature dependency of the rate, a very small temperature variation is enough to restore the energy production. Thus the models are essentially unaffected by the current uncertainty on the p(D,γ)^{3}He reaction rate. From this analysis we can conclude that the main uncertainty source on the D-burning phase in stellar models is the error on the initial deuterium abundance which can be as large as 50% as discussed in **Section 4.4**.

Recently Tumino et al. (2014) (see also Tumino et al., 2011) measured the reaction rate for two additional channels involving the D-burning, namely the D(D,p)^{3}H and the D(D,n)^{3}He processes, using the THM; such burning channels could potentially contribute to the D-burning in stars. **Supplementary Figure S4** shows, for the quoted reactions, the THM rates compared to the ones of still widely used NACRE compilation (Angulo et al., 1999), of the JINA REACLIB (Cyburt, 2004) and to the (Descouvemont et al., 2004) rates. The estimated uncertainty on the analyzed burning channels (of about 5%) are also shown. At temperatures typical of stellar deuterium burning (~10^6 K) the D(D,p)^{3}H is about 5% larger than the NACRE, while it is much larger (about 15%) than the value reported in Cyburt (2004). The differences sensitively reduce at larger temperatures, more important for cosmological calculations. If the Descouvemont et al. (2004) rate is considered, the difference with THM is very small at stellar temperatures (below 1%), while it increases at larger temperatures, reaching about 5% at $T \sim 10^9$ K.

The new THM rate for the D(D,n)^{3}He reaction is ~10% larger than the others (NACRE, JINA and (Descouvemont et al., 2004)) for temperatures smaller than about 5×10^7 K. At larger temperatures the differences reduce and for $T \gtrsim 2 \times 10^8$ K the THM rate is smaller than the others by about 5–10%. Tumino et al. (2014) evaluated the effect of the new rates in stellar models, showing that the change in the cross sections does not produce any effect on the stellar structure. The result was expected because such burning channels are quite negligible in stellar models, where D is mainly destroyed via the p(D,γ)^{3}He channel. On the contrary, these reactions could be more important for BBN (Cyburt, 2004; Coc and Vangioni, 2010). Tumino et al. (2014) estimated that the new reaction rates could result in a variation of the primordial deuterium abundance inferred from the BBN by about 2%, while an impact on the ^{7}Li abundance up to about 10% is expected.

6.2 Stellar Surface Abundance of Light Elements and Updated (p,α) Reaction Rates

The energy produced in the Li, Be and B nuclear reactions is negligible and such reactions do not affect stellar structures evolution. However, the surface abundances of light elements strongly depend on the nuclear burning (Tognelli et al., 2019). The different fragility of Li, Be and B against (p,α) destruction reactions potentially allows to investigate the characteristics of different depths of the stellar interior.

In **Supplementary Figures S5, S10** the reaction rates for the most relevant light element burning (p,α) reactions calculated with the THM are shown and compared with the JINA REACLIB and the less recent, but still widely used, NACRE rates. The results are discussed below.

6.2.1 ^{6}Li and ^{7}Li Surface Abundance and (p,α) Reaction Rates Efficiency

The first attempts to apply THM (p,α) reaction rates to pre-MS lithium surface abundance calculations were performed by Pizzone et al. (2003) and Pizzone et al. (2005) (hereafter pt05) and successively updated, after re-normalization to recently released direct data, in Lamia et al. (2012) and Lamia et al. (2013). The left panel of **Supplementary Figure S5** shows the ^{6}Li(p,α)^{3}He reaction rate obtained using the THM compared to the pt05 rate available on the JINA REACLIB page. The THM estimated rate deviates from the pt05 by about 15% at a temperature of T ≈ 10^6 K, typical of ^{6}Li burning in the pre-MS phase, a value that is larger than the current estimated uncertainty (about 10%) on the rate itself.

Lamia et al. (2013) evaluated the effect on the surface ^{6}Li abundance of the update of the ^{6}Li+p reaction rate for a range of stellar masses at three different metallicities [(Fe/H) = −0.5, −1.0, and −2.0]. **Supplementary Figure S6** shows the time evolution of the surface ^{6}Li abundance – normalized to the original value– obtained adopting the three different ^{6}Li(p,α)^{3}He reaction rates – THM, JINA (pt05), and NACRE. From **Supplementary Figure S6** it is evident that ^{6}Li depletion, at fixed burning reaction rate, varies significantly for different masses and metallicities. This can be understood recalling that the higher the metallicity (or the lower the stellar mass) the deeper and hotter the base of the convective envelope. Note that among the most massive models (i.e., M = 1.2 $M_\odot$), which have the thinnest external convective envelopes, only that with the highest metallicity [i.e., (Fe/H) = −0.5] efficiently depletes surface ^{6}Li. In the selected [Fe/H] range, the difference in the ^{6}Li depletion between the THM and NACRE models ranges from about 13% (for M = 1.2 $M_\odot$) to about 60% (for M = 1.0 $M_\odot$). The difference reduces if JINA rate is adopted, as expected due to the smaller differences between the two rates.

Right panel of **Supplementary Figure S5** shows the comparison between the THM and NACRE ^{7}Li + p reaction rate; the difference is of about 13% at a temperature of T ≈ 10^6 K, not much larger than the current uncertainty on the rate (about 10%). **Supplementary Figure S7** shows the time evolution of the surface ^{7}Li abundance for different masses when THM and NACRE ^{7}Li + p reaction rates are adopted. The differences

between the two calculations range from about 7% (for $M = 1.0\,M_\odot$) to about 25% (for $M = 0.6\,M_\odot$).

In general, the effect of adopting different ^{6}Li and ^{7}Li burning reaction rates, although not negligible, is less important than the effects due to errors in other quantities used in the computation of a stellar model, such as the original chemical composition, external convection efficiency, or the uncertainties in some other physical inputs adopted in the calculations (e.g., opacity and equation of state, see **Sec. 5.4** and the discussions in Pizzone et al., 2010 and Tognelli et al., 2012). Thus, at the moment an uncertainty on the burning reaction rate of the order of 10% is not the main error source in the determination of the surface lithium abundance in stellar models (Lamia et al., 2012; Lamia et al., 2013).

6.2.2 Lithium Depletion Boundary

In the mass range $M \approx 0.06 - 0.4\,M_\odot$ (the exact values depending on the chemical composition), ^{7}Li is completely destroyed in pre-MS in fully convective structures. The larger is the mass the higher is the temperature inside the star, and consequently the earlier is the onset of lithium burning. The larger temperature in more massive stars produces also a more efficient lithium burning, and consequently the age at which lithium is fully depleted in such convective stars strongly depends on the stellar mass. In a coeval population of stars with ages between about 15 and 350 Myr, one would expect to observe a sharp transition in very low-mass regime between stars with and without surface lithium at a given mass (corresponding to the higher stellar mass that, at the cluster age, fully destroy lithium). Such a transition, usually called the Lithium Depletion Boundary (LDB), is a powerful age indicator (see e.g., D'Antona and Mazzitelli, 1994) thanks to the connection between luminosity, mass and age. **Supplementary Figure S8** shows an example of the age vs. luminosity relation for stars located at the LDB in the mass range $[0.06 \div 0.4]\ M_\odot$.

The method of LDB has been successfully adopted to assign ages to young clusters as a competitive method to the use of isochrone fitting (e.g., Barrado y Navascués et al., 1999; Oliveira et al., 2003; Jeffries and Oliveira, 2005; Manzi et al., 2008; Dobbie et al., 2010; Jeffries et al., 2013; Binks and Jeffries, 2014; Juarez et al., 2014; Dahm, 2015; Dupuy et al., 2016; Martín et al., 2018; Martín et al., 2020 and references therein). The uncertainties on age determination through the LDB technique have been analyzed in Burke et al. (2004) and, more recently, in Tognelli et al. (2015); the main uncertainties that potentially affect the LDB age determination are those already discussed in **Section 5.4**. **Supplementary Figure S9** shows the relative age uncertainty on LDB age determination obtained by Tognelli et al. (2015) taking into account the errors on the adopted input physics and chemical composition. The shaded area has been obtained by a cumulative variation of all the considered input physics and chemical abundances within their uncertainties (going into more detail would require a too long discussion out of the purposes of this review, see the quoted paper for additional information). The uncertainty of the method depends on the stellar luminosity (or mass) at the LDB, which, in turn, translates in an age, but it is in any case lower than about 10%. As a general comment, faint stars that correspond to LDB ages of the order of 50–60 Myr ($0.06 \lesssim M/M_\odot \lesssim 0.1$) have errors of the order of about 5%, an uncertainty that increases increasing the stellar luminosity at the LDB and thus the derived age. Tognelli et al. (2015) showed that a large part of the uncertainty on the LDB ($\sim 40\%$) comes from the chemical composition indetermination while the lithium burning rate causes a variation of the LDB age of about 1%.

6.2.3 ^{9}Be and ^{10}B Surface Abundance and (p,α) Reaction Rates Efficiency

Supplementary Figure S10 shows the comparison between the recent THM reaction rates and other reaction rates used in the literature. The THM ^{9}Be(p,α)^{6}Li rate (at temperatures of few million degrees) is about 25% larger than NACRE and the uncertainty on the THM ^{9}Be burning rate is about 25% (blue dashed area in the figure). The THM reaction rate is quite similar to that in the recent NACRE II (Xu et al., 2013), even if the THM uncertainty region is sensibly smaller than that of the NACRE II rate, see (Lamia et al., 2015). Left panel of **Supplementary Figure S11** shows the comparison between the predicted surface Be abundances computed using the THM reaction rate and the NACRE reaction rate, for solar metallicity stars. The higher THM rate leads to a faster ^{9}Be destruction consequently, at the same age, models with the THM rate show a lower ^{9}Be surface abundance with respect to models with the NACRE rate. The differences in the predicted surface abundances are significant in those models where ^{9}Be is efficiently destroyed (i.e., for $M \lesssim 0.5\,M_\odot$).

We recall that in stars, ^{9}Be is destroyed through two channels: ^{9}Be(p,α)^{6}Li (R_1, the rate analyzed by Lamia et al., 2015) and ^{9}Be(p, 2α)^{2}H (R_2). The ratio $R_1/R_2 \approx 1.2$, for stellar conditions at the temperature of interest; thus the R_2 contribution to beryllium destruction is not negligible. Changing only R_1, as done in Lamia et al. (2015) affects the final beryllium abundance by a factor that is given by the R_1 reaction rate change (about 25%) multiplied by the probability that the ^{9}Be burning occurs in that channel, i.e., $25\% \times R_1/(R_1 + R_2) \approx 14\%$, thus leading to a change in the predicted Beryllium abundance lower than what expected if only R_1 channel was active in stars. The effect of the THM uncertainty on the ^{9}Be(p,α)^{6}Li rate – approximately 25% which is equal to the difference with respect to NACRE rate – is expected to produce a variation of the predicted ^{9}Be surface abundance of the same order of magnitude discussed above.

Right panel of **Supplementary Figure S10** shows the comparison between the THM and the NACRE rate for the ^{10}B(p,α)^{7}Be reaction: at temperatures of a few millions of kelvin, the THM rate is ~30% lower than the NACRE one. The error of the THM rate at the temperatures of interest is about 20%. However if the THM rate is compared with the one of the updated NACRE II Compilation (Xu et al., 2013), the differences are significantly reduced, see (Lamia et al., 2015).

The effect of the different ^{10}B(p,α)^{7}Be reaction rates on surface B abundance in low mass stars (at solar metallicity) is shown in the right panel of **Supplementary Figure S11**. The lower THM ^{10}B(p,α)^{7}Be cross section leads to a smaller ^{10}B destruction and thus to a larger surface ^{10}B abundance at a fixed age. Due to the higher ^{10}B burning temperature with respect to ^{9}Be, the effect of

reaction rate change is significant only for masses $M \lesssim 0.4\,M_{\odot}$. Also notice that the typical timescale at a fixed mass where ^{10}B is destroyed is longer than that of ^{9}Be.

For completeness in **Supplementary Figure S11** we point out for ages typical of MS evolution [e.g., $\log t \gtrsim 8.5$ for $M = 0.5\,M_{\odot}$ for the ^{9}Be abundance behavior and for $M = 0.4\,M_{\odot}$ for ^{10}B] the effect of microscopic diffusion, which leads to the settling of light elements toward the stellar interior.

Supplementary Figure S12 shows the surface logarithmic abundances of ^{9}Be and ^{10}B as a function of the effective temperature, $T_{\rm eff}$. Although observational ^{9}Be and ^{10}B abundances are still not available for the low temperature/mass regimes typical of efficient ^{9}Be and/or ^{10}B burning, it is worth to estimate the role of the improvements in nuclear physics in surface abundance predictions. The models are computed using the THM and NACRE reaction rates discussed above; we remind that $T_{\rm eff}$ is not affected by the change of the (p,α) rates. Each curve represents the abundance isochrone, i.e., the locus of models with the same age but different masses. For those models where ^{9}Be (^{10}B) burns the differences between the adoption of the NACRE and THM reaction rates can be as large as about 0.2–0.3 dex for ^{9}Be and almost 1 dex for ^{10}B.

To our knowledge, an analysis of the dependence of surface ^{9}Be or ^{10}B abundances on the errors in input physics and chemical composition adopted in the calculations is not available in the literature. However, it's a good approximation assuming a Be and B burning sensitivity to the input physics similar to that obtained for ^{7}Li, as the burning temperatures are not much different. Under this assumption, the effects of the uncertainty on (p,α) Be and B burning reaction rates is not the dominant error source for the surface abundance predictions of such elements.

7 SUMMARY AND CONCLUSION

Surface light elements abundances prediction in stellar models is a difficult task because it's affected by several errors in the adopted input physics and uncertainties in the efficiency of some physical mechanisms as e.g., convection in the stellar envelope. Moreover, pre-MS characteristics and surface light element abundances depend on the previous protostellar phase, which is the phase when the star forms. Analysis of the effects of different choices of accretion parameters (accretion rate, radius and mass of the first stable hydrostatic protostar, accretion history, accretion geometry, the amount of energy transferred from the accreted matter to the accreting star, etc..) on the subsequent pre-MS evolution have been performed in the literature. The results show that if the accretion process leads to bright and extended structures at the end of the protostellar phase the stellar characteristics (including the surface light element abundances) are very similar to those of standard (non-accreting) pre-MS models with the same final mass. The structure of a pre-MS star at the end of the accretion phase is affected by the inclusion of the protostellar accretion only for a restricted range of accretion parameters, mainly in the so called "cold accretion scenario." In these cases a significant reduction of the surface light element abundances during the protostellar phase (in contrast to standard models) has been obtained; however the position of the stars in the HR diagram is in disagreement with observations for disk stars, rising doubts about the validity of the adopted accretion parameters.

Protostellar accretion in low mass halo stars was suggested in the literature as one of the possible solutions for the cosmological lithium problem. However, theoretical calculations show that the reproduction of the Spite Plateau would require a fine tuning of the parameters that govern the protostellar phase and, more important, the models with the required Li depletion follow a pre-MS evolution in the HR diagram which is quite different to the one observed for high metallicity pre-MS stars. Comparison between theoretical predictions and observations for surface lithium abundance in young open clusters still show discrepancies. During the pre-MS phase surface Li abundance is strongly influenced by the nuclear burning as well as by the extension toward the interior of the convective envelope and by the temperature at its bottom. These last two quantities depend on the input physics adopted in the calculations (radiative opacity, atmospheric models etc..), on the assumed stellar chemical composition and on the convection efficiency in superadiabatic regions, whose precise physical treatment is not still fully available.

Comparison between predictions and observations for pre-MS stars in open clusters suggest a less efficient convection during the pre-MS phase with respect to the Main Sequence. This is true even if one takes into account the uncertainties on the results due to the errors in the adopted input physics and assumed chemical composition. A possible explanation of this result could be the fact that in 1D evolutionary codes a reduced convection efficiency could mimic the main effects of some non-standard mechanisms active in young stars, such as the presence of a not negligible magnetic field and/or surface spot coverage.

The energy produced by the Li, Be, B burning reactions is negligible, thus their effects on stellar structures are irrelevant. However, the surface abundances of light elements strongly depends on the nuclear burning and thus on the adopted reaction rates. The only nuclear burning that during the pre-MS or protostellar accretion phase affects stellar evolution is the deuterium burning. The impact on pre-MS evolution of a variation of the p(D,γ)^{3}He reaction rate by its present uncertainty (±7%) has been analyzed in the literature, finding a negligible effect on stellar models. Two other D-burning channels have been considered, namely the D(D,p)^{3}H and the D(D,n)^{3}He. However, as expected, the inclusion of such channels does not produce relevant effects on pre-MS evolution as the largest part of deuterium is destroyed via p(D,γ)^{3}He.

The effects on the other light elements surface abundance predictions of the still present (even if greatly reduced) uncertainty on (p,α) cross sections have been evaluated in detail and compared to the influence on the results of the errors in the other physics ingredients and in the stellar chemical composition. Light element (p,α) reaction rates have been recently revised through the indirect Trojan Horse method (THM), sensibly reducing their estimated uncertainty and finding

differences with previous estimates at the energies of astrophysical interest. In general, differences in the predicted surface Li, Be, B abundances if the THM or the less recent but still widely used NACRE reaction rates are adopted are significant for stars in which light elements are efficiently burned.

The current uncertainty on the ^{6}Li and ^{7}Li proton capture reaction rates is of the order of 10%. Numerical calculations show that the effects on the ^{6}Li and ^{7}Li surface abundances due to this uncertainty, although not negligible, are less important than the influence of errors in other quantities used in the computation of a stellar model. The present errors on the ^{9}Be(p,α)^{6}Li and ^{10}B(p,α)^{7}Be rates, at the temperatures of interest, are, respectively, of about 25 and 20%. Due to the higher ^{9}Be and ^{10}B burning temperature, with respect to the Li burning, the effects of the reaction rate change/uncertainty are significant only for masses lower than $M \lesssim 0.5\,M_{\odot}$ and $M \lesssim 0.4\,M_{\odot}$, respectively.

In conclusion, recent cross section measurements for light element (p,α) burning reactions sensibly reduced their uncertainty, even if it is still not negligible. Pre-Main Sequence theoretical calculations and consequently prediction for light element surface abundances are affected by several uncertainty sources: the not precise knowledge of the protostellar evolution and the efficiency of superadiabatic convection, the still present errors on the input physics adopted in the calculations and in the assumed stellar chemical composition. On the other hand, the errors on light element nuclear cross sections do not constitute the main uncertainty source for the prediction of light elements surface abundances.

AUTHOR CONTRIBUTIONS

All authors listed have made a substantial, direct, and intellectual contribution to the work and approved it for publication.

FUNDING

This work has been partially supported by INFN (Iniziativa specifica TAsP) and the Pisa University project PRA 2018/2019 “Le stelle come laboratori cosmici di fisica fondamentale.”

ACKNOWLEDGMENTS

AC acknowledges the support of the “visiting fellow” program (BVF 2019) of the Pisa University. ET acknowledges INAF-OAAb for the fellowship “Analisi dell’influenza dell’evoluzione protostellare sull’abbondanza superficiale di elementi leggeri in stelle di piccola massa in fase di pre-sequenza principale.” LL acknowledges the program “Starting Grant 2020” by University of Catania.

SUPPLEMENTARY MATERIAL

The Supplementary Material for this article can be found online at: https://www.frontiersin.org/articles/10.3389/fspas.2021.604872/full#supplementary-material

REFERENCES

Adelberger, E. G., García, A., Robertson, R. G. H., Snover, K. A., Balantekin, A. B., Heeger, K., et al. (2011). Solar fusion cross sections. II. The pp chain and CNO cycles. *Rev. Mod. Phys.* 83, 195–246. doi:10.1103/RevModPhys.83.195

Aguilera-Gómez, C., Ramírez, I., and Chanamé, J. (2018). Lithium abundance patterns of late-F stars: an in-depth analysis of the lithium desert. *A&A* 614, A55. doi:10.1051/0004-6361/201732209

Allende Prieto, C., Koesterke, L., Ludwig, H.-G., Freytag, B., and Caffau, E. (2013). Convective line shifts for the Gaia RVS from the CIFIST 3D model atmosphere grid. *A&A* 550, A103. doi:10.1051/0004-6361/201220064

Amarsi, A. M., Barklem, P. S., Asplund, M., Collet, R., and Zatsarinny, O. (2018). Inelastic O+H collisions and the O I 777 nm solar centre-to-limb variation. *A&A* 616, A89. doi:10.1051/0004-6361/201832770

Amarsi, A. M., Nissen, P. E., and Skúladóttir, Á. (2019). Carbon, oxygen, and iron abundances in disk and halo stars. Implications of 3D non-LTE spectral line formation. *A&A* 630, A104. doi:10.1051/0004-6361/201936265

Angulo, C., Arnould, M., Rayet, M., Descouvemont, P., Baye, D., Leclercq-Willain, C., et al. (1999). A compilation of charged-particle induced thermonuclear reaction rates. *Nucl. Phys. A.* 656, 3–183.

Arnett, W. D., Meakin, C., Hirschi, R., Cristini, A., Georgy, C., Campbell, S., et al. (2018). 3D simulations and MLT: II. RA-ILES results. arXiv e-prints. arXiv: 1810.04659

Arnett, W. D., Meakin, C., Viallet, M., Campbell, S. W., Lattanzio, J. C., and Mocák, M. (2015). Beyond mixing-length theory: a step toward 321D. *ApJ* 809, 30. doi:10.1088/0004-637X/809/1/30

Asplund, M. (2005). New light on stellar abundance analyses: departures from LTE and homogeneity. *ARA&A* 43, 481–530. doi:10.1146/annurev.astro.42.053102.134001

Asplund, M., Grevesse, N., Sauval, A. J., Allende Prieto, C., and Kiselman, D. (2004). Line formation in solar granulation. IV. [O I], O I and OH lines and the photospheric O abundance. *A&A* 417, 751–768. doi:10.1051/0004-6361:20034328

Asplund, M., Grevesse, N., Sauval, A. J., and Scott, P. (2009). The chemical composition of the Sun. *ARA&A* 47, 481–522. doi:10.1146/annurev.astro.46.060407.145222

Asplund, M., Grevesse, N., and Sauval, A. J. (2005). “The solar chemical composition,”. *Cosmic abundances as records of stellar evolution and nucleosynthesis*. Editors T. G. BarnesIII and F. N. Bash (San Francisco: Astronomical Society of the Pacific Conference Series), Vol. 336, 25.

Asplund, M., Lambert, D. L., Nissen, P. E., Primas, F., and Smith, V. V. (2006). Lithium isotopic abundances in metal-poor halo stars. *ApJ* 644, 229–259. doi:10.1086/503538

Audard, M., Ábrahám, P., Dunham, M. M., Green, J. D., Grosso, N., Hamaguchi, K., et al. (2014). “Episodic accretion in young stars,”. *Protostars and planets VI*. Editors H. Beuther, R. S. Klessen, C. P. Dullemond, and T. Henning, 387. doi:10.2458/azuuapress9780816531240-ch017

Gaia CollaborationBabusiaux, C., van Leeuwen, F., Barstow, M. A., Jordi, C., Vallenari, A., et al. (2018). Gaia data release 2. Observational hertzsprung-russell diagrams. *A&A* 616, A10. doi:10.1051/0004-6361/201832843

Badnell, N. R., Bautista, M. A., Butler, K., Delahaye, F., Mendoza, C., Palmeri, P., et al. (2005). Updated opacities from the opacity project. *MNRAS* 360, 458–464. doi:10.1111/j.1365-2966.2005.08991.x

Bae, J., Hartmann, L., Zhu, Z., and Gammie, C. (2013). Variable accretion outbursts in protostellar evolution. *ApJ* 764, 141. doi:10.1088/0004-637X/764/2/141

Baraffe, I., and Chabrier, G. (2010). Effect of episodic accretion on the structure and the lithium depletion of low-mass stars and planet-hosting stars. *A&A* 521, A44. doi:10.1051/0004-6361/201014979

Baraffe, I., Chabrier, G., and Gallardo, J. (2009). Episodic accretion at early stages of evolution of low-mass stars and Brown dwarfs: a solution for the observed luminosity spread in H-R diagrams? *ApJl* 702, L27–L31. doi:10.1088/0004-637X/702/1/L27

Baraffe, I., Vorobyov, E., and Chabrier, G. (2012). Observed luminosity spread in young clusters and FU Ori stars: a unified picture. *ApJ* 756, 118. doi:10.1088/0004-637X/756/2/118

Barrado y Navascués, D., Stauffer, J. R., and Patten, B. M. (1999). The lithium-depletion boundary and the age of the young open cluster IC 2391. *ApJl* 522, L53–L56. doi:10.1086/312212

Baur, G. (1986). Breakup reactions as an indirect method to investigate low-energy charged-particle reactions relevant for nuclear astrophysics. *Phys. Lett. B* 178, 135–138.

Beeck, B., Cameron, R. H., Reiners, A., and Schüssler, M. (2013). Three-dimensional simulations of near-surface convection in main-sequence stars. II. Properties of granulation and spectral lines. *A&A* 558, A49. doi:10.1051/0004-6361/201321345

Bergemann, M., Collet, R., Amarsi, A. M., Kovalev, M., Ruchti, G., and Magic, Z. (2017). Non-local thermodynamic equilibrium stellar spectroscopy with 1D and <3D> models. I. Methods and application to magnesium abundances in standard stars. *ApJ* 847, 15. doi:10.3847/1538-4357/aa88cb

Bergemann, M., Gallagher, A. J., Eitner, P., Bautista, M., Collet, R., Yakovleva, S. A., et al. (2019). Observational constraints on the origin of the elements. I. 3D NLTE formation of Mn lines in late-type stars. *A&A* 631, A80. doi:10.1051/0004-6361/201935811

Bigot, L., Mourard, D., Berio, P., Thévenin, F., Ligi, R., Tallon-Bosc, I., et al. (2011). The diameter of the CoRoT target HD 49933. Combining the 3D limb darkening, asteroseismology, and interferometry. *A&A* 534, L3. doi:10.1051/0004-6361/201117349

Binks, A. S., and Jeffries, R. D. (2014). A lithium depletion boundary age of 21 Myr for the Beta Pictoris moving group. *MNRAS* 438, L11–L15. doi:10.1093/mnrasl/slt141

Blancard, C., Cossé, P., and Faussurier, G. (2012). Solar mixture opacity calculations using detailed configuration and level accounting treatments. *ApJ* 745, 10. doi:10.1088/0004-637X/745/1/10

Boesgaard, A. M., and Novicki, M. C. (2005). Beryllium in the ultra-lithium-deficient, metal-poor halo dwarf g186-26. *ApJl* 633, L125–L128. doi:10.1086/498021

Boesgaard, A. M., Rich, J. A., Levesque, E. M., and Bowler, B. P. (2011). Beryllium and alpha-element abundances in a large sample of metal-poor stars. *ApJ* 743, 140. doi:10.1088/0004-637X/743/2/140

Böhm-Vitense, E. (1958). Über die Wasserstoffkonvektionszone in Sternen verschiedener Effektivtemperaturen und Leuchtkräfte. Mit 5 Textabbildungen. *Z. Astrophysik* 46, 108.

Bonifacio, P., Caffau, E., Ludwig, H. G., Steffen, M., Castelli, F., Gallagher, A. J., et al. (2018). Using the CIFIST grid of COBOLD 3D model atmospheres to study the effects of stellar granulation on photometric colours. I. Grids of 3D corrections in the UBVRI, 2MASS, HIPPARCOS, Gaia, and SDSS systems. *A&A* 611, A68. doi:10.1051/0004-6361/201732232

Bossini, D., Vallenari, A., Bragaglia, A., Cantat-Gaudin, T., Sordo, R., Balaguer-Núñez, L., et al. (2019). Age determination for 269 Gaia DR2 open clusters. *A&A* 623, A108. doi:10.1051/0004-6361/201834693

Burke, C. J., Pinsonneault, M. H., and Sills, A. (2004). Theoretical examination of the lithium depletion boundary. *ApJ* 604, 272–283. doi:10.1086/381242

Caffau, E., Ludwig, H.-G., Steffen, M., Freytag, B., and Bonifacio, P. (2011). Solar chemical abundances determined with a CO5BOLD 3D model atmosphere. *Sol. Phys.* 268, 255–269. doi:10.1007/s11207-010-9541-4

Caffau, E., Maiorca, E., Bonifacio, P., Faraggiana, R., Steffen, M., Ludwig, H.-G., et al. (2009). The solar photospheric nitrogen abundance. Analysis of atomic transitions with 3D and 1D model atmospheres. *A&A* 498, 877–884. doi:10.1051/0004-6361/200810859

Calvet, N., Briceño, C., Hernández, J., Hoyer, S., Hartmann, L., Sicilia-Aguilar, A., et al. (2005). Disk evolution in the orion OB1 association. *AJ* 129, 935–946. doi:10.1086/426910

Cayrel, R., Spite, M., Spite, F., Vangioni-Flam, E., Cassé, M., and Audouze, J. (1999). New high S/N observations of the (6Li)/(7) Li blend in HD 84937 and two other metal-poor stars. *A&A* 343, 923–932.

Cayrel, R., Steffen, M., Chand, H., Bonifacio, P., Spite, M., Spite, F., et al. (2007). Line shift, line asymmetry, and the $\hat{6}$Li/$\hat{7}$Li isotopic ratio determination. *A&A* 473, L37–L40. doi:10.1051/0004-6361:20078342

Chabrier, G., and Baraffe, I. (1997). Structure and evolution of low-mass stars. *A&A* 327, 1039–1053.

Charbonnel, C., Decressin, T., Amard, L., Palacios, A., and Talon, S. (2013). Impact of internal gravity waves on the rotation profile inside pre-main sequence low-mass stars. *A&A* 554, A40. doi:10.1051/0004-6361/201321277

Charbonnel, C., Deliyannis, C. P., and Pinsonneault, M. (2000). "Sinks of light elements in stars - Part III (invited paper),". *The light elements and their evolution*. Editors L. da Silva, R. de Medeiros, and M. Spite, Vol. 198, 87.

Charbonnel, C., and Primas, F. (2005). The lithium content of the Galactic Halo stars. *A&A* 442, 961–992. doi:10.1051/0004-6361:20042491

Chiavassa, A., Bigot, L., Kervella, P., Matter, A., Lopez, B., Collet, R., et al. (2012). Three-dimensional interferometric, spectrometric, and planetary views of Procyon. *A&A* 540, A5. doi:10.1051/0004-6361/201118652

Chiavassa, A., Casagrande, L., Collet, R., Magic, Z., Bigot, L., Thévenin, F., et al. (2018). The STAGGER-grid: a grid of 3D stellar atmosphere models. V. Synthetic stellar spectra and broad-band photometry. *A&A* 611, A11. doi:10.1051/0004-6361/201732147

Clarke, D., MacDonald, E. C., and Owens, S. (2004). Li abundance/surface activity connections in solar-type Pleiades. *A&A* 415, 677–684. doi:10.1051/0004-6361:20034620

Coc, A., and Vangioni, E. (2010). Big-Bang nucleosynthesis with updated nuclear data, *J. Phys. Conf. Ser. Journal of physics conference series*, 202. 012001. doi:10.1088/1742-6596/202/1/012001

Coc, A., and Vangioni, E. (2017). Primordial nucleosynthesis. *Int. J. Mod. Phys. E* 26, 1741002. doi:10.1142/S0218301317410026

Collet, R., Hayek, W., Asplund, M., Nordlund, Å., Trampedach, R., and Gudiksen, B. (2011). Three-dimensional surface convection simulations of metal-poor stars. The effect of scattering on the photospheric temperature stratification. *A&A* 528, A32. doi:10.1051/0004-6361/201016151

Copi, C. J., Schramm, D. N., and Turner, M. S. (1997). Big-bang nucleosynthesis limit to the number of neutrino species. *Phys. Rev.* 55, 3389–3393. doi:10.1103/PhysRevD.55.3389

Creevey, O. L., Thévenin, F., Boyajian, T. S., Kervella, P., Chiavassa, A., Bigot, L., et al. (2012). Fundamental properties of the Population II fiducial stars ¡ASTROBJ¿HD 122563¡/ASTROBJ¿ and ¡ASTROBJ¿Gmb 1830¡/ASTROBJ¿ from CHARA interferometric observations. *A&A* 545, A17. doi:10.1051/0004-6361/201219651

Cunha, K. (2010). "Boron abundances in the Galactic disk,". *Light elements in the universe*. Editors C. Charbonnel, M. Tosi, F. Primas, and C. Chiappini (IAU Symposium), Vol. 268, 243–248. doi:10.1017/S1743921310004199

Cyburt, R. H., Fields, B. D., Olive, K. A., and Yeh, T.-H. (2016). Big bang nucleosynthesis: present status. *Rev. Mod. Phys.* 88, 015004. doi:10.1103/RevModPhys.88.015004

Cyburt, R. H. (2004). Primordial nucleosynthesis for the new cosmology: determining uncertainties and examining concordance. *Phys. Rev.* 70, 023505. doi:10.1103/PhysRevD.70.023505

Da Rio, N., Gouliermis, D. A., and Gennaro, M. (2010a). A new method for the assessment of age and age spread of pre-main-sequence stars in young stellar associations of the magellanic clouds. *ApJ* 723, 166–183. doi:10.1088/0004-637X/723/1/166

Da Rio, N., Robberto, M., Soderblom, D. R., Panagia, N., Hillenbrand, L. A., Palla, F., et al. (2010b). A multi-color optical survey of the orion nebula cluster. II. The H-R diagram. *ApJ* 722, 1092–1114. doi:10.1088/0004-637X/722/2/1092

Dahm, S. E. (2015). Reexamining the lithium depletion boundary in the Pleiades and the inferred age of the cluster. *ApJ* 813, 108. doi:10.1088/0004-637X/813/2/108

Damone, L., Barbagallo, M., Mastromarco, M., Mengoni, A., Cosentino, L., Maugeri, E., et al. (2018). Be (n ,p) Li reaction and the cosmological lithium problem: measurement of the cross section in a wide energy range at n_TOF at CERN. *Phys. Rev. Lett.* 121, 042701. doi:10.1103/PhysRevLett.121.042701

Degl'Innocenti, S., Prada Moroni, P. G., Marconi, M., and Ruoppo, A. (2008). The FRANEC stellar evolutionary code. *Ap&SS* 316, 25–30. doi:10.1007/s10509-007-9560-2

Delgado Mena, E., Bertrán de Lis, S., Adibekyan, V. Z., Sousa, S. G., Figueira, P., Mortier, A., et al. (2015). Li abundances in F stars: planets, rotation, and Galactic evolution. *A&A* 576, A69. doi:10.1051/0004-6361/201425433

Delgado Mena, E., Israelian, G., González Hernández, J. I., Santos, N. C., and Rebolo, R. (2012). Be abundances in cool main-sequence stars with exoplanets. *ApJ* 746, 47. doi:10.1088/0004-637X/746/1/47

Delgado Mena, E., Israelian, G., González Hernández, J. I., Sousa, S. G., Mortier, A., Santos, N. C., et al. (2014). Li depletion in solar analogues with exoplanets. Extending the sample. *A&A* 562, A92. doi:10.1051/0004-6361/201321493

Dell'Omodarme, M., Valle, G., Degl'Innocenti, S., and Prada Moroni, P. G. (2012). The Pisa stellar evolution data base for low-mass stars. *A&A* 540, A26. doi:10.1051/0004-6361/201118632

Descouvemont, P., Adahchour, A., Angulo, C., Coc, A., and Vangioni-Flam, E. (2004). Compilation and R-matrix analysis of Big Bang nuclear reaction rates. *At. Data Nucl. Data Tables* 88, 203–236. doi:10.1016/j.adt.2004.08.001

Dobbie, P. D., Lodieu, N., and Sharp, R. G. (2010). IC 2602: a lithium depletion boundary age and new candidate low-mass stellar members. *MNRAS* 409, 1002–1012. doi:10.1111/j.1365-2966.2010.17355.x

Dupuy, T. J., Forbrich, J., Rizzuto, A., Mann, A. W., Aller, K., Liu, M. C., et al. (2016). High-precision radio and infrared astrometry of LSPM J1314+1320AB. II. Testing pre-main-sequence models at the lithium depletion boundary with dynamical masses. *ApJ* 827, 23. doi:10.3847/0004-637X/827/1/23

D'Antona, F., and Mazzitelli, I. (1997). Evolution of low mass stars. *Mem. Soc. Astron. Italiana* 68, 807.

D'Antona, F., and Mazzitelli, I. (1994). New pre-main-sequence tracks for M less than or equal to 2.5 solar mass as tests of opacities and convection model. *ApJS* 90, 467–500. doi:10.1086/191867

D'Antona, F., and Montalbán, J. (2003). Efficiency of convection and Pre-Main Sequence lithium depletion. *A&A* 412, 213–218. doi:10.1051/0004-6361:20031410

D'Antona, F., Ventura, P., and Mazzitelli, I. (2000). First results on pre-main-sequence evolution, including a magnetic field. *ApJ* 543, L77–L80. doi:10.1086/318172

Eggenberger, P., Haemmerlé, L., Meynet, G., and Maeder, A. (2012). Impact of rotation and disc lifetime on pre-main sequence lithium depletion of solar-type stars. *A&A* 539, A70. doi:10.1051/0004-6361/201118432

Feiden, G. A., and Chaboyer, B. (2013). Magnetic inhibition of convection and the fundamental properties of low-mass stars. I. Stars with a radiative core. *ApJ* 779, 183. doi:10.1088/0004-637X/779/2/183

Feiden, G. A., and Chaboyer, B. (2012). Reevaluating the mass-radius relation for low-mass, main-sequence stars. *ApJ* 757, 42. doi:10.1088/0004-637X/757/1/42

Feiden, G. A. (2016). Magnetic inhibition of convection and the fundamental properties of low-mass stars. III. A consistent 10 Myr age for the Upper Scorpius OB association. *A&A* 593, A99. doi:10.1051/0004-6361/201527613

Fields, B. D. (2011). The primordial lithium problem. *Annu. Rev. Nucl. Part. Sci.* 61, 47–68. doi:10.1146/annurev-nucl-102010-130445

Freytag, B., Steffen, M., Ludwig, H. G., Wedemeyer-Böhm, S., Schaffenberger, W., and Steiner, O. (2012). Simulations of stellar convection with CO5BOLD. *J. Comput. Phys.* 231, 919–959. doi:10.1016/j.jcp.2011.09.026

Fu, X., Bressan, A., Molaro, P., and Marigo, P. (2015). Lithium evolution in metal-poor stars: from pre-main sequence to the Spite plateau. *MNRAS* 452, 3256–3265. doi:10.1093/mnras/stv1384

Garcia Lopez, R. J., Rebolo, R., and Perez de Taoro, M. R. (1995). Beryllium abundances in late-type Hyades dwarf stars. *A&A* 302, 184.

Gennaro, M., Prada Moroni, P. G., and Tognelli, E. (2012). Testing pre-main-sequence models: the power of a Bayesian approach. *MNRAS* 420, 986–1018. doi:10.1111/j.1365-2966.2011.19945.x

González Hernández, J. I., Bonifacio, P., Caffau, E., Ludwig, H. G., Steffen, M., Monaco, L., et al. (2019). The Li/Li isotopic ratio in the metal-poor binary CS22876-032. *A&A* 628, A111. doi:10.1051/0004-6361/201936011

Goudelis, A., Pospelov, M., and Pradler, J. (2016). Light particle solution to the cosmic lithium problem. *Phys. Rev. Lett.* 116, 211303. doi:10.1103/PhysRevLett.116.211303

Hartmann, L., Cassen, P., and Kenyon, S. J. (1997). Disk accretion and the stellar birthline. *ApJ* 475, 770. doi:10.1086/303547

Hartmann, L., Herczeg, G., and Calvet, N. (2016). Accretion onto pre-main-sequence stars. *ARA&A* 54, 135–180. doi:10.1146/annurev-astro-081915-023347

Hartmann, L., and Kenyon, S. J. (1996). The FU orionis phenomenon. *ARA&A* 34, 207–240. doi:10.1146/annurev.astro.34.1.207

Hayashi, C., and Nakano, T. (1963). Evolution of stars of small masses in the pre-main-sequence stages. *Prog. Theor. Phys.* 30, 460–474. doi:10.1143/PTP.30.460

Hayashi, C. (1961). Stellar evolution in early phases of gravitational contraction. *PASJ* 13, 450–452.

Hillenbrand, L. A. (2009). "Age-related observations of low mass pre-main and young main sequence stars,". *The ages of stars*. Editors E. E. Mamajek, D. R. Soderblom, and R. F. G. Wyse (IAU Symposium), Vol. 258, 81–94. doi:10.1017/S1743921309031731

Hosokawa, T., Offner, S. S. R., and Krumholz, M. R. (2011). On the reliability of stellar ages and age spreads inferred from pre-main-sequence evolutionary models. *ApJ* 738, 140. doi:10.1088/0004-637X/738/2/140

Hosokawa, T., and Omukai, K. (2009a). Evolution of massive protostars with high accretion rates. *ApJ* 691, 823–846. doi:10.1088/0004-637X/691/1/823

Hosokawa, T., and Omukai, K. (2009b). Low-metallicity protostars and the maximum stellar mass resulting from radiative feedback: spherically symmetric calculations. *ApJ* 703, 1810–1818. doi:10.1088/0004-637X/703/2/1810

Hosokawa, T., Yorke, H. W., and Omukai, K. (2010). Evolution of massive protostars via disk accretion. *ApJ* 721, 478–492. doi:10.1088/0004-637X/721/1/478

Iben, I. (2013). *Stellar evolution physics*. in *Physical Processes in stellar interiors*, Vol. 1.

Ingleby, L., Calvet, N., Hernández, J., Hartmann, L., Briceno, C., Miller, J., et al. (2014). The evolution of accretion in young stellar objects: strong accretors at 3-10 myr. *ApJ* 790, 47. doi:10.1088/0004-637X/790/1/47

Jackson, R. J., and Jeffries, R. D. (2014). The effect of star-spots on the ages of low-mass stars determined from the lithium depletion boundary. *MNRAS* 445, 4306–4315. doi:10.1093/mnras/stu2076

Jeffries, R. D. (2006). Pre-main-sequence lithium depletion *(chemical abundances and mixing in stars in the milky way and its satellites*, 163. ESO ASTROPHYSICS SYMPOSIASpringer-Verlag, 163. 978-3-540-34135-2.

Jeffries, R. D. (2009). "Age spreads in star forming regions?," in *The ages of stars*. *Of* IAU symposium. Editors E. E. Mamajek, D. R. Soderblom, and R. F. G. Wyse, Vol. 258, 95–102. doi:10.1017/S1743921309031743

Jeffries, R. D. (2000). "Lithium depletion in open clusters,". *Stellar clusters and associations: convection, rotation, and dynamos*. Editors R. Pallavicini, G. Micela, and S. Sciortino (Astronomical Society of the Pacific Conference Series), Vol. 198, 245.

Jeffries, R. D., Naylor, T., Mayne, N. J., Bell, C. P. M., and Littlefair, S. P. (2013). A lithium depletion boundary age of 22 Myr for NGC 1960. *MNRAS* 434, 2438–2450. doi:10.1093/mnras/stt1180

Jeffries, R. D., and Oliveira, J. M. (2005). The lithium depletion boundary in NGC 2547 as a test of pre-main-sequence evolutionary models. *MNRAS* 358, 13–29. doi:10.1111/j.1365-2966.2005.08820.x

Jofré, P., Heiter, U., and Soubiran, C. (2019). Accuracy and precision of industrial stellar abundances. *ARA&A* 57, 571–616. doi:10.1146/annurev-astro-091918-104509

Juarez, A. J., Cargile, P. A., James, D. J., and Stassun, K. G. (2014). An improved determination of the lithium depletion boundary age of Blanco 1 and a first look on the effects of magnetic activity. *ApJ* 795, 143. doi:10.1088/0004-637X/795/2/143

Kaufer, A. (2010). "Observations of light elements in massive stars,". *Light elements in the universe*. Editors C. Charbonnel, M. Tosi, F. Primas, and C. Chiappini (IAU Symposium), Vol. 268, 317–324. doi:10.1017/S1743921310004291

King, J. R., Krishnamurthi, A., and Pinsonneault, M. H. (2000). The lithium-rotation correlation in the Pleiades revisited. *AJ* 119, 859–872. doi:10.1086/301205

King, J. R., Schuler, S. C., Hobbs, L. M., and Pinsonneault, M. H. (2010). Li I and K I scatter in cool Pleiades dwarfs. *ApJ* 710, 1610–1618. doi:10.1088/0004-637X/710/2/1610

Kunitomo, M., Guillot, T., Ida, S., and Takeuchi, T. (2018). Revisiting the pre-main-sequence evolution of stars. II. Consequences of planet formation on stellar surface composition. *A&A* 618, A132. doi:10.1051/0004-6361/201833127

Kunitomo, M., Guillot, T., Takeuchi, T., and Ida, S. (2017). Revisiting the pre-main-sequence evolution of stars. I. Importance of accretion efficiency and deuterium abundance. *A&A* 599, A49. doi:10.1051/0004-6361/201628260

Lamia, L., Mazzocco, M., Pizzone, R. G., Hayakawa, S., La Cognata, M., Spitaleri, C., et al. (2019). Cross-section measurement of the cosmologically relevant Be(n,α) He reaction over a broad energy range in a single experiment. *Astrophysical J.* 879, 23. doi:10.3847/1538-4357/ab2234

Lamia, L., Spitaleri, C., La Cognata, M., Palmerini, S., and Pizzone, R. G. (2012). Recent evaluation of the Li(p, α)He reaction rate at astrophysical energies via the Trojan Horse method. *A&A* 541, A158. doi:10.1051/0004-6361/201219014

Lamia, L., Spitaleri, C., Pizzone, R. G., Tognelli, E., Tumino, A., Degl'Innocenti, S., et al. (2013). An updated Li(p, α)He reaction rate at astrophysical energies with the trojan horse method. *ApJ* 768, 65. doi:10.1088/0004-637X/768/1/65

Lamia, L., Spitaleri, C., Tognelli, E., Degl'Innocenti, S., Pizzone, R. G., and Prada Moroni, P. G. (2015). Astrophysical impact of the updated Be(p,α)Li and B(p,α) Be reaction rates as deduced by THM. *ApJ* 811, 99. doi:10.1088/0004-637X/811/2/99

Landin, N. R., Ventura, P., D'Antona, F., Mendes, L. T. S., and Vaz, L. P. R. (2006). Non-gray rotating stellar models and the evolutionary history of the Orion Nebular Cluster. *A&A* 456, 269–282. doi:10.1051/0004-6361:20054011

Larson, R. B. (1969). Numerical calculations of the dynamics of collapsing proto-star. *MNRAS* 145, 271.

Larson, R. B. (1972). The evolution of spherical protostars with masses 0.25 M_solar to 10 M_solar. *MNRAS* 157, 121. doi:10.1093/mnras/157.2.121

Larson, R. B. (2003). The physics of star formation. *Rep. Prog. Phys.* 66, 1651–1697. doi:10.1088/0034-4885/66/10/R03

Lind, K., Amarsi, A. M., Asplund, M., Barklem, P. S., Bautista, M., Bergemann, M., et al. (2017). Non-LTE line formation of Fe in late-type stars - IV. Modelling of the solar centre-to-limb variation in 3D. *MNRAS* 468, 4311–4322. doi:10.1093/mnras/stx673

Lind, K., Melendez, J., Asplund, M., Collet, R., and Magic, Z. (2013). The lithium isotopic ratio in very metal-poor stars. *A&A* 554, A96. doi:10.1051/0004-6361/201321406

Lodders, K., Plame, H., and Gail, H. (2009). Abundances of the elements in the solar system. In *Landolt-börnstein - group VI Astronomy and astrophysics numerical data and functional relationships in science and technology volume 4B: solar system*. Edited by J.E. Trümper, 4. 44. doi:10.1007/978-3-540-88055-4_34

Lodders, K. (2010). Solar system Abundances of the elements. *Astrophysics Space Sci. Proc.* 16, 379. doi:10.1007/978-3-642-10352-0_8

Ludwig, H.-G., Freytag, B., and Steffen, M. (1999). A calibration of the mixing-length for solar-type stars based on hydrodynamical simulations. I. Methodical aspects and results for solar metallicity. *A&A* 346, 111–124.

Ludwig, H., Caffau, E., Steffen, M., Freytag, B., Bonifacio, P., and Kučinskas, A. (2009). The CIFIST 3D model atmosphere grid. *Mem. Soc. Astron. Italiana* 80, 711.

Lydon, T. J., Fox, P. A., and Sofia, S. (1992). A formulation of convection for stellar structure and evolution calculations without the mixing-length theory approximations. I. Application to the Sun. *ApJ* 397, 701. doi:10.1086/171826

Mathieu, R. D., BaraffeSimon, I. M., Stassun, K. G., and White, R. (2007). Dynamical mass measurements of pre-main-sequence stars: fundamental tests of the physics of young stars. *Protostars and Planets V*, 411–425.

MacDonald, J., and Mullan, D. J. (2012). Precision modelling of M dwarf stars: the magnetic components of CM Draconis. *MNRAS* 421, 3084–3101. doi:10.1111/j.1365-2966.2012.20531.x

Machida, M. N., Inutsuka, S.-i., and Matsumoto, T. (2010). formation process of the circumstellar disk: long-term simulations in the main accretion phase of star formation. *ApJ* 724, 1006–1020. doi:10.1088/0004-637X/724/2/1006

Machida, M. N., Inutsuka, S.-i., and Matsumoto, T. (2008). High- and low-velocity magnetized outflows in the star formation process in a gravitationally collapsing cloud. *ApJ* 676, 1088–1108. doi:10.1086/528364

Magic, Z., and Asplund, M. (2014). *Surface appearance of stellar granulation*.The Stagger-grid: a grid of 3D stellar atmosphere models - VI. arXiv e-prints. arXiv:1405.7628.

Magic, Z., Collet, R., Asplund, M., Trampedach, R., Hayek, W., Chiavassa, A., et al. (2013). The Stagger-grid: a grid of 3D stellar atmosphere models. I. Methods and general properties. *A&A* 557, A26. doi:10.1051/0004-6361/201321274

Manzi, S., Randich, S., de Wit, W. J., and Palla, F. (2008). Detection of the lithium depletion boundary in the young open cluster IC 4665. *A&A* 479, 141–148. doi:10.1051/0004-6361:20078226

Martín, E. L., Lodieu, N., and Béjar, V. J. S. (2020). Search for the sub-stellar lithium depletion boundary in the open star cluster Coma Berenices. *A&A* 640, A9. doi:10.1051/0004-6361/202037907

Martín, E. L., Lodieu, N., Pavlenko, Y., and Béjar, V. J. S. (2018). The lithium depletion boundary and the age of the hyades cluster. *ApJ* 856, 40. doi:10.3847/1538-4357/aaaeb8

Masunaga, H., and Inutsuka, S.-i. (2000). A radiation hydrodynamic model for protostellar collapse. II. The second collapse and the birth of a protostar. *ApJ* 531, 350–365. doi:10.1086/308439

Meléndez, J., Ramírez, I., Casagrande, L., Asplund, M., Gustafsson, B., Yong, D., et al. (2010). The solar, exoplanet and cosmological lithium problems. *Ap&SS* 328, 193–200. doi:10.1007/s10509-009-0187-3

Meyer, M. R., Backman, D. E., Weinberger, A. J., and Wyatt, M. C. (2007). "Evolution of circumstellar disks around normal stars: placing our solar system in context," in *Protostars and planets V*. Editors B. Reipurth, D. Jewitt, and K. Keil, 573.

Mondet, G., Blancard, C., Cossé, P., and Faussurier, G. (2015). Opacity calculations for solar mixtures. *ApJS* 220, 2. doi:10.1088/0067-0049/220/1/2

Montalbán, J., and Schatzman, E. (2000). Mixing by internal waves. III. Li and Be abundance dependence on spectral type, age and rotation. *A&A* 354, 943–959.

Mossa, V., Stöckel, K., Cavanna, F., Ferraro, F., Aliotta, M., Barile, F., et al. (2020). The baryon density of the Universe from an improved rate of deuterium burning. *Nature* 587, 210–213. doi:10.1038/s41586-020-2878-4

Muzerolle, J., Calvet, N., Briceño, C., Hartmann, L., and Hillenbrand, L. (2000). Disk accretion in the 10 MYR old T Tauri stars TW hydrae and hen 3-600a. *ApJ* 535, L47–L50. doi:10.1086/312691

Muzerolle, J., Luhman, K. L., Briceño, C., Hartmann, L., and Calvet, N. (2005a). Measuring accretion in young substellar objects: approaching the planetary mass regime. *ApJ* 625, 906–912. doi:10.1086/429483

Muzerolle, J., Megeath, S. T., Flaherty, K. M., Gordon, K. D., Rieke, G. H., Young, E. T., et al. (2005b). The outburst of V1647 orionis revealed by spitzer. *ApJ* 620, L107–L110. doi:10.1086/428832

Natta, A., Grinin, V., and Mannings, V. (2000). "Properties and evolution of disks around pre-main-sequence stars of intermediate mass," in *Protostars and planets IV*. Editors V. Mannings, A. P. Boss, and S. S. Russell, 559–588.

Nordlander, T., Amarsi, A. M., Lind, K., Asplund, M., Barklem, P. S., Casey, A. R., et al. (2017). 3D NLTE analysis of the most iron-deficient star, SMSS0313-6708. *A&A* 597, A6. doi:10.1051/0004-6361/201629202

Nordlund, A. (1982). Numerical simulations of the solar granulation. I - basic equations and methods. *A&A* 107, 1–10.

Nordlund, Å., Stein, R. F., and Asplund, M. (2009). Solar surface convection. *Living Rev. Solar Phys.* 6, 2.

Oliveira, J. M., Jeffries, R. D., Devey, C. R., Barrado y Navascués, D., Naylor, T., Stauffer, J. R., et al. (2003). The lithium depletion boundary and the age of NGC 2547. *MNRAS* 342, 651–663. doi:10.1046/j.1365-8711.2003.06592.x

Pace, G., Castro, M., Meléndez, J., Théado, S., and do Nascimento, J.-D., Jr. (2012). Lithium in M 67: from the main sequence to the red giant branch. *A&A* 541, A150. doi:10.1051/0004-6361/201117704

Palla, F., and Stahler, S. W. (1991). The evolution of intermediate-mass protostars. I - basic results. *ApJ* 375, 288–299. doi:10.1086/170188

Palla, F., and Stahler, S. W. (1992). The evolution of intermediate-mass protostars. II. Influence of the accretion flow. *ApJ* 392, 667. doi:10.1086/171468

Palla, F., and Stahler, S. W. (1993). The pre-main-sequence evolution of intermediate-mass stars. *ApJ* 418, 414. doi:10.1086/173402

Pettini, M., Zych, B. J., Murphy, M. T., Lewis, A., and Steidel, C. C. (2008). Deuterium abundance in the most metal-poor damped Lyman alpha system: converging on h. *MNRAS* 391, 1499–1510. doi:10.1111/j.1365-2966.2008.13921.x

Piau, L., and Turck-Chièze, S. (2002). Lithium depletion in pre-main-sequence solar-like stars. *ApJ* 566, 419–434. doi:10.1086/324277

Pitrou, C., Coc, A., Uzan, J.-P., and Vangioni, E. (2018). Precision big bang nucleosynthesis with improved Helium-4 predictions. *Phys. Rep.* 754, 1–66. doi:10.1016/j.physrep.2018.04.005

Pizzone, R. G., Roeder, B. T., McCleskey, M., Trache, L., Tribble, R. E., Spitaleri, C., et al. (2016). Trojan Horse measurement of the F(p,α)O astrophysical S(E)-factor. *Eur. Phys. J. A* 52, 24. doi:10.1140/epja/i2016-16024-3

Pizzone, R. G., Spampinato, C., Spartá, R., Couder, M., Tan, W., Burjan, V., et al. (2020). Indirect measurement of the He (n,p)H reaction cross section at Big Bang energies. *Eur. Phys. J. A* 56, 199. doi:10.1140/epja/s10050-020-00212-x

Pizzone, R. G., Spartá, R., Bertulani, C. A., Spitaleri, C., La Cognata, M., Lalmansingh, J., et al. (2014). Big bang nucleosynthesis revisited via trojan horse method measurements. *Astrophysical J.* 786, 112.

Pizzone, R. G., Spitaleri, C., Cherubini, S., La Cognata, M., Lamia, L., Romano, S., et al. (2010). Trojan Horse Method: a tool to explore electron screening effect. *J. Phys. Conf. Ser.* 202, 012018. doi:10.1088/1742-6596/202/1/012018

Pizzone, R. G., Spitaleri, C., Lattuada, M., Cherubini, S., Musumarra, A., Pellegriti, M. G., et al. (2003). Proton-induced lithium destruction cross-section and its astrophysical implications. *Astron. Astrophysics* 398, 423–427.

Pizzone, R. G., Tumino, A., Degl'Innocenti, S., Spitaleri, C., Cherubini, S., Musumarra, A., et al. (2005). Trojan horse estimate of bare nucleus astrophysical s (e)-factor for the li (p, α) he reaction and its astrophysical implications. *Astron. Astrophysics* 438, 779–784.

Prantzos, N. (2012). Production and evolution of Li, Be, and B isotopes in the Galaxy. *A&A* 542, A67. doi:10.1051/0004-6361/201219043

Pratt, J., Baraffe, I., Goffrey, T., Geroux, C., Viallet, M., Folini, D., et al. (2016). Spherical-shell boundaries for two-dimensional compressible convection in a star. *A&A* 593, A121. doi:10.1051/0004-6361/201628296

Primas, F. (2010). "Beryllium and boron in metal-poor stars,". *Light elements in the universe*. Editors C. Charbonnel, M. Tosi, F. Primas, and C. Chiappini (IAU Symposium), Vol. 268, 221–230. doi:10.1017/S1743921310004163

Proffitt, C. R., and Quigley, M. F. (1999). Boron abundances in early-B stars: the B 3 2065.8 angstroms line in IUE data. *American astronomical society meeting abstracts*, Vol. 195. American Astronomical Society Meeting Abstracts

Randich, S. (2010). "Lithium and beryllium in Population I dwarf stars,". *Light elements in the universe*. Editors C. Charbonnel, M. Tosi, F. Primas, and C. Chiappini (IAU Symposium), Vol. 268, 275–283. doi:10.1017/S1743921310004242

Randich, S., Primas, F., Pasquini, L., Sestito, P., and Pallavicini, R. (2007). Tracing mixing in stars: new beryllium observations of the open clusters NGC 2516, Hyades, and M 67. *A&A* 469, 163–172. doi:10.1051/0004-6361:20066218

Randich, S., Tognelli, E., Jackson, R., Jeffries, R. D., Degl'Innocenti, S., Pancino, E., et al. (2018). The Gaia-ESO Survey: open clusters in Gaia-DR1 . A way forward to stellar age calibration. *A&A* 612, A99. doi:10.1051/0004-6361/201731738

Richard, O., Michaud, G., and Richer, J. (2005). Implications of WMAP observations on Li abundance and stellar evolution models. *ApJ* 619, 538–548. doi:10.1086/426470

Richard, O., Michaud, G., Richer, J., Turcotte, S., Turck-Chièze, S., and VandenBerg, D. A. (2002). Models of metal-poor stars with gravitational settling and radiative accelerations. I. Evolution and abundance anomalies. *ApJ* 568, 979–997. doi:10.1086/338952

Rolfs, C. E., and Rodney, W. S. (1988). *Cauldrons in the cosmos: nuclear astrophysics*. Chicago, IL: Univ. Chicago Press.

Santos, N. C., Israelian, G., Randich, S., García López, R. J., and Rebolo, R. (2004). Beryllium anomalies in solar-type field stars. *A&A* 425, 1013–1027. doi:10.1051/0004-6361:20040510

Sbordone, L., Bonifacio, P., Caffau, E., Ludwig, H.-G., Behara, N. T., González Hernández, J. I., et al. (2010). The metal-poor end of the Spite plateau. I. Stellar parameters, metallicities, and lithium abundances. *A&A* 522, A26. doi:10.1051/0004-6361/200913282

Sembach, K. (2010). "Measurements of deuterium in the milky way,". *IAU symposium*. Editors C. Charbonnel, M. Tosi, F. Primas, and C. Chiappini (IAU Symposium), Vol. 268, 43–52. doi:10.1017/S1743921310003856

Sestito, P., Randich, S., Mermilliod, J. C., and Pallavicini, R. (2003). The evolution of lithium depletion in young open clusters: NGC 6475. *A&A* 407, 289–301. doi:10.1051/0004-6361:20030723

Sestito, P., and Randich, S. (2005). Time scales of Li evolution: a homogeneous analysis of open clusters from ZAMS to late-MS. *A&A* 442, 615–627. doi:10.1051/0004-6361:20053482

Siess, L., and Livio, M. (1997). On the rotational evolution of young low-mass stars. *ApJ* 490, 785. doi:10.1086/304905

Smiljanic, R., Pasquini, L., Charbonnel, C., and Lagarde, N. (2010). Beryllium abundances along the evolutionary sequence of the open cluster IC 4651 - a new test for hydrodynamical stellar models. *A&A* 510, A50. doi:10.1051/0004-6361/200912957

Somers, G., and Pinsonneault, M. H. (2014). A tale of two anomalies: depletion, dispersion, and the connection between the stellar lithium spread and inflated radii on the pre-main sequence. *ApJ* 790, 72. doi:10.1088/0004-637X/790/1/72

Somers, G., and Pinsonneault, M. H. (2015). Older and colder: the impact of starspots on pre-main-sequence stellar evolution. *ApJ* 807, 174. doi:10.1088/0004-637X/807/2/174

Spitaleri, C., Cherubini, S., del Zoppo, A., Di Pietro, A., Figuera, P., Gulino, M., et al. (2003). The trojan horse method in nuclear astrophysics. *Nucl. Phys. A.* 719, C99–C106. doi:10.1016/S0375-9474(03)00975-8

Spitaleri, C., La Cognata, M., Lamia, L., Mukhamedzhanov, A. M., and Pizzone, R. G. (2016). Nuclear astrophysics and the trojan horse method. *Eur. Phys. J. A* 52, 77.

Spitaleri, C., La Cognata, M., Lamia, L., Pizzone, R. G., and Tumino, A. (2019). Astrophysics studies with the trojan horse method. *Eur. Phys. J. A* 55, 161.

Spite, F., and Spite, M. (1982a). Abundance of lithium in unevolved halo stars and old disk stars - interpretation and consequences. *A&A* 115, 357–366.

Spite, M., Spite, F., and Bonifacio, P. (2012). The cosmic lithium problem . an observer's perspective. *Memorie della Societa Astronomica Italiana Supplementi* 22, 9.

Spite, M., and Spite, F. (2010). "Li isotopes in metal-poor halo dwarfs: a more and more complicated story,". *Light elements in the universe*. Editors C. Charbonnel, M. Tosi, F. Primas, and C. Chiappini (IAU Symposium), Vol. 268, 201–210. doi:10.1017/S1743921310004138

Spite, M., and Spite, F. (1982b). Lithium abundance at the formation of the Galaxy. *Nature* 297, 483–485. doi:10.1038/297483a0

Stahler, S. W. (1988). Deuterium and the stellar birthline. *ApJ* 332, 804. doi:10.1086/166694

Stahler, S. W., Shu, F. H., and Taam, R. E. (1980a). The evolution of protostars. I - global formulation and results. *ApJ* 241, 637–654. doi:10.1086/158377

Stahler, S. W., Shu, F. H., and Taam, R. E. (1980b). The evolution of protostars. II - the hydrostatic core. *ApJ* 242, 226–241. doi:10.1086/158459

Stahler, S. W., Shu, F. H., and Taam, R. E. (1981). The evolution of protostars. III - the accretion envelope. *ApJ* 248, 727–737. doi:10.1086/159197

Steffen, M., Cayrel, R., Caffau, E., Bonifacio, P., Ludwig, H. G., and Spite, M. (2012). Li detection in metal-poor stars: can 3D model atmospheres solve the second lithium problem?. *Memorie della Societa Astronomica Italiana Supplementi* 22, 152.

Steigman, G., Romano, D., and Tosi, M. (2007). Connecting the primordial and Galactic deuterium abundances. *MNRAS* 378, 576–580. doi:10.1111/j.1365-2966.2007.11780.x

Swenson, F. J. (1995). Lithium in halo dwarfs: the undoing of diffusion by mass loss. *ApJ* 438, L87–L90. doi:10.1086/187722

Talon, S., and Charbonnel, C. (2010). "Light elements as diagnostics on the structure and evolution of low-mass stars,". *IAU symposium*. Editors C. Charbonnel, M. Tosi, and F. Primas (& C. ChiappiniIAU Symposium), Vol. 268, 365–374. doi:10.1017/S1743921310004485

Talon, S. (2008). Mixing processes in rotating stars. *Mem. Soc. Astron. Italiana* 79, 569.

Tan, K. F., Shi, J. R., and Zhao, G. (2009). Beryllium abundances in metal-poor stars. *MNRAS* 392, 205–215. doi:10.1111/j.1365-2966.2008.14027.x

Tognelli, E., Degl'Innocenti, S., and Prada Moroni, P. G. (2012). Li surface abundance in pre-main sequence stars. Testing theory against clusters and binary systems. *A&A* 548, A41. doi:10.1051/0004-6361/201219111

Tognelli, E., Lamia, L., Pizzone, R. G., Degl'Innocenti, S., Prada Moroni, P. G., Romano, S., et al. (2019). Stellar surface abundance of light elements and updated (p,α) reaction rates. *Nuclei in the cosmos XV*, 219, 449–452. doi:10.1007/978-3-030-13876-987

Tognelli, E., Prada Moroni, P. G., and Degl'Innocenti, S. (2015). Cumulative theoretical uncertainties in lithium depletion boundary age. *MNRAS* 449, 3741–3754. doi:10.1093/mnras/stv577

Tgnelli, E., Prada Moroni, P. G., Degl'Innocenti, S., Salaris, M., and Cassisi, S. (2020). Protostellar accretion in low mass metal poor stars and the cosmological lithium problem. *A&A* 638, A81. doi:10.1051/0004-6361/201936723

Tognelli, E., Prada Moroni, P. G., and Degl'Innocenti, S. (2013). The PISA Pre-Main Sequence accreting models. *Protostars and planets VI posters*.

Tognelli, E., Prada Moroni, P. G., and Degl'Innocenti, S. (2011). The Pisa pre-main sequence tracks and isochrones. A database covering a wide range of Z, Y, mass, and age values. *A&A* 533, A109. doi:10.1051/0004-6361/200913913

Tognelli, E., Prada Moroni, P. G., and Degl'Innocenti, S. (2018). Theoretical uncertainties on the radius of low- and very-low-mass stars. *MNRAS* 476, 27–42. doi:10.1093/mnras/sty195

Tognelli, E. (2013). *The Pisa pre-main sequence stellar evolutionary models: results for non-accreting and accreting models*. Pisa, Italy: PhD dissertation, University of Pisa. Available at:https://etd.adm.unipi.it/t/etd-05312013-140950/.

Tomida, K., Tomisaka, K., Matsumoto, T., Hori, Y., Okuzumi, S., Machida, M. N., et al. (2013). Radiation magnetohydrodynamic simulations of protostellar collapse: protostellar core formation. *ApJ* 763, 6. doi:10.1088/0004-637X/763/1/6

Torres, G., and Ribas, I. (2002). Absolute dimensions of the M-type eclipsing binary YY geminorum (Castor C): a challenge to evolutionary models in the lower main sequence. *ApJ* 567, 1140–1165. doi:10.1086/338587

Trampedach, R., Asplund, M., Collet, R., Nordlund, Å., and Stein, R. F. (2013). A grid of three-dimensional stellar atmosphere models of solar metallicity. I. General properties, granulation, and atmospheric expansion. *ApJ* 769, 18. doi:10.1088/0004-637X/769/1/18

Trampedach, R., Christensen-Dalsgaard, J., Asplund, M., Stein, R. F., and Nordlund, Å. (2015). The surface of stellar models - now with more 3D simulations!. *European physical journal web of conferences*, 101. European Physical Journal Web of Conferences, 06064. doi:10.1051/epjconf/201510106064

Trampedach, R., Stein, R. F., Christensen-Dalsgaard, J., Nordlund, Å., and Asplund, M. (2014). Improvements to stellar structure models, based on a grid of 3D convection simulations - I. T(τ) relations. *MNRAS* 442, 805–820. doi:10.1093/mnras/stu889

Tremblay, P. E., Ludwig, H. G., Freytag, B., Steffen, M., and Caffau, E. (2013). Granulation properties of giants, dwarfs, and white dwarfs from the CIFIST 3D model atmosphere grid. *A&A* 557, A7. doi:10.1051/0004-6361/201321878

Tumino, A., Spartà, R., Spitaleri, C., Mukhamedzhanov, A. M., Typel, S., Pizzone, R. G., et al. (2014). New determination of the H(d,p)H and H(d, n)He reaction rates at astrophysical energies. *ApJ* 785, 96. doi:10.1088/0004-637X/785/2/96

Tumino, A., Spitaleri, C., La Cognata, M., Cherubini, S., Guardo, G. L., Gulino, M., et al. (2018). An increase in the C + C fusion rate from resonances at astrophysical energies. *Nature* 557, 687–690. doi:10.1038/s41586-018-0149-4

Tumino, A., Spitaleri, C., Mukhamedzhanov, A. M., Typel, S., Aliotta, M., Burjan, V., et al. (2011). Low-energy d+d fusion reactions via the Trojan Horse Method. *Phys. Lett. B* 700, 111–115. doi:10.1016/j.physletb.2011.05.001

Vauclair, S., and Charbonnel, C. (1995). Influence of a stellar wind on the lithium depletion in halo stars: a new step towards the lithium primordial abundance. *A&A* 295, 715.

Vaytet, N., Chabrier, G., Audit, E., Commerçon, B., Masson, J., Ferguson, J., et al. (2013). Simulations of protostellar collapse using multigroup radiation hydrodynamics. II. The second collapse. *A&A* 557, A90. doi:10.1051/0004-6361/201321423

Ventura, P., Zeppieri, A., Mazzitelli, I., and D'Antona, F. (1998). Pre-main sequence Lithium burning: the quest for a new structural parameter. *A&A* 331, 1011–1021.

Vorobyov, E. I., and Basu, S. (2010). The burst mode of accretion and disk fragmentation in the early embedded stages of star formation. *ApJ* 719, 1896–1911. doi:10.1088/0004-637X/719/2/1896

Wang, E. X., Nordlander, T., Asplund, M., Amarsi, A. M., Lind, K., and Zhou, Y. (2021). 3D NLTE spectral line formation of lithium in late-type stars. *MNRAS* 500, 2159–2176. doi:10.1093/mnras/staa3381

Watson, A. M., Stapelfeldt, K. R., Wood, K., and Ménard, F. (2007). "Multiwavelength imaging of young stellar object disks: toward an understanding of disk structure and dust evolution," in *Protostars and planets VI*. Editors B. Reipurth, D. Jewitt, and K. Keil, 523.

Xiong, D.-R., and Deng, L.-C. (2006). A re-examination of the dispersion of lithium abundance of Pleiades member stars. *ChA&A* 30, 24–40. doi:10.1016/j.chinastron.2006.01.003

Xiong, D. R., and Deng, L. (2002). The extent of the solar overshooting zone deduced from Li abundance. *MNRAS* 336, 511–519. doi:10.1046/j.1365-8711.2002.05767.x

Xu, Y., Takahashi, K., Goriely, S., Arnould, M., Ohta, M., and Utsunomiya, H. (2013). Nacre II: an update of the NACRE compilation of charged-particle-induced thermonuclear reaction rates for nuclei with mass number A<16. *Nucl. Phys.* A 918, 61–169. doi:10.1016/j.nuclphysa.2013.09.007

Conflict of Interest: The authors declare that the research was conducted in the absence of any commercial or financial relationships that could be construed as a potential conflict of interest.

The reviewer OS declared a past co-authorship with one of the authors RP to the handling editor.

Advantages of publishing in Frontiers

OPEN ACCESS
Articles are free to read for greatest visibility and readership

FAST PUBLICATION
Around 90 days from submission to decision

HIGH QUALITY PEER-REVIEW
Rigorous, collaborative, and constructive peer-review

TRANSPARENT PEER-REVIEW
Editors and reviewers acknowledged by name on published articles

Frontiers
Avenue du Tribunal-Fédéral 34
1005 Lausanne | Switzerland

Visit us: www.frontiersin.org
Contact us: frontiersin.org/about/contact

REPRODUCIBILITY OF RESEARCH
Support open data and methods to enhance research reproducibility

DIGITAL PUBLISHING
Articles designed for optimal readership across devices

FOLLOW US
@frontiersin

IMPACT METRICS
Advanced article metrics track visibility across digital media

EXTENSIVE PROMOTION
Marketing and promotion of impactful research

LOOP RESEARCH NETWORK
Our network increases your article's readership